

# Advanced VLBI Imaging

INAUGURAL-DISSERTATION

zur Erlangung des Doktorgrades der  
Mathematisch-Naturwissenschaftlichen Fakultät der  
Universität zu Köln



vorgelegt von

**Hendrik Müller**

aus Göttingen, Deutschland

Köln, 2023

Berichterstatter:

Prof. Dr. J. Anton Zensus

Prof. Dr. Jean-Luc Starck

Prof. Dr. Andreas Eckart

Beginn Promotionsphase:

01.09.2020

Dissertation abgegeben:

28.04.2023

Disputation:

18.07.2023

Dissertation angenommen von der Mathematisch-Naturwissenschaftlichen Fakultät  
der Universität zu Köln:

18.07.2023

# Erklärung

Hiermit versichere ich an Eides statt, dass ich die vorliegende Dissertation selbstständig und ohne die Benutzung anderer als der angegebenen Hilfsmittel und Literatur angefertigt habe. Alle Stellen, die wörtlich oder sinngemäß aus veröffentlichten und nicht veröffentlichten Werken dem Wortlaut oder dem Sinn nach entnommen wurden, sind als solche kenntlich gemacht. Ich versichere an Eides statt, dass diese Dissertation noch keiner anderen Fakultät oder Universität zur Prüfung vorgelegen hat; dass sie - abgesehen von unten angegebenen Teilpublikationen und eingebundenen Artikeln und Manuskripten - noch nicht veröffentlicht worden ist sowie, dass ich eine Veröffentlichung der Dissertation vor Abschluss der Promotion nicht ohne Genehmigung des Promotionsausschusses vornehmen werde. Die Bestimmungen dieser Ordnung sind mir bekannt. Darüber hinaus erkläre ich hiermit, dass ich die Ordnung zur Sicherung guter wissenschaftlicher Praxis und zum Umgang mit wissenschaftlichem Fehlverhalten der Universität zu Köln gelesen und sie bei der Durchführung der Dissertation zugrundeliegenden Arbeiten und der schriftlich verfassten Dissertation beachtet habe und verpflichte mich hiermit, die dort genannten Vorgaben bei allen wissenschaftlichen Tätigkeiten zu beachten und umzusetzen. Ich versichere, dass die eingereichte elektronische Fassung der eingereichten Druckfassung vollständig entspricht.

Köln, den 28.04.2023

A handwritten signature in black ink, appearing to read 'Heath Nite', written on a light-colored rectangular background.

sign here

---

## Zur Doktorarbeit relevante Teilpublikationen, Stand 26.07.2023<sup>1</sup>

**Müller, H.**; Behrens, C. and Marsh, D.J.E.: *An optimized Ly  $\alpha$  forest inversion tool based on a quantitative comparison of existing reconstruction methods*, 2020, MNRAS, 497, 4937-4955, part of the work has been done for the Master's thesis

**Müller, H.**; Behrens, C. and Marsh, D.J.E.: *A novel estimator for the equation of state of the IGM by Ly $\alpha$  forest tomography*, 2021, MNRAS, 503, 6202-6222, part of the work has been done for the Master's thesis

**Müller, H.** and Lobanov, A.P.: *DoG-HiT: A novel VLBI Multiscale Imaging Approach*, 2022, A&A, 666, A137

Hamaide, L.; **Müller, H.** and Marsh, D.J.E.: *Searching for Dilaton Fields in the Ly $\alpha$  forest*, 2022, Phy. Rev. D, 106, 123509, **(shared first authorship)**

**Müller, H.** and Lobanov, A.P.: *Multi-scale and multi-directional VLBI imaging with CLEAN*, 2023, A&A, 672, A26

**Müller, H.** and Lobanov, A.P.: *Dynamic and polarimetric VLBI imaging with a multiscale approach*, 2023, A&A, 673, A151

**Müller, H.** and Lobanov, A.P.: *Multiscale VLBI Imaging*, 2023, Proceedings of the 15th European VLBI Network Mini-Symposium and Users' Meeting, DOI: <https://doi.org/10.22323/1.428.0056>, partially reproduced in the chapters 2.4.3, 3.5 and 3.7

Roelofs, F.; Blackburn, L.; Lindahl, G.; Doeleman, S. S.; Johnson, Michael D.; Arras, P.; Chatterjee, K.; Emami, R.; Fromm, C.; Fuentes, A.; Knollmüller, J.; Kosogorov, N.; **Müller, H.**; Patel, N.; Raymond, A.; Tiede, P.; Traianou, T.; Vega, J.: *The ngEHT Analysis Challenges*, 2023, Galaxies, 11, 1

Chatterjee, K.; Chael, A.; Tiede, P.; Mizuno, Y.; Emami, R.; Fromm, C.; Ricarte, A.; Blackburn, L.; Roelofs, F.; Johnson, M. D.; Doeleman, S. S.; Arras, P.; Fuentes, A.; Knollmüller, J.; Kosogorov, N.; Lindahl, G.; **Müller, H.**; Patel, N.; Raymond, A.; Traiano, T.; Vega, J.: *Comparing accretion flow morphology in*

---

<sup>1</sup>Siehe Lebenslauf am Ende für eine umfassende Liste.

---

*numerical simulations of black holes from the ngEHT Model Library: the impact of radiation physics*, 2023, *Galaxies*, 11, 2

Kim, J.Y.; Savolainen, T.; Voitsik, P.; Kravchenko, E.V.; Lisakov, M.M.; Kovalev, Y.Y.; **Müller, H.**; Lobanov, A.; Sokolovsky, K.; Bruni, G.; Edwards, P.G.; Reynolds, C.; Bach, U.; Gurvits, L.I.; Krichbaum, T.; Hada, K.; Giroletti, M.; Orienti, M.; Anderson, J.M.; Lee, S.-S.; Sohn, B.-W. and Zensus, A.: *RadioAstron Space-VLBI Imaging of the jet in M87: I. Detection of high brightness temperature at 22 GHz*, 2023, *ApJ*, 952, 1

**Müller, H.**, Mus, A. and Lobanov, A.: *Using multiobjective optimization to reconstruct interferometric data. Part I*, 2023, *A&A*, 675, A60 (**shared first authorship**)

# Abstract

Very Long Baseline Interferometry (VLBI) is an observational technique developed in astronomy for combining multiple radio telescopes into a single virtual instrument with an effective aperture reaching up to many thousand kilometers and enabling measurements at highest angular resolutions. The celebrated examples of applying VLBI to astrophysical studies include detailed, high-resolution images of the innermost parts of relativistic outflows (jets) in active galactic nuclei (AGN) and recent pioneering observations of the ‘shadows’ of supermassive black holes (SMBH) in the center of our Galaxy and in the galaxy M87.

Despite these and many other proven successes of VLBI, analysis and imaging of VLBI data still remain difficult, owing in part to the fact that VLBI imaging inherently constitutes an ill-posed inverse problem. Historically, this problem has been addressed in radio interferometry by the CLEAN algorithm, a matching-pursuit inverse modeling method developed in the early 1970-s and since then established as a de-facto standard approach for imaging VLBI data.

In recent years, the constantly increasing demand for improving quality and fidelity of interferometric image reconstruction has resulted in several attempts to employ new approaches, such as forward modeling and Bayesian estimation, for application to VLBI imaging.

While the current state-of-the-art forward modeling and Bayesian techniques may outperform CLEAN in terms of accuracy, resolution, robustness, and adaptability, they also tend to require more complex structure and longer computation times, and rely on extensive finetuning of a larger number of non-trivial hyperparameters. This leaves an ample room for further searches for potentially more effective imaging approaches and provides the main motivation for this dissertation and its particular focusing on the need to unify algorithmic frameworks and to study VLBI imaging from the perspective of inverse problems in general.

In pursuit of this goal, and based on an extensive qualitative comparison of the existing methods, this dissertation comprises the development, testing, and first implementations of two novel concepts for improved interferometric image reconstruction. The concepts combine the known benefits of current forward modeling techniques, develop more automatic and less supervised algorithms for image reconstruction, and realize them within two different frameworks.

The first framework unites multiscale imaging algorithms in the spirit of compressive sensing with a dictionary adapted to the uv-coverage and its defects (DoG-HiT, DoB-CLEAN). We extend this approach to dynamical imaging and polarimetric imaging. The core components of this framework are realized in a multidisciplinary and multipurpose software *MrBeam*, developed as part of this

---

dissertation.

The second framework employs a multiobjective genetic evolutionary algorithm (MOEA/D) for the purpose of achieving fully unsupervised image reconstruction and hyperparameter optimization.

These new methods are shown to outperform the existing methods in various metrics such as angular resolution, structural sensitivity, and degree of supervision. We demonstrate the great potential of these new techniques with selected applications to frontline VLBI observations of AGN jets and SMBH.

In addition to improving the quality and robustness of image reconstruction, DoG-HiT, DoB-CLEAN and MOEA/D also provide such novel capabilities as dynamic reconstruction of polarimetric images on minute time-scales, or near-real time and unsupervised data analysis (useful in particular for application to large imaging surveys).

The techniques and software developed in this dissertation are of interest for a wider range of inverse problems as well. This includes such versatile fields such as Ly $\alpha$  tomography (where we improve estimates of the thermal state of the intergalactic medium), the cosmographic search for dark matter (where we improve forecasted bounds on ultralight dilatons), medical imaging, and solar spectroscopy.

The structure of this dissertation is as follows. We present in chapter 1 the background theory to radio astronomy, active galaxies and VLBI in general. Chapter 2 presents a detailed discussion of existing imaging algorithms, their respective advantages and disadvantages. In particular, we discuss the limitations of CLEAN, e.g. a suboptimal representation of extended emission, missing regularization, a disparity between the model and the image, and limited resolution. In order to uniform imaging techniques and software, we demonstrate a deep connection of the several imaging techniques in the spirit of inverse problems and (convex) optimization. We discuss in chapter 3 our newly proposed multi-scale imaging algorithms DoG-HiT and DoB-CLEAN in detail. In chapter 4 we present the details behind MOEA/D. DoG-HiT, DoB-CLEAN and MOEA/D are currently in application in a wide range of ongoing VLBI projects. We present a small exemplary excerpt of these applications to synthetic data and observational data in chapter 5. Furthermore, we summarize the transfer and connection to alternative, closely connected (astrophysical) inverse problems such as cosmography or solar observations. Finally, we present our conclusions in chapter 6 and discuss future developments in chapter 7.

# Zusammenfassung

Very Long Baseline Interferometry (VLBI) ist eine Beobachtungstechnik, die in der Radioastronomie entwickelt wurde. Mehrere Radioteleskope werden zu einem einzelnen, virtuellen Instrument mit einer effektiven Apertur von bis zu tausenden Kilometern kombiniert. Dies ermöglicht Beobachtungen bei höchster Winkelauflösung. Bekannte Anwendungsbeispiele von VLBI in astrophysikalischen Studien sind die detaillierten und hoch-auflösenden Bilder der innersten Jets in aktiven Galaxienkernen (AGN), und kürzliche, wegweisende Beobachtungen des "Schattens" supermassereicher schwarzer Löcher (SMBH) im Zentrum unserer Galaxie und in der Galaxie M87.

Trotz dieser und vieler anderer Erfolge von VLBI bleibt die Analyse von VLBI Daten schwierig, teilweise weil VLBI-Bildgebung ein schlecht-gestelltes inverses Problem darstellt. Historisch wurde dieses Problem in der Radiointerferometrie mit dem CLEAN-Algorithmus gelöst. CLEAN ist eine matching-pursuit Modellierungsmethode, die in den früheren 1970er entwickelt wurde, und ist seitdem der de-facto Standard-Ansatz in VLBI.

In den vergangenen Jahren haben die konstant ansteigenden Anforderungen an die Bildqualität und Genauigkeit interferometrischer Bildgebung in verschiedenen neuen Ansätzen resultiert, wie forward-modeling und Bayesianische Techniken.

Während die aktuellen forward-modeling und Bayesianischen Methoden CLEAN hinsichtlich Genauigkeit, Auflösung, Robustheit und Adaptierbarkeit verbessern, sind sie typischerweise komplizierter, benötigen länger für die Berechnung, und basieren auf der Feineinstellung einer Zahl nicht-trivialer Hyperparameter. Dies lässt Raum für die weitere Suche nach potentiell effektiveren Bildgebungsverfahren und stellt die Motivation für diese Doktorarbeit und die Fokussierung auf die Notwendigkeit algorithmische Herangehensweise aus der Perspektive inverser Probleme zu vereinheitlichen dar.

Um dieses Ziel zu erreichen, und basierend auf einem ausgedehnten qualitativen Vergleich existierender Methoden, stellt diese Doktorarbeit die Entwicklung, das Testen, und erste Anwendungen zweier neuer Konzepte für eine verbesserte Bildrekonstruktion vor. Dafür werden die bekannten Vorteile aktueller forward-modeling Techniken kombiniert, und automatisiertere und weniger überwachte Algorithmen für die Rekonstruktion entwickelt. Dies wird in zwei verschiedenen grundlegenden Strukturen realisiert.

Erstens entwickeln wir multiskalare Bildgebungsverfahren mit Basisfunktionen die datengestützt zum uv-coverage gefittet werden (DoG-HiT, DoB-CLEAN) und entwickeln diesen Ansatz weiter zur Bildgebung dynamischer Quellen und

---

zu Polarimetrie. Die Kern-komponente dieser Algorithmen sind in der interdisziplinären und multifunktionalen Software *MrBeam* implementiert.

Zweitens präsentieren wir einen genetischen, evolutionären Mehrzieloptimierungs-Algorithmus (MOEA/D) um automatisierte Bildrekonstruktionen und Hyperparameter-Optimierungen zu ermöglichen.

Diese neue Methoden verbessern existierende Methoden hinsichtlich verschiedener Metriken wie der Winkelauflösung, strukturellen Sensitivität und des Grades der Automatisierung. Wir demonstrieren das große Potenzial dieser neuen Techniken mit ausgewählten Anwendungen zu führenden VLBI Beobachtungen von AGN Jets und SMBH.

Zusätzlich zu der Verbesserung der Qualität und Robustheit der Rekonstruktion, bieten DoG-HiT, DoB-CLEAN und MOEA/D bisher nicht verfügbare Fähigkeiten wie die dynamische Rekonstruktion polarimetrischer Filme auf Zeitskalen von Minuten und die automatisierte Bildgebung in nahezu Echtzeit (insbesondere geeignet für systematische, häufige Beobachtungen).

Weiterhin sind die Techniken und die Software die für diese Dissertation entwickelt wurden von Interesse für ein größeres Gebiet inverser Probleme. Dies beinhaltet so verschiedene Felder wie Ly $\alpha$ -forest Tomographie (in welchem wir aktuelle Messungen des thermischen Zustandes des intergalaktischen Mediums verbessern), die kosmographische Suche nach dunkler Materie (in welcher wir Vorhersagen zu ultraleichten Dilatonen verfeinern), medizinische Bildgebung und solare Spektroskopie.

Die Struktur dieser Dissertation ist wie folgt. Wir präsentieren in Kapitel 1 die notwendige Theorie zu Radioastronomie, aktiven Galaxien und VLBI im Allgemeinen. Kapitel 2 beinhaltet eine detaillierte Diskussion aktueller Bildgebungsverfahren und ihrer Vor- und Nachteile. Insbesondere diskutieren wir die Limitierungen von CLEAN, beispielsweise eine suboptimale Repräsentation ausgebreiteter Emission, fehlende Regularisierung, die Ungleichheit zwischen dem Modell und dem finalen Bild, und die limitierte Auflösung. Um Bildgebungsverfahren und Software zu vereinheitlichen, zeigen wir eine tiefere Verbindung zwischen den verschiedenen Methoden auf im Rahmen inverser Probleme und (konvexer) Optimierung. Wir diskutieren in Kapitel 3 die neuen multiskalaren Algorithmen DoG-HiT und DoB-CLEAN im Detail. In Kapitel 4 präsentieren wir die Details von MOEA/D. DoG-HiT, DoB-CLEAN und MOEA/D werden momentan für eine große Zahl laufender VLBI Projekte angewendet. Wir präsentieren einen kurzen, beispielhaften Auszug dieser Anwendungen auf synthetische Daten und beobachtete Daten in Kapitel 5. Weiterhin fassen wir den Wissenstransfer zu alternativen, nahe verwandten (astrophysikalischen) inversen Problemem wie Kosmographie oder Sonnenbeobachtungen zusammen. Letztendlich, präsentieren

---

wir unsere Schlußfolgerungen in Kapitel 6 und diskutieren zukünftige Entwicklungen in Kapitel 7.

# Contents

<b>1</b>	<b>Introduction</b>	<b>1</b>
1.1	Radio Astronomy . . . . .	1
1.2	Brief History of Radio Astronomy . . . . .	3
1.3	Active Galactic Nuclei (AGN) . . . . .	3
1.4	Very Long Baseline Interferometry (VLBI) . . . . .	10
1.4.1	Radio Telescopes . . . . .	11
1.4.2	Basic Principles of Interferometry . . . . .	12
1.4.3	Very Long Baseline Interferometry . . . . .	16
1.4.4	Overview of VLBI Data Processing . . . . .	17
1.4.5	Corruption Effects . . . . .	22
<b>2</b>	<b>Imaging</b>	<b>26</b>
2.1	Scope of VLBI Imaging . . . . .	26
2.2	Inverse Problems . . . . .	27
2.2.1	General Introduction . . . . .	27
2.2.2	Regularization Theory . . . . .	29
2.2.3	Convex Optimization . . . . .	30
2.3	VLBI Data Products . . . . .	32
2.3.1	Visibilities . . . . .	32
2.3.2	Closure Quantities . . . . .	34
2.3.3	Polarimetry . . . . .	36
2.3.4	Extended Imaging Problems . . . . .	39
2.4	Imaging with CLEAN Deconvolution . . . . .	39
2.4.1	Algorithm . . . . .	39
2.4.2	Convergence . . . . .	42
2.4.3	Limitations of CLEAN . . . . .	43
2.4.4	Multiscale-CLEAN . . . . .	46
2.5	Self-calibration . . . . .	47
2.6	Forward Modeling . . . . .	48
2.6.1	MEM . . . . .	48
2.6.2	RML . . . . .	50
2.6.3	Bayesian Imaging . . . . .	52
2.6.4	Compressive Sensing . . . . .	55
2.6.5	Deep Learning . . . . .	57
2.7	Evaluation Metrics . . . . .	58
2.7.1	Accuracy . . . . .	58
2.7.2	Dynamic Range . . . . .	59
2.7.3	Resolution . . . . .	60

2.7.4	Supervision . . . . .	63
2.7.5	Robustness and Adaptability . . . . .	64
2.7.6	Numerical Performance . . . . .	65
2.8	Motivation for New Algorithms . . . . .	66
<b>3</b>	<b>Multiscale VLBI Imaging</b>	<b>68</b>
3.1	Rationale . . . . .	68
3.2	Paper 1: Müller & Lobanov 2022, A&A, 666, A137 . . . . .	70
3.3	Paper 2: Müller & Lobanov 2023a, A&A, 672, A26 . . . . .	91
3.4	Paper 3: Müller & Lobanov 2023b, A&A, 673, A151 . . . . .	116
3.5	Imaging Pipeline . . . . .	135
3.6	Software . . . . .	137
3.7	Conclusions . . . . .	139
<b>4</b>	<b>Evolutionary Imaging</b>	<b>141</b>
4.1	Paper 4: Müller, Mus, Lobanov 2023d, A&A, 675, A60 . . . . .	142
<b>5</b>	<b>Applications</b>	<b>156</b>
5.1	ngEHT Analysis Challenges . . . . .	157
5.1.1	Analysis Challenge 1+2 . . . . .	158
5.1.2	Analysis Challenge 3 . . . . .	162
5.2	EHT Projects . . . . .	166
5.2.1	2017 M87 . . . . .	166
5.2.2	Centaurus A . . . . .	172
5.2.3	3C279 . . . . .	173
5.3	AGN projects . . . . .	174
5.3.1	Parallel Cluster Computing Pipeline . . . . .	174
5.3.2	GMVA Data on 3C279 . . . . .	178
5.3.3	M87 RadioAstron . . . . .	181
5.4	Synergies . . . . .	185
5.4.1	Ly- $\alpha$ Tomography . . . . .	185
5.4.2	Ultralight Dark Matter . . . . .	194
5.4.3	Magnetic Resonance Tomography . . . . .	199
5.4.4	Solar Spectrometry . . . . .	201
<b>6</b>	<b>Conclusions</b>	<b>205</b>
<b>7</b>	<b>Outlook</b>	<b>209</b>
	<b>References</b>	<b>214</b>

## List of Figures

1.1	Sketch of the opacity of the atmosphere as a function of frequency. The image was taken from the ESO public outreach materials: <a href="https://www.eso.org/public/germany/images/atm_opacity/">https://www.eso.org/public/germany/images/atm_opacity/</a> at 23.12.2022. . . . .	2
1.2	The radio galaxy Cygnus A observed with the Very Large Array (VLA). Image was taken from <a href="http://www.aoc.nrao.edu/~ccarilli/cyga.shtml">http://www.aoc.nrao.edu/~ccarilli/cyga.shtml</a> at 02.01.2023. For details, see Carilli & Barthel (1996). . . . .	4
1.3	Illustration of the unified model of AGNs. Image from Urry & Padovani (1995). . . . .	6
1.4	Different scales of the M87 jet. Adapted from Blandford et al. (2019) under license agreement 1307729-1 with Copyright Clearance Center Inc. (CCC). Panel a: VLA observation of the core jet at 90 cm. Panel b: VLA observation of the galaxy jet at 20 cm. Panel c: VLBA observations of the black hole jet at 20 cm (Cheung et al. 2007). Panel d: VLBA observations of the innermost jet at 7 mm (Walker et al. 2018). Panel e: GMVA observations of the innermost jet at 3 mm (Kim et al. 2018). Panel f: EHT observations of the black hole shadow at 1.3 mm (Event Horizon Telescope Collaboration et al. 2019b). . . . .	8
1.5	Collimation profile of M87 as transverse radius vs function of distance to core. Image adapted from Blandford et al. (2019) under license agreement 1307729-1 with Copyright Clearance Center Inc. (CCC). . . . .	9
1.6	Blazar model proposed by A. Marscher. Image taken from Park & Algaba (2022) by CC BY.4.0. Image copyright: A. Marsher. . . . .	10
1.7	Sketch of the light and signal path in a radio telescope, taken from Encyclopedia Britannica <a href="https://cdn.britannica.com/34/4634-050-DA53D88D/Radio-telescope-system.jpg">https://cdn.britannica.com/34/4634-050-DA53D88D/Radio-telescope-system.jpg</a> at 23.12.2022. . . . .	12
1.8	Coordinate system used to express an on-sky distribution (direction cosines $l, m$ ) and baselines ( $u, v, w$ expressed in units of wavelengths). The figure is taken from Thompson et al. (2017), Fig. 3.2. by CC BY 4.0. . . . .	13
1.9	Relation between functions involved in imaging a source, adapted after Thompson et al. (2017), Fig. 5.5. . . . .	16

1.10	Panel a: Synthetic uv-coverage of the Karl G. Jansky Very Large Array (VLA) taken from the CASA documentation: <a href="https://casaguides.nrao.edu/index.php/VLA-CASA-Imaging-CASA5.5.0">https://casaguides.nrao.edu/index.php/VLA-CASA-Imaging-CASA5.5.0</a> at 23.12.2022. One can clearly see the elliptical tracks of the uv-coverage and the significant gaps between several tracks and towards the center., Panel b: uv-coverage of the 2017 EHT campaign of M87 (Fig. 2 Event Horizon Telescope Collaboration et al. 2019b). . . . .	17
1.11	Sketch of heterodyne receiver system. . . . .	18
1.12	Schematic illustration of a radio interferometer, taken from Thompson et al. (2017), Fig. 6.2. by CC BY 4.0. . . . .	20
1.13	Flowchart of the calibration after correlation. Figure taken from Janssen et al. (2022), Fig.2 by CC BY 4.0. . . . .	21
1.14	Upper panels: Dirty beam and uv-coverage for an array without gaps, i.e. a single spherical Bessel functions in the upper right panel. Bottom panel: uv-coverage and dirty beam as superposition of Bessel functions of different scales for an uv-coverage with radially symmetric gaps. . . . .	24
2.15	Overview of inverse modeling imaging methods (i.e. variants of CLEAN) that have been applied to VLBI. We spare here CLEAN methods that have been proposed for non-VLBI applications such as wide-field imaging. . . . .	40
2.16	Illustration of the CLEAN algorithm. We reformulate the problem as a deconvolution problem. The dirty map is the convolution of the dirty beam with the true image. In every iteration we search for the maximal peak in the residual and subtract the rescaled and shifted dirty beam from the dirty beam. Finally we convolve the list of all these CLEAN image with the clean map and add the last residual. . . . .	41

2.17	Illustration of the disparity issue related to CLEAN with synthetic EVN data. Upper left panel: The ground truth image. Bottom left panel: The uv-coverage. Upper middle panel: The model computed by CLEAN. The model is a set of CLEAN components. Bottom middle panel: The recovered visibilities from the CLEAN model. The model fits the observed visibility points (red points) well. However, the model does not interpolate reasonably in the gaps of the uv-coverage. Top right panel: The clean image, i.e. the clean beam convolved with the model. This image approximates the true image reasonable well. Bottom right panel: However, the predicted visibilities of the convolved image do not match the observations anymore. . . . .	44
2.18	Overview of recent forward modeling techniques and the respective software tools. . . . .	49
3.19	Multiscale Decomposition of the jet in M87. Images are adapted from Mertens et al. (2016). . . . .	70
3.20	Synthetic uv-coverage of an EHT observation. The radial distribution of visibility points has significant radial gaps (blue shaded). . . . .	70
3.21	Schematic illustration of the multiround pipeline adapted for DoG-HiT. . . . .	135
5.22	Overview over the synthetic Sgr A* models used for the second ngEHT analysis challenge. Image is reprinted from Roelofs et al. (2023) by CC BY 4.0. . . . .	160
5.23	Submissions for the second ngEHT challenge at 230 GHz for the RIAFSPOT model. Image is reprinted from Roelofs et al. (2023) by CC BY 4.0. . . . .	161
5.24	Submissions for the second ngEHT challenge at 230 GHz for the GRMHD model. Image is reprinted from Roelofs et al. (2023) by CC BY 4.0. . . . .	162
5.25	Exemption of the linearly polarized ground truth movie that was used for the third ngEHT Analysis challenge. . . . .	163
5.26	Reconstruction result with DoG-HiT for the third ngEHT Analysis challenge. The ground truth image is shown in Fig. 5.25. Synthetic observations were performed with a possible ngEHT configuration at 230 GHz. . . . .	163
5.27	Single frame comparison at $UT = [11.3, 11.5, 11.7]$ from the ground truth movie (left panels, Fig. 5.25) and the recovered frame (right panels, Fig. 5.26). . . . .	164

5.28	Reconstruction result of the GRMHD ground truth image for the third ngEHT Analysis challenge with DoG-HiT. Synthetic observations were performed with a possible ngEHT configuration at 230 GHz. . . . .	165
5.29	First ever image of a black hole shadow (Event Horizon Telescope Collaboration et al. 2019a). The image was taken from <a href="https://www.eso.org/public/germany/images/eso1907a/">https://www.eso.org/public/germany/images/eso1907a/</a> at 05.01.2023.	167
5.30	DoG-HiT reconstructions of single days of 2017 EHT observation of M87. Upper panels: High band (229 GHz). Lower panels: Low band (227 GHz). . . . .	168
5.31	Average DoG-HiT reconstruction of 2017 EHT observations of M87, i.e. the average of all reconstructions presented in Fig. 5.30.	168
5.32	MOEA/D reconstructions of M87 (Müller et al. 2023d) observed with the EHT in 2017. We show all clusters of non-dominated solutions for all four days. . . . .	169
5.33	Average DoG-HiT reconstruction of 2017 EHT observations of M87 (only high bands), averaged over all four days highlighting the extended emission component. . . . .	170
5.34	Fig. 1 of Broderick et al. (2022b). The figure shows the extended emission recovered by THEMIS as contour levels. The right panels compare the event horizon scale reconstructions with the extended jet observed with the GMVA (Kim et al. 2018). The white line indicates the edge-brightened jet opening. The extended emission towards the south-west of the ring is correlated with the jet observed at smaller frequencies. Figure is reprinted by CC.BY. 4.0. .	171
5.35	Cen A observed with the EHT. Image credit: Janssen et al. (2021). The image is taken from <a href="https://www.mpg.de/17216488/eht-centaurus-a-jet">https://www.mpg.de/17216488/eht-centaurus-a-jet</a> at 13.01.2023. . . . .	172
5.36	DoG-HiT reconstruction of Cen A. . . . .	173
5.37	DoG-HiT reconstruction of 3C279 observed with the EHT in 2017.	174
5.38	DoB-CLEAN reconstruction of BL Lac at highest angular resolution from Müller & Lobanov (2023a). The high-resolution reconstruction shows a possible edge-brightening that was not visible with CLEAN. . . . .	176
5.39	MOJAVE observations of 3C120 with data analyzed with CLEAN by the MOJAVE team. The scans are ordered in time starting from the top left (earliest) scan to the bottom right. The images are plotted in logarithmic scale. . . . .	176

5.40	MOJAVE observations of 3C120 analyzed unsupervised by DoG-HiT (blurred with a 0.5 mas beam). The scans are ordered in time. The image series is plotted in logarithmic scale. . . . .	177
5.41	The single epoch observed at 27.10.1996 from the MOJAVE sample of 3C120 analyzed with CLEAN and with DoG-HiT. . . . .	177
5.42	Left panel: uv-coverage of coherently averaged data set (60 s averaging). Right panel: Radplot of self-calibrated data set. . . . .	179
5.43	DoG-HiT reconstruction of central core region of GMVA observations of 3C279 at 14.April 2018. . . . .	179
5.44	Overview of reconstructions of 3C279 at various wavelengths. The figure is taken from Kim et al. (2020) by CC.BY 4.0. . . . .	179
5.45	Average of CLEAN, <i>ehtim</i> and DoG-HiT images guided by DoG-HiT windows. . . . .	180
5.46	Left panel: uv-coverage of RadioAstron observations of M87, Right panel: DoG-HiT reconstruction. . . . .	181
5.47	CLEAN reconstructions of M87. Reprinted from Kim et al. (2023) with permission for reprinting given by J.Y. Kim. . . . .	182
5.48	DoG-HiT reconstructions of M87 RadioAstron observations blurred to the natural beam ( $470 \times 150 \mu\text{as}$ ) and the super-resolved beam ( $200 \times 100 \mu\text{as}$ ). . . . .	182
5.49	DoB-CLEAN reconstruction of M87 with RadioAstron observations with uniform weighting. . . . .	183
5.50	Illustration of the Ly $\alpha$ forest. Light emitted by a distant quasar gets absorbed by the intervening gas, forming the feature of densely packed, narrow absorption lines known as the Ly $\alpha$ forest. Image was taken from <a href="https://news.illinois.edu/view/6367/204679">https://news.illinois.edu/view/6367/204679</a> on 10.01.2023. Graphic design is by John Webb. . . . .	186
5.51	Flowchart of the estimation of the thermal state of the IGM from inverse Ly $\alpha$ tomography. Figure adapted from Müller et al. (2021). 190	
5.52	Overview of estimates of the temperature at mean density as a function of redshift. The presented data sets are from Becker et al. (2011); Boera et al. (2014); Gaikwad et al. (2020); Garzilli et al. (2020); Hiss et al. (2018); Telikova et al. (2019); Walther et al. (2019). Image adapted from Müller et al. (2021). . . . .	191
5.53	Overview of estimations of the polytropic index $\gamma$ . The estimates are from Bolton et al. (2014); Garzilli et al. (2012); Hiss et al. (2018); Rorai et al. (2018). Image adapted from Müller et al. (2021). 192	

5.54	Overview over estimations of the photoionization rate as a function of redshift. The estimates are from Becker et al. (2013); Faucher-Giguère et al. (2008); Telikova et al. (2019). Image adapted from Müller et al. (2021). . . . .	193
5.55	Flowchart of getting constraints on the dilaton coupling in the case of non-detection, adapted from Hamaide et al. (2022). . . . .	197
5.56	Forecasted constraints for the dilaton photon coupling as a functions of the dilaton mass. The forecast shows the prediction for the UVES_SQUAD survey (Murphy et al. 2019) and a possible SKA configuration by a study of the absorption profiles by full inversion of the spectra (Hamaide et al. 2022). The MICROSCOPE results are taken from Bergé et al. (2018). Atomic spectroscopy constraints have been reported in Hees et al. (2016). The Figure is adapted from Hamaide et al. (2022). . . . .	198
5.57	Synthetic reconstruction of STIX observation. The upper left panel shows the ground truth image. The bottom right panel illustrates the uv-coverage. The reconstruction was done semi-blindly by various investigators with standard techniques of the solar spectrometry community such as CLEAN and MEM_GE (Massa et al. 2020). The other panels show reconstructions with VLBI data analysis pipelines such as <i>ehtim</i> (RML) with different weighting combinations, unsupervised by DoG-HiT and DoB-CLEAN, as well as with a Bayesian VLBI method (resolve) and by maximum entropy by constrained minimization (Con_MEM). . . . .	204
7.58	Schematic illustration of the Neural Network Tikhonov (NETT) method. The image structure with artifacts is projected to the artifacts only by an autoencoder. The autoencoder consists of an encoder network, a low-dimensional central layer, and a decoder network that is mirrored to the encoder. The regularizer is extracted from the central layer. Image adapted from ? by CC.BY 3.0. . . . .	213

## List of Tables

1	AGN Classification, adapted from the AGN lecture of W. Kollatschny in the winter semester 2016/2017, University of Göttingen.	5
2	Summary of the inversion techniques tested and acronyms used for Ly $\alpha$ forest tomography. Adapted from Müller et al. (2020). . . . .	189
3	Summary of the findings of Müller et al. (2020). Adapted from Müller et al. (2020). . . . .	189

# 1 Introduction

Since the beginning of astronomy humans used the optically visible part of the spectrum to observe the Universe, first by naked eye, then after the invention of the first telescopes with the help of magnifying optics. The visible light however is only a very narrow band of the complete spectrum and allows only a restricted view on the Universe. With upcoming radar technology in the twentieth century, radio astronomy was born and opened a complete new window to observe the astrophysical phenomena around us. Radio waves peek through dense gaseous environments and cosmic dust, uncovering a structural richness that was hidden to observations in other frequency bands. However, radio observations with single aperture telescopes have a worse resolution due to their long wavelengths. This limitation has been successfully overcome through the development of radio interferometry, and very long baseline interferometry (VLBI) in particular. VLBI combines individual radio telescopes into a virtual instrument with an effective aperture reaching up to many thousand kilometers and allowing to achieve record high angular resolution. In this chapter we introduce the basic concepts of radio astronomy and radio interferometry in particular. This chapter makes explicit use of the textbooks Burke et al. (2019), Thompson et al. (2017) and Snell et al. (2019).

## 1.1 Radio Astronomy

Radio astronomy studies the Universe across an extremely broad part of the electromagnetic spectrum, spanning over five orders of magnitude in wavelength, from submillimeter to decameter regimes. The good atmospheric transparency at cm- and m-wavelength provides the radio astronomy community with rich possibilities for ground based observations (Snell et al. 2019), see also Fig. 1.1. Continuum radio emission is produced in a wide range of astronomical objects and through several fundamental emission processes including free-free radiation, synchrotron radiation and inverse Compton radiation (Burke et al. 2019). Many of the fundamental and most actively studied emission and absorption lines also lie in the radio window, in particular the hyperfine structure line of neutral hydrogen (the HI line), with its rest frame wavelength of  $\sim 21$  cm (Ewen & Purcell 1951; Pritchard & Loeb 2012). Strong redshifting of the emission from objects in the early Universe makes the radio regime extremely relevant for cosmological studies. The prime example of this is the hydrogen ionization line emitted at the time of recombination, today known as the cosmic microwave background (CMB), which peaks at  $\sim 160$  GHz (Planck Collaboration et al. 2020).

The strength of a radio signal is expressed by its spectral flux density in units

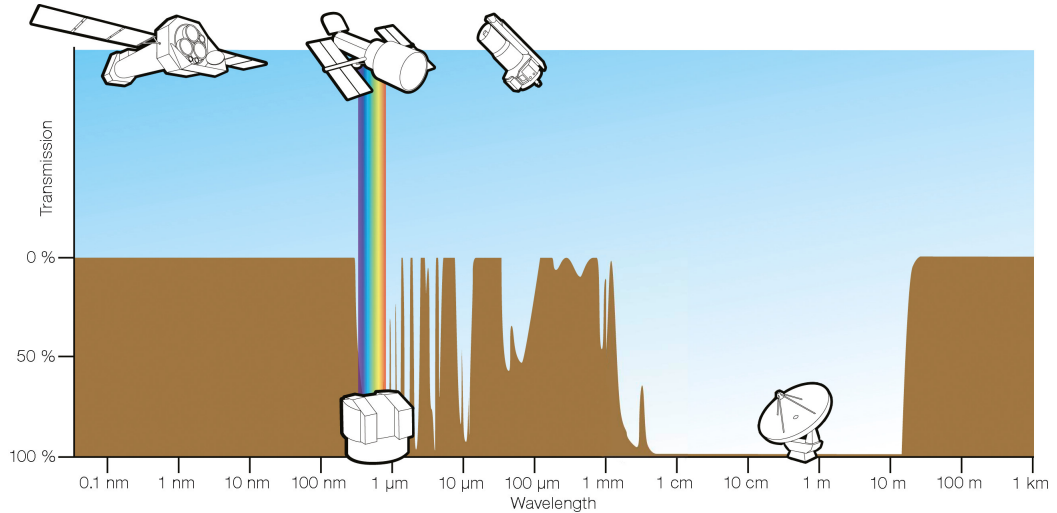


Figure 1.1: Sketch of the opacity of the atmosphere as a function of frequency. The image was taken from the ESO public outreach materials: [https://www.eso.org/public/germany/images/atm\\_opacity/](https://www.eso.org/public/germany/images/atm_opacity/) at 23.12.2022.

of Jansky:  $1 \text{ Jy} = 1 \text{ Wm}^{-2}\text{Hz}^{-1}$ , i.e. the energy flux per unit frequency and area (Thompson et al. 2017). Reflecting the predominant source of noise in radio astronomy, it is common practice to express signal strength and noise levels in terms of temperatures by relating the energy flux density to the temperature of a blackbody emitter with the same spectral flux density. Following this convention, we can classify the extent of typical radio astronomy sources in four categories (list and categorization adapted from Burke et al. 2019):

**Cold Sources** Sources emitting the blackbody radiation, with temperature of up to  $\sim 100 \text{ K}$ , including the cosmic microwave background, atomic hydrogen clouds, molecular clouds and interstellar dust.

**Warm Sources** Objects in which emission is produced by free-free radiation, e.g. in higher temperature plasma. Sources of interest are stellar photospheres, planetary nebulae and stellar winds.

**Hot Sources** Objects which are emitting nonthermal synchrotron radiation with brightness temperatures  $T_B > 10^5 \text{ K}$ , e.g. pulsars, supernovae,  $\gamma$ -ray bursts, and active galactic nuclei (AGN). We will put a special focus on AGN in the course of this dissertation.

**Maser Sources** Nonthermal maser sources with brightness temperatures up to  $10^{12} \text{ K}$ .

## 1.2 Brief History of Radio Astronomy

The first radio telescope was constructed by Karl Guthe Jansky in the thirties (Jansky 1933). Grote Reber constructed the first fully steerable radio antenna based on a parabolic reflector in 1937. Subsequently he discovered many of the strongest radio sources and obtained the first radio map of the Milky Way (Reber 1944). For almost ten years Grote Reber remained the only radio astronomer in the world. Technically, the need for advanced radar systems during World War II helped to advance the existing instruments. First breakthrough discoveries made at radio frequencies include the observation that the Sun is a strong radio source (Hey 1946), the detection of the hydrogen hyperfine structure line (Ewen & Purcell 1951), the detection of the cosmic microwave background (Penzias & Wilson 1965), the detection of the first maser in 1965 (Weaver et al. 1965) and the discovery of pulsars (Hewish et al. 1968).

In the meantime the radio astronomy evolved into an integral field of astrophysics that studies astronomical objects on all scales (Burke et al. 2019), ranging from cosmic structure formation (e.g. CMB), over galactic scales (e.g. research on active galactic nuclei and jets), and down to stellar (e.g. pulsars) and planetary astronomy. The radio window is essential to understand astrophysical phenomena. Groundbreaking observations produced in recent years include, among many others, the first image of the shadow of a supermassive black hole by the Event Horizon Telescope (Event Horizon Telescope Collaboration et al. 2019a) and ultra-sharp images of H-Tauri delivered by the ALMA telescope that demonstrate how forming planets are accumulating dust and gas in a protoplanetary disc (ALMA Partnership et al. 2015).

Radio astronomy will continue to deliver frontline observational results, with a variety of upcoming or planned next generation radio instruments such as the next generation Event Horizon Telescope (ngEHT), the Square Kilometer Array (SKA) and the next generation Very Large Array (ngVLA). These telescopes will be able to probe the Universe at an unmatched resolution, sensitivity and dynamic range. On the other hand, the upcoming decades of precision astronomy instruments require the invention of novel data analysis methods as well, in order to meet the high profile research goals of their respective missions.

## 1.3 Active Galactic Nuclei (AGN)

A variety of different types of galaxies is known by now, varying in morphology (e.g. elliptical, spiral, bulk-spiral or irregular), size, mass and bolometric luminosity. As a rough estimate of order of magnitude, ‘normal’ galaxies have an optical bolometric luminosity  $L \sim 10^9 - 10^{11} L_{\odot}$  where  $L_{\odot}$  is the luminosity of

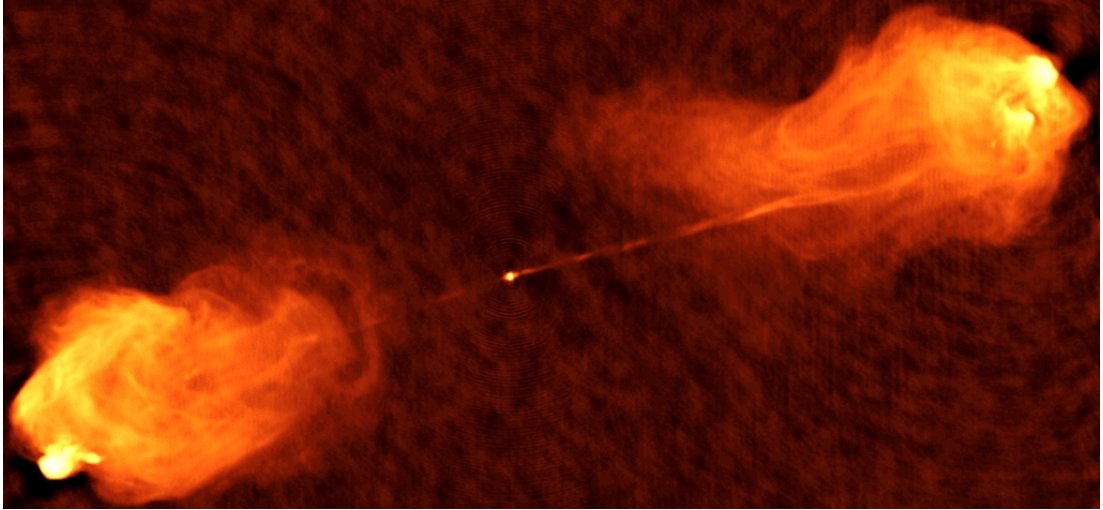


Figure 1.2: The radio galaxy Cygnus A observed with the Very Large Array (VLA). Image was taken from <http://www.aoc.nrao.edu/~ccarilli/cyga.shtml> at 02.01.2023. For details, see Carilli & Barthel (1996).

the Sun (Mo et al. 2010). Active galaxies, broadly speaking, differ from ‘normal’ galaxies by a compact, luminous core with optical bolometric brightness’s of up to  $L \sim 10^{11} - 10^{14} L_{\odot}$ . These cores form the class of active galactic nuclei (AGN). Further phenomena that have been observed in some (but not all, see the unifying model) active galaxies are highly excited emission lines and ‘forbidden’ lines, nonthermal continuum radiation in the radio regime and  $\gamma$  regime, and a rapid variability (Robson 1996). Additionally, some active galaxies exhibit a very specific morphological feature: an elongated jet which often ends in an extended lobe (Robinson & Terlevich 1994). We present an exemplary radio image of such a two-lobed jet structure in Fig. 1.2. Based on their observed morphologies and spectra, AGN have been classified in many different categories. A rough overview of the most important AGN types is provided in Tab. 1 including quasars (QSO), blazars, BL Lacertae, radio galaxies, and Seyfert galaxies (Robson 1996).

All these types of nuclear activity in galaxies are unified in the unifying model of AGN. We show a sketch of the current AGN unification scheme in Fig. 1.3. The central engine consists of a supermassive black hole (SMBH) embedded in an accretion disk. The accretion onto the central SMBH heats the gas in the surrounding disk, hence producing the compact, high brightness nucleus of an active galaxy. Broadband continuum radiation is produced in the accretion disk and in the relativistic jets ejected from the nucleus. The accretion disk is surrounded by clouds of gas producing broad emission and absorption lines in the optical spectrum of AGN (the broad line region, BLR). On larger scales, this system is surrounded by a dusty torus and by a collection of colder clouds revealed by narrow emission and absorption lines (the narrow line region, NLR). Jets are formed

Type	Host	Variability	Spectrum	Jets possible
Quasar	all	days	opt: point source, radio-loud and radio-quiet, emission lines, hard X, $\gamma$	strong
Blazar	ellipt.	days	highest luminosity, double-humped, X, $\gamma$ to TeV, compact radio core	strong
BL Lac	ellipt.	days	high luminosity, optical variable, no em./abs. lines, radio-loud	yes
Radio gal.	ellipt.	months	strong radio core: flat spectrum, jet and hotspots: steep spectrum	strong
Seyfert	spiral	months	comptonized continuum, em./abs. lines, reflection bump	weak

Table 1: AGN Classification, adapted from the AGN lecture of W. Kollatschny in the winter semester 2016/2017, University of Göttingen.

in a fraction of active galaxies and propagate in a direction which is roughly perpendicular to the plane of the accretion disk. This unifying model can explain the various types of AGN by different viewing angles (Robson 1996). We discuss radio-loud galaxies first. When observed face on, i.e. looking into the jet or close to the jet axis, strong (jetted) radio emission is visible. Moreover, due to the face on viewing, direct observations of the variable (turbulent) nature of the accretion flow and the jet are possible and explain the observed fast variability. We see these objects as blazars or, at a small angle off axis, BL Lac objects. In these objects, both narrow and broad emission lines can be observed, unless the non-thermal continuum strongly dominates the emission. The relative prominence of these two types of emission lines leads to classifying the radio-loud galaxies as broad line radio galaxies (BLRG) and narrow line radio galaxies (NLRG). Quasi stellar objects (QSO) or ‘quasars’ are the high power active galactic nuclei counterparts to radio galaxies observed at the same viewing angle. They can be further subdivided into Type I QSOs (broad lines) and Type II QSOs (narrow lines). The dusty torus absorbs, reflects and scatters the light produced in the nuclear region (Robson 1996). Active galaxies which do not have strong jets are classified as Seyfert (Sy) galaxies and radio-quiet QSO. Again, depending on the viewing angle, the geometry of the absorbing torus, the size of the broad line and the narrow line region, we subdivide Seyfert galaxies in Seyfert 1 galaxies (broad emission lines) and Seyfert 2 galaxies (narrow emission lines).

There is growing observational evidence for the unifying model since it can explain the various spectral properties, variability and morphology of active galaxies within a single and self-consistent framework (Robson 1996). The detailed physical mechanisms in the central engine that produce the compact luminous synchrotron radiation and jets are still the matter of ongoing debate. Several as-

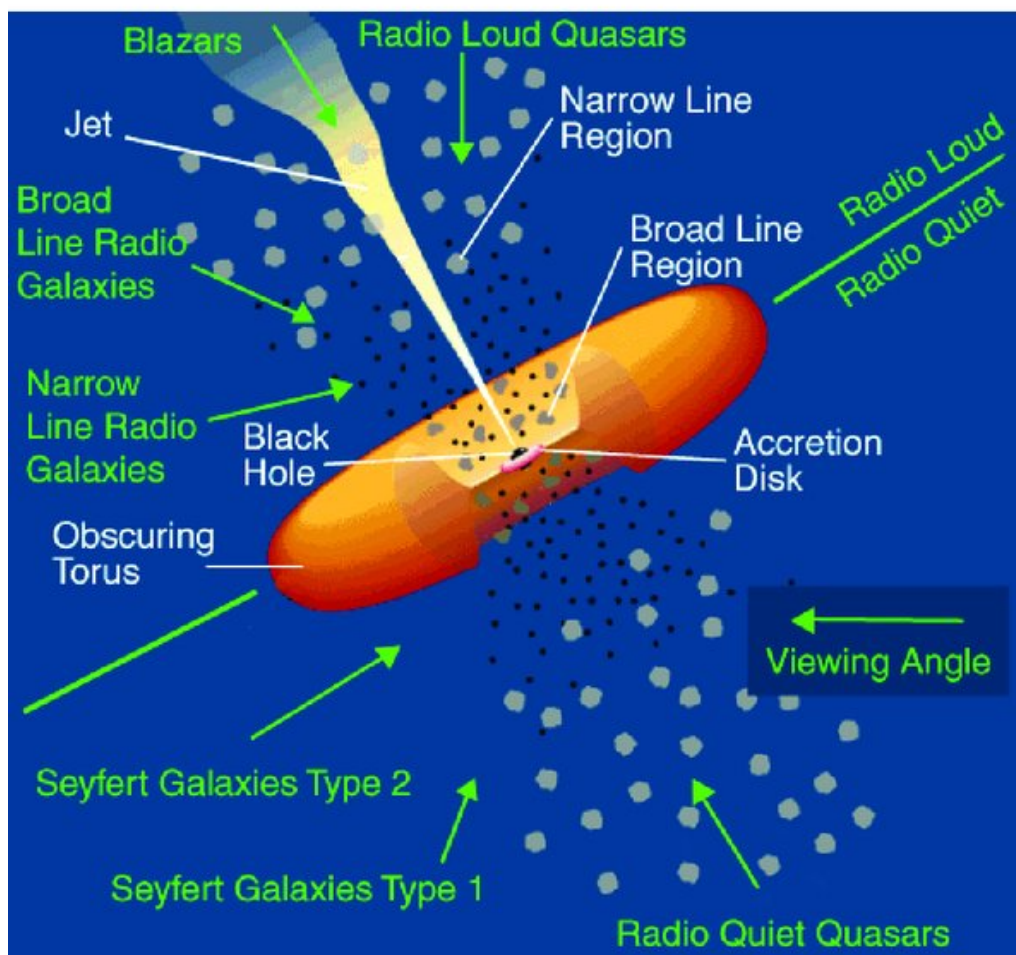
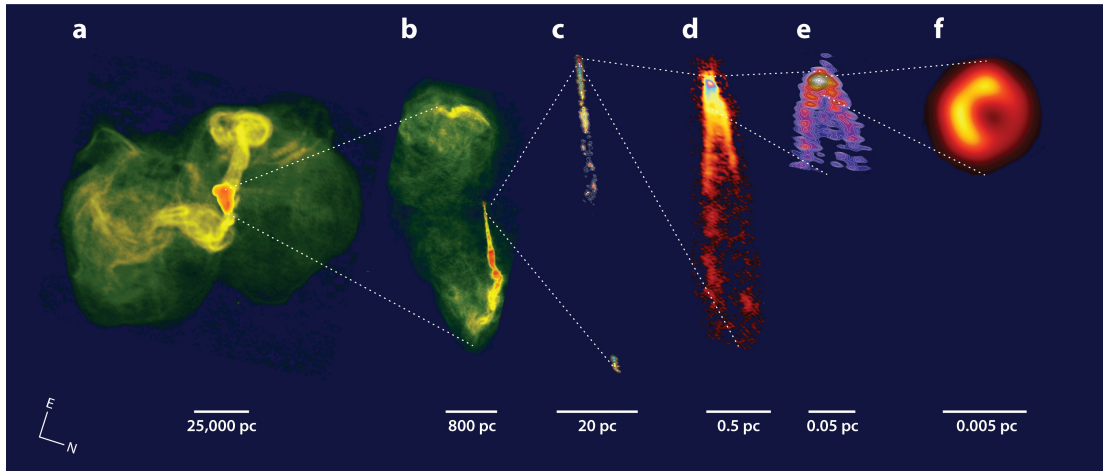


Figure 1.3: Illustration of the unified model of AGNs. Image from Urry & Padovani (1995).

trophysical probes confirmed the existence of a supermassive black hole (SMBH), i.e. by the observed motions of stars on close orbits around the central SMBH in the Milky Way (GRAVITY Collaboration et al. 2019, 2022), the gravitational lens effect (first observed by Walsh et al. 1979), the observation of relativistic iron  $K\alpha$  lines in the X-ray regime (Fabian et al. 1989, 2000) or the imaging of the black hole shadow by radio interferometry (Event Horizon Telescope Collaboration et al. 2019a, 2022a). Most alternative explanations that were proposed historically, e.g. massive stars or dense clusters, do not match to the observations. However, there are some horizonless objects such as gravastars that are proposed as alternatives to SMBH (Chirenti & Rezzolla 2016; Lobanov 2017; Mazur & Mottola 2004; Sakai et al. 2014).

Relativistic jets that are formed in a fraction of AGN are observed from meter wavelengths to  $\gamma$ -rays (Blandford et al. 2019). On large, kiloparsec scales the jets are commonly classified as the Fanaroff-Ryley (FR) types I and II (Fanaroff & Riley 1974). The FR I jets are low power, edge darkened radio sources. FR II jets are high power, edge brightened jets. We follow the review by Blandford et al. (2019) in the following description of jet properties. Blandford et al. (2019) considered three scales of jets: ‘Galaxy jets’, ‘black hole jets’ (inward extension to the gravitational radius of the central SMBH) and ‘lobe jets’ (outward extension). A multifrequency montage of these scales of the galaxy M87 is presented in Fig. 1.4. Galaxy jets are often one-sided (Lister et al. 2018; Wilkinson et al. 1977) as a result of relativistic beaming. Regular VLBI monitoring (e.g. Lister et al. 2018) demonstrated complex kinematics and dynamics of the jets on these scales, with distinct plasma condensations (jet components) expanding and moving with apparent superluminal speeds along the jet. Around a third of all observed jet components show nonradial motion while a small percentage ( $\sim 4\%$ ) even seems to move inwards (Blandford et al. 2019). This can be explained by the joint effect of relativistic shocks and plasma instabilities developing in the jet (Mertens et al. 2016). Both, clearly limb-brightened jets (e.g. Kim et al. 2018) and clearly edge-brightened jets (e.g. Giovannini et al. 2018) were observed. This probably indicates different jet anchors (Blandford et al. 2019). The richness of structural features in jets is further underlined by polarization measurements. We refer the reader here to systematic surveys of linear polarization within the MOJAVE project, e.g. Lister et al. (2018); Pushkarev et al. (2017); Zobnina et al. (2022). As an overall tendency, the fractional polarization increases with core separation with an increase towards the edge of the jet (Blandford et al. 2019).

Blandford et al. (2019) denotes the most inward portion of the jet the ‘black hole jet’. To describe this jet region, we shall recall here the main findings from the VLBI monitoring of M87 (whose innermost radio jet is the most detailed

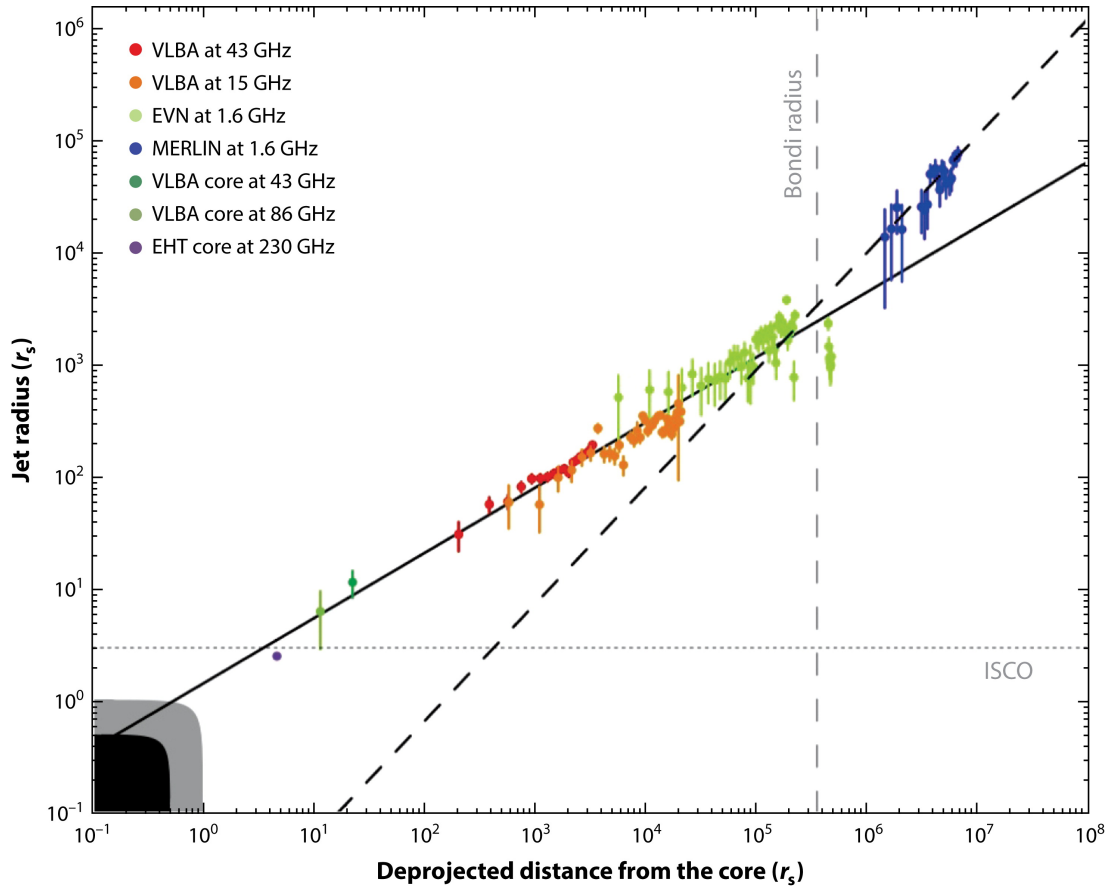


Blandford R, et al. 2019.  
*Annu. Rev. Astron. Astrophys.* 57:467–509

Figure 1.4: Different scales of the M87 jet. Adapted from Blandford et al. (2019) under license agreement 1307729-1 with Copyright Clearance Center Inc. (CCC). Panel a: VLA observation of the love jet at 90 cm. Panel b: VLA observation of the galaxy jet at 20 cm. Panel c: VLBA observations of the black hole jet at 20 cm (Cheung et al. 2007). Panel d: VLBA observations of the innermost jet at 7 mm (Walker et al. 2018). Panel e: GMVA observations of the innermost jet at 3 mm (Kim et al. 2018). Panel f: EHT observations of the black hole shadow at 1.3 mm (Event Horizon Telescope Collaboration et al. 2019b).

studied black hole jet so far) from Walker et al. (2018) reprinted in Blandford et al. (2019). The jet in M87 is two sided, with edge brightening observed both in the stronger jet and weaker counter-jet. Close to the black hole, the jet can be accelerated to superluminal speeds in a semi-parabolic shape. At the Bondi radius the jet decelerates and transforms into a conical shape. An overview of the collimation profiles is presented in Fig. 1.5. Observations of the magnetic field close to the black hole indicate a strong helical field structure (Event Horizon Telescope Collaboration et al. 2021a,b).

All in all, observations suggest that the jet acceleration and collimation appear close to the central SMBH within the Bondi radius (Blandford et al. 2019). The jet is collimated due to strong magnetic fields. Downstream the jet relativistic shocks may form and manifest themselves as superluminal jet components. We show a sketch of this blazar model in Fig. 1.6. However, the details of the jet confinement, accretion and jet launching are still not fully understood. Current theories either propose a jet launching from the rotation of the black hole (Blandford & Znajek 1977) or from the accretion disk (Blandford & Payne 1982). At extremely low and extremely high, super-Eddington accretion rates, jet formation is believed to be related to radiatively inefficient accretion flows (Blandford et al. 2019). The mechanism for the initial jet collimation and confinement is also poorly known, with strong magnetic fields proposed to play a vital role (Boccardi



 Blandford R, et al. 2019.  
*Annu. Rev. Astron. Astrophys.* 57:467–509

Figure 1.5: Collimation profile of M87 as transverse radius vs function of distance to core. Image adapted from Blandford et al. (2019) under license agreement 1307729-1 with Copyright Clearance Center Inc. (CCC).

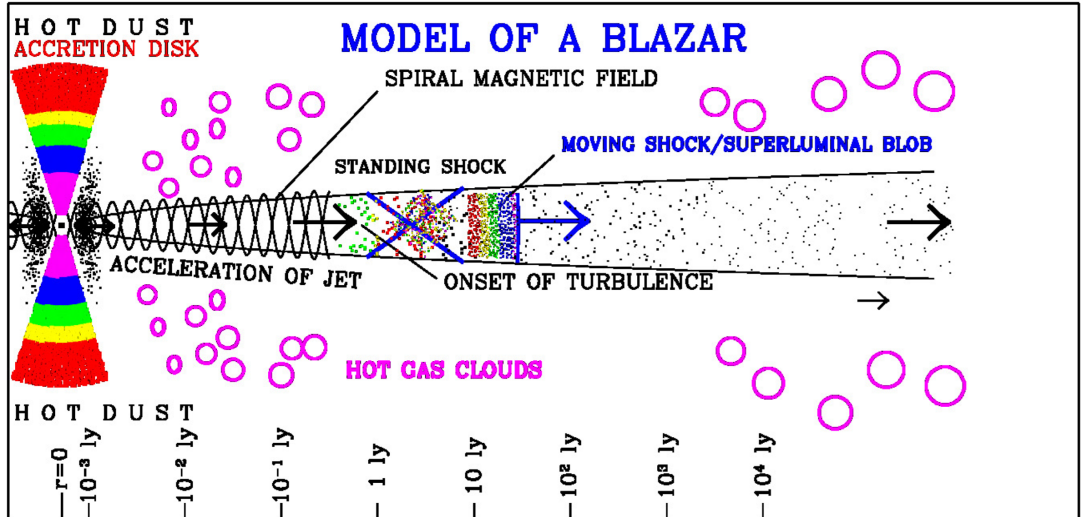


Figure 1.6: Blazar model proposed by A. Marscher. Image taken from Park & Algaba (2022) by CC BY.4.0. Image copyright: A. Marsher.

et al. 2021; Ricci et al. 2022). The possibility of jet confinement by the walls of a funnel by a ion-supported torus has also been discussed (Blandford et al. 2019). Pressure gradients in the dense ambient medium or dynamical disk winds (Globus & Levinson 2016) may as well play a role in the jet confinement. There are further open question about the physics of relativistic jets and their connection to the AGN phenomenon (see the discussion in Blandford et al. 2019). Where and how are the emitting particles accelerated in the jet? How do jets transit so rapidly from electromagnetic to particle dominance? What is the environmental impact on the formation of a jet? What physical process exactly decides whether a galaxy is active or not? What is the evolution of active galaxies and what was their role during cosmic structure formation and the reionization epoch?

## 1.4 Very Long Baseline Interferometry (VLBI)

Very long baseline interferometry (VLBI) is the prime observational technique employed for studies of relativistic jets in AGN. We discuss the fundamentals of VLBI in this chapter. We provide a short overview of radio telescopes in general, the fundamentals of interferometry, the specifics of VLBI and an overview of the data processing in VLBI. Finally, we discuss factors and effects limiting the quality of VLBI measurements. As the main result from this chapter, we introduce in Eq. (1.8) and (1.12) the forward equations will be subsequently used in the imaging algorithms developed in this dissertation.

### 1.4.1 Radio Telescopes

The prime element of a radio telescope, determining its design and performance, is the receptor of radiation or radio antenna. Depending on the observing wavelength,  $\lambda$ , three different antenna designs are common: reflector antennas ( $\lambda < 1m$ ), wire mesh-antennas ( $\lambda \sim 1m$ ) and half-wavelength dipole antennas ( $\lambda > 1m$ ) (Taylor et al. 1999). We will focus on reflector antennas for the sub-meter regime. Radio waves arriving at the reflector (aperture) are collimated and focused onto a feed horn where the signal is coherently added (Burke et al. 2019). The optical system consisting of the primary reflector (complemented, in some optical designs, by a secondary ‘subreflector’) and feed horn is called the frontend of the radio telescope. A sketch of a frontend system is shown in Fig. 1.7. However, the exact design and geometry varies from telescope to telescope due to various mounts, light paths, and electronics. Most radio dishes are made steerable in azimuth and altitude, in order to track the source during the observation time. However, there are prominent exceptions, such as the full-aperture Arecibo and FAST telescopes or the semi-aperture RATAN-600 telescope. While such telescopes have the best sensitivity for object close to the zenith, a movable secondary reflector (e.g. at Arecibo, see Cohen 2009) and a deformable surface (e.g. at FAST, see Li & Pan 2016) allow for off-zenith observations as well.

Radio antennas are not equally sensitive in any direction. The sensitivity of the antenna off-focus is described by the antenna beam pattern  $A(l, m)$  that will be introduced in the more detailed discussions in chapter 1.4.4. Moreover, the antenna beam pattern is complex, consisting of a single primary lobe and multiple secondary lobes (sidelobes). Noise from non-desirable nearby sources whose emission is received in one of the sidelobes could therefore corrupt the data sets recorded by a single antenna (Thompson et al. 2017). Another prominent factor corrupting radio observations is the radio frequency interference (RFI) signal from digital communication, satellites and other synthetic human generated radio sources (Burke et al. 2019). It is an increasingly difficult task to shield radio astronomic observations against the RFI. Radio telescopes are typically constructed in radio-quiet zones such that the interaction with RFI is minimal.

The signal accumulated at the receiving horn of the telescope is transported into the backend system where a heterodyne detector translates the detected radio waves into a time series of complex voltages (Burke et al. 2019). However, it is hard to record time series at  $GHz$ -frequencies. The heterodyne receiver therefore downsamples the recorded signal to smaller frequencies that can be digitized. The incoming signal is (analogously and digitally) filtered, mixed with a local oscillator (and hence effectively down-sampled) and finally digitized (Thompson

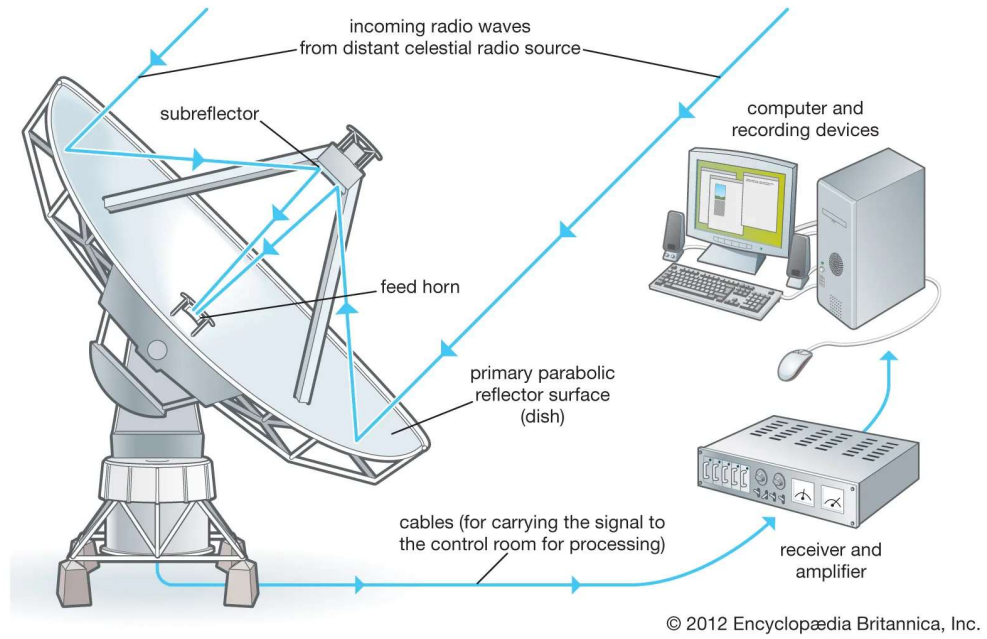


Figure 1.7: Sketch of the light and signal path in a radio telescope, taken from Encyclopedia Britannica <https://cdn.britannica.com/34/4634-050-DA53D88D/Radio-telescope-system.jpg> at 23.12.2022.

et al. 2017). We describe these steps in greater details in chapter 1.4.4.

### 1.4.2 Basic Principles of Interferometry

The following description of basic principles of radio interferometry derives from the discussion presented in chapter 3 of Thompson et al. (2017). We define a locally Euclidean coordinate system on sky at the point of the source with direction cosines  $l, m$ , see Fig. 1.8. The voltage reception pattern of an antenna  $U_A(l, m)$  is characterized by the field distribution in the antenna aperture  $\mathcal{E}(x, y)$  via (Thompson et al. 2017):

$$U_A(l, m) \propto \int \int \mathcal{E}(x, y) e^{2\pi i [lx/\lambda + my/\lambda]} dx dy, \quad (1.1)$$

where  $x, y$  are point coordinates in the antenna aperture and  $\lambda$  is the wavelength. Eq. (1.1) describes the effective interference between all points in the aperture. It implies that the voltage reception pattern and the aperture illumination function form a Fourier pair. We define the effective collecting area by the modulus of  $U_A$

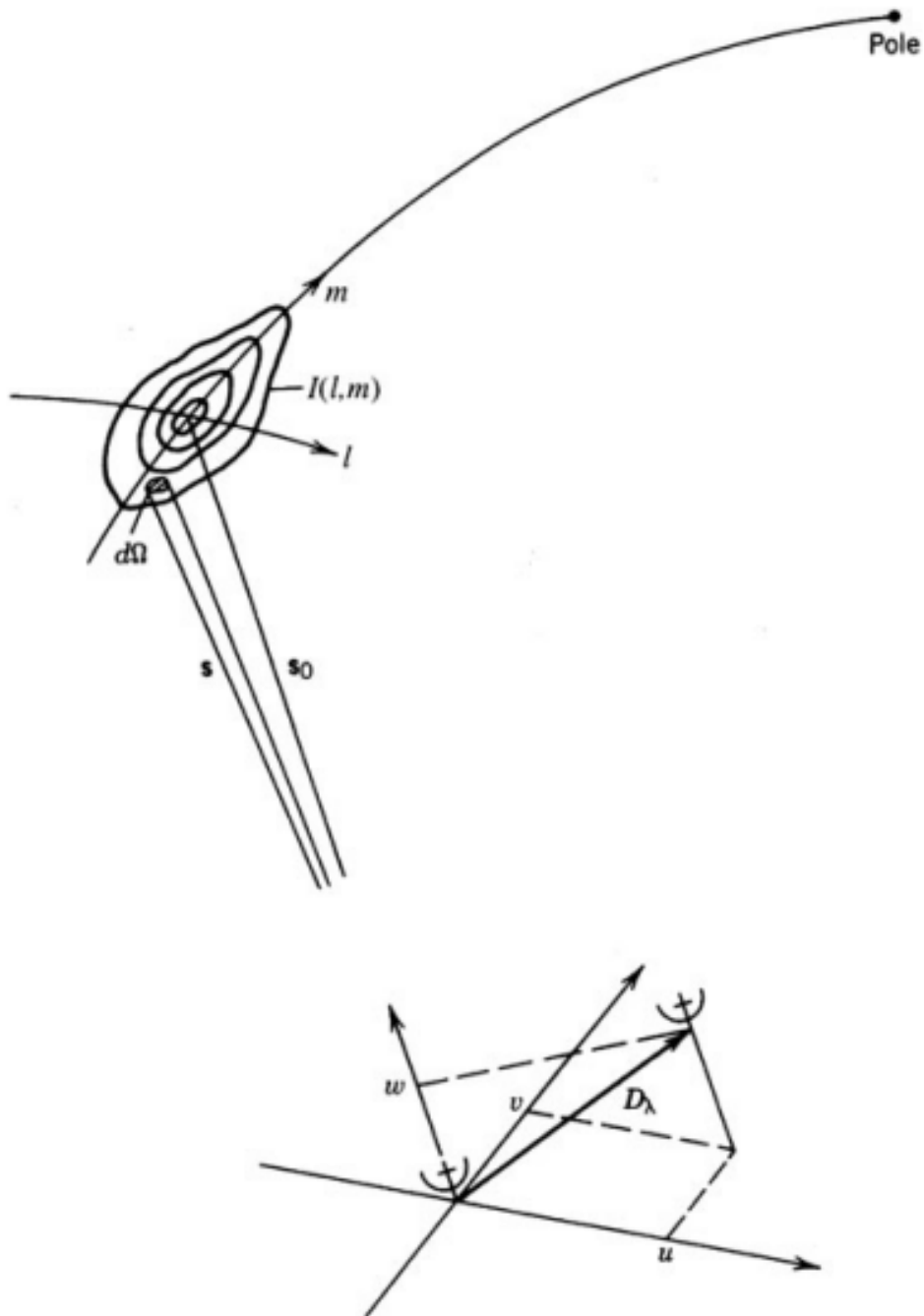


Figure 1.8: Coordinate system used to express an on-sky distribution (direction cosines  $l, m$ ) and baselines ( $u, v, w$  expressed in units of wavelengths). The figure is taken from Thompson et al. (2017), Fig. 3.2. by CC BY 4.0.

for a normalized point source, i.e. (Thompson et al. 2017):

$$\sqrt{A(l, m)} = |U_A(l, m)|. \quad (1.2)$$

From Eq. (1.1) it becomes obvious that the smallest resolvable structures on sky are limited by the longest sampled spatial Fourier frequencies, i.e. the resolution limit is of order of  $\lambda/D$  where  $D$  is the diameter of the reflector antenna. Hence, a poor resolution can be expected for single aperture telescopes operating at radio wavelengths.

Radio interferometry provides a very powerful method for overcoming the problem of poor resolution of radio telescopes. In radio interferometry an array of antennas is used. All of the array antennas simultaneously observe the same target objects, and the signals recorded at all these antennas are subsequently correlated for all pairs of the antennas. In the following we will discuss the case of an antenna pair in a simplified setup for first illustration. We first assume that the source is unresolved for both antennas, i.e. appears as a point source. If both antennas track the source, then the antenna response at antenna  $k$  to an incident field  $E(l, m)$  could be expressed as (Thompson et al. 2017):

$$C_k(t) = \int dl \int dm \int d\nu E(l, m, \nu) \sqrt{A_k(l, m)} H_k(\nu) e^{2\pi i \nu t}, \quad (1.3)$$

with a frequency  $\nu$  and a frequency response  $H_k(\nu)$ , i.e. a frequency filter function. Hence, the correlation product is:

$$r(\tau) = \lim_{T \rightarrow \infty} \frac{1}{2T} \int_{-T}^T dt C_1(t) C_2^*(t - \tau) = \lim_{T \rightarrow \infty} \frac{1}{2T} \int_{-T}^T dt \int dl dm dl' dm' d\nu d\nu' E(l, m) E^*(l', m') \sqrt{A_1(l, m) A_2(l', m')} H_1(\nu) H_2^*(\nu') e^{2\pi i \nu t} e^{-2\pi i \nu' (t - \tau)}. \quad (1.4)$$

We have to assume that the source is spatially incoherent, eliminating off-diagonal integrals in  $l'$  and  $m'$ . Moreover, we integrate out the time dependence eliminating the integral in  $\nu'$  and define the intensity as the squared field amplitude (Thompson et al. 2017):

$$I(l, m) = E(l, m) E^*(l, m). \quad (1.5)$$

Hence (Thompson et al. 2017):

$$r(\tau) = \int dl dm d\nu I(l, m) \sqrt{A_1(l, m) A_2(l, m)} H_1(\nu) H_2^*(\nu) e^{2\pi i \nu \tau}. \quad (1.6)$$

The geometric delay between the two antennas is given by the baseline array ex-

pressed by harmonic coordinates  $u, v, w$  associated to the direction cosines  $l, m, n$  ( $u, v$  define the baseline vector in the plane perpendicular to the source direction, and  $w$  is the baseline vector component along the source direction), compare Fig. 1.8. It is  $\nu_0\tau = ul + vm + w \left[ \sqrt{1 - l^2 - m^2} - 1 \right] \approx ul + vm$  with a central frequency  $\nu_0$ . The  $w$ -term becomes important in wide-field applications, but can be ignored with the small field of views of VLBI (Taylor et al. 1999). In the special case of two identical antennas with a constant antenna beam pattern across the field of view (i.e. small field of view) with an ideal narrow box frequency filter we get (Thompson et al. 2017):

$$r(u, v) = A_0 \mathcal{V}(u, v) \Delta_\nu, \quad (1.7)$$

where  $A_0$  is the combined response, and  $\Delta_\nu$  the observing bandwidth.  $\mathcal{V} = \mathcal{F}I$  are the visibilities. While Eq. (1.7) was derived in a very simplified setting, it illustrates the main idea behind radio interferometry already: The correlation product of an antenna pair gives rise to the visibilities, i.e. to the Fourier transform of the true sky brightness distribution. For a variable antenna beam pattern, the measured visibilities are related to the convolution of the power reception pattern  $A(l, m)$  and the intensity, expressed by a transfer function  $W(u, v)$  in the Fourier domain. The relation between these various antenna properties is illustrated in Fig. 1.9.

For the remainder of this dissertation we focus on the imaging problem, i.e. we assume complex visibilities as our observables from which the two-dimensional sky brightness distribution needs to be robustly reconstructed. In such generalized setting the van-Cittert-Zernike theorem holds true approximately (Burke et al. 2019; van Cittert 1934; Zernike 1938):

$$\mathcal{V}(u, v) = \int \int e^{-2\pi i(lu + mv)} I(l, m) dl dm. \quad (1.8)$$

Every antenna pair at a fixed point in time provides the visibility at one Fourier frequency  $(u, v)$  determined by the baseline between the two antennas. As the Earth rotates relative to the source, each antenna pair produces an elliptical track (for all objects with non-zero declinations) in the Fourier plane (uv-coverage) defined by the  $(u, v)$  coordinates (Taylor et al. 1999). The combination of all such uv-tracks determines the total coverage (uv-coverage) of the Fourier plane by an interferometric observation. With a fully filled uv-coverage, the true sky brightness distribution could be derived from an inverse Fourier transform. However, due to the limited number of antennas and observing time, the Fourier domain is only sparsely filled. Examples of uv-coverages with the typical elliptical tracks

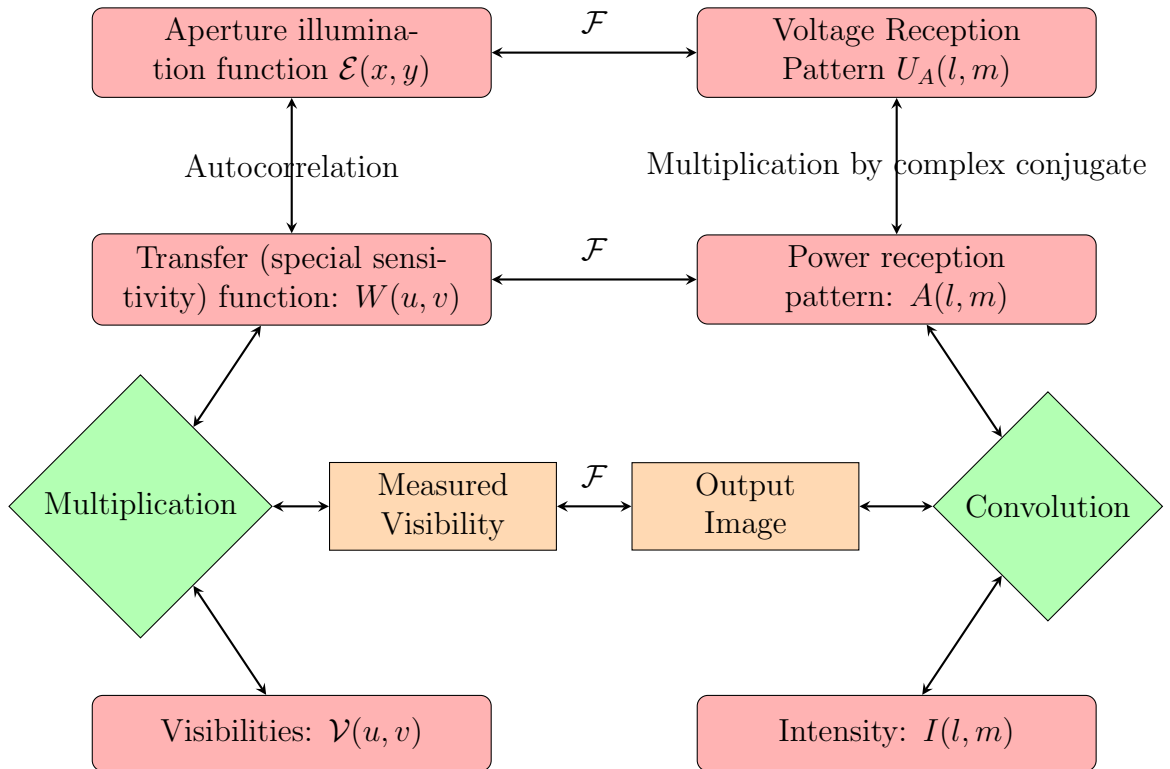


Figure 1.9: Relation between functions involved in imaging a source, adapted after Thompson et al. (2017), Fig. 5.5.

due to Earth rotation are presented in Fig. 1.10. Compared to the resolution limit of a single dish instrument,  $\theta_{\min} \sim \frac{\lambda}{D}$  with the diameter of the antenna  $D$ , we conclude by comparing Eq. (1.1) and (1.8) that the resolution limit of an interferometric array is of order:  $\theta_{\min} \sim \frac{\lambda}{B}$  where  $B$  is the longest baseline in the array (i.e. the longest  $u, v$ -distance covered by observations). Hence, the main advantages of radio interferometers are as follows: The effective collecting area of an interferometric array is the sum of the collecting areas of its antennas, and the resolution is inversely proportional to the longest distance between the antennas, which is typically much larger than the size of a single antenna. On the contrary, radio interferometers, opposed to single dish instruments, do not have a full aperture, i.e. significant gaps in the  $uv$ -coverage.

### 1.4.3 Very Long Baseline Interferometry

Very long baseline interferometry (VLBI) is a special radio interferometric technique with long baselines, up to a global scale (and in the case of space-VLBI with even longer baselines to a space antenna). As a special interferometric technique, VLBI has a special range of additional issues that distinguish it from usual radio interferometers. Among others we like to mention (Thompson et al. 2017):

- Due to the lack of short baselines and the focus on high angular resolution,

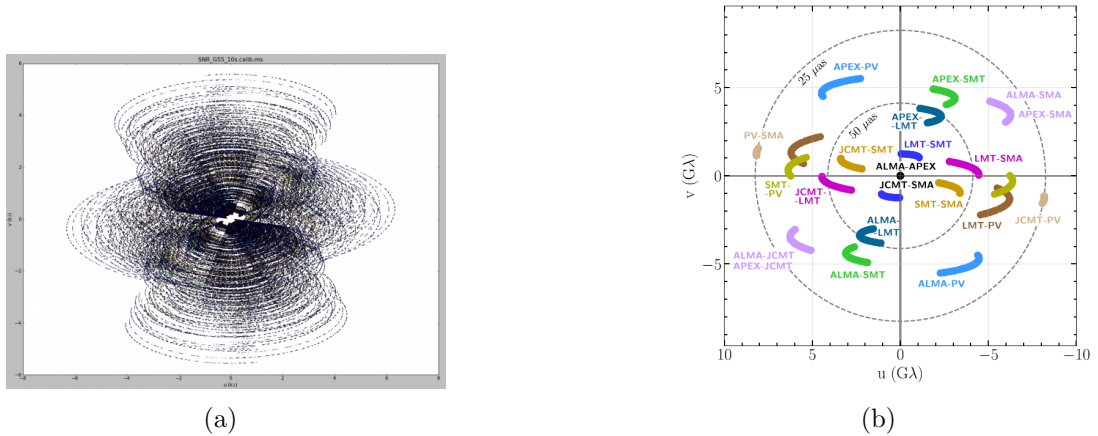


Figure 1.10: Panel a: Synthetic uv-coverage of the Karl G. Jansky Very Large Array (VLA) taken from the CASA documentation: <https://casaguides.nrao.edu/index.php/VLA-CASA-Imaging-CASA5.5.0> at 23.12.2022. One can clearly see the elliptical tracks of the uv-coverage and the significant gaps between several tracks and towards the center., Panel b: uv-coverage of the 2017 EHT campaign of M87 (Fig. 2 Event Horizon Telescope Collaboration et al. 2019b).

VLBI typically targets small fields of view. The  $w$ -projection term for wide-field applications is often ignored.

- Continental scale and global scale VLBI experiments do not contain a central master oscillator station distributing the clock signal to all participating antennas. The data sets need to be stored on harddrives instead and correlated in a post-processing step. Therefore, there is less control over the system stability and time delay, affecting most significantly the phase stability, particularly for mm-wavelengths. As a result, a thorough (self-)calibration procedure is needed.
- Due to the high angular resolution of VLBI arrays, there are few unresolved sources that can be used for calibration.
- Typically, but not necessarily, VLBI arrays are limited to a rather small number of antennas due to the high technical requirements of single antennas to participate in a VLBI experiment.

#### 1.4.4 Overview of VLBI Data Processing

We will only provide a short and simplified overview of the data analysis procedure in VLBI. The data analysis procedure generally comprises data taking, correlation, calibration and imaging. The procedure is described in more detail in the usual textbooks (Burke et al. 2019; Snell et al. 2019; Taylor et al. 1999;

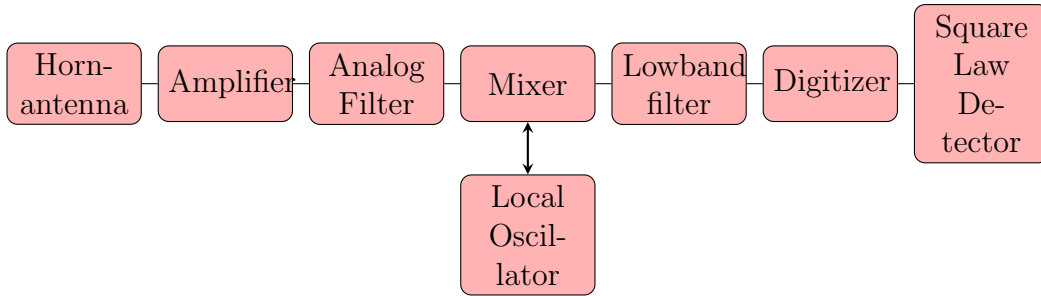


Figure 1.11: Sketch of heterodyne receiver system.

Thompson et al. 2017). We refer the interested reader also to the more recent overview of VLBI software provided in Janssen et al. (2022).

During observation the science target and (ideally unresolved) calibrator sources are observed with alternated observing scans. From the calibrator source time delays between the antennas are detected. This time delay is caused by the geometric distance and atmospheric effects, e.g. water vapor in the line of sight of single antennas. These phase solutions will work as an initial phase solution for the fringe detection. In addition to this we observe a total flux calibrator to translate the arbitrary antenna counts to physical intensities. Typically, a short measurement of the system temperature at the antennas and a pointing or focus correction is applied between the science scans.

The time series recorded by a single antenna looks like random noise due to the spatially incoherent superposition of incoming waves of the observed source and the superposition of various frequencies (Burke et al. 2019). In the following we outline the system of a generic heterodyne receiver system, although structural details of the complicated electronics would go beyond the scope of this introduction. A sketch of the different analysis steps is presented in Fig. 1.11. The detected signal is amplified by an amplifier and send through an analog bandpass filter (Thompson et al. 2017). The time series gets mixed with a local oscillator that oscillates at a frequency  $\nu_{\text{LO}}$ . Note that by the trigonometric addition theorem the relation  $2 \sin(\nu) \cos(\nu_{\text{LO}}) = \sin(\nu + \nu_{\text{LO}}) + \sin(\nu - \nu_{\text{LO}})$  holds true. Hence, by mixing the signal is separated into a low side band and a high side band. With the application of an additional analog low-band filter the frequency is effectively shifted down, such that the signal can be digitized by a digitizer with sufficiently fast temporal sampling (Burke et al. 2019). In a single dish instrument, a square-law detector and an averager pick the amplitude of the voltage pattern that is proportional to the intensity that should be measured by averaging out spatially incoherent cross terms (Burke et al. 2019).

A radio interferometer works similarly. We show a sketch of the working procedure in a radio interferometer in Fig. 1.12 (Thompson et al. 2017). If

the antennas are fiber-connected to a central station, the amplified and filtered signal is mixed with a master oscillator of a central station. After additional filtering (as outlined above) and the application of a variable phase delay, the two signals are multiplied in a multiplier and integrated in time. These two steps are called correlation (Janssen et al. 2022; Thompson et al. 2017). Hence, for a radio interferometer the correlator replaces the square-law detector and the averager. In VLBI the antennas are often not connected to a central control station and every antenna has its own local oscillator. Therefore, we copy the digitized signal on hard disk drives and correlate the data on specific supercomputer systems: correlators (Taylor et al. 1999). A high clock precision and a good initial phase solution is key to the success of the correlation, i.e. fringe detection (Janssen et al. 2022). It is worth mentioning that while software correlators are currently more common (Janssen et al. 2022), there is continued progress in the development of hardware correlators (e.g. at the Korean VLBI Network (KVN), see Lee et al. 2014c) originally introduced for processing large volumes of radio interferometry data.

After correlation, we need to calibrate the data set. We present a schematic overview of the necessary calibration steps in Fig. 1.13, adapted from Janssen et al. (2022). Delay models computed at the correlation stage are still imperfect. The data set could still suffer from corrupted data points. Moreover, the delay model at the correlation stage does not account for atmospheric fluctuations. Furthermore, we have to correct the observed data sets for instrumental effects such as cross-delay between orthogonal polarization channels and a frequency-dependent response function (bandpass) of the receiver system. We call the procedure to finetune the delay model (i.e. maximizing the correlation) fringe fitting. Now we discuss the several stages presented in Fig. 1.13 in some more detail. As a first step, the correlation output needs to be correctly loaded and converted into a uniform data format since a VLBI array is often highly heterogeneous, with a variety of different receiver systems and mounts. Moreover, we have to correct for the parallactic angles (Taylor et al. 1999). To avoid outliers that corrupt the data analysis further downstream, we flag possible statistical outliers. Next we calibrate the bandpass response of the antennas. If the bands are reasonable narrow, only a small variation from band to band could be expected. An auto-correlation analysis therefore provides initial gains per frequency bandpass. The correlator outputs are electronic counts in arbitrary units. We translate these counts into physical units by comparing to the known total fluxes of the flux-calibrator sources observed typically at the beginning and the end of the VLBI observing run. When this is not feasible, the measured antenna gains and system temperatures are applied for the flux density calibration. Next we can pre-calibrate

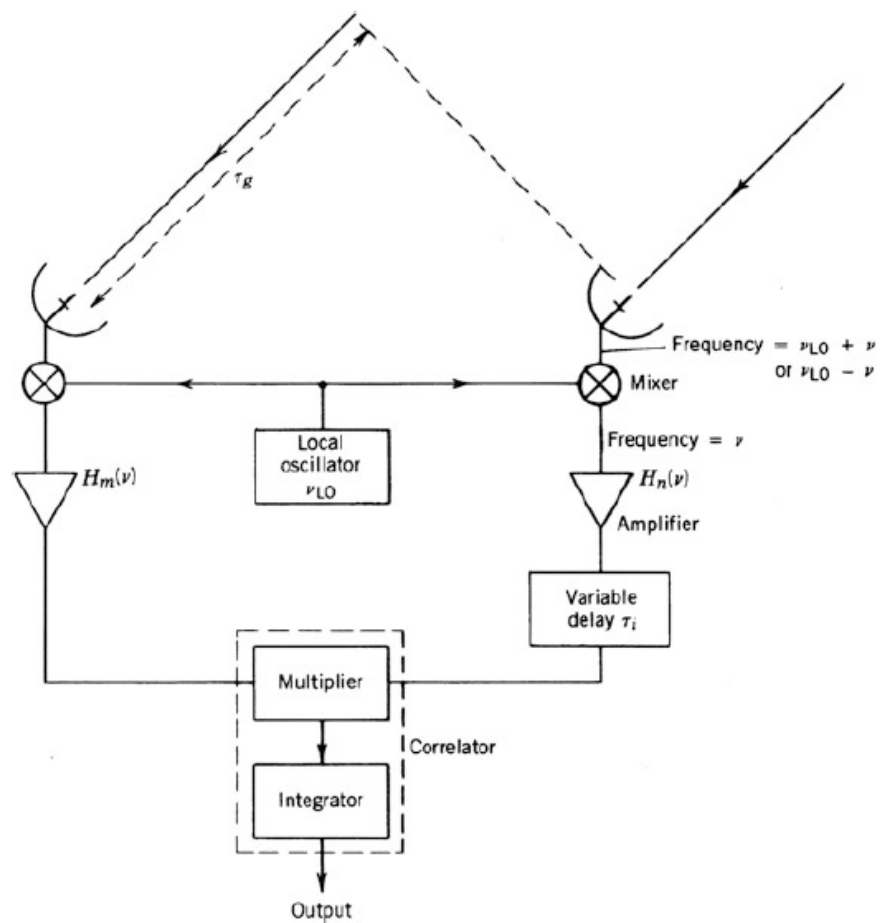


Figure 1.12: Schematic illustration of a radio interferometer, taken from Thompson et al. (2017), Fig. 6.2. by CC BY 4.0.

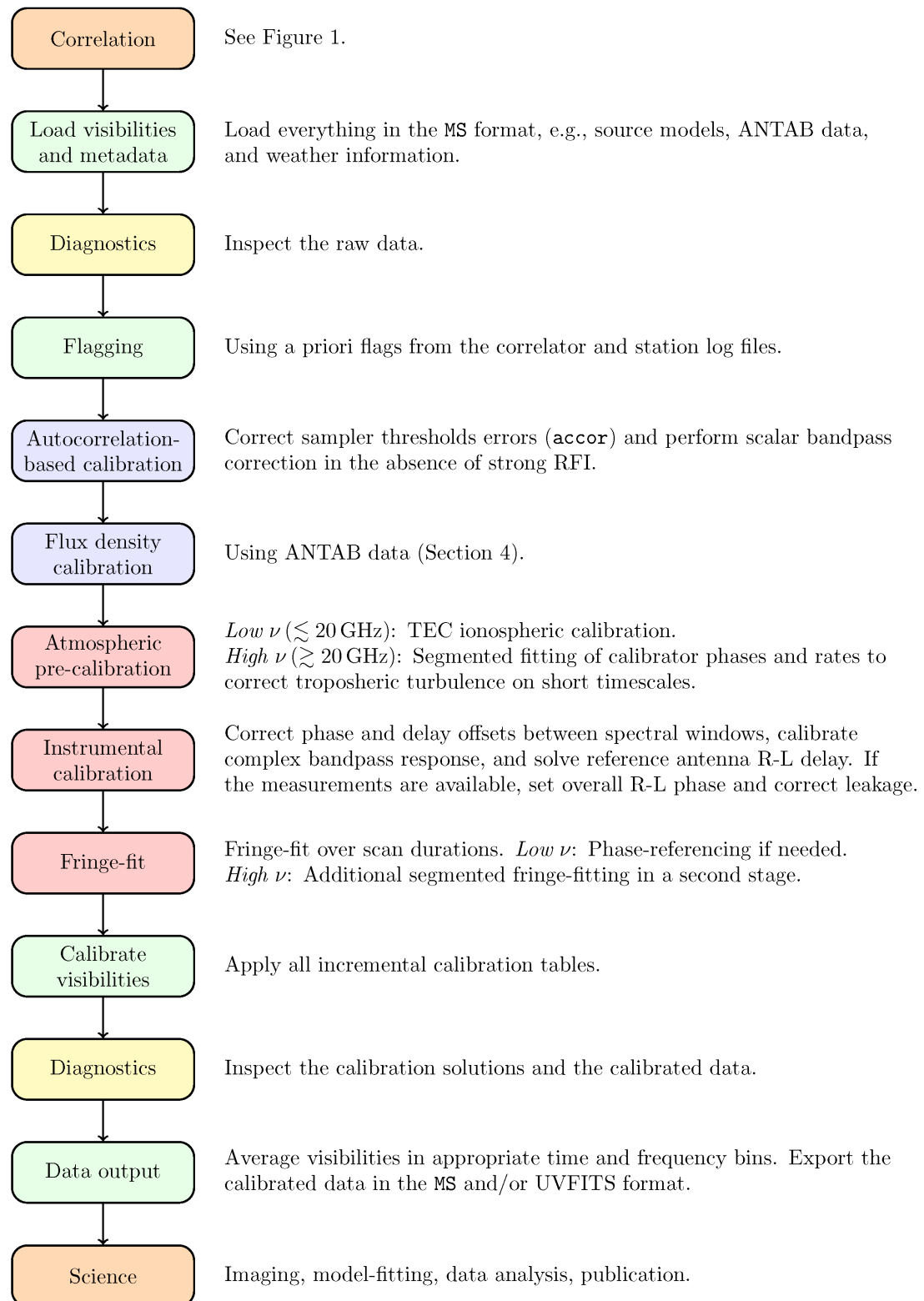


Figure 1.13: Flowchart of the calibration after correlation. Figure taken from Janssen et al. (2022), Fig.2 by CC BY 4.0.

for atmospheric phase-delays (Janssen et al. 2022). For weak sources, we use phase-referencing: during the observation the science target and the calibrator are observed in an alternating cadence. The calibrator is often a strong, ideally unresolved source. We obtain a proper delay model correction from the calibrator source and apply it to the science target (Taylor et al. 1999). Subsequently we correct for phase delays between frequency bands and polarization channels. Finally, we fit the fringes, i.e. we obtain a finer phase delay model for any baseline. The common fringe fitting method is a least square optimization with an assumed source model (Janssen et al. 2022; Schwab & Cotton 1983). Fringe fitting is a numerically expensive and time consumptive procedure, especially for heterogeneous arrays (Janssen et al. 2022). Therefore, a valid precalibration is essential to allow for local fringe finding. Ideally, the final calibrated data set would be free of systematic data corruption effects except for thermal noise. While we account for most effects during the calibration, the calibration is never perfect in practice. This is particularly the case if the source contains a rich structural complexity that was not accounted for with the simple source models during global fringe fitting. In these cases, we have to refine the calibration during the imaging (self-calibration), i.e. with a gradually evolving reconstruction we can refine the delay and sensitivity models.

Imaging is the last step in the VLBI data analysis procedure comprising a set of procedures of recovering an image from calibrated visibilities. As described by the van-Cittert-Zernike theorem, see Eq. (1.8), imaging mainly deals with an incomplete Fourier transform. However, the observed visibilities have additional data corruptions and noise effects that need to be corrected for during imaging as well (which is normally achieved through self-calibration). This hybrid approach consisting of calibration and imaging at the same stage of the data analysis is called hybrid imaging (Taylor et al. 1999). We will discuss several data corruption effects in the following subsection and describe the imaging procedure in detail in chapter 2

#### 1.4.5 Corruption Effects

With a full uv-coverage, the true image is related to the true visibilities through the Fourier transform. However, the imaging problem is complicated by two issues. First, the uv-coverage is sparse as every antenna pair at a fixed point in time provides only one Fourier frequency, and the number of antennas and observing time is limited. Second, the measured visibilities differ from the true visibilities due to noise and non-accounted antenna based (atmospheric) errors.

The effect of the uv-coverage on the final image can be well illustrated by the dirty beam or the effective point spread function (psf) of an interferometric array.

The dirty beam is the image domain response to a point source on sky, i.e. to a flat uniform Fourier transform. Hence, it is the inverse Fourier transform of the uv-coverage itself (Taylor et al. 1999):

$$B^D = \mathcal{F}^{-1} \mathbf{G} \sum_{(u,v) \in \text{uv-coverage}} \omega_{u,v} \delta(u,v) =: \mathcal{F}^{-1} \mathbf{G} \mathbf{S} \mathcal{F} \delta(0), \quad (1.9)$$

where  $\omega_{u,v}$  are possible weighting parameters,  $\mathbf{G}$  is a gridding operator that represents the uv-points on a rectangular grid accessible to a fast Fourier transform and  $\mathbf{S}$  a sampling operator that projects the visibilities to the measured, weighted visibilities and sets all non-measured visibilities to zero.

Obviously, the uv-coverage is limited to a finite support: there is a finite, longest baseline in the array. The highest sampled Fourier frequency limits the angular resolution. Even with the ideal, uniformly filled uv-coverage, i.e. if the uv-coverage would be a disk, this creates a sidelobe structure. As an illustration and for subsequent discussions it is useful to establish the Fourier transform of a disk function  $rect_R = \mathbf{1}_{\{x^2+y^2 < R^2\}}$ :

$$\mathcal{F}(rect_R)(k, \alpha) = \frac{R}{k} J_1(2\pi k R) =: f_R(k), \quad (1.10)$$

with polar coordinates  $k, \alpha$ .  $J_1$  is the first order Bessel function which is plotted in the upper right panel in Fig. 1.14. With additional gaps in the uv-coverage the sidelobe pattern becomes more complex. As an illustrating example, we consider the situation with a gap in the uv-coverage between a radius in uv-coverage  $r_1$  and  $r_2$  with  $r_1 < r_2 < R$  (where  $R$  is the limiting longest baseline). Such a simplified uv-coverage would be expressed by the function  $rect_R - rect_{r_2} + rect_{r_1}$  with a dirty beam:

$$\mathcal{F}(rect_R - rect_{r_2} + rect_{r_1})(k, \alpha) = f_R(k) - f_{r_2}(k) + f_{r_1}(k), \quad (1.11)$$

a sum of three Bessel functions, each of them introducing sidelobes at a different spatial scale, compare also Fig. 1.14. A directional dependence of the filling of the uv-coverage adds even more complexity to the pattern. Hence, the dirty beam corresponding to the uv-coverage of a real observation is a superposition of elliptical Bessel functions with a complex sidelobe pattern (see the detailed discussion in Müller & Lobanov 2023a). It is the goal of imaging to ‘clean’ these sidelobes out of the image, or equivalently to ‘fill’ the gaps in the uv-coverage with a reasonable interpolation. One specific gap is inherent to the uv-coverage in every radio interferometer: the zero point of the uv-plane and the uv-distance corresponding to the closest pair of antennas in a VLBI array, such that the

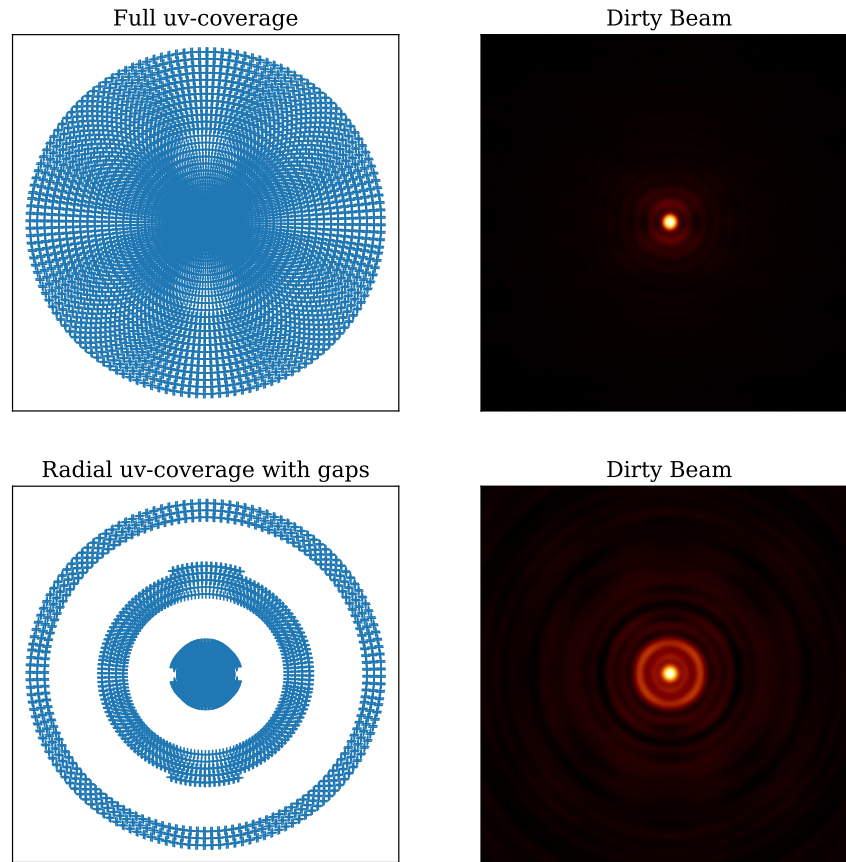


Figure 1.14: Upper panels: Dirty beam and uv-coverage for an array without gaps, i.e. a single spherical Bessel functions in the upper right panel. Bottom panel: uv-coverage and dirty beam as superposition of Bessel functions of different scales for an uv-coverage with radially symmetric gaps.

maximum structural scale to which the observation is sensitive remains restricted.

Up to now we have only discussed the situation of uniformly weighted visibilities with gaps. However, the filling factor and signal-to-noise ratio is varying for different regions of the uv-coverage, typically with a prominent overweighting of the short baselines (Taylor et al. 1999). Hence, the dirty beam is not only a superposition of elliptical Bessel functions of first order, but these constituents of the beam pattern have varying weights as well.

Moreover, the observed visibilities differ from the true visibilities by direction-independent calibration effects that can be multiplied into antenna based complex gains  $g_i$ . More details on the calibration effects that still need to be accounted for are provided in chapter 1.4.4 and Janssen et al. (2022). Additionally, the observed

visibilities are corrupted by thermal noise specific to the corresponding antenna pair  $i, j$ :  $\epsilon_{i,j}$ . The observed visibilities of an antenna pair  $i, j$  are therefore (Taylor et al. 1999):

$$V_{i,j} = g_i g_j^* \mathcal{V}(u_i, v_j) + \epsilon_{i,j}, \quad (1.12)$$

where all terms can be time-dependent in principle, i.e. the gains vary over the course of observations.

## 2 Imaging

We study the imaging problem in VLBI and some closely related inverse problems in this dissertation. This chapter serves as an overview of the background theory laying the foundation for the current developments in the image reconstruction and for the specific imaging algorithms developed and introduced in this dissertation. In general, images are reconstructed with a variety of apparently loosely connected algorithmic frameworks. We present a common language for all these methods and demonstrate their deeper connections as instances of the *generalized Tikhonov regularization* method. This is essential for achieving a same-level theoretical comparison and for providing a common basis for algorithm development. Moreover, the *generalized Tikhonov* framework and the methods and software developed in this dissertation have a wider range of applications outside of VLBI as well. We first set the scope of VLBI imaging, introduce the basic terms of inverse problems, and then discuss common data products in VLBI. We present various imaging approaches employing both inverse modeling and forward modeling and conclude with their qualitative comparison. Finally, we present the motivation for this dissertation.

### 2.1 Scope of VLBI Imaging

All radio interferometers share the same fundamental issue for imaging: the Fourier domain is undersampled. However, there are significant differences between VLBI arrays and denser arrays such as the proposed Square Kilometer Array (SKA), the Atacama Large Millimeter/submillimeter Array (ALMA), the Very Large Array (VLA) or MeerKAT regarding the proposed and used data analysis techniques. Foremost, these two data regimes (i.e. VLBI and ‘dense arrays’) vary by the number of observed visibilities (i.e. the uv-coverage), compare e.g. Fig. 1.10.

For dense arrays, the large number of antennas allows for high dynamic range reconstructions. For reconstructions at these dynamic ranges a detailed calibration is necessary. Among the calibration of gains, this includes direction-dependent gains and wide-field effects. Thermal noise would be amplified in a naive direct inversion. For this reason, regularization needs to be added: we aim to recover an optimal, high dynamic range image from noisy data and want to stabilize the reconstruction process against observational noise and data corruptions. In this sense, the problem could be approximated as a regularized deconvolution problem with an approximately injective convolution kernel (the point spread function).

In VLBI, wide-field effects are typically ignored. On the contrary, the fringes

are more unstable, such that in mm-VLBI imaging methods that are agnostic against an initial phase-calibration were proposed recently (Chael et al. 2018; Müller & Lobanov 2022). The primary issue for VLBI arrays is the small number of visibilities. The uv-coverages of VLBI experiments have significant gaps that are much more prominent than for denser arrays. The philosophy behind reconstructing an image changes slightly: we want to interpolate the observed visibilities in the gaps of the uv-coverage without introducing new (not observed) features in the map. The point spread function is clearly not injective (missing data). The undersampling of the Fourier domain, i.e. the issue of missing information, dominates the reconstruction and limits the dynamic range.

The differences between these two data regimes led to different inversion methods that have been proposed respectively. In this dissertation we focus on the VLBI side. Hence, in the following chapters we mainly focus on the missing data issue and address this multimodality of the reconstruction directly either with multiscale basis functions or with a multiobjective optimization.

## 2.2 Inverse Problems

The imaging problem can be effectively formulated in the language of inverse problems. We therefore introduce the basic concepts of inverse problems in this chapter. However, we provide only a coarse overview of the general ideas and omit derivations of the mathematically rigorous formulations. Building upon this general formulation of inverse problems, we present the basic approach how to solve them (regularization) and how to realize this numerically in the context of convex optimization.

### 2.2.1 General Introduction

Generally, we study a forward problem of the form:

$$g^\delta = FI + \epsilon_\delta, \tag{2.1}$$

with a generic forward operator  $F : \mathbb{X} \rightarrow \mathbb{Y}$  acting between Hilbert spaces  $\mathbb{X}$  and  $\mathbb{Y}$  and noise  $\epsilon_\delta$  of magnitude  $\|\epsilon_\delta\|_{l_2} = \delta$ . In the case of VLBI, the forward operator is the operator mapping the sky brightness distribution to the measured visibilities, i.e. it describes a Fourier transform, sampling and multiplication with complex gains. The forward problem reads as follows: Given the input/image  $I$ , predict the measured data (i.e. visibilities)  $g^\delta$ . The inverse problem asks the reverse question: Given the noisy observed data  $g^\delta$ , what was the input array (Kirsch 2011)?

Interestingly, even if the forward problem has analytically desirable properties, e.g. it is smooth, convex, compact, bounded or Lipschitz-continuous, the inverse problem is typically harder to solve (Kirsch 2011). We call an inverse problem well-posed, if there exists a solution (existence), the solution is unique and depends continuously on the input parameters. If one of these criteria fail, we call the inverse problem ill-posed (Hadamard & Morse 1953). This is the situation in VLBI: There are non-measured Fourier coefficients, i.e. missing information. The stability requirement is most crucial since existence and uniqueness conditions could be achieved by enlarging or shrinking the domain of possible solutions (Kirsch 2011). An ill-conditioned inverse problem is typically unstable against observational noise, i.e. the naive inversion by the pseudo-inverse operator could amplify observational noise. This is the case if the (pseudo-)inverse operator is not bounded.

A simple example of such a problem can be formulated in the context of linear inverse problems: If the sequence of singular values has a (weak) accumulation point at zero, the inverse operator (if it exists at all) will be unbounded, as the singular values of the inverse operator are the inverse of the singular values of the forward operator. A naive inversion could therefore lead to an arbitrary increase of noise effects during reconstruction. The prime example of such an analytically invertible, but ill-conditioned problem is inverting a Gaussian convolution, i.e. deblurring. A deconvolution, following the Fourier convolution theorem, would require dividing by the Fourier transform of a Gaussian filter which decreases exponentially fast to zero with Fourier frequency. Image reconstruction employing this type of deconvolution is prone to be unstable against observational noise  $\epsilon_\delta$ , and this is the typical situation in VLBI.

Another simple ill-posed inverse problem is (numerical) differentiation (Varah 1983). The corresponding forward operator is the integral operator, respectively its discretization. While there exists a simple unique solution, it is unstable against noise. The differential quotient could grow large for a noise distribution that is rapidly varying from pixel to pixel.

Inverse problems should not be confused with simple fitting problems. A linear, invertible operator between finite dimensional Hilbert spaces always has a bounded inverse: In the finite manifold of singular values, there is a well defined smallest singular value unequal to zero (invertibility). Inverse problems typically arise in infinite dimensional reconstruction problems, i.e. the reconstruction of an image (sky brightness distribution) from its sparse Fourier transform. However, in practice a pixelized finite representation, i.e. on a grid, always has to be used for computations.

## 2.2.2 Regularization Theory

For perturbed data, we aim to recover an approximation of the true solution that fits the observed (noisy) data at the level of the noise (Kirsch 2011). To this end, we call the procedure to approximate an ill-posed inverse problem by a family of single-valued, stable reconstruction problems *regularization* (Morozov 1967). There are various approaches to introduce regularization to an ill-posed problem, and they all share great similarity. We describe here the motivation behind the *generalized/non-linear Tikhonov regularization*. In the VLBI community, the same idea is known under the name Regularized Maximum Likelihood (RML) or Maximum Entropy Method (MEM). First we reformulate the problem stated in Eq. (2.1) as an optimization problem. We look for a guess solution  $\hat{I}$  such that:

$$\hat{I} \in \operatorname{argmin}_f \left\{ \left\| g^\delta - Ff \right\|^2 =: T^F(g^\delta, f) \right\}. \quad (2.2)$$

Note that the norm is always non-negative and, in the absence of noise, for the true solution  $I$ , the argument in the norm would vanish. Hence, Eq. (2.2) is equivalent to the original, non-regularized formulation of the inverse problem. The minimum is still multi-valued (ill-posedness). Moreover, in the presence of noise we find a guess solution that fits the data and the noise distribution (overfitting). Hence, a second term is added (Kirsch 2011; Landweber 1951; Tikhonov 1963a,b):

$$\hat{I}_{\alpha_\delta} \in \operatorname{argmin}_f \left\{ \left\| g^\delta - Ff \right\|^2 + \alpha_\delta R(f) =: T_{\alpha_\delta, R}^F(g^\delta, f) \right\}, \quad (2.3)$$

where  $R$  is called the regularization term and  $\alpha_\delta \in [0, \infty)$  is the regularization parameter depending on the noise level  $\delta$ . The regularization term measures the feasibility of the solution: among all the possible (pseudo-)optimal solutions (ill-posedness) we choose the one that is most feasible according to our perception of the image structure. In many cases, this prior information just includes a simplicity assumption, i.e. we recover the simplest solution that still fits the data. However, more advanced priors are possible as well (see e.g. Akiyama et al. 2017b; Chael et al. 2016, for a variety of regularization terms in VLBI). Note that  $T_{\alpha_\delta, R}^F$  is an approximation to  $T^F$ , and in particular  $T_{\alpha_\delta, R}^F \rightarrow T^F$  for  $\alpha_\delta \rightarrow 0$ . Moreover, if the regularization term  $R$  is well-chosen, every operator  $T_{\alpha_\delta, R}^F(g^\delta, \cdot)$  has a well-defined, single-valued guess solution (minimum)  $\hat{I}_{\alpha_\delta}$  that is stable against noise. Hence, as a rationale, to account for ill-posedness, we approximate the multi-valued inverse problem (formulated as an optimization problem) by a sequence of single-valued and robust objective functionals that converge to the initial inverse

problem if the noise level converges to zero (Kirsch 2011). Originally, Tikhonov regularization was proposed with an  $l^2$ -prior. However, in what follows we will apply the term *generalized Tikhonov regularization* to every regularization approach that tries to solve the reconstruction problem by minimizing a weighted sum of data fidelity terms and regularization terms:

$$\hat{I} \in \operatorname{argmin}_f \left\{ \sum_i \alpha_i S_i(g^\delta, Ff) + \sum_j \beta_j R_j(f) \right\}, \quad (2.4)$$

with data fidelity terms  $S_i$ , regularization terms  $R_j$  and regularization parameters  $\alpha_i, \beta_j$ . The data fidelity terms measure the proximity of the guess solutions to the observed data. The regularization terms measure the feasibility of the guess solutions. The regularization parameters control the tradeoff between fitting the data and feasibility of the solution. By minimizing a weighted sum of data fidelity terms and regularization terms, an optimal solutions is found that fits the data and is feasible according to the used priors.

### 2.2.3 Convex Optimization

As described in chapter 2.2.2, we solve inverse problems by minimizing a complex objective functional such as Eq. (2.4). A description of the solution of inverse problems therefore requires some background in optimization theory. A detailed overview is provided in Boyd & Vandenberghe (2004). Optimization can be broadly divided into two classes: convex and non-convex optimization. We will concentrate on convex optimization for this discussion. However, we should mention that some VLBI data products (i.e. closure quantities) and regularization terms ( $l^0$ -penalization) are not convex. Hence, for example the objective functional of the DoG-HiT algorithm is non-convex. A more rigorous convergence analysis is needed in this case and will be discussed in chapter 3.

A functional  $T : \mathbb{X} \rightarrow [0, \infty]$  is called convex if (Boyd & Vandenberghe 2004):

$$T(rx_1 + (1-r)x_2) \leq rT(x_1) + (1-r)T(x_2) \quad (2.5)$$

holds for all  $x_1, x_2 \in \mathbb{X}$  and  $r \in [0, 1]$ . Moreover, a functional is called strictly convex if strict inequality holds true. Strict convexity warrants uniqueness of the minimization problem by a simple contradiction argument: assume that  $T$  would have multiple minima. Let  $x_1 \neq x_2 \in \mathbb{X}$  be two of these  $T$ -minimizing solutions. Then every combination of the form  $x_3 = rx_1 + (1-r)x_2$  would be a smaller minimum according to strict convexity of  $T$ , i.e.  $T(x_3) < T(x_1) = T(x_2)$ , which is a contradiction to the initial assumptions.

If all terms in the objective functional would be smooth, minimization could be done with gradient based minimization procedures. The simplest minimization procedure is steepest descent (first proposed by Debye 1909), i.e. we minimize the objective in Eq. (2.4) by the iteration:

$$f \leftarrow f - \gamma \left\{ \sum_i \alpha_i \partial S_i(g^\delta, \cdot)(Ff) \nabla F(f) + \sum_j \beta_j \nabla R_j(f) \right\}, \quad (2.6)$$

with a stepsize parameter  $\gamma$ . A wide range of more sophisticated variants exist that allow for convergence acceleration, implicit schemes, additional constraints, an improved numerical performance and a more global search spectrum, e.g. acceleration by Nesterov's heavy ball algorithm (Nesterov 1983), conjugate gradient methods (Fletcher & Reeves 1964; Hestenes & Stiefel 1952), Broyden-Fletcher-Goldfarb-Shanno (BFGS) methods and its variants (Broyden 1970; Byrd et al. 1995; Fletcher 1970; Goldfarb 1970; Shanno 1970), or the Levenberg-Marquardt algorithm (Levenberg 1944; Marquardt 1963). We will not go into more details here.

Not all terms in an objective functional of the form of Eq. (2.4) are smooth. In particular, sparsity promoting regularization terms ( $l^1$ -norm, total variation) do not have a single-valued gradient. Since these terms are typically convex, we can use tools of convex optimization instead. However, there are prominent exceptions, in particular in VLBI (see chapter 3 for more details). The following paragraph is rewritten from the publication Müller & Lobanov (2022) related to this dissertation. We assume an objective functional of the form of  $T_{\alpha_S, R}^F(g^\delta, f)$ , see Eq. (2.3), for this discussion with a smooth functional  $S$  and a convex functional  $R$ , i.e. we have splitted the objective into the smooth and the convex part. In general we define the proximal-operator of a generic functional  $H$  defined on a Hilbert space  $\mathbb{X}$  by (Müller & Lobanov 2022):

$$\text{prox}_{\tau, H}(z) = \operatorname{argmin}_{s \in \mathbb{X}} \left\{ H(s) + \frac{1}{2\tau} \|s - z\|_{\mathbb{X}} \right\}. \quad (2.7)$$

If  $H$  is proper, lower-semi-continuous and convex, then  $\text{prox}_{\tau, H}$  is well-defined (Moreau 1962). We can prove now that:

$$\hat{s} \in \operatorname{argmin}_s H(s) \iff \hat{s} = \text{prox}_{\tau, H}(\hat{s}) \quad (2.8)$$

holds true independently of  $\tau \geq 0$ . A sketch of the proof is presented in Appendix A of Müller & Lobanov (2022) and reprinted in chapter 3. Hence, applied to  $T_{\alpha_S, R}^F(g^\delta, f)$ , we get the two-step minimization procedure (Combettes & Pesquet

2011):

$$f \leftarrow \text{prox}_{\tau\alpha, R}(f - \tau\nabla F(g^\delta - Ff)). \quad (2.9)$$

These types of algorithms are called forward-backward splitting as they split the iterations in a gradient-based forward step and a proximal point based backward step. Most optimization problems occurring in VLBI imaging need to be solved with these kind of minimizers due to the complexity and non-smoothness of the optimization terms involved. Again, it is worth mentioning that acceleration techniques and more advanced variants of the forward-backward splitting algorithm exist, e.g. fast iterative soft shrinkage thresholding (FISTA) first proposed by Beck & Teboulle (2009) or recently proposed primal-dual algorithms (Chambolle & Pock 2011).

Most convex optimization algorithms such as forward-backward splitting are formulated in the framework of Eq. (2.4), i.e. with only one smooth data term and one convex penalty term (Combettes & Pesquet 2011; Kirsch 2011). However, in VLBI we typically deal with a larger combination of terms (Chael et al. 2016; Event Horizon Telescope Collaboration et al. 2019b, 2022b) which makes slight extensions of the underlying optimization tools necessary. An alternative approach would be multiobjective optimization methods, i.e. evolutionary algorithms (Müller et al. 2023d; Zhang & Li 2007).

## 2.3 VLBI Data Products

In the previous subsection, we introduced the *generalized Tikhonov regularization* method as a minimization of a weighted sum of data fidelity terms and penalty terms. We focus in this chapter on the data fidelity terms, i.e. on the VLBI data products that we try to fit. We first discuss interferometric visibilities as the most important data products and then extend the discussion to more abstract data products such as closure quantities and polarimetric visibilities.

### 2.3.1 Visibilities

The prime data product coming out of an observation by a VLBI experiment are the observed visibilities  $V$ . The fit quality of a guess solution  $\hat{I}$  to the observed visibilities is typically expressed by the reduced  $\chi^2$ :

$$S_{\text{vis}}(V, \cdot) : W \mapsto \frac{1}{N_{\text{vis}}} \sum_{i=1}^{N_{\text{vis}}} \frac{|W_i - V_i|^2}{\epsilon_i^2}, \quad (2.10)$$

where  $N_{\text{vis}}$  is the number of observed visibilities,  $\epsilon_i$  the estimated thermal noise of a given visibility and  $W = \mathcal{F}\hat{I}$  the forwarded visibilities of the current guess  $\hat{I}$ . Similarly, the quality of the fit to the observed data can be expressed in the image domain by the magnitude of the residual  $I^{\text{res}}$  in natural weighting:

$$I^{\text{res}} = \mathcal{F}^{-1} \mathbf{G} \sum_{i=1}^{N_{\text{vis}}} \frac{W_i - V_i}{\epsilon_i} \delta(u_i, v_i), \quad (2.11)$$

with the gridding operator  $\mathbf{G}$  introduced earlier. Due to the unitary of the Fourier transform (i.e. the Fourier transform does not change the norm) it is:

$$\|I^{\text{res}}\|^2 = N_{\text{vis}} S_{\text{vis}}(V, W), \quad (2.12)$$

where we ignored aliasing and sampling errors due to the sampling and gridding of the Fourier coefficients. We call the initial residual corresponding to  $W = 0$  the *dirty map*:

$$I^D = \mathcal{F}^{-1} \mathbf{G} \sum_{i=1}^{N_{\text{vis}}} \frac{V_i}{\epsilon_i} \delta(u_i, v_i), \quad (2.13)$$

There exist several variants of  $S_{\text{vis}}$  in practice (and in particular for inverse modeling approaches).

First, it has become common practice in mm-VLBI to add a small systematic noise floor to the error budget to correct for non-accounted thermal errors or telescope pointing errors (Event Horizon Telescope Collaboration et al. 2019b, 2022b). Moreover, this additional noise floor would prohibit  $S_{\text{vis}}$  to be driven by single data points with nonphysically small system temperature estimates.

Second, when computing the residual, weighting schemes other than the *natural* one could be introduced (Taylor et al. 1999). A prominent alternative is *uniform* weighting. The uniform weighting accounts for the fact that in most VLBI arrays more short baselines exist than long baselines, hence large scale structures are favored. With the uniform weighting, every grid cell after the gridding gets the same weight, regardless of the number and significance of the visibility points sampled in it, thus giving more weight to the longer baselines (Taylor et al. 1999). In order to formulate different weighting schemes, let us first introduce the ungridded data weights,  $\omega_i$ , as the inverse variance by  $\omega_i = 1/\epsilon_i^2$ . Then we define the grid weights  $\mathcal{W}_i$  as the gridded inverse variances  $\omega_i$  over a grid size of  $2/\text{FOV}$  (where FOV is the field of view). The uniform weights are

(Briggs 1995):

$$w_i^{\text{uniform}} = \frac{\omega_i}{\mathcal{W}_i}. \quad (2.14)$$

Both weighting schemes are unified in the Briggs-weighting scheme (Briggs 1995):

$$w_i^{\text{robust}} = \frac{\omega_i}{1 + \mathcal{W}_k s^2} \quad (2.15)$$

$$s^2 = \frac{(5 \cdot 10^{-r})^2}{\frac{\sum_i \mathcal{W}_i^2}{\sum_i \omega_i}} \quad (2.16)$$

with Briggs robustness parameter  $r$ .

If desired, one could introduce additional weights at the gridding stage manually with a tapering function. A taper is a Gaussian function of the  $uv$ -radius that is multiplied to the observed and recovered visibilities. A taper therefore gives more weight to the short baselines. Less common, also inverse tapers were used (Event Horizon Telescope Collaboration et al. 2019b).

An important consideration arises in radio interferometry from the fact that the visibilities are complex numbers, i.e. they consist of an amplitude and a phase. After calibration, the phase is often more unstable than the amplitudes, such that it is beneficial in some cases to calculate the fit to the observed amplitudes only:

$$S_{\text{amp}}(V, \cdot) : W \mapsto \frac{1}{N_{\text{vis}}} \sum_{i=1}^{N_{\text{vis}}} \frac{(|W_i| - |V_i|)^2}{\epsilon_i^2}. \quad (2.17)$$

It should be stressed here that for all weighting schemes the functionals  $S_{\text{vis}} \circ \mathcal{F}$  is differentiable and convex.

### 2.3.2 Closure Quantities

Visibilities (amplitudes and phases) are corrupted by errors in the measured antenna gains, compare chapter 1.4.5. Hence, fidelity criteria such as  $S_{\text{vis}}$  are prone to calibration effects. Closure quantities, i.e. closure phases and closure amplitudes, are gain-independent alternatives. A closure phase is the added phase over a closed triangle of antennas  $i, j, k$ . It is (Taylor et al. 1999):

$$\Psi_{i,j,k} = \arg(V_{ij}V_{jk}V_{ki}^*) = \arg(\mathcal{V}_{ij}\mathcal{V}_{jk}\mathcal{V}_{ik}^*) + \arg(g_i g_j^* g_j g_k^* g_k g_i^*) = \arg(\mathcal{V}_{ij}\mathcal{V}_{jk}\mathcal{V}_{ik}^*),$$

in the absence of thermal noise. Hence, closure phases are independent of antenna based gains. A similar property are closure amplitudes comprising the ratio of

visibility amplitudes over a quadrangle of antennas  $i, j, k, l$  (Taylor et al. 1999):

$$A_{i,j,k,l} = \frac{|V_{i,j}||V_{k,l}|}{|V_{j,k}||V_{l,i}|} = \frac{|\mathcal{V}_{i,j}||\mathcal{V}_{k,l}|}{|\mathcal{V}_{j,k}||\mathcal{V}_{l,i}|} \times \frac{|g_i g_j^* g_k g_l^*|}{|g_i^* g_j g_k^* g_l|} = \frac{|\mathcal{V}_{i,j}||\mathcal{V}_{k,l}|}{|\mathcal{V}_{j,k}||\mathcal{V}_{l,i}|}. \quad (2.18)$$

Hence, closure amplitudes are also independent of antenna based gains. For forward modeling approaches, closure phases and closure amplitudes could be directly used as data fidelity quantities:

$$S_{\text{cph}}(V, \cdot) : W \mapsto \frac{1}{N_{\text{cph}}} \sum_{i=1}^{N_{\text{cph}}} \frac{|\Psi_i(W) - \Psi_i(V)|^2}{\epsilon_{\text{cph},i}^2}, \quad (2.19)$$

where  $N_{\text{cph}}$  is the number of independent closure phase combinations and  $\Sigma_{\text{cph},i}$  the noise on a closure phase  $\Psi_i(V)$ . Similarly we define:

$$S_{\text{ca}}(V, \cdot) : W \mapsto \frac{1}{N_{\text{ca}}} \sum_{i=1}^{N_{\text{ca}}} \frac{|A_i(W) - A_i(V)|^2}{\epsilon_{\text{ca},i}^2}, \quad (2.20)$$

with analogous notation. Instead of the amplitudes, sometimes the logarithm of the closure amplitudes is used to give more weight to small amplitudes and in particular the separation between vanishing visibilities and small signals:

$$S_{\text{cla}}(V, \cdot) : W \mapsto \frac{1}{N_{\text{cla}}} \sum_{i=1}^{N_{\text{cla}}} \frac{|\ln A_i(W) - \ln A_i(V)|^2}{\epsilon_{\text{cla},i}^2}. \quad (2.21)$$

It is important to note that Eq. (2.19), Eq. (2.20) and (2.21) are only approximations to the correct log-likelihoods for closure products, see e.g. Arras et al. (2022); Blackburn et al. (2020).

Chael et al. (2018) explored the possibility to carry out interferometric imaging using only the closure quantities, with promising results that found application in later EHT data reductions (see Event Horizon Telescope Collaboration et al. 2019b, 2022b). An important characteristics in imaging with closure quantities is the number of independent closure phases and closure amplitudes. If there are  $N_{\text{ant}}$  antennas in the array, then the number of independent visibilities at a single time is:

$$N_{\text{vis}} = \frac{N_{\text{ant}}(N_{\text{ant}} - 1)}{2}. \quad (2.22)$$

Chael et al. (2018) estimated the number of independent closure phases to be:

$$N_{\text{clp}} = \frac{(N_{\text{ant}} - 1)(N_{\text{ant}} - 2)}{2} = \left(1 - \frac{2}{N_{\text{ant}}}\right) N_{\text{vis}}. \quad (2.23)$$

and the number of independent closure amplitudes to be:

$$N_{\text{cla}} = \frac{N_{\text{ant}}(N_{\text{ant}} - 3)}{2} = \left(1 - \frac{2}{N_{\text{ant}} - 1}\right) N_{\text{vis}}. \quad (2.24)$$

Thus, there are fewer degrees of freedom in the closure quantities. These show up in two degeneracies particularly. First, closure amplitudes and closure phases are independent against the image shift, i.e. the absolute position information is not maintained. Second, closure phases and closure amplitudes are independent against rescaling the image with a constant number  $\lambda > 0$ . Hence, total flux information is also lost and therefore strict convexity is broken.

Moreover, we have to bring up the issue noted first in Lockhart & Gralla (2022a). While closure phases and closure amplitudes are independent of antenna based gains, the statistical errors of the closure quantities are not. Lockhart & Gralla (2022a) presented two natural approximations for the variance: The variable model (using data visibilities  $V$  to compute the error) and the fixed model (using the model visibilities  $W$ ). The choice affects the final reconstruction results. The  $\chi^2$ -fit quality to the closure quantities (i.e.  $S_{\text{ca}}, S_{\text{cp}}$ ) has been used in VLBI for decades to quantify the goodness of the fit independent of antenna based gains. This is simply a wrong assumption according to the findings in Lockhart & Gralla (2022a). However, application in practice demonstrated that closure-only imaging still performs very robustly against gain corruptions (e.g. compare the extensive synthetic data validations in Chael et al. 2018; Event Horizon Telescope Collaboration et al. 2019b, 2022b).

### 2.3.3 Polarimetry

Synchrotron sources show typically some degree of polarization. Let us write down the electric field as a vector with two orthogonal components in the plane (x,y) perpendicular to the direction of field propagation (Thompson et al. 2017):

$$\begin{pmatrix} E_x(t) \\ E_y(t) \end{pmatrix} = \begin{pmatrix} \tilde{E}_x(t) \cos(2\pi\nu t + \phi_x(t)) \\ \tilde{E}_y(t) \cos(2\pi\nu t + \phi_y(t)) \end{pmatrix}, \quad (2.25)$$

with frequency  $\nu$  (assuming monochromaticity), phase-shift  $\phi$  and amplitude modulation  $\tilde{E}$ . Then the Stokes parameters are defined by (Thompson et al.

2017):

$$I = \langle \tilde{E}_x^2(t) \rangle + \langle \tilde{E}_y^2(t) \rangle \quad (2.26)$$

$$Q = \langle \tilde{E}_x^2(t) \rangle - \langle \tilde{E}_y^2(t) \rangle \quad (2.27)$$

$$U = 2\langle \tilde{E}_x(t)\tilde{E}_y(t)\cos(\phi_x(t) - \phi_y(t)) \rangle \quad (2.28)$$

$$V = 2\langle \tilde{E}_x(t)\tilde{E}_y(t)\cos(\phi_x(t) + \phi_y(t)) \rangle. \quad (2.29)$$

The Stokes parameters describe the polarization state of the incoming signal. Stokes  $I$  is the total intensity, Stokes  $Q$  and  $U$  (orthogonal) linear polarization and  $V$  circular polarization. It follows directly that the inequality:

$$I^2 \geq Q^2 + U^2 + V^2 \quad (2.30)$$

holds true. We can identify the Stokes visibilities from the Stokes parameters by a Fourier transform (Thompson et al. 2017):

$$\mathcal{V}_I = \mathcal{F}I \quad (2.31)$$

$$\mathcal{V}_Q = \mathcal{F}Q \quad (2.32)$$

$$\mathcal{V}_U = \mathcal{F}U \quad (2.33)$$

$$\mathcal{V}_V = \mathcal{F}V \quad (2.34)$$

We denote the action on an electric field by Jones matrices. An antenna in the VLBI array observes the polarimetric source in two perpendicular polarization filter (either orthogonal linear polarization or opposite circular polarization, Thompson et al. (2017)). The antenna based gains could vary between both bands. Hence, gains are represented by the Jones matrix (Thompson et al. 2017):

$$\mathbf{J}_{\text{gain}} = \begin{pmatrix} g_x & 0 \\ 0 & g_y \end{pmatrix}. \quad (2.35)$$

Moreover, we have to calibrate for the rotation of the polarization surface relative to the antenna by an angle  $\theta$  (Thompson et al. 2017):

$$\mathbf{J}_{\text{rotation}} = \begin{pmatrix} \exp(i\theta) & 0 \\ 0 & \exp(-i\theta) \end{pmatrix}, \quad (2.36)$$

and the leakage between the polarization filter (Thompson et al. 2017):

$$\mathbf{J}_{\text{leakage}} = \begin{pmatrix} 1 & d_x \\ d_y & 1 \end{pmatrix}. \quad (2.37)$$

We combine these corruption effects into an antenna based Jones matrix  $\mathbf{J} = \mathbf{J}_{\text{gain}}\mathbf{J}_{\text{rotation}}\mathbf{J}_{\text{leakage}}$ . When we multiply the two polarization bands from two antennas  $i, j$  we get four correlation products. This is short noticed by the outer product  $\otimes$ :

$$\mathbf{s}_{i,j}(t) := (\mathbf{J}_i\mathbf{E}_i(t)) \otimes (\mathbf{J}_j^*\mathbf{E}_j^*(t)) = (\mathbf{J}_i \otimes \mathbf{J}_j^*)(\mathbf{E}_i(t) \otimes \mathbf{E}_j^*(t)) \quad (2.38)$$

We have shown in chapter 1.4.2 that, when we integrate the multiplied quantities over time (i.e. correlating), the resulting quantity is related to the visibilities. Exactly the same computation, but for all four components, shows now (Thompson et al. 2017):

$$\mathbf{r}_{i,j} = \langle \mathbf{E}_i(t) \otimes \mathbf{E}_j^*(t) \rangle = \begin{pmatrix} r_{i,j}^{xx} \\ r_{i,j}^{xy} \\ r_{i,j}^{yx} \\ r_{i,j}^{yy} \end{pmatrix} = \begin{pmatrix} 1 & 1 & 0 & 0 \\ 0 & 0 & 1 & i \\ 0 & 0 & 1 & -i \\ 1 & -1 & 0 & 0 \end{pmatrix} \begin{pmatrix} \mathcal{V}_I(u_{ij}, v_{ij}) \\ \mathcal{V}_Q(u_{ij}, v_{ij}) \\ \mathcal{V}_U(u_{ij}, v_{ij}) \\ \mathcal{V}_V(u_{ij}, v_{ij}) \end{pmatrix}, \quad (2.39)$$

for linear polarization, compare Eq. (2.26), (2.27), (2.28) and (2.29). The calculation for circular polarization is analogous (with a different base) and is therefore not repeated here. Hence, in polarimetry, the correlation products of each antenna pair give rise to four different visibilities corresponding to the four Stokes parameters. Similarly to our discussions in chapter 2.3.1, we can therefore also define data fidelity terms for the Stokes visibilities  $Q, U, V$ . In consistency with our notation before we denote the measured visibilities by:

$$\mathbf{s}_{i,j} = \begin{pmatrix} V_I^{ij} \\ V_Q^{ij} \\ V_U^{ij} \\ V_V^{ij} \end{pmatrix} \quad (2.40)$$

Recently Broderick & Pesce (2020) also derived closure quantities for polarimetric properties: the closure traces. We define the visibility matrix  $\mathbf{V}_{ij}$  for an antenna pair  $ij$  first:

$$\mathbf{V}_{ij} = \begin{pmatrix} V_I^{ij} + V_V^{ij} & V_Q^{ij} + iV_V^{ij} \\ V_Q^{ij} + iV_V^{ij} & V_I^{ij} - V_V^{ij} \end{pmatrix} \quad (2.41)$$

Then the trace over a quadrangle of antennas  $i, j, k, l$ :

$$Tr_{ijkl} = \frac{1}{2} \text{trace} \left( \mathbf{V}_{ij}\mathbf{V}_{kj}^{-1}\mathbf{V}_{kl}\mathbf{V}_{il}^{-1} \right) \quad (2.42)$$

is independent of the corruption matrices  $\mathbf{J}$  (Broderick & Pesce 2020). Hence,  $Tr_{ijkl}$  is independent of leakage terms, gain amplitudes, and gain phases. Closure traces have been used for calibration (Event Horizon Telescope Collaboration et al. 2021a), but not for imaging yet. A serious drawback of closure traces is its independence against rotations in the Poincare-sphere (Broderick & Pesce 2020).

### 2.3.4 Extended Imaging Problems

The classical imaging problem described above has several important extensions, including multifrequency imaging, dynamical imaging and spectral imaging. In dynamical imaging, we do not recover a single image  $I(l, m)$  from our data, but a movie  $I(l, m, t)$ , i.e. we extend the imaging problem to the time domain. For dynamical imaging, the problem is decomposed into several scans of shorter length. Instead of a quality of fit metric for the full observation, we use a quality of fit metric on each individual sub-scan. Roelofs et al. (2023) provide an overview over the current approaches for dynamical imaging. We provide a more comprehensive overview on the reconstruction of dynamics in chapter 3.4.

For spectral imaging, imaging is extended to the spectral domain. If there is an isolated emission line in the spectrum (such as the hyperfine structure line of hydrogen), the spectral dimension could be associated to the radial direction due to the Hubble redshift, e.g. compare 21 cm intensity mapping.

For multifrequency imaging, data of several frequency bands are combined. The multifrequency data set is fitted by a suitable common model with built-in spectral variability (Chael et al. 2023). For these reconstructions, the data fidelity term is a (weighted) sum of the data fidelity terms at single frequencies.

## 2.4 Imaging with CLEAN Deconvolution

The original CLEAN algorithm (Högbom 1974) and its many variants (Bhatnagar & Cornwell 2004; Clark 1980; Cornwell 2008; Müller & Lobanov 2023a; Rau & Cornwell 2011; Sault & Wieringa 1994; Schwab 1984) have been the de-facto standard in VLBI for the last decades, mainly because they are practical. We present the CLEAN algorithm in this chapter, and discuss its convergence, limitations and extensions. A schematic overview of usual CLEAN methods proposed for VLBI is presented in Fig. 2.15.

### 2.4.1 Algorithm

For CLEAN the imaging problem is equivalently reformulated as a deconvolution problem with the dirty map  $I^D$ , i.e. the first residual, compare Eq. (2.13), and

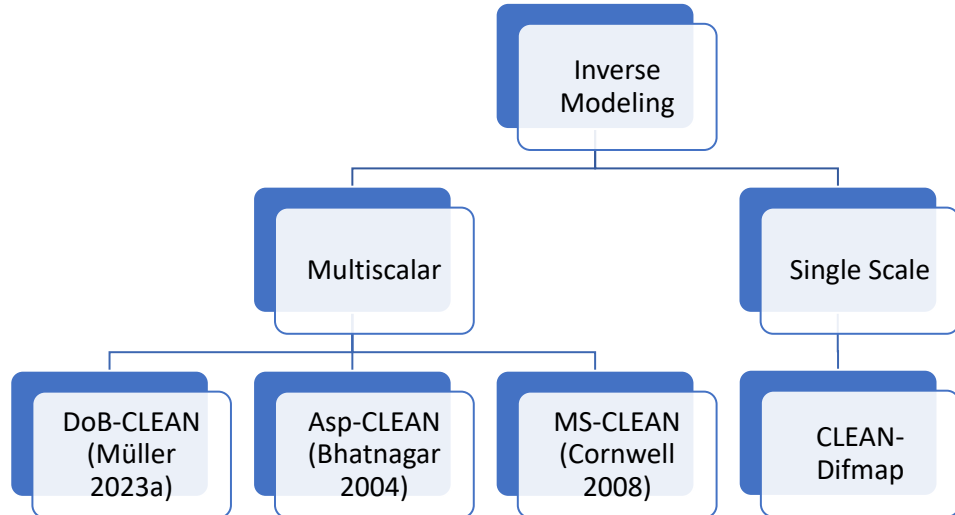


Figure 2.15: Overview of inverse modeling imaging methods (i.e. variants of CLEAN) that have been applied to VLBI. We spare here CLEAN methods that have been proposed for non-VLBI applications such as wide-field imaging.

the dirty beam  $B^D$ , see Eq. (1.9):

$$I^D = B^D * I, \quad (2.43)$$

where  $I$  is the true sky brightness distribution. As discussed in chapter 1.4.5, the dirty beam is a superposition of weighted spherical Bessel functions. The dirty beam always has a central peak (limiting resolution) and a range of sidelobes. With CLEAN, we try to reduce the sidelobes from the image. For this we define a Gaussian clean beam  $B^C$  that is fitted to the central component of the dirty beam, i.e. a beam that only contains the main lobe of the dirty beam, but not the sidelobes. CLEAN consists of the following steps (Högbom 1974), see also the sketched outline in Fig. 2.16:

1. We search for the biggest peak in the current residual. Instead of searching the complete field of view, we only look for peaks in user defined (manually drawn) search windows (CLEAN windows). The windowing in CLEAN is typically a subjective operation aimed at restricting the algorithm application to the true emission regions and excluding contributions from beam sidelobes and other potential artifacts. We store the position and the strength of the recently found peak in a list of delta-components (CLEAN components).
2. We shift the dirty beam to the position of the maximal peak in the residual and rescale it to a fraction (the CLEAN gain) of the strength of the last found maximum in the residual.

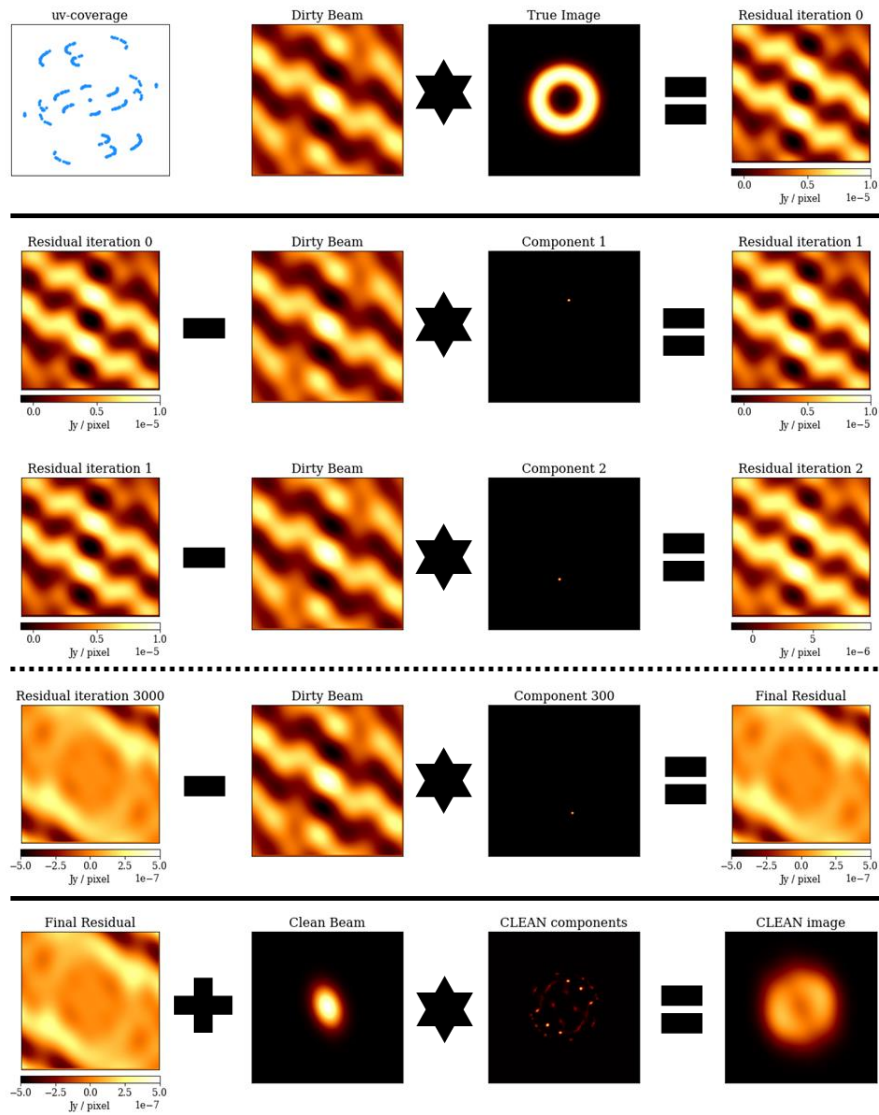


Figure 2.16: Illustration of the CLEAN algorithm. We reformulate the problem as a deconvolution problem. The dirty map is the convolution of the dirty beam with the true image. In every iteration we search for the maximal peak in the residual and subtract the rescaled and shifted dirty beam from the dirty beam. Finally we convolve the list of all these CLEAN image with the clean map and add the last residual.

3. We substitute the rescaled and reshifted dirty beam from the residual/dirty map and update the dirty map. Then we iterate these three steps again until the residual looks noise-like. This procedure is illustrated in the middle panels of Fig. 2.16.

In this way, we compute a list of CLEAN components  $\{a_0\delta(l_0, m_0), a_1\delta(l_1, m_1), \dots, a_n\delta(l_n, m_n)\}$  that approximates the initial dirty map, i.e.:

$$I^D \approx B^D * \left( \sum_{i=0}^n a_i \delta(l_i, m_i) \right). \quad (2.44)$$

The recovered physical image (the clean map) will be (compare the last row in Fig. 2.16):

$$I^C = B^C * \left( \sum_{i=0}^n a_i \delta(l_i, m_i) \right). \quad (2.45)$$

As a common practice, we add the last residual to the clean map as well.

CLEAN is a straightforward algorithm that allows for manual interaction and adjustments between its successive major cycles. The scientist performing CLEAN has the freedom to manipulate the CLEAN procedure: by drawing CLEAN windows, by reweighting the observed visibilities by a taper or by a different weighting scheme, or by calibrating and flagging the data points itself. In particular, interactive self-calibration is important in mm-VLBI where reliable phase information often is lost. The hybrid approach of interactively alternate imaging and self-calibration is called hybrid imaging and discussed in more detail in chapter 2.5.

CLEAN is a greedy matching pursuit approach to solve the imaging problem by inversely modeling the emission from the dirty image. However, it can be shown that, under certain circumstances, it can be viewed as an instance of the generalized Tikhonov method with  $l^0$  penalty term in the pixel basis and  $S_{\text{vis}}$  (with corresponding weighting scheme) as data fidelity term (Lannes et al. 1997).

### 2.4.2 Convergence

The first mathematical proof for the convergence of the CLEAN algorithm in the absence of thermal noise and antenna based gains was derived by Schwarz (1978). We will not reiterate the rigorous mathematical statement, but rather present the idea behind the convergence of CLEAN in this chapter. Let us denote the current model (list of delta components) after  $k$  CLEAN iterations by  $M_k = \left( \sum_{i=0}^k a_i \delta(l_i, m_i) \right)$ . Then  $M_{k+1}$  differs from  $M_k$  by  $\Delta M_k = \mathcal{G} r_k \delta(l_k, m_k)$  where  $\mathcal{G}$

denotes the CLEAN gain and  $r_k = \max I_k^{res}$  the maximum in the  $k$ -th residual. Let us define the sequence  $Q_k$  by:

$$Q_k = \langle I_k - I, B^D * (I_k - I) \rangle. \quad (2.46)$$

Then simple numerics shows:

$$\Delta Q_k = Q_{k+1} - Q_k = (\mathcal{G}^2 - 2\mathcal{G}) r_k^2. \quad (2.47)$$

Hence, for all gains  $\mathcal{G} \in [0, 2]$ ,  $\Delta Q_k$  is always negative. Thus,  $Q_k$  is strictly monotonically decreasing. Note that the dirty beam is positive semi-definite (Fourier transform is unitary, and the Fourier transform of the dirty beam only contains non-negative harmonics). Hence,  $Q_k$  is bounded from below by 0. Thus,  $Q_k$  is converging. Schwarz (1978) deduced convergence from here, however strict monotonicity does not prove convergence to zero. To get  $Q_k \rightarrow 0$ , we need an additional argument. Since  $Q_k$  is converging, it holds  $\Delta Q_k \rightarrow 0$ . By Eq. (2.47) we get  $r_k \rightarrow 0$ . Since  $r_k$  was defined as the maximum of the residual  $I_k^{res}$ , we see that the residuals are converging to zero array-wise as well:  $I_k^{res} \rightarrow 0$ . Schwarz (1978) obtained the CLEAN convergence to the true solution by assuming positive definiteness of the dirty beam. This may be approximately true for dense arrays with a moderate degree of undersampling, but does not hold for sparse VLBI arrays once the missing data issue becomes prevalent. Thus, we can only conclude that  $B^D * (I - I_k) \rightarrow 0$ , i.e. the difference between the true image and the CLEAN model is in the kernel of the dirty beam.

There is no proof for the convergence of CLEAN in the presence of noise. Similar arguments as before show, in the presence of noise, that  $I_k^{res} \rightarrow 0$ . However, this is prone to overfitting the noise distribution as the residual  $I_k^{res} = I - I_k + N$  is perturbed by a random noise field  $N$ . Therefore, it is crucial to stop CLEAN before the algorithm starts to overfit noise. The stopping rule plays the role of an effective regularization parameter in this case. However, a valid stopping criterion does not exist due to the unknown correlation structure of the observed visibilities and the respective noise contribution. In practice, it is rather done based on a manually inspection of the data. The problem is further complicated by the existence of calibration issues in the data, i.e. the need for self-calibration during the imaging (hybrid imaging).

### 2.4.3 Limitations of CLEAN

While being the standard imaging tool in VLBI, CLEAN has some serious limitations. We summarized these limitations in Müller & Lobanov (2023c). Here

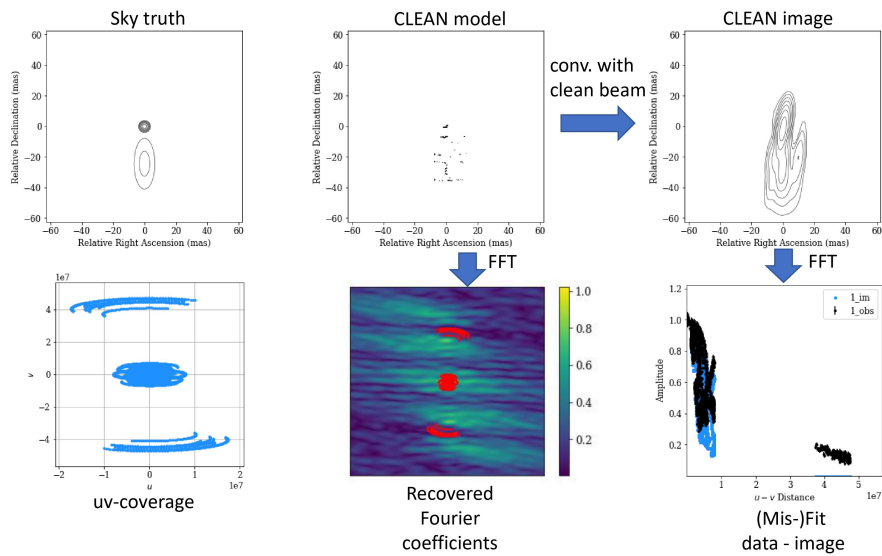


Figure 2.17: Illustration of the disparity issue related to CLEAN with synthetic EVN data. Upper left panel: The ground truth image. Bottom left panel: The uv-coverage. Upper middle panel: The model computed by CLEAN. The model is a set of CLEAN components. Bottom middle panel: The recovered visibilities from the CLEAN model. The model fits the observed visibility points (red points) well. However, the model does not interpolate reasonably in the gaps of the uv-coverage. Top right panel: The clean image, i.e. the clean beam convolved with the model. This image approximates the true image reasonable well. Bottom right panel: However, the predicted visibilities of the convolved image do not match the observations anymore.

we reprint these arguments. The following enumeration (indented text) is an excerpt of the manuscript Müller & Lobanov (2023c) accepted for publication to the Proceedings of Science as part of the conference proceeding for the 15th EVN symposium 2022 in Cork adapted to the layout of this thesis. Writing and content was compiled by me with consultation by Andrei Lobanov.

- CLEAN introduces a disparity between the model that fits the observed visibilities (list of delta components) and the final image (delta components convolved with the clean beam). This is clearly unphysical as the final images produced by CLEAN do not fit the observed visibilities anymore, e.g. compare the discussion in Müller & Lobanov (2023a)
- CLEAN does not introduce effective regularization and is therefore prone to overfitting the data, in particular in the gaps of the uv-coverage, e.g. see the discussions in Müller & Lobanov (2023a). In fact, the regularization of CLEAN relies on the user finding the correct stopping rule by hand, compare Schwarz (1978).
- CLEAN typically requires supervision by a scientist introducing a significant human bias.
- CLEAN relies on an inverse modeling approach. Hence, the success of CLEAN relies strongly on the success of the phase calibration. A forward modeling approach would be more salient as it allows the direct use of calibration-independent closure quantities (Chael et al. 2018). Moreover, a forward approach would allow straightforwardly to incorporate additional hyperparameters in the reconstruction procedure such as gains, other polarimetric channels or prior distributions (Arras et al. 2021).
- The formal resolution of CLEAN is rigidly set by the precalculated restoring beam. However, recent developments in super-resolution imaging in VLBI demonstrated that the CLEAN beam might be too conservative (Arras et al. 2021; Broderick et al. 2022b; Event Horizon Telescope Collaboration et al. 2019b; Müller & Lobanov 2022; Roelofs et al. 2023). In fact, the theoretical model fitting resolution of an VLBI array is much higher than the clean beam resolution, but only reachable if the range of possible solutions is limited by strong prior assumptions (Lobanov 2005). Since CLEAN does not make any reasonable prior assumptions compared to Regularized Maximum Likelihood (RML)

and Bayesian approaches, its resolution is worse compared to these more recent approaches.

- The representation of the image by a list of CLEAN components is disadvantageous for the reconstruction of extended emission. (Cornwell 2008)
- While CLEAN is relatively fast to apply since, after initialization, only subtractions of arrays and list searches have to be applied in the minor loop, it does not scale up well to the data science needs for the next generation of radio interferometers such as the SKA, ngEHT or ngVLA. In particular, CLEAN does not make use of modern GPU accelerated computing infrastructures.

We illustrate the serious issue that there is a disparity between the CLEAN model and the CLEAN image in Fig. 2.17. Moreover, Fig. 2.17 also illustrates the issue with missing regularization. While the measured visibilities are fitted correctly, the full Fourier transform of the fitted model (bottom, middle panel) reveals that the most dominating recovered feature (the pattern of horizontal stripes) appears in the gaps, i.e. is not measured.

#### 2.4.4 Multiscale-CLEAN

Some of the limitations of standard Högbom CLEAN (Högbom 1974) are caused by the fact that  $\delta$ -components are no well suited basis functions to represent extended emission. In particular, the prior assumption behind CLEAN, i.e. that the image is sparsely represented in the pixel basis, might be inadequate. Multiscale-CLEAN approaches (MS-CLEAN) model the image with extended basis functions to address the representation of extended emission (Bhatnagar & Cornwell 2004; Cornwell 2008; Offringa & Smirnov 2017; Starck et al. 1994; Wakker & Schwarz 1988) or to solve the disparity between the CLEAN model and the CLEAN image (Müller & Lobanov 2023a). We will discuss MS-CLEAN approaches in more detail in chapter 3 when presenting our newly proposed MS-CLEAN variant DoB-CLEAN. For a general introduction, we only summarize the basic algorithmic outline of MS-CLEAN approaches. For MS-CLEAN, we construct a dictionary of extended basis functions: either by manual selection (Cornwell 2008; Offringa & Smirnov 2017; Starck et al. 1994; Wakker & Schwarz 1988), or optimally selected based on the current residual (Bhatnagar & Cornwell 2004) or fitted to the uv-coverage (Müller & Lobanov 2023a). We perform basically the same steps (minor loop) as for CLEAN in MS-CLEAN as well. However, when we search for the maximum in the residual, we do not only search for the location in the image domain, but also across the different scales represented by the basis functions.

Once a peak is selected, we substitute a rescaled and shifted dirty beam from the residual that is convolved with the corresponding basis functions. We refer to chapter 3 for more details.

## 2.5 Self-calibration

Recall from chapter 1.4.5 that the observed visibilities differ from the true visibilities in the presence of various antenna based gain errors. The complete forward problem is stated in Eq. (1.12). Direct imaging of such visibilities accounts only for the sparsity of the observation and regularization against thermal noise. Hence, we have to deal with the gain calibration in an additional step. This procedure is called *self-calibration* (Taylor et al. 1999; Thompson et al. 2017). Assuming that we would have already a proper model for the sky brightness distribution  $\hat{I} \approx I$ , we can calibrate the gains by fitting the gains to the recovered visibilities. Let  $W_{j,k,t} = \mathcal{F}\hat{I}(u_{j,k,t}, v_{j,k,t})$  be the recovered visibilities over an antenna pair  $j, k$  at a time  $t$ , then we minimize (Thompson et al. 2017):

$$\{\hat{g}_1, \dots, \hat{g}_{N_{ant}}\} \in \operatorname{argmin}_{\{g_1, \dots, g_{N_{ant}}\}} \sum_{j=1}^{N_{ant}} \sum_{k=1, j \neq k}^{N_{ant}} \sum_{t_{jk}} \frac{|W_{j,k,t} g_j g_k^* - V_{j,k,t}|^2}{\epsilon_{j,k,t}^2}, \quad (2.48)$$

where  $N_{ant}$  is the number of antennas,  $t_{jk}$  the times of independent measurements of the visibilities over antenna pair  $j, k$ , and  $\epsilon_{j,k,t}$  as before the estimated thermal error of the visibility. The inverse gains are applied to the observed data set. The minimization problem in Eq. (2.48) is typically over-constrained. Gain variations are mainly caused by atmospheric effects such that gains could vary over the time of observation (Janssen et al. 2022). In this case we compute various gain corrections for parts of the observation rather than for the complete observation run. Moreover, in the standard VLBI data reduction packages such as *ehtim*, *AIPS* and *Difmap* we do not search for gain solutions globally, but restrict the allowed variance to an initial tolerance. The gains are complex prefactors, i.e. they consist of an amplitude and a phase. It is possible to restrict the minimization to the phases only or to the amplitudes only, if needed. A further option is to exclude single antennas explicitly from the gain calibration.

Self-calibration requires a reasonable image model  $\hat{I}$  with reasonable model visibilities  $W$ . On the other hand, imaging requires a well calibrated data set. To overcome this self-referencing, the following procedure of hybrid imaging was introduced: We do a manually fixed number of CLEAN iterations, self-calibrate the visibilities, recalculate the residual with the new visibilities and return to the first step (Taylor et al. 1999). Since phases are typically more unstable than amplitudes, it is common practice to use only phase calibration in the first

self-calibration rounds. A generic pitfall for hybrid imaging is that true image features which cause a spatial variability of the visibilities are absorbed in the gain calibration. To avoid this issue, self-calibration is often initially applied over long time intervals (allowing for a single gain solution per time interval), shifting towards shorter solution intervals at later iterations.

Self-calibration is a well established tool in VLBI by now and has proven to be useful in practice. From a mathematical perspective, hybrid imaging is comparable to a two-step gradient descent or alternate projection approach in which the array of unknowns consists of the sky brightness distribution  $I(l, m)$  and the array of gains. However, hybrid imaging is by design a local search method and may get trapped in local minima.

Lastly, we need to mention, that closure phases and closure amplitudes play a vital role in the gain calibration since they are independent of the gains in the absence of thermal noise. While these possibilities are not directly realized within CLEAN, we can use them in the interactive data manipulation and data visualization steps inherent to CLEAN as a verification. However, we should here point out one of the limitations of inverse modeling again: closure quantities cannot be used as data fidelity terms, opposed to forward modeling techniques. Additionally, the procedure of alternate imaging and self-calibration remains highly supervised, hence introducing a human bias in the analysis.

## 2.6 Forward Modeling

Recently, forward modeling techniques have been developed for VLBI. For these techniques a model is forwardly recovered by minimizing a sum of data fidelity terms and regularization terms in the spirit of Eq. (2.4). Forward modeling techniques often surpass CLEAN in dynamic range and resolution, while trading this advantage for a higher computational cost. We show a schematic overview of recently proposed, novel VLBI forward modeling techniques in Fig. 2.18.

### 2.6.1 MEM

The oldest forward modeling technique used is the Maximum Entropy Method (MEM), dating back to Frieden (1972), Ponsonby (1973) and Ables (1974). MEM assumes entropy maximization as a prior. For this discussion we follow the description of Cornwell & Evans (1985). The entropy of the guess solution  $f$  is measured by the term (Cornwell & Evans 1985):

$$R_{MEM}(f) = \sum_i f_i \ln \frac{f_i}{M_i}, \quad (2.49)$$

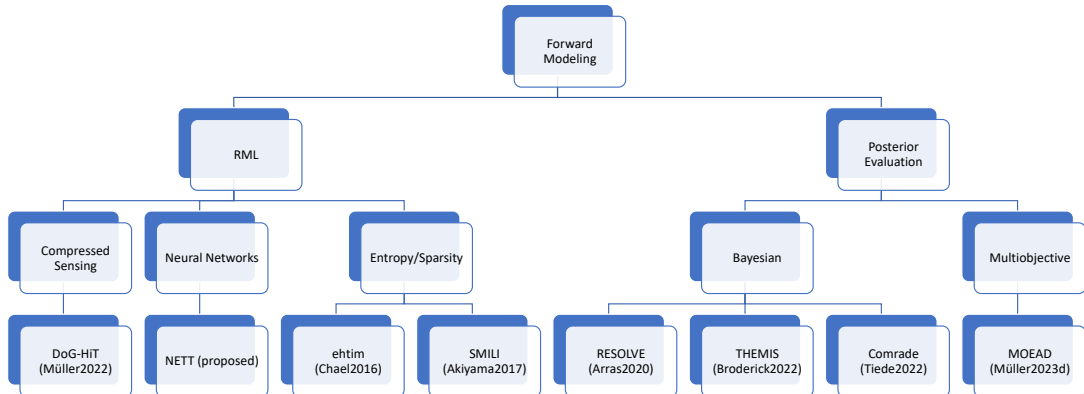


Figure 2.18: Overview of recent forward modeling techniques and the respective software tools.

with a prior distribution  $M$ . A common choice for the prior distribution is a Gaussian distribution.  $R_{MEM}$  therefore measures the simplicity of a guess solution. Cornwell & Evans (1985) proposed to use the entropy prior in the *generalized Tikhonov framework* together with the fit quality to the visibilities. Moreover, application in practice proved it beneficial to add the model flux to the optimization terms as well:

$$R_{model-flux}(f) = \int dldmf(l, m). \quad (2.50)$$

The complete objective functionals, equivalently reformulated in the language of this dissertation, reads (Cornwell & Evans 1985):

$$T_{\alpha, \beta}^{MEM}(f) = S_{\text{vis}}(V, Ff) + \alpha R_{MEM}(f) + \beta R_{model-flux}(f), \quad (2.51)$$

with measured visibilities  $V$  and forward operator  $F$ .  $T_{\alpha, \beta}^{MEM}$  is typically minimized by a gradient descent algorithm since all terms are differentiable. The Lagrangian parameters  $\alpha$  and  $\beta$  are varied during the reconstruction in order to achieve the expected values ( $\chi^2 \sim 1$ ) and expected total flux in the image (Cornwell & Evans 1985).

A wide range of alternative MEM frameworks with a slightly different definition of the entropy functional, representation of the image (i.e. by a multiscalar function) or minimization procedure were discussed in the past. We refer the interested reader to Bontekoe et al. (1994); Garsden et al. (2015); Gull & Daniell

(1979); Högbom (1979); Li et al. (2011); Maisinger et al. (2004); Mus & Marti-Vidal (2023); Narayan & Nityananda (1984, 1986); Pantin & Starck (1996); Starck et al. (2001); Thiébaud & Young (2017); Wernecke & D’Addario (1977); Wiaux et al. (2009). A comprehensive comparison between CLEAN and MEM methods is provided in Thompson et al. (2017) and Cornwell et al. (1999). CLEAN performs faster for smaller data sets, while MEM gives better performance for large data sets and large arrays. Moreover, since smoothness is built in in the prior entropy functional, MEM typically performs better for smooth, extended emission than CLEAN. Vice versa, CLEAN performs better for point sources. Narayan & Nityananda (1986) concluded that the reconstruction with MEM varied strongly with the background noise level and, in consequence, absorption features under the background noise level are poorly reconstructed.

### 2.6.2 RML

Regularized Maximum Likelihood (RML) methods are the next natural development step after the MEM algorithms. New RML capabilities were in particular developed for the data analysis of the Event Horizon Telescope (EHT), e.g. see Akiyama et al. (2017a,b); Chael et al. (2016, 2018); Event Horizon Telescope Collaboration et al. (2019b); Ikeda et al. (2016). RML methods are directly formulated in the framework of the *general Tikhonov* method by minimizing a weighted sum of data fidelity terms and regularization terms. A combination of  $S_{\text{vis}}$ ,  $S_{\text{amp}}$ ,  $S_{\text{cph}}$  and  $S_{\text{cla}}$  is used as data fidelity terms. Chael et al. (2018) demonstrated that reasonable image reconstructions could be obtained if closure phases and closure quantities are fitted directly without the use of a fit to the visibilities. Since the closure quantities are independent of the gains, this approach promises an alternative to classical self-calibration. This approach was used in Event Horizon Telescope Collaboration et al. (2019b) and Event Horizon Telescope Collaboration et al. (2022b). However, Lockhart & Gralla (2022a) demonstrated that the closure errors are not independent of the gains and the way how these are approximated affects the final image.

The MEM prior term  $R_{MEM}$  is reused in RML implementations as a regularization term. Moreover, additional regularization terms are included. We briefly introduce these terms in this chapter. Sparsity of the solution can be introduced by  $l^0$ -regularization:

$$R_{l^0}(f) = \|f\|_{l^0}. \quad (2.52)$$

However, the  $l^0$  norm is neither smooth nor convex, with all the consequential issues for the optimization procedures discussed above. Therefore, the  $l^1$  norm is

used as a convex approximation:

$$R_{l^1}(f) = \|f\|_{l^1}. \quad (2.53)$$

$R_{l^1}$  is not smooth, but has a simple proximal operator. The proximal operator of the  $l^1$ -norm is the soft shrinkage operator. A natural extension, favoring simplicity of the solution instead of sparsity, is the  $l^2$ -term:

$$R_{l^2}(f) = \|f\|_{l^2}. \quad (2.54)$$

Other than sparsity, regularization terms can be used to assume smoothness of the solution. These are expressed by the magnitude of the gradient of the current solution (assuming that it has one). We define the total variation:

$$R_{TV}(f) = \|\nabla f\|_{l^1}, \quad (2.55)$$

and the total squared variation:

$$R_{TSV}(f) = \|\nabla f\|_{l^2}. \quad (2.56)$$

$R_{TSV}$  promotes smoothness of the recovered solution, while  $R_{TV}$  promotes piecewise constant smooth functions with smooth sigmoid connections.  $R_{TV}$  is therefore best suited for the detection of edges and filaments. Finally, a total flux constraint may be used:

$$R_{flux}(f) = \left| \int \int dldm f(l, m) - c \right|, \quad (2.57)$$

where  $c$  is the compact flux. The complete optimization problem reads:

$$\hat{I} \in \underset{f}{\operatorname{argmin}} \left\{ \alpha_{vis} S_{vis}(V, Ff) + \alpha_{amp} S_{amp}(V, Ff) + \alpha_{cph} S_{cph}(V, Ff) + \alpha_{cla} S_{cla}(V, Ff) \right. \\ \left. + \beta_{l^0} R_{l^0}(f) + \beta_{l^1} R_{l^1}(f) + \beta_{l^2} R_{l^2}(f) + \beta_{TV} R_{TV}(f) + \beta_{TSV} R_{TSV}(f) + \beta_{flux} R_{flux}(f) \right\} \quad (2.58)$$

For the main software packages that implement RML imaging routines, i.e. *SMILI* and *ehtim*, the minimization is done by gradient descent optimization routines. This, however, is strictly speaking not correct since some of the aforementioned regularization terms (i.e.  $R_{l^1}$  and  $R_{TV}$ ) do not have a well defined gradient everywhere. We developed in Müller & Lobanov (2022) a framework for the mathematically more rigorous forward-backward splitting and implemented it in the software package *MrBeam*<sup>2</sup>.

<sup>2</sup><https://github.com/hmuellergoe/mrbeam>

Typically in convex optimization and inverse problems, only one data term and one regularization term is combined. In this setting, optimization algorithms such as forward-backward splitting are exact (Combettes & Pesquet 2011). An objective functional consisting of a combination of ten smooth or convex objective functionals as in Eq. (2.58) is rather unusual (Kirsch 2011) and questions the minimization by splitting algorithms. Nevertheless, the application to observational and synthetic data with the degree of undersampling present in current VLBI arrays proved that this large number of penalty terms with the correct weightings is necessary. Particularly, we refer to the synthetic data surveys presented in Event Horizon Telescope Collaboration et al. (2019b) and Event Horizon Telescope Collaboration et al. (2022b). The selected top-sets (i.e. the reconstructions that were consistent with the ground truth image) consisted of all the regularization terms mentioned in Eq. (2.58) and the reconstructions from only a subset of terms did not pass the top-set selection criteria. This issue is worsened even more when the imaging is done from the closure quantities only (Chael et al. 2018). The number of independent closure phases and closure amplitudes is smaller than the number of independent visibilities, thus introducing degeneracies (e.g. lost absolute position and lost total flux) that need to be adjusted for by the regularization terms as well.

RML methods share some basic advantages superior to CLEAN and MEM. With the correct selection of the weighting parameters  $\alpha_i$  and  $\beta_j$ , the reconstructions have a higher resolution than CLEAN (e.g. Arras et al. 2021; Event Horizon Telescope Collaboration et al. 2019b; Müller & Lobanov 2022; Roelofs et al. 2023), they are more precise, and break the degeneracy between model and image introduced by CLEAN. Moreover, they allow for the use of (self-)calibration independent terms. All in all, RML methods produce the more favorable solutions compared to CLEAN. However, as a serious drawback, the RML solution depends strongly on the choice of the regularization parameters that are unknown prior to the imaging procedure. This makes tedious parameter surveys with synthetic model data sets necessary.

### 2.6.3 Bayesian Imaging

Recent years saw an ongoing development of Bayesian imaging methods that were specially designed for VLBI: *Themis* (Broderick et al. 2020a,b), *Comrade* (Tiede 2022) and *resolve* (Arras et al. 2019, 2021; Greiner et al. 2016; Junklewitz et al. 2016). As before, let us denote the data by  $g^\delta$  and the image guess models by  $f$ . In Bayesian approaches, we are interested in the posterior probability density  $\mathcal{P}(f|g^\delta)$ . The posterior probability density distribution is related to the

Likelihood  $\mathcal{P}(g^\delta|f)$  and the prior distribution  $\mathcal{P}(f)$  by Bayes theorem:

$$\mathcal{P}(f|g^\delta) = \frac{\mathcal{P}(g^\delta|f)\mathcal{P}(f)}{\mathcal{P}(g^\delta)}. \quad (2.59)$$

We can use any VLBI data product as data term  $g^\delta$ . The most prominent ones are again the visibilities, amplitudes, and closure quantities. Let us first discuss the standard case that full complex visibilities are used as data product. The forward problem is described by Eq. (1.8) and Eq. (1.12). Let us denote, as before, the computed guess visibilities by  $W = Ff$  (ignoring gains for now). Since the additional thermal noise is assumed to be independent and Gaussian, we get the likelihood:

$$\mathcal{P}(V|f) = (2\pi)^{-N_{vis}/2} \left[ \prod_{i=1}^{N_{vis}} \frac{1}{\epsilon_i} \right] \exp\left(-\frac{N_{vis}}{2} S_{vis}(V, W)\right), \quad (2.60)$$

with the notation of chapter 2.3.1, compare Eq. (2.10). Hence, it is:

$$\ln \mathcal{P}(V|f) = \text{const.} - \frac{N_{vis}}{2} S_{vis}(V, W) \quad (2.61)$$

Similar relations can be derived for the amplitudes, and closure quantities:

$$\ln \mathcal{P}(|V||f) = \text{const.} - \frac{N_{amp}}{2} S_{amp}(V, W) \quad (2.62)$$

$$\ln \mathcal{P}(\Psi(V)|f) \sim \text{const.} - \frac{N_{cph}}{2} S_{cph}(V, W) \quad (2.63)$$

$$\ln \mathcal{P}(A(V)|f) \sim \text{const.} - \frac{N_{cla}}{2} S_{cla}(V, W), \quad (2.64)$$

in the notation of chapter 2.3.2. Note that for the closure quantities Eq. (2.63) and Eq. (2.64) are only approximations to the true log-likelihood of the closure quantities (Blackburn et al. 2020).

We encode our existing knowledge of the sky brightness distribution into the prior distribution. It is one of the great advantages of Bayesian algorithms that prior information on the spatial correlation of pixels is naturally introduced at this stage by the auto-correlation of the prior distribution  $\mathcal{P}(f)$ , i.e. we assume a Gaussian or lognormal (non-negativity) distribution with specified auto-correlation. Current applications of Bayesian imaging algorithms (e.g. Arras et al. 2022) add more layers of complexity to the determination of the correlation structure: Instead of assuming specific prior correlation function, the correlation function is determined in a non-parametric fashion. As a result, the model is more flexible and adaptable, and this can reduce biases. This highlights an additional

advantage of Bayesian frameworks: the forward model could naturally consist of any additional parameters (such as the gains) or deeper layers of the model (model components, multi-frequency representation by mean image and spectral index map, time-dynamic evolution etc.) as long as a reasonable prior distribution can be derived (e.g. compare the extensions of the classical Bayesian framework in Arras et al. 2022; Broderick et al. 2022a; Roelofs et al. 2023).

After combining the likelihood and the prior the best guess is derived by the expectation value:

$$\hat{I}_{mean} = \int f \mathcal{P}(f|g^\delta) df. \quad (2.65)$$

The higher order momenta of the distribution  $\mathcal{P}(f|g^\delta)$  describe the uncertainty of the recovered image, such as the variance:

$$\text{Var} = \int (f - \hat{I}_{mean})^2 \mathcal{P}(f|g^\delta) df. \quad (2.66)$$

We encounter here another key advantage of Bayesian approaches: they do not only recover an image representation, but also an uncertainty quantification. However, it is questionable whether these uncertainty estimates have a physical meaning as the prior distributions are often not physical, but rather chosen on a best effort basis to ensure a viable image reconstruction (Arras et al. 2021).

Bayesian methods originally appeared in Bayesian parameter estimation frameworks with a restricted number of free parameters and clearly defined prior distributions. The (infinite-dimensional) reconstruction of a function  $I(l, m)$  is a more challenging problem (and this is where the ill-posedness arises). The large number of pixels (free parameters) required to represent the image poses severe performance issues. The evaluation of integrals of the form of Eq. (2.65) is numerically expensive due to the high dimensionality. A full-dimensional Markov-Chain Monte-Carlo simulation takes often too much time (Cai et al. 2018a,b). Various solutions have been proposed in the past, e.g. in the context of Bayesian neural networks (Goan & Fookes 2020), but are only rarely translated to VLBI. Broderick et al. (2020b) tried to sample the posterior distribution exactly, thus they had to represent the image on a low-dimensional grid only with interpolation between the gridding points. Tiede (2022) translated Bayesian methods to a faster software framework to gain numerical speed. Arras et al. (2019, 2021) proposed a variational inference method called Metric Gaussian Variational Inference (Knollmüller & Enßlin 2019) for fast approximations of the posterior distribution.

Finally, we should also point out a deep connection of Bayesian imaging algo-

gorithms to the *generalized Tikhonov* method. The mean, see Eq. (2.65), could be approximated by the maximum of the posterior (MAP estimator), in particular for symmetric distributions we have:

$$\begin{aligned}\hat{I}_{mean} &\approx \operatorname{argmax}_f \mathcal{P}(f|g^\delta) \\ &= \operatorname{argmax}_f \ln \mathcal{P}(f|g^\delta) = \operatorname{argmax}_f \left\{ \ln \mathcal{P}(g^\delta|f) + \ln \mathcal{P}(f) \right\},\end{aligned}\quad (2.67)$$

where the last equality holds due to Bayes theorem Eq. (2.59). Referring to Eq. (2.61), (2.62), (2.63), (2.64) the first term resembles the data fidelity terms of RML formulations. The second term in the optimization ( $\ln \mathcal{P}(f)$ ) plays the role of the penalty term. Consider for example a Gaussian prior distribution for  $f$  with standard covariance, then  $\ln \mathcal{P}(f) \propto \|f\|_{l^2}$ . Hence, the maximum-a-posterior estimator would be equivalent to  $l^2$ -regularization.

Bayesian approaches have some advantages that are outlined above: they allow for a quantification of the image uncertainty, and they allow for the natural introduction of prior assumptions that are more difficult to express in other frameworks. On the downside, they are numerically very expensive. Moreover, the results depend strongly on the assumed prior distribution and a larger number of non-trivial hyperparameters that are unknown a-priori.

#### 2.6.4 Compressive Sensing

Compressive sensing (CS) is the signal processing technique that allows for a compression of images by a sparse representation. The technique has a wide range of applications across multiple disciplines including facial recognition, photography, image restoration or portable network graphics (Starck & Murtagh 2006). For a full discussion in the context of astronomy we refer to Candès et al. (2006); Donoho (2006); Starck & Murtagh (2006); Starck et al. (2015). The underlying idea of compressive sensing is to transform the image to another domain in which the image structure could be sparsely represented (Candès et al. 2006). As a trivial example, a monochromatic harmonic oscillation could be sparsely represented by a single data point by transforming it into the Fourier domain. For astronomical images, wavelets have been proposed with promising sparsifying properties (Line et al. 2020; Mertens & Lobanov 2015; Mertens et al. 2016; Mohan & Rafferty 2015; Starck et al. 2003; Starck & Murtagh 2006; Starck et al. 2015). In particular, we like to highlight Mertens & Lobanov (2015) who proposed the use of a sparsifying wavelet transform in the context of post-processing VLBI images of AGN jets.

Wavelets are a variant of the short-time Fourier transform that can be varied

in position, strength and in spatial scale. Hence, there are wavelets that describe the extended large scale emission and wavelets that compress small scale fluctuations. The combination of both in a single dictionary allows for a sparse (i.e. sparser than in pixel-basis) representation of the image structure. Several wavelet functions have been proposed in the past: among others the Morlet wavelet (Coupinot et al. 1992; Goupillaud et al. 1984), the Mexican-hat wavelet (Murenzi 1989), the Haar wavelet (Stollnitz et al. 1994), and difference of Gaussian wavelets (Assirati et al. 2014; Gonzalez & Woods 2006). There exist discrete á-trous versions of these wavelet functions (e.g. Mallat 1989). For a full description we refer to Starck et al. (2015). We presented in Müller & Lobanov (2022) a novel wavelet dictionary combining the difference of Gaussian wavelets with the philosophy of the á-trous wavelet decomposition. Moreover, we extended these wavelets to radially asymmetric wavelets in Müller & Lobanov (2023a).

We discussed sparsity as a relevant imaging prior already in chapter 2.6.2: The  $l^0$ -norm and  $l^1$ -norm are sparsity promoting. Moreover, sparsity in the pixel-basis is the essential prior information for the CLEAN algorithm (Lannes et al. 1997): We try to model the visibilities with as few CLEAN components as possible. However, for these approaches we assume sparsity in the pixel-basis, which may be inadequate for extended and resolved emission (compare our discussion on the limitations of CLEAN in chapter 2.4.3). For imaging algorithms that make use of compressive sensing theory, this assumption is relaxed. We represent the image by a sparsifying matrix of basis functions  $I = \Gamma\mathcal{I}$ .  $\Gamma$  is called a dictionary, while the single elements of  $\Gamma$  (the basis functions) are called atoms (Starck et al. 2015).  $\mathcal{I}$  is a set of wavelet coefficients. We propose sparsity on the array of wavelet coefficients. As in preceding chapters, we call the forward operator,  $F$ , that maps the guess image  $f$  to the measured visibilities (Fourier transform, sampling to visibility points, weighting, tapering). In its easiest formulation, imaging by compressive sensing reads (Garsden et al. 2015):

$$\hat{\mathcal{I}} \in \operatorname{argmin}_{\mathcal{I}} \{S_{\text{vis}}(V, F\Gamma\mathcal{I}) + \alpha R_{l^1}(\mathcal{I})\}, \quad (2.68)$$

with the recovered image:

$$\hat{I} = \Gamma\hat{\mathcal{I}}. \quad (2.69)$$

The similarity to RML methods is obvious. Moreover, straightforwardly, CS-imaging is an instance of the *generalized Tikhonov regularization*. It is also worth noting that some of the more complex regularization terms of RML methods, such as  $R_{TV}$  can be rewritten in the language of CS as well: it is equivalent to sparsity of the Haar-wavelets.

Similar to the RML and Bayesian approaches, the data fidelity term could be replaced by more calibration robust data terms ( $S_{\text{amp}}$ ,  $S_{\text{cph}}$ ,  $S_{\text{cla}}$  or a combination of them). Moreover, the  $l^1$  penalization could be replaced by hard thresholding ( $R_{l^0}$ ) or intermediate strategies such as iteratively reweighted  $l^1$  penalization (Candès et al. 2007). Sparsifying imaging has been applied for radio interferometry before with great success, historically first in framework of MEM (e.g. Bontekoe et al. 1994; Maisinger et al. 2004; Pantin & Starck 1996; Starck et al. 1994, 2001; Weir 1992), later in a more general setting (among others Cai et al. 2018a,b; Carrillo et al. 2012, 2014; Garsden et al. 2015; Girard et al. 2015; Li et al. 2011; Onose et al. 2016, 2017; Pratley et al. 2018). We transferred these ideas to VLBI (Müller & Lobanov 2022, 2023a,b). Moreover, for the first time, we succeeded to construct a largely unsupervised reconstruction method by choosing the dictionary data-driven (Müller & Lobanov 2022).

### 2.6.5 Deep Learning

Deep Learning techniques have been proposed successfully for various pattern recognition problems and have been used for inverse problems. Particularly we like to mention their success for magnetic resonance tomography (MRI) reconstructions, as for example demonstrated by the fastMRI challenge (Muckley et al. 2021). In MRI, a similar problem is solved, i.e. the reconstruction of an image from a sparsely sampled Fourier domain (Sodickson 2021), for more details we refer to the more detailed discussion in chapter 5.4.3. Due to these developments and the relative similarity, it is evident that these techniques are currently studied for radio interferometry as well (e.g. compare the works in Aghabiglou et al. 2022; Dabbech et al. 2022; Gheller & Vazza 2022; Terris et al. 2023). These methods promise great potential. Once trained, the networks scale well to big data sets (Terris et al. 2023). Moreover, they provide a natural way to express structured prior information that is more complicated to adapt in standard sparsifying bases (Aghabiglou et al. 2022). Applications to VLBI are however rare. Yao-Yu Lin et al. (2021) proposed an end-to-end pipeline for the classification of images. Sun et al. (2022) proposed a first network for VLBI in a plug-and-play framework. Neural Network Tikhonov (NETT) may be another powerful approach (Li et al. 2020), specifically due to its conceptual similarity to multiscale imaging methods. We discuss more prospects of NETT in chapter 7. However, due to the limited number of visibilities and the large uncertainties (e.g. phase errors) imaging in the VLBI data regime requires strong prior information. Since it remains difficult (despite the considerable recent effort) to determine how a network learned a specific structural pattern and prior information, the application of deep learning techniques to VLBI remains restricted by now.

## 2.7 Evaluation Metrics

In the previous chapter, we gave an overview over the landscape of reconstruction methods in VLBI (and radio interferometry in general). In this chapter, we present how to evaluate and compare RML and Bayesian methods with CLEAN qualitatively. We do not include deep learning methods in this comparison since they are still in the proposing stage for VLBI currently and not applied to VLBI data sets at a considerable level by now (although there is great potential for these methods). An exhaustive quantitative comparison is not always feasible and should be left for further discussion. The interested reader can be referred here to existing imaging comparisons, e.g. Arras et al. (2021); Event Horizon Telescope Collaboration et al. (2019b); Müller & Lobanov (2022); Roelofs et al. (2023). However, these comparisons should all be treated with relative caution. They only discuss various algorithms in very specific settings (e.g. for the needs of the EHT telescope). The following assessment presented below is based on generally accepted experience in practice. For the remainder of the dissertation, we will treat MEM and RML algorithms as the same, as MEM could be derived as an instance of the RML method with entropy prior. Moreover, we spare a detailed discussion of CS-methods here, and defer a detailed discussion for the conclusions of this dissertation. Except for DoG-HiT, whose development constitutes the main body of this dissertation in the following subsections, CS-based algorithms are regularly applied in radio-interferometry, but only rarely to VLBI data sets.

### 2.7.1 Accuracy

Arguably, the most important criterion of success for any new imaging algorithm is its accuracy when reconstructing synthetic data. The accuracy of the reconstruction is typically measured by the cross-correlation between the recovered image and some realization of the ground truth image representing the expected result of the perfect reconstruction. However, this metric is often not sufficient. Images of AGN jets, on which this dissertation is focused, typically consist of a bright core and much fainter extended emission. On one hand, the cross-correlation between the recovered image and the ground truth image is dominated by the reconstruction of the core-component (and hence by resolution power). On the other hand, scientific interest often lies in the extended jet structures. Hence, Roelofs et al. (2023) proposed to use the cross-correlation between the logarithms of the images instead.

Decade-long application of CLEAN has demonstrated that it works overall quite well in recovering the true image structure, except for two special cases: in the presence of wide, extended emission and when the VLBI array is very sparse.

In the first case, the CLEAN reconstruction tends to represent the smooth extended structures by a combination of discretized regions of enhanced brightness, thus creating the characteristic ‘spotty’ appearance on scales substantially larger than the primary lobe scale of the dirty beam. This particular issue could be solved by the use of extended basis functions as CLEAN components, i.e. by MS-CLEAN algorithms (Bhatnagar & Cornwell 2004; Cornwell 2008; Offringa & Smirnov 2017; Rau & Cornwell 2011; Starck et al. 1994; Wakker & Schwarz 1988). In the second case (extreme sparse uv-coverage), the amount of information available to CLEAN is very limited. The more limited the information contained in the data is, the more the reconstruction relies on the prior assumption. The extensive investigations of these matters presented in Event Horizon Telescope Collaboration et al. (2019b) and Event Horizon Telescope Collaboration et al. (2022b) proved that in this case RML and Bayesian methods lead to more reliable reconstruction results.

A number of forward modeling approaches have been developed in recent years for imaging VLBI data (Akiyama et al. 2017a,b; Arras et al. 2019, 2021; Broderick et al. 2020a,b; Chael et al. 2016, 2018; Müller & Lobanov 2022; Tiede 2022). In these publications, the respective algorithms were benchmarked against CLEAN, always outperforming classical CLEAN in accuracy of reconstructing images from synthetic data for which the exact ground truth image is always available. A thorough cross-comparison on a wider set of arrays, synthetic data sets and noise corruptions however is still pending. Furthermore, we have to mention the main theoretical issue with CLEAN here as well: the model fitted to the visibilities and the final image do not match. This issue is solved only recently for CLEAN (Müller & Lobanov 2023a), but does not occur for forward modeling techniques in general.

### 2.7.2 Dynamic Range

The dynamic range of a reconstructed image is one of the standard parameters used for specifying the quality of reconstruction. Based on the assumption that, after the imaging has ended, the final residual is noise-like, we quantify the magnitude of the noise. The dynamic range is the ratio of the recovered peak flux and the noise floor in the residual. However, a closely related, but mathematically less rigorously defined metric of image fidelity seems to be more salient here: what is the brightness of the faintest (extended) emission features that are still reliably recovered? CLEAN works overall quite well in recovering faint, extended emission with the major drawback of a fractured and disconnected reconstruction of extended emission features. The manual execution of CLEAN by an experienced astronomer is key to the success of high dynamic range imaging (Taylor et al.

1999).

Recent comparisons of VLBI data processing tools (e.g. Roelofs et al. 2023) proved that current RML and Bayesian methods outperform CLEAN in dynamic range as well in some specific settings. Moreover, current hybrid approaches (Broderick et al. 2020b; GRAVITY Collaboration et al. 2022) that combine model-fitting and imaging steps proved that fainter, formerly undetected features can reliably be recovered in the residual after the dominating bright feature has been fitted by an analytical template at a higher resolution. However, experience with applications in practice shows that fitting faint, extended emission by forward modeling is a bit more subtle: the data fidelity terms for forward modeling techniques are rather dominated by the high resolution reconstruction of the bright core component. The emission will only be reliably recovered if the correct data term weightings (RML) and priors (Bayesian) are used.

### 2.7.3 Resolution

The resolution that an imaging algorithm can achieve is a significant criterion for the evaluation of the quality of an image reconstruction. There is, however, not a unique concept for resolution. Loosely speaking, the resolution limit of an algorithm can be defined as the angular size of the smallest features that are still robustly recovered. (MS-)CLEAN has a solid resolution limit originating from the convolution with a finite beam. More recent imaging routines however demonstrated that this bound is too conservative (Event Horizon Telescope Collaboration et al. 2019b; Müller & Lobanov 2022; Roelofs et al. 2023). Forward modeling techniques utilize more advanced imaging priors that allow us to reconstruct images at higher resolutions, commonly referred to as super-resolution. In this chapter, we discuss the theoretical resolution limit of a radio interferometer showing that the general conception of super-resolution may be misleading: forward modeling techniques can achieve a resolution that is closer to the true resolution limit than CLEAN, rather than super-resolving structures.

As one possible resolution criterion we discuss the case of a Gaussian source as opposed to a point source as it was done in Lobanov (2005). The Gaussian source is still resolved, if it can be separated from the delta source with sufficient statistical significance. In order to get an analytic limit, rather than numerical, we have to make several simplifying assumption. Lobanov (2005) used the signal-to-noise ratio on the longest baseline. Here we present a novel, more rigorous calculation. We extend this procedure to a hypothesis test including all data points. We test the hypothesis, the image is a delta-peak (zero-hypothesis), against the hypothesis, the image is a Gaussian with width  $s$ . We compute the  $\chi^2$  and reject the hypothesis for  $\chi^2 > 2.7$  (90% exclusion limit). Note that the Fourier

transform of a Gaussian  $G_s(x) = \frac{1}{\sqrt{2\pi s^2}} e^{-x^2/(2s^2)}$  is given by  $e^{-k^2/(2\Sigma^2)}$  with trivial expansion to two dimensions and  $\Sigma = \frac{1}{2\pi s}$ . Hence (with  $q(u, v) = \sqrt{u^2 + v^2}$ ):

$$\begin{aligned}
 \chi^2 &= \sum_i \frac{\left(1 - e^{-k_i^2/(2\Sigma^2)}\right)^2}{\sigma_i^2} \sim \int \int dudv \frac{\rho(u, v) \left(1 - e^{-q^2/(2\Sigma^2)}\right)^2}{\sigma(u, v)^2} \\
 &= \int \int dudv \rho(u, v) \left(1 - e^{-q^2/(2\Sigma^2)}\right)^2 SNR^2 \\
 &= 2\pi SNR^2 \int dq q \rho(q) \left(1 - e^{-q^2/(2\Sigma^2)}\right)^2 \\
 &= \frac{SNR^2 N_{\text{vis}}}{\log(q_{\text{max}}/q_{\text{min}})} \int dq q^{-1} \left(1 - e^{-q^2/(2\Sigma^2)}\right)^2, \tag{2.70}
 \end{aligned}$$

where  $\rho(u, v)$  is the density of uv-points in the uv-domain and is (neglecting directional dependent patterns of the uv-coverage) approximated by a radially decreasing function:  $\rho(q) \propto q^{-2}$  with  $\int \int dudv \rho(u, v) = N_{\text{vis}}$ .  $N_{\text{vis}}$  is the number of independent visibility points and  $q_{\text{max}}$  and  $q_{\text{min}}$  denote the maximal and minimal uv-distance in the array. Moreover, we assumed that the signal to noise ratio ( $SNR$ ) is constant along the array. We use the integral exponential function:  $E_i(t) := \int_{-\infty}^x \frac{e^t}{t} dt$ . Substitution with  $t = -q^2$  shows:

$$\int_0^{q_{\text{max}}} q^{-1} e^{-q^2} dq = \frac{1}{2} E_i(-q_{\text{max}}^2) + \text{const.} \tag{2.71}$$

Hence, we have:

$$\begin{aligned}
 \int_{q_{\text{min}}}^{q_{\text{max}}} dq q^{-1} \left(1 - e^{-q^2/(2\Sigma^2)}\right)^2 &= \log(q_{\text{max}}) - \log(q_{\text{min}}) \\
 + E_i\left(\frac{-q_{\text{min}}^2}{2\Sigma^2}\right) - E_i\left(\frac{-q_{\text{max}}^2}{2\Sigma^2}\right) &+ \frac{1}{2} E_i\left(\frac{-q_{\text{max}}^2}{\Sigma^2}\right) - \frac{1}{2} E_i\left(\frac{-q_{\text{min}}^2}{\Sigma^2}\right) \tag{2.72}
 \end{aligned}$$

The following expansion holds (where  $\gamma$  is the Euler-Mascheroni constant):

$$E_i(x) = \gamma + \log(|x|) + \sum \frac{x^k}{k!k} \tag{2.73}$$

The constant terms vanish. The logarithmic terms vanish as well:

$$\begin{aligned}
 \log(q_{\text{max}}) - \log(q_{\text{min}}) + \log\left(\frac{q_{\text{min}}^2}{2\Sigma^2}\right) - \log\left(\frac{q_{\text{max}}^2}{2\Sigma^2}\right) \\
 + \frac{1}{2} \log\left(\frac{q_{\text{max}}^2}{\Sigma^2}\right) - \frac{1}{2} \log\left(\frac{q_{\text{min}}^2}{\Sigma^2}\right) &= 0 \tag{2.74}
 \end{aligned}$$

The diverging terms  $\lim_{q_{\text{min}} \rightarrow 0} \log(q_{\text{min}})$  vanish! Only the potence terms survive.

When setting  $q_{min}$  to zero, we arrive at:

$$\begin{aligned} \int_0^{q_{max}} dq q^{-1} (1 - e^{-q^2/(2\Sigma^2)})^2 &= - \sum_{k=1}^{\infty} \frac{(-1)^k}{k!k} \frac{q_{max}^{2k}}{2^k \Sigma^{2k}} + \frac{1}{2} \sum_{k=1}^{\infty} \frac{(-1)^k}{k!k} \frac{q_{max}^{2k}}{\Sigma^{2k}} \\ &= \sum_{k=1}^{\infty} \frac{(-1)^k}{k!k} \frac{q_{max}^{2k}}{\Sigma^{2k}} \frac{2^{k-1} - 1}{2^k} = 0 + \frac{1}{4} \frac{q_{max}^4}{\Sigma^4} \frac{2-1}{4} + O\left(\left(\frac{q_{max}}{\Sigma}\right)^6\right). \end{aligned} \quad (2.75)$$

Hence:

$$\chi^2 \sim \frac{SNR^2 N_{vis}}{\log(q_{max}/q_{min})} \frac{q_{max}^4}{16\Sigma^4} = \frac{\pi^4 N_{vis}}{\log(q_{max}/q_{min})} q_{max}^4 s^4 SNR^2. \quad (2.76)$$

Thus:

$$d_{lim} = \frac{1}{q_{max}} \frac{1}{\sqrt{SNR}} \left( \frac{\chi^2 \log(q_{max}/q_{min})}{\pi^4 N_{vis}} \right)^{1/4}. \quad (2.77)$$

We see that the limiting resolution scales inversely with the longest baseline and inversely with the square root of the signal-to-noise ratio, consistent with the findings in Lobanov (2005). While Eq. (2.77) was derived in a rather simplified setting, it demonstrates a key feature of the discussion about limiting resolution: The resolution of an observation is not only improved by the addition of longer baselines, but also by the signal-to-noise ratio and the number of visibilities. This has possible strategic consequences for the future of high precision VLBI measurements: The theoretical resolution limit of an array such as the GMVA+ALMA is comparable to the one of the EHT albeit observing at a smaller frequency, since the number of antennas is higher. Moreover, the rationale behind space-VLBI missions is questionable if the calibration of the space-antenna (and thus the noise level at the longest baselines) cannot be done well enough.

The CLEAN resolution does not match with the scaling presented in Eq. (2.77). If the noise level would be smaller by a constant factor on all baselines, the dirty beam would not change since the relative weighting between the visibility points stays the same. Hence, the CLEAN resolution limit does not respect the overall signal-to-noise ratio. In the extreme limit of this calculation, for infinite signal-to-noise ratio, CLEAN reconstructions still would have the same resolution limit, albeit a correct model-fitting would be possible (as long as enough degrees of freedom are observed).

General derivations of resolution limits for forward fitting techniques are more complicated. The effective resolution limits for the *general Tikhonov regularization* methods of the form Eq. (2.4) is determined by the balancing between the data terms and the regularization terms. Therefore, a general well-defined res-

olution limit such as for CLEAN cannot be given. It depends on the weighting factors, the true image, how sensitive the regularization terms are to the features of the true sky brightness distribution and the quality of the fit metrics. However, as a rule of thumb, forward modeling techniques can achieve higher resolutions, when the data have more visibility points with less noise. In this case the data terms dominate over the regularization terms that typically impose smoothness (e.g. compare the reconstructions with EHT and ngEHT configuration or single-frequency vs multifrequency reconstructions in Chael et al. 2023; Roelofs et al. 2023). Furthermore, the more sophisticated the used prior information (e.g. prior distributions, simplicity, sparsity or smoothness) match to the observed target, the better small-scale features can be detected.

All in all, the following tendency can be observed in practice: CLEAN has a well defined resolution by the pre-calculated Gaussian restoring beam. This is however too conservative (Broderick et al. 2022a; Chael et al. 2016; Event Horizon Telescope Collaboration et al. 2019b; Müller & Lobanov 2022, 2023a). The theoretical resolution limit is often much better. But this resolution can only be achieved in model-fitting approaches with a very restricted range of image structures (e.g. such as we have to assume that the image is composed of a single Gaussian and fit the parameters of this Gaussian). Forward modeling methods achieve better resolutions than CLEAN (super-resolution by a factor of 2–3) since more advanced prior information is processed at the imaging stage. Therefore, the term super-resolution is misleading. Forward modeling techniques do not super-resolve a structure, but they lean ideas of model-fitting techniques to come closer to the theoretical model fitting resolution.

#### **2.7.4 Supervision**

The necessity of human interaction during the data analysis is often a severe problem for VLBI. One reason for this is that manual image reconstruction takes a lot of time, which might be acceptable for single VLBI experiments, but is simply not acceptable for large-scale surveys. The other reason is that an intensive human interaction with the imaging procedure may introduce a subjective bias, with the resulting reconstruction becoming difficult to reproduce. An automated imaging pipeline is needed and has indeed been used, at least in part, for imaging VLBI data from large surveys such as MOJAVE (Lister et al. 2018).

CLEAN is by design strongly supervised. A scientist applying CLEAN for imaging VLBI data has to make a series of crucial decisions, such as tapering, weighting, CLEAN windows, CLEAN gains, parameters of progressive self-calibration steps, and the criterion for terminating the hybrid imaging cycle. Nearly all of these parameters are varied during the data analysis procedure in

an interactive way. Therefore it is challenging to reproduce CLEAN reconstructions. Indeed the CLEAN reconstructions provided by different scientists often differ significantly, especially for very sparse data sets with corrupted phase information.

RML and Bayesian methods are less supervised by design. They solve a well defined optimization problem without strong need for intermediate adjustments and user intervention. On the contrary, we have to specify a larger number of non-trivial hyperparameters such as the weighting terms, parameters of the prior distributions, or parameters related to the minimization procedure. As a complex, non-linear objective functional is optimized, the effect of each of these hyperparameters on the final reconstruction is way less obvious than for CLEAN. For Event Horizon Telescope Collaboration et al. (2019b, 2022b) therefore extensive parameter surveys were utilized: All possible parameter combinations were tested on a set of synthetic data sets. The top-set consisted of all hyperparameter sets that passed the synthetic data tests. This combination was then applied to the observed data. This brute-force approach, however, is computationally very expensive, specifically for data qualities that require the use full amount of terms in Eq. (2.58).

### 2.7.5 Robustness and Adaptability

Recent rapid developments of novel, and often conceptually different approaches to image reconstruction call for detailed comparisons of their relative performance, robustness, and adaptability. Many of the forward modeling techniques were developed in recent years (Akiyama et al. 2017a,b; Arras et al. 2019, 2021; Broderick et al. 2020a,b; Chael et al. 2016, 2018; Müller & Lobanov 2022, 2023a,b; Tiede 2022). They approach the VLBI imaging problem differently than CLEAN. This led to the development of completely new software packages, e.g. *ehtim*, *SMILI*, *resolve*, *Comrade*, *Themis* and *MrBeam* rather than extending the existing ones. Compared to the experience with the decade-long application of CLEAN in software packages such as *AIPS*, *Difmap* or *CASA*, the relative youth of the new software packages and their limited range of applications by now increases the danger of bugs and pitfalls (although no major bugs were identified by now). The rather simple, but matured, application of CLEAN on the contrary was found to be very robust.

As another criterion we like to bring up adaptability: How easy is it to adapt the existing imaging algorithms to closely related data analysis problems such as polarimetry, dynamic imaging or closure-only imaging. The extension of RML algorithms is very straightforward. As we already shortly discussed in chapter 2.3.4, we could easily replace the data terms by data terms tailored to the cor-

responding problem, e.g. we could use the fit quality to the closure quantities  $S_{\text{cph}}$  and  $S_{\text{cla}}$  instead of  $S_{\text{vis}}$  to be less dependent on the antenna based gains. Furthermore, the extension of the appropriate regularization terms is straightforward as well. For instance, for dynamic imaging as an additional term the temporal correlation/smoothness can be used (Müller & Lobanov 2023b; Roelofs et al. 2023). The same applies for Bayesian methods, although not all possible terms have an easy correspondent in the language of Bayesian statistics. Adapting CLEAN for dynamic imaging, spectral imaging or multifrequency imaging is harder, but possible. The data products often do not have a simple description as a deconvolution problem and explicit (correlation) prior information is more complicated to encode in the image reconstructions. For CLEAN, a series of single deconvolution problems is solved instead with cross-matching at the major cycle step (Rau & Cornwell 2011).

### 2.7.6 Numerical Performance

Finally, we discuss the numerical performance of different image reconstruction approaches. CLEAN is a numerically cheap algorithm. After initiation, the minor loops only consist of rescaling, shifting and substituting of arrays. The Fourier transform does not have to be evaluated in the minor loops. Non-linear least square minimization (first introduced by Briggs 1995) evaluate the Fourier transform in every iteration. On the other hand, CLEAN is a local optimization algorithm: it only updates the residual in the neighborhood of the maximum peak in the residual in the minor cycle iterations. A minimization based on the gradient descent updates the image at every pixel at the same time, thus less iterations are needed. Cornwell et al. (1999) concluded that MEM-reconstructions overtake CLEAN reconstructions in speed for images with more than  $10^6$  pixels. Current RML methods are even more complicated than the early MEM-algorithms. On the other hand, they make use of the enhanced computational speed with the current generation of computing systems. A *ehtim*-reconstruction of an EHT data set does not take longer than a couple of minutes right now on a standard notebook. More advanced multiscale approaches such as *DoG-HiT* (Müller & Lobanov 2022, 2023a) can take up to an hour of computation time. Bayesian algorithms however, have a worse numerical performance due to the expensive sampling of the posterior (Broderick et al. 2020a; Cai et al. 2018a,b). This is caused by the different philosophy behind Bayesian algorithms. While CS, RML, MEM and CLEAN approaches recover only one image (i.e. only approximate the maximum of the posterior distribution), Bayesian algorithms recover the complete posterior landscape with rich additional information about the uncertainty of the recovered features.

Apart from the numerical performance, the data analysis could take much more time as the existing algorithms are not unsupervised. In particular, the necessity for tedious parameter surveys delays the data analysis significantly. The same applies for CLEAN with its manual trial-and-error way of working.

## 2.8 Motivation for New Algorithms

In order to outline better the motivation for developing new algorithms for VLBI image reconstruction, we first summarize the main conclusion from the preceding discussion in this chapter. CLEAN and its variants are the de-facto standard for the VLBI data analysis. However, all CLEAN realizations have well-known limitations, such as a disparity between the model and the image or a worse representation of extended emission. In recent years, many new methods in various frameworks have been proposed: Bayesian, CS, RML and modern MEM algorithms. We have demonstrated above that while these are different perspectives on the imaging problem, they are all closely related. These new methods surpass CLEAN in most evaluation metrics such as resolution, accuracy, and adaptability, while (similarly to CLEAN) their reconstructions rely on a larger number of hyperparameters. For Bayesian and RML methods, the effect of the hyperparameters on the final reconstruction is particularly difficult to be assessed. In this dissertation we propose several competitive alternatives that combine less supervision (i.e. less sensitivity to input parameters) with the known advantages of forward modeling techniques.

Firstly, we propose a new method in the framework of RML and CS imaging methods and present steps towards an unsupervised, automated imaging pipeline. RML methods achieve their superior performance due to the combination of various data terms and regularization terms. But the result depends strongly on the a-priori unknown weights of the terms. The penalty terms promote sparsity, smoothness and simplicity respectively. These terms prove efficient, with the correct weighting, to recover high quality images. Our approach is different. We construct a novel penalty term that is as data-driven as possible. As this penalty term is inspired in an automatized fashion from the uv-coverage, i.e. the data structure itself, the penalty term is automatically tailored to the experiment. Therefore, we do not need a series of regularizers, but only one regularization term. We demonstrate that, although the optimization landscape is much easier, this new method (DoG-HiT) shares the advantages of RML methods (super-resolution, high accuracy) and even surpasses them in terms of sensitivity to extended emission (Müller & Lobanov 2022) while simultaneously providing a strong reduction in the number of free parameters used for the reconstruction.

To this end, we propose to use a wavelet dictionary fitted to the uv-coverage and utilize sparsity in the wavelet domain in the spirit of compressive sensing theory. For more details, we refer to the following chapters and Müller & Lobanov (2022, 2023a,b,c). This new method (DoG-HiT) is unsupervised (wavelet dictionary automatically selected, only one free parameter with a-priori parameter choice), topping CLEAN in all relevant metrics and being competitive to RML methods. Moreover, DoG-HiT can be used as a basis for several extensions of the standard imaging problem. Challenging extensions of the classical imaging problem, such as closure-only imaging, dynamical imaging and polarimetry, can be easily tackled with the specific, newly designed regularizer method. In particular, DoG-HiT is independent of antenna based gains by only processing closure phases and closure amplitudes. Furthermore, we succeeded to transfer the main concepts behind DoG-HiT to a second new algorithm (DoB-CLEAN) that works in the framework of CLEAN, and thus allows for an iterative data manipulation and data investigation (Müller & Lobanov 2023a). DoB-CLEAN successfully overcomes some of the known limitations of CLEAN.

Complementary to the wavelet based approach, we propose a multiobjective evolutionary algorithm (MOEA/D) as a viable alternative. With MOEA/D we probe the complete set of locally optimal (non-dominated) solutions with respect to the input parameters: the Pareto front (Zhang & Li 2007) which spans a hypersurface in the domain of possible solutions. These solutions appear to be clustered in clusters of coincident solutions (Müller et al. 2023d). All solutions in the Pareto front are mathematically optimal. With this technique we are able to investigate the range of all reasonable images that fit the data similar in philosophy to a Bayesian exploration, although an interpretation of the clusters as a Bayesian posterior would be an over-interpretation (Müller et al. 2023d). Imaging now deals with the question of choosing the most natural image among all possible images clusters. We present a selection criterion based on the principle of least action and benchmark its performance on synthetic and observational data. In that way, MOEA/D provides a completely data-driven and unsupervised best guess reconstruction with an additional robustness estimate.

As a side product we have designed and developed the novel imaging software *MrBeam* and contributed significantly to *regpy*. *MrBeam* and *regpy* implement iterative regularization of the *general Tikhonov method* with the tools of convex optimization. Such a modular software package is of interest also outside of the VLBI community. Thus, we were able to contribute with this work significantly to such versatile fields such as Ly $\alpha$  tomography (Müller et al. 2020, 2021), the search for dark matter (Hamaide et al. 2022), medical imaging (MRI) and solar observations.

### 3 Multiscale VLBI Imaging

We present in this chapter the novel multiscale imaging algorithms DoG-HiT and DoB-CLEAN. First we recall the motivation and main idea behind the project. Then we show the main publications relevant for this dissertation. Finally, we present the imaging pipeline and an overview of the software tools used in practice. The publications presented in this chapter are in this order:

- **Müller, H.** and Lobanov, A.P.: *DoG-HiT: A novel VLBI Multiscale Imaging Approach*, 2022, A&A, 666, A137. Conceptualization: H.M., A.L., methodology/software: H.M., formal data analysis: H.M., writing/editing: H.M., A.L.. — Müller & Lobanov (2022), **Paper 1**
- **Müller, H.** and Lobanov, A.P.: *Multi-scale and multi-directional VLBI imaging with CLEAN*, 2023, A&A, 672, A26. Conceptualization: H.M., A.L., methodology/software: H.M., formal data analysis: H.M., writing/editing: H.M., A.L.. — Müller & Lobanov (2023a), **Paper 2**
- **Müller, H.** and Lobanov, A.P.: *Dynamic and polarimetric VLBI imaging with a multiscale approach*, 2023, A&A, 673, A151. Conceptualization: H.M., A.L., methodology/software: H.M., formal data analysis: H.M., writing/editing: H.M., A.L.. — Müller & Lobanov (2023b), **Paper 3**
- **Müller, H.** and Lobanov, A.P.: *Multiscale VLBI Imaging*, 2023, Proceedings of the 15th European VLBI Network Mini-Symposium and Users' Meeting, DOI: <https://doi.org/10.22323/1.428.0056>. Conceptualization: H.M., A.L., methodology/software: H.M., writing/editing: H.M., A.L.. — Müller & Lobanov (2023c), partially reproduced in Sec. 3.5 and in Sec. 3.7.

#### 3.1 Rationale

Our prime goal is to define a data-driven regularizer, allowing for unsupervised imaging. Recalling from chapter 2, the imaging problem can be understood as a deconvolution problem. During the deconvolution, the sidelobes arising in the dirty image due to gaps in the uv-coverage ought to be suppressed. To achieve this, we aim to interpolate the fit in the Fourier domain to the uv-gaps. In this perspective, the rationale behind DoG-HiT is easy to explain: we want to find the simplest, physically reasonable model that fits the visibilities. These requirements, i.e. fitting the visibilities while being physically reasonable and as simple as possible, can be translated to the Fourier domain as follows:

- We have to ensure that the recovered model fits the observed visibilities, i.e. we have to minimize a reasonable data-fidelity term in the objective functional. To be less dependent on the phase and amplitude calibration, we propose to use closure phases  $S_{\text{cph}}$  and closure amplitudes  $S_{\text{cla}}$  here.
- The recovered model should be physically reasonable, i.e. free of secondary sidelobes and reasonably smooth. Hence, the interpolation in the Fourier domain has to satisfy the same requirements: we want to smoothly interpolate the fit to the gaps of the uv-coverage.
- The model should be as simple as possible to fit the observed data reasonably. In particular, we do not want to induce image features that are mainly compressed by Fourier frequencies in the gaps of the uv-coverage, i.e. by not measured visibilities. This requirement is particularly important for VLBI observations with a high sparsity.

From these three points, it becomes obvious that spatial scales covered by observations need to be clearly distinguished from those not covered by observations. To this end, we use specially designed wavelets as basis functions. The image is decomposed by these basis functions. Following the Fourier deconvolution theorem, convolution with a basis function in the image domain is equivalent to multiplication by its Fourier transform in the Fourier domain. Hence, the decomposition by a dictionary of basis functions can be equivalently understood as a multiplication by spatial frequency filters in the Fourier domain. We make use of this idea to separate covered from non-covered scales. By fitting the filters to the uv-coverage, some of the basis functions compress the image scales corresponding to the gaps of the coverage and should hence be smoothly suppressed (simplicity). As an additional requirement, the basis functions itself have to be smooth and free of sidelobes to allow for physically reasonable reconstructions.

The following publications present a series of developements for DoG-HiT over the course of the last years. In Müller & Lobanov (2022), we presented the initial description of the method, and we demonstrated its capabilities on synthetic data. In Müller & Lobanov (2023a), we discussed which set of basis functions would be optimal. We extended DoG-HiT to multidirectional dictionaries, difference of spherical Bessel functions as basis functions, and presented for the first time the idea of switching between two dictionaries. Furthermore, in Müller & Lobanov (2023a) we combined and translated the ideas behind DoG-HiT and our findings about optimal dictionaries to a novel MS-CLEAN framework. In Müller & Lobanov (2023b) we extended DoG-HiT to dynamic imaging and polarimetry. A concise overview of the current state of DoG-HiT and DoB-CLEAN, combining

all these developments together, and adding a total flux calibration step to the pipeline was presented in Müller & Lobanov (2023c).

### 3.2 Paper 1: Müller & Lobanov 2022, A&A, 666, A137

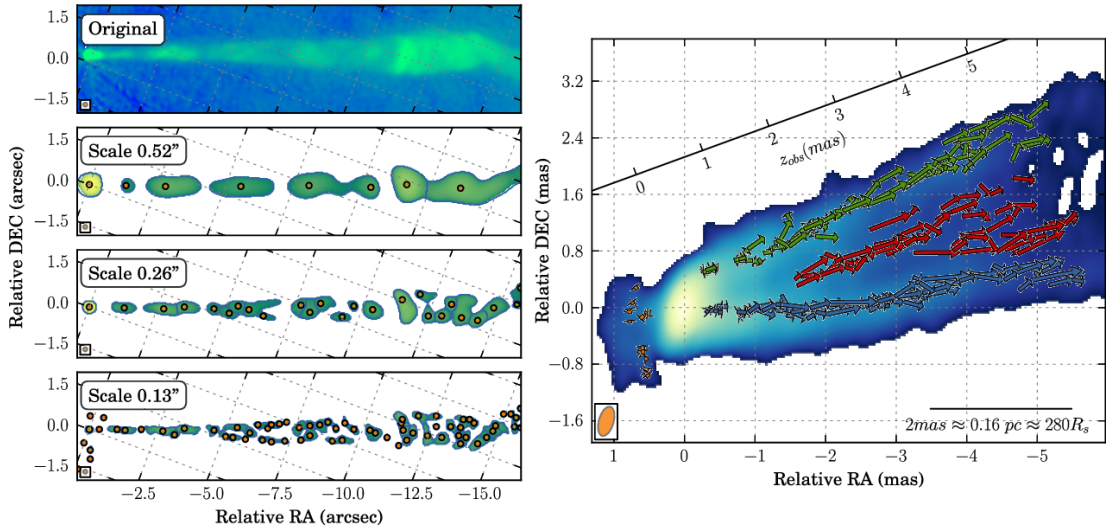


Figure 3.19: Multiscale Decomposition of the jet in M87. Images are adapted from Mertens et al. (2016).

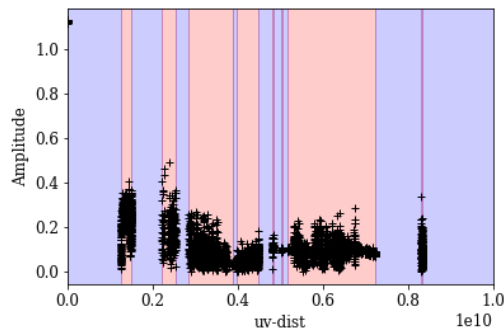


Figure 3.20: Synthetic uv-coverage of an EHT observation. The radial distribution of visibility points has significant radial gaps (blue shaded).

We present the basic DoG-HiT publication in this subsection. The project on multiscale VLBI imaging was mainly inspired by the recent successes of wavelet transforms in sparse representation of image features that are typical for the primary VLBI targets, i.e. for AGN core-jet structures. One example of such application is provided by the jet segmentation presented in Mertens & Lobanov (2015) and Mertens et al. (2016). Mertens & Lobanov (2015) demonstrated that an AGN jet can be effectively decomposed with a wavelet transform into subbands of a specific spatial scale, compare e.g. Fig. 3.19. This procedure has been used to divide the jet into spatial components by a watershed segmentation and track

these components in time to infer the dynamics within the jet. In this work, we transferred the ideas and the software of Mertens & Lobanov (2015); Mertens et al. (2016) to the visibility domain and studied their use for VLBI imaging. To this end, we are primarily focused on EHT data reductions and on addressing the problem of missing spatial frequencies inherent to interferometric data. The radial distribution of the visibility points, see Fig. 3.20, has clearly separable covered visibilities and uncovered gaps. DoG-HiT is designed to identify these gaps and turn this spatial information in a strong prior information.

Multiscalar RML imaging algorithms have been proposed before (e.g. Carrillo et al. 2012, 2014; Garsden et al. 2015; Girard et al. 2015; Li et al. 2011; Mouri Sardarabadi et al. 2016; Onose et al. 2016, 2017; Pantin & Starck 1996; Pratley et al. 2018; Starck et al. 2001; Wiaux et al. 2009). DoG-HiT presents the first variant that was directly developed for application in VLBI. It differs from previous attempts by using a different wavelet transform (fitted to the uv-coverage to account for the typical gaps in the VLBI uv-coverages), the use of non-linear and non-convex, but calibration-agnostic data terms, the minimization procedure and data-analysis pipeline.

## DoG-HiT: A novel VLBI multiscale imaging approach

H. Müller, and A. P. Lobanov

Max-Planck-Institut für Radioastronomie, Auf dem Hügel 69, Bonn 53121, Germany  
 e-mail: [hmueller@mpi-fr-bonn.mpg.de](mailto:hmueller@mpi-fr-bonn.mpg.de); [alobanov@mpi-fr-bonn.mpg.de](mailto:alobanov@mpi-fr-bonn.mpg.de)

Received 1 February 2022 / Accepted 14 June 2022

### ABSTRACT

**Context.** Reconstructing images from very long baseline interferometry (VLBI) data with a sparse sampling of the Fourier domain ( $uv$ -coverage) constitutes an ill-posed deconvolution problem. It requires application of robust algorithms, maximizing the information extraction from all of the sampled spatial scales, and minimizing the influence of the unsampled scales on image quality.

**Aims.** We develop a new multiscale wavelet deconvolution algorithm, DoG-HiT, for imaging sparsely sampled interferometric data, which combines the difference of Gaussian (DoG) wavelets and hard image thresholding (HiT). Based on DoG-HiT, we propose a multistep imaging pipeline for analysis of interferometric data.

**Methods.** DoG-HiT applies the compressed sensing approach to imaging by employing a flexible DoG wavelet dictionary, which is designed to adapt smoothly to the  $uv$ -coverage. It uses closure properties as data fidelity terms only, initially, and performs nonconvex, nonsmooth optimization by an amplitude-conserving and total-flux-conserving, hard thresholding splitting. DoG-HiT calculates a multiresolution support as a side product. The final reconstruction is refined through self-calibration loops and imaging with amplitude and phase information applied for the multiresolution support only.

**Results.** We demonstrate the stability of DoG-HiT, and benchmark its performance against image reconstructions made with the CLEAN and regularized maximum-likelihood (RML) methods using synthetic data. The comparison shows that DoG-HiT matches the super-resolution achieved by the RML reconstructions and surpasses the sensitivity to extended emission reached by CLEAN.

**Conclusions.** The application of regularized maximum likelihood methods, outfitted with flexible multiscale wavelet dictionaries, to imaging of interferometric data, matches the performance of state-of-the-art convex optimization imaging algorithms and requires fewer prior and user-defined constraints.

**Key words.** techniques: interferometric – techniques: image processing – techniques: high angular resolution – methods: numerical – galaxies: jets – galaxies: nuclei

### 1. Introduction

In very long baseline interferometry (VLBI), signals recorded at individual radio antennas are combined (correlated) in order to sample angular scales inversely proportional to pairwise antenna separations projected onto the plane of the incoming wavefront. Described by the van Cittert–Zernike theorem, the correlation product (visibility) of the signals recorded at two antennas at a given time is given by a single spectral harmonic corresponding to a single spatial frequency of the Fourier transform of the observed sky brightness distribution (see [Thompson et al. 1994](#)). From a complete sampling of spatial frequencies, the true image could be revealed by the inverse Fourier transform. However, the practical limitations on the number of antennas, observing bandwidth, and observing time often result in a situation where VLBI data provide only sparse sampling ( $uv$ -coverage) of the spatial frequencies (or “Fourier domain”), below the Nyquist–Shannon sampling rate.

The development of powerful imaging algorithms such as CLEAN ([Högbom 1974](#)) and their decade long successful application in VLBI studies demonstrated that a reliable reconstruction of the true sky brightness distribution is still possible under a strong assumption that the sky brightness distribution is compressible as a sum of point sources. CLEAN and its many variants (e.g., [Clark 1980](#); [Schwab 1984](#)) work well not only for compact structures but also for extended emission. CLEAN

is still broadly used, mainly because it is practical. However, frontline VLBI applications, such as millimeter- or space-VLBI, demand better imaging tools that would alleviate the known limitations of CLEAN and provide super-resolution, multiscale decompositions, and a high dynamic range.

Multiresolution imaging routines based on the greedy matching pursuit procedure, inherent to CLEAN, have been developed for decades now ([Wakker & Schwarz 1988](#); [Starck et al. 1994](#); [Bhatnagar & Cornwell 2004](#); [Cornwell 2008](#); [Rau & Cornwell 2011](#)). These studies build upon the great success of compressed sensing theory (e.g., [Candès et al. 2006](#); [Donoho 2006](#)), namely that an image can be sparsely represented in a suitable set of basis functions (atoms). Even the CLEAN algorithm (sparsity in pixel basis; [Lannes et al. 1997](#)) and total variation regularization methods (sparsity of the Haar wavelet) could be understood in this way.

Imaging algorithms based on wavelets attract close attention from the astronomy community because they stand out as extremely helpful in the analysis and compression of image features on multiple scales ([Starck & Murtagh 2006](#); [Starck et al. 2015](#); [Mertens & Lobanov 2015](#); [Line et al. 2020](#)). Both extended emission features and small-scale structures are well compressible with wavelets. Moreover, wavelets of varying scales are sensitive to different ranges of visibilities, allowing the user to incorporate information about the radially distributed positions of gaps in the  $uv$ -coverage in the imaging procedure. Hence,

sparsity in the wavelet domain is a strong and interesting image prior for the radio aperture synthesis imaging problem.

The past five decades have seen an ongoing development of regularized maximum likelihood (RML) methods for interferometric imaging, in particular with the development of image entropy regularizers such as the maximum entropy method (MEM; e.g., Frieden 1972; Narayan & Nityananda 1986; Wiaux et al. 2009; Li et al. 2011; Garsden et al. 2015; Thiébaud & Young 2017). The RML methods have been applied particularly extensively for imaging with the Event Horizon Telescope (EHT; e.g., Ikeda et al. 2016; Akiyama et al. 2017b,a; Chael et al. 2018; Event Horizon Telescope Collaboration 2019). In a typical RML application, the image is recovered by simultaneously minimizing a data fidelity term, which measures the proximity of the recovered solution to the true data, namely visibilities and/or closure properties, and a set of regularization terms, which measure the feasibility of the recovered solution. It has been demonstrated that  $l_1$ -penalty terms promote sparsity in the image domain. Hence, RML algorithms and the progress in convex optimization (Beck & Teboulle 2009; Combettes & Pesquet 2009) provide a powerful framework for respecting sparsity during image deconvolution.

However, the deficiencies of  $uv$ -coverages, inherent to such interferometric instruments as the EHT or the space VLBI mission *RadioAstron*, pose additional challenges. Compressed sensing approaches applied to data from such arrays are capable, in principle, of recovering the significant structure of the target (achieving small data fidelity terms), while suppressing any additional noise-induced image features and sidelobes (achieving small penalty terms). However, in VLBI observations the sidelobes and the true image structure often become comparable in their magnitudes. The suppression of structure due to image sparsity affects the recovered data significantly. A more advanced treatment of image features, in other words a more advanced differentiation between observed emission and noisy structures induced by  $uv$ -gap, and an amplitude conserving optimization strategy are needed. Furthermore, an unsupervised approach for blind imaging is desired.

Random and systematic noise factors in the final image can be induced at various steps of the analysis. In particular, errors resulting from  $uv$ -coverage deficiencies and antenna-based noise factors (calibration issues, thermal noise) depend on the location of the trace of the antenna pair in the  $uv$ -plane. Hence, these errors are scale and direction dependent. We need a novel algorithm that can deal with this, in other words one that can automatically decompose noisy features from signal features. This is a task that is suitable for wavelets in the first instance, since they decompose the image into a sequence of scales. Direction-dependent information is more difficult to compress and will not be addressed in this paper.

In this paper, we present a new multiscale wavelet imaging algorithm built upon the compressed sensing approach. Our method goes beyond standard sparsity, promoting imaging algorithms by applying a more stringent separation of significant image features from noise contributions, by using an adaptive wavelet dictionary and suppressing the noise-induced artifacts in a novel amplitude-conserving hard thresholding algorithm. This algorithm is well suited for dealing with high-level sidelobes such as those typically found in the data from the EHT or space-VLBI observations.

An important feature of the algorithm is that the initial selection of the scales in the wavelet dictionary is derived from the  $uv$ -coverage of observations, and not from any assumptions about the structure of the target source. We utilize current

state-of-the-art optimization algorithms to solve the resulting RML minimization problem, but amend the imaging pipeline by a hard thresholding sparsity term based on the multiresolution support, which allows us to retain necessary image information while suppressing noisy scales. We deal with potential residual calibration deficiencies of the data by first using only the gain-invariant closure quantities for imaging and then, after identifying and suppressing noise contributions, imaging the full data with an optimized, fixed multiresolution support. The resulting objective functional for minimization is not convex and not smooth, which requires employing nonconvex and nonsmooth optimization strategies. We present a final imaging pipeline that is immediately applicable to VLBI data. This imaging pipeline requires considerably fewer parameters than typical RML pipelines, thereby presenting a viable step toward a more unsupervised imaging approach.

We test our pipeline routine on test images that were recently used to verify the modern generation of RML image routines (Tiede et al. 2020). For incomplete  $uv$ -coverages, our algorithm performs better than the canonical CLEAN algorithm and its multiscale variants, owing to the flexibility of the dictionary (allowing it to be adapted to a specific  $uv$ -coverage of the array), the sparse representation of astronomical images in the wavelet basis (compared to the representation with the CLEAN or MS-CLEAN components), and the correct treatment of scale-dependent noise properties.

## 2. Theory

This section summarizes the relevant theory and background for different aspects of the new algorithm. We focus primarily on application of wavelets for deconvolution in aperture synthesis and on specific aspects of the optimization procedures applied to sparsely sampled data.

### 2.1. Aperture synthesis

In interferometric observations, every antenna in the array records the electromagnetic field of an incoherent sky brightness distribution  $I(x, y)$ , where  $x$  and  $y$  are angular coordinates on the sky. Following the van Cittert–Zernike theorem, the cross-correlation between the signals recorded by two antennas over a baseline  $(u, v)$  (spatial frequencies in units of wavelengths) is given by the Fourier transform of  $I(x, y)$  at this baseline:

$$\mathcal{V}(u, v) = \iint e^{-2\pi i(xu+yv)} I(x, y) dx dy, \quad (1)$$

where  $\mathcal{V}$  is the complex visibility. This relation holds under assumptions of a flat wavefront and a small field-of-view approximation. Every antenna pair, at a fixed time, gives rise to a specific baseline. The projection of a baseline on a plane orthogonal to the direction to the target shifts smoothly by time due to Earth rotation describing the typical elliptical traces in  $uv$ -coverages. However, due to the small number of antennas in VLBI arrays, the coverage of measurements in the  $uv$ -domain remains sparse. In particular, gaps in the  $uv$ -coverage introduce sidelobes and artefacts in the recovered image. When inverting the Fourier transform (to produce  $I^D$ ), the result can be written as a convolution:

$$I^D = B * I, \quad (2)$$

where  $I^D$  is the dirty image, meaning the inverse Fourier transform of the (tapered) observed visibilities, and  $B$  is the dirty

beam, meaning the inverse Fourier transform of the (tapered) projection onto measured baselines in the Fourier codomain.

Aperture synthesis imaging is the problem of recovering the true distribution  $I(x, y)$  from a discrete, sparse set of observed visibilities. This procedure could also be understood as a deconvolution problem, see Eq. (2). The incomplete  $uv$ -coverage introduces direction- and scale-dependent sidelobe patterns in the dirty image and the dirty beam. Deconvolution, in this case, becomes an ill-posed inverse problem. In particular, the solution to the imaging problem in Eq. (2) is, strictly speaking, not unique as Fourier harmonics are missing from the observation (historically called the “invisible distributions”). A successful deconvolution method must be able to identify and categorize these invisible distributions and minimize their impact on the restored image.

Image restoration is further complicated by the variable thermal noise and signal-to-noise ratio (S/N) of visibility measurements. The visibility S/N is systematically reduced at long baselines. As the antenna sensitivity enters the reconstruction at specific scales and directions, determined by the position of the baseline corresponding to a given antenna pair, the noise becomes scale and direction dependent.

Various calibration issues also need to be addressed during image restoration. Systematic direction-independent calibration errors can be factorized into multiplicative station-based gains  $g_i$  (where the index  $i$  denotes the antenna in the array), affecting the relation between the observed visibilities  $V_{ij}$  and the true visibilities  $\mathcal{V}_{ij}$ :

$$V_{ij} \approx g_i g_j^* \mathcal{V}_{ij} + N_{ij}, \quad (3)$$

where  $N_{ij}$  denotes thermal noise on the baseline. In particular, phase information is typically only available after a calibration by an ad hoc initial model. In standard imaging approaches (e.g., in CLEAN), the problem of calibration is typically addressed through a hybrid imaging approach. In this case, an initial image is first produced using the a priori set of instrumental gains, and then the gain terms are solved for, as in Eq. (3), in order to enforce consistency with the current image guess (with the solution typically obtained by a gradient descent approach or self-calibration). These two steps are repeated iteratively until the desired image quality is reached. In this way, alternating self-calibration and imaging steps converge to a self-contained model description, consistent with the observed and self-calibrated data.

Some of the calibration issues can be circumvented by employing closure quantities computed from combinations of visibilities that are independent of antenna-based gain errors. The closure phase,  $\Psi_{ijk}$ , is the phase over a triangle of antennas  $i, j, k$ :

$$\Psi_{ijk} = \arg(V_{ij} V_{jk} V_{ki}). \quad (4)$$

The closure amplitude,  $A$ , is the ratio of amplitudes over a square of antennas  $i, j, k, l$ :

$$A_{ijkl} = \frac{|V_{ij}| |V_{kl}|}{|V_{ik}| |V_{jl}|}. \quad (5)$$

Not all closure triangles and closure squares are independent, which leads to the number of total observables being reduced. We assume that at a specific time  $N$ , antennas are observing simultaneously. This gives rise to  $N(N-1)/2$  independent baselines, while there are only  $(N-1)(N-2)/2$  independent closure

phases, and  $N(N-3)/2$  independent closure amplitudes (Chael et al. 2018). Hence, the number of observables is reduced by a fraction of  $1-2/N$  for closure phases, and  $1-2/(N-1)$  for closure amplitudes.

## 2.2. Deconvolution

Historically, the imaging problem described by Eq. (2) has been addressed through inverse modeling, that is, by CLEAN (Högbom 1974), which can be classified as a greedy, matching pursuit algorithm. The problem is first translated into a deconvolution problem by taking the inverse Fourier transform of the visibilities. Hence, CLEAN needs to perform this inversion on calibrated complex visibilities at every stage. The deconvolution problem is therefore solved by inverse modeling; CLEAN searches iteratively for the position of the maximum in the residual image, stores this in a list of delta-components, and updates the residual by subtracting the rescaled and shifted dirty beam from the residual image. In multiscale variants of CLEAN, the delta components are replaced by more sophisticated extended basis functions (Bhatnagar & Cornwell 2004; Cornwell 2008; Rau & Cornwell 2011). In recent years, there has been a continued development of imaging by forward modeling (e.g., Garsten et al. 2015; Akiyama et al. 2017b; Chael et al. 2018) in which Eq. (1) is solved by fitting a model solution to the visibilities, by minimizing the error in some cost functional (data fidelity term). With this forward modeling approach, RML methods can work directly on the closure quantities or a mix of data products in order to reduce the influence of calibration errors on the reconstruction. Regularization and missing information are dealt with by simultaneously minimizing a penalization term, which promotes the desired image features (i.e., sparsity, smoothness, or small entropy). The resulting minimization problem is then solved by standard numerical optimization algorithms, such as a gradient descent algorithm.

A major advantage of the work presented in this paper is the use of novel basis functions (i.e., wavelets). We will discuss them in more detail in Sect. 2.3. These wavelets are extended and allow a more thorough analysis of the  $uv$ -coverage of the observations. The basis functions used in the (MS-)CLEAN and RML methods do not typically offer this kind of analysis. The standard CLEAN (Högbom 1974) algorithm models the image as a set of delta functions. Its multiscale variants use some version of truncated Gaussian functions (see the discussions in Cornwell 2008). RML methods utilize pixel grids.

## 2.3. Wavelets

The continuous wavelet transform (CWT) could be understood as an extension of the Fourier transform (Starck et al. 2015), in which the Fourier decomposition in the frequency domain is amended by a windowing of the measurement domain with a specially designed analyzing wavelet function. In the definition of Grossmann et al. (1989), the CWT related to an analyzing wavelet  $\Phi(t)$  operates in one dimension on the space of square integrable functions so that

$$I \mapsto W(a, b) = \frac{1}{\sqrt{a}} \int I(t) \Phi^* \left( \frac{t-b}{a} \right) dt = I * \tilde{\Phi}_a(b), \quad (6)$$

where  $\tilde{\Phi}_a(t) = \frac{1}{\sqrt{a}} \Phi^* \left( \frac{-t}{a} \right)$ ,  $a$  is the scale parameter, and  $b$  is the position parameter. Hence, the CWT effectively performs a number of convolutions with dilated versions of the analyzing wavelet  $\Phi$ . There are different choices for analyzing wavelet

functions, including the Morlet wavelet (Goupillaud et al. 1984; Coupinot et al. 1992), the Haar wavelet (Stollnitz et al. 1994), the Mexican-hat wavelets (Murenzi 1989), and discrete versions (e.g., see Mallat 1989; Starck et al. 2015, and references therein).

In this work we are using difference of Gaussian (DoG) wavelets that are commonly applied to approximate Mexican-hat wavelets (Gonzalez & Woods 2006; Assirati et al. 2014):

$$\begin{aligned} \Phi_{\text{DoG}}^{\sigma_1, \sigma_2}(x, y) &= \frac{1}{2\pi\sigma_1^2} \exp\left(\frac{-r(x, y)^2}{2\sigma_1^2}\right) - \frac{1}{2\pi\sigma_2^2} \exp\left(\frac{-r(x, y)^2}{2\sigma_2^2}\right) \\ &= G_{\sigma_1} - G_{\sigma_2}, \end{aligned} \quad (7)$$

where necessarily  $\sigma_1 \leq \sigma_2$ , and  $G_{\sigma_j}$  denotes a Gaussian with standard deviation  $\sigma_j$ .

Wavelets in the image domain (convolution) directly translate to masks in the Fourier domain (pointwise multiplication):

$$\mathcal{F}\Phi_{\text{DoG}}^{\sigma_1, \sigma_2}(u, v) \propto \exp(-2\pi^2\sigma_1^2q(u, v)^2) - \exp(-2\pi^2\sigma_2^2q(u, v)^2), \quad (8)$$

where  $q(u, v)$  denotes the radius in Fourier domain.

Of special interest for image compression is the discrete wavelet transform, in particular the à trous wavelet transform (also called the starlet transform). In a nutshell, the à trous wavelet transform aims to compute a sequence of smoothing scales  $c_j$  by convolving the image with a discretized smoothing kernel dilated by  $2^j$  pixels, where  $j$  labels the scale and ranges from 0 up to a final smoothing scale  $J$ . Wavelet scales are defined as the difference of two smoothing scales:

$$\omega_j = c_j - c_{j+1}. \quad (9)$$

The last smoothing scale  $c_J$  is added to the set of wavelet scales resulting in the set:  $[\omega_0, \omega_1, \dots, \omega_{J-1}, c_J]$ . This set decomposes the initial image into subbands  $\omega_j$ , each of them containing information on spatial scales from  $2^j\rho$  to  $2^{j+1}\rho$ , where  $\rho$  is the smallest scale in the image, namely the width of the smoothing kernel (which is often chosen to be close to the pixel scale). The set is complete in the sense that the image at the limiting resolution  $c_0$  can be recovered by summing all scales:

$$c_0 = \sum_j \omega_j + c_J. \quad (10)$$

The à trous wavelet transform has a wide range of applications and was successfully applied to radio interferometry previously (e.g., Li et al. 2011; Garsden et al. 2015). However, the à trous wavelet decomposition, by construction, allows only for scales with the widths of  $2^0, 2^1, 2^2, 2^3, \dots$  pixels. In this study, we are interested in obtaining a more flexible selection of scales in order to adapt the scales to the  $uv$ -coverage and differentiate better between well- and poorly constrained spatial scales.

Therefore, we propose constructing a continuous wavelet decomposition out of DoG wavelets in the same way as the à trous wavelet transform was constructed out of a discretized smoothing kernel. We select an ascending sequence of widths  $\sigma_0 \leq \sigma_1 \leq \dots \leq \sigma_J$  and compute the smoothing scales  $c_j$  by convolution with Gaussians that have widths  $\sigma_j$ , namely  $c_j = I * G_{\sigma_j}$ . The wavelet scales  $\omega_j$  are then set by

$$\omega_j = c_j - c_{j+1} = I * \Phi_{\text{DoG}}^{\sigma_j, \sigma_{j+1}}, \quad (11)$$

which sufficiently approximates the Mexican hat wavelet scales.

We call a set of basis functions in compressed sensing a “dictionary”, while the basis functions themselves are called “atoms”

of the dictionary. The term dictionary is also used for the linear mapping that evaluates a coefficient array of these atoms (Starck et al. 2015). The set of DoG wavelet functions  $\Phi_{\text{DoG}}^{\sigma_j, \sigma_{j+1}}$ , together with the last smoothing scale  $G_{\sigma_J}$ , builds a multiscale dictionary  $\Gamma$ :

$$\Gamma : (I_0, I_1, I_2, \dots, I_J) \mapsto \sum_{j=0}^{J-1} \Phi_{\text{DoG}}^{\sigma_j, \sigma_{j+1}} * I_j + G_{\sigma_J} * I_J. \quad (12)$$

The atoms of the dictionary  $\Gamma$  are the wavelets  $\Phi_{\text{DoG}}^{\sigma_j, \sigma_{j+1}}$  and  $G_{\sigma_J}$ . By construction, see also Eq. (10), all atoms in the dictionary sum to  $G_{\sigma_0}$ , which (given that  $\sigma_0$  should be chosen very small, i.e.,  $G_{\sigma_0}$  is a delta peak at the pixel scale) indicates that the dictionary  $\Gamma$  has full rank.

Another crucial property of the dictionary  $\Gamma$  is that the integral of the atoms  $\Phi_{\text{DoG}}^{\sigma_j, \sigma_{j+1}}$  is vanishing. Hence, only the final smoothing scale  $G_{\sigma_J}$  transports the total flux in the image.

The subbands  $I_j$  hold the information of the image at a respective scale described by  $\sigma_j$  and  $\sigma_{j+1}$ . We will denote the collection of subbands of an image  $I$  by  $\mathcal{I} = \{I_1, I_2, \dots, I_J\}$  for the rest of the paper. However, even if  $I = \Gamma(I_1, I_2, \dots, I_J)$  holds, it is usually  $I_j \neq \omega_j$  due to the nonorthogonality of the DoG wavelet functions. Nevertheless,  $\omega_j$  should provide a reasonable initial guess if one tries to find an array  $\mathcal{I} = \{I_1, I_2, \dots, I_J\}$  that satisfies  $I = \Gamma\mathcal{I}$ .

#### 2.4. Sparsity-promoting regularization

We apply sparsity-promoting regularization in the generalized Tikhonov framework:

$$\hat{\mathcal{I}} \in \operatorname{argmin}_{\mathcal{I}} [S(F\Gamma\mathcal{I}, V) + \alpha R(\mathcal{I})], \quad (13)$$

where  $S$  is the data fidelity term, which measures the proximity between the recovered visibilities  $F\Gamma\mathcal{I}$  and the observed visibility data,  $V$ . The term  $F$  denotes mapping of the image intensity onto the visibilities, meaning it computes a tapered and weighted projection of the Fourier transform of  $x$  on a discrete and fixed sampling. The term  $R$  denotes the regularization term, which measures the feasibility of the guess  $\mathcal{I}$ . The parameter  $\alpha$  controls the bias between both terms. The final recovered image solution is then:

$$\hat{I} = \Gamma\hat{\mathcal{I}}. \quad (14)$$

The data fidelity terms used for this paper are introduced as follows. Let  $\mathcal{V} = F\Gamma\mathcal{I}$  denote the visibility data predicted from the current guess. We quantify the proximity between the predicted and measured visibilities by the effective  $\chi^2$ -distance between them,

$$S_{\text{vis}}(\mathcal{V}, V) = \frac{1}{N_{\text{vis}}} \sum_{i=1}^{N_{\text{vis}}} \frac{|\mathcal{V}_i - V_i|^2}{\Sigma_i^2}, \quad (15)$$

where  $N_{\text{vis}}$  is the number of visibilities and  $\Sigma_i$  the estimated thermal noise of a given visibility. This  $\chi^2$  corresponds directly to a log-likelihood, given uncorrelated Gaussian thermal noise on the different baselines. In addition to this, we also use similar distances defined for three additional quantities: (a) the distance between the measured and predicted visibility amplitudes,

$$S_{\text{amp}}(\mathcal{V}, V) = \frac{1}{N_{\text{vis}}} \sum_{i=1}^{N_{\text{vis}}} \frac{(|\mathcal{V}_i| - |V_i|)^2}{\Sigma_i^2}; \quad (16)$$

(b) the distance between the measured and predicted closure phases,

$$S_{\text{cph}}(\mathcal{V}, V) = \frac{1}{N_{\text{cph}}} \sum_{i=1}^{N_{\text{cph}}} \frac{|\Psi_i(\mathcal{V}) - \Psi_i(V)|^2}{\Sigma_{\text{cph},i}^2}, \quad (17)$$

where  $N_{\text{cph}}$  is the number of closure phase combinations,  $\Sigma_{\text{cph},i}$  the noise on a closure phase  $\Psi_i(V)$ , and  $\Psi_i(\mathcal{V})$  denotes the respective closure phase computed from the array of predicted visibilities,  $\mathcal{V}$ ; and finally, (c) the distance between the measured and predicted closure amplitudes,

$$S_{\text{cla}}(\mathcal{V}, V) = \frac{1}{N_{\text{cla}}} \sum_{i=1}^{N_{\text{cla}}} \frac{|\ln A_i(\mathcal{V}) - \ln A_i(V)|^2}{\Sigma_{\text{cla},i}^2}, \quad (18)$$

with similar conventions as for the closure phases. We would like to note here that Eqs. (17) and (18) are only approximate expressions for the correct log-likelihoods for closure products (e.g., Blackburn et al. 2020; Arras et al. 2022). These approximations and the combinations of them are applied in Sect. 4 for the analysis of test data.

It is known that sparsity is promoted by convex pseudonorm functionals as a regularization term (Starck et al. 2015), for example by a term of the form:

$$R_{l_0}(\mathcal{I}) = \|\mathcal{I}\|_{l_0} = \sum_{j=0}^J \sum_i w_j |I_j^i|, \quad (19)$$

with weights  $w_j = \max_{\text{DoG}} \Psi_j^{\sigma_j, \sigma_{j+1}}$  (see our discussion in Sect. 3.1) and  $i$  referring to the pixels in the subbands.

Another type of regularization term used for this work are characteristic functions, incorporating a total flux  $f$  constraint

$$R_{\text{flux}}(I, f) = \begin{cases} 0 & \text{total flux of } I = f \\ \infty & \text{else,} \end{cases} \quad (20)$$

or a multiresolution support,  $M$ , such that

$$R_{\text{mrs}}(\mathcal{I}, M) = \begin{cases} 0 & \mathcal{I} \neq 0 \text{ only in } M \\ \infty & \text{else.} \end{cases} \quad (21)$$

The multiresolution support  $M$  is a subdomain of the parameter space occupied by  $\mathcal{I} = \{I_1, I_2, \dots, I_J\}$ , and it comprises the coefficients in  $\mathcal{I}$  that are allowed to be unequal to zero. In this sense,  $R_{\text{mrs}}$  could be understood as a compact flux constraint (i.e., all coefficients in the subbands  $I_1, I_2, \dots, I_J$  outside of a compact core region are constrained to zero), a multiscale constraint (i.e., all coefficients within one uncovered subband  $I_j$  are set to zero), or a combination of both.

### 2.5. Optimization

We use a flexible dictionary of DoG wavelets and minimize Eq. (13) directly with convex optimization algorithms. Generally, a gradient descent algorithm could be used for this task, as long as the data fidelity term and the penalty term are smooth (i.e., possess a gradient). However, for sparsity-promoting algorithms, the penalty term is typically nonsmooth, meaning that the  $l_0$ -norm is not differentiable. In numerical optimization, it is common practice to use the  $l_1$ -norm as a convex approximation to the nonconvex  $l_0$ -functional stated above (e.g., Starck et al. 2015). As the  $l_1$ -norm is also not smooth (preventing gradient descent algorithms from being used), powerful optimization

strategies were developed in numerical mathematics that typically outperform smooth approximations to the  $l_1$ -norm. Several of such optimization strategies have been recently applied to aperture synthesis as well (Li et al. 2011; Carrillo et al. 2012, 2014; Garsden et al. 2015; Girard et al. 2015; Onose et al. 2016, 2017; Mouri Sardarabadi et al. 2016; Akiyama et al. 2017b,a; Cai et al. 2018a,b; Chael et al. 2018; Pratley et al. 2018; Event Horizon Telescope Collaboration 2019). These algorithms depend on the proximal point operator instead of the gradient. However, in the present work we are addressing a slightly more advanced problem of maintaining sufficient contrast in the image, and hence we are interested in the  $l_0$  functional instead of its common convex approximation  $l_1$ . Moreover, this will allow us to construct a multiresolution support later on. Relying on the overall success of proximal-point-based algorithms to deal with this kind of optimization problem, we nevertheless attempt to address our minimization problem using a proximal-point-based optimization.

In the following, we describe the basic properties of the proximal\_point operator. If  $H$  is a proper, convex and lower semicontinuous functional on a Hilbert space  $\mathbb{X}$ , then the proximity operator of  $H$  is defined as the mapping (Moreau 1962):

$$\text{prox}_{\tau, H}(z) = \underset{s \in \mathbb{X}}{\text{argmin}} \left\{ H(s) + \frac{1}{2\tau} \|s - z\|_{\mathbb{X}}^2 \right\}, \quad (22)$$

and  $\text{prox}_{\tau, H}$  is well defined (i.e., there is a unique single-value minimum). For a convex, proper and lower semicontinuous objective functional, such as the right hand side of Eq. (22), the zero element is in the subdifferential of the functional at the point of the minimum. Hence,  $\hat{s} := \text{prox}_{\tau, H}(z)$  satisfies:

$$z - \hat{s} \in \tau \partial H[\hat{s}]. \quad (23)$$

The power of proximal operators comes from their fixed-point property. It follows directly from Eqs. (22) and (23), that:

$$\hat{s} \in \underset{s}{\text{argmin}} H(s) \iff \hat{s} = \text{prox}_{\tau, H}(\hat{s}) \quad (24)$$

independently of  $\tau \geq 0$ . For a sketch of the proof see Appendix A.

Hence, we can solve the minimization in Eq. (13) by fixed-point iterating the proximity operator. This procedure is exact, in the sense that convergence proofs are available (e.g., Martinet 1972). For the combination of a smooth term (data-fidelity term) and a nonsmooth term (penalty term), we use a two-step splitting minimization strategy consisting of a gradient descent step for the data fidelity term and one proximity step for the penalty term (Combettes & Pesquet 2009). The forward-backward splitting algorithm is outlined in its general framework in Table 1. The two-step splitting is realized during the last step of the algorithm, when the current guess is updated by a proximal step and a gradient descent step.

Interestingly, despite being derived in the context of convex optimization, there are also local convergence proofs available for the cases when  $S$  and  $R$  are not convex, but the penalty term remains lower semicontinuous and proper, and satisfies the technical Kurdyka-Łojasiewicz property (e.g., see Attouch et al. 2013; Ochs et al. 2014; Xiao et al. 2015; Boj et al. 2016; Liang et al. 2016 or Bao et al. 2016 for a connection to wavelets). This is of special interest for radio aperture synthesis as the data fidelity terms  $S_{\text{amp}}$ ,  $S_{\text{cph}}$ , and  $S_{\text{cla}}$  are indeed not convex. Local convergence to a steady point is known, and under some circumstances even global convergence could be proven (compare the discussion in Liang et al. 2016). Application in practice shows that,

**Table 1.** Forward–backward splitting for the minimization of  $S + R$ .

<b>Input:</b> $S, R : \mathbb{X} \mapsto \mathbb{R}$ (convex)
<b>Input:</b> $\text{grad } S$ is $L$ -Lipschitz continuous
Step size: $\tau \in (0, 2/L)$ , typical choice: $\tau = 1/\ \text{grad}(S)\ ^2$
Initial guess: $x_0 \in \mathbb{X}$
<b>while</b> $i = 0, 1, 2, \dots$ <b>do</b>
$x_{i+1} = \text{prox}_{\tau R}(x_i - \tau \text{grad} S(x_i))$

given a reasonable initial guess, local minima could be avoided (Starck et al. 2015).

One may wonder if the difficulty with convex nonsmooth penalty functionals is now just transported to the probably troublesome minimization problem in the definition of the proximity operator in Eq. (22). But the proximity operator is known for a large number of examples and the computation is often not more time-consuming than one Landweber iteration. For example, for the  $l_0$ -functional, the proximity operator is (e.g., Starck et al. 2015):

$$\text{prox}_{\tau, \|\cdot\|_{l_0}}(z) = \begin{cases} z & |z| > \sqrt{2\tau} \\ \text{sign}(z)[0, z] & |z| = 0 \\ 0 & |z| < \sqrt{2\tau} \end{cases}, \quad (25)$$

where the signum and absolute value are meant to be evaluated pointwise. This not always a single value, since the  $l_0$  norm is not convex. The proximal point operator of characteristic functions is the projection on the support of the characteristic function; in the case of multiresolution support, this is the function that nullifies all coefficients outside the multiresolution support, and in the case of the total flux, it is the function that projects the current guess to the guess with the correct total flux.

### 3. Pipeline

#### 3.1. Outline

We use the same notations as in the previous subsections:  $V$  are the observed visibilities,  $f$  the prior compact total flux,  $\Gamma$  the dictionary of composed of DoG wavelets, and  $F$  the linear mapping of the image intensity to the tapered visibilities. The core of our imaging method concerns solving the following optimization problem:

$$\hat{\mathcal{J}} \in \text{argmin}_{\mathcal{J}} \left[ S_{\text{cph}}(F\Gamma\mathcal{J}, V) + S_{\text{cla}}(F\Gamma\mathcal{J}, V) + \alpha \cdot R_{l_0}(\mathcal{J}) + R_{\text{flux}}(\mathcal{J}, f) \right], \quad (26)$$

where we choose the maximum of the corresponding DoG wavelet function as weights  $\omega_j$ . We have only one regularization parameter  $\alpha$  that controls the amount of suppression by hard thresholding. We like to emphasize the main motivations behind this optimization problem.

Firstly, we use the more flexible DoG dictionary here, see Eq. (12). This allows us to adapt the dictionary to the  $uv$ -coverage by separating scales that are well covered by observations from those that are less accurately constrained by observations. This will allow us to better suppress the signal from the latter scales.

Secondly, we initially use the closure properties as the data fidelity term, as a measure to reduce the effect of possible antenna-based calibration errors. Chael et al. (2018) demonstrated that this information is sufficient to recover the image when using strong regularization priors. In later imaging rounds,

that is after several self-calibration steps, we also start to include amplitude and phase information.

Thirdly, we use hard thresholding ( $l_0$  pseudonorm regularization), which promotes sparsity. In the few works addressing multiscalar imaging for radio aperture synthesis (Li et al. 2011; Carrillo et al. 2012, 2014; Garsden et al. 2015; Onose et al. 2016, 2017; Mouri Sardarabadi et al. 2016; Pratley et al. 2018), often the  $l_1$ -norm is used as a convex approximation to  $R_{l_0}$ . This is standard for sparsity-promoting inverse problems (e.g., Starck et al. 2015). However, the  $l_1$ -norm suppresses both the image features and noisy structures. As it is important to preserve the amplitude on the well-covered scales, we resort to using the nonconvex  $l_0$ -pseudonorm as penalization. We weight the  $l_0$  pseudonorms by the maximal peak of the corresponding DoG wavelet basis function. This is done to prevent the scale selection having a strong effect on the choice of the best regularization parameter. In principle these weighting parameters could be considered as free regularization parameters as well. However, to meet our requirement of constructing an algorithm that is as unbiased and data-driven as possible, we restrict them in this work to the choice that seems most reasonable.

It should be noted that  $S_{\text{cph}}$ ,  $S_{\text{cla}}$ , and  $R_{l_0}$  are invariant against rescaling the coefficients  $x$  (atoms) by a scale factor  $\lambda \in \mathbb{R}$ . To select the most feasible solution along this line, we select the one that matches the prior compact total flux.

There are more possible regularization terms available, for example the total variation or the total squared variation terms that are applied for the EHT imaging (Event Horizon Telescope Collaboration 2019). However, finding suitable weighting parameters for the different data terms and penalty terms is somewhat unintuitive for such different types of regularizations. This task often requires large parameter surveys with feasible synthetic data. We aim to find a largely unsupervised algorithm with only a few free parameters.

Our optimization problem differs significantly from previous multiscalar RML imaging approaches (e.g., Li et al. 2011; Carrillo et al. 2012, 2014; Garsden et al. 2015; Girard et al. 2015; Onose et al. 2016, 2017; Mouri Sardarabadi et al. 2016; Cai et al. 2018a,b; Pratley et al. 2018). They used the starlet transform as a dictionary (which we replaced by the DoG dictionary), the distance of observed and predicted visibilities as the data fidelity term (which we replaced by closure properties), and  $l_1$  penalty terms (which we replaced by  $l_0$  penalization).

Nevertheless, our algorithm shares some similarities with RML reconstructions. The unpenalized minimization of the data fidelity terms yields a high-resolving reconstruction that fits the observed data points with a fidelity that is (too) high, but that provides clearly unphysical, highly oscillating fits of the visibilities in the gaps of the  $uv$ -coverage. Total variation and total squared variation penalization effectively smooth the recovered model to a reasonable extent, where the amount of smoothing is controlled by the trade-off between the data fidelity term and the penalization term. We achieve a similar effect by modeling the brightness density distribution with (as few as possible) smooth, extended basis functions.

#### 3.2. Pipeline

The data fidelity terms  $S_{\text{cph}}$  and  $S_{\text{cla}}$ , and the regularization term  $R_{l_0}$ , are not convex. Therefore, the minimization problem stated in Eq. (26), strictly speaking, may not have a single-value minimum. Therefore, a careful imaging pipeline helping global convergence is needed. It should also be noted that the representation of the image in wavelet scales is an overcomplete

representation. Due to the resulting large arrays, computation could be slow. Computation time can, in principle, be reduced when starting from a reasonable initial guess instead of a flat image or a Gaussian prior.

On the other hand, the solution of Eq. (26) returns an adequate calibration image  $\hat{I} = \Gamma\hat{x}$  and computes, on the fly, a multiresolution support  $M$  (all the pixels that are unequal to zero). Further imaging rounds, including the self-calibrated visibilities, allow the solution to vary only in the multiresolution support, and thus could sharpen the image further while respecting the sparsity assumption thanks to the multiresolution support. This approach is realized within the following imaging pipeline:

The first imaging round consists of “single scalar flux constraining imaging”: We minimize the term:

$$\hat{I}_1 \in \operatorname{argmin}_I S_{\text{amp}}(FI, V) + S_{\text{cph}}(FI, V) + S_{\text{cla}}(FI, V) + R_{\text{flux}}(I, f), \quad (27)$$

where no dictionary is involved. We do this by the fast minimization method available in the `scipy` package. In fact, this imaging round is similar to the first imaging round with the `ehtim` imaging package for [Event Horizon Telescope Collaboration \(2019\)](#). This imaging round is used for finding a reasonable initial guess in order to reduce the overall computation time. We convolve the result with the instrument clean beam (to avoid local minima) and only use a few iterations, meaning it is an incomplete decomposition. Finally, we have to find a wavelet coefficient array  $\mathcal{J}^1$  that satisfies  $\hat{I}_1 = \Gamma\mathcal{J}^1$ . To satisfy Eq. (10), we copy the intensity  $\hat{I}_1$  in every scale  $\hat{J}_j^1 = \hat{I}_1$ , where  $j$  denotes the scale in use.

The second imaging round consists of “multiscalar closure property hard thresholding imaging”: This imaging round is the heart of the new algorithm. We solve Eq. (26) using a forward–backward splitting approach. We start from the initial guess  $\mathcal{J}^1$  computed in the first imaging round and compute a scale discrete guess in order to minimize Eq. (26). We start from the largest scales only (setting all other subbands to zero), successively adding smaller scales and larger thresholds. We stop at the scale at which the functional (26) is minimal, in other words at the smoothing when accuracy of the fit and sparsity penalization balance. Lastly, we reestimate the thresholds for each scale individually starting from the smallest scales. We then minimize, starting from this initial guess, the functional with a forward–backward splitting strategy. We will explain this forward–backward splitting minimization strategy in Sect. 3.3. An outline of the round 2 imaging algorithm is presented in Table 2.

The third imaging round consists of “multiresolution imaging with visibility amplitudes”: We self-calibrate the data with the image guess derived in the second image round. Moreover, we compute the multiresolution support  $M$  from the result  $\hat{\mathcal{J}}^2$  of the second imaging round, that is to say, we choose all nonzero elements of the multiscalar coefficient array  $\hat{\mathcal{J}}^2$  as multiresolution support. We now solve the problem:

$$\hat{\mathcal{J}}^2 \in \operatorname{argmin}_{\mathcal{J}} S_{\text{amp}}(F\Gamma\mathcal{J}, V) + S_{\text{cph}}(F\Gamma\mathcal{J}, V) + S_{\text{cla}}(F\Gamma\mathcal{J}, V) + R_{\text{mrs}}(\mathcal{J}, M). \quad (28)$$

This is solved by a simple gradient descent algorithm starting from the initial guess  $\hat{\mathcal{J}}^3$  in which only the gradient with respect to the coefficient in the multiresolution support is computed.

The fourth imaging round is “multiresolution imaging with full visibilities”: after another self-calibration step, we solve the

imaging problem:

$$\hat{\mathcal{J}}^4 \in \operatorname{argmin}_{\mathcal{J}} S_{\text{vis}}(F\Gamma\mathcal{J}, V) + R_{\text{mrs}}(\mathcal{J}, M), \quad (29)$$

by a gradient descent algorithm that only varies coefficients in the multiresolution support analog to the third imaging round.

For the last, fifth imaging round we do “single scalar visibility imaging”: We set all pixels with negative flux to zero flux and increase the match to the observed visibilities by a gradient descent algorithm that minimizes  $S_{\text{vis}}(FI, V)$  in the pixel scale starting from  $\hat{I}^5 = \Gamma\hat{x}^5$ .

The last three imaging rounds (in particular round 5) are optional and only refine the reconstruction. This will be discussed in our demonstration on synthetic data in Sect. 4.

### 3.3. Minimization algorithm

We now discuss the minimization algorithm used to minimize Eq. (26). All other imaging rounds are based on smooth gradient descent minimization algorithms (rounds 3–5) or a smooth Newton-type minimization (round 1). But Eq. (26) is neither convex nor smooth. However, the data fidelity terms are smooth with Lipschitz continuous derivatives and the  $l_0$  pseudonorm is proper and lower-semicontinuous, and satisfies the Kurdyka–Lojasiewicz property (e.g., [Liang et al. 2016](#)). Thus, the forward–backward splitting algorithm 1 remains applicable, see our discussion in Sect. 2.5. Additionally, we recall that  $S_{\text{cph}}$ ,  $S_{\text{cla}}$ , and  $R_{l_0}$  are invariant against rescaling the coefficient array by a scalar factor  $\lambda$ . We therefore propose the following iterative scheme: we first minimize  $S_{\text{cph}}(F\Gamma x, V) + S_{\text{cla}}(F\Gamma x, V) + \alpha \cdot R_{l_0}(x)$  by a fixed number of forward–backward splitting iterations, and then we rescale the coefficient array by a scale factor, such that  $I = \Gamma x$  has a total flux matching the prior compact flux (leaving the data fidelity terms and regularization terms unaffected). Then we proceed with our forward–backward splitting algorithm, performing rescaling again, and so on. The complete procedure is outlined in Table 2. The needed proximal operator for the  $l_0$  pseudonorm is computed in Eq. (25).

Iterative reweighted  $l_1$ -regularization proposed by [Candès et al. \(2007\)](#) provides an alternative approach to solving optimization problems with nonconvex  $l_0$ -terms and is more common than our forward–backward scheme. However, our rescaling approach to match the total flux would affect the reweighting step of the reweighted  $l_1$ -regularization method. Thus, it would introduce an additional layer of complexity in solving the optimization problem. This would fail our requirement of a preferably simple imaging algorithm with a small number of parameters to specify.

### 3.4. Selection of scales

Our DoG-wavelet dictionary is flexible in the sense that the Gaussian widths could be chosen to adapt to the  $uv$ -coverage. Hence, the selection of scales is data driven (e.g., by the  $uv$ -coverage) and should be performed automatically. In this section we discuss the automatic scale-width selection and outline the key points of this approach.

The Fourier transform of a two-dimensional DoG wavelet is a ring shaped mask, see Eq. (8). It is reasonable to select the masks such that well-covered regions of the  $uv$ -space and poorly covered regions are separated. However, for very sparse arrays, there are no really well covered scales. In this situation, our selection should be also driven by the assertion that all the data points belonging to the same antenna pair should be covered in one scale.

**Table 2.** Wavelet forward–backward splitting: pipeline round 2.

---



---

<p><b>Input:</b> Visibilities: <math>V</math></p> <p><b>Input:</b> Stepsize: <math>\tau</math> (chosen artificially, such that algorithm converges)</p> <p><b>Input:</b> Regularization Parameter: <math>\alpha</math></p> <p><b>Input:</b> Total flux: <math>f</math></p> <p>Define a dictionary of basis functions(wavelets): <math>\Gamma</math></p> <p>Define a forward operator: <math>G : \mathcal{S} \mapsto \mathcal{F}\Gamma\mathcal{S}</math> (note <math>G</math> is linear)</p> <p>Define a data-fidelity functional: <math>df : \mathcal{S} \mapsto S_{\text{ica}}(V, G\mathcal{S}) + S_{\text{cph}}(V, \Gamma\mathcal{S})</math></p> <p>Precompute gradient of data-fidelity functional: <math>df'[\mathcal{S}]</math></p> <p>Define a penalty term: <math>pen : \mathcal{S} \mapsto  \text{support}(x) </math> (<math>l_0</math>-norm)</p> <p>Precompute proximal operator of penalty term: <math>prox_\tau</math> (hard shrinkage operator, Eq. (25))</p> <p><math>\mathcal{S}</math> = initialguess</p> <p>Define grid of possible thresholds: <math>t_i</math></p> <p><b>for</b> <math>i = 1, 2, 3, \dots</math> <b>do</b></p> <p style="padding-left: 20px;">Hard thresholding: <math>test_i = prox_{t_i}(\mathcal{S})</math></p> <p style="padding-left: 20px;"><math>min_i = df(test_i) + \alpha pen(test_i)</math></p> <p>Find minimum <math>i</math> and update initial guess <math>\mathcal{S} = prox_{t_i}(\mathcal{S})</math></p> <p><math>min_{tot} = min_i</math></p> <p><b>for</b> <math>j = 0, 1, 2, \dots, J</math> <b>do</b></p> <p style="padding-left: 20px;"><b>for</b> <math>i = 1, 2, 3, \dots</math> <b>do</b></p> <p style="padding-left: 40px;">Hard thresholding single scale: <math>test_{i,j} = \{\mathcal{S}_1, \dots, prox_{t_i}(\mathcal{S}_j), \dots, \mathcal{S}_j\}</math></p> <p style="padding-left: 40px;"><math>min_{i,j} = df(test_{i,j}) + \alpha pen(test_{i,j})</math></p> <p style="padding-left: 40px;"><b>if</b> <math>min_{i,j} &lt; min_{tot}</math> <b>then</b></p> <p style="padding-left: 60px;"><math>min_{tot} = min_{i,j}</math></p> <p style="padding-left: 60px;"><math>\mathcal{S}_j = prox_{t_i}(\mathcal{S}_j)</math></p> <p><b>while</b> stopping-rule 1 <b>do</b></p> <p style="padding-left: 20px;"><b>while</b> stopping-rule 2 <b>do</b></p> <p style="padding-left: 40px;"><math>\mathcal{S} = \mathcal{S} - \tau \cdot df'[\mathcal{S}]</math></p> <p style="padding-left: 40px;"><math>\mathcal{S} = prox_{\tau\alpha}(\mathcal{S})</math></p> <p style="padding-left: 20px;"><math>\mathcal{S} = \mathcal{S} \cdot f / \text{sum}(\Gamma\mathcal{S})</math></p> <p>Compute Multiresolution support <math>M = \{\mathcal{S} \neq 0\}</math></p> <p><b>Output:</b> <math>\mathcal{S}</math> is approximate minimizer to Eq. (26)</p> <p><b>Output:</b> <math>\hat{I} = \Gamma\mathcal{S}</math> is an approximation to the true sky brightness distribution</p> <p><b>Output:</b> As a byproduct <math>M</math> is a reasonable multi-resolution support</p>	<p>► Precompute needed data terms and operators</p> <p>► Find initial image thresholding by minimizing Eq. (26) on a predefined grid of thresholds</p> <p>► Start forward–backward iterations from this guess</p>
--	---

---

We present a sketch of our automatic scale selection in Fig. 1. We unpack the array of  $uv$ -distances of the full array, sort it in increasing order (black dots in Fig. 1), and search for jumps between two consecutive data points that exceed a certain threshold. These jumps clearly appear at gaps in the  $uv$ -coverage (most visible between the blue and orange lines in Fig. 1, respectively between the green and the red lines). We store the  $uv$ -distances at which these gaps appear and select the DoG wavelet widths by the mean of the consecutive distances (represented by horizontal colored lines in Fig. 1).

As a demonstration, we apply this procedure to the EHT 2017 array. In Fig. 2, we show our masks and the data points in  $uv$ -space. The width information of the scales shown in Fig. 2 is given in Table 3. We also mention in Table 3 which scale is most sensitive to which antenna pair (i.e., what the selection criterion was for this scale). As all DoG wavelets satisfy the zero integral property of wavelets, the only flux-transporting scale is the smoothing scale  $G_{\sigma_j}$ .

The smallest scale in our set has a width of 9.96  $\mu\text{as}$ , which corresponds to 5.02 pixels in our discretization. For the sake of

completing our dictionary of wavelet functions so that Eq. (10) remains satisfied, we complete our sets of scales down to the pixel size by adding DoG wavelets according to the widths of one, two, and four pixels. This, however, will turn out to be less relevant, as these scales will be suppressed by the algorithm automatically, see Sect. 4.2.

## 4. Tests with synthetic data

### 4.1. Testdata

We test our algorithm on the same set of synthetic data that were recently used for testing feature extraction from the EHT data (Tiede et al. 2020). In particular, we use a crescent, a disk, a double Gaussian, and a ring structure.

The crescent is described by the equation (Tiede et al. 2020):

$$I(r, \theta) = I_0(1 - s \cos(\theta - \xi)) \frac{\delta(r - r_0)}{2\pi r_0}. \quad (30)$$

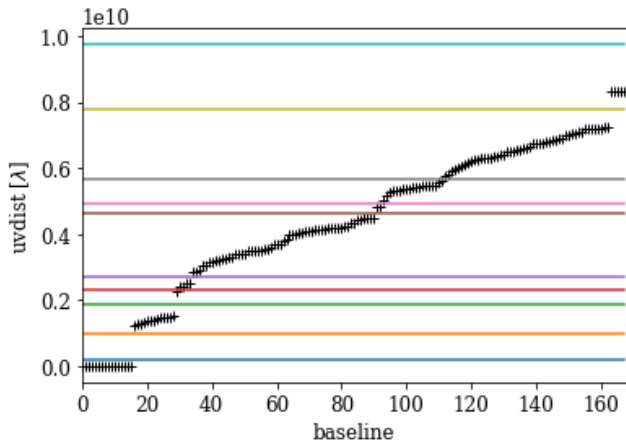


**Fig. 1.** Sketch of the automatic scale selection. The sorted array of  $uv$ -distances is plotted with black points. This array has clearly visible jumps (gaps in radial  $uv$ -coverage). We identify these jumps and assign scalar widths to them (horizontal colored lines).

**Table 3.** Widths of DoG wavelets and their main sensitivity to the  $uv$ -coverage, i.e., which antenna pair is mainly covered by these scales.

Scale	$\sigma_1 \rightarrow \sigma_2$ ( $\mu\text{as}$ )	Main Sensitivity
0	0.84 $\rightarrow$ 1.69	Unresolved
1	1.69 $\rightarrow$ 3.37	Unresolved
2	3.37 $\rightarrow$ 4.23	Unresolved
3	4.23 $\rightarrow$ 5.78	PV-SMA/JCMT
4	5.78 $\rightarrow$ 6.66	Gap
5	6.66 $\rightarrow$ 7.06	AA/AP-JCMT/SMA, AA/AP-PV
6	7.06 $\rightarrow$ 12.18	AA/AP-SMT, SMT-PV, LMT-PV
7	12.18 $\rightarrow$ 14.13	AA/AP-LMT, JCMT/SMA-LMT
8	14.13 $\rightarrow$ 17.55	JCMT/SMA-SMT
9	17.55 $\rightarrow$ 33.69	Gap
10	33.69 $\rightarrow$ 39.81	LMT-SMT
11	39.81	AA-AP, JCMT-SMA

**Notes.** Different scales are most sensitive either to specific baselines or the gaps in the  $uv$ -coverage. The three smallest scales were added to complete the dictionary down to the pixel size and compress unresolved structures.

We use  $\xi = 180^\circ$ ,  $r_0 = 22 \mu\text{as}$ ,  $s = 0.46$ , and  $I_0 = 0.6 \text{ Jy}$ . The crescent is then convolved with a Gaussian with a full width at half maximum (FWHM) of  $10 \mu\text{as}$ . The disk is a disk of diameter  $70 \mu\text{as}$ . The disk is then convolved with a Gaussian with FWHM  $10 \mu\text{as}$ .

The double Gaussian image consists of two Gaussian peaks with a FWHM of  $20 \mu\text{as}$ . The first Gaussian is placed at the origin and has a flux of  $0.27 \text{ Jy}$ . The second Gaussian is placed  $30 \mu\text{as}$  to the east and  $12 \mu\text{as}$  to the south. It has a flux of  $0.33 \text{ Jy}$ .

The ring has radius of  $22 \mu\text{as}$  and a total flux of  $0.6 \text{ Jy}$ . The ring is convolved with a Gaussian with a FWHM of  $10 \mu\text{as}$ .

We simulate visibility data from the test images with the help of the `ehtim` package, using the EHT 2017 array at  $229 \text{ GHz}$ . We mimic the observation with the `observe_same` option, assuming the same systematic noise levels, observation intervals, and correlation times as for the EHT observations (Event Horizon Telescope Collaboration 2019). We assume phase and gain calibration, but add thermal noise.

We aim to study the image on a  $128 \times 128$  pixel grid with  $1 \mu\text{as}$ -pixels. However, to avoid boundary effects in the computation (the largest chosen Gaussian has a FWHM of already  $93.75 \mu\text{as}$ ), we widen the field of view by a factor of two. Moreover, we use 129 pixels instead of 128 pixels to discretize narrow central Gaussians correctly. We have defined 12 different wavelet scales. Thus, we are attempting to solve for  $12 \times 129 \times 129 \approx 2 \times 10^5$  parameters in the multiscale imaging rounds.

#### 4.2. Imaging pipeline

In this subsection, we use with the crescent image to demonstrate the stability of our imaging pipeline and present some key features. We show in Fig. 3 the imaging results obtained from the crescent test data after different imaging rounds. The image after the second imaging round is shown in the upper right panel, and the final image after the fifth imaging round is shown in the lower right panel. The essential image structure is already recovered after the second imaging round (multiscalar imaging with closure properties). This indicates that the multiscalar imaging approach might also be applicable to badly calibrated data and that satisfactory image quality could be achieved even without self-calibration loops. Nevertheless, the use of the amplitudes and full visibility data (imaging rounds 3–5, lower panels) refines the recovered structures, and increases coincidence with observed visibilities. Moreover, the steady improvement of the image quality shown in Fig. 3 demonstrates that our amplitude conserving hard thresholding approach works as intended. We observe a strong contrast between the ring feature and the inner depression (due to sparsity) while the amplitude and total flux is conserved. This would not be available with soft thresholding.

We demonstrate in Fig. 4 that our final image fits the observed visibilities well. The hard thresholding approach suppresses emission that is not significant for fitting the visibilities, but it does not break the fit to the observed data as soft thresholding would do. In fact, we successfully separated between significant image structures (fitting the visibilities) and noise induced features (very small sidelobe level in the final image).

We present the multiscalar composition of the image in more detail in Fig. 5. The panels of Fig. 5 suggest that different scales are sensitive to different parts of the final image, for example an extended Gaussian component (bottom right panel), the ring feature with a central negative peak to compensate for this extended emission (middle panels), or the asymmetry of the crescent (bottom left panel). The final high-resolution and high-contrast image is only visible when summing all the single-scale images. Additionally, we present in Fig. 4 the fit to the data from the single scales only for some selected single scales, namely the ones that have the largest signal according to Fig. 5. In the Fourier domain, the various scales are mostly sensitive to varying parts of the  $uv$ -coverage, from the short baselines (scales 9 and 11), over the middle baselines (scale 6), to the longest PV-SMA/JCMT baselines (scale 4) as designed. Moreover, Fig. 5 demonstrates that there are certain scales that are completely suppressed due to the sparsity-promoting imaging pipeline (the smallest scales, top panels). Consequently, there is no signal at these scales in Fig. 5. This is reasonable as these scales are sensitive mainly to fine structures, that could only be sampled at baselines longer than the maximum baseline in the data. Moreover, it is noticeable that the scale that is most sensitive to the longest baselines (PV-SMA/JCMT, the fourth scale in Fig. 5) is completely suppressed. That, however, does not necessarily mean these data points do not affect the reconstruction anymore. As can be seen in the ring-like masks presented in

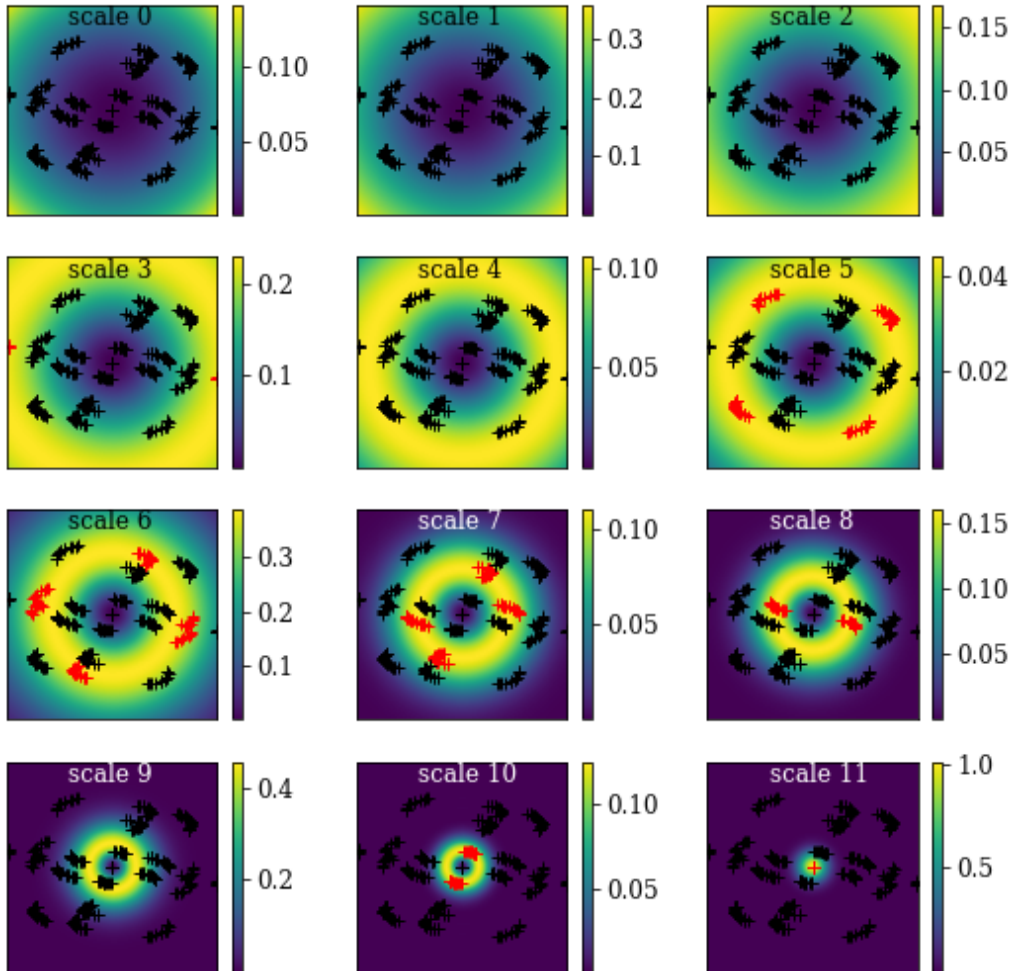


**Fig. 2.** Observed  $uv$ -coverage (black and red points) of the EHT data array (observation of M87 on 5 April 2017) and masks defined by the DoG wavelets listed in Table 3 (color maps). The masks are the Fourier transform of the respective wavelets and they define ring-like filters in Fourier domain. The visibilities highlighted by a specific filter are plotted in red.

Fig. 2, these data points, in fact, affect all other scales as well (as the Fourier masks are not steep Heaviside functions), but with reduced importance. However, the suppression of this scale could be a hint that further improvement of the method may be available by treating the weighting coefficients  $w_j$  in Eq. (19) as free parameters.

#### 4.3. Proof of concept

One of the principal ideas of this paper is to define a flexible wavelet dictionary that adapts smoothly to the  $uv$ -coverage. We now prove this concept. We present in Fig. 6 a reconstruction with the complete pipeline, with the selection of scales specified in Table 3, and with a coarser grid that would be available, for instance, with the less flexible à trous wavelet transform (right panel):  $\tilde{\Sigma} = [1, 4, 8, 32]$  (in units of  $1.98 \mu\text{s}$  pixels). We used only every second power of two here for demonstration purposes, to enhance the effect of a less fine grid of scales.

The crescent structure is much more robustly recovered with our selection of scales. This is expected, as illustrated by Fig. 5. The smaller scales respond to different aspects of the fine structure of the crescent test image, such as the ring-like emission, the narrow central ring line or the southern emission peak. The

larger scales compress the extended emission. The final high-resolution image is only visible by the sum of all these scales. The artificial selection of scales  $\tilde{\Sigma}$  has a less complex separation of scales. The complex conglomerate of multiple structure features has to be compressed in only one or two scales. Due to the coarse gridding of widths in  $\tilde{\Sigma}$ , the algorithm is forced to utilize to small scales, which are not able to compensate the bad fitting of the unconstrained minimization. Our automatic scale selection outperforms this rigid choice of scales because of a more suitable smoothing and thresholding due to adaptive steps in the scale selection, and hence a more rigorous compression of structure information.

That said, it should be mentioned again that the wavelet dictionaries are complete regardless of the selection of scales. Hence, theoretically, the same image can be represented by both wavelet dictionaries regardless of the special choice of scales. The dependency of the reconstruction on the selection of scales is induced by the imaging pipeline (we recall that the objective functional is not convex, and thus only convergence to a local minimum can be assured). It is easier to recover the image feature at a specific scale, if this scale is well covered by measurements, which helps global convergence with our imaging pipeline. On the other hand, a deconvolution at a less well covered scale is

H. Müller and A. P. Lobanov: DoG-HiT: A novel VLBI multiscale imaging approach

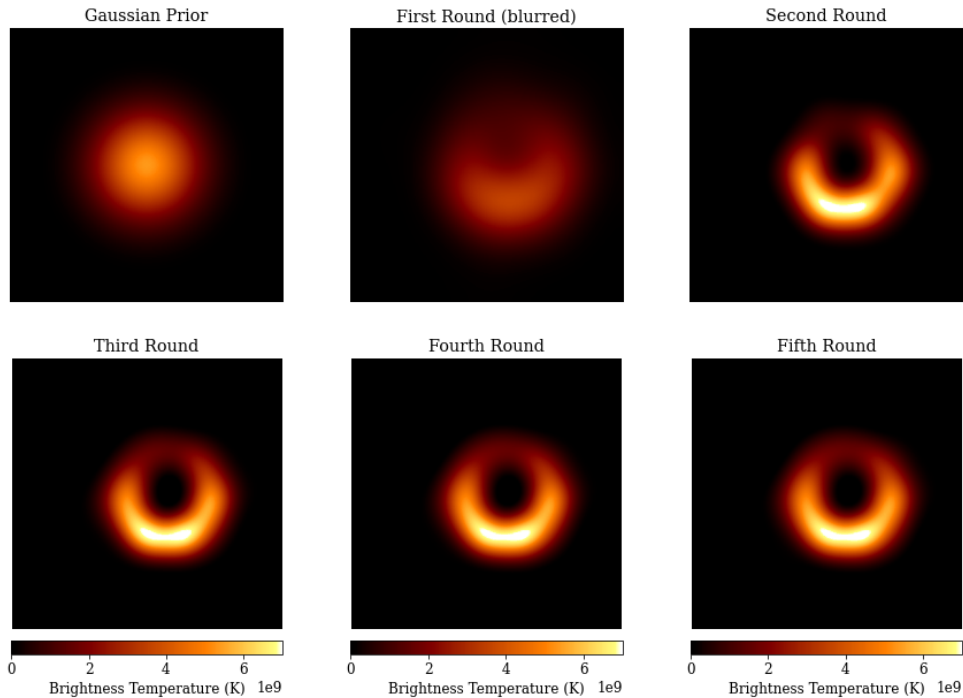


**Fig. 3.** Imaging results of the crescent at various steps of the imaging pipeline. *Upper left:* Gaussian prior image. *Upper middle:* initial guess, result after round 1 blurred by the  $20 \mu\text{as}$  beam. *Upper right:* after imaging round 2. *Bottom left:* after imaging round 3. *Bottom middle:* after imaging round 4. *Bottom right:* final image after imaging round 5.

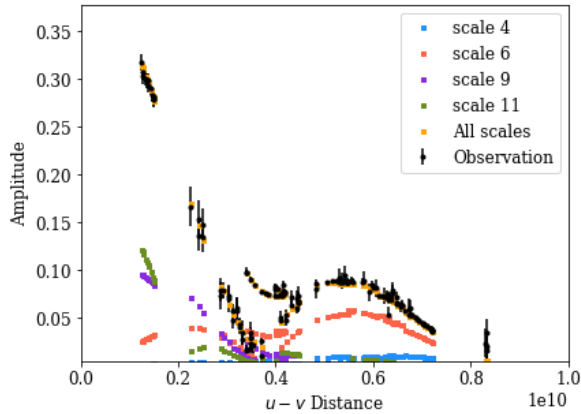


**Fig. 4.** Observed amplitudes (black) and recovered visibilities (yellow) as functions of  $uv$ -radius for the crescent test data. Moreover, we show the fit of single scales for some selected scales (blue, red, purple, green).

more uncertain and would possibly fail in the reconstruction of some features.

One may ask now whether progressively refining the grid of scales could further increase the accuracy of image restoration. Whilst, in principle, this is expected, it also comes with the cost of increased computation time and requires more complexity. In this regard, our automatic scale selection may be viewed as a viable optimum and data-driven approach.

#### 4.4. Regularization parameter

Our algorithm depends on significantly fewer critical parameters that need to be specified by the user. The user only needs

to define the regularization parameter  $\alpha$  that controls the size of the penalty term, in contrast to the RML methods, which require multiple penalty terms (e.g., with MEM, 11, TV, TSV ... penalty terms), balanced by the term weightings. All other parameters in DoG-HiT are determined automatically from data; the widths of the DoG dictionary are defined by the automatic procedure described in Sect. 3.4 and the total flux could be identified with the zero-spacing flux, which can be measured or estimated. Parameters corresponding to the numerical minimization methods (stepsize, number of iterations, relative tolerance) have only a minor impact on the final result, as long as convergence is assured. We present a more quantitative analysis of the impact of the regularization parameter  $\alpha$  on the reconstruction in Appendix B. In short, if the regularization parameter is too small, the visibilities are overfitted by a greedy model with a high background level. For higher regularization parameters, the penalty term becomes more important; the background flux level is decreased and the greedy, blobby model becomes more uniform. Thus, the best fit is achieved. On the other hand, if the regularization parameter chosen is too big, the sparsity penalization dominates the objective functional. The hard thresholding suppresses significant image information and the image is badly fitted with a small number of large wavelet scales.

## 5. Comparison to alternative imaging algorithms

We compare our image reconstruction with the image reconstructions by standard Högbom CLEAN and the RML method available in the ehtim software package. We utilize the weighting of the data terms for RML reconstructions that was used for [Event Horizon Telescope Collaboration \(2019\)](#) and apply their

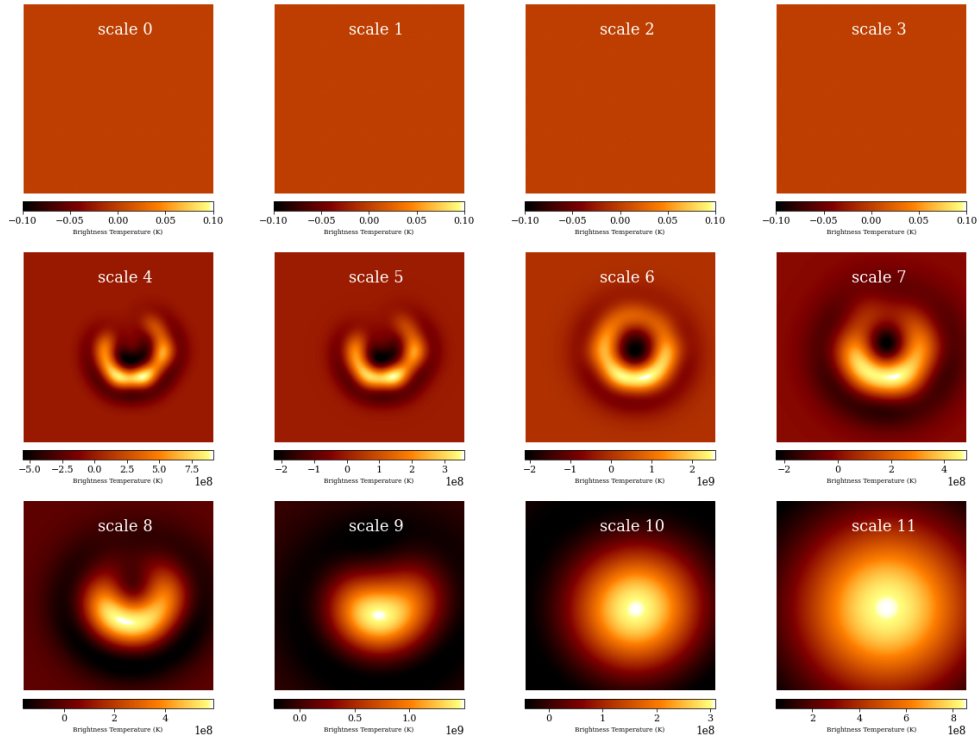


**Fig. 5.** Multiresolution image after imaging round 4. Each panel shows the recovered images from one scale only. The scales are computed with the DoG method with the widths defined in Table 3. The images is shown for every scale in increasing order *from the upper left to the lower right*.

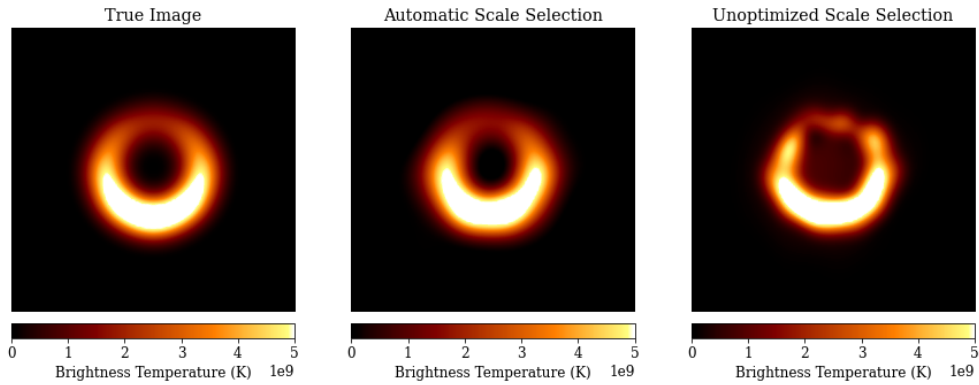


**Fig. 6.** Reconstruction of the crescent image. *Left panel:* true image. *Middle panel:* reconstruction with the selection of scales specified in Table 3. *Right panel:* reconstruction with scale widths that are a power of two (discrete wavelet transform).

four-round imaging pipeline published in the EHT data release<sup>1</sup>. The CLEAN reconstructions are performed with the circular window available in the EHT data release<sup>2</sup> and are restored with a  $20 \mu\text{as}$  restoring beam. It is worth noting that the RML scripts used for this imaging were extensively optimized for the observations of M87 with the EHT, and so excellent reconstructions are expected for this comparison with RML. On the other hand, in contrast to DoG-HiT, these excellent reconstructions required many different parameters to be specified.

<sup>1</sup> Available under <https://github.com/eventhorizontelescope/2019-D01-02>

<sup>2</sup> <https://github.com/eventhorizontelescope/2019-D01-02>

### 5.1. Qualitative comparison

We show in Fig. 7 our test image reconstructions on the set of test data presented in Sect. 4.1. Our image reconstruction shows a greater resolution than the CLEAN images. Moreover, we achieve a greater contrast between image features and background noise levels than the CLEAN algorithm, (i.e., sharper edges in the recovered images).

Compared to the powerful RML imaging method, our algorithm achieves comparable resolutions. This is surprising, as we probe the observed images with extended basis functions. In particular, we are able to recover some of the fine structure that is not visible in the RML reconstructions. We find the correct crescent-shaped north–south asymmetry in the crescent image, the fine

H. Müller and A. P. Lobanov: DoG-HiT: A novel VLBI multiscale imaging approach

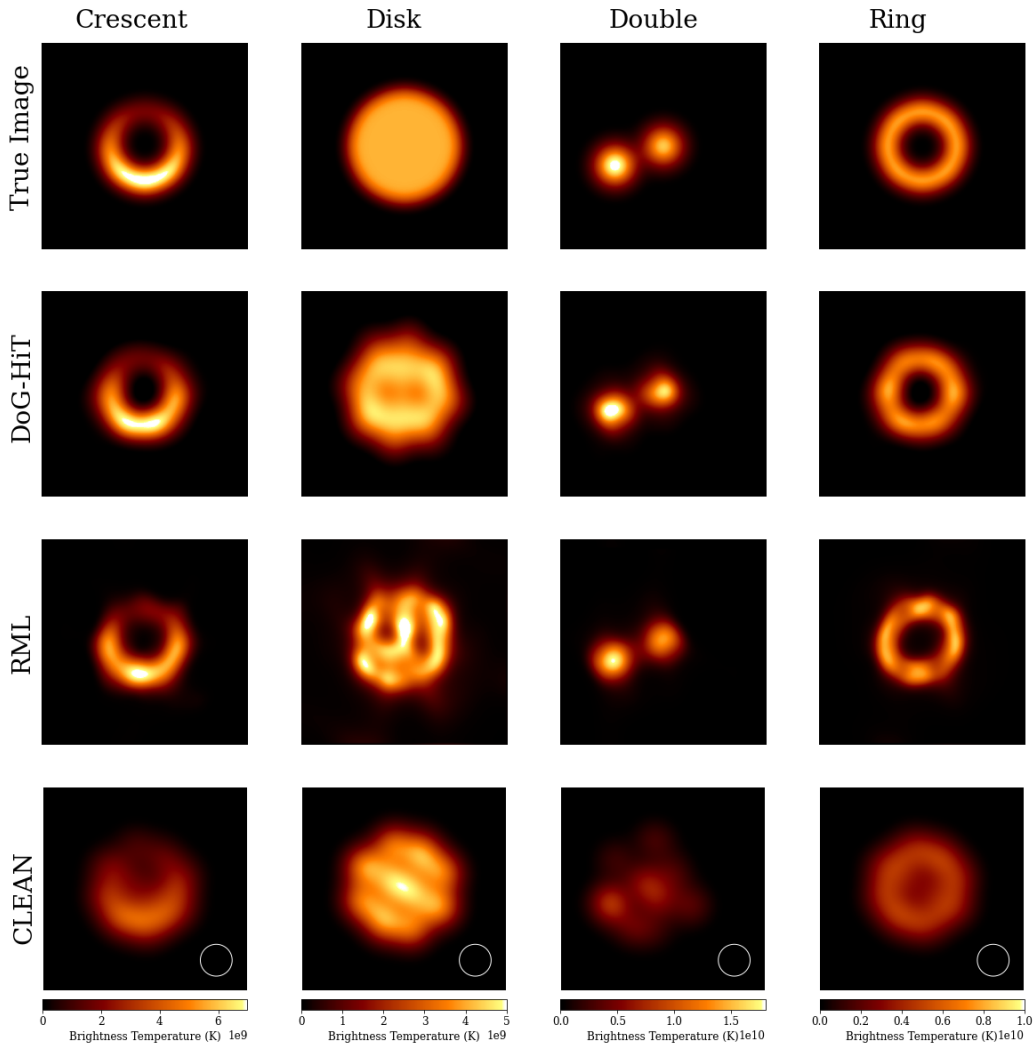


**Fig. 7.** Comparison of the reconstructions with various imaging algorithms. We show in the *upper line* the true images (crescent, disk, double, ring). In the *second to fourth lines*, we present the image reconstructions with DoG-HiT, RML, and CLEAN, respectively.

ring ridgeline in the ring image, and the correct peak values in the double Gaussian image. Moreover, we find a greater contrast between the ring-like features in the ring and crescent images, and the central depression, compared to the contrast observed in RML image. However, the inner “no-emission” radius is smaller than in the true images with DoG-HiT, while the spherical shape remains better recovered. This region is significantly better recovered by the RML algorithm. Moreover, RML appears to perform better in resolving the ring and crescent features transversely.

Notably, our algorithm also succeeds in the reconstruction of smooth extended emission (e.g., of the disk image). The reconstruction of the disk is quite accurate and comparable to the reconstruction with CLEAN. It does not manifest the greedy image disk features or background emission present in the RML reconstruction. The ring image demonstrates that DoG-HiT is able to fit uniform emission (ring extension) and sharp features (ring edges) simultaneously. The CLEAN reconstruction of the ring lacks the proper reconstruction of the sharp ring edges and the central depression. The RML reconstruction fits the central depression well, but the ring brightness distribution is less

homogeneous than in the DoG-HiT reconstruction. In this way DoG-HiT combines the major advantages of RML reconstructions (super-resolving structures) and CLEAN (high dynamic range sensitivity to extended structures), and at the same time reduces the drawbacks of both of these two methods. It should, therefore, be well suited for imaging problems arising in the context of EHT observations, in which the demand for the recovery of information contained on the smallest accessible scales requires simultaneous robust imaging of extended structures (jet). The performance of DoG-HiT under these conditions will be discussed in Sect. 6, using simulated data with a wide range of spatial scales.

### 5.2. Quantitative comparison

We now compare the various imaging algorithms in a more quantitative way, using a measure of their relative error,

$$\text{err} = \frac{\|\text{recovered solution} - \text{exact image}\|}{\|\text{exact image}\|}. \quad (31)$$

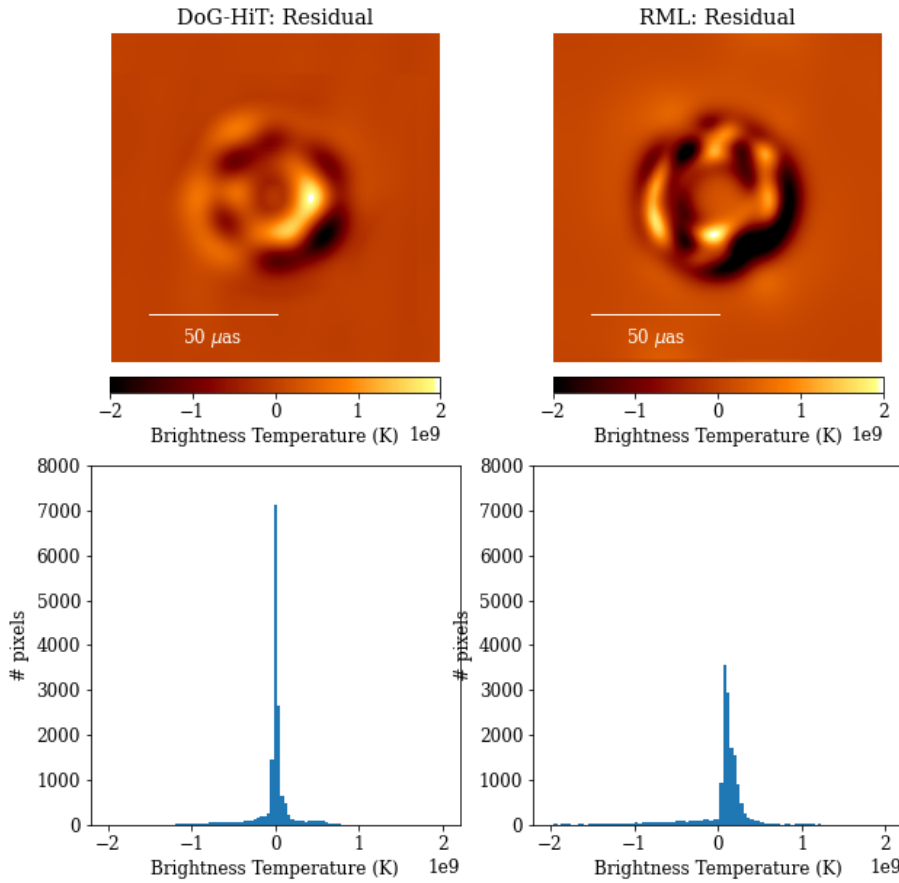


**Fig. 8.** Residuals of the reconstructions with DoG-HiT (*left*) and RML (*right*) for the ring image. *Upper panels:* true image subtracted from the reconstructed image. *Lower panels:* histogram of the residual distribution.

**Table 4.** Relative errors of the reconstructions shown in Fig. 7.

Blurring		Crescent	Disk	Double	Ring
0 $\mu$ as	DoG-HiT	0.156	0.138	0.167	0.139
	RML	0.16	0.266	0.164	0.211
	CLEAN	1.121	1.282	1.427	1.082
10 $\mu$ as	DoG-HiT	0.219	0.144	0.191	0.215
	RML	0.238	0.219	0.234	0.245
	CLEAN	0.294	0.568	0.658	0.285
20 $\mu$ as	DoG-HiT	0.414	0.203	0.402	0.411
	RML	0.433	0.275	0.443	0.441
	CLEAN	0.399	0.156	0.556	0.396

We present the relative errors of the reconstructions in Table 4. The comparison may be somewhat unfair for CLEAN, given the large beam size compared to the size of the structures, but a final convolution with a synthetic point spread function is the common standard in radio astronomy. We present the relative error of the reconstruction both without blurring (as is standard for RML and DoG-HiT) and with blurring by one-half of the beam size and the full beam size (as is standard for CLEAN). The super-resolving DoG-HiT reconstructions worsen with a larger restoring beam, while for CLEAN the opposite is true. DoG-HiT wins the challenge for three of the four test images (crescent, disk, ring) and performs similar to RML for narrow structures (crescent, double). Overall, we can conclude that DoG-HiT is

able to achieve a similar precision as current imaging algorithms, but alleviates some of the limitations of both CLEAN (no super-resolution) and RML methods (sensitivity to smooth extended features).

We present in Fig. 8 the residuals of the reconstructions of the ring feature with RML and with DoG-HiT. The residuals for both imaging methods are ring-shaped and spatially correlated, indicating that there is still not recovered structure. However, the histograms of the residuals in the lower panels of Fig. 8 demonstrate a very good reconstruction overall. The pixel residual distribution is well approximated by a narrow Gaussian distribution in both cases. Nevertheless, the residual distribution for DoG-HiT is slightly more narrow and less skewed, which agrees well with the overall slightly smaller relative error listed in Table 4.

### 5.3. Transverse resolution

We study the transverse resolution of the algorithms with the crescent image in this section. We present in Fig. 9 the profiles of the true (blue) and the recovered crescent images in the north–south direction at central right ascension. We recover the correct double peak structure with north–south asymmetry, both with the RML method and with DoG-HiT. CLEAN is not able to reproduce this fine structure sufficiently. Regarding transverse resolution of the ring features and the central depression, RML and DoG-HiT perform equally well, approximately recovering the correct widths of the Gaussian blurred ring and the correct depth of the central depression. However, DoG-HiT recovers a

zero-flux central depression, which is not captured in the true image. We computed the blurring beam size that maximizes the correlation between the (blurred) true image and the recovered images to quantify the resolutions. The largest correlation between the DoG-HiT reconstruction and the true image was achieved if the true image was blurred by a beam with widths  $6.1 \mu\text{s}$ . That means that DoG-HiT was able to reproduce image features down to a resolution of approximately  $6 \mu\text{s}$ . For the RML reconstruction, we found a maximal correlation for a beam of  $5.2 \mu\text{s}$ , similar to DoG-HiT. This resolution is expected due to the reverse taper of  $5 \mu\text{s}$  applied in the ehtim pipeline. For CLEAN we found a width of  $19.7 \mu\text{s}$ , coinciding well with the applied point spread function of the array.

#### 5.4. Simplicity and performance

The five imaging steps presented in Sect. 3.2 may not appear as a simple approach to imaging. However, one should recall that this strategy resembles typical steps in the imaging of interferometric data with CLEAN (imaging in several loops of cleaning and self-calibration). Hence, our lengthy pipeline is not more complex than automatic cleaning scripts.

More importantly, DoG-HiT only takes into account a very limited number of regularization parameters, namely only the prior guess for the total flux and the biasing parameter  $\alpha$ , which controls the weight of the hard thresholding regularization term (see Eq. (26)). Apart from these parameters, only solver related choices such as stepsize or relative tolerances need to be specified. This is a first step toward a more unsupervised imaging algorithm in which crucial choices for the imaging procedure (i.e., selection of window or regularization parameters) come directly from data and are not manually selected during the analysis.

The down side of this simplicity is that DoG-HiT is also less flexible compared to RML methods. RML methods combine different type of penalizations and prior assumptions that could be relatively weighted according to specifications of a certain data set. While it is promising news that wavelet sparsity-promoting algorithms are similar to RML methods, or in some settings, perform better, this conclusion cannot be automatically generalized. In particular, more advanced calibration issues could add an additional layer of complexity to the problem. Furthermore, the hard thresholding method used in DoG-HiT may limit the dynamic range of the reconstruction (i.e., the minimal flux that can be recovered). A more rigorous study of this drawback should be made in subsequent works and applications.

Furthermore, a serious disadvantage of our algorithm is that it presently requires considerably more time and computing resources than the fast RML methods. This is because the image is represented by an overcomplete dictionary of wavelet scales.

## 6. Physical source model

To demonstrate the performance of the algorithm on structures covering a wider range of spatial scales, we present here a DoG-HiT image reconstruction made from synthetic data from the first ngEHT Analysis Challenge<sup>3</sup>, which emulate the black hole shadow and the jet base in M87 as observed with a possible ngEHT configuration (Roelofs et al. 2022). The ngEHT is a planned, but not finally proposed, future global VLBI array, designed to produce real time movies of the dynamics in the extreme vicinity of a black hole and the innermost jet region

<sup>3</sup> Available under <https://challenge.ngeht.org/challenge1/>

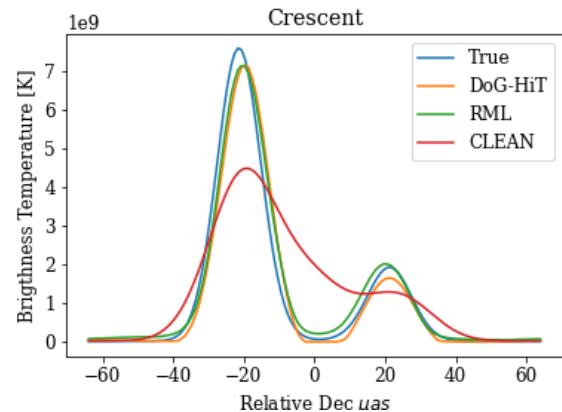
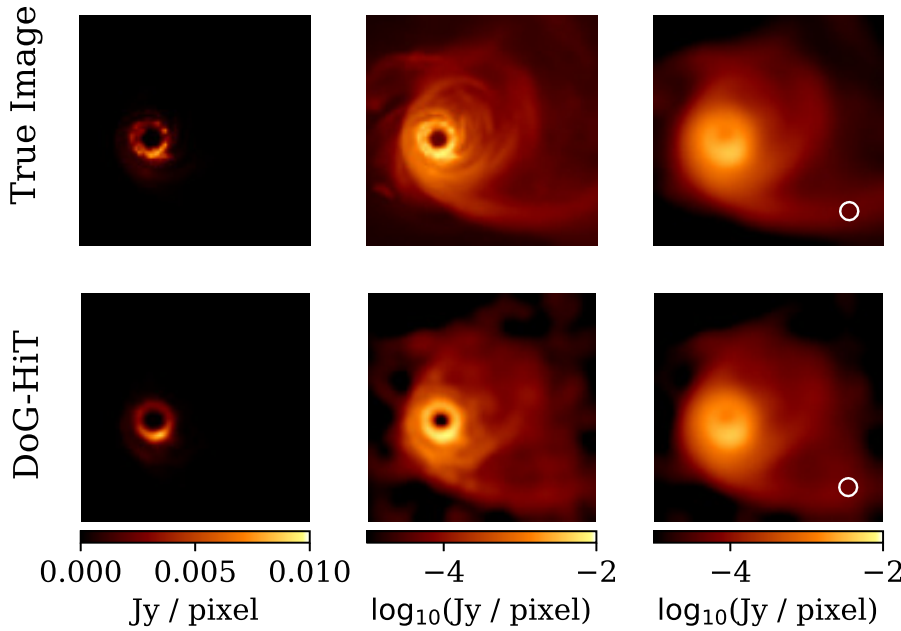


Fig. 9. Profiles of the recovered crescent images in the north-south direction and central right ascension.

(Doeleman et al. 2019). The ngEHT will build upon the enormous success of the EHT and will extend the EHT science with higher dynamic ranges, sensitivity, and resolution. It is believed that it will deliver novel groundbreaking results for the formation of jets, accretion physics, and general relativity tests (Doeleman et al. 2019). In particular, the dense  $uv$ -coverage (including short baselines) and high sensitivity of the ngEHT, compared to the current EHT, allow for the reconstruction of the extended jet emission. The reconstruction and the true image are compared in Fig. 10 in linear (left column) and logarithmic (middle and right column) scales, with the latter employed to highlight the extended emission. The simulated source structure is taken from a MAD GRMHD simulation of a rapid spinning black hole surrounded by an accretion disk with electron heating from reconnection (Roelofs et al. 2022; Mizuno et al. 2021; Fromm et al. 2022). The simulated visibilities are calculated for a possible template ngEHT configuration at 230 GHz that is used throughout the ngEHT Analysis Challenge (Roelofs et al. 2022) and might be realized in the final concept of the array. It contains the 11 current EHT sites (ALMA, APEX, GLT, IRAM-30 m, JCMT, KP, LMT, NOEMA, SMA, SMT, SPT) and ten additional stations from the list of Raymond et al. (2021, BAR, OVRO, BAJA, NZ, SGO, CAT, GARS, HAY, CNI, GAM). HAY, OVRO, and GAM are 37-, 10.4-, and 15-m antennas, respectively. All of the remaining additional antennas are assumed to be of 6 m in diameter. The synthetic visibilities are simulated with a 10-s averaging time and with alternating 10-min observation scans and 10-min gaps. The resulting  $uv$ -coverage is presented in Fig. 11. For more information on the generation of the ground truth image and the synthetic observation, we refer the interested reader to the description of the ngEHT Analysis Challenge available at the link listed in footnote 3.

The DoG-HiT reconstruction in Fig. 10 accurately represents the central ring-like structure. This is expected, judging from the successful reconstructions obtained in Sect. 5.1 on the compact crescent images from a much sparser synthetic observation. In addition to this, Fig. 10 demonstrates that DoG-HiT also reproduces the extended emission from the jet base (middle and right panels) very well. The structural details of the jet base are compressed on much larger scales than the smaller ring feature, and are less bright (hence only visible in logarithmic scale). This result demonstrates the ability of DoG-HiT to work on images with a wide range of spatial scales and a large dynamic range.



**Fig. 10.** Reconstruction of synthetic M87 observation with a possible ngEHT array taken from the ngEHT Analysis Challenge (Roelofs et. al. 2022). The true image is presented in the upper panels, and the reconstruction with DoG-HiT in the lower panels. The left panels show the ground truth and the recovered images in linear scale, the middle panels in logarithmic scale (i.e., highlighting the extended emission from the jet basis), and the right panels compare the ground truth and the recovered image, both smoothed with a restoring beam of 20  $\mu$ as.

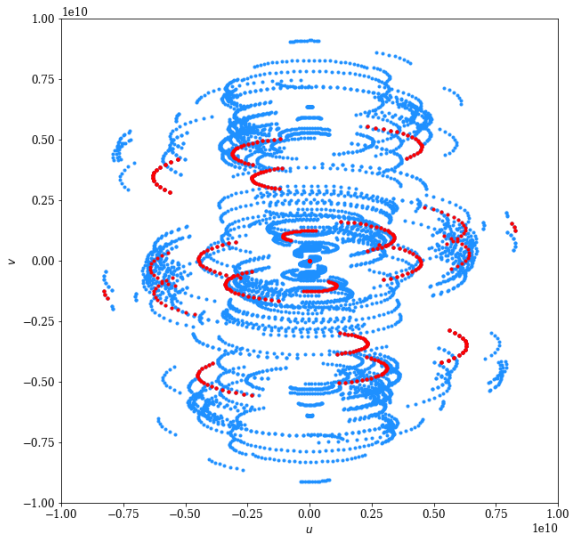


**Fig. 11.**  $uv$ -coverage of a synthetic ngEHT observation of M87 at 230 GHz. The  $uv$ -coverage with the EHT 2017 antennas only is plotted in red. For more details, see Roelofs et. al. (2022).

## 7. Conclusion

In this paper, we presented a novel interferometric imaging algorithm that is capable of adapting to the Fourier domain coverage of observations and is particularly applicable to sparse  $uv$ -coverages. Our imaging algorithm models the image as a sum of the difference of Gaussians wavelet functions. This wavelet dictionary is more flexible than the usual discrete à trous wavelet transform and allows us to select the scales to adapt to the  $uv$ -coverage.

We formulate the imaging problem as an optimization problem with an objective functional consisting of the reduced  $\chi^2$  of the recovered closure properties (closure phase and logarithmic closure amplitudes) and an  $l_0$ -pseudonorm sparsity term in the

wavelet domain. As this objective functional is still invariant against rescaling of the image guess, we also add a total flux constraint. The resulting objective functional is nonsmooth and nonconvex, but could be solved by an iterative hard thresholding splitting algorithm for which local convergence to a steady point is known. Due to nonconvexity, global convergence cannot be assured, but practice shows that local minima could be avoided by proper initial guesses. Our algorithm is an amplitude- and total-flux-conserving algorithm, in contrast to schemes using soft thresholding. Together with a more thorough separation of image features and sidelobes by a flexible wavelet dictionary analysis, this is expected to bring significant improvements in imaging of VLBI data with strongly varying and scale-dependent noise.

We present a complete imaging pipeline ready for application. Our imaging pipeline consists of five imaging rounds, where we refine the initial imaging results from the closure properties in an iterative imaging, self-calibration loop, which uses the amplitude and phase information. We apply, for the first time, a multiresolution constraint for these refinement steps. Moreover, we prove the stability of our pipeline in practice on synthetic data.

Comparisons of imaging performance on the synthetic data show that DoG-HiT achieves super-resolution and outperforms CLEAN in the reconstruction of fine structure (super-resolving) and that it is comparable to RML methods in terms of accuracy of reconstruction. DoG-HiT succeeds in the reconstruction of smooth extended emission components, where it outperforms RML. It effectively combines the strengths of CLEAN and RML methods, and reduces their specific weaknesses. DoG-HiT should therefore be well suited for application to targets with a wide range of spatial scales, for which it may outperform current RML reconstructions in the context of better recovering smoother emission on large scales. We have demonstrated this capability on a synthetic data set from the first ngEHT challenge, with excellent reconstructions achieved for of both the small-scale inner ring-like structure and the faint, larger-scale emission from the jet base. It should also be noted that the DoG-HiT reconstruction accurately reproduces features with a

H. Müller and A. P. Lobanov: DoG-HiT: A novel VLBI multiscale imaging approach

strong contrast between emission and the background. At the same time, DoG-HiT presently introduces some systematic inaccuracies (e.g., a limited dynamic range) into the reconstruction, and this needs to be addressed in future works.

*Acknowledgments.* We thank F. Roelofs, C. Fromm, L. Blackburn, G. Lindahl, A. Raymond, S. Doeleman and the team of the ngEHT Analysis Challenge for providing their data set and for useful discussions. H.M. received financial support for this research from the International Max Planck Research School (IMPRS) for Astronomy and Astrophysics at the Universities of Bonn and Cologne. Software availability: We will make our imaging pipeline and algorithms publicly available soon as part of the software package MrBeam (<https://github.com/hmue11ergoe/mrbeam>). MrBeam makes use of the publicly available ehtim (Chael et al. 2018), regpy (Regpy 2019), and WISE software packages (Mertens & Lobanov 2015).

## References

- Akiyama, K., Ikeda, S., Pleau, M., et al. 2017a, *AJ*, **153**, 159  
Akiyama, K., Kuramochi, K., Ikeda, S., et al. 2017b, *ApJ*, **838**, 1  
Arras, P., Frank, P., Haim, P., et al. 2022, *Nat. Astron.*, **6**, 259  
Assirati, L., Silva, N. R., Berton, L., Lopes, A. A., & Bruno, O. M. 2014, *J. Phys.: Conf. Ser.*, **490**, 012020  
Attouch, H., Bolte, J., & Svaiter, B. 2013, *Math. Programm.*, **137**, 91  
Bao, C., Dong, B., Hou, L., et al. 2016, *Inverse Probl.*, **32**, 115004  
Beck, A., & Teboulle, M. 2009, *SIAM J. Imaging Sci.*, **2**, 183  
Bhatnagar, S., & Cornwell, T. J. 2004, *A&A*, **426**, 747  
Blackburn, L., Pesce, D. W., Johnson, M. D., et al. 2020, *ApJ*, **894**, 31  
Boş, R., Csetnek, E., & Szilard Csaba, L. 2016, *EURO J. Comput. Optim.*, **4**, 3  
Cai, X., Pereyra, M., & McEwen, J. D. 2018a, *MNRAS*, **480**, 4154  
Cai, X., Pereyra, M., & McEwen, J. D. 2018b, *MNRAS*, **480**, 4170  
Candès, E., Romberg, J., & Tao, T. 2006, *IEEE Trans. Inform. Theory*, **52**, 489  
Candès, E., Wakin, M., & Boyd, S. 2007, *J. Fourier Anal. Applic.*, **14**, 877  
Carrillo, R. E., McEwen, J. D., & Wiaux, Y. 2012, *MNRAS*, **426**, 1223  
Carrillo, R. E., McEwen, J. D., & Wiaux, Y. 2014, *MNRAS*, **439**, 3591  
Chael, A. A., Johnson, M. D., Bouman, K. L., et al. 2018, *ApJ*, **857**, 23  
Clark, B. G. 1980, *A&A*, **89**, 377  
Combettes, P., & Pesquet, J. 2009, *Fixed-Point Algorithms for Inverse Problems in Science and Engineering*, 49  
Cornwell, T. J. 2008, *IEEE J. Sel. Top. Signal Process.*, **2**, 793  
Coupinot, G., Hecquet, J., Auriere, M., & Futaully, R. 1992, *A&A*, **259**, 701  
Doeleman, S., Blackburn, L., Dexter, J., et al. 2019, *Bull. Am. Astron. Soc.*, **51**, 256  
Donoho, D. 2006, *IEEE Trans. Inform. Theory*, **52**, 128  
Event Horizon Telescope Collaboration (Akiyama, K., et al.) 2019, *ApJ*, **875**, L4  
Frieden, B. R. 1972, *J. Opt. Soc. Am.*, **62**, 511  
Fromm, C. M., Cruz-Orsorio, A., Mizuno, Y., et al. 2022, *A&A*, **660**, A107  
Garsden, H., Girard, J. N., Starck, J. L., et al. 2015, *A&A*, **575**, A90  
Girard, J. N., Garsden, H., Starck, J. L., et al. 2015, *J. Instrum.*, **10**, C08013  
Gonzalez, R. C., & Woods, R. E. 2006, *Digital Image Processing*, 3rd edn. (New Jersey: Prentice Hall)  
Goupillaud, P., Grossmann, A., & Morlet, J. 1984, *Geoexploration*, **23**, 85  
Grossmann, A., Kronland-Martinet, R., & Morlet, J. 1989, In *Wavelets: Time-Frequency Methods and Phase Space* -1, 2  
Högbom, J. A. 1974, *A&AS*, **15**, 417  
Ikeda, S., Tazaki, F., Akiyama, K., Hada, K., & Honma, M. 2016, *PASJ*, **68**, 45  
Lannes, A., Anterrieu, E., & Marechal, P. 1997, *A&AS*, **123**, 183  
Li, F., Cornwell, T. J., & de Hoog, F. 2011, *A&A*, **528**, A31  
Liang, J., Fadili, J., & Peyré, G. 2016, in *Advances in Neural Information Processing Systems*, eds. D. Lee, M. Sugiyama, U. Luxburg, I. Guyon, & R. Garnett, (Curran Associates, Inc.), 29, 4035  
Line, J. L. B., Mitchell, D. A., Pindor, B., et al. 2020, *PASA*, **37**, e027  
Mallat, S. G. 1989, *IEEE Trans. Pattern Anal. Mach. Intell.*, **11**, 674  
Martinet, B. 1972, *Comptes Rendus Acad. Sci. Paris*, **1274**, 163  
Mertens, F., & Lobanov, A. 2015, *A&A*, **574**, A67  
Mizuno, Y., Fromm, C. M., Younsi, Z., et al. 2021, *MNRAS*, **506**, 741  
Moreau, J. 1962, *Comptes Rendus Hebdomadaires Séances Acad. Sci., Paris*, **255**  
Mouri Sardarabadi, A., Leshem, A., & van der Veen, A.-J. 2016, *A&A*, **588**, A95  
Murenzi, R. 1989, in *Wavelets. Time-Frequency Methods and Phase Space*, eds. J.-M. Combes, A. Grossmann, & P. Tchamitchian, 239  
Narayan, R., & Nityananda, R. 1986, *ARA&A*, **24**, 127  
Ochs, P., Chen, Y., Brox, T., & Pock, T. 2014, *SIAM J. Imaging Sci.*, **7**, 1388  
Onose, A., Carrillo, R. E., Repetti, A., et al. 2016, *MNRAS*, **462**, 4314  
Onose, A., Dabbech, A., & Wiaux, Y. 2017, *MNRAS*, **469**, 938  
Pratley, L., McEwen, J. D., d’Avezac, M., et al. 2018, *MNRAS*, **473**, 1038  
Rau, U., & Cornwell, T. J. 2011, *A&A*, **532**, A71  
Raymond, A. W., Palumbo, D., Paine, S. N., et al. 2021, *ApJS*, **253**, 5  
Regpy 2019, regpy: Python tools for regularization methods, <https://github.com/regpy/regpy>  
Roelofs, F., et al. 2022, *Galaxies*, in press  
Schwab, F. R. 1984, *AJ*, **89**, 1076  
Starck, J. L., & Murtagh, F. 2006, *Astronomical Image and Data Analysis* (Springer)  
Starck, J.-L., Bijaoui, A., Lopez, B., & Perrier, C. 1994, *A&A*, **283**, 349  
Starck, J.-L., Murtagh, F., & Fadili, J. 2015, *Sparse Image and Signal Processing: Wavelets and Related Geometric Multiscale Analysis*, 2nd edn, 1  
Stollnitz, E., Deroose, T., & Salesin, D. 1994, *IEEE Comput. Graph. Applic.*, **15**  
Thiébaud, É., & Young, J. 2017, *J. Opt. Soc. Am. A*, **34**, 904  
Thompson, A., Moran, J., & Swenson, G. 1994, *Interferometry and Synthesis in Radio Astronomy* (Krieger Publishing Company)  
Tiede, P., Broderick, A. E., & Palumbo, D. C. M. 2020, *ApJ*, submitted [arXiv:2012.07889]  
Wakker, B. P., & Schwarz, U. J. 1988, *A&A*, **200**, 312  
Wiaux, Y., Jacques, L., Puy, G., Scaife, A. M. M., & Vanderghynst, P. 2009, *MNRAS*, **395**, 1733  
Xiao, J., Ng, M. K.-P., & Yang, Y.-F. 2015, *IEEE Trans. Image Process.*, **24**, 1587

$\alpha$	0	$10^{-3}$	$10^{-2}$	$10^{-1}$	$10^0$	$10^1$
crescent	0.345	0.17	0.148	0.148	0.169	0.254
disk	0.202	0.164	0.154	0.137	0.138	0.231

**Table B.1.** Relative error of the DoG-HiT reconstruction with varying assumptions on the regularization parameter  $\alpha$ .

### Appendix A: Fixed point property of proximity operators

Let  $\hat{x} \in \operatorname{argmin}_x H(x)$  and let  $x \in \mathbb{X}$ . Then it is:

$$H(x) + \frac{1}{2\tau} \|x - \hat{s}\|_{\mathbb{X}} \geq H(\hat{s}) + \frac{1}{2\tau} \|\hat{s} - \hat{s}\|_{\mathbb{X}}, \quad (\text{A.1})$$

as  $\hat{s}$  is in the argmin of  $H$  and  $\tau \geq 0$ . Vice versa, let  $\hat{s}$  be the solution to  $\hat{s} = \operatorname{prox}_{\tau H}(\hat{s})$ , then it follows, see Eq. (23):

$$0 = \hat{s} - \hat{s} \in \tau \partial H[\hat{s}], \quad (\text{A.2})$$

which suffices to show that for a convex, proper, and lower semicontinuous functional,  $\hat{x}$  is in the argmin of  $H$ .

### Appendix B: Variation of the regularization parameter

In this subsection we discuss the impact of the regularization parameter  $\alpha$ . We show in Fig. B.1 the reconstruction of the crescent image and of the disk image, with varying regularization parameter  $\alpha$ . The leftmost panels show the true image, and the panels to the right of that show the unconstrained reconstructions (e.g.,  $\alpha = 0$ ). The middle panels show, from left to right, the reconstruction results obtained with increasing values of  $\alpha$ . In Table B.1 we present the relative precisions (31) of the different reconstructions. The reconstructions are worse for  $\alpha$  that is too small or too big. The best-fit value lies somewhere in between.

The reconstructions for very small  $\alpha$  show a greedy resolving model that is too fine, which differs significantly from the true image. Moreover, fainter sidelobes and background emission are visible in the reconstruction. These models overfit the observed visibilities, in other words, the observed visibilities are fitted exactly, but the gaps in the uv-coverage are filled by high-oscillating fits.

For intermediate  $\alpha$ , the reconstruction is best. The unconstrained reconstruction is modeled with few (due to sparsity) extended, smooth wavelet functions. This approach effectively smooths the fit to the visibilities and fills the gaps in the uv-coverage with smooth fits. In this spirit, the sparsity approach in the wavelet basis has a similar effect on the data, such as total variation, total squared variation, and maximum entropy penalizations. Moreover, sidelobes in the image are suppressed by the hard thresholding.

At the other end of the table, the reconstructions worsen again for reconstruction parameters that are too large. In these cases, the penalty term dominates the objective functional in the forward-backward minimization. The image is modeled with too few wavelet scales. The result is a blurry reconstruction. Moreover, the hard thresholding minimization procedure cuts significant fainter features, for instance, the northern emission in the crescent test image (upper most right panel in Fig. B.1).

H. Müller and A. P. Lobanov: DoG-HiT: A novel VLBI multiscale imaging approach

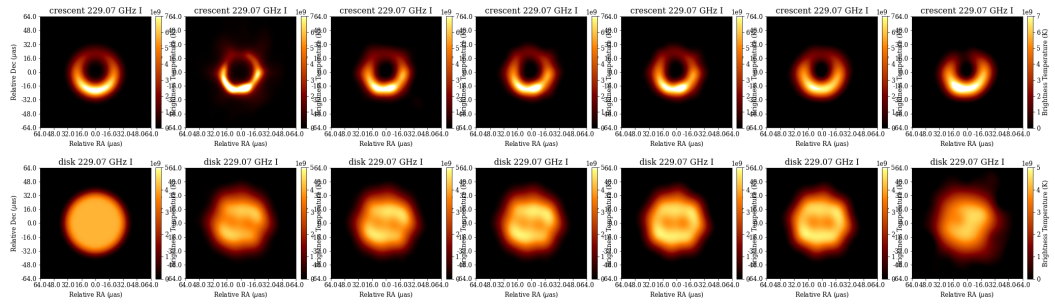


**Fig. B.1.** Reconstructions with varying regularization parameter  $\alpha$ . Leftmost panels: True images. Middle panels from left to right:  $\alpha \in \{0, 10^{-3}, 10^{-2}, 10^{-1}, 10^0, 10^1\}$ .

### 3.3 Paper 2: Müller & Lobanov 2023a, A&A, 672, A26

We present in this subsection the second VLBI imaging publication for this dissertation Müller & Lobanov (2023a). This is the natural continuation of the work started in Müller & Lobanov (2022). Inspired by the success of combining several multiscale transforms (e.g. Carrillo et al. 2013; Starck et al. 2003), we extend here the multiscalar dictionaries to a series of multidirectional dictionaries. We introduce a second wavelet dictionary by difference of spherical Bessel functions which are best suited to represent both scale and directional properties of the uv-coverage. With these two dictionaries at hand, we introduce for the first time the concept of swapping the dictionaries during image reconstruction. The following manuscript uses this concept for developing a multiscale CLEAN framework (DoB-CLEAN), departing from the forward modeling framework discussed in Müller & Lobanov (2022). We illustrate the conceptual motivation for DoB-CLEAN first, before we present the manuscript.

CLEAN has several limitations. One of the theoretically most severe issues for VLBI experiments is the need to convolve the set of CLEAN components with the rigidly fixed, Gaussian CLEAN restoring beam after the minor and major loops have ended. This limits the achievable resolution and introduces an unphysical disparity between the model fitted to the visibilities and the final (convolved) image. As a naive approach to resolve this conflict, one could try to fit the residual directly with the final image  $I^C$ , i.e. solve a problem of the kind:

$$I^D \approx B^D * I^C = B^D * B^C * \left( \sum_{i=0}^n a_i \delta(l_i, m_i) \right), \quad (3.1)$$

instead of solving Eq. (2.44) and Eq. (2.45). However, such an approach would quickly start to diverge since the main lobe of the dirty beam  $B^D$  is convolved with the clean beam  $B^C$  smearing out the residuals. In order to avoid divergence, we replace the clean beam with a set of extended multiscalar basis functions  $\{\Phi_0, \Phi_1, \dots, \Phi_k\}$ , i.e.:

$$I^D \approx B^D * I^C = B^D * \left( \sum_{i=0}^n a_i \Phi_{j_i}(l_i, m_i) \right). \quad (3.2)$$

If the basis functions would be constructed such that they are orthogonal to the kernel of the dirty beam, i.e. if  $B^D * \Phi_j \approx \Phi_j$ , the divergence due to smearing would be solved. However, it turns out that wavelets that satisfy this property (i.e. that are fitted to the uv-coverage), would have to contain sidelobes on their own, and hence promote unphysical solutions. We therefore define a second set

of basis functions  $\{\tilde{\Phi}_0, \tilde{\Phi}_1, \dots, \tilde{\Phi}_k\}$  that only approximate the main lobe of the wavelets  $\Phi_j$ . We reduce the residual in the way described by Eq. (3.2), but the final CLEAN model will be:

$$I^C = \sum_{i=0}^n a_i \tilde{\Phi}_{j_i}(l_i, m_i). \quad (3.3)$$

This procedure is similar in philosophy to the approach in the canonical CLEAN and looks like a standard multiscale version of CLEAN at first glance. However, there is a subtle difference. We can update the residual with the model  $I^C$  without divergence since the basis functions are already extended. Hence, the convolution with the multiscale equivalent of the clean beam takes place within the minor loops (before the residual is updated) now and a final, unphysical convolution with a clean beam is not needed anymore. This solves the disparity between the model and the image in CLEAN and allows for super-resolution in the reconstruction. For more details, we refer to the following manuscript.

DoB-CLEAN transfers the algorithmic ideas behind DoG-HiT to a CLEAN framework and cures most of the issues and limitations related to CLEAN by this. Moreover, the subtle updates introduced to DoB-CLEAN compared to MS-CLEAN approaches (i.e. swapping between two different dictionaries, convolution within the minor loop, scale-selection criterion), are done under the surface within the minor loop. The interface could be used in exactly the same way (MS-)CLEAN was used in VLBI for decades. Hence, we decrease the hurdle to adapt to a novel imaging framework for the user and make use of the extensive experience of astronomers. A more detailed comparison to MS-CLEAN algorithms (e.g. Bhatnagar & Cornwell 2004; Cornwell 2008; Offringa & Smirnov 2017; Rau & Cornwell 2011; Starck et al. 1994; Wakker & Schwarz 1988) can be found in the following manuscript. We want to highlight here however, that MS-CLEAN and DoB-CLEAN were proposed for different data regimes. MS-CLEAN was developed for the reconstruction of extended emissions in which the representation by CLEAN components is suboptimal. DoB-CLEAN is developed specifically for the reconstruction at the highest possible resolution in a sparse VLBI experiment. That implies significant algorithmic differences between classical MS-CLEAN and DoB-CLEAN. For MS-CLEAN the multiscale basis functions are used to represent extended emission uniformly, for DoB-CLEAN they are used to distinguish between covered and non-covered Fourier coefficients.

# Multiscale and multidirectional very long baseline interferometry imaging with CLEAN

H. Müller and A. P. Lobanov

Max-Planck-Institut für Radioastronomie, Auf dem Hügel 69, Bonn 53121, Germany  
 e-mail: [hmueller@mpi-fr-bonn.mpg.de](mailto:hmueller@mpi-fr-bonn.mpg.de); [alobanov@mpi-fr-bonn.mpg.de](mailto:alobanov@mpi-fr-bonn.mpg.de)

Received 2 August 2022 / Accepted 27 January 2023

## ABSTRACT

**Context.** Very long baseline interferometry (VLBI) is a radio-astronomical technique whereby the correlated signal from various baselines is combined into an image of the highest possible angular resolution. Due to the sparsity of the measurements, this imaging procedure constitutes an ill-posed inverse problem. For decades, the CLEAN algorithm has been the standard choice in VLBI studies, despite it bringing on some serious disadvantages and pathologies that are brought on by the requirements of modern frontline VLBI applications.

**Aims.** We developed a novel multiscale CLEAN deconvolution method (DoB-CLEAN) based on continuous wavelet transforms that address several pathologies in CLEAN imaging. We benchmarked this novel algorithm against CLEAN reconstructions on synthetic data and reanalyzed BL Lac observations of RadioAstron with DoB-CLEAN.

**Methods.** The DoB-CLEAN method approaches the image via multiscale and multidirectional wavelet dictionaries. Two different dictionaries were used: 1) a difference of elliptical spherical Bessel functions dictionary fitted to the  $uv$ -coverage of the observation that is used to sparsely represent the features in the dirty image; 2) a difference of elliptical Gaussian wavelet dictionary that is well suited to represent relevant image features cleanly. The deconvolution was performed by switching between the dictionaries.

**Results.** DoB-CLEAN achieves a super-resolution compared to CLEAN and remedies the spurious regularization properties of CLEAN. In contrast to CLEAN, the representation via basis functions has a physical meaning. Hence, the computed deconvolved image still fits the observed visibilities, in contrast to CLEAN.

**Conclusions.** State-of-the-art multiscale imaging approaches seem to outperform single-scale standard approaches in VLBI and are well suited to maximize the extraction of information in ongoing frontline VLBI applications.

**Key words.** techniques: interferometric – techniques: image processing – techniques: high angular resolution – methods: numerical – galaxies: nuclei – galaxies: jets

## 1. Introduction

Very long baseline interferometry (VLBI) is a radio-interferometric technique that achieves an unmatched angular resolution. An array of single-dish antennas altogether form an instrument with angular resolution determined by the wavelength and longest separation between two antennas in the array (Thompson et al. 2017). The signal recorded at each antenna pair is correlated. The correlation product (visibility) is proportional to the Fourier-transform of the true sky-brightness distribution (van Cittert-Zernike theorem), where the spatial frequency is specified by the baseline separating the two antennas recording. In principle, the true image could be revealed from a complete sampling of the  $uv$ -space by an inverse Fourier transform. However, since an interferometer is a sparse array of single antennas with a limited number of baselines, the coverage of Fourier coefficients ( $uv$ -coverage) is often sparse and has significant gaps (Thompson et al. 2017). This makes imaging, namely, the procedure of creating an image from the correlated antenna outputs, an ill-posed inverse problem.

The imaging problem (inverse Fourier transform from sparsely sampled data) is often expressed equivalently as a deconvolution problem, namely, the dirty image (inverse Fourier transform of visibilities) is modeled as the convolution of the

dirty beam (inverse Fourier transform of mask) and the true sky brightness distribution (Thompson et al. 2017).

CLEAN and its variants (Högbom 1974; Clark 1980; Schwab 1984) have been the standard in VLBI imaging for decades and are still widely used. CLEAN models the image iteratively as a set of point sources: CLEAN searches for the position of the maximum in the residual image, stores the intensity and the position in a list of delta-components, and updates the residual by subtracting the rescaled and shifted dirty beam from the residual image. Despite the general success of CLEAN in VLBI applications, a number of issues have arisen thus far: CLEAN is less precise than recently developed regularized maximum likelihood (RML) methods (Akiyama et al. 2017b,a; Chael et al. 2018; Event Horizon Telescope Collaboration 2019; Müller & Lobanov 2022) and Bayesian approaches (Arras et al. 2021), particularly when the true sky brightness distribution is uniform and extended, it offers a poorer resolution and relies on manual input from the astronomer performing the imaging to achieve a convergence to the true solution. Moreover, the sequential nature inherent to CLEAN makes CLEAN slow compared to modern optimization algorithms that were developed in an environment of parallel CPU computing facilities.

From a theoretical point of view, CLEAN is inadequate. An imaging procedure needs to satisfy two basic requirements.

Firstly, the final image needs to fit the observed visibilities. Secondly, among all possible solutions that fit the data (i.e., among the kernel spanned by the convolution with the dirty beam), the imaging procedure should select the image that is most reasonable, namely, the one that interpolates the gaps in the  $uv$ -coverage in the most reasonable way. CLEAN can only achieve one of these goals simultaneously. CLEAN separates between a model (the list of delta-components) that fits the observed data and the final image (the model convolved with a clean beam) that is thought to be a reasonable approximation to the true sky brightness distribution. However, strictly speaking, the final image that CLEAN produces in VLBI (and that is used in further studies) no longer provides a reasonable data fit.

In fact, the regularizing property of CLEAN is questionable as well. While CLEAN typically provides decent fits for the  $uv$ -tracks that were observed, the (typically not plotted) fit in the gaps in the  $uv$ -coverage is sometimes clearly unphysical, we will discuss this attribute in more detail in Sect. 4. A more thorough imaging approach is needed that takes the distribution of gaps in the  $uv$ -coverage in account and provides more control over the non-measured Fourier coefficients.

Most of these issues are caused by CLEAN modeling of the image as a sequence of delta components which is inadequate to describe extended image features in real astronomical images. One possible solution is the use of multiscale algorithms that model the image as a set of extended basis functions of different scales (Wakker & Schwarz 1988; Starck et al. 1994; Bhatnagar & Cornwell 2004; Cornwell 2008; Rau & Cornwell 2011; Müller & Lobanov 2022). While this is a great step forward in imaging, MS-CLEAN methods have not been widely adopted in frontline VLBI applications in the past. This is because the selection of suitable basis functions greatly affects the fitting procedure as various scales are sensitive to various parts of the  $uv$ -coverage and do not necessarily solve the problem of missing regularization in CLEAN, namely, the unphysical fits in the gaps of the  $uv$ -coverage. To also address this problem of missing regularization, we propose a more data-driven approach here: the basis functions are selected in a way that they fit to the  $uv$ -coverage, namely, they define masks in the Fourier domain that are separate between visibilities covered by observations and visibilities that are not covered by observations (gaps in the  $uv$ -coverage). The features from the latter should be suppressed during imaging, namely, the unphysical fit in the gaps occurring during CLEAN should be smoothed and regularized. As the  $uv$ -coverage of an observation is typically not circularly symmetric, we propose (for the first time) not only a multiscale, but also a multidirectional set of basis functions (i.e., dictionary).

In this way, our procedure allows for a more thorough separation between reliable image information, namely, image features introduced by regions in the Fourier domain that are covered by data and “invisible distributions,” that is, image features that are most sensitive to regions of the  $uv$ -coverage that are not covered by observations. This is certainly needed to match our second basic requirement for an imaging algorithm for frontline VLBI arrays; among all possible solutions, the one that is most physical (regularized) should be selected.

In this paper, we present an approach to constructing a suitable multiscale and multidirectional dictionary for imaging and implementing this dictionary in a CLEAN-like algorithm called DoB-CLEAN (difference of elliptical Bessel functions CLEAN) that fits in the normal workflow that radio astronomers are used to.

## 2. Theory

### 2.1. Background

A radio interferometer observes a source with all antennas available in the array at the same time. The source typically appears point-like per antenna in the constructed array. The interferometric observation, however, reveals image features at a much greater resolution. We denote the (incoherent) sky-brightness distribution of the source by  $I(l, m)$ . Here,  $l$  and  $m$  denote spatial on-sky coordinates. The recorded signals are correlated for each antenna pair at a fixed time. The antenna pair is specified by a corresponding separation vector  $(u, v)$ , namely, spatial frequencies in units of wavelengths, which is called baseline. While the Earth continues to rotate over the period of observations, the projected baselines vary as well, leading to the typical elliptical tracks in the  $uv$ -coverage. Described by the van-Cittert-Zernike theorem (assuming the small-field approximation and a flat wavefront), the correlation product at a single baseline is the Fourier coefficient of the true sky brightness distribution at this baseline (Thompson et al. 2017):

$$\mathcal{V}(u, v) = \iint I(l, m) e^{-2\pi i(lu + mv)} dl dm. \quad (1)$$

These Fourier coefficients are referred to as the “visibilities.”

Imaging is the problem of recovering the on-sky distribution,  $I$ , from the measured complex visibilities,  $\mathcal{V}$ . From a full sample of the  $uv$ -domain, this could be achieved by an (gridded) inverse Fourier transform. However, every antenna pair at a particular instance in time gives rise to only one Fourier coefficient. Hence, the limited number of available antennas and the limited amount of observation time only allow for a very sparse coverage of the  $uv$ -domain.

For imaging with CLEAN (Högbom 1974), Eq. (1) is equivalently reformulated as a deconvolution problem. The observed visibilities are gridded on a regular grid and possibly weighted – for instance, by baseline-dependent S/N and in the case of uniform weighting, by the number of data points per cell. The gridding cells corresponding to unmeasured Fourier coefficients are set to zero. The dirty image  $I^D$  is now defined as the inverse Fourier transform of the gridded (and weighted) observed visibilities. Furthermore, the dirty beam  $B^D$  is the response to a synthetic point-source, namely, the inverse Fourier transform of the gridding (and weighting) alone. It is:

$$I^D = B^D * I. \quad (2)$$

The imaging problem is now translated into a deconvolution problem. The dirty image and the dirty beam contain significant sidelobes that are caused by the gaps in the  $uv$ -coverage, that is, the cells in the Fourier domain that are initialized with zero during gridding. These sidelobes are “cleaned,” that is, suppressed, by deconvolution. Hence, the deconvolution process can also be understood as an approach to interpolate the observed measured visibilities to the gaps.

Among the sparsity of the observed Fourier coefficients, the imaging procedure has to deal with further complications: scale-dependent thermal noise on different baselines and direction-independent calibration issues. The former complication is addressed by weighting the visibilities by their thermal noise level. The latter complication is factored in station-based multiplicative gains. In particular, the relative phase is often unknown in VLBI imaging. Station-based gains are corrected by

gain-self-calibration loops alternating with deconvolution iterations. In principle, more complex calibration errors could also occur, which cannot be factored in station-based gains at all.

## 2.2. CLEAN

CLEAN directly solves the deconvolution in Eq. (2) by iteratively subtracting the dirty beam from the residual. Classical CLEAN (Högbom 1974) approaches the image as a sequence of point sources. Hence, once the position of a new component is found, the dirty beam is shifted to this position and rescaled to the intensity in the residual image at that location multiplied with some gain parameter. The residual image is updated by subtracting the shifted and rescaled dirty beam. The list of delta-components constitutes the model that CLEAN computes to fit the observed visibilities.

It is crucial for CLEAN to find a proper location of the next component. This is handled mostly manually by the astronomer by specifying search-windows for the next components. This procedure has proven successful, particularly in the presence of calibration errors. However, the iterative windowing, flagging, and self-calibration lacks reproducibility. Within the specified window, the location of the next component is found by the location of the peak in the current residual image. However, this is only approximately correct. If the assumption behind CLEAN, namely, that the true sky brightness distribution is modeled by a sum of point-sources, were true and we would ignore thermal noise for one moment, the current residual ( $I^D$ ) could be envisioned as the convolution of the dirty beam  $B^D$  with the sum of point sources that are unmodeled by CLEAN until this step ( $\{\delta_l\}$  with intensities  $a_l$ ):

$$I^D = \sum_l a_l B^D * \delta_l. \quad (3)$$

The most efficient selection criterion would be to find the largest of these unmodeled point sources, namely, the largest  $a_l$ . CLEAN takes the largest peak in the residual instead. This might not always be the optimal choice since overlapping sidelobes from different emission features can suppress real emission and can create a false source when the sidelobes are constructively added. In practice, this subtle difference however was not found to cause problems. However, we would like to note that the new multiscale CLEAN (DoB-CLEAN) algorithm that we propose in Sect. 3 is based on the same assumption (see Sect. 3.4).

After the final CLEAN-iteration, the list of delta components is typically convolved with a clean beam that represents the resolution limits of the instrument. Moreover, the last residual is added to the final image. This step is of direct meaning for the regularizing property of CLEAN: how does CLEAN fit the gaps in the  $uv$ -coverage? Again we assume the model of point-sources from Eq. (3). Let us assume that CLEAN has computed a guess model:  $M = \sum_l \hat{a}_l \delta_l$ , where the weights,  $\hat{a}_l$ , should approximate the true weights,  $a_l$ , sufficiently well. Then, the final residual,  $R$ , reads:

$$R = I^D - B^D * M = B^D * \left( \sum_l (a_l - \hat{a}_l) \delta_l \right), \quad (4)$$

and the final model:

$$I^M = M + R = B^D * \sum_l a_l \delta_l + (\mathbb{1} - B^D) * \sum_l \hat{a}_l \delta_l, \quad (5)$$

where  $\mathbb{1}$  denotes the identity operator. The sum is decomposed in a part that corresponds to the measured Fourier coefficients – the first term, convolution with dirty beam sets the Fourier coefficients in the gaps exactly to zero) and a part that corresponds to the uncovered gaps in the  $uv$ -coverage; and the second term, convolution with an “invisible” beam  $Id - B$  that is exactly zero for the measured Fourier coefficients and unequal to zero in the gaps. Hence, the model should always fit the data correctly (first term) in the unphysical, ideal situation of an infinite field of view and uniform weighted data without thermal noise and calibration errors. It becomes obvious that CLEAN (assuming that the  $\hat{a}_l$  values are good approximations to the true weights) interpolates the uncovered gaps in the  $uv$ -coverage by assuming that the same pattern of delta components could be used to describe these signals once they were measured. This, however, is problematic primarily for two reasons: first, the  $uv$ -coverage of a real VLBI array shows rich radial (e.g., a denser coverage on short baselines) and direction-dependent structural patterns (e.g., highly elliptical  $uv$ -tracks for some antenna pairs that give rise to only a few directions in the  $uv$ -domain). It is far from obvious that these different regions in the Fourier domain should encode the same feature. It is more likely that the small-scale structure hidden on short baselines and the large-scale structure on long baselines show less similarity. A more rigorous multiscale (and multidirectional) approach is needed to separate these different structural features and to take the structural pattern of the  $uv$ -coverage into account. Secondly, the convergence rates and fitting properties in the presence of thermal noise remain unclear (Schwarz 1978). In practice, the CLEAN model often results in severe overfitting when not stopped early enough. This problem is solved by convolving the final model by the clean beam, that is, the fits to the usual more-poorly-covered long baselines are generally suppressed. However, this only trades the problem of overfitting for a limited resolution that is challenged by modern state-of-the-art imaging algorithms and for an unphysical separation between the final image (that is used for further analysis, but does not fit the visibilities due to the convolution with the clean beam that causes disparity from the observed visibilities) and a model (that fits the visibilities, but is not useful for image analysis). Again a more rigorous multiscale approach that improves the separation between gaps and covered regions in the  $uv$ -coverage (and suppresses the overfits in former one) is desired.

The regularization introduced by CLEAN can also be visualized in the image-domain instead of the Fourier domain: here, the extrapolation into gaps in the fit translates into suppressing sidelobes in the dirty image. Sidelobes are suppressed as the basis functions (delta-functions) are sidelobe-less and the dirty image and the dirty beam consist of the same sidelobe pattern. Hence, deconvolution suppresses sidelobes by subtracting the sidelobe pattern of the dirty beam from the residual. As we go on to discuss later in this paper, this stands be a major difference with regard to our new DoB-CLEAN algorithm.

## 2.3. Multiscale CLEAN and wavelets

Multiscale-CLEAN (MS-CLEAN) methods have been proposed in the past (Bhatnagar & Cornwell 2004; Cornwell 2008) to mitigate the problems detailed above. In a nutshell, the point-like basis functions from CLEAN are replaced by smooth, positive, extended basis functions that are suitable for representing the image structure. Bhatnagar & Cornwell (2004) used adaptive scale pixels (Asp) which could, in principle, compress any

shape. [Cornwell \(2008\)](#) specified this and used tapered, truncated parabolas, namely, a function with a minor difference with regard to Gaussians (i.e., they have a finite support). In particular, [Cornwell \(2008\)](#) mentions that Gaussians would be possible as well, as long as a very high dynamic range is not desired or image-plane support constraints are required. Our new method is based on the spirit of MS-CLEAN developed in these works. However, we fit the image with a completely different wavelet-based dictionary resulting in a different imaging procedure. We explain how we theoretically compare our new algorithm with standard MS-CLEAN approaches in more detail in Sect. 4.2.

#### 2.4. Alternative imaging approaches

CLEAN and its variants ([Högbom 1974](#); [Clark 1980](#); [Schwab 1984](#); [Bhatnagar & Cornwell 2004](#); [Cornwell 2008](#); [Rau & Cornwell 2011](#)) have been the standard method in VLBI for the last decades. They remain in use due to their practical nature that allows the astronomer to interact with the imaging manually, to manipulate the data set and to self-calibrate the data set during imaging. We therefore aim to keep this workflow for our new proposed procedure. However, we like to mention the many modern methods developed for VLBI. This includes regularized maximum likelihood (RML) methods (e.g., [Carrillo et al. 2012](#); [Garsden et al. 2015](#); [Akiyama et al. 2017b](#); [Chael et al. 2018](#); [Müller & Lobanov 2022](#)) as well as Bayesian reconstructions (e.g., [Junklewitz et al. 2016](#); [Cai et al. 2018a,b](#); [Arras et al. 2019, 2021](#); [Broderick et al. 2020b,a](#)). In comparison to CLEAN, the problem is solved by forward modeling instead of inverse modeling.

### 3. Algorithm

#### 3.1. Overview

We demonstrated in [Müller & Lobanov \(2022\)](#) how a multiscale approach can improve imaging performance. Our algorithm was based on a wavelet-based sparsity promoting (compressed sensing) approach in the RML fashion. In this paper, we are interested in a more CLEAN-like algorithm as this working procedure is well established within the VLBI community. In particular, we are proposing a new version of MS-CLEAN ([Cornwell 2008](#)), but for the first time we are selecting the basis functions in a way that they fit to the  $uv$ -coverage. This provides an optimal selection between observed image features and sidelobes induced by  $uv$ -coverage defects.

We model the true image by a set of extended basis functions (a dictionary)  $\Psi = \{\Phi_0, \Phi_1, \dots\}$  instead of delta functions, that is,  $I = \Psi x$  with some coefficient array  $x$ . We try to recover the coefficient array  $x$  from the data and infer the recovered image from there by applying the dictionary on  $x$  once more, the recovered image will be  $I = \Psi x$  (where  $x$  is the recovered array of coefficients). The basis functions,  $\Phi_i$ , have some connection to the Fourier domain: convolving with  $\Phi_i$  in the image domain is equivalent to multiplying with the Fourier transform,  $\mathcal{F}\Phi_i$ , in the Fourier domain. The basis functions of the dictionary therefore define filters in the Fourier domain which allow for information on the  $uv$ -coverage to be injected during the imaging procedure, namely, every basis function,  $\Phi_i$ , compresses features of a specific set of baselines.

Here, we consider which basis functions are most efficient in that regard. For the sake of optimally representing the image, we seek basis functions that are smooth, sidelobe-free,

and positive (cf. the selection of basis functions in [Cornwell 2008](#)). An optimal fitting of the  $uv$ -coverage calls for basis functions that provide steep radial masks in the Fourier domain and that are optimally orthogonal on each other as desired. These are demonstrably contradicting requirements. Typical orthogonal wavelet functions (e.g., Daubechies wavelets) already contain wide sidelobes ([Starck et al. 2015](#)). Therefore, we are dealing with two different dictionaries: with a dictionary of (radially) orthogonal wavelets,  $\Psi^{\text{DoB}}$ , referred to as the “difference of Bessel” (DoB) in the following, which enables the optimized handling of masks in the Fourier domain and with a dictionary of smooth and clean wavelets,  $\Psi^{\text{DoG}}$ , that can be used best to describe image features, referred to as “difference of Gaussian (DoG) in the following”. The two wavelet dictionaries are related to each other such that latter one (the image-driven dictionary  $\Psi^{\text{DoG}}$ ) contains only the central peak (without sidelobes) of the wavelets in the former one (the Fourier domain driven dictionary  $\Psi^{\text{DoB}}$ ). This is a similar approximation to that of CLEAN and MS-CLEAN via the transition from the dirty beam to the clean beam, namely, by fitting a central Gaussian component to dirty beam pattern.

The CLEANing procedure is done with  $\Psi^{\text{DoB}}$ . We represent the dirty image by  $I^D = B^D * (\Psi^{\text{DoB}} x)$  and iteratively recover the coefficient array,  $x$ , by CLEAN loops, that is, we iteratively search for the maximum peak, store this in a list of multiscale components and update the residual. The list of multiscale components for the final image, however, is convolved with  $\Psi^{\text{DoG}}$ , instead of  $\Psi^{\text{DoB}}$ . In this sense, representing the model by shifted and rescaled DoB wavelets does not suppress sidelobes in the image (since the basis functions  $\Psi^{\text{DoB}}$  contain sidelobes on their own), but works as a feature-finder algorithm that decomposes the dirty image into a list of (extended) multiscale basis functions. These are then replaced by more regular basis functions that compress the same image features (the same scales), but suppress the long elongating sidelobes. This is done in an alternating iterative procedure with iterative updates of the residual map: we represent the dirty image by the dictionary,  $\Psi^{\text{DoB}}$ , by CLEAN loops; we compute a guess solution by replacing the dictionary,  $\Psi^{\text{DoB}}$ , with the dictionary,  $\Psi^{\text{DoG}}$ ; we update the residual image and repeat these steps until the residual image is noise-like. As opposed to CLEAN, the suppression of sidelobes is not done by finding the CLEAN components and subtracting the dirty beam from the image, but by replacing  $\Psi^{\text{DoB}}$  with  $\Psi^{\text{DoG}}$ .

In our previous paper [Müller & Lobanov \(2022\)](#), we presented a novel wavelet dictionary based on the DoG method, which proved flexible enough to compress information about the  $uv$ -coverage of the observation. Thus, we reused this dictionary for the image domain,  $\Psi^{\text{DoG}}$ . It is the canonical extension to orthogonal wavelets to replace the Gaussians in the construction of the DoG wavelets by modified Bessel functions of the same width (i.e., the central peak of the Bessel functions has the same width as the Gaussians). The Fourier transform of modified Bessel functions is a uniform disk, hence, the Fourier transforms of difference of Bessel (DoB) wavelets are uniform rings. These have non-overlapping support in the Fourier domain, hence, they are orthogonal. We therefore construct the wavelets for fitting the  $uv$ -coverage,  $\Psi^{\text{DoB}}$ , out of DoB wavelets. Moreover, we present ways to extend this concept also to direction-dependent wavelets. Some examples of our sequence of wavelets and their corresponding filter in Fourier domain are presented in Fig. 1. Moreover, we present the cross-section of two example wavelets in Figs. 2 and 3, demonstrating the correspondence between DoB wavelet scales and DoG wavelets. We present more details on this in the subsequent subsections.

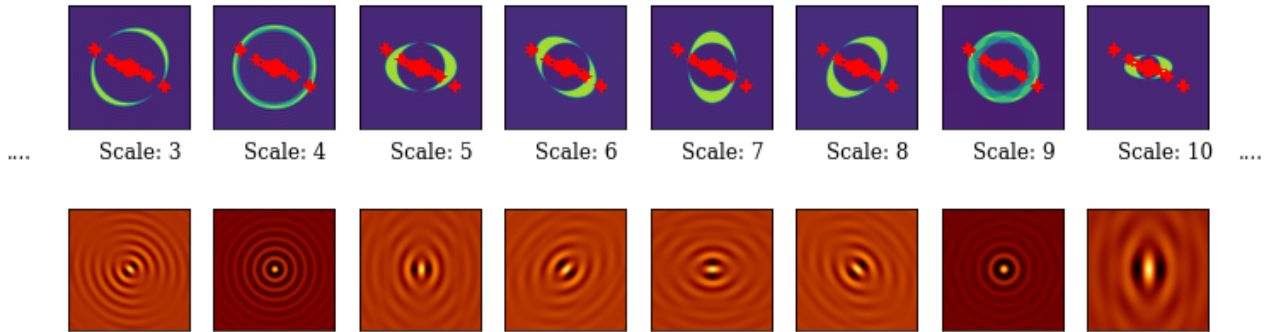


**Fig. 1.** Illustration of the used wavelet scales,  $\Phi_{\text{DoB}}$ , fitted to a synthetic RadioAstron  $uv$ -coverage in image and Fourier domain. Scales of various radial widths (scales 3, 4, scales 5–9, and scale 10) and four different elliptical directions are shown. The scales are fit to the  $uv$ -coverage, as they are sensitive to gaps or covered coefficients, respectively. Upper panel: Fourier transform of the wavelet scales and the synthetic RadioAstron  $uv$ -coverage (red points). Lower panels: respective wavelet basis function in image domain.

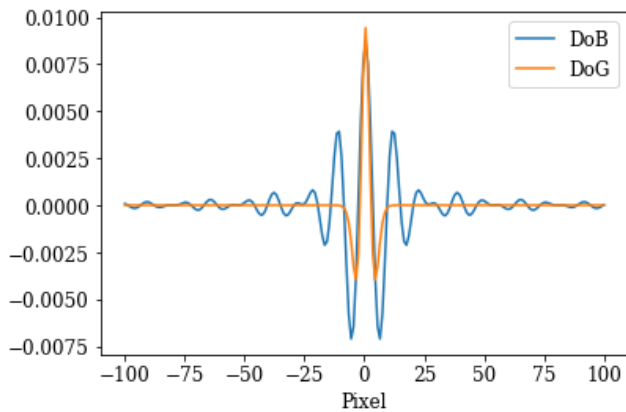


**Fig. 2.** Cross-section of the DoB and DoG wavelet scale 5 presented in Fig. 1. The DoB-wavelet fits the central peak, but suppresses the extended sidelobes.

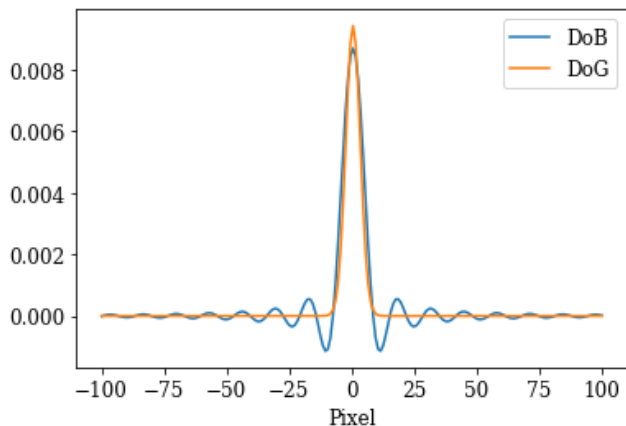


**Fig. 3.** Cross-section of the DoB and DoG wavelet scale 7 presented in Fig. 1. The DoB wavelet fits the central peak, but suppresses the extended sidelobes.

### 3.2. Wavelet-basis functions

We explain in this section the design of the wavelet functions used in this work. As discussed in Sect. 3.1, we aim to find a suitable dictionary,  $\Psi^{\text{DoG}}$ , that is flexible in its radial scales and

smooth to compress image features best, and a dictionary,  $\Psi^{\text{DoB}}$ , that corresponds to the same radial (and angular) scales and provides an optimal analysis masks in the  $uv$ -domain. Our wavelet dictionaries are based on the design of DoG wavelets that we successfully applied to VLBI imaging in Müller & Lobanov (2022). We first summarize the construction of the DoG wavelet dictionary from Müller & Lobanov (2022), then we discuss the straightforward extensions to difference of Bessel functions (DoB) and angular wavelet dictionaries. For more details we refer to Müller & Lobanov (2022).

One of the most frequently applied continuous wavelet functions is the “Mexican hat” wavelet (Murenzi 1989; Starck et al. 2015), which is known to offer image compressions for a wide range of model images. The Mexican hat wavelet is effectively a (rescaled) Laplacian of Gaussian (Gonzalez & Woods 2006). Hence, it is well approximated by the corresponding differential quotient for small variations (Assirati et al. 2014), which we call a DoG wavelet in the following:

$$\Phi_{\text{DoG}}^{\sigma_1, \sigma_2}(x, y) = \frac{1}{2\pi\sigma_1^2} \exp\left(\frac{-r(x, y)^2}{2\sigma_1^2}\right) - \frac{1}{2\pi\sigma_2^2} \exp\left(\frac{-r(x, y)^2}{2\sigma_2^2}\right), \quad (6)$$

$$= G_{\sigma_1} - G_{\sigma_2}, \quad (7)$$

where, necessarily,  $\sigma_1 \leq \sigma_2$  and  $G_{\sigma_j}$  denotes a Gaussian with standard deviation  $\sigma_j$ .

In the past, discrete à trous wavelet decompositions have been of special interest in radio astronomy (Starck & Murtagh 2006; Starck et al. 2015; Mohan & Rafferty 2015; Mertens & Lobanov 2015; Line et al. 2020). These wavelet decompositions (called starlets) were successfully applied to imaging and image segmentation. A starlet decomposition can be computed quickly by a hierarchical upstream filtering instead of repeated convolutions in high dimensions. The image is iteratively convolved with a small filter which has typically a small support of only a couple of coefficients. The filter is applied on the output of the preceding filtering operation, respectively. In this way, a sequence of smoothed images is computed, which we denote following our notation in Müller & Lobanov (2022) by  $c_j$ , where  $j \in [0, 1, 2, \dots, J]$  labels the scale. Thus, the scales,  $c_j$ , are smoothed copies of the original (full resolution) image smoothed by  $2^j \rho$  pixels, where  $\rho$  is the limiting resolution of filter kernel in units of pixels. Wavelets are computed by the difference method:

$$\omega_j = c_j - c_{j+1}, \quad (8)$$

such that each wavelet scale,  $\omega_j$ , compresses the image information on spatial scales between  $2^j\rho$  pixels and  $2^{j+1}\rho$  pixels. The sequence of discrete à trous wavelets is completed by the final smoothing scale  $c_J$ . The set  $[\omega_0, \omega_1, \omega_2, \dots, \omega_{J-1}, c_J]$  is an over-complete representation of the original information, that is, no information is lost or suppressed during convolution. In particular, the image at limiting resolution,  $c_0$ , is recovered by all scales by an easy superposition:

$$c_0 = \sum_{j=0}^{J-1} \omega_j + c_J. \quad (9)$$

This property proved to be key to our application of wavelets in Müller & Lobanov (2022).

While discrete à trous wavelets are very successful in the compression of image information, they are less flexible than a continuous wavelet transform due to the inherent upsampling by a factor of two. Hence, they lack the ability to fit sufficiently to the more complex  $uv$ -coverage of real VLBI arrays. Therefore, we defined a flexible wavelet dictionary out of DoG wavelets in the same procedure as was done for the à trous wavelet: we defined an increasing set of widths  $[\sigma_0, \sigma_1, \sigma_2, \dots, \sigma_J]$  and computed the filtered scales of the original image by convolving with Gaussians, that is,  $c_j = G_{\sigma_j} * I$  (where  $I$  denotes the original image). It is (compare Müller & Lobanov 2022):

$$\omega_j = c_j - c_{j+1} = \Phi_{\text{DoG}}^{\sigma_j, \sigma_{j+1}} * I, \quad (10)$$

and the complete set of scale satisfies the completeness relation Eq. (9) again. If the original image,  $I$ , is noisy, the scales,  $\omega_j$ , will be noisy as well with a scale-specific noise-level. All in all, the DoG wavelet decomposition operation reads:

$$\Psi^{\text{DoG}} : I \mapsto [\Phi_{\text{DoG}}^{\sigma_0, \sigma_1} * I, \Phi_{\text{DoG}}^{\sigma_1, \sigma_2} * I, \dots, G_{\sigma_J} * I]. \quad (11)$$

Convolutions in the image domain translate to multiplicative masks in the Fourier domain. The Fourier transform of a DoG wavelet is a difference of non-normalized Gaussian functions:

$$\mathcal{F}\Phi_{\text{DoG}}^{\sigma_j, \sigma_{j+1}}(u, v) \propto \exp(-2\pi^2\sigma_j^2 q(u, v)^2) - \exp(-2\pi^2\sigma_{j+1}^2 q(u, v)^2), \quad (12)$$

which defines ring-like masks in the  $uv$ -domain, as described in Müller & Lobanov (2022). To have steep and orthogonal masks, however, we propose to replace Gaussians in the construction of wavelets by spherical Bessel functions. Hence:

$$\Phi_{\text{DoB}}^{\tilde{\sigma}_j, \tilde{\sigma}_{j+1}}(x, y) = \frac{1}{\tilde{\sigma}_j r(x, y)} J_1(2\pi r(x, y)/\tilde{\sigma}_j) - \frac{1}{\tilde{\sigma}_{j+1} r(x, y)} J_1(2\pi r(x, y)/\tilde{\sigma}_{j+1}), \quad (13)$$

where  $J_0$  denotes the Bessel function of first order and  $\tilde{\sigma}_j$  represents the widths of the Bessel functions. The widths for the DoB wavelets,  $\tilde{\sigma}$ , are typically not the same as the widths that we use for the DoG-wavelets. In fact, we determine  $\tilde{\sigma}_j$  first by fitting DoB wavelets to the  $uv$ -coverage, as described in Sect. 3.3, then we select the widths for the DoG wavelets,  $\sigma_j$ , such that the correlation between DoB wavelet and DoG wavelet is maximal (see our demonstration in Figs. 2 and 3).

In 2D, it is:

$$\mathcal{F}^{-1}(1_K)(r) = \frac{K}{r} J_0(2\pi Kr) =: \tilde{J}_{1/K}(r), \quad (14)$$

where  $1_K$  is a disc with a radius of  $K$  in the Fourier domain. Hence, the Fourier transform of the DoB wavelet is a ring-shaped mask with step-like cross-section:

$$\mathcal{F}(\Phi_{\text{DoB}}^{\tilde{\sigma}_j, \tilde{\sigma}_{j+1}})(k) = 1_{1/\tilde{\sigma}_j}(k) - 1_{1/\tilde{\sigma}_{j+1}}(k). \quad (15)$$

All DoB wavelets are therefore orthogonal to each other, as the Fourier transform is a unitary operation and the wavelets,  $\Phi_{\text{DoB}}^{\tilde{\sigma}_j, \tilde{\sigma}_{j+1}}$ , have non-overlapping support in the Fourier domain.

Up until now, we have only discussed the case of radially symmetric wavelets. To match the patterns in  $uv$ -coverages of real VLBI arrays, a direction-dependent dictionary is desired as well. This extension is straightforward by replacing the radial symmetric Gaussian-Bessel functions via elliptical beams. We now demonstrate the construction of direction-dependent wavelet dictionary for the DoG wavelets. The construction for DoB wavelets is analogous.

We start with radial widths  $[\sigma_j]$ , and  $N$  angles  $\alpha_0, \alpha_1 = \alpha_0 + \frac{2\pi}{N}, \dots, \alpha_{N-1} = \alpha_0 + \frac{2\pi}{N}(N-1)$  equidistantly distributed on a circle. We then calculate radial Gaussians  $G_{\sigma_j}^r$  and elliptical Gaussians  $G_{\sigma_j, \sigma_{j+1}, \alpha_i}^e$  with major axis  $\sigma_{j+1}$  and minor axis  $\sigma_j$  rotated by an angle  $\alpha_i$ . Hence, when decomposing an image  $I$  we compute filtered smoothed, radial bands  $c_j^r = G_{\sigma_j}^r * I$  and elliptical bands  $c_{j,i}^e = G_{\sigma_j, \sigma_{j+1}, \alpha_i}^e * I$  and compute the wavelets via:

$$\omega_{j,i} = c_j^r - c_{j,i}^e. \quad (16)$$

Due to the combination of radial wavelets and elliptical wavelets,  $\omega_{j,i}$  has a single directionality that is necessary to capture the direction dependence. Moreover, a construction in the spirit of Eq. (16) allows to complete the dictionary easily, that is, to satisfy a completeness property similar to Eq. (9). We completed the set of wavelets with the residual scales  $\omega_{j,N} = \frac{1}{B_j} \sum_{i=0}^{N-1} c_{j,i}^e - c_{j+1}^r$  (where  $B$  is a normalization constant such that  $\|\omega_{j,N}\| = \|\omega_{j,N-1}\|$  for a response to a delta source). The final smoothing scale is  $\omega_J = c_J^r$ . We present the complete action of the dictionaries  $\Psi^{\text{DoG}}$  and  $\Psi^{\text{DoB}}$  in Appendix A. The complete set of wavelet scales  $\{\omega_{j,i}, \omega_J\}$  satisfies a completeness property again:

$$Nc_0^r = \sum_{j=0}^{J-1} \left( \sum_{i=0}^{N-1} \omega_{j,i} + B_j \omega_{j,N} \right) + N\omega_J. \quad (17)$$

### 3.3. Radial widths

In this subsection, we explain which widths  $\sigma_0 < \sigma_1 < \dots < \sigma_J$  were selected to get an optimal fit to the  $uv$ -coverage. The selection of these basis functions has to be done prior to the imaging procedure. The basis functions are selected in a way that they allow for an optimal separation between covered Fourier coefficients and unsampled Fourier coefficients, such that some wavelet basis functions compress Fourier information that is covered by data and the remaining one compress scalar information that has not been observed (gaps). The only important criterion here is whether a scale is sampled or not. For the selection of scales we do not process the signal strength or phase observed in the visibilities. Hence, at this stage, only the  $uv$ -coverage is processed. During the imaging a least-square fit to the visibilities at every scale will be done, with an effective suppression of the non-covered scales.

This selection is similar to the procedure that we already proposed in Müller & Lobanov (2022). We selected the radial

widths only, while the angular elliptical beams are always constructed from the same array of angles equidistantly distributed on a circle at all radial scales,  $\sigma_j$ .

The angle offset,  $\alpha_0$ , was chosen to be the rotation of the major axis in the clean beam. For the selection of the radial scales, we extract the array of  $uv$ -distances, sort this array in increasing order, and look for jumps in the sorted new array. If the increase from one component in the sorted array to the next one exceeds some (manually chosen) threshold, we store the radial baseline lengths,  $q(u, v)$ , for the two neighboring data points in a list of lengths in the Fourier domain. We translate these lengths in the Fourier domain into an increasing list of radial widths of spherical Bessel functions in the image plane  $[\sigma_i]$  by inverting. Finally, we complete this list: if there is an index,  $i$ , such that  $2\sigma_i < \sigma_{i+1}$ , we add a scalar width  $\sigma = (\sigma_{i+1} + \sigma_i)/2$  to avoid to large gaps between consecutive widths.

The resulting DoB wavelet dictionary fits the  $uv$ -coverage well, as can be seen in the comparison of the Fourier filters presented in Fig. 1. As a next step, we have to find the radial widths for the DoG wavelets. We recall that the DoB wavelets were constructed with the à trous differential method. We constructed the DoG wavelets in the same way. Thus, we fit the Gaussians with varying radial widths to the central peaks of the spherical Bessel functions of widths  $[\sigma_i]$ . We then constructed the DoG wavelets by the differential method from these Gaussians. The resulting DoG wavelets approximate the central peaks of the DoB-wavelets, but without the wide sidelobes of the DoB wavelets. This is demonstrated in Figs. 2 and 3. A sequence of examples of selected DoB scales and the respective Fourier transform masks is shown in Fig. 1.

The threshold parameter used in this procedure to identify the gaps in the  $uv$ -coverage is a free parameter. If it is chosen too large, smaller gaps will be skipped. If it is chosen too small, the number of selected basis functions increases and samples the  $uv$ -coverage more accurate than might be necessary. In this work, the threshold has always been chosen such that the most obvious radial gaps are kept and the number of basis functions does not exceed 50 to assure good numerical performance, but this may vary based on the array configuration.

### 3.4. Scale-selection criterion

We assume orthogonal wavelet functions,  $\Phi_j$ , where  $j$  is the count of the scale.

We then assume the true image,  $I$ , is modeled via a sum of wavelets:

$$I = \sum_{j,n,l} a_{j,n,l} \Phi_{j,n} * \delta_l, \quad (18)$$

where  $j$  labels the (radial) scale in use,  $n$  labels the angle of the ellipse, and  $l$  labels the pixels in the image (position of the wavelet). This assumption is well motivated by the great success that wavelet-based segmentation, image compression, and decomposition have in radio astronomy (Starck et al. 2015; Mertens & Lobanov 2015; Line et al. 2020); and, in particular, better motivated than the implicit pixel-based CLEAN assumption. We note that if we replace one scale,  $\Phi_j$ , by two smaller scales,  $\Phi_{j_1}$  and  $\Phi_{j_2}$ , satisfying  $\Phi_j = 2\Phi_{j_1} = 2\Phi_{j_2}$ , it would hold that  $a_j = a_{j_1} = a_{j_2}$ . Hence, the magnitude of  $a_{j,n,l}$  does not depend on the relative size of the corresponding wavelet. Thus, in every CLEAN iteration, we would like to find the biggest  $a_{j,n,l}$  still in the dirty image. However, some scales are not covered in the data. We therefore update our goal: we want to find

the biggest  $a_{j,n,l}$  still in the residual for which the corresponding wavelet basis function  $\Phi_{j,n}^{\text{DoB}}$  corresponds to sampled Fourier coefficients. How much a scale is covered in the data is measured by the dirty beam: if one scale is covered (i.e., the Fourier coefficients compressed by this scale are sampled), the product  $\|\mathcal{F}\Phi_{j,n}^{\text{DoB}} \cdot S\| = \|\Phi_{j,n}^{\text{DoB}} * B^{\text{D}}\|$  is large and vice versa (where  $S = \mathcal{F}B^{\text{D}}$  is a pixel-based mask in the Fourier domain). We therefore formulate our selection criterion as follows: we want to find the scale,  $j$ , angle,  $n$ , and position,  $l$ , such that:

$$\{j, n, l\} \in \operatorname{argmax} \frac{\|\Phi_{j,n} * B^{\text{D}}\|}{\|\Phi_{j,n}\|} a_{j,n,l} \quad (19)$$

is maximal and whereby  $B^{\text{D}}$  denotes the dirty beam. The question at hand is how we can fulfill this criterion in the selection of peaks. We note that the model parameters  $a_{j,n,l}$  are not known to us. In fact, we want to determine them from the dirty image (in the following labeled as  $I^{\text{D}}$ ).

We demonstrate that we can fulfill our criterion if we convolve the dirty image with the beam:

$$B^{\phi} = \frac{1}{\|\Phi_{i,m} * B^{\text{D}}\| \|\Phi_{i,m}\|} \Phi_{i,m} * B^{\text{D}} \quad (20)$$

and search for the maximum over the scales,  $i$ , the angle,  $m$ , and the position of the peak,  $k$ , namely,  $\{i_{\max}, m_{\max}, k_{\max}\} \approx \{j, n, l\}$ . In fact, when we search for the peak over all these scales, we solve the optimization problem:

$$\{i, m, k\} \in \operatorname{argmax}_{i,m,k} \frac{1}{\|\Phi_{i,m} * B^{\text{D}}\| \|\Phi_{i,m}\|} (\Phi_{i,m} * B^{\text{D}} * I^{\text{D}})(k). \quad (21)$$

A detailed proof of this identification, namely, showing that we matched our selection criterion Eq. (20) with the optimization strategy Eq. (21), is presented in Appendix B.

### 3.5. Pseudocode and implementation

We summarize the parameters of DoB CLEAN in Algorithm 1. First, we computed the dirty image,  $I^{\text{D}}$ , and the dirty beam,  $B^{\text{D}}$ , as usual for CLEAN. We then fit the scale widths  $\{\tilde{\sigma}_i\}$  to the  $uv$ -coverage as described in Sect. 3.3. Out of these scale-widths,  $\{\tilde{\sigma}_i\}$ , we constructed the DoB wavelet dictionary,  $\Psi_{\text{clean}}^{\text{DoB}}$ , via the difference method from modified Bessel functions. We find the widths of the corresponding DoG wavelet dictionary by fitting the central peak of the modified Bessel functions with Gaussian functions. We define the DoG wavelet dictionary,  $\Psi_{\text{clean}}^{\text{DoG}}$ , via the difference method again from these Gaussians.

From Sect. 3.4, we recall that for the weights of the different scales and for the selection of the correct scales, the convolution of our wavelet functions with the dirty beam plays a vital role, as seen in Eq. (21). We therefore absorbed the dirty beams in the definition of the dictionaries to reduce computational cost, namely, we computed a “dirty” DoB wavelet dictionary:  $\Psi_{\text{dirty}}^{\text{DoB}} = D * \Psi_{\text{clean}}^{\text{DoB}}$ .

Now, before the cleaning process starts, we can precompute the data products required for the cleaning iterations later on. We decomposed the dirty image by  $\Psi_{\text{dirty}}^{\text{DoB}}$  for the multiscale search of the maximal peak in the residual during the minor loop. We have to use the “dirty” dictionary here according to our scale-selection criterion Eq. (21). Moreover, we have to decompose

**Algorithm 1:** Wavelet CLEAN algorithm.

**Require:** Dirty Image:  $I^D$   
**Require:** Dirty Beam:  $B^D$   
**Require:** gain:  $g$   
**Require:** scale-widths for Wavelet-decomposition (DoB):  $\{\tilde{\sigma}_j\}$   
 fitted to  $uv$ -coverage

Define “clean” DWT by difference of Bessel functions with scales  $\tilde{\sigma}_j$ :  $\Psi_{\text{clean}}^{\text{DoB}}$ .

Fit Gaussian functions to the central peaks of the Bessel functions, define a difference of Gaussians (DoG) dictionary by these fits:  $\Psi_{\text{clean}}^{\text{DoG}}$ . We note that this dictionary approximates the Bessel dictionary, but without the sidelobes.

Define “dirty” DWT by DoB with “dirty” scales  $\hat{\sigma}_j$ :  $\Psi_{\text{dirty}}$ , where  $\Psi_{\text{dirty}}^{\text{DoB}} = \Psi_{\text{clean}}^{\text{DoB}} * B^D$

Decompose dirty image by  $\Psi_{\text{dirty}}^{\text{DoB}}$ :  $I^D = \sum I_j^D$ ,

Decompose dirty beam by  $\Psi_{\text{clean}}^{\text{DoB}}$ :  $B^D = \sum B_j^D$ ,

Decompose the scales of the dirty beam by  $\Psi_{\text{dirty}}^{\text{DoB}}$ :  $B_j^D = \sum B_{ij}^D$ .

Find normalization constants:  $n_j = \max(B_j^D)$ ,

Normalize beam and psf by  $n_j$ :  $B_{ij}^D = B_{ij}^D/n_j \dots$  for all  $i$  and  $j$ .

Find weights:  $w_j = \frac{1}{\|\Psi_{\text{dirty}}^{\text{DoB}}\| \|\Psi_{\text{clean}}^{\text{DoB}}\|}$  (these weights were proven to be optimal).

Initialize restoring image:  $M = 0$ ,

**while** residual not noise-like **do**,

**while** number of maximal iterations not reached **do**,

        Find Maximum of  $[w_j \cdot \text{abs}(I_j)]$  searching over scales  $j$  and pixels  $k$ ,

        Store maximum  $I_j^k \cdot \delta_j^k$  in list of components,

        For every scale  $l$ :  $I_l = I_l - g \cdot I_j^k \cdot \text{shift}(B_{lj}^D, k)$ ,

$M = M + \sum g \cdot I_j^k \cdot \Psi_{\text{clean}}^{\text{DoG}} \delta_j^k$ ,

    Update dirty image/residual:  $I^D = I^D - B^D * M$ ,

    Reinitialize the decomposition:  $\Psi_{\text{dirty}}^{\text{DoB}}$ :  $I^D = \sum I_j^D$ ,

    optional: self-calibration,

    optional: project solution to positive values.

Add residual image:  $M = M + \sum I_j^D$ ,

**Ensure:**  $M$  is approximation to true sky image.

the dirty beam by our set of basis function that will represent the image in the first instance, that is, by  $\Psi_{\text{clean}}^{\text{DoB}}$ . These scales of the dirty beam  $B_j^D$  are then subtracted from the residual during the minor loop of the CLEAN iterations. It is further beneficial to compute the subtraction from the image-scales,  $I_j$ , scale-by-scale independently, instead of subtracting the complete beam  $B_j^D$  from the residual and recomputing the image-scale decomposition newly every iteration. Hence, we precomputed the scalar decomposition of the beam-scales,  $B_j^D$ , by the “dirty” dictionary,  $\Psi_{\text{dirty}}^{\text{DoB}}$ , as well. Moreover, we normalize these beams by their maximal peak. We note that these data products ( $B_{ij}^D$ ) have to be computed only once before the CLEAN loops start until the

dirty beam is changed (due to a new weighting scheme, flagging of data, and other operations). Later on, only convolutions of these wavelets with delta-components have to be computed. Hence, we can compute the subtractions of the multiscale beams very efficiently by shifting and rescaling the precomputed beam scales  $D_{i,j}$ . Finally, we precomputed the multiscale weights,  $w_j$ , explained in Sect. 3.4 – more specifically, the denominator in Eq. (21).

As outlined previously, we carried out the CLEANing procedure by iterating between a CLEAN loop (with DoB wavelets as basis functions, i.e., the inner loop) and switching between dictionaries (from DoB dictionary to DoG dictionary, i.e., the outer loop). In the inner loop, we iteratively search for the largest peak among the image scales and we store the position, the scale, and intensity in a list of delta components. We then update the residual scale-by-scale by subtracting the recently found component. After a sufficient number of iterations, we compute a model  $M$  by summing our stored delta components, but applying the dictionary,  $\Psi_{\text{clean}}^{\text{DoG}}$ , instead of the dictionary,  $\Psi_{\text{clean}}^{\text{DoB}}$  (outer loop). After this switch of dictionaries, we have to reinitialize the residual and the residual scales for the next DoB-CLEAN runs. At this step, further data manipulation steps, such as flagging, self-calibration, thresholding the image, or projecting to positive fluxes, could also be applied as required, depending on the data set under consideration. We also refer to Fig. 5, where we demonstrate the working procedure of DoB-CLEAN on one of the synthetic data sets that are used in Sect. 4. The dirty beam is successfully cleaned out of the image by the representation by DoB wavelets (small residual). However, the wavelets itself contain sidelobes and, hence, the DoB model has these sidelobes as well. By switching to DoG wavelets, we get a physical and smooth model that still fits the visibilities.

### 3.6. Comparison to CLEAN and MS-CLEAN

DoB-CLEAN succeeds over CLEAN by using a multi-resolution approach to imaging. This allows for a better separation between image features and sidelobes. Hence, DoB-CLEAN provides more reasonable regularization. Thus, we repeat the regularization analysis presented in Eqs. (4)–(5). We assume that the true model is expressed as:

$$I = \sum_l a_l \Psi_l^{\text{DoB}}. \quad (22)$$

We note that although the wavelet functions  $\Psi_l^{\text{DoB}}$  contain clearly unphysical sidelobe structures, this is not a stronger assumption than the point source assumption that we did for the analysis of CLEAN, namely, Eq. (2), due to the completeness of the wavelet dictionary, as in Eq. (9). The dirty image is then:

$$I^D = \sum_l a_l \Psi_l^{\text{DoB}} * B^D \approx \sum_i a_i \Psi_i^{\text{DoB}} * B^D, \quad (23)$$

where the indices,  $i$ , are a typically sparse subset of the space of indices,  $l$ . This harvests one of the main advantages of DoB-CLEAN over CLEAN. While the sparsity assumption that is hard-coded in CLEAN is somewhat dubious, in particular if extended structures are studied, DoB-CLEAN tries to sparsely represent the dirty image with a dictionary especially designed for this purpose. The wavelet functions that correspond to scales in the Fourier domain that are not covered can be omitted in the sum above (the convolution with the dirty beam vanishes)

and the sparsity assumption is really fulfilled. The dirty image is modeled by:

$$M^D = \sum_i \hat{a}_i \Psi_i^{\text{DoB}}, \quad (24)$$

where  $\hat{a}_i$  denotes the estimated approximations to the true coefficients,  $a_i$ , calculated by DoB-CLEAN. The cleaned image model reads:

$$M = \sum_i \hat{a}_i \Psi_i^{\text{DoG}}. \quad (25)$$

Hence, the residual is:

$$R = I^D - B^D * M \approx B^D * \sum_i [a_i \Psi_i^{\text{DoB}} - \hat{a}_i \Psi_i^{\text{DoG}}]. \quad (26)$$

Thus:

$$I^M = M + R = B^D * \sum_i a_i \Psi_i^{\text{DoB}} + (\mathbb{1} - B^D) * \sum_i \hat{a}_i \Psi_i^{\text{DoG}}. \quad (27)$$

Again we recover the correct data fit for the covered scales. In the second term we process information from covered scales only (indices  $i$ ). We therefore extrapolate the data fit to the gaps in the  $uv$ -coverage by the same core-information as the signal from the covered scales (the DoG-wavelets fit the central peak of the DoB-wavelets), but we suppress the sidelobes. This can be translated to the Fourier domain in that we copy the same information that we recovered from covered scales in the uncovered scales as well, but the importance decreases with distance from the covered Fourier coefficients. We, therefore, in contrast to CLEAN, recover the final model from the measured visibility points only and suppress the information in the gaps to a level, such that the final recovered model appears smooth and free of sidelobes, but no image features are hidden in the gaps. This seems to be an optimal criterion for us given the sparsity of the measured visibilities. We will expand more on how CLEAN and DoB-CLEAN fit the gaps in the  $uv$ -coverage in Sect. 4.4.

The replacing of DoB wavelets by DoG wavelets is similar to a multiscale variant of replacing the dirty beam by the clean beam as done for CLEAN. However, there are subtle differences. For DoB-CLEAN, the convolution is not done as a final step, but takes place within the minor loop, such that the new residuals are computed after convolution with  $\Psi_i^{\text{DoG}}$ . Moreover, in comparing with Algorithm 1, we replace, in the minor loop, the “dirty” scales,  $\Psi_{\text{dirty}}^{\text{DoB}} = \Psi_{\text{dirty}}^{\text{DoB}} * B^D$ , with the “clean” scales,  $\Psi_{\text{clean}}^{\text{DoG}}$ . Since the basis functions are already extended and fit to the  $uv$ -coverage (i.e., the limiting resolution) a final additional convolution with a clean beam is not needed. This convolution is unphysical as it introduces a disparity between the model fitted to the visibilities and the final image. Our algorithm directly computes a clean (i.e., free of sidelobes) model that fits to the visibilities and that matches our perception of astronomical reality – in other words, it solves this disparity.

We go on to briefly discuss the convergence of DoB-CLEAN at this point. If the model is composed of extended DoG wavelet functions with widths equivalent to the limiting resolution, an additional convolution with the dirty beam to compute the residual could smear out the model image even more and cause divergence. This however is prevented by the scale selection criterion Eq. (21). Since we convolve the dirty image another time with the dirty beam to find the optimal scale, we select smaller scales (already respecting the fact that another convolution for the computation of the residual will smear out features).

DoB-CLEAN is based on the ideas pioneered in multiresolution CLEAN methods (Bhatnagar & Cornwell 2004; Cornwell 2008; Rau & Cornwell 2011). However, our new method has some significant differences. Most obviously, we use different dictionaries than in previous works. MS-CLEAN basis functions are selected on a best effort basis manually (Cornwell 2008). Asp-CLEAN (Bhatnagar & Cornwell 2004) is a variant of MS-CLEAN in which the proper scale widths of the basis functions (Asps) are selected by a fit to the data alternating with the minor loop iterations. Asp-CLEAN therefore shares some more philosophical similarities with DoB-CLEAN than standard MS-CLEAN. However, the basic outline remains the same: basis functions are selected based on the image domain to describe the perceived image structure best, thereby solving practical issues related to CLEAN in representing extended emission. Cornwell (2008) defined three requirements for such basis functions: each basis function should be astrophysically plausible, as well as radially symmetric, and the shape should allow support constraints (although the latter one can be weakened). In contrast, our dictionaries are designed on different requirements: we designed wavelet basis functions,  $\Psi^{\text{DoB}}$ , that fit to the  $uv$ -coverage, namely, those that sparsely represent the dirty image. Hence, in contrast to MS-CLEAN and Asp-CLEAN, our selection of scales is purely driven by the instrument – with no perception of the image structure. This highlights a difference that is strictly specific to Asp-CLEAN: in Asp-CLEAN, the applied scales are meant to optimally fit the observed visibilities in every iteration and this selection strongly affects the minor loop iterations. In DoB-CLEAN, it is only the  $uv$ -coverage, and not the visibilities, that is used to define scales and the selection of which scales fits the visibilities ideally is controlled by the minor loop. Moreover, we use, for the first time, a multidirectional dictionary. These requirements are not compatible. This has a couple of consequences that cause DoB-CLEAN to differ from MS-CLEAN algorithms. MS-CLEAN and Asp-CLEAN use the minor and major loops to suppress sidelobes (compare our discussion in Sect. 2.2) by a sparse representation of the true model. DoB-CLEAN uses the minor and major loop of CLEAN to find a sparse representation of the dirty image (not the true image). This makes the use of a second dictionary,  $\Psi^{\text{DoG}}$ , and a switch between both dictionaries needed. Sidelobes are suppressed by replacing the DoB wavelets (with large sidelobes) by the DoG wavelets (without sidelobes). Also,  $\Psi^{\text{DoB}}$  features some more advantages: it is orthogonal in radial dimension. Hence, in the DoB-CLEAN scalar features that, for example, only affect intermediate baselines, but not long or small baselines, can be expressed sparsely, while in MS-CLEAN and Asp-CLEAN, every basis function necessarily affects the shortest baselines. In particular, there is only one scale,  $c_J$ , that transports flux in the image (compare Eqs. (8) and (9)), all other scales have an integral of zero. The orthogonality offers the additional advantage that a solid scale-selection criterion could be derived (see Sect. 3.4), in contrast to Cornwell (2008), where the selection of the correct scale is done in an ad hoc manner by manually choosing a specific scale-bias. We, however, select for the first time the scale that provides the largest correlation to the dirty image. Moreover, the basis function dictionary is complete. Hence, opposite to Asp-CLEAN and MS-CLEAN, there is no doubling of information compressed at different scales.

All in all, compared to CLEAN and MS-CLEAN, DoB-CLEAN succeeds in two important aspects. First, the regularization property (i.e., how to fill the gaps in  $uv$ -coverage) is more reasonable. Second, in CLEAN (Högbom 1974) and in MS-CLEAN (Cornwell 2008), the final model is blurred

with the clean beam, which causes an unphysical separation between model and image as described in the introduction. In DoB-CLEAN however, the basis functions are already extended functions that represent the image features well and are used to fit to the visibilities. Thus, a final convolution with the clean beam is (theoretically) not needed in making the computed image the same as the computed model.

### 3.7. Software and pipeline

The method has been implemented in the new software package MrBeam, which makes explicit use of ehtim (Chael et al. 2018) and regpy (Regpy 2019). We designed the user interface to resemble standard VLBI software packages such as Difmap (Shepherd 1997). This has several practical benefits: it resembles a method of working that is common and familiar to scientists. Hence, MrBeam allows for the typical tools of interactive manipulation, visualization and inspection of data known from CLEAN softwares: interactive drawing of CLEAN windows (search masks for peaks in the residual), the option for various weighting schemes, taperings and flagging of data, a hybrid self-calibration routine, and so on. This proved practical in the past to address data corruption and calibration issues. However, the practical use of interactive tools remains restricted to small arrays in MrBeam as the multiscale image decompositions have to be recomputed every time the weights or gains have been updated.

In principle, DoB-CLEAN needs two stopping rules to be specified. Firstly, we have to specify after how many iterations we want to stop the overall CLEANing procedure (stopping rule 1 in Algorithm 1). Secondly, we have to determine for how many iterations do we want to represent the image with DoB wavelets before we perform the change to the DoG wavelets (stopping rule 2 in Algorithm 1). The former stopping-rule is defined by the noise level of the observation and the current residual. We do not provide a quantitative stopping criterion here but stopped the iterations whenever the residual image looked Gaussian-like and the residuals were not reduced significantly with further iterations. For the latter stopping rule, changing the dictionaries every iteration proved to be the most practical solution, that is, we updated the model image every iteration.

The fitting of the observed visibilities by extended, specially-designed basis functions proved to be helpful in introducing regularization. However, to account for every un-fitted source of flux in the final image, it could be beneficial to clean the already-cleaned residual with several Högbom CLEAN iterations on the complete field to improve the fit to observed visibilities. We provide such an option in the software package *imagingbase* underlying this work. However, this finalization step was not found to amend the final model on a level that is visible by eye.

Lastly, we would like to comment on the use of CLEAN windows. In standard Högbom CLEAN, windows are essential in the early iterations of the CLEANing and self-calibration to separate the essential true sky brightness distribution from sidelobes. After several iterations the residual is smaller, the sidelobes are suppressed and the underlying image structure becomes visible. The windows can be drawn larger. However, for DoB-CLEAN drawing sophisticated windows did not prove to be essential at all. The sidelobe structure of the beam is imprinted in the basis functions of the DoB wavelet dictionary and the role of the convolution with the dirty beam is in particular represented, for the first time, in our scale-selection criterion. The maximal correlation is achieved when the multiscale component is centered in the sidelobe structure and components are not falsely set in the

sidelobes, but rather where the true sky brightness distribution is located. Hence, for our tests on synthetic data in Sect. 4, we imaged with DoB-CLEAN on the complete field of view without setting any window.

### 3.8. Post-processing

The multiscale and multidirectional decomposition offers rich possibilities for post-processing. The multiscale dictionary  $\Psi$  provides control over the fit of the model in the gaps within the  $uw$ -coverage. This is a great advantage of DoB-CLEAN. In particular, we can identify the image features that are present in the observation and those that are not covered. The signal from the latter is suppressed. In this sense, we end up constructing a mostly sidelobe-free representation of the robustly-measured image information. However, we can use this information as well to reintroduce missing scales in the observation to the image. This step should be done with relative caution as we are adding extrapolated signals.

We implemented and tested the most natural approach to reintroduce missing information in the image, namely, by interpolating between neighboring scales. For that we first have to identify which scales are labeled as uncovered (i.e., which scales do we have to add to the image in post-processing). We can use the scale-selection criterion here again: we define a threshold  $t$  (usually we use  $t = 0.1$ ), compute the initial dirty beam with uniform weighting, and label scales as missing if:

$$\frac{\|\Psi_l^{\text{DoB}} * B^{\text{D}}\|}{\|\Psi_l^{\text{DoB}}\|} < t. \quad (28)$$

For each of these missing scales, we search for the next smaller scale in the same direction (for elliptical scales) and the next larger scale in the same direction and interpolate the coefficient array for the missing scale between these two. We evaluated the performance of post-processing by missing scales in Sect. 4.4. In a nutshell, adding missing (not measured) scales to the image proved useful to suppress artifacts that are introduced by gaps in the  $uw$ -coverage. However, this option should be used only with relative caution as signal is predicted for Fourier coefficients that are not constrained by observations, that is, false image features could be added to the reconstruction when the adding of the missing scales is overdone. While it is a natural choice to interpolate the missing scale from adjacent scales, this does not always have to be the best option. This is in particular true when the structures at various scales have only a small correlation as common for example in VLBI studies of jets powered by an active galactic nuclei (AGN). The bright small-scale features (VLBI-core, innermost jet) and the large scale features (extended jet emission) can vary in morphology, localization and orientation (e.g., compare the multifrequency studies in Kim et al. 2020, with highly varying morphologies between scales). Recent progress in multifrequency observations, and the ongoing combination of short baseline and long baseline arrays (and, consequently, the desire to map galactic structures on a range of spatial scales) may further highlight the issue raised above.

### 3.9. Numerical challenges

In this subsection, we present some numerical issues and challenges for DoB-CLEAN and possible strategies to resolve them.

As the DoB wavelets are designed to define steep, orthogonal masks in the  $uw$ -domain, we have to deal with the Gibbs-phenomenon at the edges of these masks. We found that the field

of view should be large enough, such that roughly ten sidelobes of the spherical Bessel functions still fit in it to avoid numerical issues by the Gibbs phenomenon. Additionally, it proved beneficial to fight the rapid accumulation of numerical errors by reinitializing the decomposition of the dirty image from time to time.

Low-level negative fluxes are introduced into the images by the basis functions itself and have to be negated by neighboring scales (see the completeness relation Eq. (9)). However, this also reveals the great advantage of DoB-CLEAN over CLEAN. Due to the completeness relation Eq. (9) and the explicit allowance of negative wavelet coefficients, every structure in the current model could, in principle, be deleted again or completely altered and partly negated by other scales in later iterations. This is more difficult in CLEAN, where falsely set components (e.g., due to corrupted data, calibration issues, or falsely-identified windows) are typically removed from the model by flagging them manually. Hence, DoB-CLEAN interacts well with extended starting models similar to the working procedure standard in RML methods (iterative imaging with a new starting model and blurring). We therefore have a new RML-inspired ad hoc method to avoid negative fluxes in the final image: alternating with imaging we threshold (and blur) the image to the significant flux and reinitialize the residual and the DoB-CLEAN parameters with the thresholded model as a starting model.

After some iterations we project the recovered model to the significant fluxes – that is: we threshold the model by a small fraction, typically one percent of the peak flux, and, in particular, projecting all negative fluxes to zero; then we blur the image by the nominal resolution. We take this image as a proper starting model for the next imaging rounds. We recompute the residual and the corresponding decomposition and proceed with the CLEANing with the thresholded model as a starting model. This strategy is well motivated, every high dynamic range image structure that might be falsely deleted from the model, is reintroduced in the newly computed residual and will be reintroduced to the model in the subsequent CLEANing loops. In particular, a worse resolution after blurring will be corrected later by readding small-scale DoG wavelets that shift power from larger scales to smaller scales. As a weaker version of this strategy, we also can project only the negative fluxes to zero flux (i.e., use a zero-percentage threshold) and recompute the residuals that had proved to be sufficient in some cases. This blurring strategy is not a necessary requirement for DoB-CLEAN, but it does serve as an alternative way to guide the imaging, similar to how it is done with tapers in CLEAN; however, here, it is translated into the image domain due to the simple possibility to read any missing small-scale structure at a later point in the iterations.

## 4. Tests on synthetic data

### 4.1. Synthetic data

In the following, we explain how we checked our imaging algorithm on several test images. For these purpose, we chose a range of test images presenting various source structures and  $uv$ -coverages: we study a synthetic image with a Gaussian core and faint ellipse observed with EVN coverage (Gaussian-evn), a double-sided core dominated synthetic source with a synthetic ring-like  $uv$ -coverage (dumbbell-ring), and a synthetic observation of BL Lac with RadioAstron (blac-space).

The Gaussian-evn model consists of a small Gaussian with width of 5 mas (0.5 Jy) and a (faint) elliptical blob with semi-axes of 50 mas and 20 mas directed to the south (0.5 Jy).

The elliptical source is shifted by 100 mas to the south. The Gaussian-evn model is chosen to artificially approximate typical core-jet structures. The model is plotted in the first panel of Fig. 4. We synthetically observe the model with a past EVN configuration from Lobanov et al. (2011) and observed the synthetic source by the software ehtim (Chael et al. 2018) with the observe\_same option. The  $uv$ -coverage of this observation is plotted in panel five of Fig. 4.

The dumbbell-ring model consists of an ellipse with 50 mas times 500 mas semi-axes (1 Jy) centered at the middle, a Gaussian with width 2 mas (0.3 Jy), and a second negative Gaussian with with 5 mas (−0.3 Jy). The Gaussians and ellipse were chosen in a way that no negative flux appears in the model. The source model is presented in panel 1 of row 2 of Fig. 4. We observed the source for testing purposes with a synthetic instrument with ring-like  $uv$ -coverage; for this reason, we placed artificial antennas equally spaced from the south pole, observed the synthetic source, and flagged out all baselines that did not involve the central station. From this uniform  $uv$ -distribution we then introduced two significant radial gaps by flagging. The corresponding  $uv$ -coverage is presented in Fig. 4 (panel 5 of row 2).

Finally, we took RadioAstron observations of BL Lac as a more physical source model. We took the natural weighted image from Gómez et al. (2016) as the true source structure (see panel 1, row 3 in Fig. 4) and observed it, again with the observe\_same option, with the array of that observation. The corresponding (time-averaged)  $uv$ -coverage is plotted in Fig. 4 (panel 5 row 3). All the observations had thermal noise added, but without adding phase or amplitude calibration errors.

### 4.2. Qualitative comparison

Figure 4 presents the reconstructions of our three synthetic sources with DoB-CLEAN (second column) and with CLEAN (third column: final CLEAN image, fourth column: CLEAN model). For the blac-space model, a set of rectangular windows that constrain the flux to the lower half of the image was used. For the Gaussian-evn and the dumbbell-ring reconstructions, no particular window was used. Figure 5 presents an outline for the imaging procedure done for the dumbbell-ring example. We remove the dirty beam successfully during the minor loop, but represent the image by a multiscale set of DoB wavelets that contain sidelobes on its own. By replacing the DoB wavelets by DoG wavelets, we get a physically meaningful result, from which we recompute a significantly reduced residual.

We show additionally in Fig. 6, a comparison of the DoB-CLEAN reconstruction with MS-CLEAN reconstructions. For the MS-CLEAN reconstructions we used in all three examples a dictionary consisting of a delta component and Gaussians with one, two, and three times the width of the clean beam.

The DoB-CLEAN reconstructions were very successful overall. The core-jet-like structures were well represented, even if the array configuration was extremely sparse. The representation of the wider, extended emission, in particular in the Gaussian-evn example is excellent, opposed to CLEAN. As expected a similar effect is achieved by MS-CLEAN reconstructions opposed to Högbom CLEAN (compare the upper panels in Figs. 4 and 6). The reconstructions of the wide-field Gaussian-evn structure in Fig. 6 is of similar quality between DoB-CLEAN and MS-CLEAN. Moreover, the DoB-CLEAN reconstruction allows for the reconstruction of small scales simultaneously, as demonstrated with the two-component core in the blac-space image (indicating a good use of space-baselines).

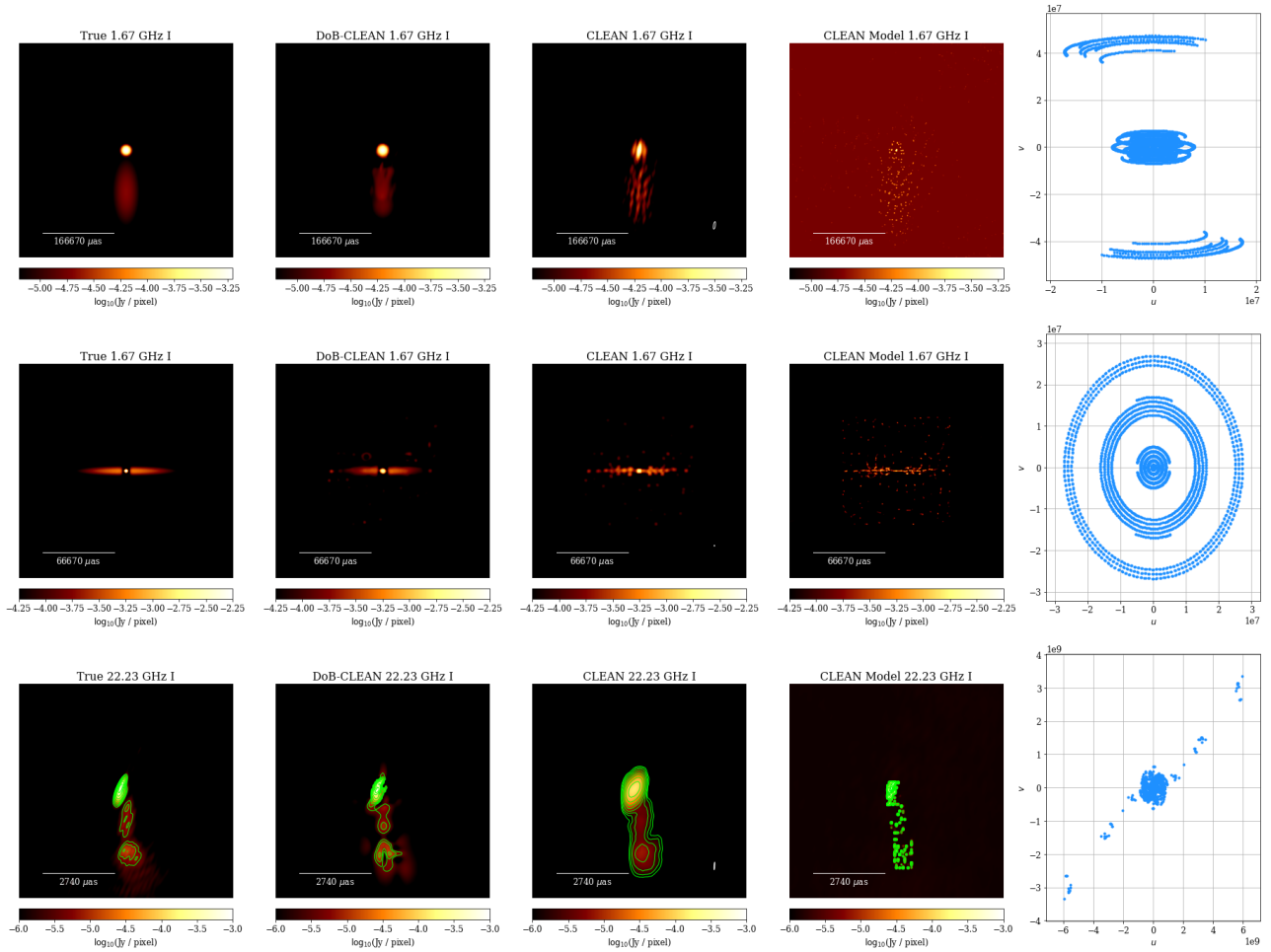


**Fig. 4.** Comparison of reconstructions of synthetic data. First row: Gaussian-evn; second row: dumbbell-ring; third row: bllac-space, with various algorithms. First column: true image, second column: DoB-CLEAN reconstruction. Third column: CLEAN image. Fourth column: CLEAN model. Fifth column:  $uv$ -coverage of the synthetic observations. Contour levels for the bllac-space example are [0.5%, 1%, 2%, 4%, 8%, 16%, 32%, 64%] of the peak flux.

When comparing to CLEAN (third column), it becomes obvious that DoB-CLEAN achieves super-resolution. It reliably recovers structures smaller than the clean beam, particularly in the bllac-space example, even if these structures are faint compared to the central core region (fainter by a factor  $\approx 100$ – $1000$  for bllac-space). This super-resolving feature, however, does not come at the price of reduced sensitivity to extended emission as discussed above. MS-CLEAN reconstructions are bound to the clean beam resolution as well, thus ending up outperformed by DoB-CLEAN in terms of resolution as well.

We present in the fourth column of Fig. 4 the single CLEAN model, that is, the composition of delta components. We recall that we identified the mismatch between the final image and the CLEAN model that fits the data as a main theoretical disadvantage of CLEAN. The same applies for MS-CLEAN. In fact, the model maps are no useful description of the source structure in either way. DoB-CLEAN directly computes a model with physical meaning. The reconstructions shown here match the model fitted to the visibilities. Hence, the cleaning with DoB-CLEAN leaves a similar final residual (dominated by thermal noise) as the standard Högbom CLEAN, but with a much more useful

source model. In this sense, DoB-CLEAN produces more robust source structures.

While CLEAN and MS-CLEAN reconstructions are overall quite successful as well, we identify several qualitative metrics in which DoB-CLEAN clearly outperforms CLEAN and MS-CLEAN. All in all, we conclude from here that DoB-CLEAN seems to be an improvement over CLEAN in terms of resolution (achieving super-resolution), robustness (model matches to final image), and sensitivity to extended emission. The latter advantage becomes obvious, particularly for the Gaussian-evn data set in which the CLEAN beam is much smaller than the extended elliptical source structure, leading to a fractured reconstruction opposed to the smooth extended emission recovered by DoB-CLEAN.

### 4.3. Performance tests

We go on to use the Gaussian-evn example for a set of additional tests to study the features and performance of DoB-CLEAN further.

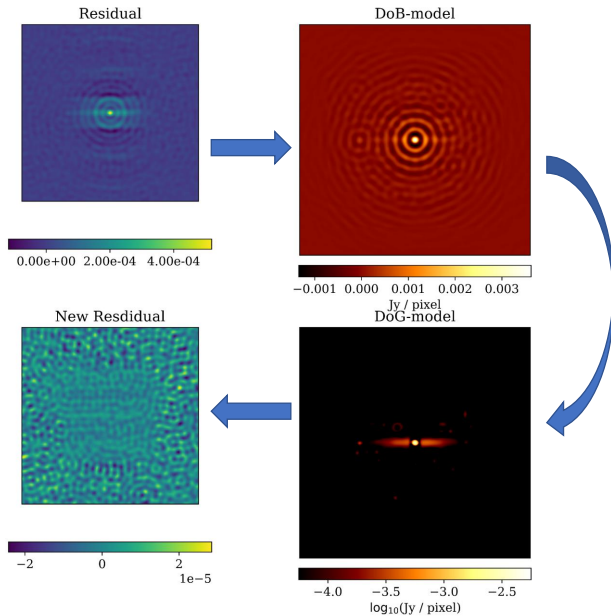


**Fig. 5.** Sketch of the imaging iterations for the dumbbell-ring example. Upper left: initial residual. Upper right: we remove the dirty beam by computing a multiscale model composed of DoB wavelets. The panel presents the recovered model  $\sum g \cdot I_j^k \cdot \Psi_{\text{clean}}^{\text{DoB}} \delta_j^k$  (notation from Algorithm 1). Bottom right: we replace the DoB wavelets by DoG wavelets:  $\sum g \cdot I_j^k \cdot \Psi_{\text{clean}}^{\text{DoB}} \delta_j^k$  getting a physically reasonable model that still fits the data. Bottom left: final updated residual computed from the DoG-model. Iterations continue if needed.

To discuss the advantage of super-resolution further, we redid the Gaussian-*evn* observation and reconstruction, but with a source structure scaled down by a factor of four in size to highlight the signal on longer baselines more. We present our reconstructions in Fig. 7. The extended, elliptical emission is still very well recovered by DoB-CLEAN. The small Gaussian core is overestimated in size due to the large beam size and a smaller central core component becomes visible as a signal from the long baselines. However, the CLEAN reconstruction again has bigger issues with the beam size and the (elliptical) beam shape. This example demonstrates the potential for super-resolving structures at the size of the clean beam with DoB-CLEAN.

With this excellent performance at hand for small source structures that require super-resolution, we advance on this statement by studying the Gaussian-*evn* source example with synthetic RadioAstron observations (as space-VLBI observations are typically designed to study sources at the highest resolution). VLBI observations with space antennas, however, pose a new range of challenges: the special *uv*-coverage leading to highly elliptical beams, a bad signal-to-noise ratio on the long space baselines, and the complex calibration of the space baselines. In this study we ignored calibration issues, but we considered highly scale-dependent noise by mirroring a real observation (Gómez et al. 2016). We took the Gaussian-*evn* source, scaled it down in size from a field of view of  $1''$  to a field of view of  $16 \text{ mas}$  (e.g., by a factor of  $\approx 16$ ) and synthetically observed it with RadioAstron. Our reconstructions are shown in Fig. 8. This test run again solidifies the problem that CLEAN reconstructions seem to have for highly elliptical beams. DoB-CLEAN works

better in this regard, recovering a clearly visible core and a disconnected, approximately elliptical, extended emission pattern without many sidelobes. However, compared to the reconstructions that we presented in Fig. 7, the reconstruction is worse due to the sparsity at small scales (long baselines). The circular Gaussian core-component is represented by a dumb-bell structure instead, the elliptical faint emission is recovered by two connected Gaussian blobs. The dumb-bell structure is a consequence of relative sparsity at small scales as it represents the typical structure that a single scale out of the difference of elliptical beams dictionary features. Basically, only the scale oriented in the direction described by the longer-elongating space baselines is selected, all other scales at this radial width are suppressed. All in all, we can conclude that DoB-CLEAN is capable of reconstructing super-resolved images even with such challenging arrays such as RadioAstron, although a higher level of artifacts is visible at higher resolution.

It is difficult to quantify the amount of super-resolution in general. Since the limiting resolution is not limited by a well-defined beam convolution, but, instead, due to the balancing between fitting the visibilities and a multiscale sparsity assumption. The achievable resolution depends both on the specifics of the instrument (i.e., *uv*-coverage and scale-dependent noise-level) and the source structure itself. To get a rough impression of the resolution that is achievable with DoB-CLEAN we apply the following strategy: we observe the Gaussian-*evn* source model with RadioAstron coverage (see Fig. 9) and with EVN coverage (see Fig. 10). Iteratively, we minimize the source size (by keeping the same image array, but minimizing the pixel size, i.e., the field of view). Each time, we carried out a reconstruction with DoB-CLEAN and blur the (minimized) ground truth images on a predefined fine grid of circular Gaussian blurring kernels. We computed the correlation of the blurred synthetic ground truth images and the reconstructions in any case (left panels in Figs. 9 and 10). The correlation curves look reasonable with a clearly identifiable maximal peak. We show the blurring kernel size with the maximal correlation for the smallest source sizes in the right panels. If the source is that small that it becomes unresolved by DoB-CLEAN, the blurring kernel size needs to converge from below roughly towards the limiting resolution: indeed, the maximum correlation is roughly constant within the errorbars indicating an effective resolution for a RadioAstron configuration of  $\sim 20 \mu\text{as}$  (beam:  $\sim 290 \times 31 \mu\text{as}$ ) and an effective resolution for an EVN resolution of  $\sim 2 \text{ mas}$  (beam:  $\sim 18 \times 4 \text{ mas}$ ). Hence, a moderate super-resolution by a factor of 2–3 might be possible. However, while the representation of super-resolved features with wavelets is clearly more reasonable than a representation with delta components, we have to note that the reconstruction problem at a higher resolution is also more challenging and artifacts that are usually hidden under the convolution with the beam can be expected (and are visible, e.g., in Fig. 8).

Finally, we study the effect of thermal noise on the reconstruction. For this purpose we again observed the Gaussian-*evn* example, but this time, we added a constant thermal noise on all baselines at a level such that the final signal-to-noise ratio is approximately one. The reconstructions are presented in Fig. 11. Comparing the reconstruction shown in Fig. 4, the source structures recovered by DoB-CLEAN and CLEAN remain relatively unaffected. Faint, blobby background sidelobes as expected from Gaussian noise are introduced to the CLEAN image. In DoB-CLEAN, the effect is different: a coronal emission around the central component is introduced. This feature, however, is very weak and can only be seen at high dynamic range. This coronal

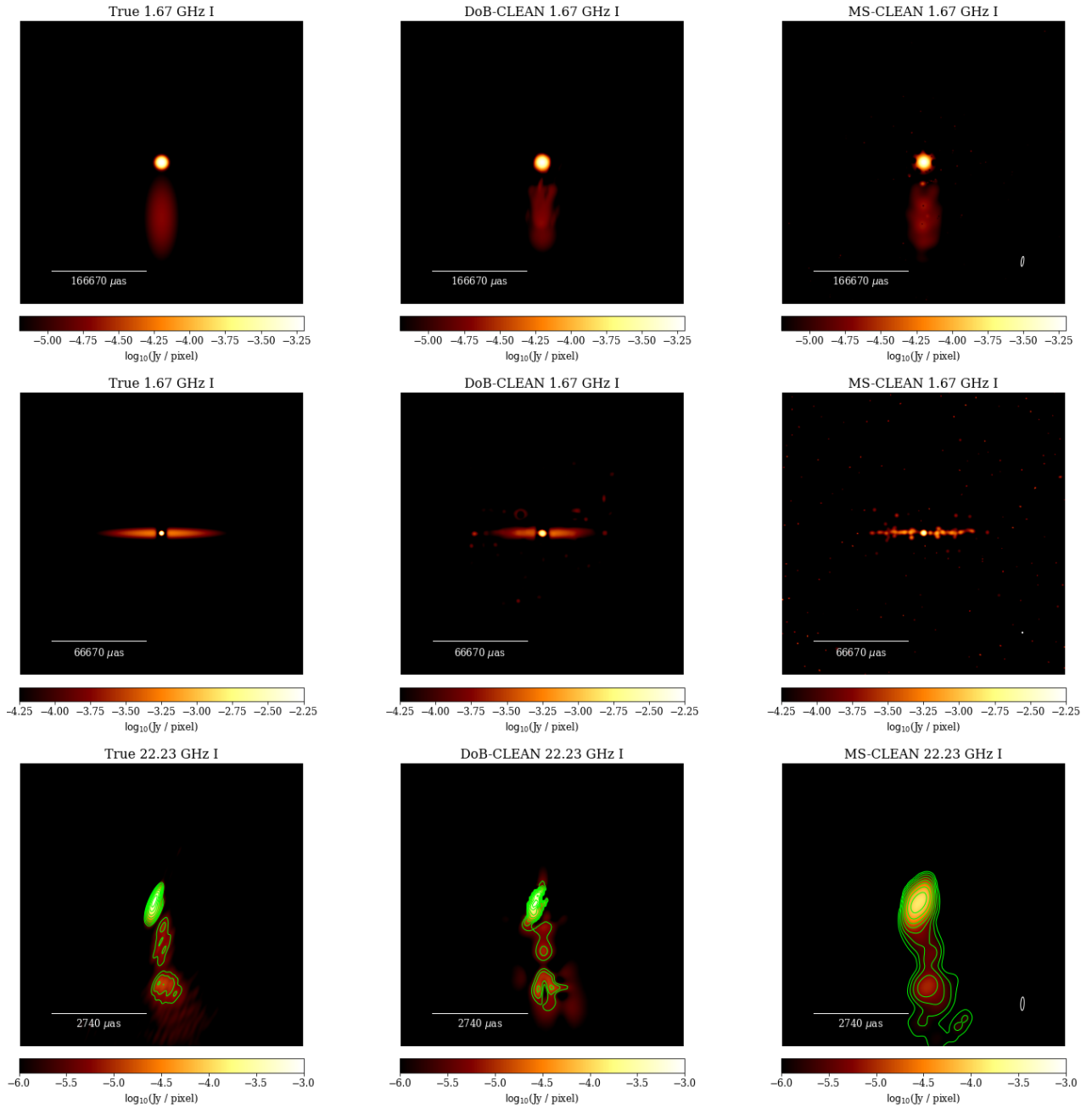


**Fig. 6.** Comparison of reconstructions on synthetic data. First row: Gaussian-evn; second row: dumbbell-ring; third row: bllac-space, with various algorithms. First column: true image; second column: DoB-CLEAN reconstruction; third column: MS-CLEAN image. Contour levels for the bllac-space example are [0.5%, 1%, 2%, 4%, 8%, 16%, 32%, 64%] of the peak flux.

feature has to be noted as an explicit image artifact that DoB-CLEAN introduces in the image when studying noisy images at high dynamic range.

#### 4.4. Artifacts compared to CLEAN

We now compare DoB-CLEAN to CLEAN with the Gaussian-evn example with a reduced source size, as seen in Fig. 7, with special emphasis on the image artifacts introduced by these algorithms. We present the complete Fourier transform of

the true image and the reconstructions (DoB-CLEAN, CLEAN model, and final CLEAN image) in Fig. 12. In the upper row, we show the amplitude of the Fourier transform of the true source model and the  $uv$ -points over-plotted in red. In the lower panels, we show the fit between the measured and observed visibilities. Standard imaging software such as Difmap typically only show the latter ones indicating a successful fit of the observed visibilities for both CLEAN (i.e., the model) and DoB-CLEAN. However, the complete Fourier transform reveals that this might be inadequate. The CLEAN reconstruction shows a

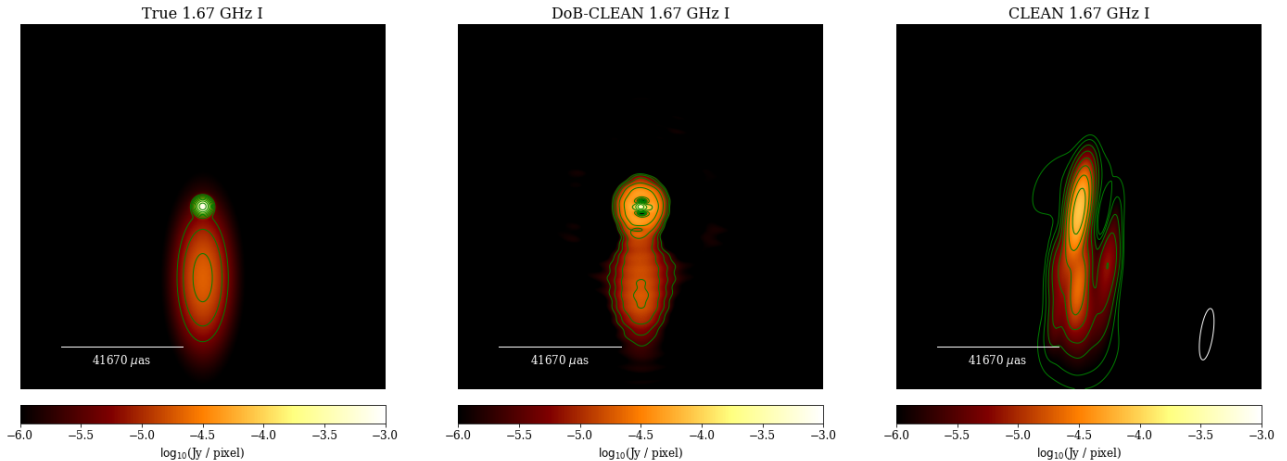


**Fig. 7.** Reconstructions of the Gaussian-evn test case, but with smaller source size. The contour levels are [0.5%, 1%, 2%, 4%, 8%, 16%, 32%, 64%] of the peak flux.

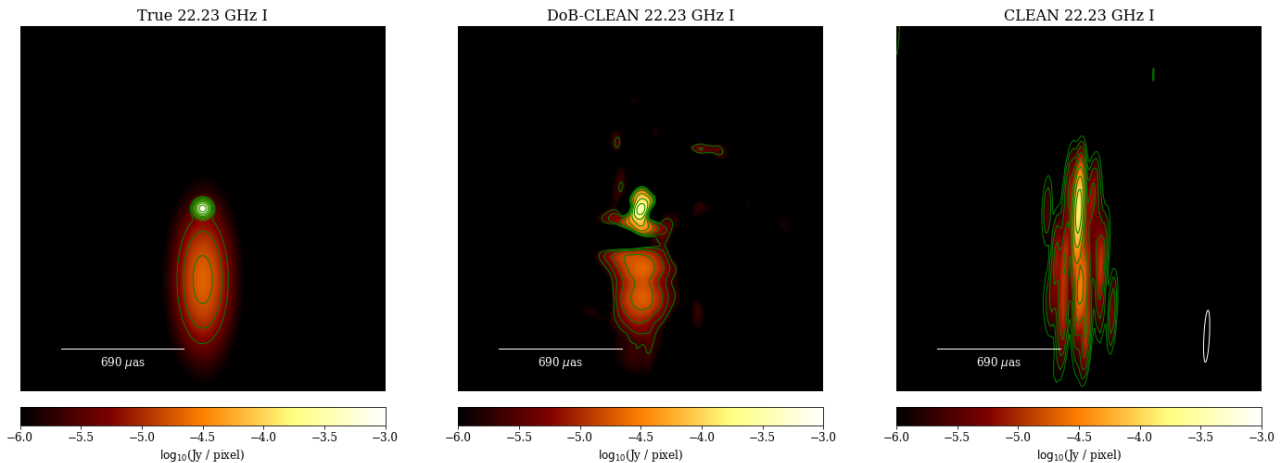


**Fig. 8.** Reconstructions of the Gaussian-evn test case with RadioAstron  $uv$ -coverage. The contour levels are [0.5%, 1%, 2%, 4%, 8%, 16%, 32%, 64%] of the peak flux.

rich, periodic structure in the Fourier domain, in the gap between short and long baselines, but also at baselines longer than the observed ones. These structures in the gaps are not motivated by any measured visibility and, in particular, they are very slightly correlated with the signal measured at long baselines. This particular CLEAN problem is solved by convolving with the clean beam, but at the cost of a worsened fit of the final image to the observed visibilities (compare the bottom panel for the CLEAN image). The DoB-CLEAN reconstruction shows a much better fit to the Fourier coefficients. The signal in the large gap between short and long baselines is suppressed as well as the unphysical signal on Fourier coefficients longer than the longest baselines, but the fit to the observed baselines remains excellent.

Due to this suppression, minimal structural information is added in the gaps and only the robust, measured image information is processed. However, comparing to the true Fourier transform, this also gives rise to some possible problems in the imaging procedure: as the  $uv$ -coverage is sparse and contains a prominent gap with unmeasured Fourier coefficients, there is image information in this gap that is not recovered in the final image with DoB-CLEAN. In particular, this gap introduces the

spurious image structure visible in Fig. 7 in the core component. The core Gaussian is recovered by a small DoG component compressed by the longest baselines in the array and a wider Gaussian component compressed by the shorter baselines. The missing scale (i.e., a missing DoG-scale to satisfy completeness) is visible in the final image by the ring-like feature of weak flux sources around the inner component. While imaging only robust image features with a reduced sidelobe level would appear to be an optimal solution for imaging, these kinds of structures are a clear indicator of missing amplitudes on non-measured baselines. As explained in Sect. 3.8, DoB-CLEAN, as opposed to CLEAN, offers a unique way to identify these problems and to re-add these uncovered scales in the image. We demonstrate the usefulness of this approach in Fig. 13. With an increasing fraction of added missing scales, the interpolated flux in the gap becomes more prominent (upper panels). The artifact in the core component vanishes (bottom panels). When overdoing the interpolation however (i.e., adding too much information on small scales or long baselines), the elliptical extended emission gets erroneously estimated. Hence, when applied to observational data, this interpolation option should be used with

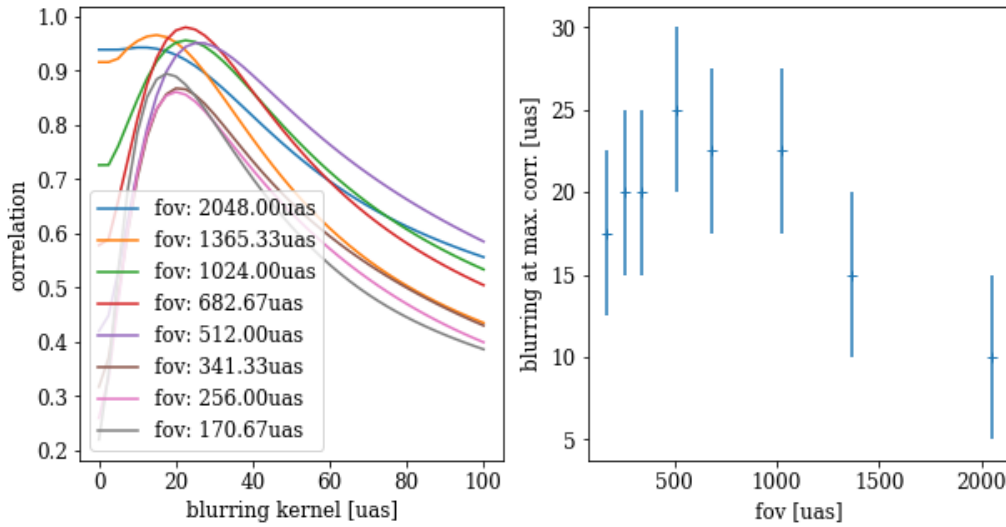


**Fig. 9.** Illustration of the estimation procedure for the effective resolution of DoB-CLEAN. Left panel: correlation between DoB-CLEAN reconstructions for varying source sizes with RadioAstron synthetic observation of the Gaussian-evt ground truth image and the blurred ground truth images. Right panel: blurring at maximal correlation as a function of source size (field of view).

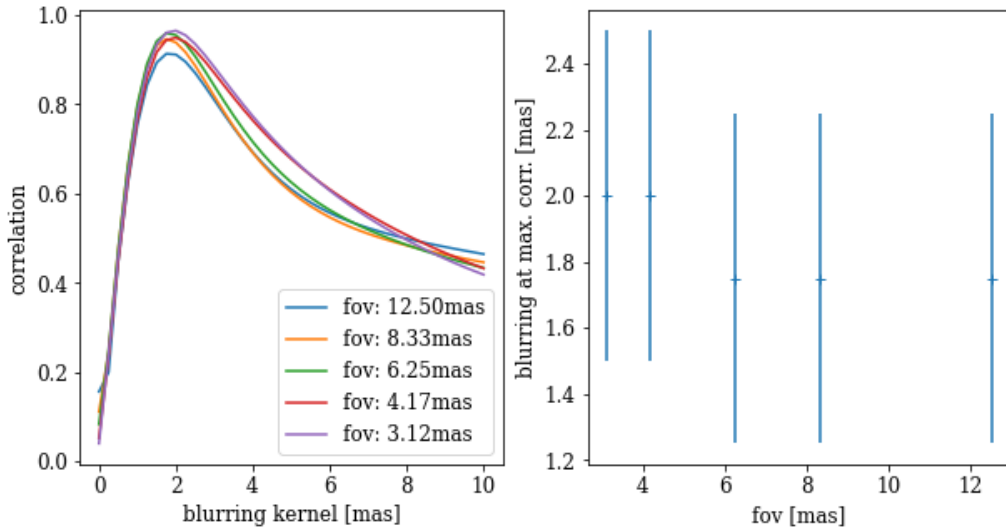


**Fig. 10.** Illustration of the estimation procedure for the effective resolution of DoB-CLEAN as in Fig. 9, but with EVN coverage.

relative caution as we are interpolating structural information in the image that is (in principle) unmeasured.

## 5. BL Lac

### 5.1. Data

We reanalyzed the public data set of BL Lac observations with RadioAstron (Gómez et al. 2016), as described in this section as an additional test with real observational data. In what follows, we summarize these observations and for more detailed information, we refer to Gómez et al. (2016). BL Lac was observed at 22 GHz on November 10 and 11, 2013. Due to some technical problems, BL Lac was only observed by 15 correlated antennas (instead of the 26 possible in the array). The data set was correlated at the DiFX correlator at the Max-Planck-Institut für Radioastronomie (MPIfR). Data reduction and calibration took

place with AIPS and Difmap (Shepherd 1997). We used the self-calibrated data set of Gómez et al. (2016) as a starting point for reconstructions with DoB-CLEAN.

### 5.2. Reconstructions

We present our reconstruction results with DoB-CLEAN in Fig. 14. Moreover, we show our reconstructions blurred with the corresponding clean beam in Fig. 15.

Comparing our imaging results blurred with the clean beam (Fig. 15) to the reconstruction results with CLEAN (Fig. 16), we identify very similar structures, in particular, for natural weighting. We identify the central core with an elliptic shape and the two connected Gaussian blobs to the south. Some of the fine-structure in the CLEAN image is visible in the DoB-CLEAN image as well, such as the shape of the core or the orientation of the components in the jet. However, there are also some

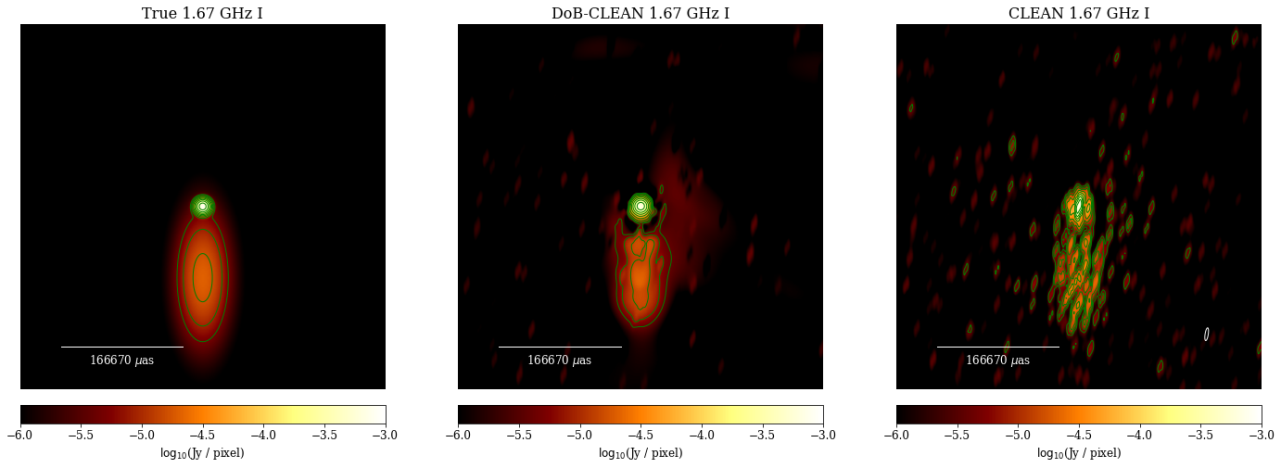


**Fig. 11.** High dynamic range reconstructions of the Gaussian-evn test case, but higher thermal noise level. The contour levels are [0.5%, 1%, 2%, 4%, 8%, 16%, 32%, 64%] of the peak flux.

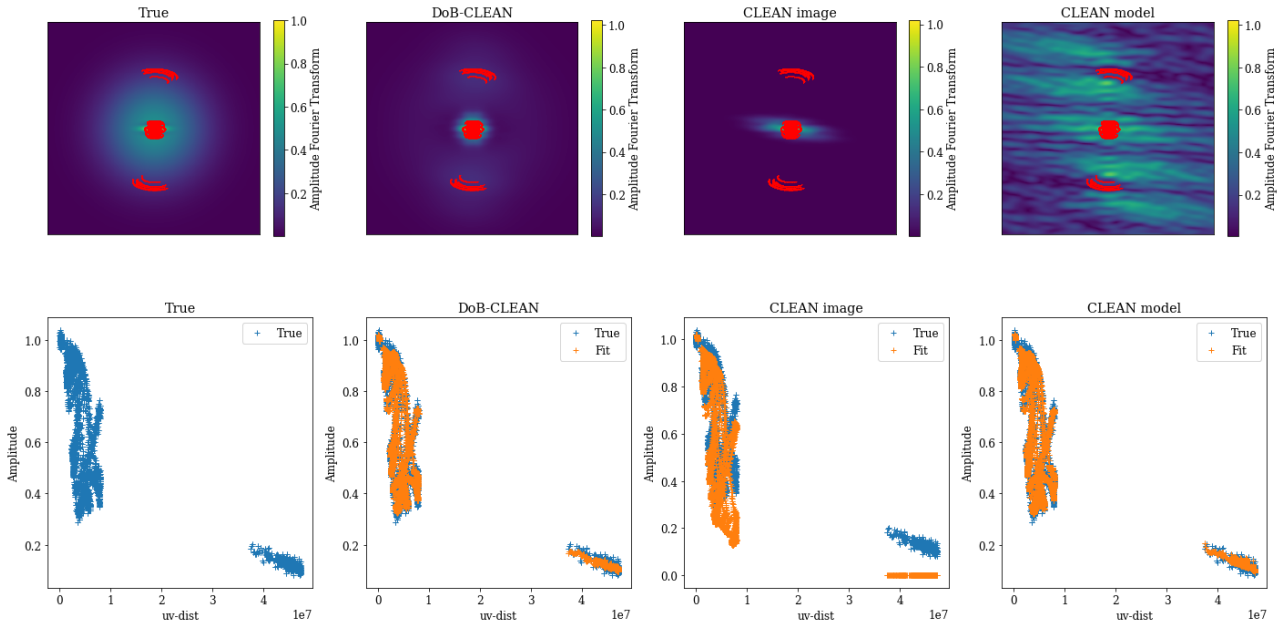
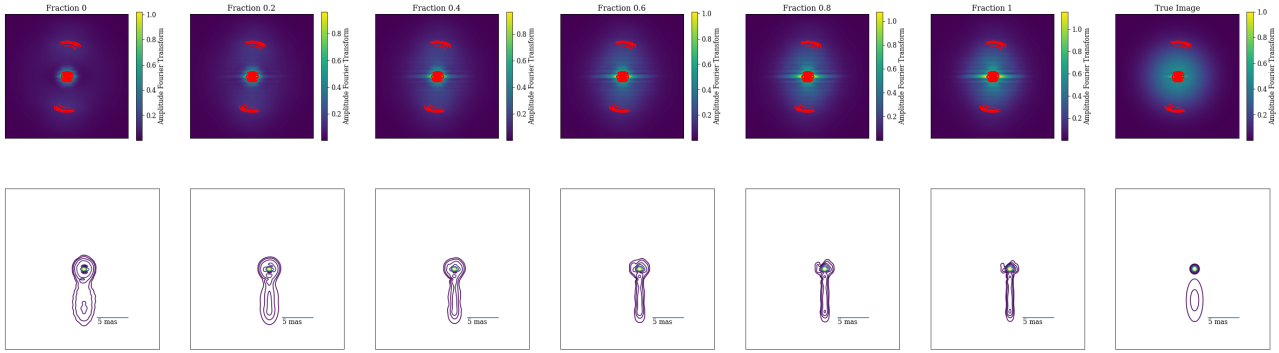


**Fig. 12.** Comparison of the fits of the Gaussian-evn synthetic data reconstruction in the Fourier domain. Upper panels: complete Fourier transform of reconstructions (true, DoB-CLEAN, CLEAN image, and CLEAN model), with  $uv$ -coverage over-plotted (red crosses). Lower panels: Radplot showing the fit of the recovered model to the observed visibilities. It is only for DoB-CLEAN that the fit is successful (lower panels) and the Fourier transform of the model is physically reasonable (upper panels).

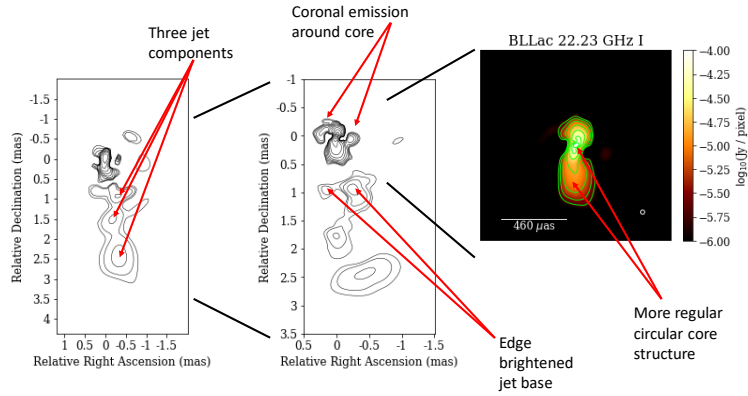
slight differences, such as the faint emission to the north-east that is not related to the jet. This emission could be an artifact of DoB-CLEAN reconstructions, as compared to the typical image artifacts that we discussed in Sect. 4.2, which are caused by the intrinsic sidelobes in the basis functions. In the middle panels, we show the reconstructions with uniform weighting, and in the right panels, a zoom-in on the central core region with uniform weighting. These reconstructions with their more highly resolved structures better highlight the core region. Overall, the similarity between the blurred DoB-CLEAN images (Fig. 15) and the CLEAN images (Fig. 16) is beneficial in uniform weighting, particularly in the zoom-in panels into the core. Interestingly,

CLEAN finds stronger extended emission. Moreover, we find a possible edge-brightened structure in the reconstructions with DoB-CLEAN that is not apparent in the CLEAN images.

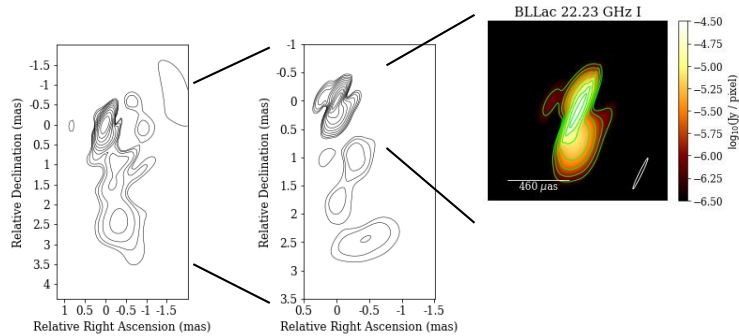
We demonstrated that DoB-CLEAN allows for super-resolution and the actual model computed features a physical model, in contrast to CLEAN. We present in Fig. 14 the DoB-CLEAN reconstructions at full resolution. In fact, Fig. 14 shows more highly resolved structures of a narrow jet. We would like to mention some features that become visible in the full resolution DoB-CLEAN reconstructions, as opposed to the blurred reconstructions.



**Fig. 13.** Fourier transform of recovered data with DoB-CLEAN (upper panels) and the recovered model (lower panels) in the Gaussian-evn test case. From left to right: missing (not measured) scales are interpolated from the covered scales with a higher fraction. The most right panels show the true image. The used contour-levels are [1%, 2%, 4%, 8%, 16%, 32%, 64%] of the peak flux.



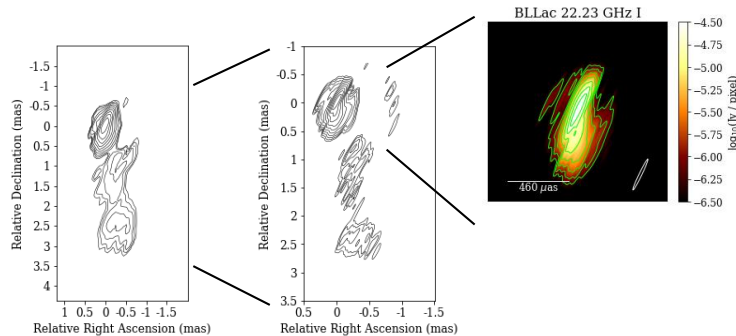
**Fig. 14.** BL Lac reconstructions with DoB-CLEAN at full resolution with natural weighting (left pane), uniform weighting (middle panel) and uniform weighting with smaller pixel size zoomed in the central core region (right panel). The contour levels are: [0.1,0.2,0.4,0.8,1.6,3.2,6.4,12.8,25.6,51.2]% ([0.025, 0.05, 0.1,0.2,0.4,0.8,1.6,3.2,6.4,12.8,25.6,51.2]%, [0.8,1.6,3.2,6.4,12.8,25.6,51.2]%) of the respective peak brightness.



**Fig. 15.** BL Lac reconstructions with DoB-CLEAN blurred with the clean beam with natural weighting (left panel), uniform weighting (middle panel) and uniform weighting with smaller pixel size zoomed in the central core region (right panel). The contour levels are: [0.1,0.2, 0.4,0.8, 1.6,3.2,6.4,12.8,25.6,51.2]% ([0.025, 0.05, 0.1,0.2,0.4,0.8,1.6,3.2,6.4,12.8,25.6,51.2]%, [0.8,1.6,3.2,6.4,12.8,25.6,51.2]%) of the respective peak brightness.

As visible in the natural-weighted image, we can identify three (instead of two) peaks in the jet emission and the central jet component is now resolved. Moreover, we observe a core structure of a very narrow central core component surrounded by a wider coronal emission. This structure cannot be seen with CLEAN or DoB-CLEAN at lower resolution as the feature is blurred out by the clean beam. We note that when comparing the reconstructions of the innermost core region, for instance, in

the right panels in Figs. 16 and 15, also the CLEAN reconstructions show signs of a quasi-coronal emission around the core, namely, emission to the north-west and to the south-east of the central core component. However, in making a comparison to our discussions in Sect. 4, it is also possible that this feature is caused by missing scales in the reconstruction. A further analysis of this feature with alternative super-resolving algorithms, namely, RML algorithms (Chael et al. 2018; Müller & Lobanov

Müller, H., and Lobanov, A. P.: *A&A proofs*, manuscript no. aa44664-22

**Fig. 16.** BL Lac reconstructions with DoB-CLEAN blurred with the clean beam with natural weighting (left panel), uniform weighting (middle panel) and uniform weighting with smaller pixel size zoomed in the central core region (right panel). The contour levels are: [0.1,0.2,0.4,0.8,1.6,3.2,6.4,12.8,25.6,51.2]% ([0.1,0.2,0.4,0.8,1.6,3.2,6.4,12.8,25.6,51.2]%, [0.8,1.6,3.2,6.4,12.8,25.6,51.2]%) of the respective peak brightness.

2022), is fully desired but we leave this aspect for subsequent works.

We observe a sign of possible edge-brightening in the jet base due to a second component towards the left. This was not observed with CLEAN reconstructions. This structural feature is also visible in the blurred DoB-CLEAN reconstructions, as shown in the middle panel of Fig. 15. Furthermore, the core structure in CLEAN and blurred DoB-CLEAN has a double-elliptical shape, as seen by comparing the right panels in Figs. 16 and 15. With the full-resolution DoB-CLEAN reconstructions, we see a more regular, circular reconstruction of the core, with a clearly visible jet basis in the innermost region.

While a concordance between all reconstructions is generally very high, the novel DoB-CLEAN reconstructions demonstrate some possible features that are different from CLEAN reconstructions, especially at the highest angular resolution. Some of them could be connected to imaging artifacts either by DoB-CLEAN or standard Högbom CLEAN. We discuss the robustness of these features in Appendix C in more detail. In a nutshell, both the possible edge-brightening and the coronal emission around the core could be associated with a common sidelobe pattern. The information regarding which emission is real and which emission is thought of to be caused by sidelobes is highly uncertain. This example once more highlights the need for more variety in the choice of reconstruction methods in VLBI. More work is required on the innermost jet in BL Lac with more modern methods based on Bayesian and RML approaches to establish a better concordance between various methods. This aspect will be the subject of subsequent works.

## 6. Conclusion

In this work, we develop the novel multiscale imaging algorithm DoB-CLEAN, which is based on the framework of CLEAN with the goal to still allow the straightforward manual manipulation and calibration of data that has proven successful in the VLBI community over recent decades. However, DoB-CLEAN addresses some pathologies of the CLEAN algorithm: CLEAN has spurious regularization properties, is inadequate to describe extended emission, and introduces a separation between the model fitted to the observed visibilities and the final astronomical image. These pathologies are mainly caused by CLEAN approaching the image as a set of delta functions. DoB-CLEAN basically replaces these CLEAN components by wavelets that

compress radial and directional information in parallel. The wavelet dictionary is fitted to the  $uv$ -coverage which provides a more data-driven approach to imaging. Sidelobes are suppressed by switching between a wavelet dictionary of steep, orthogonal masks in the Fourier domain and a sidelobe free representation in the image domain.

We implemented DoB-CLEAN and benchmarked its performance against CLEAN reconstructions on synthetic data. DoB-CLEAN succeeds over CLEAN in terms of resolution and accuracy. It removes the separation between model and image, that is, DoB-CLEAN fits a model to the  $uv$ -coverage that, in fact, has a physical meaning. The biggest plausible advantage of DoB-CLEAN, however, is the control it offers over the fit in the gaps of the  $uv$ -coverage offered by the multiscale wavelet dictionary. First, this helps to prevent overfitting and fosters image robustness (i.e., only measured, robust image features are measured). Second, this offers rich opportunities for post-processing, that is, identifying missing scales and missing image features in the observation and imaging. These post-processing capabilities are also of general interest as they offer a way to identify an uncertainty estimate of cleaned features in VLBI observations.

Despite these great advantages, DoB-CLEAN does not solve any problem related to the sparsity of the  $uv$ -coverage. The lack of certain scales in the observation can introduce artifacts in the DoB-CLEAN imaging results when completely suppressed. Moreover, the basis functions have negative flux; that is to say that on a low level, it is still present in the final images (i.e., the dynamic range remains limited).

Finally, we applied DoB-CLEAN to some existing and already calibrated data from RadioAstron observations of BL Lac. The reconstructions with DoB-CLEAN and with CLEAN share certain similarities when blurred to the same resolution, but there are also some visible differences that may alter the scientific interpretation, especially at the highest resolution. This, once more, elucidates the need for more variety in the imaging algorithms used in frontline VLBI observations to establish concordance between them and robustness of the scientific interpretation. We address this issue in subsequent works.

## References

- Akiyama, K., Ikeda, S., Pleau, M., et al. 2017a, *AJ*, **153**, 159
- Akiyama, K., Kuramochi, K., Ikeda, S., et al. 2017b, *ApJ*, **838**, 1
- Arras, P., Frank, P., Leike, R., Westermann, R., & Enßlin, T. A. 2019, *A&A*, **627**, A134
- Arras, P., Bester, H. L., Perley, R. A., et al. 2021, *A&A*, **646**, A84

A&amp;A 672, A26 (2023)

- Assirati, L., Silva, N. R., Berton, L., Lopes, A. A., & Bruno, O. M. 2014, *J. Phys.: Conf. Ser.*, **490**, 012020
- Bhatnagar, S., & Cornwell, T. J. 2004, *A&A*, **426**, 747
- Broderick, A. E., Gold, R., Karami, M., et al. 2020a, *ApJ*, **897**, 139
- Broderick, A. E., Pesce, D. W., Tiede, P., Pu, H.-Y., & Gold, R. 2020b, *ApJ*, **898**, 9
- Cai, X., Pereyra, M., & McEwen, J. D. 2018a, *MNRAS*, **480**, 4154
- Cai, X., Pereyra, M., & McEwen, J. D. 2018b, *MNRAS*, **480**, 4170
- Carrillo, R. E., McEwen, J. D., & Wiaux, Y. 2012, *MNRAS*, **426**, 1223
- Chael, A. A., Johnson, M. D., Bouman, K. L., et al. 2018, *ApJ*, **857**, 23
- Clark, B. G. 1980, *A&A*, **89**, 377
- Cornwell, T. J. 2008, *IEEE J. Sel. Top. Signal Process.*, **2**, 793
- Event Horizon Telescope Collaboration (Akiyama, K., et al.) 2019, *ApJ*, **875**, L4
- Garsden, H., Girard, J. N., Starck, J. L., et al. 2015, *A&A*, **575**, A90
- Gómez, J. L., Lobanov, A. P., Bruni, G., et al. 2016, *ApJ*, **817**, 96
- Gonzalez, R., & Woods, R. 2006, *Digital Image Processing*, 3rd edn.
- Högbom, J. A. 1974, *A&AS*, **15**, 417
- Junklewitz, H., Bell, M. R., Selig, M., & Enßlin, T. A. 2016, *A&A*, **586**, A76
- Kim, J.-Y., Krichbaum, T. P., Broderick, A. E., et al. 2020, *A&A*, **640**, A69
- Line, J. L. B., Mitchell, D. A., Pindor, B., et al. 2020, *PASA*, **37**, e027
- Lobanov, A. P., Horns, D., & Muxlow, T. W. B. 2011, *A&A*, **533**, A10
- Mertens, F., & Lobanov, A. 2015, *A&A*, **574**, A67
- Mohan, N., & Rafferty, D. 2015, Astrophysics Source Code Library [record ascl:1502.007]
- Müller, H., & Lobanov, A. P. 2022, *A&A*, **666**, A137
- Murenzi, R. 1989, in *Wavelets. Time-Frequency Methods and Phase Space*, eds. J.-M. Combes, A. Grossmann, & P. Tchamitchian, 239
- Rau, U., & Cornwell, T. J. 2011, *A&A*, **532**, A71
- Regpy. 2019, "regpy: Python tools for regularization methods", <https://github.com/regpy/regpy>
- Schwab, F. R. 1984, *AJ*, **89**, 1076
- Schwarz, U. J. 1978, *A&A*, **65**, 345
- Shepherd, M. C. 1997, *ASP Conf. Ser.*, **125**, 77
- Starck, J. L., & Murtagh, F. 2006, *Astronomical Image and Data Analysis* (Springer)
- Starck, J.-L., Bijaoui, A., Lopez, B., & Perrier, C. 1994, *A&A*, **283**, 349
- Starck, J.-L., Murtagh, F., & Fadili, J. 2015, *Sparse Image and Signal Processing: Wavelets and Related Geometric Multiscale Analysis*, 2nd edn., 1
- Thompson, A. R., Moran, J. M., & Swenson, George W., J. 2017, *Interferometry and Synthesis in Radio Astronomy*, 3rd edition
- Wakker, B. P., & Schwarz, U. J. 1988, *A&A*, **200**, 312

## Appendix A: Dictionaries

The dictionaries used in this paper are as follows::

$$\begin{aligned}
 \Psi^{DoG} : I \mapsto & [G_{\sigma_0}^r * I - G_{\sigma_0, \sigma_1, \alpha_0}^e * I, G_{\sigma_0}^r * I - G_{\sigma_0, \sigma_1, \alpha_1}^e * I, \dots, G_{\sigma_0}^r * I - G_{\sigma_0, \sigma_1, \alpha_{N-1}}^e * I, \frac{1}{B_0} \sum_{i=0}^{N-1} G_{\sigma_0, \sigma_1, \alpha_i}^e * I - G_{\sigma_1}^r * I, \\
 & G_{\sigma_1}^r * I - G_{\sigma_1, \sigma_2, \alpha_0}^e * I, \quad \dots \quad , G_{\sigma_1}^r * I - G_{\sigma_1, \sigma_2, \alpha_{N-1}}^e * I, \frac{1}{B_1} \sum_{i=0}^{N-1} G_{\sigma_1, \sigma_2, \alpha_i}^e * I - G_{\sigma_2}^r * I, \\
 & G_{\sigma_2}^r * I - G_{\sigma_2, \sigma_3, \alpha_0}^e * I, \quad \dots \quad , G_{\sigma_2}^r * I - G_{\sigma_2, \sigma_3, \alpha_{N-1}}^e * I, \frac{1}{B_2} \sum_{i=0}^{N-1} G_{\sigma_2, \sigma_3, \alpha_i}^e * I - G_{\sigma_3}^r * I, \\
 & \vdots \\
 & G_{\sigma_{J-1}}^r * I - G_{\sigma_{J-1}, \sigma_J, \alpha_0}^e * I, \quad \dots \quad , G_{\sigma_{J-1}}^r * I - G_{\sigma_{J-1}, \sigma_J, \alpha_{N-1}}^e * I, \frac{1}{B_{J-1}} \sum_{i=0}^{N-1} G_{\sigma_{J-1}, \sigma_J, \alpha_i}^e * I - G_{\sigma_J}^r * I, \\
 & G_{\sigma_J}^r * I]
 \end{aligned}$$

and:

$$\begin{aligned}
 \Psi^{DoB} : I \mapsto & [\tilde{J}_{\tilde{\sigma}_0}^r * I - \tilde{J}_{\tilde{\sigma}_0, \tilde{\sigma}_1, \alpha_0}^e * I, \tilde{J}_{\tilde{\sigma}_0}^r * I - \tilde{J}_{\tilde{\sigma}_0, \tilde{\sigma}_1, \alpha_1}^e * I, \dots, \tilde{J}_{\tilde{\sigma}_0}^r * I - \tilde{J}_{\tilde{\sigma}_0, \tilde{\sigma}_1, \alpha_{N-1}}^e * I, \frac{1}{B_0} \sum_{i=0}^{N-1} \tilde{J}_{\tilde{\sigma}_0, \tilde{\sigma}_1, \alpha_i}^e * I - \tilde{J}_{\tilde{\sigma}_1}^r * I, \\
 & \tilde{J}_{\tilde{\sigma}_1}^r * I - \tilde{J}_{\tilde{\sigma}_1, \tilde{\sigma}_2, \alpha_0}^e * I, \quad \dots \quad , \tilde{J}_{\tilde{\sigma}_1}^r * I - \tilde{J}_{\tilde{\sigma}_1, \tilde{\sigma}_2, \alpha_{N-1}}^e * I, \frac{1}{B_1} \sum_{i=0}^{N-1} \tilde{J}_{\tilde{\sigma}_1, \tilde{\sigma}_2, \alpha_i}^e * I - \tilde{J}_{\tilde{\sigma}_2}^r * I, \\
 & \tilde{J}_{\tilde{\sigma}_2}^r * I - \tilde{J}_{\tilde{\sigma}_2, \tilde{\sigma}_3, \alpha_0}^e * I, \quad \dots \quad , \tilde{J}_{\tilde{\sigma}_2}^r * I - \tilde{J}_{\tilde{\sigma}_2, \tilde{\sigma}_3, \alpha_{N-1}}^e * I, \frac{1}{B_2} \sum_{i=0}^{N-1} \tilde{J}_{\tilde{\sigma}_2, \tilde{\sigma}_3, \alpha_i}^e * I - \tilde{J}_{\tilde{\sigma}_3}^r * I, \\
 & \vdots \\
 & \tilde{J}_{\tilde{\sigma}_{J-1}}^r * I - \tilde{J}_{\tilde{\sigma}_{J-1}, \tilde{\sigma}_J, \alpha_0}^e * I, \quad \dots \quad , \tilde{J}_{\tilde{\sigma}_{J-1}}^r * I - \tilde{J}_{\tilde{\sigma}_{J-1}, \tilde{\sigma}_J, \alpha_{N-1}}^e * I, \frac{1}{B_{J-1}} \sum_{i=0}^{N-1} \tilde{J}_{\tilde{\sigma}_{J-1}, \tilde{\sigma}_J, \alpha_i}^e * I - \tilde{J}_{\tilde{\sigma}_J}^r * I, \\
 & \tilde{J}_{\tilde{\sigma}_J}^r * I]
 \end{aligned}$$

where  $G_{\sigma}^r$  denotes a two-dimensional radially symmetric (normalized) Gaussian function with standard deviation  $\sigma$  and  $G_{\sigma_1, \sigma_2, \alpha}^e$  a 2D elliptical (and normalized) Gaussian function with minor axis,  $\sigma_1$ , and major axis,  $\sigma_2$ , that is rotated by an angle  $\alpha$ .  $\tilde{J}_{\sigma}^r$  is a 2D radially symmetric modified Bessel function, namely,  $\tilde{J}_{\sigma}^r(r) = \frac{1}{\sigma r} J_1(2\pi r/\sigma)$  and  $\tilde{J}_{\sigma_1, \sigma_2, \alpha}^e$  is the elliptical analog with a minor axis of  $\sigma_1$ , major axis of  $\sigma_2$ , and rotation angle  $\alpha$ .

## Appendix B: Proof for the selection criterion

It is:

$$\begin{aligned}
 & \operatorname{argmax}_{i,m,k} \frac{1}{\|\Phi_{i,m} * B^D\| \|\Phi_{i,m}\|} (\Phi_{i,m} * B^D * I^D)(k) \\
 &= \operatorname{argmax}_{i,m,k} \frac{1}{\|\Phi_{i,m} * B^D\| \|\Phi_{i,m}\|} (\Phi_{i,m} * B^D * B^D * I)(k) \\
 &= \operatorname{argmax}_{i,m,k} \frac{1}{\|\Phi_{i,m} * B^D\| \|\Phi_{i,m}\|} \left( \Phi_{i,m} * B^D * B^D * \sum_{j,n,l} a_{j,n,l} \Phi_{j,n} * \delta_l \right)(k) \\
 &= \operatorname{argmax}_{i,m,k} \frac{1}{\|\Phi_{i,m} * B^D\| \|\Phi_{i,m}\|} \left( \Phi_{i,m} * B^D * \delta_k * B^D * \sum_{j,n,l} a_{j,n,l} \Phi_{j,n} * \delta_l \right) \quad (0) \\
 &= \operatorname{argmax}_{i,m,k} \sum_{j,n,l} a_{j,n,l} \left\langle \frac{1}{\|\Phi_{i,m} * B^D\| \|\Phi_{i,m}\|} \Phi_{i,m} * B^D * \delta_k, B^D * \Phi_{j,n} * \delta_l \right\rangle \quad (B.1)
 \end{aligned}$$

At this point we have to make an approximation. The maximum of the sum is approximately achieved at the maximal summand (this approximation also lies behind the minor loop of standard CLEAN, compare our discussion in Sect. 2.2). In other words, we solve:

$$\begin{aligned}
 & \operatorname{argmax}_{i,m,k} \max_{j,n,l} a_{j,n,l} \left\langle \frac{1}{\|\Phi_i * B^D\| \|\Phi_{i,m}\|} \Phi_{i,m} * B^D * \delta_k, \Phi_{j,n} * B^D * \delta_l \right\rangle \\
 &= \operatorname{argmax}_{i,m,k} \max_{j,n} a_{j,n,k} \left\langle \frac{1}{\|\Phi_{i,m} * B^D\| \|\Phi_{i,m}\|} \Phi_{i,m} * B^D, \Phi_{j,n} * B^D \right\rangle \quad (B.2)
 \end{aligned}$$

where equality holds since  $\Phi * B^D$  is centrally peaked.

It is:

$$\langle \Phi_{i,m} * B^D, \Phi_{j,n} * B^D \rangle = 1_{i,j} \langle \Phi_{i,m} * B^D, \Phi_{i,n} * B^D \rangle, \quad (B.3)$$

as the DoB wavelet functions of varying radial widths have distinct supports in the Fourier domain. Hence, we are left with the argmax-problem:

$$\operatorname{argmax}_{i,m,k} \max_n a_{j,n,k} \frac{1}{\|\Phi_{i,m} * B^D\| \|\Phi_{i,m}\|} \langle \Phi_{i,m} * B^D, \Phi_{i,n} * B^D \rangle \quad (B.4)$$

Then:

$$\begin{aligned}
 & \max_{i,m,k,n} a_{j,n,k} \frac{1}{\|\Phi_{i,m} * B^D\| \|\Phi_{i,m}\|} \langle \Phi_{i,m} * B^D, \Phi_{i,n} * B^D \rangle \\
 & \leq \max_{i,m,k,n} a_{j,n,k} \frac{1}{\|\Phi_{i,m} * B^D\| \|\Phi_{i,m}\|} \|\Phi_{i,m} * B^D\| \|\Phi_{i,n} * B^D\| \\
 &= \max_{i,m,k,n \neq N} a_{j,n,k} \frac{\|\Phi_{i,n} * B^D\|}{\|\Phi_{i,m}\|} \\
 &= \max_{i,k,n \neq N} a_{j,n,k} \frac{\|\Phi_{i,n} * B^D\|}{\|\Phi_{i,n}\|}, \quad (B.5)
 \end{aligned}$$

where the last equality holds since  $\|\Phi_{i,n1}\| = \|\Phi_{i,n2}\|$  for every  $n1, n2$ . This maximum gets reached exactly for  $m = n$ . Hence, our selection criterion Eq. 20 is met by this procedure.

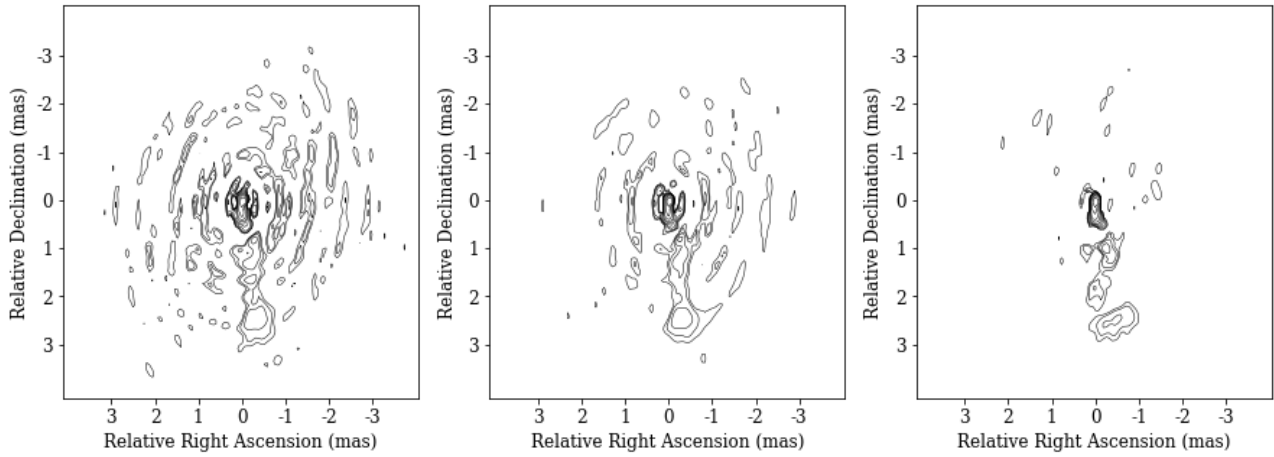
## Appendix C: Reliability of features recovered with DoB-CLEAN

We now discuss the reliability of the new features recovered in the reanalysis of the BL Lac observations with DoB-CLEAN.

Two features are in particular outstanding at highest resolution: the coronal emission around the core, and the possible sign of an edge-brightening. We have demonstrated in Sect. 4 that DoB-CLEAN addresses several pathologies of CLEAN, allows for moderate super-resolution and more accurate representation of extended emission. However, as was also demonstrated in Sect. 4, these advantages come to the cost of low-level imaging artifacts, in particular for the more challenging problem of recovering images with super-resolution (i.e., when not convolving with a beam). It is therefore unknown from a-priori how reliable the image features observed with DoB-CLEAN really are. Does DoB-CLEAN resolve some features that were not visible with CLEAN since DoB-CLEAN processes the  $uv$ -coverage more seriously? Or does vice versa DoB-CLEAN pick up on some artifacts that were suppressed by CLEAN since the interactive data manipulation (self-calibration, tapering, CLEAN-windows, flagging, ...) is more natural in CLEAN?

We present in Fig. C.1 the progress of the CLEANing procedure with DoB-CLEAN on the BL Lac data set. The residuals show a ring-like sidelobe structure that indicates the missing of certain scales in the not yet fully converged reconstructions. These scales will be added during later iterations as can be seen from the final reconstruction, namely, the vanishing residual, in the most-right panel. However, the progress of the DoB-CLEAN procedure highlights a specific requirement: since the image is composed by a sequence of wavelet sub-bands that each encode information on a specific spatial scale (i.e., the scale of the ring-like sidelobe pattern, the scale of the second ring-like sidelobe-pattern, ...) a final and clean reconstruction result will be only achievable if the various scales enter the recovered image with the correct weighting relative to each other. If one scale is over-weighted by the reconstruction procedure, the recovered image will contain sidelobes at this spatial scale as well. The correct relative weighting of scales is taken into account by our scale-selection criterion that was proven to be optimal in the absence of calibration issues. However, this fosters an important essential in the application to real, observational data: the self-calibration procedure needs to produce well estimates to the true gains such that no scale will be preferred or suppressed as a consequence of gain variations. Vice versa, the absence of sidelobe emission in the final reconstruction, see the most-right panel in Fig. C.1, indicates that the calibration and imaging procedure is consistent and was successful.

We note that the coronal emission around the central core component appears at the size of the first sidelobe scale, while the second edge-brightened blob left to the main jet-feature corresponds well to the second sidelobe scale (see Fig. C.1). This questions the robustness of the presence (DoB-CLEAN) or absence (CLEAN) of these image features. According to our reasoning above, we admit that DoB-CLEAN might be more prone than CLEAN to capture on sidelobe artifacts. However, the overall success of the reconstruction points towards a robust recovery. Moreover, also the CLEAN reconstructions seem to indicate emission to the north-west and south-east of the central core component, comparable to the coronal emission found with DoB-CLEAN (e.g., compare the most right panels in Fig. 16 and 14, working towards consistency). Typically, in CLEAN-like algorithms (such as CLEAN and DoB-CLEAN), the decision which emission is true and which emission is thought to be caused by a sidelobe is answered manually by setting proper CLEAN windows and by self calibration. A final answer regarding which reconstruction is more correct cannot be answered here. We recommend the use of a RML based method that fit the closure quantities instead of the visibilities (e.g., Chael et al.

Müller, H., and Lobanov, A. P.: *A&A proofs*, manuscript no. aa44664-22

**Fig. C.1.** Progress of the cleaning with DoB-CLEAN. Shown is the sum of the recovered image and the residual after 4000 iterations (left panel), 5000 iterations and phase self-calibration (middle panel) and the final ground-only image (right panel). The contour levels are [0.1,0.2,0.4,0.8,1.6,3.2,6.4,12.8,25.6,51.2]% of the peak brightness.


2018; Müller & Lobanov 2022) for consecutive works to build concordance between various reconstructions.

### 3.4 Paper 3: Müller & Lobanov 2023b, A&A, 673, A151

We present in this chapter the third paper in the line of works regarding multiscale VLBI imaging Müller & Lobanov (2023b). In this work, we include the multidirectional, multiscale dictionaries proposed in Müller & Lobanov (2023a) in DoG-HiT and extend DoG-HiT to both polarimetry and dynamic reconstructions. This research is inspired particularly by the future planning of the EHT and the ngEHT project (Doeleman et al. 2019), with their primary goals to produce polarimetric movies at the event horizon scales. Such movies are expected to uncover much stronger constraints on the nature of accretion and the launching of the innermost jet (Doeleman et al. 2019). The movie reconstruction problem is particularly challenging, probably presenting the most challenging imaging problem in VLBI so far. It requires the image reconstruction algorithm to be able to deal with super-resolution (to resolve the event horizon), fast dynamics, polarimetry, relatively sparse, heterogeneous arrays and poor data quality (due to the high frequency).

In the following manuscript, we utilize the multiresolution support to achieve these goals with a multiscale constrained minimization strategy as pioneered by Murtagh et al. (1995); Starck & Murtagh (1994). We conclusively demonstrate, albeit at somewhat lower fidelity in comparison to static reconstruction, that we can recover, in an unsupervised fashion, dynamic changes of polarized emission occurring on minute timescales. This achievement presently cannot be matched by any other reconstruction algorithm applied to EHT/ngEHT image reconstruction, thus signifying a major algorithmic milestone on the way toward reaching the scientific goals of the next generation of VLBI arrays. It should further be mentioned that the multiresolution support is a rather simple constraint that could be easily transferred to other RML and Bayesian frameworks. We expect great improvements in movie quality from such a combined hybrid approach.

## Dynamic and polarimetric VLBI imaging with a multiscale approach

H. Müller  and A. P. Lobanov

Max-Planck-Institut für Radioastronomie, Auf dem Hügel 69, Bonn 53121, Germany  
 e-mail: [hmueller@mpi-fr-bonn.mpg.de](mailto:hmueller@mpi-fr-bonn.mpg.de); [alobanov@mpi-fr-bonn.mpg.de](mailto:alobanov@mpi-fr-bonn.mpg.de)

Received 7 November 2022 / Accepted 20 March 2023

### ABSTRACT

**Context.** Due to the limited number of antennas and the limited observation time, an array of antennas in very long baseline interferometry (VLBI) often samples the Fourier domain only very sparsely. Powerful deconvolution algorithms are needed to compute a final image. Multiscale imaging approaches such as DoG-HiT have recently been developed to solve the VLBI imaging problem and show promising performance: they are fast, accurate, unbiased, and automatic.

**Aims.** We extend the multiscale imaging approach to polarimetric imaging, to reconstructions of dynamically evolving sources, and finally to dynamic polarimetric reconstructions.

**Methods.** These extensions (mr-support imaging) utilize a multiscale approach. The time-averaged Stokes  $I$  image was decomposed by a wavelet transform into single subbands. We used the set of statistically significant wavelet coefficients, the multiresolution support (mr-support), computed by DoG-HiT as a prior in a constrained minimization manner; we fitted the single-frame (polarimetric) observables by only varying the coefficients in the multiresolution support.

**Results.** The Event Horizon Telescope (EHT) is a VLBI array imaging supermassive black holes. We demonstrate on synthetic data that mr-support imaging offers ample regularization and is able to recover simple geometric dynamics at the horizon scale in a typical EHT setup. The approach is relatively lightweight, fast, and largely automatic and data driven. The ngEHT is a planned extension of the EHT designed to recover movies at the event horizon scales of a supermassive black hole. We benchmark the performance of mr-support imaging for the denser ngEHT configuration demonstrating the major improvements the additional ngEHT antennas will bring to dynamic polarimetric reconstructions.

**Conclusions.** Current and upcoming instruments offer the observational possibility to do polarimetric imaging of dynamically evolving structural patterns with the highest spatial and temporal resolution. State-of-the-art dynamic reconstruction methods can capture this motion with a range of temporal regularizers and priors. With this work, we add an additional simpler regularizer to the list: constraining the reconstruction to the multiresolution support.

**Key words.** techniques: interferometric – techniques: image processing – techniques: high angular resolution – methods: numerical – galaxies: nuclei – galaxies: jets

### 1. Introduction

In very long baseline interferometry (VLBI) the signals recorded at single antennas are correlated to achieve spatial resolution that would not be achievable with single-dish instruments. The correlation product of every antenna pair at a fixed time is the Fourier coefficient (visibility) of the true sky brightness distribution with a Fourier frequency determined by the projected spatial vector joining two antennas (baseline). As the Earth rotates during the observing run, baselines rotate on elliptical tracks in the Fourier domain, hence filling up the Fourier plane (uv-plane) continuously. However, due to the limited number of antennas and the limited amount of observing time, the coverage of Fourier coefficients (uv-coverage) is sparse. The procedure to recover the true sky brightness distribution from these sparsely covered Fourier coefficients is called VLBI imaging.

It is a long-standing frontline goal in astronomy to recover images of the shadow of a supermassive black hole. The Event Horizon Telescope (EHT) is a globally spanning VLBI array that observes at 230 GHz (with a recent upgrade to 345 GHz). With the combination of global baselines and short baselines, the EHT achieves the angular resolution that is needed to capture

the first image of the black hole shadow in M87 (Event Horizon Telescope Collaboration 2019a) and in the Milky Way (Event Horizon Telescope Collaboration 2022a). The next-generation Event Horizon Telescope (ngEHT) is a planned extension of the EHT (Doeleman et al. 2019; Johnson et al. 2023). It will produce movies of the accretion onto the central black hole Sgr A\* at the scales of the event horizon (Roelofs et al. 2023; Emami et al. 2023). The dynamic timescales for these observations are very short. Observations of Sgr A\* in the submillimeter (Bower et al. 2015; Wielgus et al. 2022) and near-infrared regime (GRAVITY Collaboration 2018a,b) confirm that Sgr A\* is time-varying on timescales as short as 30 min. The predicted innermost stable circular orbit (ISCO) period varies between 4 min and roughly 30 min, depending on the spin of the black hole. Palumbo et al. (2019) concluded that a well-sampled baseline coverage on timescales of ~30 min is needed to recover the source dynamics.

CLEAN (Högbom 1974) and its many variants (Clark 1980; Schwab 1984; Wakker & Schwarz 1988; Bhatnagar & Cornwell 2004; Cornwell 2008; Rau & Cornwell 2011; Müller & Lobanov 2023) have served the community well for decades, but are recently being challenged by forward-imaging approaches in

the spirit of regularized maximum likelihood (RML) methods (Narayan & Nityananda 1986; Wiaux et al. 2009; Garsden et al. 2015; Ikeda et al. 2016; Chael et al. 2016, 2018; Akiyama et al. 2017b,a; Event Horizon Telescope Collaboration 2019b; Müller & Lobanov 2022) and Bayesian approaches (Arras et al. 2019, 2021; Broderick et al. 2020a,b). Recently we developed new multiresolution tools for performing VLBI imaging (Müller & Lobanov 2022, 2023). For these multiscale approaches we designed special wavelet-based basis functions (difference of Gaussian and difference of spherical Bessel functions) and fitted the basis functions to the uv-coverage. In this way we define smooth basis-functions that are well suited to describe (compress) the recovered image features by encoding information about the uv-coverage itself. Some wavelets are most sensitive to gaps in the uv-coverage, while others are most sensitive to covered Fourier coefficients. While the signal from the latter should be recovered, the signal from former are suppressed (effectively avoiding overfitting).

As a byproduct of these multiscale imaging algorithms, we compute the multiresolution support (mr-support; Müller & Lobanov 2022): a set of wavelet parameters that are deemed statistically significant to represent the recovered image features. The multiresolution support encodes various information about the recovered image. First, it implements a support constraint (to determine where the emission is located in the image). Second, it encodes a spatial constraint (to understand which spatial scales are needed to represent the image features at these locations). In particular, the second prior information is determined by the spatial scales that are present in the data (i.e., covered by baselines in the observation). We demonstrated in Müller & Lobanov (2022) that the multiresolution support is a powerful prior information very well suited to refining the imaging procedure. In Müller & Lobanov (2022) we proposed the addition of amplitudes and phases to the data terms and the removal of any regularizer term, in order to solve the resulting optimization problem by only updating the coefficients in the multiresolution support. The fit to the observed visibilities improved, but without the addition of spurious artifacts that are typical of overfitting.

Among Stokes  $I$  imaging, full polarimetric imaging is of interest for the VLBI community, both theoretically (Blandford & Znajek 1977; Hardee et al. 2007; Kramer & MacDonald 2021) and observationally (e.g., Gómez et al. 2011, 2016; Hovatta et al. 2012; Zamaninasab et al. 2014; Pötzl et al. 2021; Ricci et al. 2022, among many others), in particular at event horizon scales (Event Horizon Telescope Collaboration 2021a,b). In polarimetric imaging the recorded data are separated into several polarized subbands and recombined in the four Stokes parameters. Essentially, we have four Stokes parameters ( $I$ ,  $Q$ ,  $U$ ,  $V$ ) and corresponding polarized visibilities. Hence, the problem that we aim to solve for the other three Stokes parameters is the same as for Stokes  $I$ : recovering a signal from a sparse measurement of the Fourier coefficients. However, there are some slight differences. While the Stokes  $I$  image is necessarily nonnegative (and used during imaging as a prior), this does not have to be true for Stokes  $Q$ ,  $U$ , and  $V$ . Moreover,  $I^2 \geq Q^2 + U^2 + V^2$  applies.

The multiresolution support is a well-suited prior to be applied to the polarimetric imaging when the Stokes  $I$  image is already done. The support constraint of the multiresolution support encodes the information that linear and circular polarized emission theoretically can only appear at locations where total intensity (Stokes  $I$ ) is greater than zero. This might not reflect the observation situation in every case. Sometimes the Stokes  $I$  signature cannot be retrieved with the spatial sensitivity of the interferometer, while the more localized (e.g., due to Faraday

rotation) polarized structural pattern is visible. However, in most VLBI studies this pathological situation does not appear and support constraint is a good approximation. Moreover, the spatial constraint adheres to the fact that the polarimetric visibilities have the same uv-coverage as total intensity visibilities (i.e., the same spatial scales, those covered by uv-coverage, are present in the polarized images).

Another domain of current research is the study of dynamic sources, such as Sgr A\*. We study in this case the static imaging of a dynamically evolving source as in Event Horizon Telescope Collaboration (2022b), and the dynamic reconstruction of a movie (Roelofs et al. 2023). In this work we focus on the latter problem. Data sets of dynamic sources pose additional challenges. Due to the short variability timescale, the effective uv-coverage in every frame is not sufficient for efficient snapshot imaging. Modern approaches utilize a temporal correlation instead, in a Bayesian framework (Bouman et al. 2018; Broderick et al. 2022; Roelofs et al. 2023) or as temporal regularizer in the RML framework (Johnson et al. 2017; Bouman et al. 2018; Chael et al. 2022; Roelofs et al. 2023). Moreover, the variability of the source could be misidentified with the calibration of the gains (Event Horizon Telescope Collaboration 2022b).

Again, the multiresolution support (computed for the time-averaged image) encodes prior information that is very desirable for dynamic imaging. The support constraint encodes the information that every location of an emission spike appearing during the observation is present also in the mean image. The uv-coverage of the full observation run is the sum of the uv-coverage of the single frames. Hence, the spatial constraint also provides a powerful image prior for dynamic imaging; the multiresolution support only allows spatial scales that are present in the mean image (in the full observation run), which means that the fit in the gaps of the uv-coverage remains under control. On the other hand, the spatial constraint allows for the addition of the spatial scales to single frames that might be not represented in the uv-coverage of this single frame, but in earlier or later snapshots. However, we note that there may be a bias toward larger scales since the mean image suppresses small-scale structures present in only part of the individual frames.

Based on the success of the approach presented in Müller & Lobanov (2022) of only changing the coefficients in the multiresolution support to introduce effective regularization, we propose the same approach for static polarimetric imaging and dynamic imaging. As outlined above, the multiresolution support is well suited to be used as a regularizer in these problems as it exactly encodes the prior information that is needed. As we solve two quite different extensions to the standard VLBI imaging with the same approach, it is natural to use the same approach for the combined problem: a dynamic polarimetric reconstruction.

## 2. Theory

### 2.1. VLBI

As described by the van Cittert–Zernike theorem, the visibilities  $\mathcal{V}$  are related to the true sky-brightness distribution  $I(x, y)$  by a two-dimensional Fourier transform under reasonable assumptions (Thompson et al. 2017):

$$\mathcal{V}_I(u, v) = \int \int e^{-2\pi i(xu+yv)} I(x, y) dx dy =: \mathcal{F}I(u, v). \quad (1)$$

From a full coverage of the Fourier coefficients (visibilities) the true sky brightness distribution could be computed by an

inverse Fourier transform. However, in VLBI the  $uv$ -coverage is very sparse with significant gaps. This makes the problem of recovering the image an ill-posed inverse problem. The polarized quantities are measured at every antenna with orthogonal polarimetric filters (linear or circular). The cross-correlation of these signals gives rise to the polarimetric Stokes  $I$  parameters and their respective polarimetric visibilities:

$$\mathcal{V}_I = \mathcal{F}I, \quad (2)$$

$$\mathcal{V}_Q = \mathcal{F}Q, \quad (3)$$

$$\mathcal{V}_U = \mathcal{F}U, \quad (4)$$

$$\mathcal{V}_V = \mathcal{F}V. \quad (5)$$

Here  $I$  is the total brightness,  $Q$  and  $U$  the linear polarizations, and  $V$  the fraction of circular polarization. By construction it is

$$I^2 \geq Q^2 + U^2 + V^2. \quad (6)$$

## 2.2. Imaging

Imaging with the CLEAN algorithm and its variants (Högbom 1974; Schwab 1984; Wakker & Schwarz 1988) were the standard in VLBI imaging for the last decades. In CLEAN the imaging problem is equivalently reformulated as a deconvolution problem,

$$I^D = B^D * I, \quad (7)$$

where  $I^D$  is called the dirty map (the inverse Fourier transform of all measured, and probably reweighted, Fourier coefficients) and  $B^D$  is called the dirty beam (the dirty map of a synthetic delta source). The astronomer using CLEAN determines some search windows for components; CLEAN looks for the maximum peak in the residual in this window (minor loop) and subtracts the shifted and rescaled dirty beam from the residual (major loop). This procedure is iterated until the residual is noise-like. In this way, CLEAN models the image as a set of delta functions. Finally, these components are restored with a restoring beam (clean beam) that fits the central peak of the dirty beam. CLEAN is an inverse modeling approach to the imaging problem.

Recently, forward-modeling approaches have gained interest in the community in the framework of RML (Akiyama et al. 2017a; Chael et al. 2018; Müller & Lobanov 2022) and Bayesian methods (Arras et al. 2019; Broderick et al. 2020a,b). These methods seem to outperform classical CLEAN in terms of speed, spatial resolution, sensitivity, and precision, in particular when the  $uv$ -coverage is sparse (e.g., Event Horizon Telescope Collaboration 2019b; Arras et al. 2021; Müller & Lobanov 2022; Roelofs et al. 2023). On the other hand, these forward-modeling methods require the fine-tuning of some hyperparameters and regularization parameters, despite the recent effort to reduce this dependence (Müller & Lobanov 2022). For the remainder of this manuscript we focus on RML methods, and ignore Bayesian approaches for now.

In RML a sum of data fidelity terms and penalty terms is minimized

$$\hat{I} \in \operatorname{argmin}_I \sum_i \alpha_i S_i(I) + \sum_j \beta_j R_j(I), \quad (8)$$

where the data fidelity term  $S_i$  measures the fidelity of the recovered solution  $I$  to the observed data (i.e., polarized visibilities) and the regularization terms  $R_j$  measure the fidelity of

the guess image  $I$ . The regularization parameters  $\alpha_i$  and  $\beta_j$  are manually set weights that balance data fidelity and regularization terms. Typical choices for the data terms are chi-square values to the observed (polarimetric) visibilities, and related calibration independent quantities such as closure phases and closure amplitudes. For the regularization terms a wide range of regularizers has been applied in the past, for example sparsity promoting regularization (11, 12), smoothness constraints (total variation, total squared variation), hard constraints (total flux, non-negativity), entropy maximization (MEM), and multiscale decompositions (hard thresholding on scales). The regularization terms introduce regularization to the ill-posed imaging problem. By balancing the data terms and the regularization terms, we select a possible guess solution that fits the data (small data terms) and is robust against noise and artifacts (small penalty terms). We demonstrated in previous works (Müller & Lobanov 2022) that a support constraint has the same regularization effect. By constraining the space of free parameters to the multiresolution support we were able to refine the fit to the observed data in later imaging rounds.

## 2.3. Wavelets

The basis behind multiscale approaches are multiscale dictionaries. In Müller & Lobanov (2022) we proposed the use of radial-symmetric difference of Gaussian (DoG) wavelets, and extended them to directional dependent basis functions in Müller & Lobanov (2023). Moreover, we introduced in Müller & Lobanov (2023) steep quasi-orthogonal basis functions to study the Fourier domain by difference of Bessel functions (DoB). Both dictionaries (DoG and DoB) are related to each other: the DoG wavelets approximate the central peak of the DoB wavelets, but do not contain the wider sidelobes of latter ones. In what follows we quickly summarize these wavelet dictionaries. For more detailed information we refer to Müller & Lobanov (2022, 2023).

Wavelets have a wide range of applications in image compression. The most widely used continuous wavelet is the Mexican-hat wavelet which is a rescaled second-order derivative of a Gaussian (Lagrangian of Gaussians; Starck et al. 2015). The difference of Gaussian method offers some viable approximation to Mexican hat wavelets. A DoG wavelet is described by two width parameters  $\sigma_1, \sigma_2$ :

$$\begin{aligned} \Phi_{\text{DoG}}^{\sigma_1, \sigma_2}(x, y) &= \frac{1}{2\pi\sigma_1^2} \exp\left(-\frac{r(x, y)^2}{2\sigma_1^2}\right) - \frac{1}{2\pi\sigma_2^2} \exp\left(-\frac{r(x, y)^2}{2\sigma_2^2}\right) \\ &= G_{\sigma_1} - G_{\sigma_2}. \end{aligned} \quad (9)$$

The Fourier transform of these DoG wavelets define ring-like filters in the Fourier domain:

$$\mathcal{F}\Phi_{\text{DoG}}^{\sigma_j, \sigma_{j+1}}(u, v) \propto \exp(-2\pi^2\sigma_j^2 q(u, v)^2) - \exp(-2\pi^2\sigma_{j+1}^2 q(u, v)^2). \quad (10)$$

The extension to DoB wavelets is natural. We replace the DoG wavelets by spherical Bessel functions:

$$\begin{aligned} \Phi_{\text{DoB}}^{\tilde{\sigma}_j, \tilde{\sigma}_{j+1}}(x, y) &= \frac{1}{\tilde{\sigma}_j r(x, y)} J_1(2\pi r(x, y)/\tilde{\sigma}_j) - \frac{1}{\tilde{\sigma}_{j+1} r(x, y)} J_1(2\pi r(x, y)/\tilde{\sigma}_{j+1}). \end{aligned} \quad (11)$$

Moreover, the extension of both wavelets to directional dependent basis functions is straightforward as well. The radial coordinates just need to be replaced by elliptical ones.

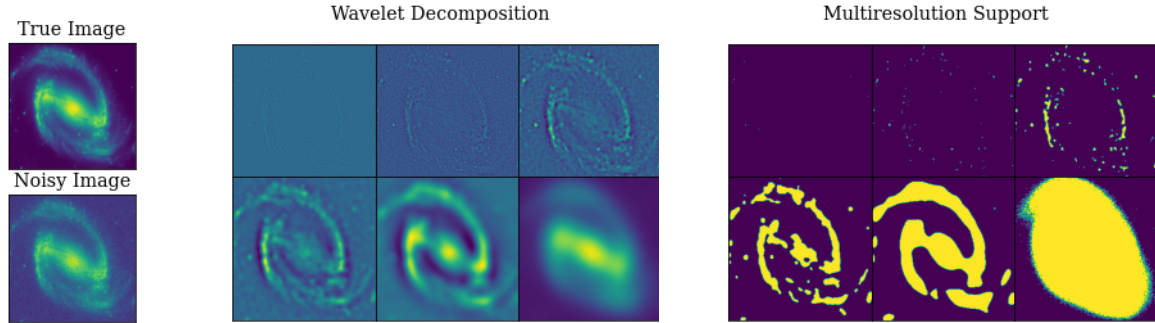


**Fig. 1.** Illustration of wavelet decomposition and multiresolution support of an astronomical image. Left panels: true image and true image with additional Gaussian noise; middle panels: Wavelet decomposition of the noised image with the DoG wavelet dictionary computed with filter sizes  $\sigma_0 = 1, \sigma_1 = 2, \sigma_2 = 4, \dots, \sigma_5 = 32$  pixels; right panels: multiresolution support computed by thresholding the wavelet scales to the scale-dependent noise plotted as a mask with value 1 (coefficient in the support) or 0 (coefficient not in the multiresolution support).

The wavelet decomposition is composed from the wavelet basis functions from a sequence of increasing widths  $\sigma_0 \leq \sigma_1 \leq \dots \leq \sigma_J$ :

$$\Psi^{\text{DoG}} : I \mapsto \mathcal{I} = [\Phi_{\text{DoG}}^{\sigma_0, \sigma_1} * I, \Phi_{\text{DoG}}^{\sigma_1, \sigma_2} * I, \dots, G_{\sigma_J} * I], \quad (12)$$

$$\Psi^{\text{DoB}} : I \mapsto \mathcal{I} = [\Phi_{\text{DoB}}^{\sigma_0, \sigma_1} * I, \Phi_{\text{DoB}}^{\sigma_1, \sigma_2} * I, \dots, J_{\sigma_J} * I]. \quad (13)$$

For direction dependent dictionaries we use elliptical Gaussians and Bessel functions instead. For more details we refer to our discussion in Müller & Lobanov (2023). The multiscale dictionary is the adjoint of the multiscale decomposition (in what follows called  $\Gamma$ )

$$\Gamma : \mathcal{I} = \{I_0, I_1, I_2, \dots, I_J\} \mapsto \sum_{i=0}^{J-1} \Phi_{\text{DoG}}^{\sigma_i, \sigma_{i+1}} * I_i + G_{\sigma_J} * I_J, \quad (14)$$

with an analogous action for DoB wavelets and multidirectional wavelets. The complete action of the multiscale and multidirectional wavelet decomposition is presented in the appendix.

#### 2.4. DoG-HiT

Our novel algorithm for doing dynamic polarimetric reconstructions is an extension of the DoG-HiT algorithm (Müller & Lobanov 2023). We summarize this algorithmic framework in this section. DoG-HiT models the image by a radial symmetric wavelet dictionary  $\Psi^{\text{DoG}}$ . The Fourier transform of the basis functions of the dictionary (atoms) are sensitivity filters in the Fourier domain. Hence, by fitting the widths of the Gaussians to the uv-coverage, we define wavelets that are most sensitive to measured Fourier coefficients and wavelets that are most sensitive to gaps in the uv-coverage. The signal of the former should be kept, while the lack of the latter atoms causes sidelobes in the image. In this way the dictionary allows for a better separation between measured features (covered by baselines) and uncovered artifacts. We interpolate the signal in the gaps by the smooth nature of the basis functions, but suppress the signal in the gaps to a level where overfitting is prohibited. All in all, we solve the minimization problem (Müller & Lobanov 2022):

$$\hat{\mathcal{I}} \in \text{argmin}_{\mathcal{I}} [S_{\text{cph}}(F\Gamma\mathcal{I}, \mathcal{V}) + S_{\text{cla}}(F\Gamma\mathcal{I}, \mathcal{V}) + \beta \cdot \|\mathcal{I}\|_p + R_{\text{flux}}(\mathcal{I}, f)]. \quad (15)$$

Here  $S_{\text{cph}}$  and  $S_{\text{cla}}$  denote the  $\chi^2$  fit to the closure phases and closure amplitudes, respectively, and  $R_{\text{flux}}$  denotes a characteristic function on the total flux of the guess solution. We

use the pseudo-norm  $\|\cdot\|_p$  (i.e., the number of non-zero coefficients) as a sparsity promoting regularization term weighted with a regularization parameter  $\beta$ . Equation (15) is solved by a forward-backward splitting algorithm alternated with rescaling the emission to a predefined total flux (Müller & Lobanov 2022). The final recovered solution is:

$$\hat{I} = \Gamma\hat{\mathcal{I}}. \quad (16)$$

The regularization parameter  $\beta$  is the only free parameter that needs to be chosen manually by the user. The number of free parameters is therefore much smaller than the number of free parameters for RML methods such as ehtim (Chael et al. 2016, 2018) or SMILI (Akiyama et al. 2017b,a) since the penalty term is chosen data-driven. We demonstrated in Müller & Lobanov (2022) that although the optimization landscape is much simpler, the reconstructions obtained by DoG-HiT are competitive to RML reconstructions. Moreover, we only fit closure phases and closure amplitudes for DoG-HiT in Eq. (15) (i.e., the reconstruction is robust against instrumental gain corruptions). Next, we use the model computed by DoG-HiT for self-calibration (i.e., we determine the gains).

#### 2.5. Multiresolution support

A specific property of the multiscale decompositions is the multiresolution support. Mertens & Lobanov (2015) paved the way for the application of the multiresolution support in the analysis of active galactic nucleus (AGN) jets. The multiresolution support is a set of wavelet components that are statistically significant (Starck et al. 2015). We decompose a noisy image by a wavelet dictionary:  $[I_0, I_1, I_2, \dots, I_J] = \Psi I$ . Moreover, we compute the scale-dependent noise level  $s_j$  by decomposing a Gaussian white noise field with the same wavelet dictionary. Given a threshold  $k_s$ , we can define a set of statistically significant wavelet coefficients with the criterion that  $\|I_j(x, y)\| \geq k_s s_j$ , where the noise level is approximated by the variance from an emission-free region of the image scale  $I_j$  (i.e., far away from the center). The multiresolution support for a celestial ground truth image from the EHT imaging challenges<sup>1</sup> is illustrated in Fig. 1.

The multiresolution support encodes two different types of prior information about the model. First, it encodes a support constraint (i.e., it defines the position of significant emission spikes in the field of view). Second, the multiresolution support contains information about the spatial scales that are present in

<sup>1</sup> <http://vlbiimaging.csail.mit.edu/>

the observation. In sparse VLBI arrays, this is dominated by the uv-coverage (i.e., by which spatial scales are covered by observed baselines in the Fourier domain). As various wavelet basis functions are most sensitive to various baselines or gaps in the uv-coverage, the information about which spatial scales are covered by observations is directly imprinted in the multiresolution support. This is especially true for the direction-dependent DoG and DoB wavelets used for DoG-HiT that were fitted to the uv-coverage (i.e., that were developed to allow an optimal separation between covered features and gaps in the uv-coverage).

DoG-HiT solves the minimization of Eq. (15) with a forward-backward splitting algorithm. The backward projection step is the application of the proximal-point operator of the  $l^0$  penalization function, which is a hard thresholding (Müller & Lobanov 2022). Hence, all insignificant wavelet coefficients are set to zero. DoG-HiT therefore computes an approximation of the multiresolution support as a byproduct. This support was used to further refine rounds in the imaging (Müller & Lobanov 2022).

The computation of the multiresolution support as a byproduct of DoG-HiT highlights an essential improvement of DoG-HiT compared to CLEAN regarding supervision. The support of significant emission is found by DoG-HiT automatically, while it has to be selected in CLEAN by the user-defined CLEAN windows. DoG-HiT is therefore less user-biased and provides (compared to standard RML frameworks and CLEAN) an essential step toward unsupervised VLBI imaging.

### 3. Algorithms

We outline in this section the algorithms used for static polarimetry, dynamic Stokes  $I$  imaging, and dynamic polarimetry. In what follows we call these algorithms mr-support imaging.

#### 3.1. Stokes $I$

Static Stokes  $I$  images are constructed with DoG-HiT with the five round pipeline presented in Müller & Lobanov (2022). However, in that work we used only radially symmetric wavelets. As an extension, we used the multi-directional dictionaries developed in Müller & Lobanov (2023) for this work (i.e., we replaced the circular symmetric Gaussians by elliptical Gaussians). Moreover, we used a grid search in Müller & Lobanov (2022) to find a proper starting point for the forward-backward splitting minimization iterations of DoG-HiT. Since the backward step in the minimization is essentially a hard thresholding, we tried different scale-dependent thresholds in an equidistant grid to minimize Eq. (15), and used the setting of the minimum as the starting point for the forward-backward iterations. For this manuscript, we used the same grid search, but applied the orthogonal DoB wavelets in the grid search, while still using the DoG wavelets in the imaging rounds of the pipeline. We do not focus on the Stokes  $I$  reconstruction in this work as these extensions are rather straightforward and minor, and the focus of the manuscript is on an extension of DoG-HiT to polarimetry. We recall one of the main advantages of DoG-HiT: the algorithm works mainly unsupervised with a minimal set of free parameters, hence adding a minimal human bias in the imaging procedure.

#### 3.2. Polarimetry

For polarimetric reconstructions we first reconstruct a Stokes  $I$  image with DoG-HiT and solve for the gains by self-calibrating to the final output (DoG-HiT relies on calibration independent

closure quantities). As a second step, we solve for the polarimetric Stokes parameters  $Q$ ,  $U$ , and  $V$ . We take the multiresolution support computed by DoG-HiT for the Stokes  $I$  imaging and constrain the space of free parameters to all wavelet coefficients in the multiresolution support. We then solve for  $Q$ ,  $U$ ,  $V$  by minimizing the fit to  $\mathcal{V}_Q, \mathcal{V}_U, \mathcal{V}_V$  with a gradient descent algorithm, but only allow coefficients in the multiresolution support to vary. In summary we solve the following problems:

$$\begin{aligned} \hat{Q} &\in \operatorname{argmin}_{Q=\{Q_0, \dots, Q_n\}, Q_j(x,y)=0 \text{ whenever } \hat{I}_j(x,y)=0} [S_Q(FTQ, \mathcal{V}_Q)], \\ \hat{U} &\in \operatorname{argmin}_{U=\{U_0, \dots, U_n\}, U_j(x,y)=0 \text{ whenever } \hat{I}_j(x,y)=0} [S_U(FTU, \mathcal{V}_U)]. \end{aligned} \quad (17)$$

Here  $\{\hat{I}_0, \dots, \hat{I}_n\} =: \hat{\mathcal{I}}$  are the recovered wavelet coefficients for the Stokes  $I$  image as in Sect. 2.4, and  $S_U$  and  $S_Q$  are the  $\chi^2$  fit qualities to the Stokes  $Q$  and  $U$  visibilities. The side condition  $Q_j(x, y) = 0$  whenever  $\hat{I}_j(x, y) = 0$  denotes the constraint that we only vary coefficients in the multiresolution support.

The multiresolution support is a well-suited regularizer here; the support constraint encodes the side-condition Eq. (6) effectively, which means that polarized emission is only allowed to appear at locations in the images in which we found relevant emission in total intensity. While this inequality Eq. (6) holds true theoretically in any case, in practice the pathological situation could occur that due to the instrumental effect a non-detection of Stokes  $I$  does not rule out polarimetric structures. With this caveat in mind, we assume for the rest of the manuscript that inequality Eq. (6) holds true in observations as well. Moreover, the polarimetric visibilities have the same uv-coverage as the Stokes  $I$  visibility. The spatial constraint of the multiresolution support describes which spatial scales are statistically significant to describe the emission in the image, which in the case of sparse VLBI arrays is dominated by the uv-coverage (i.e., which spatial scales are compressed by which baselines and whether these baselines are measured). Hence, we already computed the multiresolution support as a byproduct in DoG-HiT to study the uv-coverage of the observation, and get control over overfitting in the gaps of the uv-coverage by suppressing the respective atoms of the dictionary. This effective regularization can be copied to the polarized visibilities as the uv-coverage is the same.

Moreover, we would like to note once again that the multiresolution support is a completely data driven property computed as a sideproduct by DoG-HiT. Hence, the reconstruction of polarimetric properties still relies on a minimal set of hyperparameters and remains largely unsupervised.

We fitted complex polarimetric visibilities directly here, which requires that a good polarization calibration is already available. However, the method is easy to adapt to more realistic situations since it is (opposed to CLEAN) a forward-modeling technique. First, instead of a constrained  $\chi^2$  minimization to the complex visibilities, one could just optimize the fit to the visibility-domain polarization fraction as in Johnson et al. (2015). Second, the minimization in Eq. (17) is done iteratively, where the most important features are recovered first and gradually more detailed features are recovered at later iterations. Hence, with a similar philosophy to how self-calibration interacts with CLEAN, we could run the minimization for some iterations and do the calibration on the current model, then continue the minimization and calibration in an alternating manner.

#### 3.3. Dynamic Stokes $I$

For dynamic Stokes  $I$  imaging, we first reconstruct a static image with DoG-HiT. For this work we assume that the static image of

a dynamically evolving source might be a good approximation to the mean image during the time of observation. This might be true in particular if the source structure contains some persistent structure during the complete observing run, as could be expected for Sgr A\* in EHT observations with a persistent shadow in rotating hotspot models (Tiede et al. 2020). However, based on the dynamics of the target, it may be difficult to recover a decent fit to the data with a static image. In this work we applied a procedure inspired by the strategy in Event Horizon Telescope Collaboration (2022b); we added a systematic noise-floor on every baseline to account for variability. However, we did not repeat the sophisticated noise modeling applied in Event Horizon Telescope Collaboration (2022b).

We computed the multiresolution support by the static mean image. Then we cut the observation in single frames and reconstruct images at every frame independently. All frames together make up the dynamic movie reconstruction. However, due to the shortness of single frames, snapshot imaging is not possible due to the sparsity of the uv-coverage. Again, we propose using the multiresolution support instead. We minimize the  $\chi^2$  for every single frame observation independently for every frame in a gradient descent algorithm (using the mean image as an initial guess), but only allow coefficients in the multiresolution support to vary.

The multiresolution support is a well-suited regularizer here as well; if the static image is a good approximation to the mean image, the static image contains all the locations of emission in the field of view. If at some time an emission spike occurs at a specific location, this emission spike should be visible in the mean as well. Hence, the support constraint encodes information about the location of emission at single frames. This assumption comes with the caveat that short-lived small-scale features may be not strong enough in the mean image and excluded later from the dynamic reconstructions due to the multiresolution support. However, we also doubt that such a feature would be visible with the much sparser uv-coverage of single scans, and therefore would not be recovered. Moreover, the uv-coverage of the complete observation is the sum of the observations of the single frames. In single frame observations there are three different categories of Fourier coefficients and/or baselines: the ones measured by observations in this single frame (very sparse), the ones that are not measured during the time of the single frame but will be measured at later (earlier) times in the observation, and the baselines that are not measured at all due to the sparsity of the array. By doing constrained optimization (constrained by the multiresolution support) to the single frame observation we fit the first class of baselines, copy the solution over from the initial guess (mean image) for the second class of baselines, and suppress the last class of baselines by the multiresolution support. Hence, the spatial constraint implemented by the multiresolution support is a well-suited prior to do dynamic imaging.

The reasonable assumption of temporal correlation between scans (e.g., by a regularizer term favoring temporal smoothness) is not used explicitly for mr-support imaging. However, this assumption can be included in the dynamic reconstruction straightforwardly. Instead of fitting the visibilities with a constrained minimization approach, we can minimize the sum of a quality metric for the fit to the visibilities and a temporal regularization term, but only vary the coefficients in the multiresolution support. However, for this work we restricted ourselves to reconstructions without penalization on the temporal evolution such that now new regularization parameters are introduced and the reconstruction remains automatic and completely data-driven.

Moreover, this means that all scans can be computed in parallel, allowing for fast computations.

### 3.4. Dynamic polarimetry

We propose the same procedure for polarized imaging and dynamic Stokes  $I$  imaging: fitting the respective visibilities with a gradient descent approach, while only varying coefficients in the multiresolution support computed by DoG-HiT. It is therefore natural to utilize this approach for dynamic polarimetry as well. We propose the following strategy. First, reconstruct a static Stokes  $I$  image by DoG-HiT and compute the multiresolution support. Then cut the observation in single frames and solve for dynamics and polarimetry together by fitting to  $\mathcal{V}_I, \mathcal{V}_Q, \mathcal{V}_U, \mathcal{V}_V$  together in single frames independently, but only vary coefficients in the multiresolution support.

## 4. Synthetic data tests

### 4.1. Synthetic observations

We tested the capabilities for mr-support imaging for polarimetric image reconstructions. We tested three different source models (static polarized Sgr A\* model, a slowly rotating crescent, and a rapidly rotating crescent) with two different arrays (EHT and a possible ngEHT configuration). A thorough comparison of existing imaging approaches for dynamic polarimetry is in preparation and will be deferred to a later work. For more details we also refer to the ngEHT analysis challenges Roelofs et al. (2023), and in particular the upcoming third challenge<sup>2</sup> in which we compete with mr-support imaging. We review our submission to the third challenge in Sect. 4.5.

We observe the synthetic ground truth images and movies with the array of the EHT 2022 observations and added thermal noise according to the measured SEFDs of the 2017 observation campaign (Event Horizon Telescope Collaboration 2019b). We used ten-minute cycles consisting of five minutes of continued observation with an integration time of ten seconds and a gap of five minutes off-source (mimicking calibration, pointing scans). This cycle time is of special interest when discussing dynamic reconstructions as the five-minute gaps essentially limit the temporal resolution. The data sets were scan-averaged prior to the imaging procedure.

As ngEHT configuration we took the EHT 2022 array configuration (i.e., ALMA, APEX, GLT, IRAM-30 m, JCMT, KP, LMT, NOEMA, SMA, SMT, SPT) and added ten additional antennas from the list of Raymond et al. (2021), as was done for the ngEHT Analysis challenges (Roelofs et al. 2023): HAY (34 m), OVRO (10.4 m), GAM (15 m), BAR, BAJA, NZ, SGO, CAT, GARS, CNI (all 6 m). We added instrumental noise according to the size of the telescopes, but did not add further calibration errors. As a ground truth we took the slowly rotating crescent model with a rotation period of one hour. As for the EHT 2022 coverage, the ground truth movie was observed with a cycle of five minutes on-source and a five-minute gap and an integration time of ten seconds (ten minutes on-source with a two-minute gap in the quickly rotating crescent example).

As a static synthetic test image we took a synthetic Sgr A\* image out of the ehtim software package (Chael et al. 2018). The true image model is presented in Fig. 2. For the dynamic

<sup>2</sup> <https://challenge.ngeht.org/challenge3/>

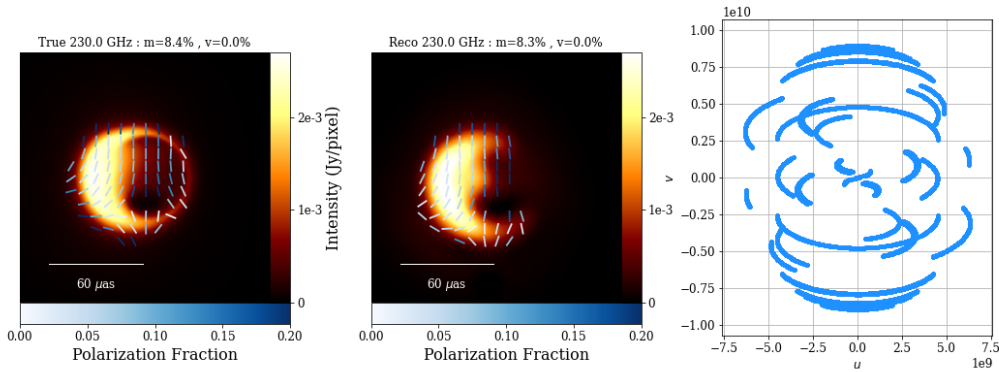


**Fig. 2.** Static, polarimetric reconstruction with mr-support imaging on synthetic data. Left panel: static polarization ground truth; middle panel: static reconstruction with mr-support imaging; right panel:  $uv$ -coverage of synthetic observation (EHT 2022 array).

## True Movie

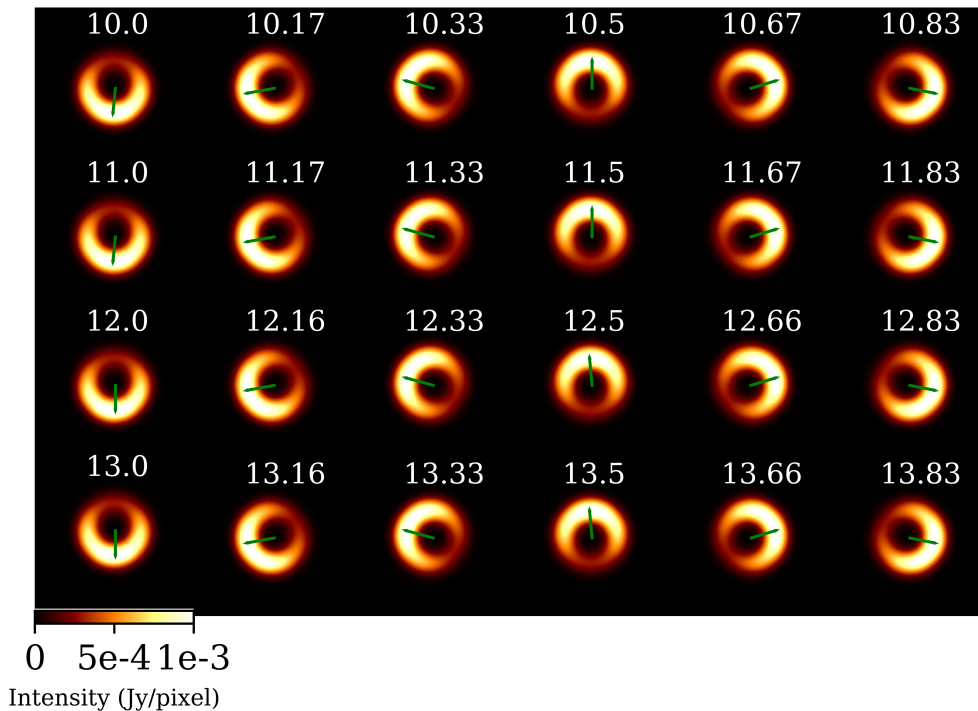


**Fig. 3.** Synthetic ground truth dynamic movie (slowly rotating crescent) in the time interval between 10 UT and 14 UT. The green arrow ranges from the image center to the position of the brightest pixel in the frame, hence illustrating the orientation of the crescent.

Stokes  $I$  imaging we used a crescent model (Tiede et al. 2022),

$$I(r, \theta) = I_0(1 - s \cos(\theta - \xi)) \frac{\delta(r - r_0)}{2\pi r_0}, \quad (18)$$

with the following parameters:  $I_0 = 0.6 \text{ Jy}$ ,  $s = 0.46$ , and  $r_0 = 22 \mu\text{as}$ . To account for dynamics roughly similar to rotating hotspot models (Tiede et al. 2020) we let the crescent rotate clockwise. One rotation period takes one hour which is roughly comparable to the flux variability timescale of the SGR A\* light curve (Wielgus et al. 2022). The synthetic ground truth image is presented in Fig. 3. To illustrate the orientation of the crescent, we also show a green arrow from the image center to the location

of the brightest pixel in the image in Fig. 3. For polarized movies we have to add polarization. For the sake of simplicity, here we used a simpler model to test the capabilities of dynamic polarimetry: we added a constant linear polarized structure at 10% (no circular polarization) with a rotating EVPA. To separate the dynamic polarimetric reconstruction from effects of the Stokes  $I$  imaging, the rotation of the EVPAs is counter-clockwise (rotation of Stokes  $I$  was clockwise) and has a different rotation period of two hours instead of one hour as for the Stokes  $I$  images.

As an additional model we also test a rapidly rotating crescent model with an orbital period time of twenty minutes. We show the ground truth movie in Fig. 4. The constant EVPA

## True Movie

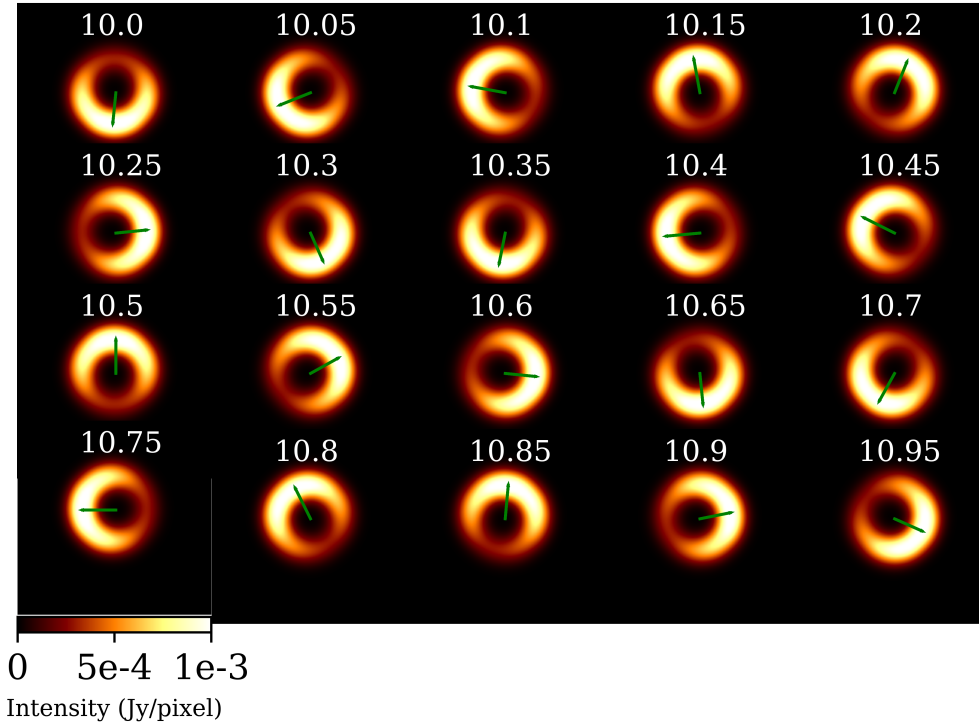


Fig. 4. True movie for fast rotating crescent.

pattern rotates counter-clockwise in one hour. The advance time between scans that is used for pointing and calibration limits the temporal resolution. For an array as sensitive as the ngEHT a smaller gap time might be possible. We therefore synthetically observed the rapidly rotating movie with a cycle of ten minutes of scientific observation (ten seconds of integration time) and a two-minute gap.

#### 4.2. Static polarization with EHT coverage

We fitted the scales to the uv-coverage first with the procedure outlined in Müller & Lobanov (2022) and Müller & Lobanov (2023): we searched for jumps in the sorted distribution of uv-distances that exceed a threshold, and we selected the radial scales accordingly. We defined nine radial scales and used four different angles, resulting in 36 scales to represent the uv-coverage. The Stokes  $I$  image was recovered with DoG-HiT (Müller & Lobanov 2022) using the multi-directional dictionaries introduced in (Müller & Lobanov 2023), as described in Sect. 3.1. As presented in Sect. 3.2, we then computed the multiresolution support. The multiresolution support is presented in Fig. 5. Some scales that are most sensitive to gaps in the uv-coverage are suppressed completely, while other scales encode various parts of the emission structure, for example the ring-like emission (scale 34 and scale 35), the extended emission structure (scale 30 and 32), the fine crescent structure (e.g., scale 4, 7, 9, 14, and 24), or the bright spot to the left of the crescent (e.g., scale 0, 2, and 10). The minimization to the polarized visibilities was done with the limited-memory

Broyden–Fletcher–Goldfarb–Shanno (BFGS) algorithm (Byrd et al. 1995), as implemented in Scipy (Jones et al. 2001). To assert global convergence, we blurred the Stokes  $Q$  and  $U$  image of the reconstruction with the nominal resolution and redo the minimization with a gradient descent procedure.

We show the final reconstruction result in Fig. 2. The reconstruction of the Stokes  $I$  image is relatively successful. The crescent-like shadow image is overall well recovered. However, there are some finer structures that are not recovered by DoG-HiT: the closing of the ring by a thin line toward the right and the fainter structure inside the ring. The linear polarized emission is overall very well recovered. The total fraction of linear polarized light and the overall direction of the electromagnetic vector position angles (EVPA) in the north–south direction are well recovered. The synthetic ground truth image contains a greater number of complex local structures for example a rotation of the EVPA in the bottom left of the image toward the east–west direction. This shift is partly visible in the recovered image as well, although the amount of rotation is smaller.

All in all, this example demonstrates that even for a very challenging and sparse array such as the EHT 2022 array the polarimetric reconstruction with support imaging is quite successful in both the overall structure, but also in the reconstruction of more localized polarimetric structures with a size of  $\approx 5 \mu\text{as}$ . Thus, similar to the DoG-HiT reconstruction for the Stokes  $I$  image, mr-support polarimetry seems to offer mild super-resolution. Interestingly, super-resolution and a good fit to the polarized visibilities is offered without introducing artifacts in the image. This demonstrates the power of the regularization approach.

Müller, H. and Lobanov, A. P.: A&A proofs, manuscript no. aa45393-22

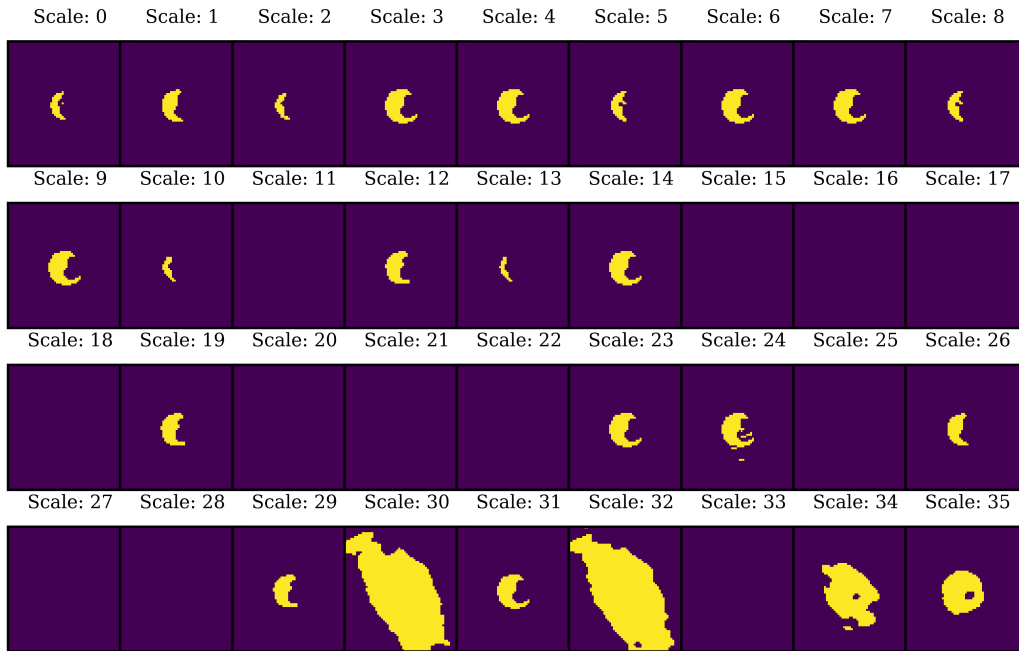


Fig. 5. Multiresolution support for the reconstruction of the static polarization example with EHT coverage.

### Recovered Movie

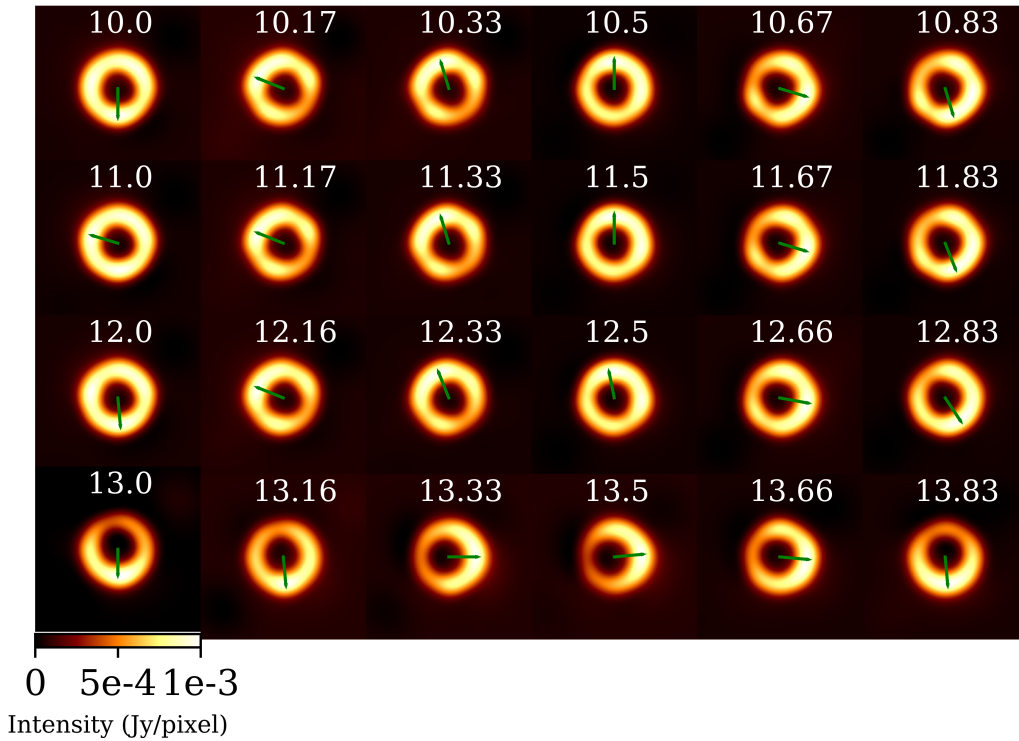


Fig. 6. Recovered solution (recovered with mr-support imaging) for slowly rotating crescent observed with the EHT.

## Recovered Movie

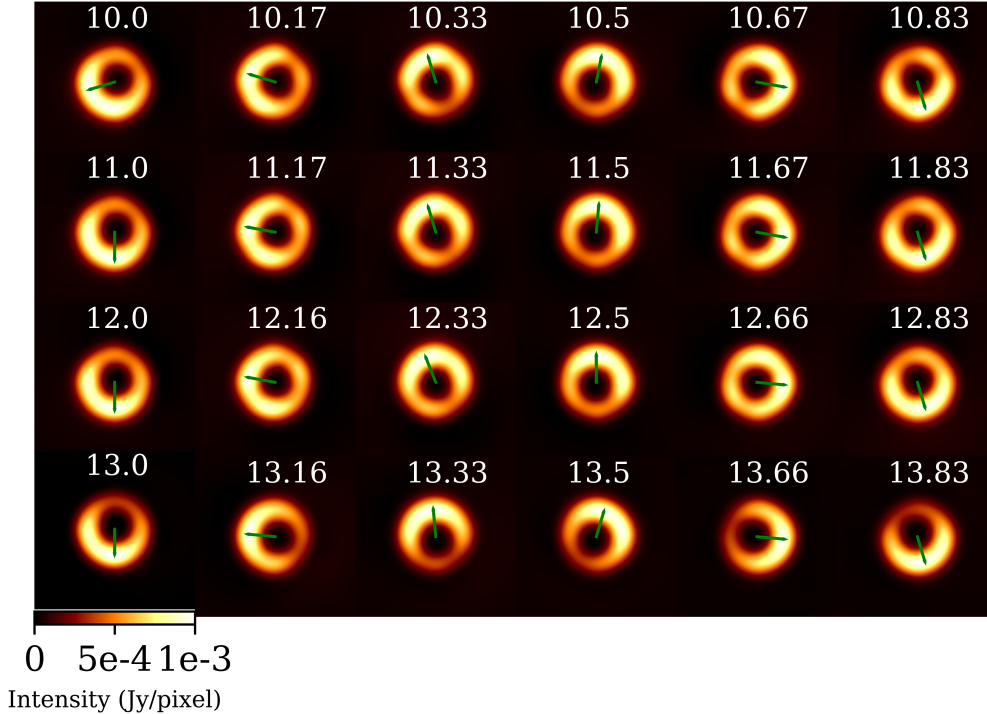


Fig. 7. Same as Fig. 6, but for slowly rotating crescent observed with the ngEHT.

#### 4.3. Dynamic Stokes I

The synthetic slowly rotating crescent movie was observed as described in Sect. 4.1 with a ten-minute cycle with EHT coverage. According to this temporal resolution, we cut the observation into frames with a length of ten minutes for the dynamic reconstruction. The reconstruction was then done with the mr-support approach in the best time window  $t \in [10 \text{ UT}, 14 \text{ UT}]$  (Farah et al. 2022) as outlined in Sect. 3.3. As a first step we fitted a symmetric ring model to the data, created a mean image with DoG-HiT with the fitted ring model as an initial guess, and then we solved sequentially for every frame by mr-support imaging with the support calculated from the mean. As an initial guess for the single frame imaging with mr-support imaging we used the reconstruction of the respectively preceding frame (or the mean in case of the first frame).

We present the reconstruction results in Fig. 6. The single frames all show a circular structure with a radius of  $\approx 22 \mu\text{s}$ . Moreover, nearly all frames have an asymmetry of a crescent. However, the crescent asymmetry is less prominent than in the true image. As for the true dynamic movie, we illustrate the orientation of the crescent by an arrow from the center to the brightest pixel in the reconstruction. Following the orientations of the recovered crescents in Fig. 6 a clear rotation with an orbital period of one hour is visible. The orientation of the recovered crescents match in most frames with the synthetic ground truth except for some notable exceptions at 11 UT (no asymmetry recovered at all), and 13.16 UT–13.5 UT (incorrect orientations). In particular the latter could be a consequence of taking the reconstruction at the preceding frame as an initial guess for the

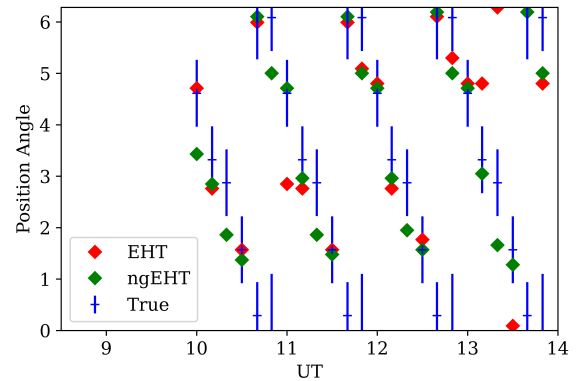


Fig. 8. True position angle (blue) and the recovered position angle recovered with mr-support imaging for an EHT configuration (red) and ngEHT configuration (green) for the slowly rotating crescent model. The error bars reflect the change in position angle in the true source model within a ten-minute scan (cycle length of synthetic observation).

next frame, and hence the false recovery at 13.16 UT also affects all the following frames.

We present in Fig. 7 the reconstruction result for a slowly rotating crescent with ngEHT coverage. The reconstruction of the crescent is excellent at every frame with high contrast images. The single-frame images do not show additional image artifacts. Although the additional ngEHT antennas have rather high thermal noise levels, the much improved density of the array effectively stabilizes against thermal noise. Strikingly the orientation of the crescents matches the ground truth very well. We

## Recovered Movie

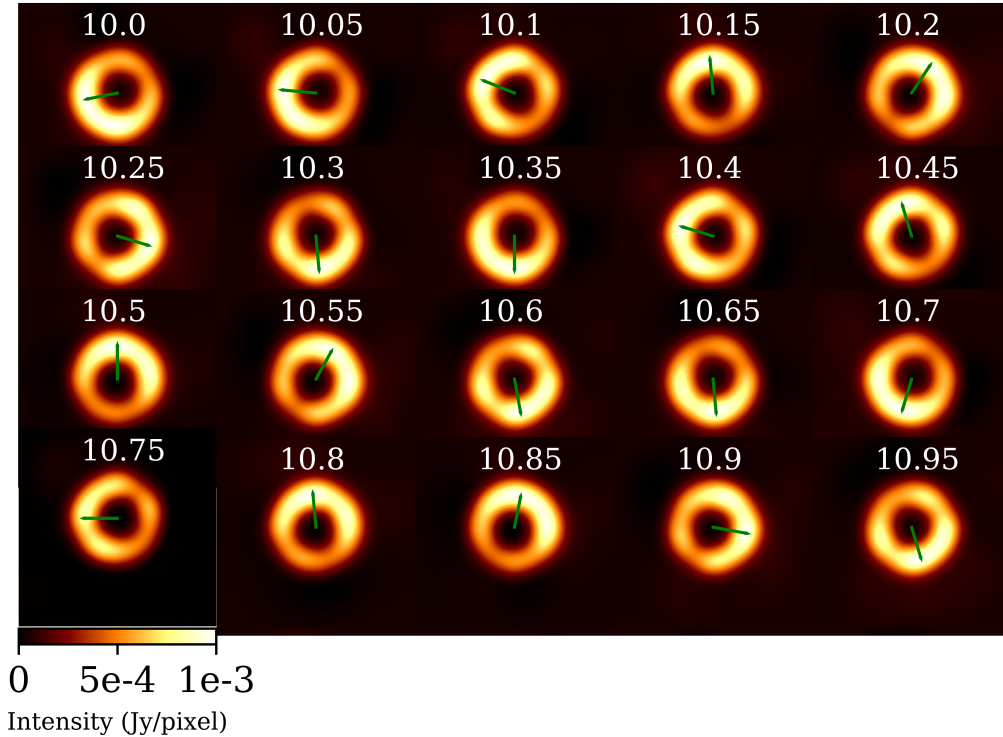


Fig. 9. Reconstruction of rapidly rotating crescent observed with the ngEHT.

present in Fig. 8 a comparison between the true position angles and the recovered ones with an error by the temporal smearing due to the scan length.

The ngEHT array is much denser than the EHT configuration of 2022. This enhances the possible temporal resolutions. We therefore also studied the possibility to observe faster rotating structures at the event horizon with the fast rotating crescent model. The dynamic reconstruction was done in this case in frames of three minutes in length. The faster orbital period and the shorter frame length complicate the reconstruction procedure: there are fewer observation points per single frame, which raises the problem of sparsity. Moreover, due to the shorter dynamical timescale and the smaller number of observing points per single frame, the scan-averaged visibility points worsen the signal-to-noise ratio by a factor of  $\sqrt{3}$  compared to the slower rotating crescent. The reconstruction results for dynamic Stokes  $I$  imaging with mr-support imaging are shown in Fig. 9. The crescent is observed at every frame. Additionally, the overall orientation matches quite well. However, the quality of the reconstruction decreases compared to the slowly rotating crescent, as can be expected: the asymmetry of the crescents is less clear and the orientation is slightly off by roughly 15 degrees in some frames.

All in all, we observe that with mr-support imaging we recover the correct image structure very well, including overall shadow feature, crescent asymmetry, and orientation, for most frames in the observation. Again, we note that these particular successful reconstructions do not suffer from introducing image artifacts despite the sparsity of the uv-coverage, especially in

single frame observations. This, once again, demonstrates the regularizing property of the mr-support approach.

#### 4.4. Dynamic polarimetry

As outlined in Sect. 3.4 we did the dynamic reconstruction of the Stokes  $I$  channel first. Hence, we copied the reconstructions from Sect. 4.3, and then added polarization frame by frame by mr-support imaging. Similar to our procedure presented in Sect. 4.2 we first minimized the data terms (fit to polarized visibilities) with a BFGS minimization procedure, blurred the reconstructed polarized images with the nominal resolution, and minimized the fit with a gradient descent procedure starting from the blurred image as an initial guess.

The reconstruction results in the time window  $t \in [10UT, 11UT]$  are presented in Fig. 10 for a slowly rotating crescent model with EHT coverage. The relatively simple polarized structure is well recovered in each frame. While the recovered images show some local variation from the overall orientation, the larger scale EVPA orientation matches for all frames. The fraction of polarized linearly polarized light is surprisingly well recovered. Again, despite some local variations in the recovered EVPA, the challenging reconstruction does not show image artifacts.

In Fig. 11 we present the reconstruction of the slowly rotating crescent observed with the ngEHT. The quality of the reconstruction improved compared to the reconstructions presented in Fig. 10. The global orientation of the EVPAs is well recovered

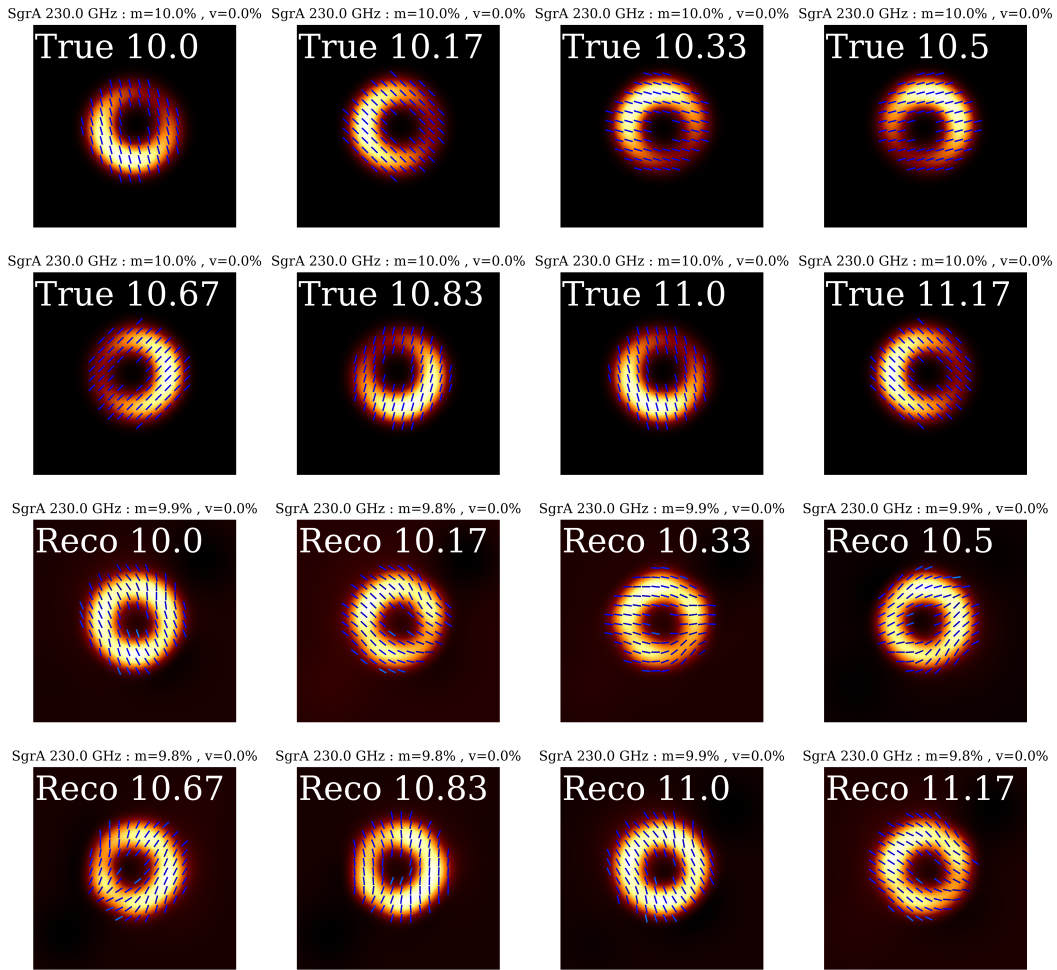


**Fig. 10.** True (upper panels) and recovered (lower panels) test images with full Stokes polarization for the slowly rotating crescent. The mr-support imaging approach recovers the true large-scale orientation of the EVPA.

for every frame. In the reconstructions with the EHT configuration we also observed some local variations from the overall polarimetric structure. These can no longer be observed in the reconstructions with ngEHT coverage.

We present the dynamic polarimetry reconstruction with mr-support imaging of the rapidly rotating crescent in Fig. 12. The reconstruction of the polarimetric structure (i.e., the rotation of the EVPAs) remains excellent. These results suggest that mr-support imaging could handle dynamic polarimetric structural features at the event horizon with realistic dynamic timescales.

#### 4.5. ngEHT analysis challenge

In addition to the rather simple synthetic data tests presented in the previous subsections, we show here the reconstructions by mr-support imaging for the third ngEHT Analysis challenge<sup>3</sup>. The ngEHT Analysis challenges are a series of semi-blind data challenges to evaluate the performance of algorithms for the planned ngEHT instrument (Roelofs et al. 2023). The ngEHT is a planned instrument to recover (polarimetric) movies at event horizon scales (Doeleman et al. 2019).

<sup>3</sup> <https://challenge.ngeht.org/>

The ground truth movies produced for the ngEHT Analysis challenge resemble the current theoretical state-of-the-art in simulations (Roelofs et al. 2023; Chatterjee et al. 2023). Here we present the reconstructions of a RIAF model of Sgr A\* (Broderick et al. 2016) with a shearing hotspot (Tiede et al. 2020) with hotspot parameters inspired by GRAVITY Collaboration (2018a). The data sets were observed with the EHT array and with the ngEHT arrays that we used for the geometric data sets as well. In contrast to the proof of concept with geometric models, the ngEHT challenge data contain the full set of data corruptions that may be expected from real observations (Roelofs et al. 2023) simulated with the SYMBA package (Roelofs et al. 2020) including atmospheric turbulence, atmospheric opacity, pointing offsets, a scattering screen, and thermal noise specific to each antenna. However, no polarization leakage was added to the data. For more information we refer to Roelofs et al. (2023) and the challenge website<sup>4</sup>. The data sets were network calibrated as it is standard in the EHT data processing (Event Horizon Telescope Collaboration 2022b). The ngEHT Analysis challenge is particularly well suited as a verification data set since the challenge

<sup>4</sup> <https://challenge.ngeht.org/>

Müller, H. and Lobanov, A. P.: A&A proofs, manuscript no. aa45393-22

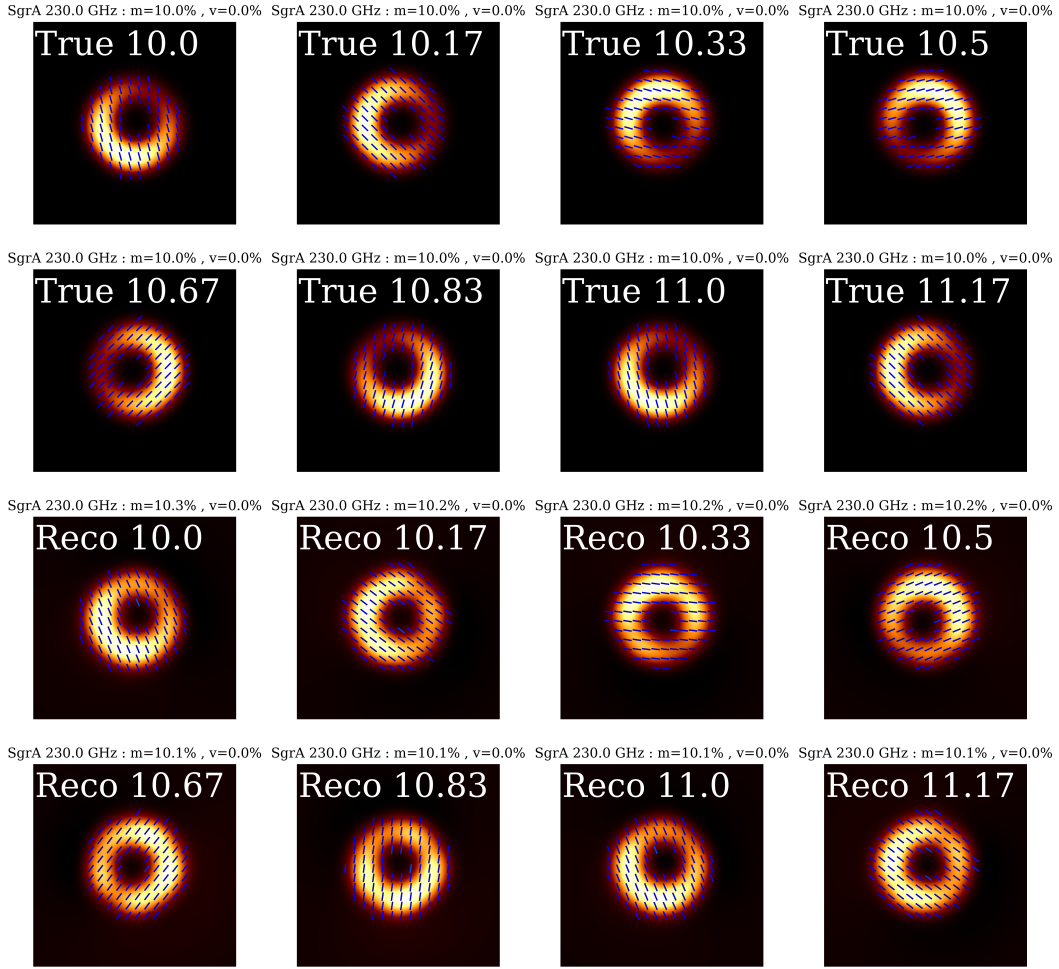


Fig. 11. Same as Fig. 10, but for slowly rotating crescent observed with the ngEHT.

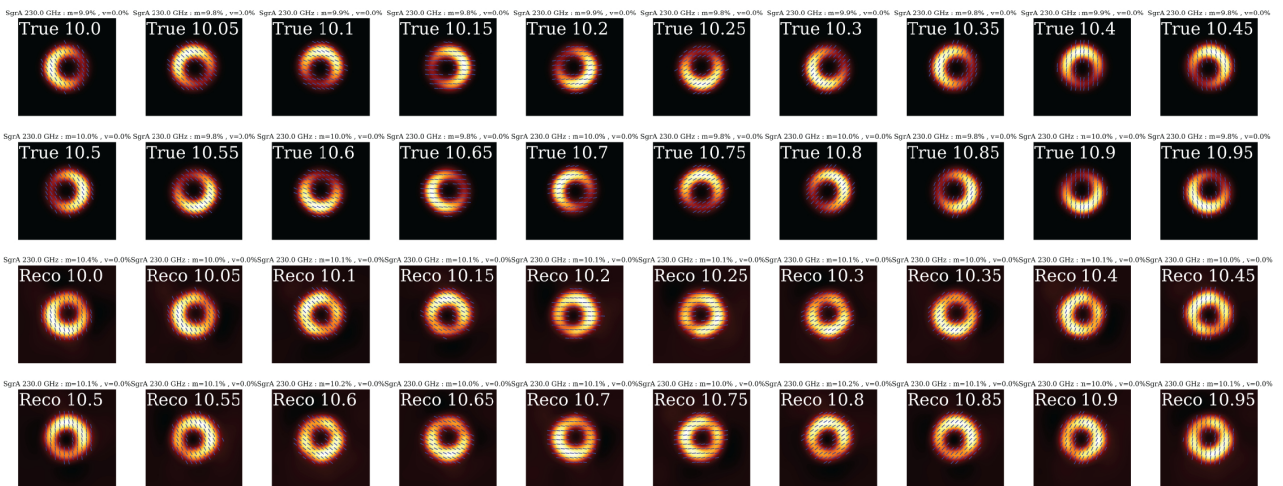
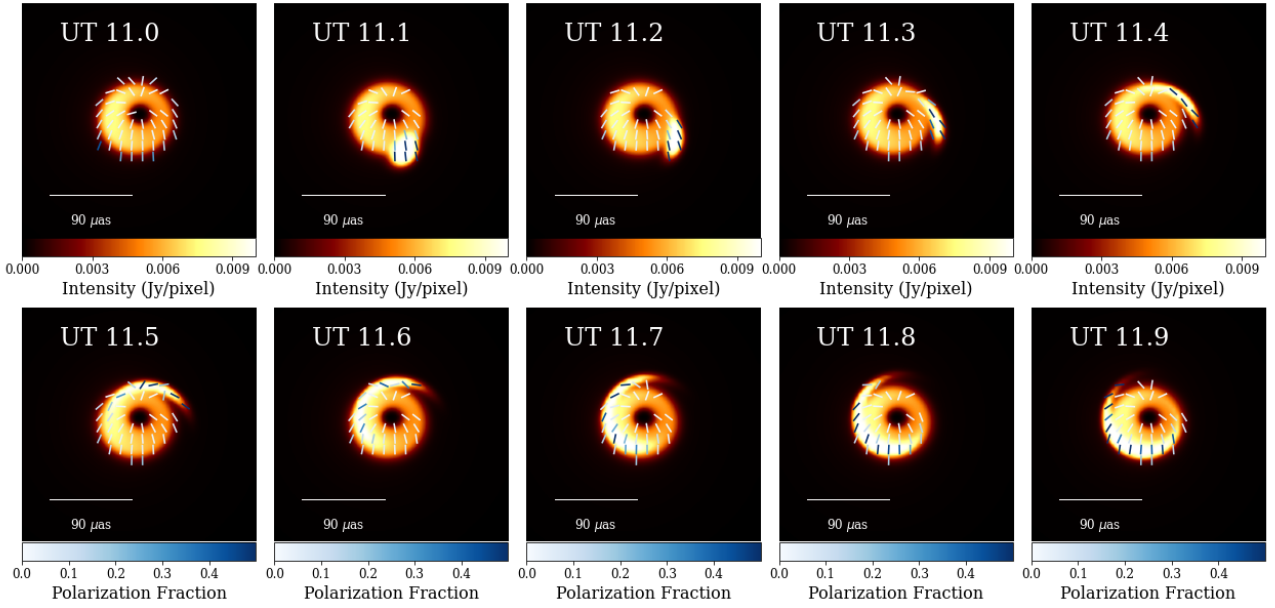
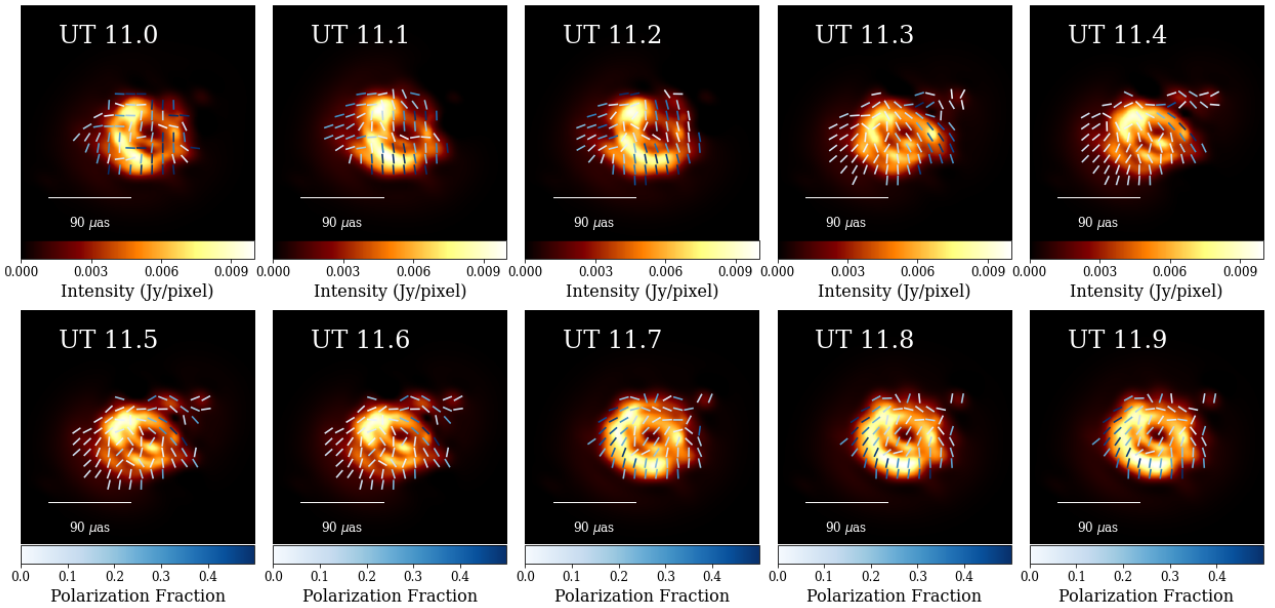


Fig. 12. Polarimetric reconstruction of fast rotating crescent with ngEHT coverage.



**Fig. 13.** Synthetic ground truth movie of Sgr A\* used for the third ngEHT Analysis challenge. The model is a RIAF model with a semianalytic shearing hotspot.



**Fig. 14.** Reconstruction of the movie plotted in Fig. 13 with mr-support imaging for the third ngEHT Analysis challenge.

was done blindly; neither the source files nor the specific data corruptions were made public to the analysis teams.

We show the ground truth movie in Fig. 13. A static (but not desattered) image was recovered by DoG-HiT with a systematic error budget of 2%. The static image is computed by DoG-HiT in a completely unsupervised way from closure quantities. We used this calibration-independent model to calibrate the data set on long time intervals (1 h). Next we calculated the multiresolution support and cut the image into frames of six minutes. The dynamic reconstruction was done with mr-support imaging. We self-calibrated the data set in every single

observing frame during the procedure. Then we added polarization in every frame.

The recovered movie is presented in Fig. 14. Moreover, we show magnified panels of selected frames in Fig. 15. The single frames all show a ring-like structure with a central depression. Compared to the ground truth frames, the reconstructed images have a worse quality due to the rapid variability, systematics, and sparse coverage. Moreover, an interstellar scattering screen was added to the data that was not removed during the imaging procedure. The reconstruction of the shearing hotspot motion is more challenging. We recover an approaching hotspot to the right of

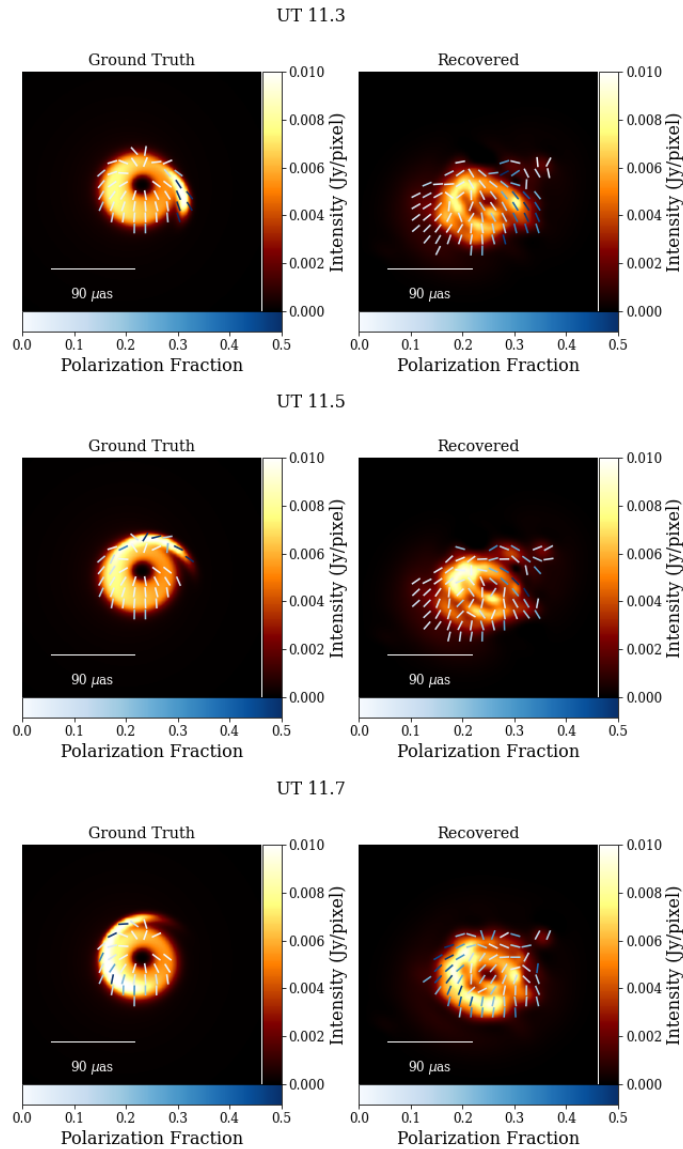


**Fig. 15.** Selected frames of reconstructions shown in Figs. 13 and 14 at times UT 11.3 (upper panels), UT 11.5 (middle panels), and UT 11.7 (lower panels).

the ring at UT 11.3 (upper panels in Fig. 15), an extended (polarized) tail to the northwest (top right) from UT 11.3 until UT 11.6 (middle panels in Fig. 15), and a clearly visible arc of larger intensity within the ring to the southeast (bottom left) from UT 11.7-UT 11.9 (bottom panels in Fig. 15). These features are consistent with the hotspot motion of the ground truth movie. While we recover some motion related to the hotspot motion, a continuously evolving movie was not recovered. This is a result of the rather bad simulated weather conditions and the observation cadence for the third challenge: the source was (synthetically) observed for ten minutes followed by a gap of ten minutes. While mr-support imaging sufficiently recovers some (scattered) hotspot related features in the frames that have observed visibilities, the algorithm does not contain an interpolation scheme to the scans without observations, it just assumes the starting point (i.e., the preceding frame). Hence, we do not recover an evolving

movie, but several frames (e.g., UT 11.5 and UT 11.6 or UT 11.7 until end) show the same image structure.

The synthetic ground truth polarization is less dynamic and hence easier to recover. We recover the overall radially-conic EVPA pattern in every frame with minor small-scale perturbations from the ground truth (which may also be related to the different Stokes  $I$  images). Moreover, the recovered polarization fraction matches the true one. As a more detailed feature we successfully recover a larger fractional polarization for the shearing hotspots that follows the hotspot motion.

The presented data set mimics one of the most challenging VLBI data analysis problems so far with various data corruptions, high frequencies (i.e., phase instabilities), fast dynamics and polarimetric structures, the need for super-resolution, and a sparse VLBI uv-coverage. As expected, the reconstruction quality with mr-support imaging is degraded compared to the

rather simple geometric data tests discussed above. However, the application already highlights the potential of mr-support imaging to do unsupervised, super-resolving, dynamical, and polarimetric imaging together. This presents a unique capability in the landscape of existing imaging algorithms by now, and in particular a domain of research in which CLEAN remains limited due to its lack of resolution, its high demand of human supervision and calibration, and the lack of support for dynamical reconstructions.

## 5. Conclusions and outlook

We presented in this manuscript a novel algorithmic approach to do static polarimetry, dynamic imaging and finally dynamic polarimetry. The approach was based on our previous works on multiscale imaging (Müller & Lobanov 2022, 2023) and the multiresolution support in particular. The multiresolution support encodes important information about the emission structure on one hand (which spatial scales are present in the image and where) and the uv-coverage on the other hand (which of these spatial scales is measured by baselines). Hence, the multiresolution support is well suited to introduce regularization for challenging extensions to the standard VLBI imaging problem in the spirit of constrained minimization: we optimize the fit to the respective data terms (chi-squared to frame-by-frame visibilities or to polarized visibilities), but vary the wavelet coefficients only in the multiresolution support.

We demonstrated with applications to simple geometric synthetic observations the power of this approach. The mr-support constraint suppressed the introduction of image artifacts, and hence provided ample regularization. Moreover, the approach is flexible enough to allow for the reconstruction of both dynamically evolving structures and polarimetric structures. Moreover, the blind application to more complex movies of the third ngEHT Analysis challenges demonstrated that the algorithm may also provide reasonable reconstructions with real data corruptions in one of the most challenging VLBI imaging problems, although the quality of the reconstruction is degraded.

Mr-support imaging shares the basic advantage of multiscale approaches that are fitted to the uv-coverage. The static reconstructions are done with DoG-Hit which is completely data driven and largely automatic without many hyperparameters (Müller & Lobanov 2022). The same applies for the extension to dynamics and polarimetric quantities. No further specific regularization terms (with corresponding weights) were introduced, rather the reconstruction was regularized again by the data-driven multiresolution support, which is determined by the uv-coverage and baseline-noise. Hence, mr-support imaging is blind and unbiased as well. However, we recognized an important bottleneck for the dynamic reconstructions with mr-support imaging: the static average image needs to approximate the true time-averaged image quite well.

An extension to RML approaches to dynamic imaging (i.e., the addition of temporal regularizers) is straightforward as well. We note that due to the lack of regularization parameters controlling the temporal correlation, mr-support imaging basically calculates images with rich structures from the extreme sparsity of a single scan independently of preceding and proceeding scans. That indicates that the multiresolution support information is a rather strong prior information that, once a reasonable static model is established, allows for the handling of extreme sparsity in the data.

The geometric test observations tested throughout this study are rather simple. First, we neglected circular polarization for

the purpose of simplicity. We note that we only added thermal noise to the observations and no phase and amplitude errors. This does not affect the reconstruction of the static Stokes  $I$  image (neither for a static source nor for a dynamically evolving source) since DoG-Hit uses the closure quantities as data terms only (Müller & Lobanov 2022). However, phase and amplitude calibration errors could affect the subsequent mr-support imaging rounds since for every frame the (polarized) visibilities are used instead of the closure quantities. Hence, we assume that it is possible to solve for the (polarized) self-calibration with the time-averaged mean image. This does not necessarily have to be true, but might be a good approximation when the dynamic timescale of the source and the dynamic timescale of the gain-variability are different allowing a gain self-calibration with the mean image (compare, e.g., Wielgus et al. 2022; Event Horizon Telescope Collaboration 2022b).

Moreover, while a rotating crescent movie might be a good approximation to a rotating hotspot model in the first instance, the model is only a rough approximation to the range of models for the dynamics at the horizon scale. The same applies to the rather simple polarization model used. We therefore tested the algorithm in the blind third ngEHT Analysis challenge as well. Due to the systematic errors added to the synthetic data, the reconstructions are worse than in the previous data tests; however, mr-support imaging, for the first time, is able to recover super-resolved polarized movies in an unsupervised way. This is a unique capability among all currently existing VLBI imaging algorithms. Furthermore, we expect further significant improvements from including a temporal regularizer in the dynamic imaging and from more sophisticated strategies for the static image reconstruction, in particular from frameworks that already demonstrated to be able to recover fast dynamics such as ehtim or StarWarps.

Finally, the application of the same ground truth movie to a possible ngEHT array configuration demonstrates the improvements that the ngEHT project will bring to dynamic reconstructions. The quality of the fits to Stokes  $I$  and polarimetric properties improves. With a ngEHT configuration it is even possible to recover structural patterns on dynamic timescales of about  $\sim 10$ – $20$  min and therefore what can be expected from real observations.

*Acknowledgements.* We thank the team from the ngEHT Analysis challenge lead by Freek Roelofs, Lindy Blackburn and Greg Lindahl for the chance to use and publish their synthetic data set for this work. Special thanks goes in particular to Paul Tiede for providing the RIAFSPOT model of SGR A\*. HM received financial support for this research from the International Max Planck Research School (IMPRS) for Astronomy and Astrophysics at the Universities of Bonn and Cologne. This work was partially supported by the M2FINDERS project funded by the European Research Council (ERC) under the European Union's Horizon 2020 Research and Innovation Programme (Grant Agreement No. 101018682). Our imaging pipeline and our software is available online as MrBeam software tool (<https://github.com/hmuellergoe/mrbeam>). Our software makes use of the publicly available ehtim (Chael et al. 2018), regpy (<https://github.com/regpy/regpy>), and WISE software packages (Mertens & Lobanov 2015).

## References

- Akiyama, K., Ikeda, S., Pleau, M., et al. 2017a, *AJ*, 153, 159
- Akiyama, K., Kuramochi, K., Ikeda, S., et al. 2017b, *ApJ*, 838, 1
- Arras, P., Frank, P., Leike, R., Westermann, R., & EnBlin, T. A. 2019, *A&A*, 627, A134
- Arras, P., Bester, H. L., Perley, R. A., et al. 2021, *A&A*, 646, A84
- Bhatnagar, S., & Cornwell, T. J. 2004, *A&A*, 426, 747
- Blandford, R. D., & Znajek, R. L. 1977, *MNRAS*, 179, 433
- Bouman, K. L., Johnson, M. D., Dalca, A. V., et al. 2018, *IEEE Transac. Comput. Imaging*, 4, 512

Müller, H. and Lobanov, A. P.: A&amp;A proofs, manuscript no. aa45393-22

- Bower, G. C., Markoff, S., Dexter, J., et al. 2015, *ApJ*, 802, 69
- Broderick, A. E., Fish, V. L., Johnson, M. D., et al. 2016, *ApJ*, 820, 137
- Broderick, A. E., Gold, R., Karami, M., et al. 2020a, *ApJ*, 897, 139
- Broderick, A. E., Pesce, D. W., Tiede, P., Pu, H.-Y., & Gold, R. 2020b, *ApJ*, 898, 9
- Broderick, A. E., Gold, R., Georgiev, B., et al. 2022, *ApJ*, 930, 1
- Byrd, R. H., Lu, P., & Nocedal, J. 1995, *SIAM J. Sci. Stat. Comput.*, 16, 1190
- Chael, A. A., Johnson, M. D., Narayan, R., et al. 2016, *ApJ*, 829, 11
- Chael, A. A., Johnson, M. D., Bouman, K. L., et al. 2018, *ApJ*, 857, 23
- Chael, A., Chan, C.-K., Klbouman, et al. 2022, <https://doi.org/10.5281/zenodo.6519440>
- Chatterjee, K., Chael, A., Tiede, P., et al. 2023, *Galaxies*, 11, 12
- Clark, B. G. 1980, *A&A*, 89, 377
- Cornwell, T. J. 2008, *IEEE J. Selected Topics Signal Process.*, 2, 793
- Doeleman, S., Blackburn, L., Dexter, J., et al. 2019, *BAAS*, 51, 256
- Emami, R., Tiede, P., Doeleman, S. S., et al. 2023, *Galaxies*, 11, 12
- Event Horizon Telescope Collaboration (Akiyama, K., et al.) 2019a, *ApJ*, 875, L1
- Event Horizon Telescope Collaboration (Akiyama, K., et al.) 2019b, *ApJ*, 875, L4
- Event Horizon Telescope Collaboration (Akiyama, K., et al.) 2021a, *ApJ*, 910, 43
- Event Horizon Telescope Collaboration (Akiyama, K., et al.) 2021b, *ApJ*, 910, 48
- Event Horizon Telescope Collaboration (Akiyama, K., et al.) 2022a, *ApJ*, 930, L12
- Event Horizon Telescope Collaboration (Akiyama, K., et al.) 2022b, *ApJ*, 930, L14
- Farah, J., Galison, P., Akiyama, K., et al. 2022, *ApJ*, 930, 1
- Garsden, H., Girard, J. N., Starck, J. L., et al. 2015, *A&A*, 575, A90
- Gómez, J. L., Roca-Sogorb, M., Agudo, I., Marscher, A. P., & Jorstad, S. G. 2011, *ApJ*, 733, 11
- Gómez, J. L., Lobanov, A. P., Bruni, G., et al. 2016, *ApJ*, 817, 96
- GRAVITY Collaboration (Abuter, R., et al.) 2018a, *A&A*, 615, L15
- GRAVITY Collaboration (Abuter, R., et al.) 2018b, *A&A*, 618, L10
- Hardee, P., Mizuno, Y., & Nishikawa, K.-I. 2007, *Ap&SS*, 311, 281
- Högbom, J. A. 1974, *A&AS*, 15, 417
- Hovatta, T., Lister, M. L., Aller, M. F., et al. 2012, *AJ*, 144, 105
- Ikeda, S., Tazaki, F., Akiyama, K., Hada, K., & Honma, M. 2016, *PASJ*, 68, 45
- Johnson, M. D., Fish, V. L., Doeleman, S. S., et al. 2015, *Science*, 350, 1242
- Johnson, M. D., Bouman, K. L., Blackburn, L., et al. 2017, *ApJ*, 850, 172
- Johnson, M. D., Akiyama, K., Blackburn, L., et al. 2023, *Galaxies*, 11, 61
- Jones, E., Oliphant, T., Peterson, P., et al. 2001, SciPy: Open source scientific tools for Python [Online; accessed 2015-08-25]
- Kramer, J. A., & MacDonald, N. R. 2021, *A&A*, 656, A143
- Mertens, F., & Lobanov, A. P. 2015, *A&A*, 574, A67
- Müller, H., & Lobanov, A. P. 2022, *A&A*, 666, A137
- Müller, H., & Lobanov, A. P. 2023, *A&A*, 672, A26
- Narayan, R., & Nityananda, R. 1986, *ARA&A*, 24, 127
- Palumbo, D. C. M., Doeleman, S. S., Johnson, M. D., Bouman, K. L., & Chael, A. A. 2019, *ApJ*, 881, 62
- Pötzl, F. M., Lobanov, A. P., Ros, E., et al. 2021, *A&A*, 648, A82
- Rau, U., & Cornwell, T. J. 2011, *A&A*, 532, A71
- Raymond, A. W., Palumbo, D., Paine, S. N., et al. 2021, *ApJS*, 253, 5
- Ricci, L., Boccardi, B., Nokhrina, E., et al. 2022, *A&A*, 664, A166
- Roelofs, F., Janssen, M., Natarajan, I., et al. 2020, *A&A*, 636, A5
- Roelofs, F., Blackburn, L., Lindahl, G., et al. 2023, *Galaxies*, 11, 12
- Schwab, F. R. 1984, *AJ*, 89, 1076
- Starck, J.-L., Murtagh, F., & Fadili, J. 2015, *Sparse Image and Signal Processing: Wavelets and Related Geometric Multiscale Analysis*, 2nd edn (Cambridge: Cambridge University Press), 1
- Thompson, A. R., Moran, J. M., & Swenson, George W., J. 2017, *Interferometry and Synthesis in Radio Astronomy*, 3rd edn. (Berlin: Springer)
- Tiede, P., Pu, H.-Y., Broderick, A. E., et al. 2020, *ApJ*, 892, 132
- Tiede, P., Broderick, A. E., & Palumbo, D. C. M. 2022, *ApJ*, 925, 122
- Wakker, B. P., & Schwarz, U. J. 1988, *A&A*, 200, 312
- Wiaux, Y., Jacques, L., Puy, G., Scaife, A. M. M., & Vanderghaynst, P. 2009, *MNRAS*, 395, 1733
- Wielgus, M., Marchili, N., Martí-Vidal, I., et al. 2022, *ApJ*, 930, L19
- Zamaninasab, M., Clausen-Brown, E., Savolainen, T., & Tchekhovskoy, A. 2014, *Nature*, 510, 126

### Appendix A: Wavelet dictionaries

This section is adapted from Müller & Lobanov (2023). The dictionaries used in this paper are as follows:

$$\begin{aligned}
 \Psi^{DoG} : I \mapsto & [G_{\sigma_0}^r * I - G_{\sigma_0, \sigma_1, \alpha_0}^e * I, G_{\sigma_0}^r * I - G_{\sigma_0, \sigma_1, \alpha_1}^e * I, \dots, G_{\sigma_0}^r * I - G_{\sigma_0, \sigma_1, \alpha_{N-1}}^e * I, \sum_{i=0}^{N-1} G_{\sigma_0, \sigma_1, \alpha_i}^e * I - G_{\sigma_1}^r * I, \\
 & G_{\sigma_1}^r * I - G_{\sigma_1, \sigma_2, \alpha_0}^e * I, \quad \dots \quad , G_{\sigma_1}^r * I - G_{\sigma_1, \sigma_2, \alpha_{N-1}}^e * I, \sum_{i=0}^{N-1} G_{\sigma_1, \sigma_2, \alpha_i}^e * I - G_{\sigma_2}^r * I, \\
 & G_{\sigma_2}^r * I - G_{\sigma_2, \sigma_3, \alpha_0}^e * I, \quad \dots \quad , G_{\sigma_2}^r * I - G_{\sigma_2, \sigma_3, \alpha_{N-1}}^e * I, \sum_{i=0}^{N-1} G_{\sigma_2, \sigma_3, \alpha_i}^e * I - G_{\sigma_3}^r * I, \\
 & \vdots \\
 & G_{\sigma_{J-1}}^r * I - G_{\sigma_{J-1}, \sigma_J, \alpha_0}^e * I, \quad \dots \quad , G_{\sigma_{J-1}}^r * I - G_{\sigma_{J-1}, \sigma_J, \alpha_{N-1}}^e * I, \sum_{i=0}^{N-1} G_{\sigma_{J-1}, \sigma_J, \alpha_i}^e * I - G_{\sigma_J}^r * I, \\
 & G_{\sigma_J}^r * I].
 \end{aligned}$$

Here  $G_{\sigma}^r$  denotes a radial Gaussian function with a standard deviation  $\sigma$  and  $G_{\sigma_1, \sigma_2, \alpha}^e$  an elliptical Gaussian with major semiaxis  $\sigma_1$ , minor semiaxis  $\sigma_2$ , and angle  $\alpha$ . The DoB dictionary is composed in the same way by replacing Gaussians with spherical Bessel functions,

$$\begin{aligned}
 \Psi^{DoB} : I \mapsto & [\tilde{J}_{\tilde{\sigma}_0}^r * I - \tilde{J}_{\tilde{\sigma}_0, \tilde{\sigma}_1, \alpha_0}^e * I, \tilde{J}_{\tilde{\sigma}_0}^r * I - \tilde{J}_{\tilde{\sigma}_0, \tilde{\sigma}_1, \alpha_1}^e * I, \dots, \tilde{J}_{\tilde{\sigma}_0}^r * I - \tilde{J}_{\tilde{\sigma}_0, \tilde{\sigma}_1, \alpha_{N-1}}^e * I, \sum_{i=0}^{N-1} \tilde{J}_{\tilde{\sigma}_0, \tilde{\sigma}_1, \alpha_i}^e * I - \tilde{J}_{\tilde{\sigma}_1}^r * I, \\
 & \tilde{J}_{\tilde{\sigma}_1}^r * I - \tilde{J}_{\tilde{\sigma}_1, \tilde{\sigma}_2, \alpha_0}^e * I, \quad \dots \quad , \tilde{J}_{\tilde{\sigma}_1}^r * I - \tilde{J}_{\tilde{\sigma}_1, \tilde{\sigma}_2, \alpha_{N-1}}^e * I, \sum_{i=0}^{N-1} \tilde{J}_{\tilde{\sigma}_1, \tilde{\sigma}_2, \alpha_i}^e * I - \tilde{J}_{\tilde{\sigma}_2}^r * I, \\
 & \tilde{J}_{\tilde{\sigma}_2}^r * I - \tilde{J}_{\tilde{\sigma}_2, \tilde{\sigma}_3, \alpha_0}^e * I, \quad \dots \quad , \tilde{J}_{\tilde{\sigma}_2}^r * I - \tilde{J}_{\tilde{\sigma}_2, \tilde{\sigma}_3, \alpha_{N-1}}^e * I, \sum_{i=0}^{N-1} \tilde{J}_{\tilde{\sigma}_2, \tilde{\sigma}_3, \alpha_i}^e * I - \tilde{J}_{\tilde{\sigma}_3}^r * I, \\
 & \vdots \\
 & \tilde{J}_{\tilde{\sigma}_{J-1}}^r * I - \tilde{J}_{\tilde{\sigma}_{J-1}, \tilde{\sigma}_J, \alpha_0}^e * I, \quad \dots \quad , \tilde{J}_{\tilde{\sigma}_{J-1}}^r * I - \tilde{J}_{\tilde{\sigma}_{J-1}, \tilde{\sigma}_J, \alpha_{N-1}}^e * I, \sum_{i=0}^{N-1} \tilde{J}_{\tilde{\sigma}_{J-1}, \tilde{\sigma}_J, \alpha_i}^e * I - \tilde{J}_{\tilde{\sigma}_J}^r * I, \\
 & \tilde{J}_{\tilde{\sigma}_J}^r * I],
 \end{aligned}$$

with radial spherical Bessel function  $\tilde{J}^r$  and elliptical Bessel function  $\tilde{J}^e$ .

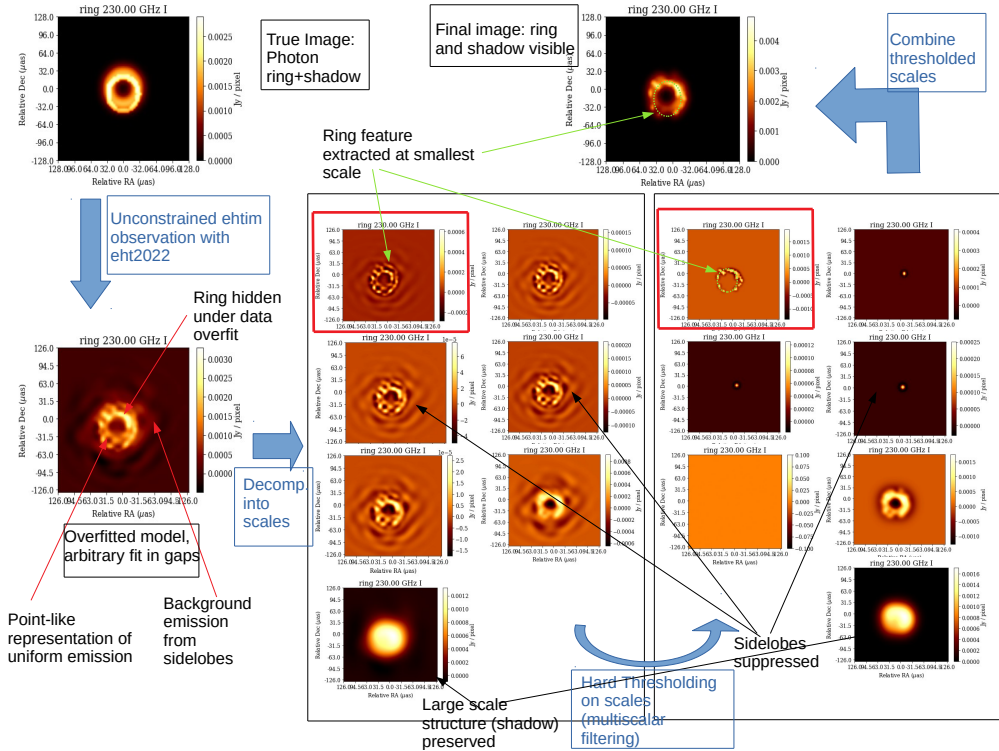


Figure 3.21: Schematic illustration of the multiround pipeline adapted for DoG-HiT.

### 3.5 Imaging Pipeline

DoG-HiT could be applied directly to the observed data set. However, we find that it performs best with a multistep imaging pipeline that was first proposed in Müller & Lobanov (2022). We present a schematic overview of this pipeline in Fig. 3.21. With ongoing developments, e.g. the multidirectional dictionaries and the dictionary-switch proposed in Müller & Lobanov (2023a) or a total flux calibration step, we updated our data analysis pipeline since its initial invention. The new pipeline was outlined in Müller & Lobanov (2023c). The following text in this subsection are two excerpts from chapter 2.1. and chapter 2.3 of that manuscript adapted for the layout of this dissertation.

<sup>3</sup> “For imaging we want to fit the observed visibilities (data-fidelity) with a clean model (i.e. no sidelobes) with the least number of independent model parameters while no image features corresponding to Fourier coefficients in the gaps in the uv-coverage should be induced. Hence, we proposed a compressed sensing approach for DoG-HiT (Müller & Lobanov 2022):

$$\hat{\mathcal{I}} \in \operatorname{argmin}_{\mathcal{I}} \left[ \chi_{\text{cph}}^2(\Gamma\mathcal{I}, V) + \chi_{\text{cla}}^2(\Gamma\mathcal{I}, V) + \alpha \cdot \|\mathcal{I}\|_{l_0} + R_{\text{flux}}(\mathcal{I}, f) \right], \quad (3.4)$$

<sup>3</sup>From Müller & Lobanov (2023c), Sec. 2.1

where  $\mathcal{I}$  is the array of wavelet coefficients,  $\alpha$  is the regularization parameter balancing the data fidelity and sparsity promoting penalization, and  $R_{\text{flux}}$  is an indicator function total flux constraint for the total flux  $f$ .  $\Gamma$  denotes the wavelet dictionary, and as before  $V$  the observed visibilities. We use the fit quality to the closure phases  $\chi_{\text{cph}}^2$  and logarithm of closure amplitudes  $\chi_{\text{cla}}^2$  respectively such that the reconstruction is independent from antenna based gains. As visible from Eq. (3.4), we compose the image from multiscale functions that are fitted to the uv-coverage and use a sparsity promoting penalization  $\|\cdot\|_{l_0}$  penalty term on the wavelet coefficients to suppress any wavelet scales mostly sensitive to the gaps in the uv-coverage.”

<sup>4</sup> “While in principle Eq. (3.4) could be minimized directly, more accurate reconstruction were obtained by a multiround imaging pipeline for Stokes I imaging first proposed in Müller & Lobanov (2022). However, the practical application of this approach Kim et al. (2023); Roelofs et al. (2023) has revealed the need to refine this imaging strategy as follows:

1. First we find a proper initial guess.
  - We do an unpenalized reconstruction with the software package *ehtim* first, i.e. we use amplitudes, closure phases and closure amplitudes and deactivate any regularization terms except for the total flux regularization. The computed solution  $I^1$  works as an initial guess, but still shows imaging artifacts due to missing regularization.
  - Next we find a multiscale representation of the initial guess. Due to the completeness property DoB-wavelet dictionaries Müller & Lobanov (2023a), it is a viable parametrization to copy  $I^1$  at every scale, i.e.  $\mathcal{I}^1 = \{I^1, I^1, \dots, I^1\}$
  - Then we use a grid-search to find an initial guess for the minimization of Eq. (3.4). The  $\|\cdot\|_{l_0}$  penalty term effectively computes a hard thresholding step (proximal-point operator of the  $l_0$ -norm). We therefore minimize Eq. (3.4) on a grid of predefined hard threshold parameters, allowed to vary from scale to scale:  $\mathcal{I}^2$
2. Now we do the DoG-HiT imaging step. Up to now DoB-wavelets were used to fit the observed visibilities. Naturally we switch to DoG-wavelets now, as described in Müller & Lobanov (2023a), by copying the guess  $\mathcal{I}^2$ , but replacing the dictionary. We then minimize Eq. (3.4) directly with the forward-backward splitting algorithm developed

---

<sup>4</sup>From Müller & Lobanov (2023c), Sec. 2.3

in Müller & Lobanov (2022) and recover the guess image by applying the wavelet dictionary  $\Gamma$  to the array of wavelet coefficients:  $I^3 = \Gamma \mathcal{I}^3$ .

3. The result can be further refined in alternate imaging and calibration rounds
  - We calibrate the total flux, since the closure quantities are invariant against rescaling array with a constant value. We compute the fit of the guess solution  $\Gamma [\delta \mathcal{I}^3]$  to the amplitudes with a varying constant parameter  $\delta \in \mathbb{R}$ , peaking around the rescaling parameter  $\delta_{\text{best}}$  that is necessary to reach the correct total flux. Finally, we do phase-self-calibration.
  - As a byproduct of step 2 we get a representation of the multiresolution support (Müller & Lobanov 2023b). It is expressed as a set of statistically significant wavelet coefficients (see Mertens & Lobanov 2015, for an application in astrophysical context). This information is used in further imaging rounds as constrained minimization prior, i.e. we fit the observed visibilities but vary only coefficients in the multiresolution support.
  - We add amplitudes to the array of observables and do imaging starting from  $\delta_{\text{best}} I^3$  as an initial guess with the constrained minimization approach with the multiresolution support. After amplitude and phase calibration, we replace closure phases and closure amplitudes by full visibilities and redo the minimization.”

### 3.6 Software

DoG-HiT and DoB-CLEAN have been implemented in the novel software package *MrBeam*. *MrBeam* implements an interface between *regpy* for iterative regularization methods in general (Regpy 2019), *ehtim* for the handling of VLBI data sets (Chael et al. 2016) and *WISE* for the handling of multiscalar transforms (Mertens & Lobanov 2015). In particular, we extended the functionality of *regpy* by tools of convex optimization. *MrBeam* is written in python in an object-oriented paradigm. The modularity of *MrBeam* allows for quick adaption and application also outside of VLBI. The main classes of *regpy* (domains, operators and solver) treat the various components of an inverse problem independently. Hence, the same solver that were developed in this dissertation, are easily transferable to other inverse problems as long as an implementation of the forward problem exists (as long with its derivative, the adjoint of the derivative and the proximal-operator). Moreover, an automatic internal handling of operator and

functional combinations (chaining, linear combinations, definition of operators on product spaces etc.) allows for simple code writing on the top-level. The most important features and capabilities of *MrBeam* can be summarized as follows:

- *MrBeam* and *regpy* implement the basic tools of inverse problems in a general setting. As already mentioned, only a generic implementation of the forward operator is needed. All solvers that are implemented in *scipy*, and additionally advanced smooth solvers (Gradient descent, iterative Gauss-Newton, Newton-CG, Landweber, Lanczos-Preconditioned Newton, ...) and convex optimization algorithms are available (e.g. forward-backward splitting, FISTA, Douglas-Rachford, ...).
- *MrBeam* implements explicitly the new algorithm DoG-HiT (Müller & Lobanov 2022). It provides a top-set handler for easy coding.
- DoB-CLEAN (Müller & Lobanov 2023a) and CLEAN are available in *MrBeam*. *MrBeam* provides an interactive interface inspired by *Difmap*, but with the plotting options of *ehtim*, to allow a convenient way of working.
- *MrBeam* supports full polarimetric imaging and dynamical imaging with a multiscalar approach as well (Müller & Lobanov 2023b).
- *MrBeam* is fully compatible with *ehtim*. Thus, it can make use of the rich functionality provided by *ehtim*, such as dynamic imaging (Bouman et al. 2018), or multifrequency imaging (Chael et al. 2023). Vice versa, *MrBeam* can be installed as an add-on package to *ehtim*. It extends the functionality of *ehtim* by multiscalar penalty terms, an advanced handling of domains by Gram matrices (mimicking the correlation matrices in Bayesian methods) and a wide range of convex solvers that are not available in *ehtim* right now.
- *MrBeam* provides an extension point to neural networks implemented in *keras* or *tensorflow* as well. Additionally, support for genetic algorithms and particle swarm optimization is build in.
- *MrBeam* has a tested parallelization strategy implemented.

Deriving from their high adaptability, *MrBeam* and *regpy* have found applications also outside of VLBI with necessary modifications. We like to mention in particular the *reglyman* software that we developed for Ly $\alpha$  forest tomography (Müller et al. 2020, 2021) and the search for fuzzy dark matter (Hamaide et al. 2022). For more details we refer to chapter 5.4.1 and chapter 5.4.2.

### 3.7 Conclusions

We shall summarize the main advantages of DoG-HiT here, deriving from a detailed summary of the algorithm presented in Müller & Lobanov (2023c). We therefore print another excerpt of this manuscript here adapted to the layout of the dissertation.

“We benchmarked the performance of DoG-HiT against CLEAN in Müller & Lobanov (2022), see also Fig. 1 and Fig. 2 [*in Müller & Lobanov (2023c)*]. DoG-HiT performs better than CLEAN in terms of accuracy and resolution. Moreover, DoG-HiT introduces an effective regularization through its sparsity promoting regularization approach and solves the disparity between a model and a final image necessarily inherent to CLEAN reconstructions. Furthermore, we demonstrated in Müller & Lobanov (2023a) that multiscale and multidirectional wavelet sparsity approaches (such as DoB-CLEAN and DoG-HiT) also have the potential to outperform CLEAN and classical MS-CLEAN Cornwell (2008) in terms of wide-field imaging, i.e. in the uniform representation of extended emission. Hence, DoG-HiT effectively deals with the most notorious limitations of CLEAN.

DoG-HiT presents a significant step towards unsupervised imaging. Since the regularization term (sparsity of wavelet coefficients of a wavelet dictionary fitted to the uv-coverage) is data-driven and chosen completely automatically, there is only one free parameter in the objective functional (the regularization parameter  $\alpha$ ), thus making extended parameter surveys needless. Moreover, benchmarking of DoG-HiT against state-of-the-art imaging RML methods demonstrates that DoG-HiT allows for reconstructions of the same quality (resolution) or sometimes even better quality than RML methods (extended emission, dynamic range), although the regularizer landscape is considerably simpler. DoG-HiT requires the evaluation of a fast Fourier transform and an application of multiscale dictionary at every iteration. Since the wavelet dictionary has to be allocated only once before the iterations start and the evaluation of the wavelet dictionary is only a matrix-array operation, DoG-HiT remains comparable fast to RML methods, significantly outperforming CLEAN.

DoG-HiT provides the multiresolution support as a byproduct and this has been proven beneficial in the reconstruction of dynamic movies and polarimetric images Müller & Lobanov (2022, 2023b). Hence, in a straightforward manner DoG-HiT can also recover polarimetric movies without the introduction of any additional regularization or temporal correlation terms. Thus, for these applications DoG-HiT remains largely unsupervised despite

the increased complexity of the reconstruction problem.

DoG-HiT is in active use for a wide range of ongoing (polarimetric) mm-VLBI projects such as observations of 3C279, OJ287 and CenA with the EHT in 2017, or observations of 3C279 with the GMVA in 2018 (Müller & Lobanov 2023c). Moreover, it has been applied to lower frequencies for observations of M87 with RadioAstron (Kim et al. 2023). Furthermore, an application to the complete MOJAVE archive of 3C120 demonstrated convincingly the potential of DoG-HiT for survey observations: we were able to reanalyze  $\sim 100$  epochs in roughly  $\sim 15$  minutes with the highly parallelized and fully automated DoG-HiT algorithm and obtained images at higher resolution and comparable dynamic range (Müller & Lobanov 2023c). Based on the success of DoG-HiT in this variety of observations, we expect great improvements for EVN images. In particular, we expect improvements for combined EVN+eMerlin observations since the wide range of accessible baselines (short baselines from eMerlin combined together with the global baselines of the EVN) makes the use of a multiscalar algorithm that recovers large scale structures and small scale structures in parallel necessary. This benefit is studied in particular in an ongoing study of the Crab Nebula observed with the EVN+eMerlin array in 2022.

DoG-HiT and its extensions are publicly available as part of the *MrBeam* software package under the url: <https://github.com/hmuellergoe/mrbeam>.”

## 4 Evolutionary Imaging

In this chapter, we present a novel imaging algorithm based on evolutionary optimization, i.e. a genetic algorithm. The publication presented in this chapter is:

- **Müller, H.**, Mus, A. and Lobanov, A.: *Using multiobjective optimization to reconstruct interferometric data. Part I*, 2023, A&A, 675, A60 (**shared first authorship**). Conceptualization: H.M., A.M., A.L., methodology/software: H.M.,A.M., formal data analysis: H.M.,A.M., writing/editing: H.M., A.M., A.L.— Müller et al. (2023d), **Paper 4**

Up until now, recalling our discussions in chapter 3, our efforts for introducing unsupervised and optimally performing image reconstruction algorithms have been centered around the idea of drastically reducing the number of free parameters by selecting the penalty term data-driven. Here we discuss a different strategy focusing on devising a procedure combining unsupervised imaging with equally unsupervised identification of the preferred image reconstruction out of a set of hyperparameter driven solutions to the imaging problem. The solutions computed in a parameter survey for an RML method effectively sample a hypersurface in the multidimensional space of all possible solutions, i.e. they approximate the so called Pareto front. A solution to a multi-objective optimization problem is called Pareto optimal if the further optimization of one specific functional automatically worsens another one. However, the sampling of this hypersurface is not optimal. Many solutions with similar data term and penalty term weightings describe very similar solutions, while other parts of the parameter space are poorly sampled. Hence, we change the strategy. Instead of searching for a single solution representing a global result of the optimization problem, we attempt to find the complete hypersurface of possible solutions. Such a multi-objective optimization problem is difficult to be addressed with the standard tools of convex analysis. In this work, we develop a novel approach which allows us to address this problem with the help of the genetic algorithm representing a broader class of evolutionary algorithms.

The multi-objective genetic algorithm (MOEA/D) proposed here has the potential to replace parameter surveys that have to be employed essentially in all RML image reconstructions. Every solution along the Pareto front is a mathematically optimal solution that fits the data and is related to a specific regularization weight combination. In contrast to parameter surveys, the computation of this set of candidate solutions is computed in parallel with significant cross-talk. The Pareto front divides into clusters of image morphologies representing the full set of locally ‘optimally-balanced’ solutions. These clusters of solutions

that fit the undersampled data with a physically reasonable model is the primary product of the imaging procedure and provides an estimate for the robustness of image features as well. Moreover, we discuss approaches to find the most natural guess among these solutions based on a least action principle and demonstrate its performance on synthetic data. Thus, we select the most likely representant completely unsupervised from the data only. This has a potential to drastically accelerate the imaging procedure, in particular for the Event Horizon Telescope (EHT), since extensive synthetic data creation, parameter surveys and top-set selection may be not needed anymore.

MOEA/D is faster than any Bayesian global exploration technique. Therefore, it scales well to needs of more challenging data reconstruction problems such as polarimetry or dynamical imaging. MOEA/D is in particular interesting for dynamical imaging reconstructions, since the sparsity of the snapshot uv-coverage and the gaps for calibration scans require a global exploration technique that explores all local minima and estimates the robustness of the reconstruction.

Finally, we would like to highlight the difference between a multiobjective optimization algorithm and Bayesian global exploration techniques. First of all, Pareto optimality is a different approach to optimization. Bayesian approaches still sample the posterior by balancing the likelihood and prior terms. While genetic algorithms are stochastic in its nature as well (random mutation, mating of randomly selected parents), they do not compute a posterior distribution, but rather the set of locally optimal modes for a multimodal problem. Bayesian imaging algorithms select a preferred mode by the assumed prior distribution.

#### **4.1 Paper 4: Müller, Mus, Lobanov 2023d, A&A, 675, A60**

# Using multiobjective optimization to reconstruct interferometric data. Part I

Hendrik Müller<sup>1,\*</sup>, Alejandro Mus<sup>2,3,\*</sup>, and Andrei Lobanov<sup>1</sup>

<sup>1</sup> Max-Planck-Institut für Radioastronomie, Auf dem Hügel 69, 53121 Bonn (Endenich), Germany  
 e-mail: [hmueller@mpi-fr-bonn.mpg.de](mailto:hmueller@mpi-fr-bonn.mpg.de)

<sup>2</sup> Departament d'Astronomia i Astrofísica, Universitat de València, C. Dr. Moliner 50, 46100 Burjassot, València, Spain  
 e-mail: [alejandro.mus@uv.es](mailto:alejandro.mus@uv.es)

<sup>3</sup> Observatori Astronòmic, Universitat de València, Parc Científic, C. Catedrático José Beltrán 2, 46980 Paterna, València, Spain

Received 21 February 2023 / Accepted 24 April 2023

## ABSTRACT

**Context.** Imaging in radioastronomy is an ill-posed inverse problem. However, with increasing sensitivity and capabilities of telescopes, several strategies have been developed in order to solve this challenging problem. In particular, novel algorithms have recently been proposed using (constrained) nonlinear optimization and Bayesian inference.

**Aims.** The Event Horizon Telescope (EHT) Collaboration convincingly investigated the fidelity of their image reconstructions with large surveys, solving the image reconstruction problem with different optimization parameters. This strategy faces a limitation for the existing methods when imaging active galactic nuclei: Large and expensive surveys solving the problem with different optimization parameters are time-consuming. We present a novel nonconvex, multiobjective optimization modeling approach that gives a different type of claim and may provide a pathway to overcome this limitation.

**Methods.** To this end, we use a multiobjective version of the genetic algorithm (GA): the Multiobjective Evolutionary Algorithm Based on Decomposition, or MOEA/D. The GA strategies explore the objective function by evolutionary operations to find the different local minima and to avoid becoming trapped in saddle points.

**Results.** First, we tested our algorithm (MOEA/D) using synthetic data based on the 2017 EHT array and a possible EHT plus next-generation EHT configuration. We successfully recover a fully evolved Pareto front of nondominated solutions for these examples. The Pareto front divides into clusters of image morphologies representing the full set of locally optimal solutions. We discuss approaches to find the most natural guess among these solutions and demonstrate its performance on synthetic data. Finally, we apply MOEA/D to observations of the black hole shadow in Messier 87 with the EHT data in 2017.

**Conclusions.** The MOEA/D is very flexible and faster than any other Bayesian method, and it explores more solutions than regularized maximum likelihood methods. We have written two papers to present this new algorithm. In the first, we explain the basic idea behind multiobjective optimization and MOEA/D, and we use MOEA/D to recover static images. In the second paper, we extend the algorithm to allow dynamic and (static and dynamic) polarimetric reconstructions.

**Key words.** techniques: interferometric – techniques: image processing – techniques: high angular resolution – methods: numerical

## 1. Introduction

Very long baseline interferometry (VLBI) is a radio interferometric technique. All antennas in the array observe the same source at the same time. The recorded signals at each antenna pair in the array are correlated gradually sampling the Fourier transform of the true image brightness distribution of the observed source with Fourier frequencies determined by baselines projected on the sky plane. Imaging, that is, the procedure of creating an image from sparsely sampled Fourier coefficients (visibilities), is a challenging ill-posed inverse problem.

Three main families of imaging algorithms in radioastronomy have been proposed by the community: CLEAN-based algorithms (Högbom 1974; Clark 1980; Bhatnagar & Cornwell 2004; Cornwell 2008; Rau & Cornwell 2011; Müller & Lobanov 2023a); maximum entropy-based and regularized maximum likelihood-based (RML) algorithms (Cornwell & Evans 1985; Chael et al. 2016, 2018; Akiyama et al. 2017a,b; Müller & Lobanov 2022); and Bayesian-based algorithms (Broderick et al.

2020; Arras et al. 2021; Tiede 2022). Since the point spread function (PSF) has a nonvanishing kernel (i.e., missing data), there is not a unique image reconstruction. The solution to the unpenalized optimization problem is multivalued. This inherent degeneracy is addressed by the regularizer either by imposing support constraints manually (by placing “CLEAN windows”) in CLEAN or by adding a penalty term (in RML) to the objective functional. However, the result is that only one representative solution is recovered, and it does not reflect the problem of missing data due to the fact that more than one model fits the visibilities and a unique mathematically ideal solution does not exist. Instead, for these methods the problem of missing data could be addressed by testing the reconstructions with different combinations of penalizations, as done in *Event Horizon Telescope Collaboration* (2019, 2022). Alternatively, the third family (i.e., the Bayesian methods) can be used, as it imposes a prior distribution and looks for all possible images that fit the data, but the high computational cost makes this approach very slow, and it requires powerful machines.

The RML methods minimize the weighted sum of a data fidelity term (ensuring proximity to the observed data) and a

\* The first two authors contributed equally to this work.

regularization term (ensuring simplicity and fidelity of the guess solution). Viable regularization terms used in frontline VLBI applications, such as observations with the Event Horizon Telescope (EHT), include total flux and non-negativity constraints, smoothness assumptions (total variation, total squared variation), entropy functionals, and sparsity priors. For more details, we refer to the discussion in [Event Horizon Telescope Collaboration \(2019\)](#). More recently, multiscalar penalization terms have been proposed ([Müller & Lobanov 2022, 2023b](#)). Most RML techniques use local search techniques by quasi-Newton approaches. While the reconstructions are generally excellent, with improvements compared to CLEAN in resolution, accuracy, and dynamic range in particular for very sparse data (see e.g., the comparisons in [Event Horizon Telescope Collaboration 2019, 2022](#); [Müller & Lobanov 2022](#); [Roelofs et al. 2023](#)), this strategy does come with two major drawbacks.

The first drawback is that the landscape of the objective is highly complex. Hence, local optimization strategies could easily become trapped in local minima instead of reaching the global minimum. Since station-based gains have a priori known uncertainties (which can however be unbound in one direction in the case of uncharacterized telescope errors) that need to be self-calibrated during the imaging, current RML pipelines use the closure phases and closure amplitudes instead of the visibilities in a first round of self-calibration ([Event Horizon Telescope Collaboration 2019, 2022](#)). The hybrid imaging problem (i.e., the common reconstruction of the gains and the image in alternating imaging and self-calibration rounds) is nonconvex. Similarly, the projection to the calibration independent closure quantities is nonconvex as well, and therefore the use of gradient descent-based optimization strategies is further questioned (i.e., the optimization problem is multimodal. Although this issue may be addressed effectively by systematic tests of various starting models, regularization parameter combinations, and reconstruction methods (as done in [Event Horizon Telescope Collaboration 2019, 2022](#)), a more global optimization strategy is desired.

The second issue is that with a larger number of possible regularization terms that need to be combined to achieve an ideal image, a priori, which selection of weighting parameters to choose is not known. This problem is typically solved with a brute force approach: a library of synthetic data is created that needs to be studied with every possible parameter combination (parameter survey). Only the parameter combination that passes several acceptance criteria will be used for the analysis of the real observational data. This procedure is tedious and time consuming. Moreover, the process is poorly motivated. The set of test images could impact the top set selection and thus the quality of the reconstruction. A multiobjective algorithm that evolves the subspace of nondominated solutions in parallel and selects the ideal hyperparameter array automatically is therefore needed.

Overall, applications to very sparse VLBI data sets, such as in [Event Horizon Telescope Collaboration \(2019, 2022\)](#), were successful in addressing both of the issues raised above related to the multimodality and multiobjectivity of the problem by parameter surveys, combining the reconstructions by different methods and teams, and by extensive testing of the data set. This strategy allowed for strong indications of the fidelity of the ring-like appearance of the black hole shadow. In this work, we build upon the success of such a survey strategy in identifying the fidelity of the recovered images but look for a reformulation of the problem that allows for a faster, less time-consuming alternative. We present a novel imaging algorithm that provides an independent, alternative claim on the morphology of the image. Moreover, this algorithm may provide the possibility to accelerate parameter

surveys. To this end, we present a novel formulation for RML-like problems to adapt to the multimodality and multiobjectivity of the problem. All the solutions calculated in a parameter survey span a subspace of “optimally balanced” (or more correctly, nondominated solutions). Instead of computing this subspace by independent optimizations on a regular grid of coordinates and selecting the best representant (i.e., computing a parameter survey), we aim for the complete subspace to be the result of our optimization procedure. This new modeling consists of solving a multiobjective optimization problem (MOP) where the objective function is a combination of the most used regularizing terms in the current RML methods ([Chael et al. 2016, 2018](#); [Akiyama et al. 2017a,b](#)). We solve this problem by using the global search technique of genetic algorithms (GA), in particular we utilize the Multiobjective Evolutionary Algorithm Based on Decomposition (MOEA/D) algorithm ([Zhang & Li 2007](#)). In this way, we avoid falling into one local minimum, and we ensure more diversity in the solutions. We compute a set of candidate solutions that are nondominated (i.e., optimal with respect to the corresponding regularization). Our strategy is similar in philosophy to the parameter surveys for RML methods but not equivalent to them since we use a different optimality concept. Instead of searching over several hyperparameter combinations, we jointly evolve the solutions to all hyperparameter combinations together (i.e., we speed up the exploration of hyperparameters drastically through genetic crosstalk of similar regularizer weight combinations). In a subsequent paper, we will extend the problem to capture dynamics (and then to reconstruct “movies” instead of snapshots) and polarimetry.

In contrast to CLEAN and RML methods, we do not recover only one representative solution. Instead, the hypersurface of all nondominated (locally optimal) models is recovered. Every model in this surface of possible solutions corresponds to a specific regularizer weight combination, and they are all explored in parallel. This diversity of solutions represents the full set of possible image morphologies. To find the most natural solution within this hypersurface, we propose two different approaches: one, by calculating the minimal distance to the ideal point and, two, by looking for accumulation points. Though Bayesian methods are able to reconstruct a set of candidate solutions related to the multimodality of the problem as well, the parameter space they explore makes their time performance low (they require quite a few hours or days of computation) for that scope, despite there being considerable recent progress in speeding up their performance (e.g., [Knollmüller & Enßlin 2019](#); [Tiede 2022](#)) and Bayesian methods having been consequently applied, even for large data sets (e.g., [Arras et al. 2021](#); [Tychoniec et al. 2022](#)). In contrast, the set of candidate solutions computed by MOEA/D does not have a Bayesian interpretation as a posterior distribution, and hence it does not allow for an uncertainty quantification.

The paper is divided as follows: in Sect. 2, we describe the basics of VLBI measurements and imaging reconstruction using RML methods. In Sects. 3 and 4, we give a short overview of multiobjective optimization, and we introduce the terms that will be useful later together with a global search technique used to solve these types of problems. We present the model of our problem in Sect. 5. Every solution of this problem is an optimal image. We test our algorithm and we discuss several points in Sect. 6 (synthetic data) and Sect. 7 (real data). For all of these tests, we use self-calibrated data. In Sect. 8, we run the algorithm in data that is not self-calibrated, and we study the importance of the initial point to constrain the problem when there is not a self-calibration model in the case of sparse uv coverage, while

in cases with better uv coverage, any extra constraint is needed to recover the intrinsic source structure. The main part of this first paper ends in Sect. 9, which contains the conclusions of the work. Further appendixes are included to avoid an unnecessary extension.

## 2. VLBI measurements and imaging

An interferometer consists of a set of  $T$  telescopes observing the same source at the same time. The signal recorded at two independent stations is correlated. This correlation product is called visibility  $\mathcal{V}(u, v)$  with harmonic coordinates  $(u, v)$  determined by the baseline of the antenna pair. The true sky brightness distribution  $I(l, m)$  and  $\mathcal{V}$  are related by the van-Cittert-Zernike theorem (Thompson et al. 1994):

$$\mathcal{V}(u, v) = \iint I(l, m) e^{-2\pi i(lu+mv)} dl dm. \quad (1)$$

With a full aperture, the true image could be recovered from the visibilities by an inverse Fourier transform. However, for VLBI, only a sparse subsample of the Fourier coefficients is measured. We call the subsample of measured Fourier frequencies the UV coverage. The measured visibilities along one pair of antennas (indexed with  $i, j \in 1, 2, \dots, T$ ) at a time  $t$  is corrupted by station-based gains  $g_i$  and additional thermal noise  $N_{i,j}$  specific to the baseline such that the measured visibility on this baseline reads:

$$V(i, j, t) = g_i g_j^* \mathcal{V}(i, j, t) + N_{i,j}. \quad (2)$$

Closure quantities are gain-independent quantities derived from the observed visibilities, that is, the closure phases over a triangle of antennas  $i, j, k \in \{1, 2, \dots, T\}$  are:

$$\Psi_{ijk} = \arg(V_{ij} V_{jk} V_{ki}), \quad (3)$$

and the closure amplitudes over a rectangle of antennas  $i, j, k, l \in \{1, 2, \dots, T\}$  are:

$$A_{ijkl} = \frac{|V_{ij}| |V_{kl}|}{|V_{ik}| |V_{jl}|}. \quad (4)$$

For RML methods, we optimize not only a single but several objective functionals (Chael et al. 2016, 2018; Akiyama et al. 2017a,b; Event Horizon Telescope Collaboration 2019; Müller & Lobanov 2022). These include data fidelity terms that measure the fidelity of the guess solution to the observed data, for example, the fit quality to the visibilities:

$$S_{\text{vis}}(\mathcal{V}, V) = \frac{1}{N_{\text{vis}}} \sum_{i=1}^{N_{\text{vis}}} \frac{|\mathcal{V}_i - V_i|^2}{\Sigma_i^2}, \quad (5)$$

with the number of observed visibilities  $N_{\text{vis}}$ , visibilities of the guess solution  $\mathcal{V}_i$ , and error  $\Sigma_i$ . Moreover, the fit to the amplitudes:

$$S_{\text{amp}}(\mathcal{V}, V) = \frac{1}{N_{\text{vis}}} \sum_{i=1}^{N_{\text{vis}}} \frac{(|\mathcal{V}_i| - |V_i|)^2}{\Sigma_i^2} \quad (6)$$

to the closure phases:

$$S_{\text{cph}}(\mathcal{V}, V) = \frac{1}{N_{\text{cph}}} \sum_{i=1}^{N_{\text{cph}}} \frac{|\Psi_i(\mathcal{V}) - \Psi_i(V)|^2}{\Sigma_{\text{cph},i}^2} \quad (7)$$

and closure amplitudes:

$$S_{\text{cla}}(\mathcal{V}, V) = \frac{1}{N_{\text{cla}}} \sum_{i=1}^{N_{\text{cla}}} \frac{|\ln A_i(\mathcal{V}) - \ln A_i(V)|^2}{\Sigma_{\text{cla},i}^2} \quad (8)$$

could be used. Regularization terms measure the feasibility of the solution to fit the data with a model that is as simple as possible. Usual choices include a flux constraint  $f$ :

$$R_{\text{flux}}(I, f) = \left\| \int \int I(l, m) dl dm - f \right\|, \quad (9)$$

where  $f$  is the total flux together with norm constraints:

$$R_{l1}(I) = \|I\|_{l1}, \quad (10)$$

$$R_{l2}(I) = \|I\|_{l2}, \quad (11)$$

smoothness priors

$$R_{\text{tv}}(I) = \int \|\nabla I\| dl dm, \quad R_{\text{tsv}}(I) = \sqrt{\int \|\nabla I\|^2 dl dm}, \quad (12)$$

and an entropy functional

$$R_{\text{entr}}(I) = \int \int I \ln\left(\frac{I}{M}\right) dl dm, \quad (13)$$

where  $M$  denotes the brightness distribution of a model image.

In RML methods, these terms are added with corresponding weighting parameters (e.g.,  $\alpha, \beta, \dots, \iota \in \mathbb{R}$ ) to create the full objective functional  $\mathcal{F}$ :

$$\mathcal{F} = \alpha S_{\text{vis}} + \beta S_{\text{amp}} + \gamma S_{\text{clp}} + \delta S_{\text{cla}} + \epsilon R_{\text{flux}} + \zeta R_{l1} + \eta R_{l2} + \theta R_{\text{tv}} + \iota R_{\text{tsv}} + \kappa R_{\text{entr}}. \quad (14)$$

The joined minimization of  $S_{\text{vis}}$ ,  $S_{\text{amp}}$ ,  $S_{\text{clp}}$ , and  $S_{\text{cla}}$  combines redundant information (e.g., the information encoded by the closure amplitudes is also encoded in the amplitudes), a potential weak point of the forward modeling techniques. In Sect. 8, we show how our algorithm works with terms that are only closure dependent.

## 3. Multiobjective optimization

A multiobjective (minimization) optimization problem in its general form can be stated as (Pardalos et al. 2017)

Problem 1 (MOP standard form)

$$\begin{aligned} \min_{x \in D} \quad & F(x) := (f_1(x), \dots, f_n(x)), \\ \text{subject to} \quad & x \in D \subset \mathbb{R}^m, \end{aligned} \quad (\text{MOP})$$

where  $D$  is the decision space,  $\mathbb{R}^n$  is the space of objectives, and  $F : D \rightarrow \mathbb{R}^n$  is the vector-valued multiobjective optimization functional whose individual components  $f_i : D \rightarrow \mathbb{R}$ ,  $i = 1, \dots, n$  are an objective functional. The feasible set  $D \subset \mathbb{R}^m$  is generally expressed by a number of inequality constraints  $D = \{x \in \mathbb{R}^m \mid c_i(x) \leq 0, i = 1, \dots, n\}$ . This is the setting of our work.

It is common to find discrepancies between objectives, meaning a single point  $x \in D$  that minimizes (maximizes) all the  $f_i$

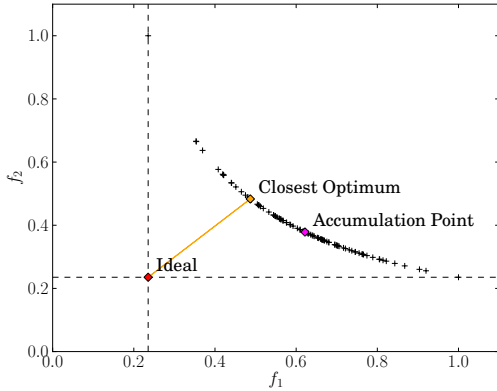


**Fig. 1.** Schematic illustration of the Pareto front for two given functions ( $f_1$  and  $f_2$ ), its ideal point, and two concepts for the most natural preferred points.

simultaneously does not exist (Pardalos et al. 2017). Therefore, the goal of the MOP is to find the best compromise among all of the objectives. This compromise is defined by means of a special set of solutions: the Pareto front  $P_{\mathbb{R}^m}(F)$  (Pardalos et al. 2017).

The Pareto front consists of the Pareto optimal (nondominated) solutions in the space of objectives. A point  $x^* \in D$  is considered Pareto optimal (nondominated) if there is no point  $x \in D$  such that  $f_i(x) \leq f_i(x^*)$ ,  $\forall i = 1, \dots, m$  and  $f_j(x) < f_j(x^*)$  for at least one  $j = 1, \dots, m$ . In other words, we call a point  $x^* \in D$  Pareto optimal if the further optimization in one objective automatically has to worsen another objective functional.

In general,  $P_{\mathbb{R}^m}(F)$  cannot be found analytically. In particular, most of the efforts are devoted to approximating  $P_{\mathbb{R}^m}(F)$  or identifying characteristic members (Pardalos et al. 2017). The selection of these represent members should be carefully done to avoid unfeasible, long running times or small diversity among the solutions. We also point out that the Pareto front represents a novel approach in VLBI to the multiple data and regularization terms discussed in Sect. 2. With the weighted sum approach (Eq. (14)) and with varying parameter combinations  $\{\alpha, \beta, \dots, t\}$ , we calculated a hypersurface that effectively approximates the Pareto front.

The Pareto front is bound by the nadir and the ideal objective vectors (see for instance Pardalos et al. 2017). While the nadir is not used in this work (we refer the reader to the bibliography for a clear definition), the ideal objective vector is the element  $l = (l_1, \dots, l_m)$  on  $D$  such that each component  $l_i$  is computed by (compare also Fig. 1):

$$l_i = \inf_{x \in P_{\mathbb{R}^m}(F)} f_i(x), \quad i = 1, \dots, m. \quad (15)$$

In this work, we used this vector to define a metric used to return one representative image, despite all the images belonging to the Pareto front being equally valid solutions.

Among all the possible strategies used to approximate the Pareto front (we refer the reader to the recent summary Sharma & Chahar 2022, for a comprehensive overview), the so-called multiobjective evolutionary algorithms (MOEAs) have been found to be efficient approaches. In this work, we used MOEA/D (Zhang & Li 2007; Li & Zhang 2009). This technique first obtains  $P_{\mathbb{R}^m}(F)$  by solving a set of scalar functionals associated with the objectives in a collaborating manner via an evolutionary algorithm. This cooperative strategy allows for

the handling of large-scale optimization problems by decomposing them into smaller scale subproblems (Tsurkov 2001). The MOEA/D has a high search ability for continuous, combinatorial, and multiobjective optimization. The MOEA/D also has a lower complexity than other algorithms. It is out of the scope of this paper to do a comparison of algorithms for solving MOP, and we thus refer the reader to Xin-She & Xing-Shi (2019) for more details on the multiple variants of algorithms solving MOP.

#### 4. MOEA/D

Nonconvex problems, as Prob. (MOP-MOEA/D), generally have more than one optimal solution. Such solutions are called “local optimal solutions”. Gradient- or Hessian-based algorithms are questionable in such types of problems because they are only able to return the first local solution they find. We refer the reader to Mus & Marti-Vidal (in prep.) for a longer discussion on the initial point dependence in nonconvex problems. In this section, we summarize a global search strategy called MOEA/D, which was first proposed in Zhang & Li (2007), that overcomes this issue. For more details, we refer to Zhang & Li (2007); Li & Zhang (2009); Xin-She & Xing-Shi (2019).

The MOEA/D algorithm solves the optimization problem with a genetic algorithm. Genetic algorithms are inspired by natural evolution. At every generation, a population of solutions is created from the preceding generation. We calculated the evolution from one generation to the next generation by genetic operations, that is, by random mutation of the single representants (genes) in the population and mating (i.e., mixing) of randomly selected parents in the parent generation.

In MOEA/D, the problem is decomposed in single problems either by a Tchebycheff decomposition or by a weighted sum decomposition. For this work, we focus on the weighted sum decomposition due to its philosophical similarity to established RML reconstructions in VLBI (Chael et al. 2016, 2018; Johnson et al. 2017; Akiyama et al. 2017b). We defined weight arrays  $\lambda^1 = \{\lambda_0^1, \lambda_1^1, \dots, \lambda_m^1\}$ ,  $\lambda^2 = \{\lambda_0^2, \lambda_1^2, \dots, \lambda_m^2\}, \dots$  that are related to the objective functionals  $f_1, f_2, \dots, f_m$ . Every weight array was normalized:

$$\lambda_i^j \in [0, 1], \quad \forall i, j, \quad (16)$$

$$\sum_{i=1}^m \lambda_i^j = 1, \quad \forall j. \quad (17)$$

Prob. (MOP) was decomposed into solving single optimization problems by a weighted sum approach:

$$x^j \in \operatorname{argmin}_x \sum_{i=1}^m \lambda_i^j f_i(x). \quad (18)$$

The nondominated single solutions in  $\{x^j\} \in D \subset \mathbb{R}^n$  approximated the Pareto front. The optimization was done with a genetic algorithm that interchanges information between several genes in one population at every iteration. For details, we refer the reader to Zhang & Li (2007) and Li & Zhang (2009). In a nutshell, we defined the closest neighborhoods  $U_B(\lambda^j)$  around every weight array  $\lambda_j$ . The update step consisted roughly of the following substeps performed for every  $j$ : first we selected two random indices  $k, l$  from the neighborhood  $U_B(\lambda^j)$ . Second, we generated a new solution  $y^j$  through genetic operations from  $x^k$  and  $x^l$ , that is, by random mutation and crossover among different candidates. Third, we updated all the solutions in the neighborhood, that is, for all indices  $n \in U_B(\lambda^j)$  we set  $x^n = y$  if

$\sum_{i=1}^m \lambda_i^n f_i(y^j) < \sum_{i=1}^m \lambda_i^n f_i(x^n)$ . Finally, we found the nondominated solutions. Next, we proceed with the next update step, i.e. we reiterated the four substeps outlined above until convergence is achieved. The MOEA/D algorithm therefore evolves the population at every point in the Pareto front at the same time. Moreover, it preserves diversity since isolated neighborhoods are protected from each other.

## 5. Modelization of the problem

To model the problem, we chose seven objective functionals:

$$f_1 := \alpha S_{\text{vis}} + \beta S_{\text{amp}} + \gamma S_{\text{clp}} + \delta S_{\text{cla}} + \zeta R_{l1}, \quad (19)$$

$$f_2 := \alpha S_{\text{vis}} + \beta S_{\text{amp}} + \gamma S_{\text{clp}} + \delta S_{\text{cla}} + \theta R_{\text{tv}}, \quad (20)$$

$$f_3 := \alpha S_{\text{vis}} + \beta S_{\text{amp}} + \gamma S_{\text{clp}} + \delta S_{\text{cla}} + \tau R_{\text{tsv}}, \quad (21)$$

$$f_4 := \alpha S_{\text{vis}} + \beta S_{\text{amp}} + \gamma S_{\text{clp}} + \delta S_{\text{cla}} + \eta R_{l2}, \quad (22)$$

$$f_5 := \alpha S_{\text{vis}} + \beta S_{\text{amp}} + \gamma S_{\text{clp}} + \delta S_{\text{cla}} + \epsilon R_{\text{flux}}, \quad (23)$$

$$f_6 := \alpha S_{\text{vis}} + \beta S_{\text{amp}} + \gamma S_{\text{clp}} + \delta S_{\text{cla}} + \kappa R_{\text{entr}}, \quad (24)$$

$$f_7 := \alpha S_{\text{vis}} + \beta S_{\text{amp}} + \gamma S_{\text{clp}} + \delta S_{\text{cla}}. \quad (25)$$

Therefore, the nonconvex multiobjective problem to be solved is

Problem 2 (MOP for imaging reconstruction)

$$\begin{aligned} \min_{x \in D} \quad & F(x) := (f_1(x), \dots, f_7(x)), \\ \text{subject to} \quad & x \in \mathbb{R}_+^{\text{Npix}}. \end{aligned} \quad (\text{MOP-MOEA/D})$$

This modelization is flexible and it is easy to include new regularization functionals. Due to Eq. (17), the weighted sum decomposition with weights array  $\{\zeta, \epsilon, \eta, \theta, \tau, \kappa, 1 - \zeta - \epsilon - \eta - \theta - \tau - \kappa\}$  is equivalent to Eq. (14). Hence, every item in the Pareto front corresponds to the optimal solution of a single hyperparameter combination (thus replacing parameter surveys). Moreover, this selection of the objective functionals ensures that the optimization is compatible with the data in every optimization direction (i.e., every  $f_j$  assures fit quality to the data). In contrast to the parameter surveys that were proposed for RML methods but are numerically unfeasible and poorly motivated, all the solutions corresponding to a specific regularizer weight combination  $\lambda^j$  are evolved together in our approach. Due to the genetic mixing of neighboring solutions, MOEA/D shares information between the solutions for similar weight arrays  $\lambda^j$  and is improved in this regard compared to parameter surveys that calculate the solutions independently. However, we mention that while the similarity to parameter surveys constitutes the main motivation behind the application of MOEA/D for VLBI imaging, Pareto optimality is a slightly different optimization concept.

Although we use the combined objectives  $f_1, \dots, f_7$  for the MOEA/D, during postprocessing we examine the front related to the penalty terms  $R_{l1} \propto f_1 - f_7$ ,  $R_{\text{tv}} \propto f_2 - f_7$ , .... For more details, we refer to Sect. 6.2, where we show examples of different Pareto fronts. We plotted the Pareto front in the first row as projections onto the three-dimensional domain. In the second row, we present the same front but with different projections. Every single point in these plots corresponds to an image recovered for a specific weighting combination. When inspecting the front, we identified several disjoint clusters. These clusters demonstrate several image morphologies that become visible when changing the weight parameter combinations. The image diversity within one cluster, however, is small. We found the clusters by a standard clustering algorithm. First, we renormalized every

axis such that the values were in the range  $[0, 1]$ . Then for every point, we found the respective neighbors (where a point is classified as a neighbor when the relative distance between them in the seven-dimensional space spanned by  $[f_1, \dots, f_7]$  is larger than some threshold). Finally, we classified all data points that were connected by a path of neighbors as being part of the same cluster.

We mention that every solution in the Pareto front is an optimal solution with respect to the multiobjective optimization problem. Mathematically, there is no preferred solution. All image morphologies in the different clusters are mathematically reasonable solutions that fit the data. Therefore, the Pareto front is the main output of MOEA/D representing the fact that there is not a single preferred image due to missing Fourier coefficients, and it presents an illustration of possible image features that are similar in philosophy to Bayesian algorithms (draws from the posterior distribution) and the survey of images produced in a parameter surveys. However, it is standard in VLBI imaging to select one image that is most natural with respect to scientific perception. We therefore present two strategies for finding the most natural image among all optimal solutions. These two strategies are illustrated in Fig. 1.

In one strategy, we can first define the ideal point following Eq. (15). As the ideal point is the point that would be optimal in every objective, it can be found by identifying the cross section of the minimum in every single objective (see Fig. 1). The ideal, however, has no physical meaning since it is not a solution of the Prob. (MOP-MOEA/D). A natural choice for a single image would thus be the recovered solution in the Pareto front that has the shortest (Euclidean) distance to the ideal point.

As a second strategy, we can look for accumulation points. Every cluster of solutions represents a locally optimal image morphology. We assumed that most solutions may cluster among the most natural solutions, while the edges of the parameter space with more exotic solutions are less sampled. To find a natural representative image, we therefore look for the points with the highest number of close neighbors: the accumulation point of the cluster.

The traditional multiobjective optimization theory lacks a standard methodology to address the challenge of solution selection, which entails the identification of a representative solution from an entire set of solutions comprising the Pareto front. Although a few strategies have been put forth in the literature (for instance Schwind et al. 2014, 2016), there is no consensus on an optimal approach. In this paper, we introduce two distinct criteria for solution selection: the accumulation point and the closest image to the ideal. Notably, any method that yields an image belonging to the Pareto front is a valid method of selecting a mathematical solution for the given problem.

## 6. Verification on synthetic data

### 6.1. Synthetic data

We tested our algorithm on the four synthetic geometric models (double, crescent, disk, and ring) that were used for the imaging verification by the EHT in 2017 (Event Horizon Telescope Collaboration 2019). For each model, two observational data sets were generated, one based on the EHT array of 2017 (coverage and thermal noise level of the 2017 observations of M87 on April 5) and the other based on a possible EHT plus ngEHT configuration (Roelofs et al. 2023) including ten additional stations, a quadrupled bandwidth, and an enhanced frequency coverage. We simulated synthetic data at 230 GHz and added thermal

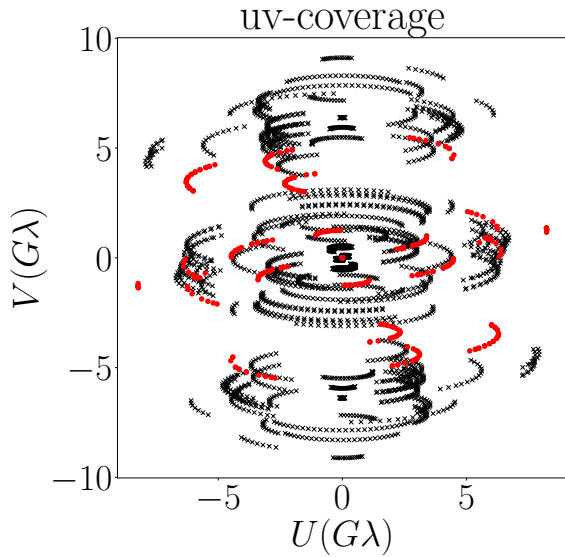


**Fig. 2.** uv coverage for M87 on April 11, 2017. The red dots show EHT, and the black crosses indicate ngEHT at 345 GHz.

noise according to the expected systematic noise levels used for Roelofs et al. (2023).

The geometric models were the same that were used for imaging verification in Event Horizon Telescope Collaboration (2019) and Müller & Lobanov (2022). The size of the ring, crescent, and disk mimics the size of the famous black hole shadow in Messier 87 (M87; Event Horizon Telescope Collaboration 2019). The ring and crescent have a radius of  $22 \mu\text{as}$ , and the disk has a diameter of  $70 \mu\text{as}$ . The double image mimics a completely different image structure that has features comparable to 3C279, as seen by the EHT (Kim et al. 2020). All geometric models were normalized to a total flux of  $0.6 \text{ Jy}$ . Moreover, we blurred the geometric models with a  $10 \mu\text{as}$ -blurring kernel before synthetically observing them in order to avoid sharp edges.

### 6.2. EHT + ngEHT array

Figure 2 depicts the UV coverage of the EHT plus ngEHT array. The crosses and points together form the full EHT plus ngEHT array. The UV plane is less sparse for the combined EHT and ngEHT instrument, thus leading to improved constraints on the inverse problem, which remains ill posed. To mimic the uncertainty in the phases we performed the reconstruction from the amplitudes and closure quantities only as was proposed in Chael et al. (2018); Müller & Lobanov (2022) and applied in Event Horizon Telescope Collaboration (2019, 2022). In particular we used the data term combination  $\alpha = 0$  and  $\beta = \gamma = \delta = 1$ . The weights were chosen on a grid with ten steps in every dimension, giving rise to 3003 parameter combinations that satisfy Eq. (17). We used a genetic algorithm with 4000 iterations. Moreover, we set the hyperparameters related to the genetic operations to the default values proposed in Li & Zhang (2009). For more details on the optimal choice of the genetic parameters (e.g., mating probability, random mutation size, and number of iterations), we refer the reader to Appendix A. Moreover, we added an overall scaling to every penalty term that was found to be ideal. For more details, we refer the reader to Appendix A. We selected

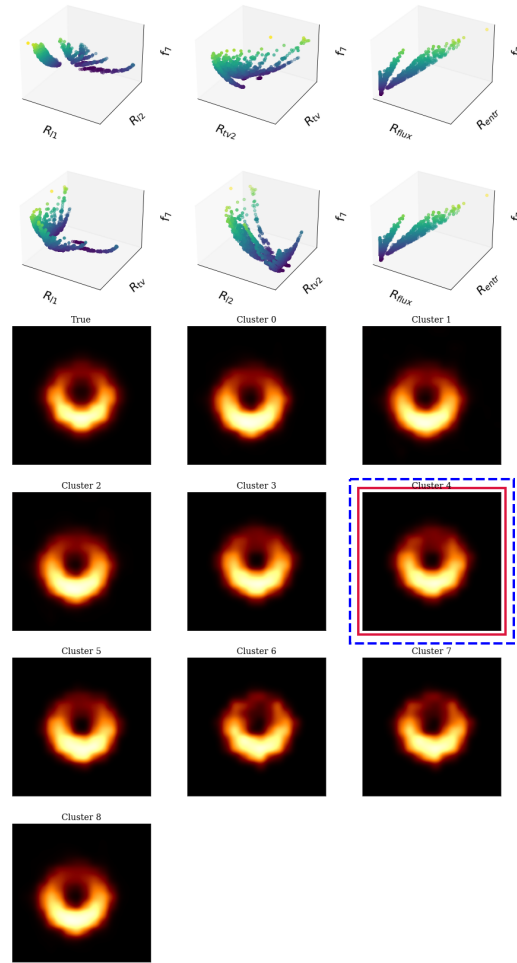


**Fig. 3.** Solution space of the MOEA/D. First two rows: Pareto front for the crescent case using the EHT + ngEHT array. The first panel of the solution clusters (top-left corner) shows the true image. The Pareto front is a seven-dimensional hypersurface. We illustrate the Pareto front with six projections. The six projections show the correlation between two regularizers and their values with respect to  $f_7$  (data fidelity term, only functional). The bluer the points are, the lower the value for  $f_7$ . Bottom two rows: solution clusters (following rows) for the crescent case using the EHT + ngEHT array. The family of solutions can be grouped into eight clusters. The red box surrounding the cluster indicates the preferred solution by the accumulation point strategy, while the blue box is the solution closest to the ideal.

a  $40 \mu\text{as}$  Gaussian as a prior. The entropy functional was computed relative to this prior image. Moreover, we had to choose an initial population for MOEA/D. Instead of starting from a pre-imaging model, we started the MOEA/D algorithm from a random distribution. Every gene in the initial population was drawn independently from a uniform distribution with values between 0 and  $1 \text{ Jy}$ . Finally, all the initial genes in the initial population were re-scaled to the respective compact flux.

We show our results for the four geometric models in Figs. 3–6. The Pareto front is a hypersurface in a seven-dimensional space (six penalty terms and one combined data term). We plotted the front as a series of three projections into the three-dimensional space (respectively two penalty terms and the data term) in the top-row panels of Figs. 3–6. Upon a first

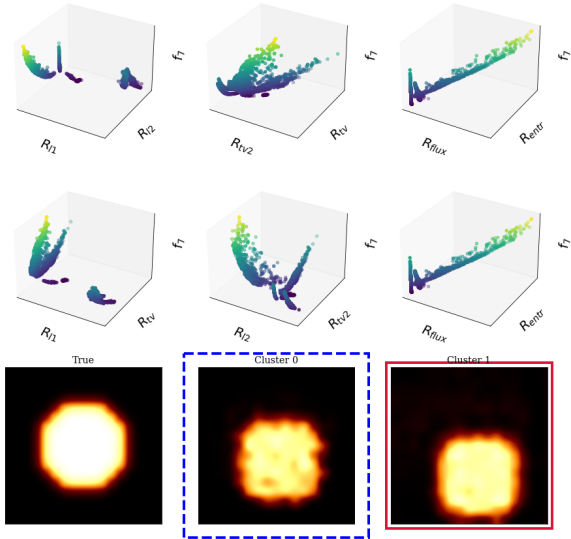


Fig. 4. Same as Fig. 3 but for the disk model.

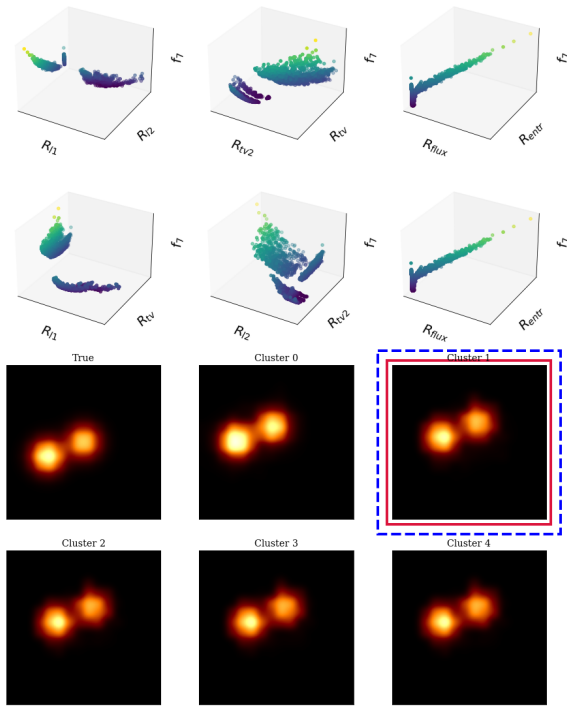


Fig. 5. Same as Fig. 3 but for the double model.

observation, we saw that the entropy, total flux constraint, and data term are strongly correlated since a wrong total flux or source size worsens the fit to the observed amplitudes.

When inspecting specific fronts, we observed that  $R_{I1}$  and  $R_{I2}$  as well as  $R_{IV}$  and  $R_{ISV}$  seemed to be correlated. That is reasonable, as these regularization terms promote a similar prior information (sparsity and smoothness, respectively). In the second-row panels of Figs. 3–6, we present the same Pareto front, but this time we combined the terms with conflicting assumptions (smoothness versus sparsity), that is, the various prior assumption that we aim to balance with an RML

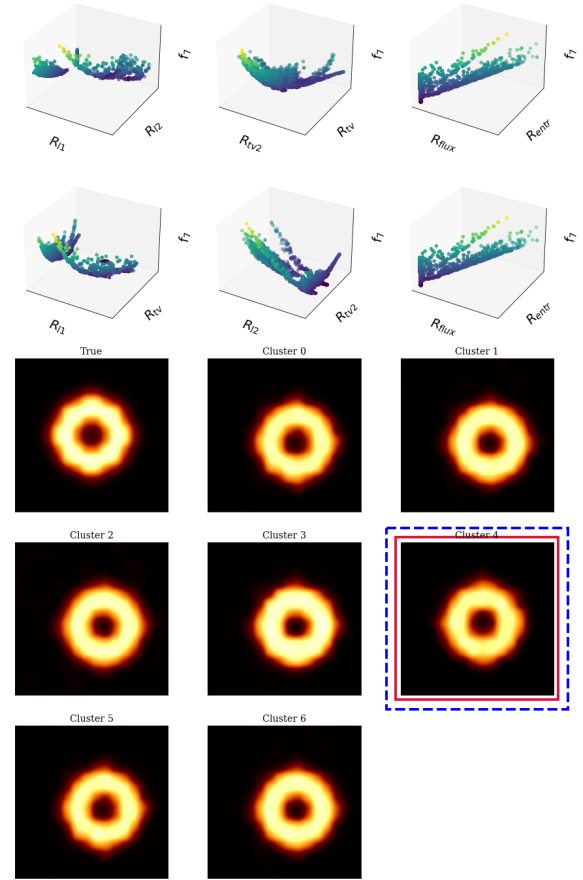
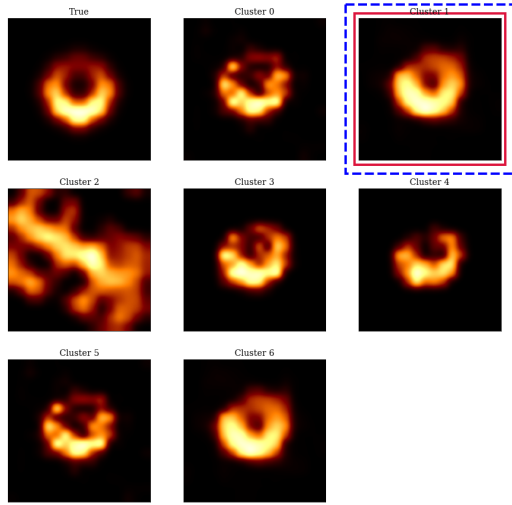


Fig. 6. Same as Fig. 3 but for the ring model.

method. As expected, we observed an anti-correlation in most cases. The Pareto front represents all optimal balances along this line of conflicting assumptions. In consequence, the front became divided into a varying number of clusters. The diversity of the images within every cluster is small, but the diversity from one cluster to the next cluster is significant. In the lower panels of Figs. 3–6, we show the ground truth image (top left) and a single representant (the accumulation point) of every cluster. We also show the solution that is preferred by the accumulation point selection criterion (i.e., the one that has the largest number of close neighbors), and we show the solution that is preferred by the closest optimum criterion. The two criteria coincide except in the disk model, but in all cases, the algorithm selected a reasonable reconstruction. For all four geometric models, the reconstruction is quite successful. The image features are recovered very well, although MOEA/D seems to slightly prefer blurred reconstructions.

### 6.3. EHT array

Figure 2 shows the UV coverage of the supermassive black hole M87 during the 2017 EHT observation campaign. The poor coverage of the campaign made the imaging more challenging, in particular since we were limited to the closure quantities. This resulted in a more difficult optimization problem, as demonstrated by the enhanced diversity in the population in the case of GA. The reconstruction was done with 5000 iterations and



**Fig. 7.** Solution clusters for the crescent case using the EHT array. The first panel (top-left corner) shows the true image. The red box surrounds the cluster indicated by the accumulation point strategy, while the blue box highlights the cluster closest to the ideal.

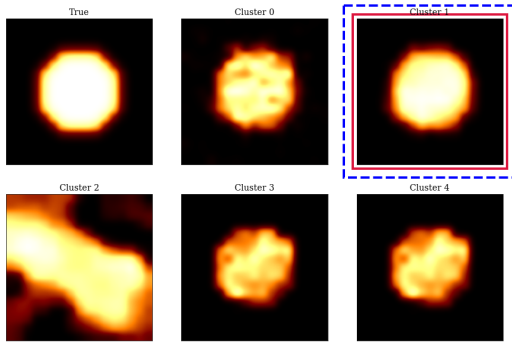


**Fig. 8.** Same as Fig. 7 but for the disk model.

a random starting point. Moreover, we used the same genetic parameters as used for the EHT plus ngEHT data sets.

We show the recovered clustered images for all for geometric models in Figs. 7–10. The recovered images show a wide variety of image morphologies. There are reasonably well-produced (but slightly blurred) reconstructions (e.g., cluster 1 and 6 for the crescent; cluster 1 and 4 for the ring). Moreover, we observed over-resolved reconstructions (e.g., cluster 0 and cluster 4 for the crescent; cluster 0 and cluster 5 for the double structure). Since every point in the Pareto front has a one-to-one correspondence to a specific weight vector combination  $\{\lambda_i^j\}$ , we could investigate which solutions were causing the over-resolved structural patterns. As expected, these solutions are at the edge of the Pareto front with a dominating sparsity term. Finally, we found some clusters that show phantom repetition of the same structures (e.g., cluster 2 and 3 for the ring; cluster 2 for the disk). These secondary phantom images are not unusual for image reconstructions given the combination of visibility phase uncertainty and poor UV coverage. This issue is addressed in RML algorithms either by surveying the correct balancing of various regularization terms (Event Horizon Telescope Collaboration 2019, 2022) or by a multiscale-based hard thresholding (Müller & Lobanov 2022). An analysis of the reconstructions in MOEA/D showed

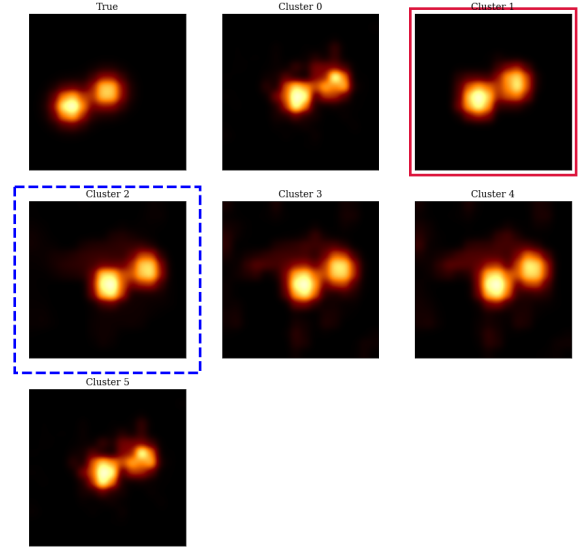


**Fig. 9.** Same as Fig. 7 but for the double-source model.

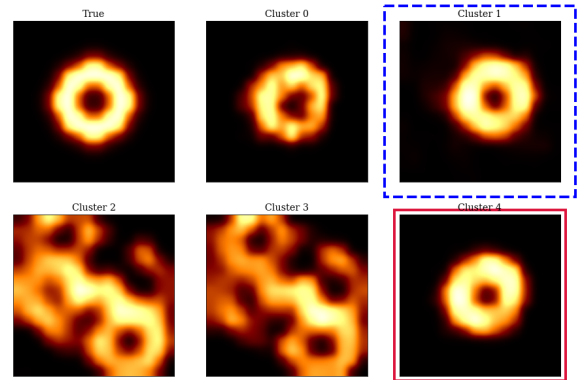


**Fig. 10.** Same as Fig. 7 but for the ring model.

that these solutions are related to the unpenalized reconstruction. This result can be well explained by the dirty beam. In particular, the cluster 2 reconstruction of the disk example resembles the dirty image, that is, the unpenalized reconstruction converges to the dirty image, as it is the easiest solution that fits the data.

For all four geometric models, we selected well-reconstructed cluster images using the accumulation point strategy and the closest neighbor strategy. These strategies may give rise to a completely data-driven image reconstruction without the need of parameter surveys. Among all the optimal images, we selected the best by looking for the image with the most close neighbors in the Pareto front.

## 7. Real data

We applied our algorithm to real data taken during the 2017 EHT campaign (Papers I–VI). We reconstructed images of M87 and the calibrator source 3C279 using the UV fit files available on the official webpage of the EHT<sup>1</sup>. To obtain the image, we used the best-parameter setting discussed in Sect. 6. For this work, we

<sup>1</sup> <https://eventhorizontelescope.org/for-astronomers/data>

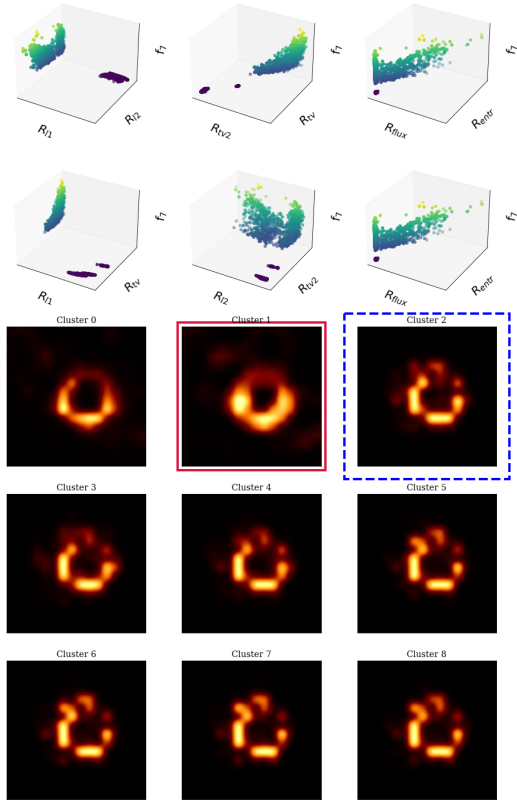


**Fig. 11.** Relative Pareto fronts (top two lines) and clustered images for M87 on April 11 (bottom three lines).

considered three variants of a data reduction pipeline: First, we used a random starting point and a random prior (Scenario A). Second, we tested a random starting point and a Gaussian prior (Scenario B). Finally, we used the image with less  $\chi^2$  (obtained with `ehtim` without any regularizer) as a starting point and a Gaussian prior (Scenario C). Although we only discuss Scenario C in this section, the remaining scenarios can be found in Appendix C. We emphasize the importance of the initial points in real data, in particular when there is sparse UV coverage. To avoid including unnecessary information in the paper, we only show the Pareto front and clustered images. We note that the convergence of the algorithm has been already shown in Sect. 6.

Messier 87 was observed across four days: April 6, 7, 10, and 11 (see for example Paper I). The reconstructions for all days can be found in Appendix B. Figure 11 depicts the set of clustered solutions for the day of April 11. Cluster 0 and cluster 1 present a good ring structure. Indeed, the representant for cluster 1 was chosen as the preferred image reconstruction, and it is very similar to the one published by the EHT. The rest of clusters have more subtle differences. The three “families” in the Pareto front can be observed in this figure.

## 8. Closure-only imaging

In this paper, we consider  $\alpha$  to be zero and  $\beta, \gamma, \delta$  to be different from zero. Hence, the reconstruction we present is independent from the highly unstable phase calibration, but the reconstruction only works properly if the data set has an amplitude that is self-calibrated, as described in Readhead & Wilkinson (1978). The aim of self-calibration is to adjust the complex gains of an

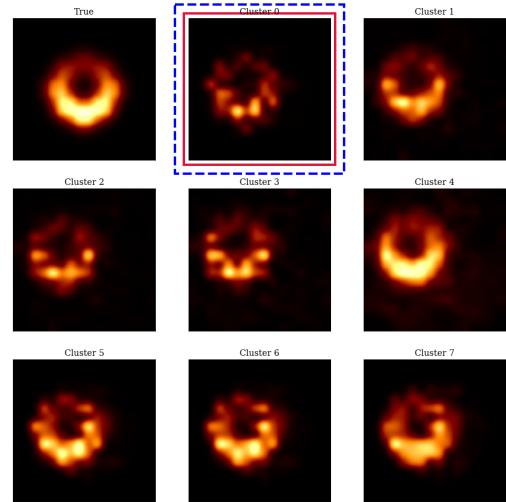


**Fig. 12.** Cluster solutions for the case of the EHT+ngEHT data with noise included and not self-calibrated. The starting point is a random distribution in the pixels.

interferometer by iteratively comparing the calibrated visibilities to an improved model. An accurate modeling of the source structure is crucial for the correct convergence of self-calibration (see for instance Martí-Vidal & Marcaide 2008; Mus et al. 2022).

In this section, we try our algorithm on non-self-calibrated data from the April 11 real EHT data and EHT plus ngEHT data. For this case, when the algorithm is applied to non-self-calibrated data, the nonclosure related fitting weights ( $\alpha$  and  $\beta$ ) are set to zero, that is, only the closure phases and the closure amplitudes are fitted, as suggested by Chael et al. (2018); Müller & Lobanov (2022). Moreover, setting  $\alpha = \beta = 0$  solves the redundancy of data terms that we mention in Sect. 2.

The reconstruction problem becomes more challenging since the number of independent closure phases and closure amplitudes are smaller than the number of independent visibilities, that is, the data consistency is less constraining (Kulkarni et al. 1991; Chael et al. 2018; Blackburn et al. 2020). Moreover, we mention that  $S_{\text{cph}}$  and  $S_{\text{cla}}$  are only approximations to the true likelihoods (Lockhart & Gralla 2022).

Figure 12 shows the set of solutions recovered using the EHT plus ngEHT array and a random brightness distribution on the pixels as starting point. We observed that MOEA/D is able to recover the intrinsic source structure even when self-calibration is not performed, although the obtained images are not as good as the ones obtained with a self-calibrated amplitude data term (i.e.,  $\beta \neq 0$ ). We note that the selection criteria for optimal solutions seemed to not select the optimal solution in this case.

In Fig. 13, we present the reconstructions for the real M87 EHT data. The poorer the UV coverage, the less constrained the optimization problem was. In the case of self-calibrated data, the problem is biased by the self-calibration model. If there were not a “biased” model, there would be more degrees of freedom, due to the smaller number of independent closure quantities. The larger number of degrees of freedom is translated into more local minima, and in consequence, there are more clusters. We highlight that the starting point is even more crucial in the case of non-self-calibrated data (i.e., without amplitude consistency), particularly when the UV coverage is sparse. Since a closure-only data set is less constraining than fitting fully calibrated visibilities, it is harder for the method to converge by

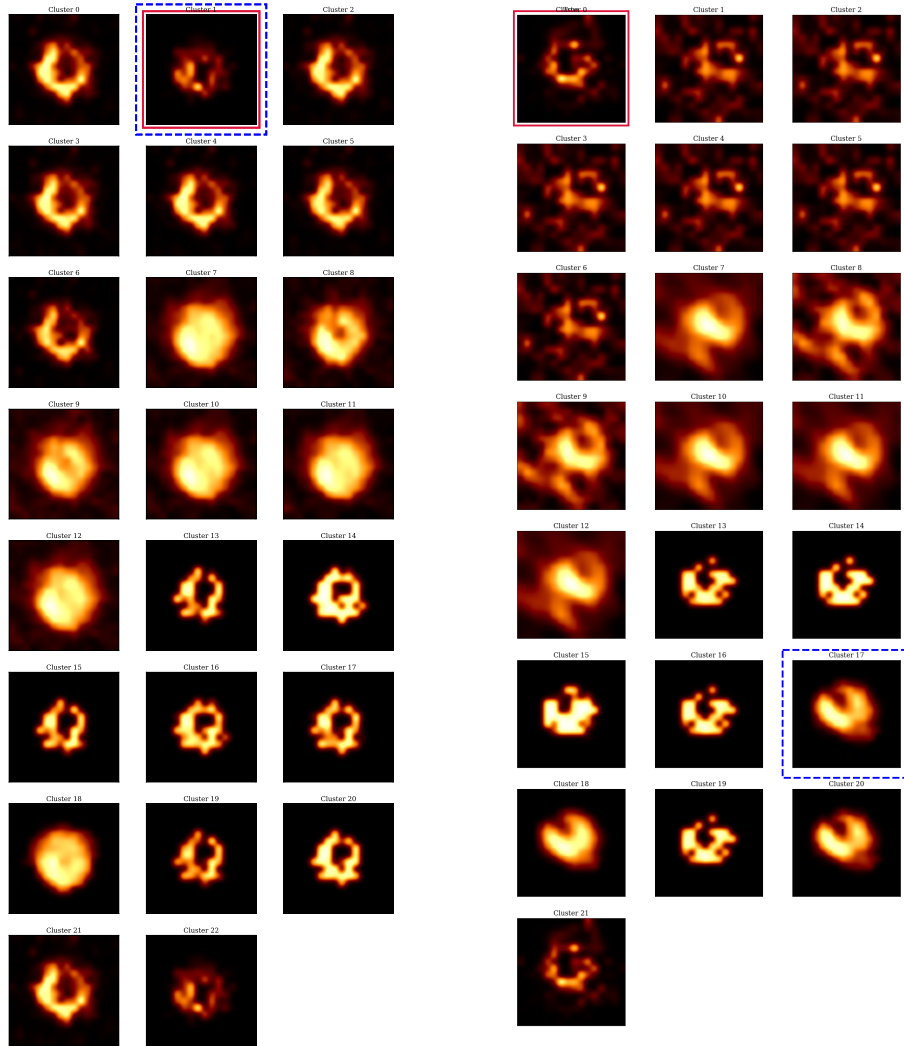


**Fig. 13.** Clusters of solutions for the case of M87 on the April 11, 2017 EHT campaign. The starting points are a ring (left panel) and Gaussian (right panel) and play an important role in constraining the solutions in absence of a self-calibration model.

random mutation and random genetic mixing. For the left panel of Fig. 13, we used a ring as the starting point, and for the right panel, we used a Gaussian distribution. While we recovered a ring with a central depression in most of the clusters in the first case, in the second, one less ring-like structure was recovered, but it can still be seen. Hence, the intrinsic structure of the source is predominant in the data even when considering a distribution not related with the real structure as a starting point.

The quality of the obtained solutions was the worst when only closure quantities were fitted. Nevertheless, we could use one of the clusters for creating a nonbiased model for self-calibration and rerun MOEA/D with updated amplitude information. Another alternative is to use this selected cluster as the initial point and to run the MOEA/D. In this way, the MOEA/D is run iteratively, improving the starting point.

## 9. Summary and conclusions

Imaging in radioastronomy is an ill-posed inverse problem, and it is particularly difficult when UV coverage is very sparse, as is the

case of global VLBI observations. Several strategies to overcome such a challenge using algorithms have been developed, and they can be classified into three main families: CLEAN methods, (constrained) nonlinear optimization methods, and Bayesian approaches. Each algorithm family has its advantages and disadvantages. For example, optimization methods are considerably faster than Bayesian ones, but they lack a global posterior exploration, and therefore a large, highly expensive parameter survey is then required. On the other side, Bayesian methods explore a huge set of parameters, but they have slow performance compared to nonlinear optimization methods and CLEAN, in particular for large data sets. We have identified two specific issues related to the imaging problem, namely, the problem is multimodal and multiobjective.

In this work, we have presented a novel multiobjective formulation based on evolutionary algorithms that overcomes these problems. We computed a set candidate of solutions that are nondominated (i.e., optimally balanced): the Pareto front. A parameter survey is not required anymore with this approach since the complete Pareto front of optimal solutions is evolved

in parallel, considerably speeding up the time required by standard RML approaches to obtain a set of solutions. Furthermore, the result of parameter surveys depends on the set of test images. This issue does not arise for MOEA/D.

Moreover, the MOEA/D is a global search technique that is less likely to get trapped in local extrema. Therefore, we are able to recover a full subset of solutions that are the best compromise of multiple objective functionals. Every candidate solution in the Pareto front is related to a specific hyperparameter combination.

The MOEA/D algorithm is faster than any Bayesian approach, but it does not explore a posterior distribution. Nonetheless, it is very flexible, allowing for the introduction of new regularizers very easily without exponentially increasing the computing complexity. We created a clustering algorithm to group the “similar” solutions. Then, we implemented two different techniques to choose the representative image between all clusters. All of the clusters are mathematically valid images, and therefore any other criterion to choose one among all can also be used.

We successfully tested our algorithm in four synthetic models (double, disk, ring, and crescent) using a sparse array (EHT 2017) and a more complete instrumental configuration (EHT + ngEHT). Finally, we ran our algorithm in real 2017 EHT M87 data. In this work, we discussed the role of various regularization terms and their impact in a multiobjective framework. In a subsequent work, we will focus on the data terms. That is, we will include a wider variety of (nonredundant) data term combinations in the multiobjective formulation (also including dynamic and polarimetric data products), study their role in more detail, and extend MOEA/D to dynamic and polarimetric observations.

*Acknowledgements.* A.M. and H.M. have contributed equally to this work. This work was partially supported by the M2FINDERS project funded by the European Research Council (ERC) under the European Union’s Horizon 2020 Research and Innovation Programme (Grant Agreement No. 101018682) and by the MICINN Research Project PID2019-108995GB-C22. A.M. also thanks the Generalitat Valenciana for funding, in the frame of the GenT Project CIDE-GENT/2018/021 and the Max Planck Institut für Radioastronomie for covering the visit to Bonn which has made this possible. H.M. received financial support for this research from the International Max Planck Research School (IMPRS) for Astronomy and Astrophysics at the Universities of Bonn and Cologne. The authors thank Michael Janssen for his valuable comments to improve this work. We will make our imaging pipeline and our software available soon in the second release of MrBeam (<https://github.com/hmuellergoe/mrbeam>). Our software makes use of the publicly available ehtim (Chael et al. 2016, 2018), regpy (<https://github.com/regpy/regpy>), MrBeam (Müller & Lobanov 2022, 2023b,a) and pygmo (Biscani & Izzo 2020) packages.

## References

- Akiyama, K., Ikeda, S., Pleau, M., et al. 2017a, *AJ*, 153, 159  
Akiyama, K., Kuramochi, K., Ikeda, S., et al. 2017b, *ApJ*, 838, 1  
Arras, P., Bester, H. L., Perley, R. A., et al. 2021, *A&A*, 646, A84  
Bhatnagar, S., & Cornwell, T. J. 2004, *A&A*, 426, 747  
Biscani, F., & Izzo, D. 2020, *J. Open Source Softw.*, 5, 2338  
Blackburn, L., Pesce, D. W., Johnson, M. D., et al. 2020, *ApJ*, 894, 31  
Broderick, A. E., Pesce, D. W., Tiede, P., Pu, H.-Y., & Gold, R. 2020, *ApJ*, 898, 9  
Chael, A. A., Johnson, M. D., Narayan, R., et al. 2016, *ApJ*, 829, 11  
Chael, A. A., Johnson, M. D., Bouman, K. L., et al. 2018, *ApJ*, 857, 23  
Clark, B. G. 1980, *A&A*, 89, 377  
Cornwell, T. J. 2008, *IEEE J. Selected Topics Signal Process.*, 2, 793  
Cornwell, T. J., & Evans, K. F. 1985, *A&A*, 143, 77  
Event Horizon Telescope Collaboration (Akiyama, K., et al.) 2019, *ApJ*, 875, L4  
Event Horizon Telescope Collaboration (Akiyama, K., et al.) 2022, *ApJ*, 930, L14  
Högbom, J. A. 1974, *A&AS*, 15, 417  
Johnson, M. D., Bouman, K. L., Blackburn, L., et al. 2017, *ApJ*, 850, 172  
Kim, J.-Y., Krichbaum, T. P., Broderick, A. E., et al. 2020, *A&A*, 640, A69  
Knollmüller, J., & Enßlin, T. A. 2019, ArXiv e-prints [arXiv:1901.11033]  
Kulkarni, S. R., Prasad, S., & Nakajima, T. 1991, *J. Opt. Soc. Am. A*, 8, 499  
Li, H., & Zhang, Q. 2009, *IEEE Trans. Evol. Comput.*, 13, 284  
Lockhart, W., & Gralla, S. E. 2022, *MNRAS*, 509, 3643  
Martí-Vidal, I., & Marcaide, J. M. 2008, *A&A*, 480, 289  
Müller, H., & Lobanov, A. P. 2022, *A&A*, 666, A137  
Müller, H., & Lobanov, A. P. 2023a, *A&A*, 672, A26  
Müller, H., & Lobanov, A. 2023b, *A&A*, 673, A151  
Mus, A., Martí-Vidal, I., Wielgus, M., & Stroud, G. 2022, *A&A*, 666, A39  
Pardalos, P. M., Žilinskas, A., & Žilinskas, J. 2017, *Non-Convex Multi-Objective Optimization* (Berlin: Springer)  
Rau, U., & Cornwell, T. J. 2011, *A&A*, 532, A71  
Readhead, A. C. S., & Wilkinson, P. N. 1978, *ApJ*, 223, 25  
Roelofs, F., Blackburn, L., Lindahl, G., et al. 2023, *Galaxies*, 11, 12  
Schwind, N., Okimoto, T., Konieczny, S., Wack, M., & Inoue, K. 2014, 2014 *IEEE 26th International Conference on Tools with Artificial Intelligence*, 170  
Schwind, N., Okimoto, T., Clement, M., & Inoue, K. 2016, *Proceedings of the Fifteenth International Conference on Principles of Knowledge Representation and Reasoning, KR’16* (AAAI Press), 601  
Sharma, S., & Chahar, V. 2022, *Archives Comput. Methods Eng.*, 29, 3  
Thompson, A., Moran, J., & Swenson, G. 1994, *Interferometry and Synthesis in Radio Astronomy* (USA: Krieger Publishing Company)  
Tiede, P. 2022, *J. Open Source Softw.*, 7, 4457  
Tsurkov, V. 2001, *Large Scale Optimization* (Berlin: Springer), 51  
Tychoniec, L., Guglielmetti, F., Arras, P., Enßlin, T., & Villard, E. 2022, *Phys. Sci. Forum*, 5, 52  
Xin-She, Y., & Xing-Shi, H. 2019, *Mathematical Foundations of Nature-Inspired Algorithms, Springer Briefs in Optimization* (Berlin: Springer)  
Zhang, Q., & Li, H. 2007, *IEEE Trans. Evol. Comput.*, 11, 712

## Appendix A: Parameter survey

The genetic evolution from one generation to the next generation in MOEA/D is calculated by genetic mixing and random mutation. These operations are controlled by specific control parameters. For full details, we refer to Li & Zhang (2009). Following the algorithmic outline presented in Sec. 4, assume that  $k, l$  are randomly selected indices in the neighborhood  $U_B(\lambda^j)$ . We aim to compute a new solution  $y^j$  by genetic mixing and random mutation. The genetic mixing is (Li & Zhang 2009):

$$y_i^j = \begin{cases} x_i^j + F \cdot (x_i^k - x_i^l) & \text{with probability CR} \\ x_i^j & \text{with probability } 1 - \text{CR}. \end{cases} \quad (\text{A.1})$$

Random mutation can be written as (Li & Zhang 2009):

$$y_i^j = \begin{cases} x_i^j + \sigma_i \cdot (b_i - a_i) & \text{with probability } p_m \\ x_i^j & \text{with probability } 1 - p_m \end{cases}, \quad (\text{A.2})$$

where  $a_i$  and  $b_i$  are the lower and upper bound of the current decision vector. The magnitude of mutation is controlled by  $\sigma_i$  (Li & Zhang 2009):

$$\sigma_i = \begin{cases} (2 \cdot \text{rand})^{\frac{1}{\eta+1}} - 1 & \text{if } \text{rand} < 0.5 \\ 1 - (2 - 2 \cdot \text{rand})^{\frac{1}{\eta+1}} & \text{otherwise} \end{cases}, \quad (\text{A.3})$$

where  $\text{rand}$  is a random number uniformly distributed in  $[0, 1]$ . Overall, we have four control parameters: two related to the genetic mixing ( $F, CR$ ) and two related to the polynomial mutation ( $p_m, \eta$ ). Moreover, the number of genes per generation and the number of generations are free parameters. A false combination of hyperparameters could keep MOEA/D from reaching convergence (e.g., if the random mutation is too small) or from having diversity in the solution (e.g., if the genetic mating appears too often). Thus, we started from the default choices suggested in Li & Zhang (2009) and surveyed several parameter combinations for the crescent example with EHT coverage. We changed  $F \in [0.1, 0.5, 0.9]$ ,  $\eta \in [5, 20, 50]$  and changed the grid of the weighting combinations to  $10^7, 30^7, 100^7$ , and  $500^7$  weight combinations. Moreover, we tested 1000, 3000, and 5000 iterations. Except for parameters far out of the standard range (i.e.,  $F = 0.9$ ), the performance was overall quite similar, with a tendency toward more generations, a smaller number of weight arrays, and genetic parameters close to those that were found to be optimal in Li & Zhang (2009). So we used  $CR = 1$ ,  $F = 0.5$ ,  $\eta = 20$ , and  $p_m = 0.9$  for this manuscript. The number of weight parameter combinations was limited to  $10^7$  combinations to keep the algorithm reasonably fast. Moreover, our investigation of more parameter combinations did not suggest an improved performance. Using 3000 – 5000 iterations seems sufficient and is also supported by the frozen-in-convergence condition of the decision vectors at these generations.

In MOEA/D, we solved problems of the form:

$$x^j \in \operatorname{argmin}_x \sum_{i=1}^m \lambda_i^j f_i(x), \quad (\text{A.4})$$

with the objective functionals discussed in Sec. 5. Every point in the Pareto front represents a solution optimal with respect to the local parameter combination. In this way, we tested the output of RML imaging with several parameter configurations. However, due to the normalization of  $\lambda^j$  and the limited grid size, the weighting parameters for different optimization terms differ only

by one order of magnitude. Since the regularization terms are not normalized with respect to the pixel size (e.g., TV-pseudonorm or  $l^1$ -norm change when a smaller pixel size is used), we had to re-scale the regularization terms to a similar order of magnitude of impact before running MOEA/D. We varied the pre-factor for  $R_\rho$ ,  $R_\rho$ ,  $R_{\text{TV}}$ , and  $R_{\text{TSV}}$  between  $[1, 10, \text{and } 100]$  and the pre-factor for entropy regularization between  $[0.1, 1, \text{and } 10]$ . The parameter combinations were tested on synthetic EHT and EHT plus ngEHT data for all four models, with optimal combinations for entropy re-scaling found to be by 0.1 or one, for  $l^2$  re-scaling to be by a factor of ten, for  $l^1$  re-scaling to be by a factor of one, and for total variation and total squared variation re-scaling to be by a factor of one or ten.

## Appendix B: M87 in all epochs

In this appendix, we extend the results of M87 shown in Sect. 7 with the reconstructed images for the rest of the epochs. Figure B.1 depicts the image reconstructions for M87 on April 5, 6, and 10. In all of them the preferred image is the one presenting the clearest ring structure.

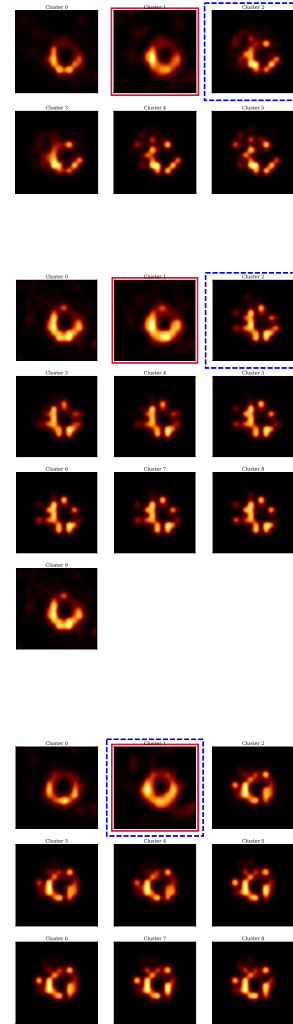


**Fig. B.1.** Image reconstructions of M87 2017 EHT observations. From top to bottom: April 5, April 6, and April 10.

### Appendix C: M87 reconstructed using different starting points

In this appendix, we present two reconstructions for M87 April 11 using 1) random brightness pixel distribution and 2) ring model as starting points, respectively. Figure C.1 shows the different clusters of the obtained solutions. As expected, starting with a ring morphology helps the convergence of the algorithm. Nevertheless, even when starting with a random brightness distribution on the pixels, we can recover a ring structure, which is a robust signature of the presence of a ring in the data. Also notable is the lesser degree of diversity presented with the geometric model. This could be due to the robust constraints that the random brightness distribution starting point imposes.

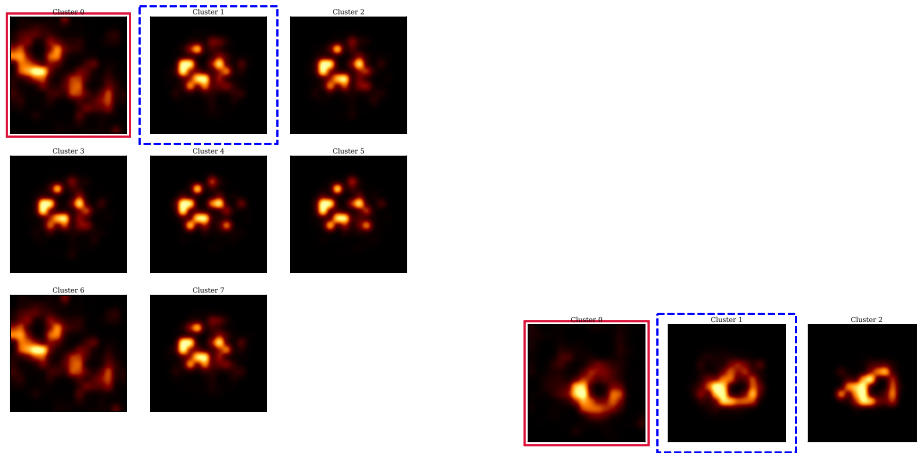


**Fig. C.1.** Set of solutions obtained supposing a random starting point (left panel) and ring starting point (right panel).

## 5 Applications

The techniques introduced in the previous chapters have been tested and applied in a variety of settings. In this chapter, we do not discuss all ongoing imaging projects, but rather present some exemplary applications. First, we summarize the scoring of DoG-HiT in the ngEHT Analysis Challenges for imaging synthetic VLBI data at 230 and 345 GHz. Then we present the DoG-HiT, DoB-CLEAN and MOEA/D contributions to imaging the EHT data (presenting only the results from published projects), space VLBI data from RadioAstron, and ground VLBI data from the Global Millimeter VLBI Array (GMVA) and the Very Long Baseline Array (VLBA). Finally, we present synergies to closely related scientific problems. Relevant publications for this chapter are:

- **Müller, H.**; Behrens, C. and Marsh, D.J.E.: *An optimized Ly  $\alpha$  forest inversion tool based on a quantitative comparison of existing reconstruction methods*, 2020, MNRAS, 497, 4937-4955. Conceptualization: H.M., C.B., D.M., methodology/software: H.M., formal data analysis: H.M., writing/editing: H.M., C.B., D.M., part of the work was done for the Master's thesis.
- **Müller, H.**; Behrens, C. and Marsh, D.J.E.: *A novel estimator for the equation of state of the IGM by Ly $\alpha$  forest tomography*, 2021, MNRAS, 503, 6202-6222. Conceptualization: H.M., C.B., D.M., methodology/software: H.M., formal data analysis: H.M., writing/editing: H.M., C.B., D.M., part of the work was done for the Master's thesis.
- Hamaide, L.; **Müller, H.** and Marsh, D.J.E.: *Searching for Dilaton Fields in the Ly $\alpha$  forest*, 2022, Phys. Rev. D, 106, 123509 (**shared first authorship**). Conceptualization: L.H., H.M., D.M., methodology/software: L.H., H.M., formal data analysis: L.H., H.M., writing/editing: L.H., H.M., D.M..
- Roelofs, F; Blackburn, L.; Lindahl, G.; Doeleman, S. S.; Johnson, Michael D.; Arras, P.; Chatterjee, K.; Emami, R.; Fromm, C.; Fuentes, A.; Knollmüller, J.; Kosogorov, N.; **Müller, H.**; Patel, N.; Raymond, A.; Tiede, P.; Traianou, T.; Vega, J.: *The ngEHT Analysis Challenges*, 2023, Galaxies, 11, 1. Contribution: Participation in challenges (data analysis), contribution of main results for challenge 2, participation in discussions and conceptualization, writing/editing.
- Chatterjee, K.; Chael, A.; Tiede, P.; Mizuno, Y.; Emami, R.; Fromm, C.; Ricarte, A.; Blackburn, L.; Roelofs, F.; Johnson, M. D.; Doeleman, S. S.; Arras, P.; Fuentes, A.; Knollmüller, J.; Kosogorov, N.; Lindahl, G.; **Müller,**

**H.**; Patel, N.; Raymond, A.; Traianou, T.; Vega, J.: *Comparing accretion flow morphology in numerical simulations of black holes from the ngEHT Model Library: the impact of radiation physics*, 2023, 11, 2. Contribution: Participation in challenges, participation in discussions and conceptualization.

- Kim, J.Y.; Savolainen, T.; Voitsik, P.; Kravchenko, E.V.; Lisakov, M.M.; Kovalev, Y.Y.; **Müller, H.**; Lobanov, A.; Sokolovsky, K.; Bruni, G.; Edwards, P.G.; Reynolds, C.; Bach, U.; Gurvits, L.I.; Krichbaum, T.; Hada, K.; Giroletti, M.; Orienti, M.; Anderson, J.M.; Lee, S.-S.; Sohn, B.-W. and Zensus, A.: *RadioAstron Space-VLBI Imaging of the jet in M87: I. Detection of high brightness temperature at 22 GHz*, 2023, 2023, ApJ, 952, 1. Contribution: Submitting a second, validation image from the self-calibrated data set.

In order to maintain the main focus of this dissertation, we only provide summaries of these works in this chapter.

## 5.1 ngEHT Analysis Challenges

The ngEHT Analysis Challenges are a series of data analysis competitions that explore the scientific capabilities of a possible ngEHT configuration and its algorithmic needs (Roelofs et al. 2023). The ngEHT is a planned future array that should extend the current capabilities of the EHT (Doeleman et al. 2019). In particular, the ngEHT is expected to deliver robust reconstructions of dynamics at the event horizon scale, i.e. movies of the dynamic changes in the innermost regions of the accretion disk in Sgr A\* and M87, and provide much stronger constraints on the physics of accretion and jet launching (Ricarte et al. 2023). The increased observing bandwidth, improved uv-coverage (in particular at short baselines), and signal-to-noise ratio, together with algorithmic improvements such as multifrequency imaging (Chael et al. 2023), should allow for a more reliable reconstruction at high dynamic range, and possibly the reconstruction of extended jet emission together with the black hole shadow (Roelofs et al. 2023). The Analysis Challenges target in particular the reconstruction of dynamic movies with various techniques. In the following subsection we summarize the findings of Chatterjee et al. (2023) and Roelofs et al. (2023). Contributions to these Challenges were made by providing submissions with an early version of DoG-HiT. Finally, we present first results of the not-yet published third challenge.

### 5.1.1 Analysis Challenge 1+2

Details on the synthetic data generation can be found in Chatterjee et al. (2023). In short, a rapidly spinning black hole embedded in an accretion disk is simulated. Two different types of simulations are explored. First, a radiatively inefficient accretion flow (RIAF) model is considered, i.e. a semi-analytic description of sub-Eddington, radiatively-inefficient and geometrically thick accretion. The accretion flow is semi-analytically modeled by phenomenological models of the electron temperature, electron density, magnetic field and velocity profile (Chatterjee et al. 2023). A rotating hotspot is introduced by the analytic prescription in Tiede et al. (2020).

Second, a MAD GRMHD simulation (magnetically arrested disk gravity relativistic magneto-hydrodynamics simulation) has been considered with details given in Chatterjee et al. (2023); Fromm et al. (2022); Mizuno et al. (2021). Specifically, a two-temperature GRMHD simulation is used, evolving the electrons alongside the ions by calculating the electron entropy separately (Chatterjee et al. 2023; Mizuno et al. 2021). Chatterjee et al. (2023) provided a comparison between the various simulations regarding the dynamics at the horizon scale. Overall the different models and simulations show great consistency in all relevant properties except for the electron temperature (Chatterjee et al. 2023).

Roelofs et al. (2023) deals with the reconstruction (imaging) of dynamic movies with realistic observing artifacts. Effects of atmospheric turbulence, atmospheric opacity (mimicking average spring weather conditions), and pointing offsets were simulated with SYMBA (Roelofs et al. 2020). Moreover, a stellar scattering screen and antenna-specific thermal noise levels were introduced. An EHT configuration is compared to a possible ngEHT configuration with ten additional antennas. The challenge was conducted blindly. For Sgr A\*, a GRMHD model and a RIAF model was provided for reconstructions. Furthermore, Roelofs et al. (2023) also discuss the reconstruction of M87 movies with extended jet emission. However, we participated with DoG-HiT only in the reconstruction of the rapidly spinning Sgr A\* models and will therefore focus on this part of the challenge. Nevertheless, we refer the interested reader to chapter 6 of Müller & Lobanov (2022) for an exemplary reconstruction of extended emission with the ngEHT configuration taken from Roelofs et al. (2023), also reprinted in this thesis in chapter 3. The analysis challenge consisted of two initial rounds: a static source model to test the setup (Challenge 1), and a dynamic source reconstruction (Challenge 2). We only contributed to the latter part of the challenge. We show the ground truth source models in Fig. 5.22. Submissions from a variety of groups representing various dynamic imaging approaches were compared. These

included multiscale approaches (DoG-HiT, Müller & Lobanov 2023b), RML reconstructions (*ehtim*, Chael et al. 2016, 2018), and Bayesian approaches (*resolve*, *starwarps*, Arras et al. 2019, 2021; Bouman et al. 2018). In a nutshell, all these algorithms approach the reconstruction of a movie by the reconstruction of a series of images (scans) with a temporal regularization added in the corresponding framework. In *ehtim*, a temporal smoothness penalty term (imposing correlation from scan to scan) is added to the set of regularization terms. For *resolve*, a temporal correlation is built into the prior model, i.e. the prior distribution of the scans is lognormal with specified correlation in spatial and temporal dimension. A hybrid approach is adopted in *starwarps* using a RML framework to fit the observed visibilities from scan to scan independently, and a Bayesian step to forward dynamic evolution from one scan to the next scan (Bouman et al. 2018). The dynamic movie reconstructions with DoG-HiT are described in detail in Müller & Lobanov (2023b), reprinted in chapter 3 in this dissertation. However, we participated in Roelofs et al. (2023) with an earlier, not yet finished version of the DoG-HiT pipeline. After we recovered the static mean image and computed the multiresolution support, we used the Bayesian forwarding step of *starwarps* with a multiresolution support constraint instead of an independent scan-by-scan fitting as we proposed in Müller & Lobanov (2023b).

The synthetic ground truth movies are displayed in Fig. 5.22. The reconstructions by various methods are shown in Fig. 5.23 for the RIAFSPOT model and Fig. 5.24 for the GRMHD models. As expected the reconstructions with ngEHT coverage are much better than the reconstructions with the current EHT setup. In particular, no algorithm could robustly recover from the simulated EHT data the dynamical evolution of emission at the event horizon scale, for any of the synthetic models used (Roelofs et al. 2023). On the contrary, the ngEHT dynamic reconstructions for the RIAFSPOT model clearly indicate a rotating, shearing hotspot motion. Best overall performance can be observed with *starwarps* and *ehtim*. However, these reconstructions utilize strong ring priors (Roelofs et al. 2023) that may be inadequate in practice and require significant user input (such that reconstructions submitted by two different scientists can differ significantly). DoG-HiT on the contrary is unsupervised and still recovers (although less clearly) the black hole shadow and some evidence for dynamics.

The reconstructions for the GRMHD models, see Fig. 5.24, are less successful due to the fast dynamic time scale of the object ( $\sim 1$  min). While no method was able to convincingly recover the rapid dynamics, all method succeed to recover the crescent-like mean image (Roelofs et al. 2023).

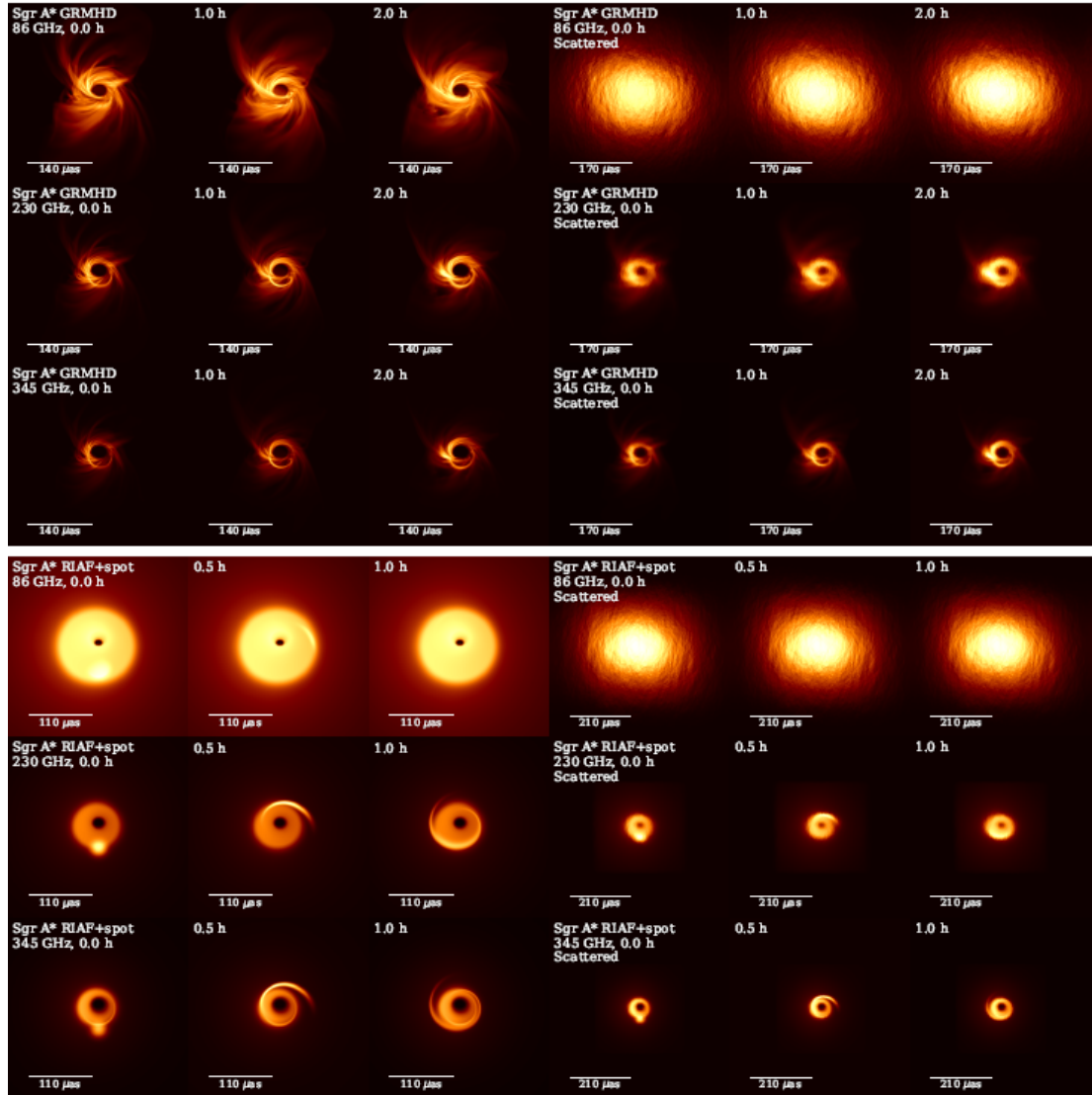


Figure 5.22: Overview over the synthetic Sgr A\* models used for the second ngEHT analysis challenge. Image is reprinted from Roelofs et al. (2023) by CC BY 4.0.

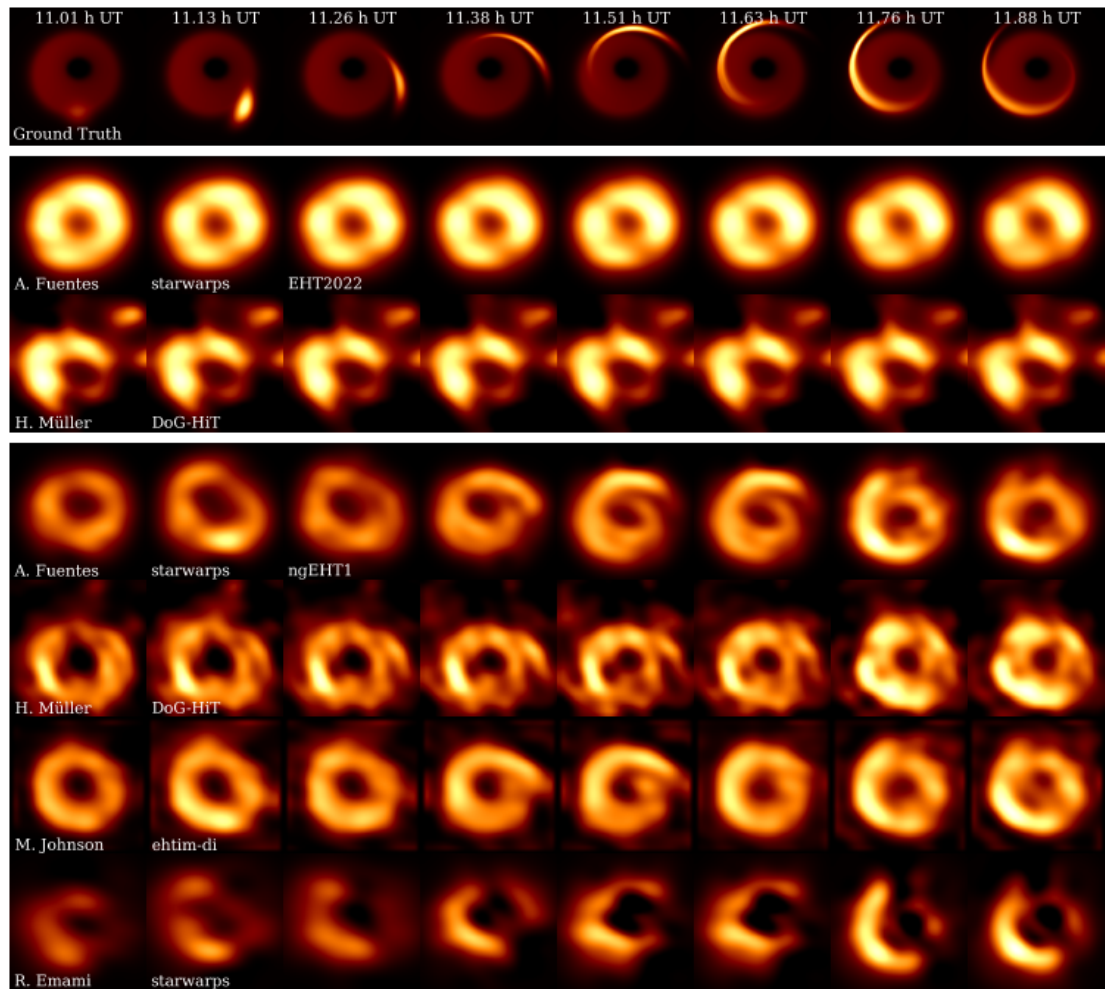


Figure 5.23: Submissions for the second ngEHT challenge at 230 GHz for the RIAFSPOT model. Image is reprinted from Roelofs et al. (2023) by CC BY 4.0.

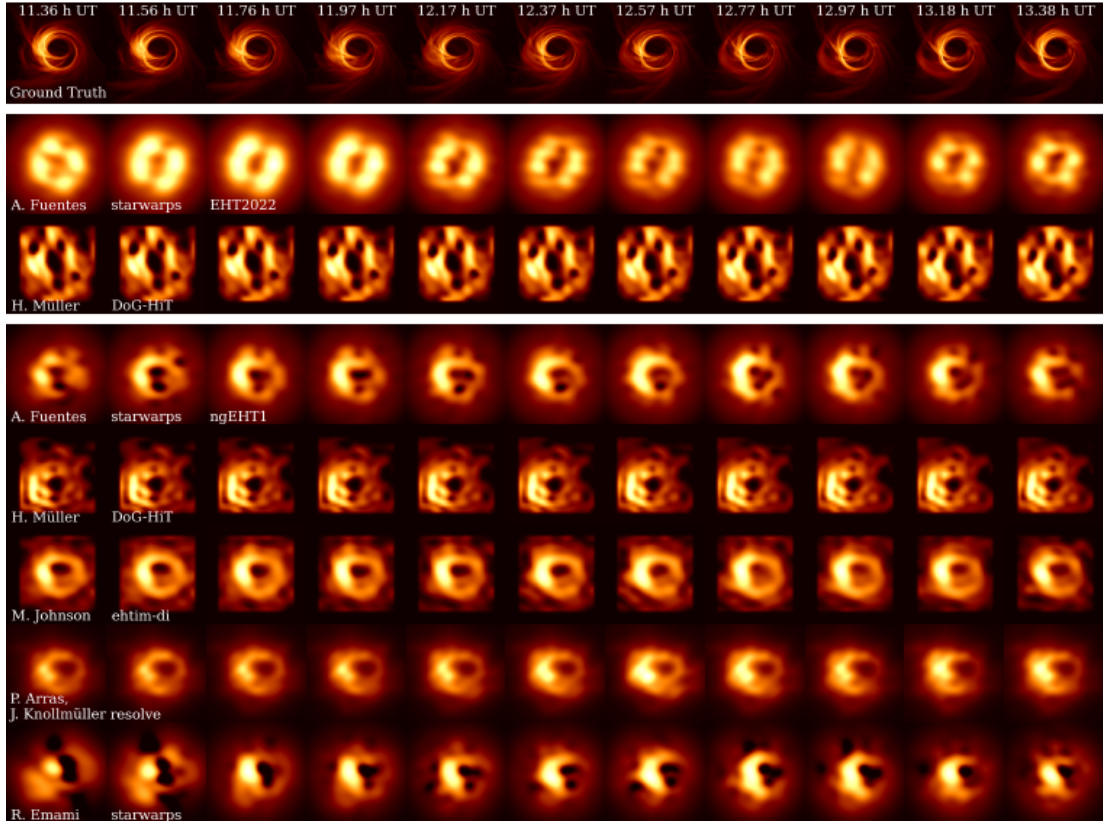


Figure 5.24: Submissions for the second ngEHT challenge at 230 GHz for the GRMHD model. Image is reprinted from Roelofs et al. (2023) by CC BY 4.0.

### 5.1.2 Analysis Challenge 3

The third ngEHT Analysis Challenge extends the first two challenges presented in Roelofs et al. (2023) to dynamical polarimetry. Therefore, they are an important test for the dynamical polarimetry capabilities of DoG-HiT. In the third challenge, we were able to participate using the full DoG-HiT algorithm presented in Müller & Lobanov (2023b), updating the dynamical Stokes I submission in the process as well. Here we repeat and expand the discussion of Müller & Lobanov (2023b), chapter 3.4. The fully polarized ground truth RIAFSPOT movie is printed in Fig. 5.25. The recovered movie is shown in Fig. 5.26. For better illustration, we also show a comparison of single frames in Fig. 5.27. The reconstruction was done from synthetic ngEHT observations, see Roelofs et al. (2023) for more details. The reconstruction is overall quite successful. We would like to mention as well, that the challenge is not a reconstruction that compares various algorithms on a rather clean data set, but contains the full set of realistic data corruptions for relatively bad weather conditions in a semi-blind setting (i.e. the ground-truth movie was not known to the participants in the challenge). In total intensity, the black hole shadow as well as signs of dynamics are well recovered. We recover the approaching hotspot at the start of the reconstruction (right to the ring at

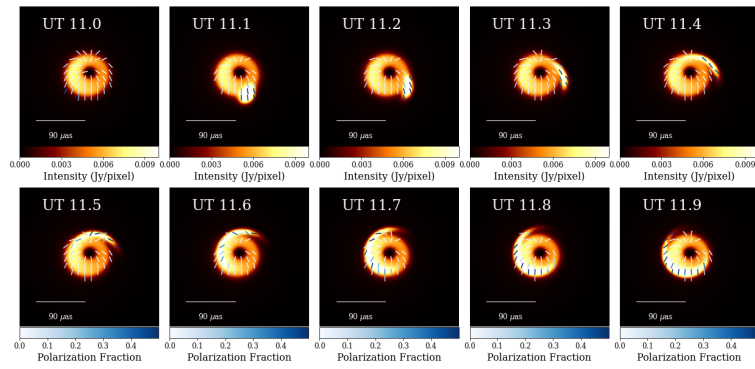


Figure 5.25: Exemption of the linearly polarized ground truth movie that was used for the third ngEHT Analysis challenge.

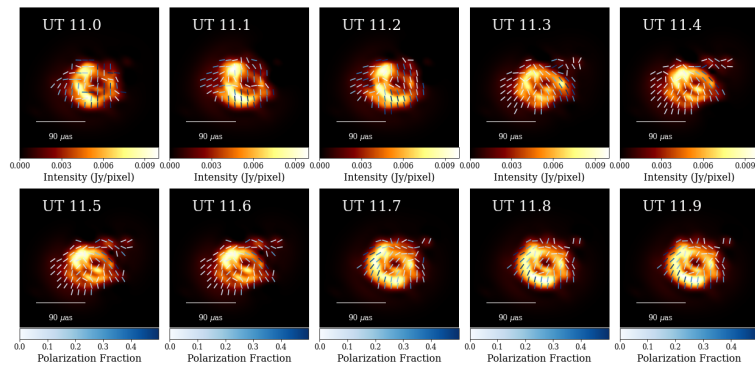


Figure 5.26: Reconstruction result with DoG-HiT for the third ngEHT Analysis challenge. The ground truth image is shown in Fig. 5.25. Synthetic observations were performed with a possible ngEHT configuration at 230 GHz.

UT 11.3), extended hotspot emission at UT 11.5 and the shearing hotspot as a region of higher emission within the black hole shadow at UT 11.7, see Fig. 5.27. The global polarization pattern is very stable and is recovered well in every single frame. Moreover, we recover the polarization pattern of the hotspot (EVPA following the hotspot motion) and the larger polarization fraction for the hotspot.

As a second movie, we study the GRMHD movie which is also plotted in Fig. 5.22. The moving EVPA pattern can be retrieved from the website of the ngEHT Analysis challenge <sup>5</sup>. We show our reconstruction with the full version of DoG-HiT in Fig. 5.28. While we have succeeded to recover the average ring shadow image, we do not succeed to recover the fast variability of the simulation. This is consistent with the findings of Roelofs et al. (2023) in which none of the proposed algorithms was able to recover the rapid variability of the total intensity. This

<sup>5</sup><https://challenge.ngeht.org/challenge3/>

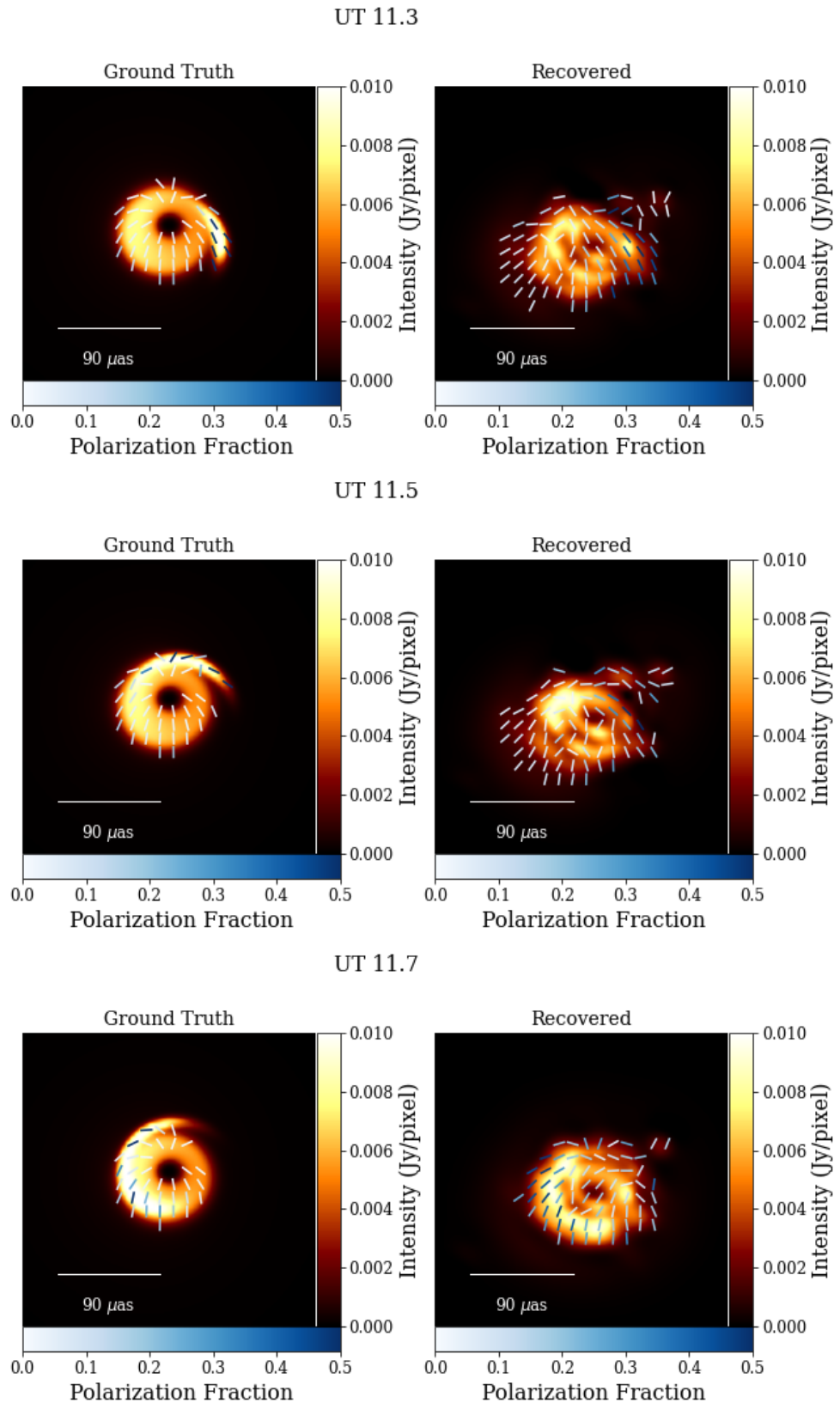


Figure 5.27: Single frame comparison at  $UT = [11.3, 11.5, 11.7]$  from the ground truth movie (left panels, Fig. 5.25) and the recovered frame (right panels, Fig. 5.26).

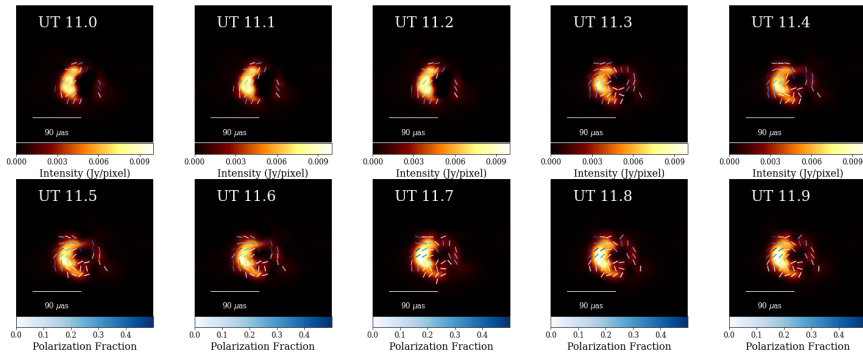


Figure 5.28: Reconstruction result of the GRMHD ground truth image for the third ngEHT Analysis challenge with DoG-HiT. Synthetic observations were performed with a possible ngEHT configuration at 230 GHz.

is partly caused by the observation cadence of the synthetic observations. The source is dynamically evolving on very short timescales, while the observation has ten-minute gaps (for calibration). Interpolating these key-frames is not possible anymore if the source is changing drastically within ten minutes. Hence, for movie-making, a faster switch between calibrator and science target is needed. We recover a circular polarization pattern in every single frame consistent with the ground truth movie. Furthermore, the recovered polarization fractions match the ground truth. Overall, although a rapidly, polarimetric movie of the GRMHD data set cannot be recovered, the reconstructions for the third ngEHT Analysis challenge (specifically for the RIAFSPOT model) demonstrate that DoG-HiT is able to find reasonable polarimetric models even for fast evolving source models.

At the time of submission of this dissertation, this was the only reconstruction that was submitted to the third challenge. A detailed comparison to other algorithms is therefore not possible at this stage. The reconstruction with DoG-HiT demonstrates well the overall potential of the approach. The option to recover rapidly evolving polarimetric movies at the event horizon scale is currently a unique capability among all existing imaging algorithms. Consistent movies with complex polarization information are recovered in an unsupervised framework, without enforcing temporal correlation between scans. The single frames are recovered independently from each other with a prior information introduced by the multiresolution support derived from the averaged mean image. Hence, the success of the reconstruction demonstrates that the effective prior information provided by the multiresolution support is strong enough to allow the reconstruction of complex source features from the uv-coverage of a single frame. An extension to the regularization terms used by Bayesian methods or RML methods for temporal regularization is rather straightforward. Hence, a combination of

multiscalar sparsity promoting imaging and state-of-the-art RML methods might be a tool that allows the consistent detection of faster dynamics at the event horizon already with EHT coverage, i.e. with already existing data. We propose this investigation for a consecutive work.

## 5.2 EHT Projects

The Event Horizon Telescope (EHT) is a global VLBI array that operates at 230 GHz with a recent extension to 345 GHz. Owing to the combination of very long global baselines and high frequencies, it reaches an angular resolution of  $\sim 20 \mu\text{as}$ . In 2017, the collaboration famously managed to observe the black hole shadow in M87 (Event Horizon Telescope Collaboration et al. 2019a) and of Sgr A\* (Event Horizon Telescope Collaboration et al. 2022a). DoG-HiT, MOEA/D and DoB-CLEAN are in regular use for ongoing EHT projects, in particular for the data analysis of the data sets observed in 2018 (however the results from this analysis are still under embargo by the EHT Consortium). We present here the data re-analysis of selected, already published data sets from the 2017 observing campaign. These reconstructions were performed independently from the data analyses published by the EHT (Event Horizon Telescope Collaboration et al. 2019b; Janssen et al. 2021; Kim et al. 2020) and relied only on closure quantities, i.e. are agnostic to the gain calibration in aforementioned works. Hence, the reconstructions presented in the following subsections are independent verifications.

### 5.2.1 2017 M87

M87 has been observed by the EHT in 2017. In 2019, the first ever image of a black hole shadow was released to the public (Event Horizon Telescope Collaboration et al. 2019a), see Fig. 5.29. The image was constructed independently by four different teams. Two teams used CLEAN, two further teams used RML methods (*ehtim*, *SMILI*). The image showed a prominent ring with a brightness asymmetry towards the south. Meanwhile, this structure has been independently verified with Bayesian methods (Arras et al. 2022; Event Horizon Telescope Collaboration et al. 2021a; Sun et al. 2022), advanced model-fitting (Lockhart & Gralla 2022a) and CLEAN (Carilli & Thyagarajan 2022), but was also criticized (Miyoshi et al. 2022). We show our reconstructions with DoG-HiT for single days and single bands in Fig. 5.30 and the band- and day-averaged mean in Fig. 5.31. The reconstruction was performed on scan-averaged data with the systematic noise levels reported in Event Horizon Telescope Collaboration et al. (2019b). We were able to recover the famous black hole shadow with the unsupervised,

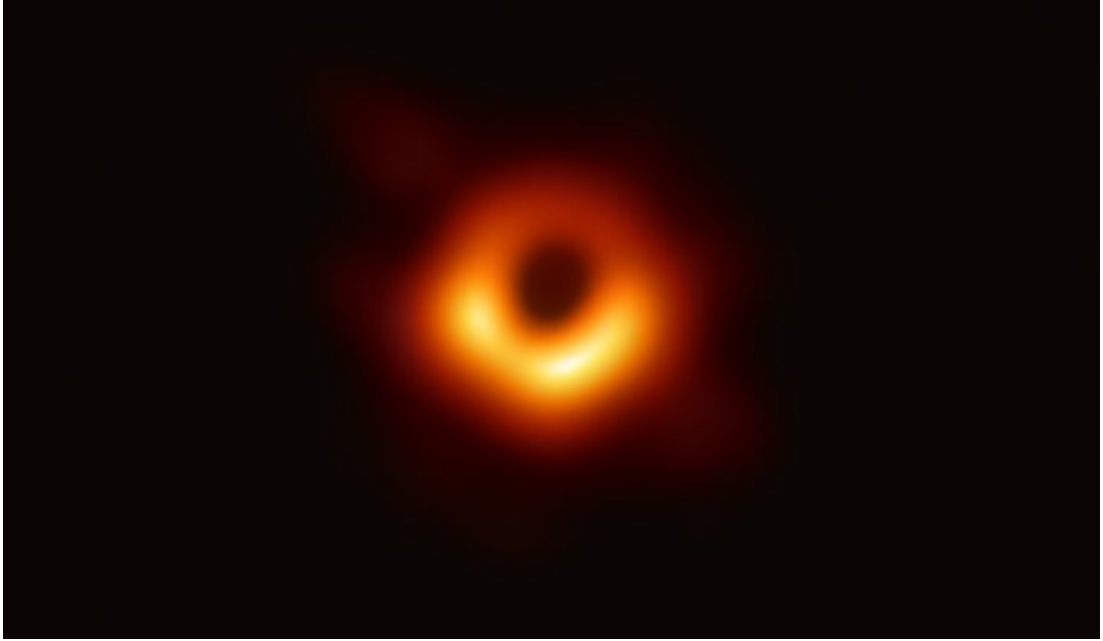


Figure 5.29: First ever image of a black hole shadow (Event Horizon Telescope Collaboration et al. 2019a). The image was taken from <https://www.eso.org/public/germany/images/eso1907a/> at 05.01.2023.

phase-insensitive DoG-HiT approach in only a few minutes of computation! This is a considerable achievement, given the lengthy, year-long data analysis procedure that went into the reconstruction with CLEAN and RML methods in Event Horizon Telescope Collaboration et al. (2019b). The ring size, orientation and overall day-to-day dynamics are consistent with the EHT observation. However, we observe a slightly smaller compact flux: 0.48 Jy instead of  $\sim 0.6$  Jy as reported in Event Horizon Telescope Collaboration et al. (2019b). Moreover, our reconstruction shows an enhanced asymmetry. We recover some substructure in the ring. The asymmetry is caused by two prominent blobs of higher intensity: one elongated from the south to the south-east and one more Gaussian-like in the south-west. A similar structure was also visible in Fig. 5.29, but with a swapped order (elongated component to the west). This elongated structure to the south-east was already observed by Arras et al. (2022). Furthermore, the dynamics among the four days is consistent with the results reported in Arras et al. (2022) as well.

We reprint in Fig. 5.32 the MOEA/D reconstructions of M87 from Müller et al. (2023d). As described in chapter 4.1, every cluster of solutions describes a reasonable, mathematically optimal solution to the imaging problem. With the accumulation point criterion (red box) we select on all four days solutions that are close to the ones preferred by *ehtim* (Event Horizon Telescope Collaboration et al. 2019b) and DoG-HiT, see Fig. 5.30. That means, the image reported

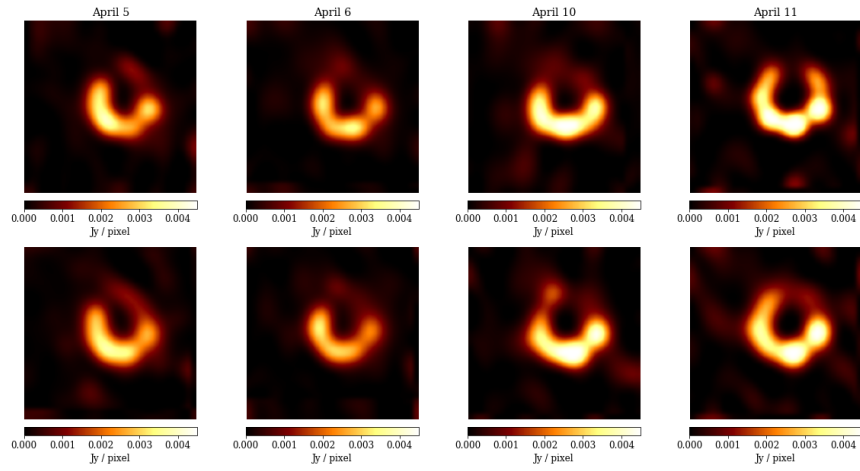


Figure 5.30: DoG-HiT reconstructions of single days of 2017 EHT observation of M87. Upper panels: High band (229 GHz). Lower panels: Low band (227 GHz).

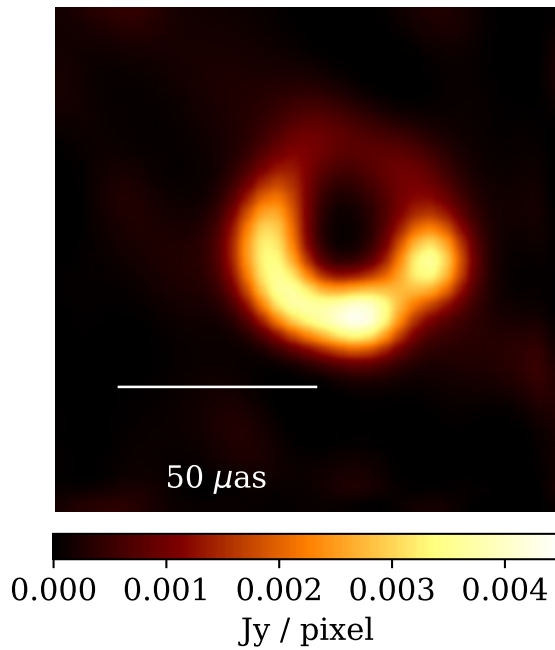


Figure 5.31: Average DoG-HiT reconstruction of 2017 EHT observations of M87, i.e. the average of all reconstructions presented in Fig. 5.30.

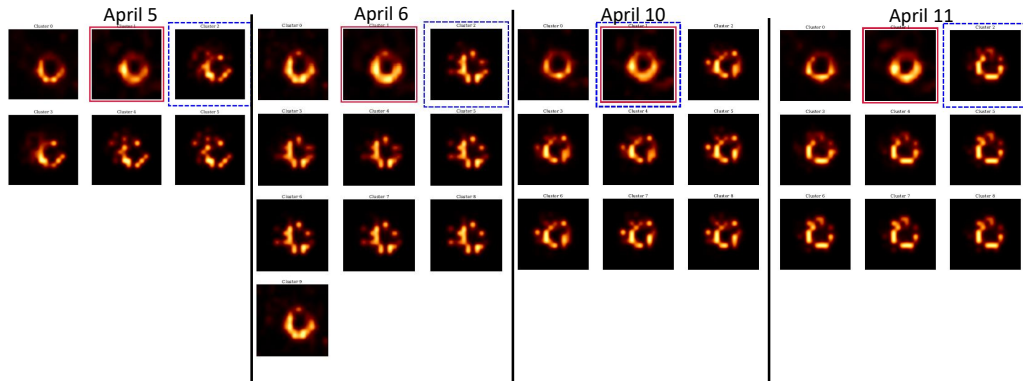


Figure 5.32: MOEA/D reconstructions of M87 (Müller et al. 2023d) observed with the EHT in 2017. We show all clusters of non-dominated solutions for all four days.

by Event Horizon Telescope Collaboration et al. (2019b) seems to be the most natural among the range of all possible solutions. Moreover, MOEA/D finds alternative clusters that correspond to models that fit the data as well. All these modes show a clear ring structure, rebuttal to the arguments in Miyoshi et al. (2022). This is a strong evidence for the robustness of the EHT detection of the ring-like structure in M87 attributed to the "black hole shadow".

Several re-analyses reported the existence of a south-western spot (Arras et al. 2022; Broderick et al. 2022b) that may be related to the apex of the jet. Following the arguments of Broderick et al. (2022b) this remarkable result is achieved by a hybrid fitting approach: A narrow ring is fitted to the visibilities, such that faint extended emission can be recovered in the residual. Broderick et al. (2022b) prominently announced the first detection of a narrow ring. This approach was criticized by Lockhart & Gralla (2022b) who reached an inconclusive result in regards to the detection of a narrow ring. Comparing the clusters computed by MOEA/D presented in Fig. 5.32, we see that there are certain clusters (cluster 0 for all days) that favor a narrow ring. These solutions are recovered at the edges of the Pareto front, but are mathematically optimal solutions to the imaging problem with respect to the prior information as well. We can confirm from this study that the narrow ring is consistent with the data and is a natural local accumulation point of the imaging procedure. However, a thicker ring is consistent with the data as well and favored by our least square principle selections. A final answer which solution to prefer can therefore not be given with the current data quality. However, resolving the debate between Broderick et al. (2022b) and Lockhart & Gralla (2022b), MOEA/D confirms that both reconstructions are reasonable and just probe different parts of the parameter space.

Hybrid modeling (i.e. the combination of imaging and modeling Broderick et al. 2020b, 2022b) utilizes an interesting feature about imaging: some methods,

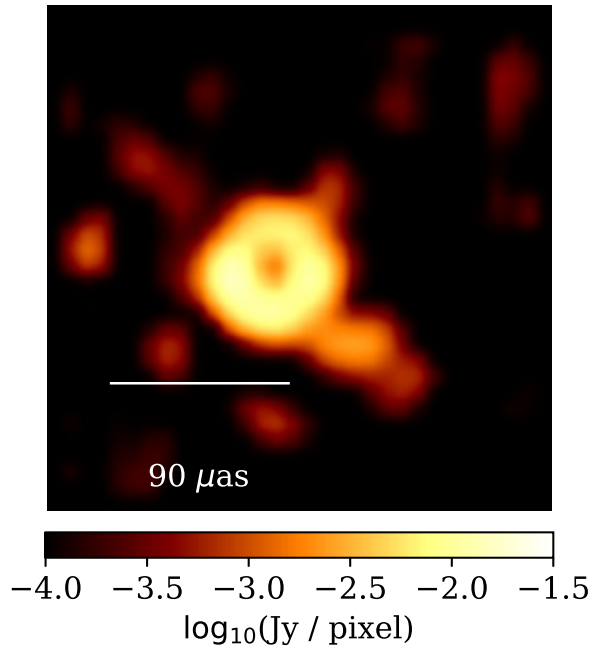


Figure 5.33: Average DoG-HiT reconstruction of 2017 EHT observations of M87 (only high bands), averaged over all four days highlighting the extended emission component.

such as model-fitting, provide superior resolution that is needed to resolve the ring, while other methods show a better performance for extended emission. A combination of the methods could therefore enable us to recover both structural features. However, the conflicting resolution between fitting a narrow ring and an imaging round questions the results: how much of the extended emission is absorbed in the model-fitting parameters of the ring and vice versa? We propose an alternative approach here that resolves the issue of conflicting resolutions. We have demonstrated in Müller & Lobanov (2022) that DoG-HiT provides super-resolution. Further, we demonstrated the power to smoothly represent extended emission features with the same basis functions with DoB-CLEAN in Müller & Lobanov (2023a). We therefore propose to search for extended emission related to the jet in M87 with DoG-HiT. To this end we relax the compact flux assumption in DoG-HiT (i.e. we used a smaller regularization parameter  $\alpha = 0.01$  instead of  $\alpha = 0.1$ ) and widened the field of view.

We show our reconstruction in Fig. 5.33. Some extended emission towards the south-west of the ring was detected that is consistent with the findings in Broderick et al. (2022b), compare Fig. 5.34. However, we recover a more elongated structure. The correct location is difficult to retrieve from the data due to the lack of closure triangles at short baselines. All in all, we can confirm the detection of an extended jet emission in the data from 2017 EHT observations of M87.

Figure 10, from  
 Avery E. Broderick et al 2022 *Astrophys. J.* 935 doi:10.3847/1538-4357/ac7c1d  
<https://dx.doi.org/10.3847/1538-4357/ac7c1d>  
 © 2022. The Author(s). Published by the American Astronomical Society.

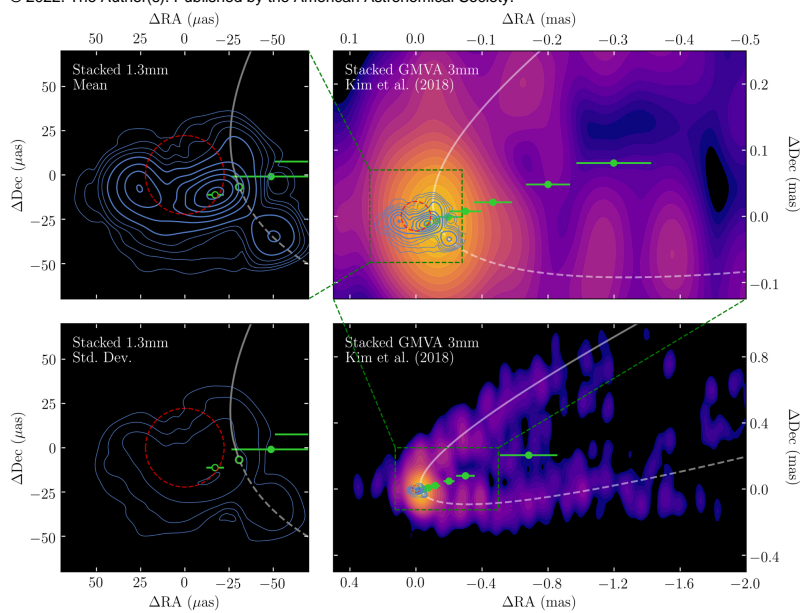


Figure 5.34: Fig. 1 of Broderick et al. (2022b). The figure shows the extended emission recovered by THEMIS as contour levels. The right panels compare the event horizon scale reconstructions with the extended jet observed with the GMVA (Kim et al. 2018). The white line indicates the edge-brightened jet opening. The extended emission towards the south-west of the ring is correlated with the jet observed at smaller frequencies. Figure is reprinted by CC.BY. 4.0.

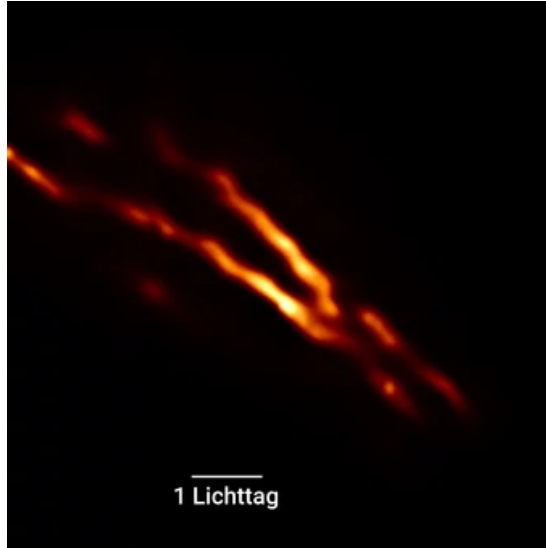


Figure 5.35: Cen A observed with the EHT. Image credit: Janssen et al. (2021). The image is taken from <https://www.mpg.de/17216488/eht-centaurus-a-jet> at 13.01.2023.

Broderick et al. (2022b) compared the extended emission to the direction of the larger-scale jet observed at 3mm with the GMVA (Kim et al. 2018) and concluded that the extended component is expected from the base of a jet launched close to the event horizon of the black hole, further supporting a spin-driven outflow launched by the Blandford-Znajek mechanism (Broderick et al. 2022b).

### 5.2.2 Centaurus A

Centaurus A (Cen A) was observed in the 2017 EHT campaign and subsequently calibrated and imaged by Janssen et al. (2021), who reported various challenges during the imaging process. For instance, the EHT uv-coverage is limited in the direction of the Cen A jet. Among all the non-horizon AGN sources observed by the EHT in 2017, Cen A proved to be the most challenging to image with significant discrepancies across different imaging methods. Due to the already established performance of DoG-HiT on ‘easier’ data sets such as M87, it is therefore an important additional test to study the performance for Cen A, in particular since DoG-HiT is unsupervised (and may resolve the discrepancies between different methods). Here we show an alternative verification of the imaging of Cen A. We show the reconstruction of Cen A presented in Janssen et al. (2021) in Fig. 5.35. For comparison we show the DoG-HiT reconstruction in Fig. 5.36. Both images match surprisingly well given the quality of the data set showing the prominent edge-brightened jet. However, we do not find the counter-jet with DoG-HiT, a feature that was already questioned in Janssen et al. (2021).

The polarimetric analysis of Cen A is still ongoing (and omitted here following

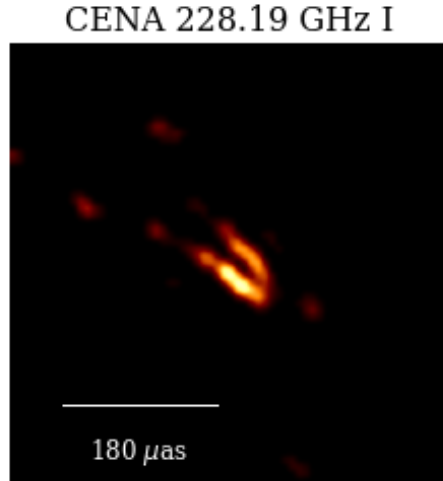


Figure 5.36: DoG-HiT reconstruction of Cen A.

the embargo rules of the EHT). DoG-HiT plays a significant role in it. The polarimetric analysis is further complicated by several data issues originating from corrupting large scale structure and rotation across IF bands. The data issues that the large scale structure is posing highlights another benefit of DoG-HiT: There may be significant polarization also outside the visible Stokes I contours. This feature could be possibly explained by the special uv-coverage of EHT observations: due to the lack of short baselines, extended emission cannot be observed with high significance. Polarized structures residing in the wider extended jet may be more localized, e.g. due to local Faraday rotation, and then become visible again with the uv-coverage of the EHT experiment. Such an effect is explicitly excluded in EHT polarimetry software such as *ehtim*, *DMC* and *Themis* by utilizing the inequality (2.30), although that may be not sufficient. DoG-HiT allows to relax this assumption as the multiresolution support also allows substantial polarized emission in low-intensity parts of the image, i.e. replaces a strong spatial support prior information with a weaker scalar support prior that is determined by the uv-coverage.

### 5.2.3 3C279

In 2017, 3C279 was observed by the EHT as a calibrator source, and an image obtained from this observation was published by Kim et al. (2020). We present a re-analysis of this data set in Fig. 5.37 for all four days of observation. The image shows the same prominent double structure observed by Kim et al. (2020). The images are best recovered on the last two days. On these days a horizontally elongated core structure is visible. It has been speculated whether this structure

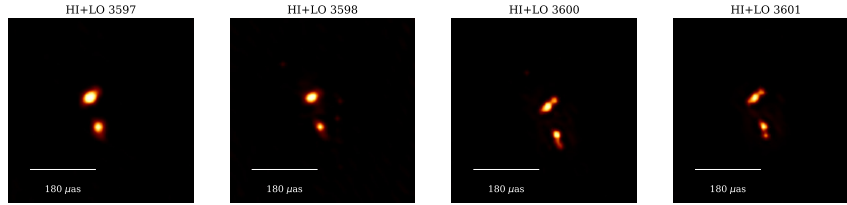


Figure 5.37: DoG-HiT reconstruction of 3C279 observed with the EHT in 2017.

might indicate a wide jet basis that may be launched from the accretion disk (Kim et al. 2020). The images at the first two days are less well constrained due to a worse uv-coverage. These images illustrate an important feature regarding the resolution of DoG-HiT: the resolution is determined by the balancing between the data fidelity terms and the regularization terms. For the first two days, compared to the last two days, the penalty term dominates the objective since the data term is less sensitive. The resulting resolution gets worse.

### 5.3 AGN projects

DoG-HiT and DoB-CLEAN were developed with a special focus on the EHT and its planned successors. Additionally, applications to lower frequency arrays have been tested recently as well. Among others, we report here on reconstructions of 3C120 within the MOJAVE, observations of 3C279 with the Global mm-VLBI Array (GMVA), and observations of M87 with RadioAstron. These applications demonstrate additional features developed for *MrBeam* in the course of this dissertation in order to meet the requirements of the corresponding experiment: a fully parallelized data analysis pipeline implemented on the central computing cluster of the Max-Planck Computing and Data Facility (MPCDF). Moreover, we develop tools for interacting with CLEAN and strategies to deal with highly elliptical beams.

#### 5.3.1 Parallel Cluster Computing Pipeline

The MOJAVE program has monitored AGN jets for over twenty years already (Lister et al. 2018). The program studies the dynamic evolution of jets, e.g. the movement of hotspots downstream the jet across epochs. 3C120 is one of the sources with a prominent, transversely resolved and edge-brightened jet (Casadio 2016; Zabora et al. 2022). Recent theoretical and observational work suggest that edge-brightening in jets may be related to a helical magnetic field (among others Gabuzda et al. 2018; Gabuzda 2021; Gómez et al. 2016; Kramer & MacDonald 2021), e.g. by the detection of a transverse rotation measure gradient. Observa-

tions at highest angular resolution, e.g. of Cen A (Janssen et al. 2021), 3C279 (Kim et al. 2018), M87 (Kim et al. 2023), 3C84 (Giovannini et al. 2018) or 3C345 (Pötzl et al. 2021) back this statement on a variety of scales. A reanalysis of a RadioAstron 22 GHz observation of BL Lac with the super-resolving algorithm DoB-CLEAN (Müller & Lobanov 2023a) showed a possible edge-brightening close to the black hole that was not visible with CLEAN reconstructions, see also Fig. 5.38. For more details we refer to our detailed discussion in chapter 3.3. It has been speculated recently whether edge-brightening is a common feature among all jets that only recently became visible with the increased resolution and dynamic range of current VLBI experiments (Gabuzda 2021). Many different explanations have been proposed in the past including Kelvin-Helmholtz instabilities, magnetic reconnection, particle acceleration at the edges of the jet, a velocity difference between the central spine and outer sheath of the jet and a helical magnetic field carried by the jet (Gabuzda 2021).

The claim whether most jets show edge-brightening as an intrinsic features at highest resolution could be already tested with existing data since novel super-resolving algorithms such as DoG-HiT allow for the reconstruction of reliable image features with a 2-3 times higher resolution. Based on these findings, we propose to test edge-brightening by a reanalysis of already existing MOJAVE data sets with a super-resolving imaging algorithm. To this end we use MOJAVE data sets due to their high number of observed epochs, comparable data quality among the epochs, and the availability of calibrated and flagged data sets (Lister et al. 2018).

The high number of MOJAVE data sets poses a severe problem for a manually driven, thorough reanalysis. However, since all epochs have similar data properties (signal-to-noise ratio, goodness of fit, stability of phase-calibration), an unsupervised imaging algorithm such as DoG-HiT may be optimal for surveying applications. It achieves super-resolution and an accuracy and performance superior to CLEAN (Müller & Lobanov 2022) while keeping to a minimum the necessity for interactive controls (Müller & Lobanov 2023c). Thus, we implemented DoG-HiT on the super-computer cluster *raven* of the Max Planck Computing and Data Facility. We developed top-level scripts dedicated to the needs of the computing system that allow the fully parallized image analysis of a huge number of data sets in a completely automatized way.

As a first test of the infrastructure, we reanalyzed all 3C120 epochs observed with MOJAVE. The CLEAN reconstructions by the MOJAVE team (Lister et al. 2018) are shown in Fig. 5.39. Every panel shows the reconstruction of a single epoch. In the single epochs, the AGN core (the brightest, most left component) and an extended jet is visible. The jet contains several hotspots whose motion

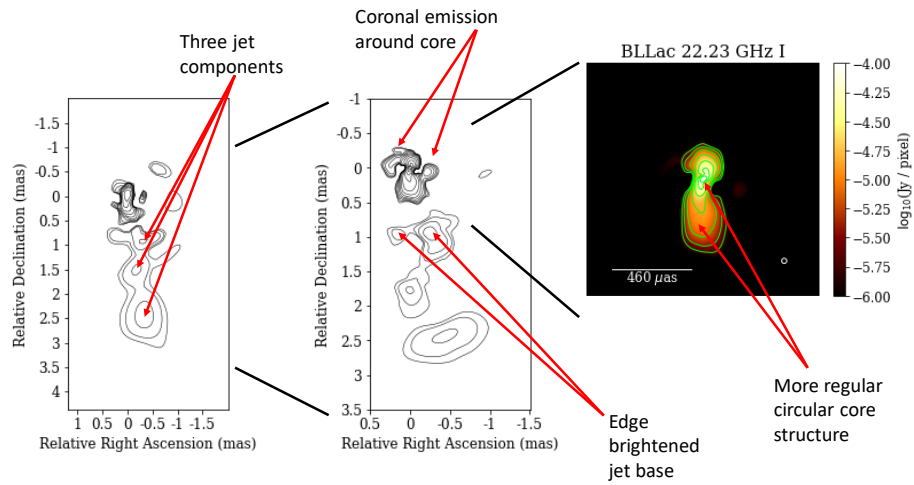


Figure 5.38: DoB-CLEAN reconstruction of BL Lac at highest angular resolution from Müller & Lobanov (2023a). The high-resolution reconstruction shows a possible edge-brightening that was not visible with CLEAN.

### MOJAVE 3C120: CLEAN

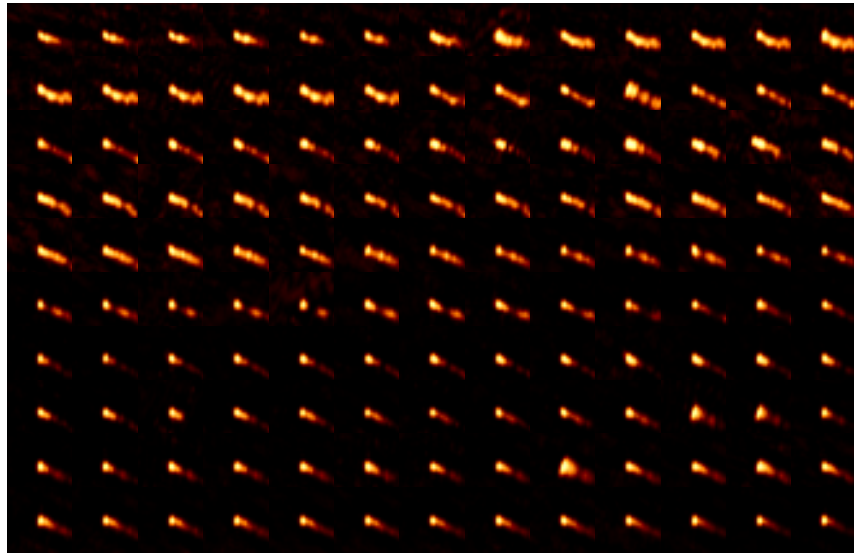


Figure 5.39: MOJAVE observations of 3C120 with data analyzed with CLEAN by the MOJAVE team. The scans are ordered in time starting from the top left (earliest) scan to the bottom right. The images are plotted in logarithmic scale.

## MOJAVE 3C120: MrBeam (DoG-HiT)

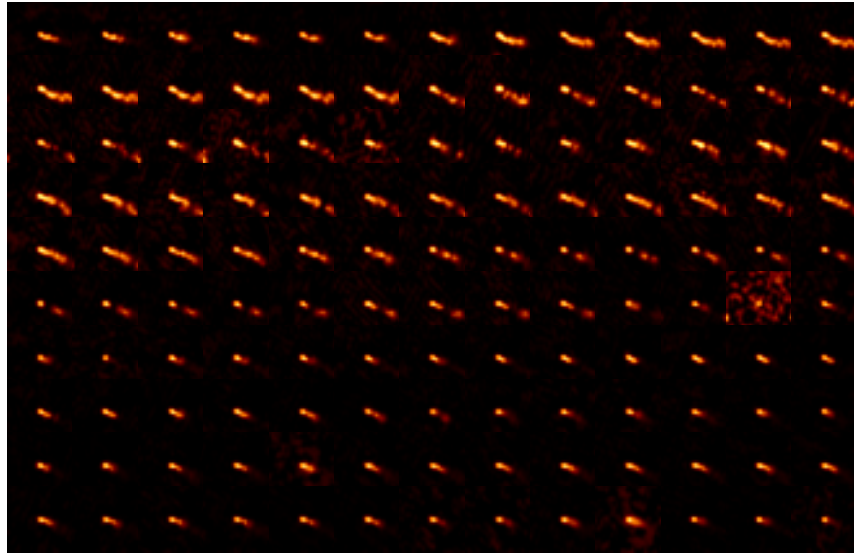


Figure 5.40: MOJAVE observations of 3C120 analyzed unsupervised by DoG-HiT (blurred with a 0.5 mas beam). The scans are ordered in time. The image series is plotted in logarithmic scale.

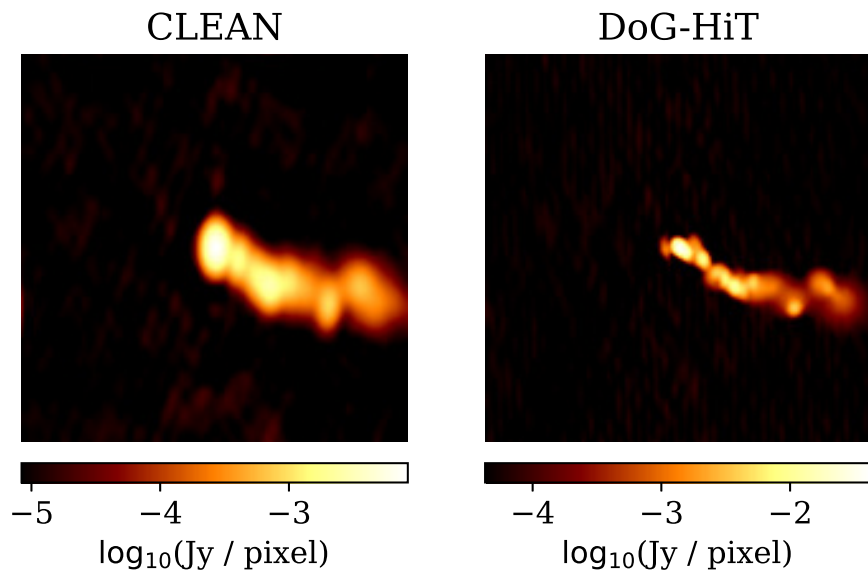


Figure 5.41: The single epoch observed at 27.10.1996 from the MOJAVE sample of 3C120 analyzed with CLEAN and with DoG-HiT.

downstream the jet are traced by MOJAVE, thus providing key observations of the dynamics within the jet. We show the reconstructions with DoG-HiT in Fig. 5.40. Moreover, for better illustration we also show the reconstructions of a single epoch in Fig. 5.41. Comparing the CLEAN and the DoG-HiT reconstructions shows that the overall structures match quite well. The automatized DoG-HiT reconstruction failed in only one epoch to reproduce an image comparable to the CLEAN reconstruction. As expected, the DoG-HiT reconstructions reveal structural features at a higher resolution, indicating that the jet may be composed of a larger number of small, moving enhanced emission regions (more and finer than observed with CLEAN) surrounded by a cocoon of faint extended emission, i.e. compare the randomly selected single epoch presented in Fig. 5.41. While the DoG-HiT reconstructions reveal structural features that were not observable with CLEAN, an edge-brightening as a generic feature of jets when recovered at highest spatial resolution is not detected, at least for 3C120. The non-detection at 15 GHz is most likely the compound result of a steep spectral index of the emission in the outer layers of the jet, compounded by the reduced emission and structural sensitivity of VLBI data at 15 GHz. This work and the existing pipeline will be extended to a larger sample of sources within MOJAVE in a consecutive work, to allow proper statistics.

The current application of DoG-HiT to the 3C120 epochs observed by MOJAVE constitutes the largest-scale application of DoG-HiT to date. It proves the capability of the software to deal with real, observational data, thus matching well to the needs of large imaging surveys done with VLBI. Applying DoG-HiT in an unsupervised fashion and at the high level of parallelization, we were able to analyze a set of 130 VLBA observations in roughly ten minutes, a procedure that took us weeks to months of manually imaging before!

### 5.3.2 GMVA Data on 3C279

3C279 has been observed with the GMVA at 3mm on 14.04.2018. Here we report on the final investigation of this data set with DoG-HiT. The full analysis of these data is still in progress. The final image will be built by achieving consistency among several methods, i.e. DoG-HiT, RML and CLEAN. Benefiting from its unsupervised nature, fast processing and stability against calibration effects, DoG-HiT provides important guiding to the other methods that require more thorough calibration and manual input at an early stage of analysis. Apart from the the image itself, we present here the developments that were undertaken to provide the imaging guidance by DoG-HiT.

We show the uv-coverage and the observed amplitudes after self-calibration and imaging in Fig. 5.42. The data set has been coherently averaged over time

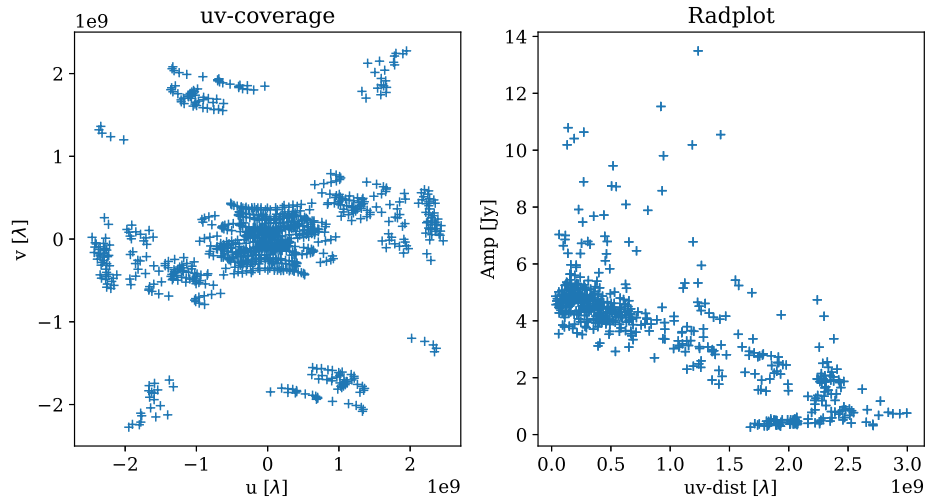


Figure 5.42: Left panel: uv-coverage of coherently averaged data set (60 s averaging). Right panel: Radplot of self-calibrated data set.

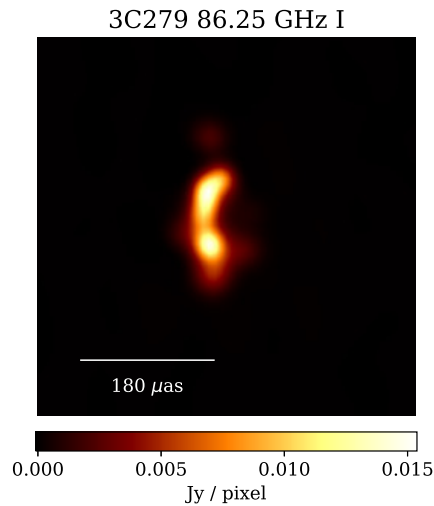


Figure 5.43: DoG-HiT reconstruction of central core region of GMVA observations of 3C279 at 14.April 2018.

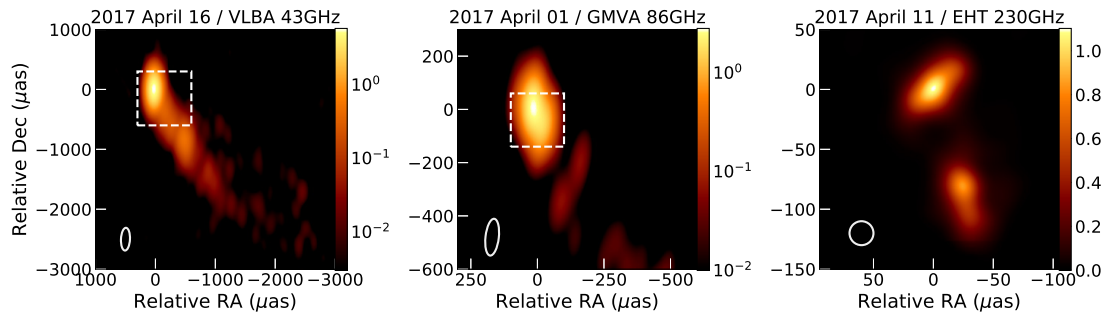


Figure 5.44: Overview of reconstructions of 3C279 at various wavelengths. The figure is taken from Kim et al. (2020) by CC.BY 4.0.

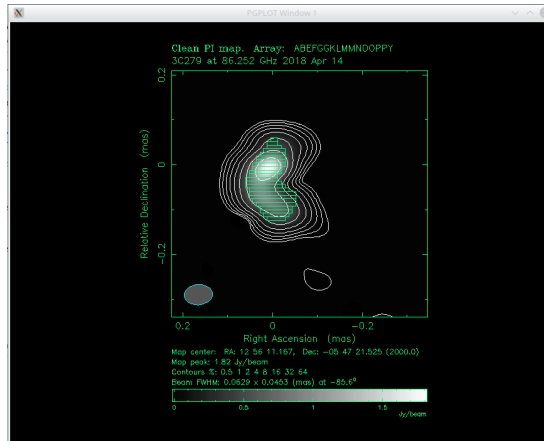


Figure 5.45: Average of CLEAN, *ehtim* and DoG-HiT images guided by DoG-HiT windows.

intervals of 60 s in length. For imaging, we followed the multistep procedure outlined in chapter 3.5. In particular, we emphasize that in the first rounds only closure quantities are used. Gains are calibrated with the closure-only solution on a dynamic time scale of 1 hour. The amplitudes of most antennas behave well, with Mauna Kea as a serious outlier, probably due to the low declination of the source or pointing issues. The imaging procedure was focused on a high resolution reconstruction of the features close to the core, in order to constrain better the compact flux. We present our DoG-HiT reconstruction in Fig. 5.43. As a comparison, we show the reconstructions from 2017 with the VLBA (7 mm), the GMVA (3.5 mm) and the EHT (1.3 mm) in Fig. 5.44. The overall jet direction and two-component structure of the innermost jet can be well reconciled with the images obtained from the 2017 data. However, the reconstruction of 2018 shows two components connected by a smooth curve (probably related to a bent jet) instead of two disconnected components.

Verification for this image comes from alternative data analysis methods, i.e. CLEAN and *ehtim*. Moreover, the GMVA image will be used for guiding the imaging of EHT data. On the CLEAN side, the most important prior information that needs to be introduced in the imaging algorithm manually, is the selection of the CLEAN windows. We can extract CLEAN windows out of the DoG-HiT reconstructions by a simple threshold: we include every pixel in the CLEAN mask that has a brightness greater than 10% of the peak flux in the image. To make this rather simple procedure work, the DoG-HiT and the future CLEAN image have to be aligned by maximizing a 2D correlation between the structures in the two images, because the absolute positional information is not preserved by either imaging algorithm. The average image (averaged over methods normalized to same peak flux) with the driving windows overplotted is shown in Fig. 5.45.

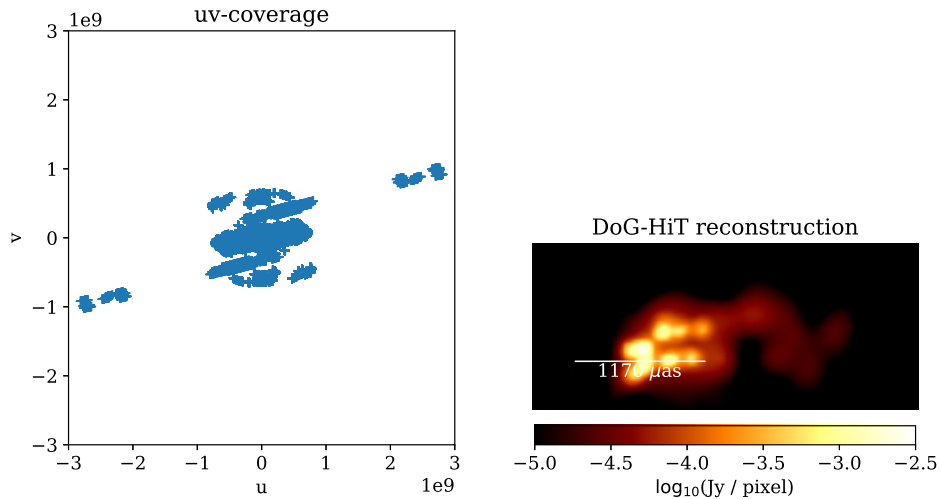


Figure 5.46: Left panel: uv-coverage of RadioAstron observations of M87, Right panel: DoG-HiT reconstruction.

### 5.3.3 M87 RadioAstron

M87 was observed with RadioAstron at 22 GHz in February 2014. Here we present a short summary of the findings in Kim et al. (2023) in which DoG-HiT and DoB-CLEAN reconstructions were used for verification of the image fidelity and the robustness of the recovered features.

The source was observed with the RadioAstron satellite and a sensitive ground array consisting of 21 antennas. The longest uv-spacing probed by the observation was  $11 \text{ G}\lambda$ . However, fringes were only detected up to  $\sim 3 \text{ G}\lambda$ . This is equivalent to an effective resolution of  $\sim 150 \mu\text{as}$  (Kim et al. 2023). We show the uv-coverage of the observation in Fig. 5.46. The data set has been correlated in Bonn. Fringe finding and evaluation of the data quality was performed with *PIMA* and *AIPS* with no initial fringes found to the space antenna, but with high signal-to-noise ratio fringes detected for all of the ground antennas, except for the Australia Telescope Compact Array (ATCA) and the Mopra antenna (Kim et al. 2023). To guide the fringe fitting on the space baselines, we mapped the source first with the ground array alone with CLEAN. This image has been loaded to AIPS to refine the fringe fitting on the space baselines. With this procedure, fringes up to  $\sim 2.8$  times the Earth diameter have been detected (Kim et al. 2023) and were used for the final imaging. The final imaging has been performed with CLEAN by adopting the CLEAN windows from the ground only image.

Due to the unstable fringes, and the sparse uv-coverage on long (space-) baselines, the reconstruction of small scale features is relatively uncertain. To examine the reliability of the recovered features, the imaging scripts have been verified on synthetic data (for more details Kim et al. 2023). Moreover, the CLEAN

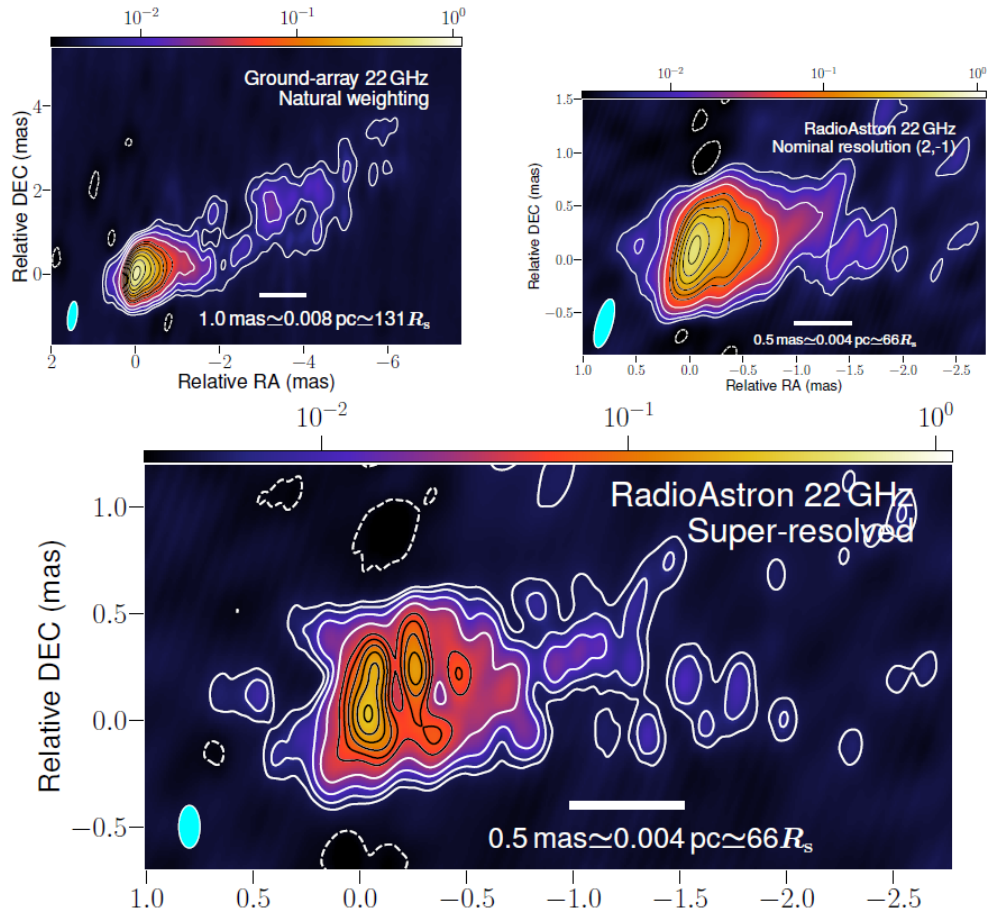


Figure 5.47: CLEAN reconstructions of M87. Reprinted from Kim et al. (2023) with permission for reprinting given by J.Y. Kim.

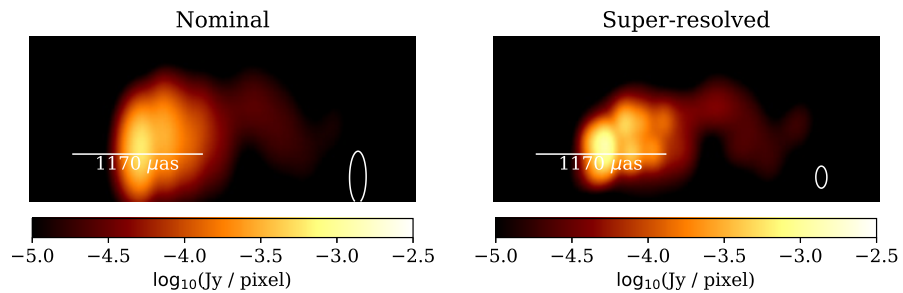


Figure 5.48: DoG-HiT reconstructions of M87 RadioAstron observations blurred to the natural beam ( $470 \times 150 \mu\text{as}$ ) and the super-resolved beam ( $200 \times 100 \mu\text{as}$ ).

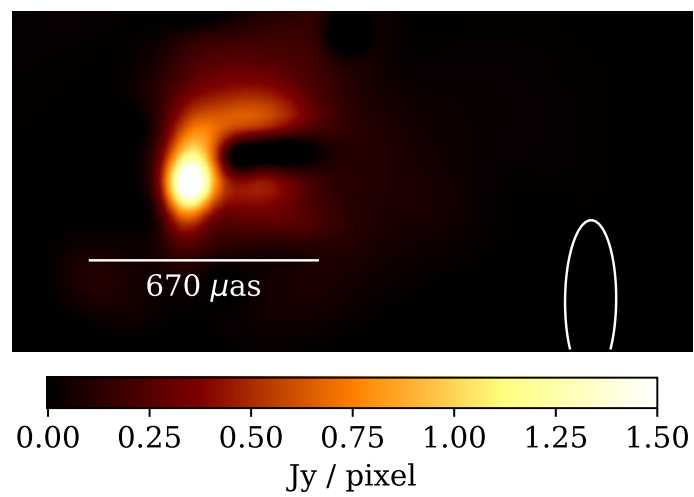


Figure 5.49: DoB-CLEAN reconstruction of M87 with RadioAstron observations with uniform weighting.

imaging was carried out independently by several different people. Due to the focus on high resolution, an independent cross-verification with a super-resolving algorithm (that is easy to handle) was desired as well. Even more salient, to explore the structural patterns with CLEAN at high angular resolution, a cross-verification with a super-resolving CLEAN like algorithm builds towards consistency. Hence, DoG-HiT and DoB-CLEAN were applied from the early stage of the analysis onward to provide alternative verification and guidance for CLEAN. The DoG-HiT reconstruction is shown in the right panel of Fig. 5.46. We present the CLEAN reconstructions with natural weighting and super-uniform weighting in Fig. 5.47. For comparison, we also show the DoG-HiT reconstructions blurred with the natural and the uniform beam in Fig. 5.48 and the DoB-CLEAN reconstruction in Fig. 5.49.

The reconstructions have converged to a consistent high resolution image of M87, with DoG-HiT and DoB-CLEAN reconstructions more focused on the core region of the source due to computational limitations on the field of view. The core brightness, strongly edge-brightened innermost jet (very clearly visible with DoB-CLEAN) and overall jet shape and width has been recovered consistently by all methods. In particular, DoG-HiT guided the reconstructions towards a verification of the detection of an edge-brightened counter-jet. The core shows a prominent X-shaped structure. There is, however, a specific discrepancy: In the CLEAN reconstructions, the brightest component is the southern core component of the double-lobed core. For DoG-HiT and DoB-CLEAN, it was the northern one.

The images show a core that is elongated in north-south direction, more than the beam resolution (Kim et al. 2023). This is consistent among various methods, but has not been observed in VLBI before. There seems to be a more complicated substructure in the core that becomes visible with high angular resolution indicating that the intrinsic size of the core is larger at longer wavelengths (Kim et al. 2023). The counter-jet has been detected consistently with all of the imaging methods. Strong edge-brightening, both in the jet and in the counter-jet indicates that the central engine might be located close to the VLBI core (Kim et al. 2023; Walker et al. 2018). The brightness temperature of the core is at least  $T_B \sim 10^{12}$  K. Such a high core brightness temperature exceeds the limit set by inverse Compton cooling (see Blandford et al. 2019) and may require Doppler boosting or an intrinsically high brightness distribution due to a continuous injection of energetic particles in the jet (Kim et al. 2023).

## 5.4 Synergies

DoG-HiT, DoB-CLEAN and MOEA/D are implemented in the software package *MrBeam* that extends *ehtim* and *regpy*. For a more detailed discussion, we refer to chapter 3.6. In a nutshell, *MrBeam* and *regpy* are modular software packages that provide a framework for inverse problems and iterative regularization methods in general. Due to this, several developments done for this dissertation found fields of applications outside of VLBI as well.

### 5.4.1 Ly- $\alpha$ Tomography

In this subsection we summarize the findings of Müller et al. (2020) and Müller et al. (2021).

The Ly $\alpha$  forest comprises densely packed, narrow absorption lines bluewards the Ly $\alpha$  absorption line in the spectra of distant quasars. It is caused by absorption of light of the background quasar by the intergalactic medium (IGM), e.g. see Bi & Davidsen (1997); McQuinn & Upton Sanderbeck (2016) as well as the illustration in Fig. 5.50. The light emitted by a background quasar passes through the IGM on its path towards us. The IGM consists of overdense regions (clouds) and underdense regions (see e.g. the maps in Lee et al. 2014b, 2016). An overdense region absorbs a bigger portion of the light than an underdense region. Hence, the amount of absorption is related to the density of the IGM (Bahcall & Salpeter 1965; Gunn & Peterson 1965). Due to the cosmic redshift, every wavelength in the spectrum can be associated with a specific position along the line of sight. This view on the Ly $\alpha$  forest is supported by studies of the line-widths (Tytler et al. 2004), cosmological simulations (Palanque-Delabrouille et al. 2013, 2015) and the studies of the probability of transmission (Rollinde et al. 2013).

The inverse problem referred to as Ly $\alpha$  forest tomography is to recover the neutral hydrogen density along a single line of sight and to interpolate the recovered neutral hydrogen densities along neighboring lines of sights in order to recover the three-dimensional cosmic density field. These problems are similar to VLBI imaging: along the line of sight we approximately solve a deconvolution problem, the three dimensional reconstruction is a sparsely sampled interpolation problem. Several techniques have been proposed in the past to achieve this goal, e.g. the Richardson-Lucy inversion scheme (Nusser & Haehnelt 1999), Wiener filtering (Pichon et al. 2001), statistical reconstructions (Gallerani et al. 2011; Kitaura et al. 2012) and inversion by non-linear optimization (Müller et al. 2020). Furthermore, the success of wavelet decomposition of the forest for constraining the thermal state of the IGM from the spectra (Garzilli et al. 2012; Lidz et al. 2010) suggests a future application of a multiscale, wavelet-based reconstruction

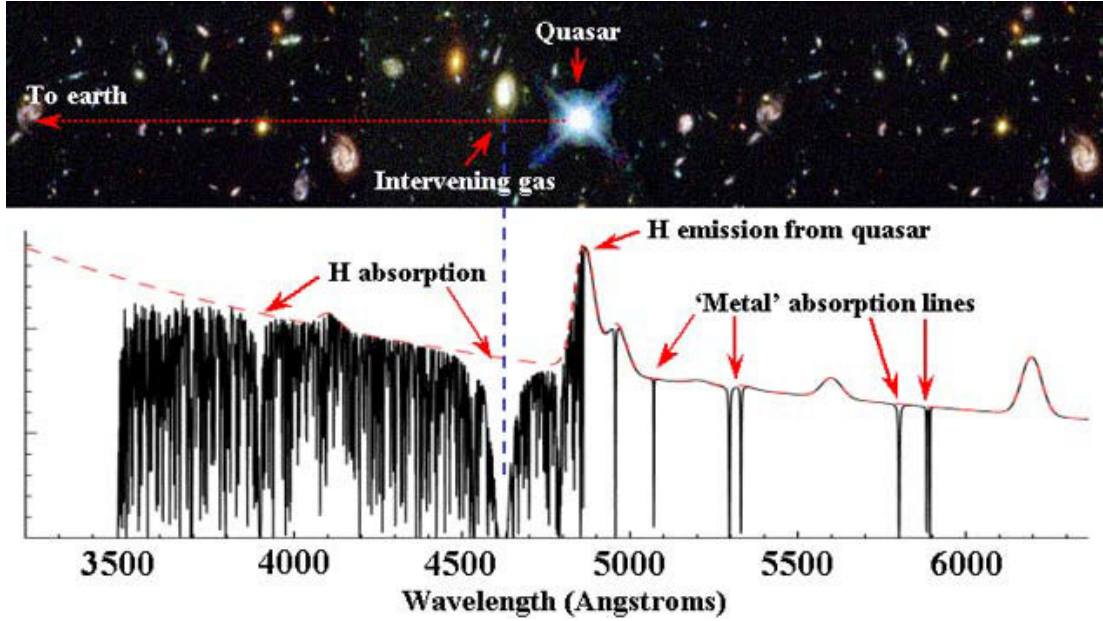


Figure 5.50: Illustration of the Ly $\alpha$  forest. Light emitted by a distant quasar gets absorbed by the intervening gas, forming the feature of densely packed, narrow absorption lines known as the Ly $\alpha$  forest. Image was taken from <https://news.illinois.edu/view/6367/204679> on 10.01.2023. Graphic design is by John Webb.

technique. The density distribution of the IGM is of great interest for the astrophysics community. Fully three dimensional reconstructions have been used to detect protoclusters (Lee et al. 2016; Stark et al. 2015), to study dark matter (Hamaide et al. 2022) and cosmic voids (Krolewski et al. 2018), as well as the statistical properties of the large scale structures in the cosmic web (Caucchi et al. 2008; Lee et al. 2014b; Lee & White 2016; Ozbek et al. 2016).

The one-dimensional inverse problem of recovering the Ly $\alpha$  signal along the line of sight at high resolution is complicated by the thermal model of the IGM. The single absorption lines are broadened by thermal broadening. This can be described by a convolution with the generic profile of an absorption line, known as the Voigt profile (Gallerani et al. 2006; Müller et al. 2020):

$$\tau(z_0) = \sigma_0 c \int_{\text{LOS}} dx(z) \frac{n_{\text{HI}}(x, z)}{1+z} \times \mathcal{H}(v_{\text{H}}(z_0) - v_{\text{H}}(z) - v_{\text{pec}}(x, z), b(x, z)), \quad (5.1)$$

where  $\tau$  is the optical depth,  $z, z_0$  are redshift coordinates,  $\sigma_0$  is the effective Ly $\alpha$  cross-section,  $n_{\text{HI}}$  is the neutral hydrogen density and  $v$  is the Hubble velocity.  $\mathcal{H}$  is the Voigt profile with width  $b$ . The thermal broadening  $b$  scales with the current temperature in the IGM. The temperature  $T$  in the IGM is related to the baryonic fractional density perturbation  $\delta_b$  by a power law (Hui & Gnedin 1997;

Müller et al. 2020):

$$T(x, z) = T_0(z)\delta_b^{2\beta}, \quad (5.2)$$

where  $T_0$  is the temperature at the mean density. The quantity  $\gamma = 1 + 2\beta$  is called the polytropic index. Under the assumption that hydrogen and helium are highly ionized in the post-reionization epoch, the final operator reads as (Müller et al. 2020):

$$\begin{aligned} \tau(z_0) \approx & \int_{\text{LOS}} dx \mathcal{A}(z(x)) \cdot n_{\text{HI}}^\zeta(x) \\ & \times \exp\left(-C(x) \cdot \frac{[v_{\text{H}}(z_0) - v_{\text{H}}(z(x)) - v_{\text{pec}}(x)]^2}{n_{\text{HI}}^\epsilon(x)}\right), \end{aligned} \quad (5.3)$$

with parameters:

$$\mathcal{A}(z) = \frac{\sigma_0 c}{\sqrt{\pi}(1+z)} \sqrt{\frac{m_p}{2k_B T_0}} \left( \frac{\mu_e \alpha_0}{\Gamma(z)} \left[ \frac{\Omega_b \rho_c}{\mu m_p} \right]^2 T_0^{-0.7}(z)(1+z)^6 \right)^{\beta/\alpha}, \quad (5.4)$$

$$\zeta = \frac{\alpha - \beta}{\alpha}, \quad (5.5)$$

$$C(z) = \frac{m_p}{2k_B T_0} \left( \frac{\mu_e \alpha_0}{\Gamma(z)} \left[ \frac{\Omega_b \rho_c}{\mu m_p} \right]^2 T_0^{-0.7}(z)(1+z)^6 \right)^\epsilon, \quad (5.6)$$

$$\epsilon = \frac{2\beta}{\alpha}. \quad (5.7)$$

For a detailed proof, we refer to our work in Müller et al. (2020). Here  $m_p$  is the mass of the proton,  $k_B$  is the Boltzmann constant,  $\mu_e = 2 \cdot (2 - Y)/(4 - 3Y)$  and  $\mu = 2/(4 - 3Y)$  with helium fraction  $Y$ ,  $\Gamma$  is the photoionization rate,  $\alpha_0$  is the recombination rate at mean temperature,  $\Omega_b$  is the cosmic baryon matter fraction,  $\rho_c$  is the critical density of the Universe, and  $\alpha = 2 - 1.4\beta = 2.7 - 0.7\gamma$ . As can be seen from Eq. (5.3), the convolution kernel scales with the density again. Hence, the forward operator  $n_{\text{HI}} \mapsto \tau$  is strictly speaking not a convolution and consequently non-linear. The inversion  $\tau \mapsto n_{\text{HI}}$  is therefore more complex and ill-posed. Because of this, advanced inversion methods have to be applied. At this point, the synergy with VLBI imaging becomes evident. The same tools and frameworks that were implemented for *regpy* and *MrBeam* to deal with the minimization of complex objectives in VLBI imaging, need to be implemented for the analysis of Ly $\alpha$  tomography as well.

In Müller et al. (2020), we compared already existing one-dimensional Ly $\alpha$  tomography algorithms that recover the density at highest resolution along the line of sight. Here we report about the main findings. The field of Ly $\alpha$  for-

est tomography was pioneered by Nusser & Haehnelt (1999) who utilized a fast Richardson-Lucy implementation (which is a linearized deconvolution algorithm). Pichon et al. (2001) proposed a Wiener filtering step for the interpolation between neighboring lines of sight and an iterative Gauss-Newton iteration for the one-dimensional reconstruction. Effectively, this is an RML regularization with a weighted  $l^2$  penalty term, with weights computed by the matter auto-correlation function. Gallerani et al. (2011) used for the first time a completely statistical approach by matching overdensity probabilities with the probability distribution of the observed optical depths (probability conservation). This approach, however, does not include regularization. A regularized version has been proposed by us in Müller et al. (2020). We present an overview of the acronyms used in this chapter in Tab. 2. A tabular overview of the key findings of Müller et al. (2020) is presented in Tab. 3. Overall the IRGN method is most precise and robust, but also takes the most time. RL is similarly precise, but scales bad to noisy images. PC is less accurate, and also lacks regularization against noise, i.e. it is unstable in the presence of noisy data. On the contrary, PC utilizes a statistical approach (conservation of probabilities). Only assumptions on the matter power spectrum are processed, no assumptions on the detailed emission and photoionization have to be made, i.e. the forward operator Eq. (5.3) is not used explicitly. Due to this advantage, PC reconstructions are independent of wrong assumptions on the a-priori unknown photoionization rate, polytropic index and temperature at mean density  $T_0$ . RPC combines the best of both worlds. We use the  $l^2$ -norm of the match of the overdensity and absorption probability density distributions as data fidelity term and the total squared variation as penalty term (Müller et al. 2020). Hence, we reformulate the Ly $\alpha$  tomography problem in the framework of the *generalized Tikhonov method* such that it can be easily implemented and realized within the framework provided by *regpy* and *MrBeam*. RPC is robust against noise (regularization introduced by the smoothness promoting total squared variation penalty term) and still independent from the exact parameters of the forward model.

In our second Ly $\alpha$  forest paper (Müller et al. 2021), we extended this approach to an estimation strategy of the thermal history of the IGM. Again, we will only provide a short overview. With two different inversion schemes at hand (RPC and IRGN), we recover the neutral hydrogen density with both schemes. One scheme (RPC) is independent of the temperature at mean density  $T_0$  and the power law index  $\beta$ . The other scheme (IRGN) depends strongly on the choice of  $T_0$  and  $\beta$ . Hence, these reconstructions only match if we assumed the correct thermal parameters for the IRGN reconstruction. Additionally, the IRGN reconstructions provide an independent way to constrain  $\beta$  and  $T_0$  as well by examining the  $\chi^2$  of

Table 2: Summary of the inversion techniques tested and acronyms used for Ly $\alpha$  forest tomography. Adapted from Müller et al. (2020).

Method	Acronym	Type	Priors	Reference
Richardson-Lucy	RL	Deterministic, Iterative	EOS	Nusser & Haehnelt (1999)
Explicit Bayesian/ Iterative Gauss Newton/ Wiener Filter	} IRGN	Bayesian, Iterative	EOS, $P_\Delta$	Pichon et al. (2001)
Probability Conservation		PC		
Regularized Prob. Cons.	RPC	Statistical, Iterative	$P_\Delta$	Müller et al. (2020)

Table 3: Summary of the findings of Müller et al. (2020). Adapted from Müller et al. (2020).

	RL	IRGN	PC	RPC
Computation Time	$\propto N_{\text{pix}}^2$ sometimes many iterations	$\propto N_{\text{pix}}^2$ large constant	$\propto N_{\text{pix}} \log N_{\text{pix}}$ no iterations needed	$\propto N_{\text{pix}} \log N_{\text{pix}}$ fast iterations
High S/N Reconstruction				
→ Large Overdensities	underestimated	underestimated	underestimated	underestimated
→ Mean Overdensities	very precise	very precise	precise	precise
→ Underdensities	precise	precise	moderate	moderate accuracy
→ No. Peaks	precise	precise	overestimated	slightly overestimated
Robustness				
→ Against Noise	unstable	robust	unstable	robust
→ Against Systematics	robust	unstable	independent	independent

the fit to the observed spectrum. Since the weighted  $l^2$  penalization term includes the matter auto-correlation matrix (i.e. the matter power spectrum),  $\chi^2 \sim 1$  is only possible for a correct configuration of the temperature at mean density  $T_0$  and polytropic index  $\beta$ . This property has been first observed by Pichon et al. (2001). If the local temperature  $T(z)$  is overestimated, i.e. thermal broadening is overestimated, a correct fit to the observed optical depths is not possible anymore. If the thermal broadening is underestimated, we overfit the data.  $T_0$  and  $\beta$  affect the size of the thermal broadening in a similar way (see Eq. (5.2)) and are hence degenerate. However, with two independent measurements (by comparing RPC and IRGN reconstructions, and by exploring the IRGN reconstructions) both parameters could be uniquely determined. Details on the estimation procedure in the philosophy of inversion are provided in Müller et al. (2021). We reprint the flowchart of this novel estimation procedure in Fig. 5.51.

We applied this novel estimation pipeline in Müller et al. (2021) to a subset of the UVES\_SQUAD spectra (Murphy et al. 2019). The subset has been selected based on the quality of the spectra, their redshift and resolution (Müller et al. 2021). The reconstruction results yield novel estimations of the temperature of the IGM at redshift  $z \sim 2.5$ , the polytropic index  $\gamma$  and the photoionization rate  $\Gamma$ , see Fig. 5.52, 5.53 and Fig. 5.54. The results are consistent with previous measurements yielding an average temperature of  $\sim 13000$  K and a power-law index

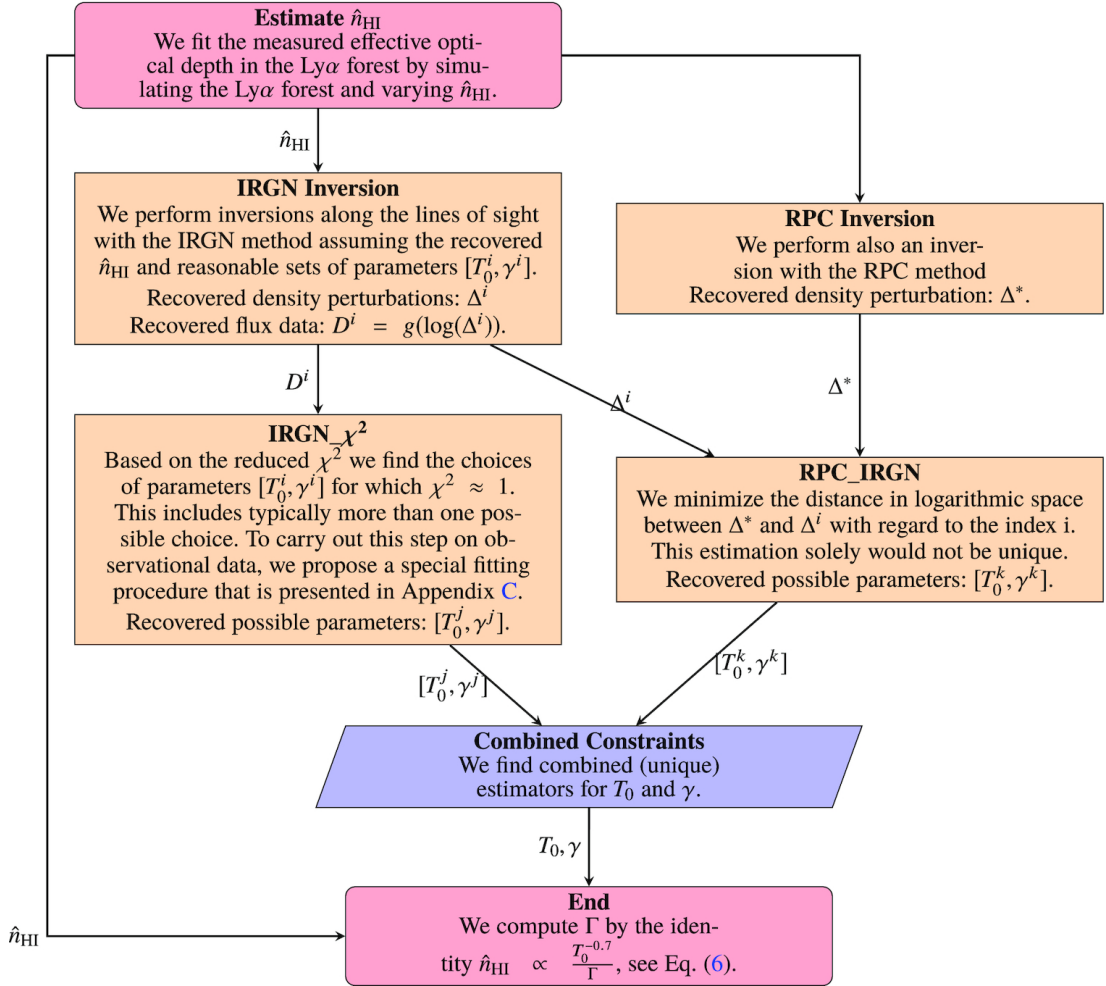


Figure 5.51: Flowchart of the estimation of the thermal state of the IGM from inverse Ly $\alpha$  tomography. Figure adapted from Müller et al. (2021).

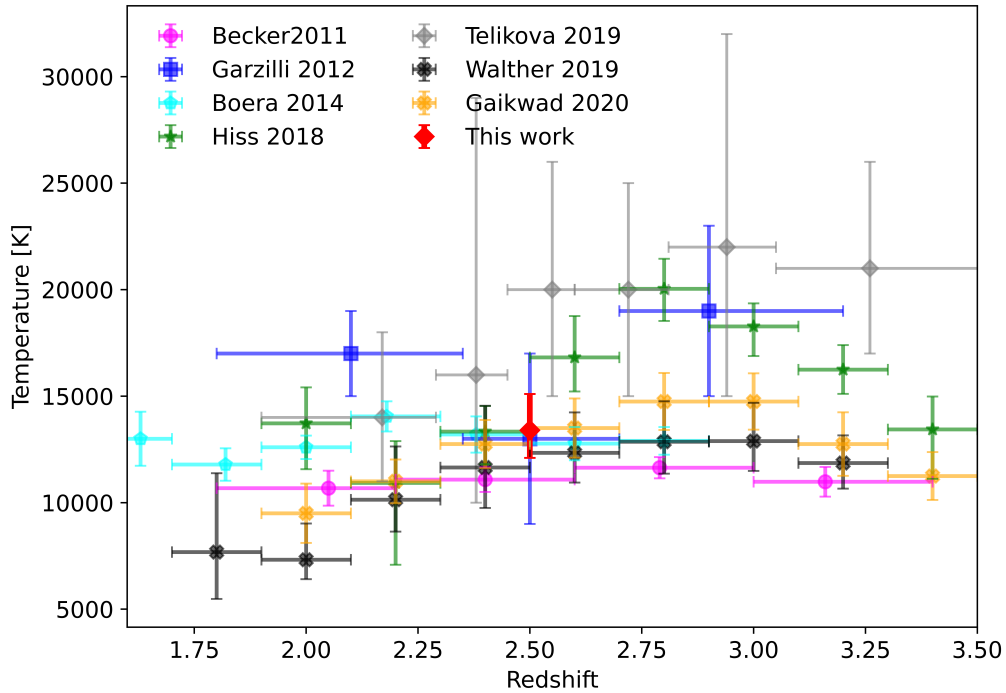


Figure 5.52: Overview of estimates of the temperature at mean density as a function of redshift. The presented data sets are from Becker et al. (2011); Boera et al. (2014); Gaikwad et al. (2020); Garzilli et al. (2020); Hiss et al. (2018); Telikova et al. (2019); Walther et al. (2019). Image adapted from Müller et al. (2021).

$\gamma \sim 1.4$ . Moreover, the method improves in accuracy over previous estimation procedures such as Voigt profile fitting (pioneered by Schaye et al. 2000). The uncertainties obtained are competitive against other recent estimates, although in our work they are drawn from a much smaller redshift bin and hence a much smaller sample of absorption lines (Müller et al. 2021).

Finally, we would like to mention that the biggest uncertainty in the data analysis is introduced by the unknown peculiar velocities (Müller et al. 2021). However, recent developments in the reconstructions of full three-dimensional tomographic maps (e.g. Horowitz et al. 2019; Porqueres et al. 2019, 2020) would allow for the sampling of the velocity field. Lee et al. (2014a) investigated the requirements for tomographic maps concluding that as long as the thermal absorption profile does not have to be resolved, tomographic maps are feasible already at low spectral resolution ( $R \sim 1000$ ). Our simulations (Hamaide et al. 2022; Hand et al. 2018; Müller et al. 2020, 2021) demonstrated that the velocity field is varying only mildly on small scales due to the small Jeans scale of baryonic matter, i.e. the suppression of small-scale fluctuations by thermal pressure (Choudhury et al.

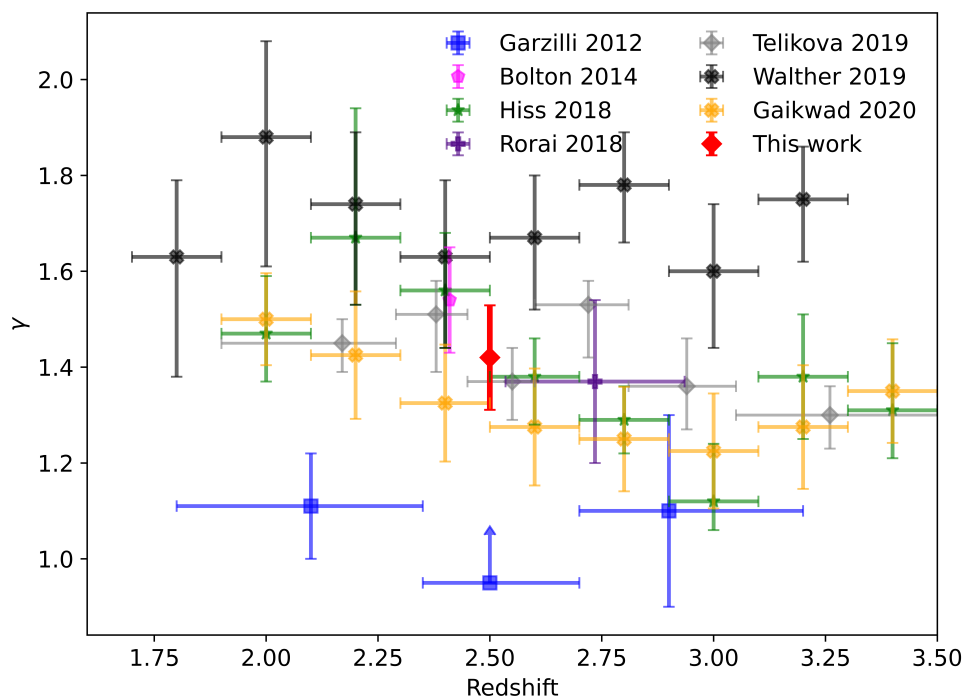


Figure 5.53: Overview of estimations of the polytropic index  $\gamma$ . The estimates are from Bolton et al. (2014); Garzilli et al. (2012); Hiss et al. (2018); Rorai et al. (2018). Image adapted from Müller et al. (2021).

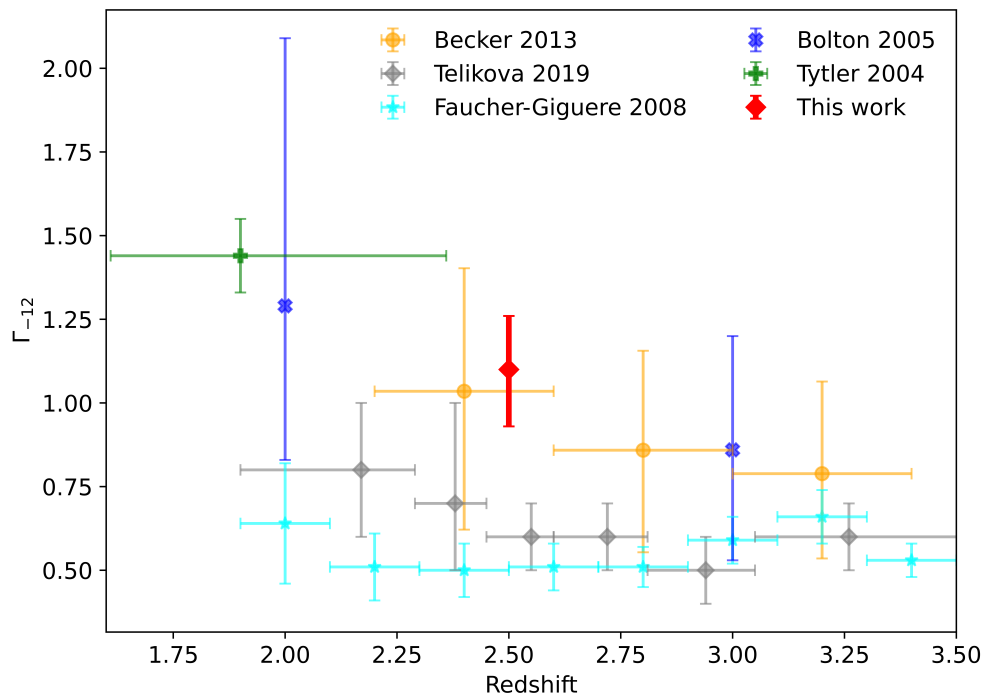


Figure 5.54: Overview over estimations of the photoionization rate as a function of redshift. The estimates are from Becker et al. (2013); Faucher-Giguère et al. (2008); Telikova et al. (2019). Image adapted from Müller et al. (2021).

2001; Gallerani et al. 2006; Zaroubi et al. 2006). Hence, a low-resolution tomographic survey combined with a high spectral resolution observation of the Ly $\alpha$  forest in a single quasar may alleviate the peculiar velocity problem and allow for uncertainties in the temperature estimation of about  $\sim 100$  K on small redshift bins (Müller et al. 2021). In particular, such a three dimensional reconstructions shares great synergies with VLBI imaging. VLBI imaging could be understood equivalently as the problem of filling the gaps in the uv-coverage with reasonable information regarding to prior assumptions, such as smoothness. For Ly $\alpha$  forest tomography, the transverse space of sightlines is only sparsely sampled (compared to the spectral resolution along a single line of sight). Hence, with respect to prior knowledge on the power spectrum of the matter density perturbations, we solve a similar interpolation problem. Even closer to the field of radio interferometry, the concepts that are discussed here are applicable to 21 cm intensity mapping as well and are proposed to be probed by the SKA (Santos et al. 2015). The emission profile of the 21 cm line is affected by thermal broadening in a similar way as for the Ly $\alpha$  line. While cosmographic probes by 21 cm intensity mapping are still in development, this technique promises impressive results for cosmographic, three-dimensional maps of the diffuse IGM. The large field of view, and the high resolution (i.e. narrow frequency bands) along the line of sights, may give unique insights in the nature of the IGM, dark matter and the epoch of reionization.

These works (Müller et al. 2020, 2021) demonstrate the multidisciplinary background of a work dealing with inverse problems in general. The project shares great synergies with VLBI imaging by using the same software tools, and more abstract the same top-level framework and functionality (solving the inverse problem of sparsely sampled data by convex optimization with iterative algorithms).

#### 5.4.2 Ultralight Dark Matter

In this subsection we summarize the results of Hamaide et al. (2022). The publication was written as a shared first-authorship publication, with a shared first-authorship between Louis Hamaide and myself. I contributed to this work at all stages of preparation, i.e. to the conceptualization, implementation, data analysis and writing/editing. The manuscript presents a novel idea of constraining ultralight dark matter particles by a full reconstruction of the matter distribution in the Universe. For the first time, a full (non-linear) inversion scheme has been proposed to extract quantities of fundamental physics. The work demonstrates once more the multidisciplinary benefit of designing an inversion framework in general by the means of convex optimization and the potential behind such approaches to constrain frontline physical applications. The work is related to the main body of this dissertation by utilizing the same software tool (*regpy*, *MrBeam*) that was

developed for VLBI imaging and the same algorithmic framework (solving an ill-posed inverse problem by convex optimization) in general. Therefore, the basic implementation of this approach shares great synergy and dual development with the work that was pursued for this dissertation. As mentioned in the preceding chapter, the synergy is particularly strong since we deal with a typical undersampling problem in the case of three-dimensional Ly $\alpha$  forest tomography. Within the scope of this dissertation, we only provide a short summary of the results presented in Hamaide et al. (2022) and in particular spare most of the technical details related to the (string-) theoretical background of dilatons.

Scalar degrees of freedom of string theory arising in low energy effective theories after compactification such as moduli, dilatons and radions (Arvanitaki et al. 2015; Becker et al. 2006) have been proposed as constituents of dark matter. The value of these scalar degrees of freedom is determined by the local minimum in some potential, e.g. a simple mass term in case of dilatons (although more complex potentials have been investigated recently as well, e.g. Arvanitaki et al. 2015; Marsh 2011). Fields that are displaced from that local minimum at early times start a damped oscillation around the minimum. The relic oscillations may contribute to dark matter at current times (Turner 1983).

The dilaton couples to all fields in the standard model via the Einstein field metric (Arvanitaki et al. 2015), in particular to the electromagnetic sector. Hence, we have the action with the scalar dilaton field  $\phi$  (Hamaide et al. 2022):

$$\mathcal{S} = \int dx^4 \sqrt{|g|} \left( \frac{1}{2} \partial_\mu \phi \partial^\mu \phi - V(\phi) + \mathcal{L}_{\text{SM}} + \mathcal{L}_{\phi, \text{int}} \right)$$

$$\mathcal{L}_{\phi, \text{int}} = \frac{\sqrt{4\pi}}{M_{\text{Pl}}} \phi \left( \frac{d_e}{4e^2} F_{\mu\nu} F^{\mu\nu} - d_{m_e} m_e \epsilon \bar{\epsilon} \right), \quad (5.8)$$

where  $\mathcal{L}_{\text{SM}}$  is the Standard Model Lagrangian and  $\mathcal{L}_{\phi, \text{int}}$  is the dilaton interaction term. As in the usual notation,  $|g|$  describes the determinant of the metric,  $F_{\mu\nu}$  the electromagnetic field tensor,  $M_{\text{Pl}}$  is the Planck mass and  $\epsilon$  is an electron spinor wavefunction.  $e$  is the charge of an electron,  $m_e$  the mass of an electron and  $d_e$  and  $d_{m_e}$  the coupling constants of the dilaton respectively. In Hamaide et al. (2022), we proposed to study the effect of dilatons on the profile of absorption lines. The coupling of the dilatons to the electromagnetic sector is essentially a second-order correction of the electromagnetic Lagrangian that we absorb into the electromagnetic mass term (Hamaide et al. 2022):

$$\mathcal{L}_{\text{EM}} = -\frac{1 - d_e \kappa \phi}{4e^2} F_{\mu\nu} F^{\mu\nu} \approx -\frac{1}{4(1 + d_e \kappa \phi) e^2} F_{\mu\nu} F^{\mu\nu}$$

$$\alpha \rightarrow \alpha + \delta\alpha = \alpha(1 + d_e \kappa \phi), \quad (5.9)$$

where  $\alpha = e^2/4\pi$  is the fine structure constant with electric charge  $e$  and  $\kappa = \sqrt{4\pi}/M_{\text{Pl}}$ . The coupling to dilatons affects the cosmic fine-structure constant. The perturbation of the fine-structure constant is varying with time according to the damped oscillations of the dilaton field  $\phi$ . The amplitude of the dilaton field, and hence the amplitude of the oscillations of the fine-structure constant, scales with the local dark matter density by biasing taking into account the power spectrum cutoff of dilatons at high spatial scales compared to ordinary matter (Bauer et al. 2020; Foster et al. 2018):

$$\langle \phi_r \rangle = \sqrt{2\rho_\phi(\mathbf{x}, t)/m_\phi} \quad (5.10)$$

Note that the wavelength of the astrophysically most significant hydrogen absorption lines (i.e. Ly $\alpha$  and the 21 cm line) depends on the value of the fine-structure constant. A change in the value of the fine-structure constant would shift the wavelength of the absorption line. Since the dilaton field is oscillating during the time a photon passes through a dark matter halo at high redshift, the corresponding absorption line is shifted toward both shorter and longer wavelength respective to the photon wavelength. This affects the profile of an absorption line by additional broadening. The detailed formulation of the novel absorption profiles is provided in Hamaide et al. (2022). In a nutshell, we separate three different regimes. If the light crossing time through a single pixel in spectral resolution is smaller than the oscillation time (i.e. for very small masses  $m_\phi < 10^{-28}$  eV) we resolve out the dilaton oscillations and observe a line-shifting effect. The dilaton field is evolved deterministically. If the pixel crossing time is larger than the oscillation time, but smaller than the coherence time (for masses  $10^{-28}$  eV  $< m_\phi < 10^{-24}$  eV), we have to average over oscillations giving rise to an additional broadening of the absorption line. The evolution of the field is not fixed deterministically, but we rather have to draw the local field amplitude from a Rayleigh distribution for each coherence interval (Centers et al. 2021; Hamaide et al. 2022). If the pixel crossing time is even longer than the coherence time, the dark matter modes start to decohere. So in this case, we average a Rayleigh distribution instead of drawing from it.

These effects can be observed in the Ly $\alpha$  forest and with 21 cm-intensity mapping. However, the absorption profile is degenerate with the profile of the underlying density distribution. How can we separate between the scenarios that the absorption line is broadened by the effect of dilatons or that the size of the absorbing hydrogen cloud is larger than thought? At this point, a full inversion in the spirit of convex optimization was proposed using the software tools developed for *regpy* and *MrBeam*. Even more salient, we propose to solve the fully

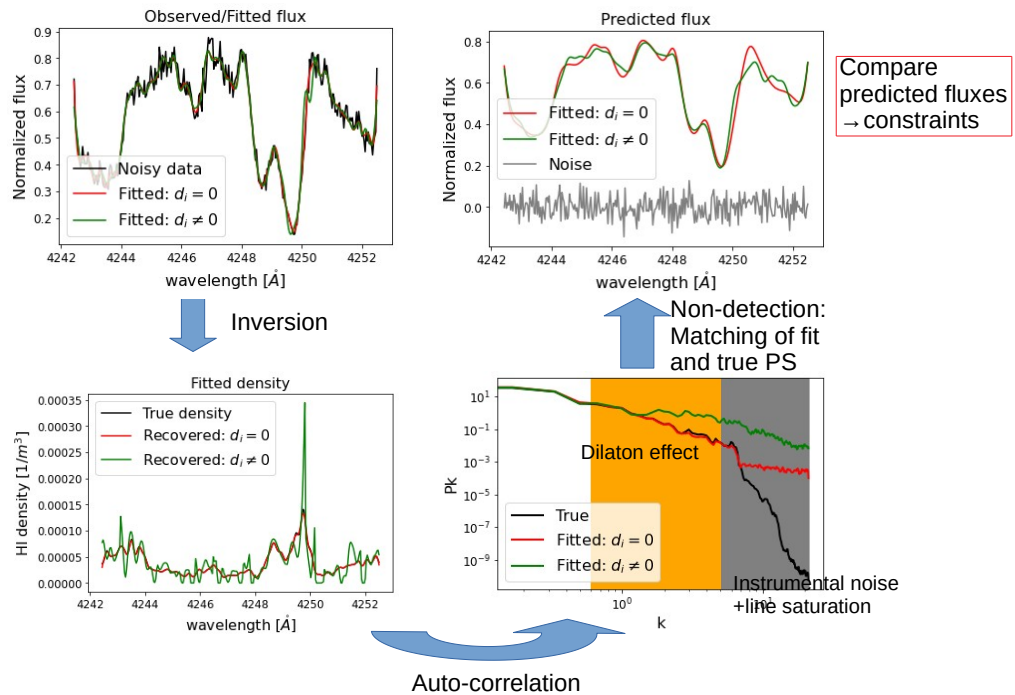


Figure 5.55: Flowchart of getting constraints on the dilaton coupling in the case of non-detection, adapted from Hamaide et al. (2022).

three-dimensional density reconstruction problem to correct for non-accounted peculiar velocities. In general, we propose to do an astrophysically independent reconstruction of the matter distribution first, and then constrain the mass and coupling to the dilaton field by fitting the observed spectra with that known matter distribution. For very small masses, i.e. when the line-shifting applies, it may be possible with sufficient accuracy by alternative probes (standard candles, galaxy count, Ly $\beta$  forest) to detect the signal (Hamaide et al. 2022). In most cases however, a probe of the matter distribution that is independent of astrophysics is not available. In these cases, we have to infer the dilaton mass and the dilaton coupling in the inversion procedure as well with the help of advanced inversion algorithms, similar in spirit to the procedure that we proposed in Müller et al. (2021). We therefore proposed an inversion strategy that gradually tests various dark matter configurations (Hamaide et al. 2022). We present an outline of our procedure in Fig. 5.55. The basic idea is that we can tell whether a reconstruction was successful or not by comparing the reconstruction to the theoretically known matter power spectrum. Only if we take the correct line broadening/shifting into account when we recover the neutral hydrogen density along the line of sight (in the Ly $\alpha$  forest or in 21 cm intensity maps respectively) the recovered density field has the correct power spectrum. When studying non-detection (i.e. with the aim

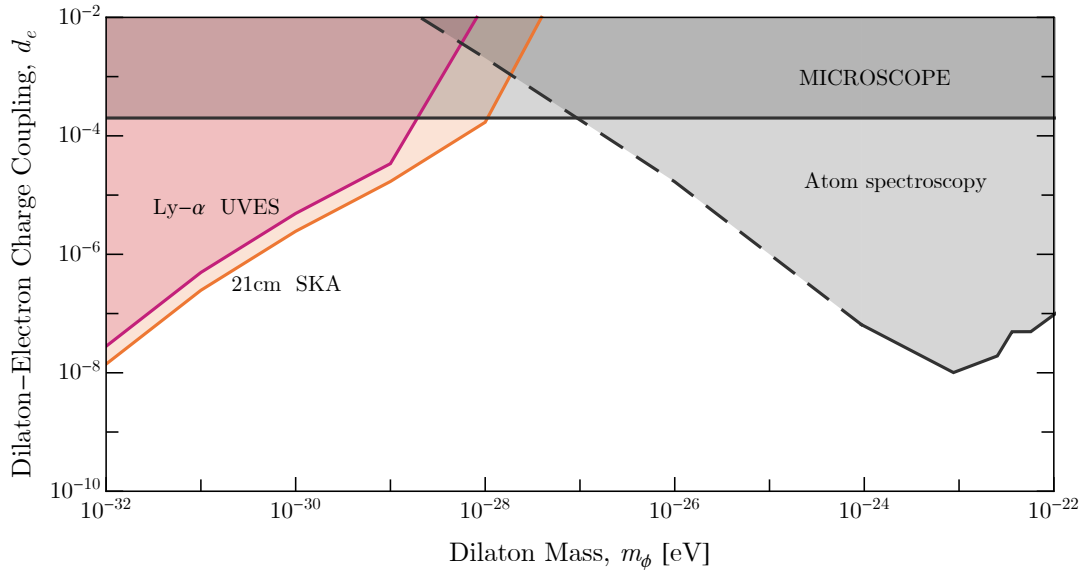


Figure 5.56: Forecasted constraints for the dilaton photon coupling as a functions of the dilaton mass. The forecast shows the prediction for the UVES\_SQUAD survey (Murphy et al. 2019) and a possible SKA configuration by a study of the absorption profiles by full inversion of the spectra (Hamaide et al. 2022). The MICROSCOPE results are taken from Bergé et al. (2018). Atomic spectroscopy constraints have been reported in Hees et al. (2016). The Figure is adapted from Hamaide et al. (2022).

of giving constraints on the abundance of dilaton dark matter), the recovered density would have the correct power spectrum while reconstructions with non-vanishing dilaton coupling would fail this test. For more details on this, and in particular on the computation of the theoretical power spectrum in the presence of fuzzy dark matter, we refer to our manuscript Hamaide et al. (2022). We compute constraints on the dilaton coupling at every mass by forecasting. Once the recovered density passes the power spectrum test, we assume that the recovered density matches the true density distribution reasonably well. Moreover, we assume that the dominating source of error is the observational noise of the spectrum (Hamaide et al. 2022). So we predict the spectrum from the recovered density distribution with various dilaton masses and couplings including the effect of dilatons on the profile of the absorption lines. We compare the recovered spectra to the observed spectra and reject a model once the predicted spectra and the observed spectra differ significantly given the noise level of the observed spectrum, i.e. if  $\chi^2 > 2.7$  (Hamaide et al. 2022).

This is the first time that an astrophysical inversion of the matter distribution has been successfully used to constrain the nature of ultralight, scalar dark matter. In Hamaide et al. (2022) we tested the approach on synthetic data and forecasted constraints that can be achieved from the UVES\_SQUAD sample and

future surveys with the Square Kilometer Array (SKA). We show the projected forecasts in Fig. 5.56. The SKA provides a unique radio-interferometric probe to study the clustering of dark matter on cosmic scales. Although the expected signal is weaker for the 21 cm lines than for  $\text{Ly}\alpha$ , the combinations of a large field of view, fast surveying capabilities, high sensitivity and narrow spectral bandwidths of the SKA compensate for this in a statistically manner. At ultralight masses, the forecasted constraints from already existing data sets exceed the constraints that come from fifth-force experiments (e.g. MICROSCOPE) and atom spectroscopy.

### 5.4.3 Magnetic Resonance Tomography

Magnetic resonance imaging (MRI) is a non-invasive medical tomography and diagnostics method. The first MRI system was constructed by Lauterbur (Lauterbur 1973) in a Nobel prize awarded work. For further illustrations, it is beneficial to present a short introduction to the general working procedure of an MRI system here, adapted from Sodickson (2021). Note that some atoms (in particular hydrogen) have a weak magnetic dipole moment due to their nuclear spin. With the application of a strong external magnetic field these magnetic dipole moments get aligned with the direction of the external magnetic field (para-magnetism). With the short-time application of a second, high-frequency magnetic field, the dipole magnetic orientation is deflected out of the parallel plane. The transverse magnetization starts to rotate around the overall longitudinal magnetization with the Lamor-frequency inducing a small electric voltage. If the second, transverse magnetic field is turned off, the dipoles align with the overall magnetization again with an atom-specific relaxation time. The relaxation time differs significantly for various types of tissue and organic material. Hence, a time-averaged image of the induced electrical current allows for non-invasive tomographic imaging. It should be mentioned here, that while all MRI systems depend on the basic physical concept of nuclear spin resonance, the details of the systems and their practical implementation vary a lot. Hence, the summary given above works only as a rough overview over the functioning of an MRI system. In particular, we would like to mention that MRI systems have to work in the near-field such that typical far-field approximations (i.e. parallel beam directions) do not apply.

Simple imaging in this way, with a single coil-profile (i.e. space encoding), would limit the resolution to roughly the wavelength of the induced electromagnetic radiation, i.e. to radio wavelengths. This is not enough to resolve the small scale details that are important for diagnostics. The solution is frequency encoding. For this, the exciting magnetic fields are applied with various gradients, where the local magnetic field strength determines the frequency of oscillation.

Hence, the atoms along the slice of detection are out of phase with a spatial frequency determined by the gradient of the magnetic field and the time of the excite- and read-out procedure. In short, a spatially averaged measurement of the electric currents encodes a Fourier coefficient of the true tomographic image. By the combination of several coils and magnetic gradients, the Fourier domain (conveniently called the k-space) gets filled up. However, the limited number of coils, the limited magnetic field strength and most significantly the limited time (to reduce the stress for the patient) limit the k-space coverage.

The forward problem in MRI can therefore be stated in the following way (Uecker et al. 2010):

$$y_j(t) = \int_{\Omega} d\vec{x} \rho(\vec{x}) c_j(\vec{x}) e^{-i\vec{k}(t)\vec{x}}, \quad (5.11)$$

where  $y_j$  are the signals received in channel  $j$  and  $\rho$  is the density that we try to observe.  $c_j$  are sensitivity masks for various coils. Only a fraction of all Fourier frequencies  $\vec{k}$  are sampled in time on typical k-space trajectories. The synergies to VLBI are obvious. Eq. (5.11) shares great similarities with the van-Cittert-Zernike theorem. Moreover, the coil profiles play a similar role such as gain factors in VLBI. In both problems, the major issue (ill-posedness) arises due to undersampling in the Fourier domain. Moreover, it has been recognized that the structural features that are recovered in radio interferometry and MRI are similar (Sodickson 2021).

The synergy to MRI is most salient in dynamic, real-time applications. In an MRI scan we could in principle sample the complete k-space when sufficient time is given. However, shorter measurement times are desired. In case of dynamic imaging the short scan length limits the k-space trajectories significantly. Although strong synergies exist, the proposed solutions are not always the same. Dynamic MRI reconstructions were first proposed with a sliding window scheme (e.g. MRI fluoroscopy Riederer et al. 1988), similar in philosophy to dynamically CLEANing scans in parallel in VLBI (Sault & Wieringa 1994; Stewart et al. 2011). MRI data acquisition is accelerated by parallel imaging strategies, i.e. GRAPPA (Griswold et al. 2002), SENSE (Pruessmann et al. 1999) or SMASH (Sodickson & Manning 1997). These strategies use the idea that in each single-coil image signal superposition occurs with different weights according to the local coil sensitivities. Historically, MRI sequences sampled the data in Cartesian coordinates, with non-Cartesian sampling schemes proposed in Pruessmann et al. (2001); Seiberlich et al. (2007). A finer temporal resolution can be achieved by imaging with priors by mixing spatial and temporal encoding schemes (Huang et al. 2005). The shortest time resolution (sparsest data) is achieved by methods of modern convex

optimization, i.e. by constrained reconstructions (Liang et al. 1992), compressive sensing (Lustig et al. 2008) and regularized non-linear inversion (Zu et al. 2013). Uecker et al. (2010) propose a framework to do real-time MRI by simultaneously fitting the observed data and the coil profiles. We refer to the review presented in Nayak et al. (2020) for more details.

These recent approaches by non-linear optimization are in line with the recent progress in VLBI (dynamic) imaging, in particular with RML methods. Bayesian methods that achieved momentum in VLBI recently are less common in the MRI community. On the contrary, MRI imaging shows interest in neural network based imaging algorithms and demonstrated their great potential (Ravishankar 2021; Sodickson 2021). These methods are less common in radio astronomy, but there is recent progress (compare the recent progress in Aghabiglou et al. 2022; Dabbech et al. 2022; Sun et al. 2022; Terris et al. 2023). Potential for mutual interaction and development between VLBI and MRI is great. Common research questions and synergies are for example: what framework (i.e. inverse modeling, RML, compressive sensing, Bayesian or AI based) is best suited for short-scan imaging? What is the optimal set of prior information (e.g. prior distributions, simplicity, smoothness or network-learned priors) and how are they implemented in the different frameworks? What can VLBI learn from the coil sensitivity calibration in MRI regarding gain calibration and vice versa? Which k-space trajectories were most successful in MRI and what does that mean for the optimal placing of antennas in novel radio interferometers? In both fields, the amount of data will increase in near future. What are the strategies to deal with these amount of data and to scale up the algorithms to upcoming big-data challenges?

The first step to study synergies in more detail is to unify the software in both fields. This has not been done so far. Therefore, we combined, for the first time, MRI applications implemented in *binder* and *regpy* with the VLBI standard software *ehtim* in the single software package *MrBeam*. This will allow to address some or all of the questions stated above.

#### 5.4.4 Solar Spectrometry

Solar spectrometry as carried out with the Spectrometer/Telescope for Imaging X-rays (STIX) presents another field of great synergy across different disciplines. STIX is one of the instruments installed on the ESA mission Solar Orbiter. Its primary goal is to observe the hot plasma in the Solar corona. The Solar corona has temperatures of several million degrees much larger than the surface temperature of the Sun. The details behind the heating process, however, remain unsolved (Krucker et al. 2020). STIX contains several subcollimators. Each of

these subcollimators contains a combination of grids. This hardware configuration decomposes the image as a (sparsely sampled) Fourier transform (Krucker et al. 2020) and STIX observes complex visibilities. The imaging problem is described by the van-Cittert-Zernike theorem, e.g. Eq. (1.8). The imaging problem is therefore the same as for VLBI. There are, however, some differences. Due to the small number of visibilities (compare the uv-coverage in Fig. 5.57) the achievable dynamic range is  $\sim 10$ . The synergy is therefore greatest to VLBI snapshot imaging. Moreover, while it became more common in mm-VLBI to do the imaging without phase-information (Chael et al. 2018; Müller & Lobanov 2022), for STIX well-calibrated visibility-phases are in principle available. There is nevertheless effort to exclude visibility-phases from the imaging for STIX as well (Massa et al. 2021).

Imaging routines that were proposed for STIX include Back-Projection (Hurford et al. 2002), CLEAN (Högbom 1974), Expectation Maximization (Benvenuto et al. 2013), Maximum Entropy Methods (Bong et al. 2006; Massa et al. 2020; Schmahl et al. 2007), and compressed sensing approaches (Duval-Poo et al. 2018; Felix et al. 2017). We developed an interface between STIX data formats and *Mr-Beam* to systematically study STIX data sets with the tools of VLBI as well. In this way, we add modern multiscale algorithms (e.g. DoB-CLEAN and DoG-HiT Müller & Lobanov 2022, 2023a), as well state-of-the-art RML methods (*ehtim* reconstructions with various regularization parameters combinations), Bayesian reconstructions (e.g. *resolve*, Arras et al. 2021) and a novel approach for Maximum Entropy imaging by constrained minimization (Con\_MEM) to the picture of available methods. We benchmark the performance of various imaging techniques on synthetic data in Fig. 5.57. We synthetically observed a ground truth image (a real observation reconstruction result) with the STIX instrument and added thermal Poisson noise in consistency with the instrumental properties. The ground truth image is shown in the upper left panel in Fig. 5.57. The remaining panels show several test reconstructions with STIX methods (CLEAN, MEM\_GE) and VLBI data methods (RML, DoG-HiT, DoB-CLEAN, Bayesian, Con\_MEM). MEM\_GE (Massa et al. 2020) is a maximum entropy method based on convex optimization (forward-backward splitting) with an iterative step size adaption and presents the current state-of-the-art for STIX imaging. The resolution and dynamic range is clearly superior to CLEAN due to the extreme sparsity of the array. RML reconstructions are compatible to MEM\_GE, but only if the correct weighting combination is used. In particular, reconstructions that assume smoothness (total variation) are worse. For the correct weighting however (L1+MEM) we recover the best among all reconstructions. DoG-HiT was designed to overcome this ambiguity in the selection of regularization parameters. Indeed we find a

reasonable reconstruction with DoG-HiT that is close to optimal and comparable to MEM\_GE. For MEM\_GE and RML-MEM methods, a weighted sum between a data fidelity term and an entropy (and probably more penalty terms) is solved. Con\_MEM is similar in philosophy, but follows a different strategy. We restrict the  $\chi^2$  of the observation to 1 and minimize the entropy along this axes with the Byrd-Omojokun Trust Region Sequential Least Square Programming algorithm (Lalee et al. 1998). The result is comparable to the reconstructions done with weighted sum entropy methods. Bayesian reconstructions rank among the best solutions (MEM\_GE, RML-MEM, DoG-HiT, Con\_MEM), but the computational effort is much higher. Finally, we present the DoB-CLEAN (Müller & Lobanov 2023a) reconstruction as well. The reconstruction clearly advances over standard CLEAN, but is worse than the quality achieved with forward modeling techniques.

All in all, these simple tests demonstrate the potential that VLBI algorithms may have for STIX as well. In particular, the forward modeling techniques based on entropy and multiscalar transforms have great potential. A more comprehensive comparison of existing methods on a wider range of test images and observation modalities is planned, but deferred for a future work.

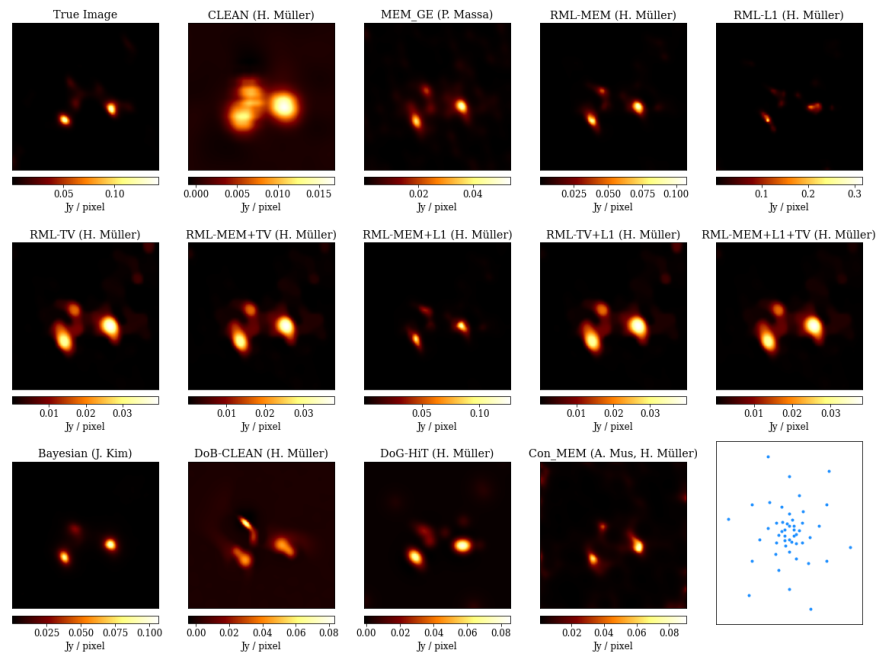


Figure 5.57: Synthetic reconstruction of STIX observation. The upper left panel shows the ground truth image. The bottom right panel illustrates the uv-coverage. The reconstruction was done semi-blindly by various investigators with standard techniques of the solar spectrometry community such as CLEAN and MEM\_GE (Massa et al. 2020). The other panels show reconstructions with VLBI data analysis pipelines such as *ehtim* (RML) with different weighting combinations, unsupervised by DoG-HiT and DoB-CLEAN, as well as with a Bayesian VLBI method (resolve) and by maximum entropy by constrained minimization (Con\_MEM).

## 6 Conclusions

The founding idea of VLBI and astronomical interferometry as a whole lies in correlating signals recorded simultaneously by any given pair of antennas participating in an observation of an emitting object in the sky and combining the products of these correlations together in order to reconstruct the spatial distribution of the observed emission. The correlation product obtained for each of those antenna pairs is approximately (owing to thermal noise and instrumental contributions to the measured correlation) the Fourier transform of the true sky brightness distribution with a Fourier frequency determined by the antenna pair baseline projected on the sky plane. Limitations inherent to interferometric observations on their duration, the number of participating antennas, and the span of the observing frequency bandwidth result in the Fourier domain being only sparsely sampled by the measured Fourier coefficients. VLBI imaging is therefore an ill-posed inverse problem to retrieve the true sky brightness distribution from the observed data, i.e. to solve an inverse Fourier transform from sparsely sampled and corrupted observations. Specifically for global/continental VLBI, in contrast to denser radio interferometric arrays, the missing data issue (gaps in uv-coverage, phase-information) dominates the reconstruction. The imaging problem is ill-posed.

Historically, the solution for this problem has been most often sought in inverse modeling, most prominently exemplified by the CLEAN algorithm. In recent years, various forward modeling approaches have been also considered for this purpose, including Regularized Maximum Likelihood, Maximum Entropy, Bayesian methods, and Compressive Sensing approaches. We demonstrated in this dissertation that all these methods, while addressing the problem from different perspectives and with different priors, share deep similarities in the framework of inverse problems and convex optimization embracing the generalized Tikhonov method. In this dissertation we present a novel imaging software tool *MrBeam* and contributed to the iterative regularization software *regpy* that implements this framework directly in general and builds towards unification of VLBI software.

CLEAN is the de-facto imaging technique of choice in VLBI, mainly because it is practical. A comparison between different algorithms however demonstrates that forward modeling techniques typically score better than CLEAN in terms of accuracy, resolution, adaptability, and (under some circumstances) dynamic range. Moreover, they address successfully several conceptual limitations related to CLEAN, e.g. the disparity between the computed model and image, and the divergence of reconstruction in the presence of noise. Furthermore, we demon-

strate with a simplified analytic calculation that the resolution limit in CLEAN is too conservative. On the other hand, superior modern imaging algorithms are more complex and need significant supervision, i.e. the finetuning of non-trivial hyperparameters.

This dissertation represents a significant step toward development of fully unsupervised imaging algorithms that still have the significant benefits of RML methods. To this end, we propose to use as few regularizers as possible and select them as data-driven as possible. We utilize a sparsity promoting multiscale approach in the spirit of compressive sensing theory and use it as the basis for developing the DoG-HiT algorithm. The multiscale dictionary in this approach is fitted to the uv-coverage, i.e. allows for an unsupervised optimal separation between observed and non-observed features. DoG-HiT is the first multiscale VLBI algorithm that also encodes directional dependence. The DoG-HiT reconstructions are comparable in accuracy and resolution (and even superior in the presence of extended emission) to state-of-the-art RML reconstructions, and significantly superior to CLEAN in terms of precision and resolution. Moreover, DoG-HiT remains fast and has a significantly simpler optimization parameter landscape than RML methods or Bayesian approaches, establishing itself as a nearly completely unsupervised and automatic image reconstruction method. An additional advantageous feature of DoG-HiT is that it processes only (less calibration sensitive) closure quantities and estimates the total compact flux in a self-consistent way. We also provide a variation of DoG-HiT formulated in the framework of MS-CLEAN algorithms: DoB-CLEAN. DoB-CLEAN addresses the limitations of CLEAN effectively and is superior to CLEAN in terms of resolution, representation of extended emission and stability (regularization). At the same time the working procedure (alternating self-calibration, mapping, and interactive data editing) remains the same.

DoG-HiT is easily adaptable to more challenging VLBI data analysis problems and has been already extended to dynamical imaging and polarimetry. Applications of DoG-HiT to imaging synthetic ngEHT data derived from numerical models with dynamically changing source structure have demonstrated the enormous potential of the approach, achieving comparable reconstruction quality than many more complex algorithms but with a less complex optimization landscape. For these applications, the multiresolution support is used as prior information, but no temporal smoothness is assumed. DoG-HiT provides the unique capability to recover polarimetric features at event horizon scales on dynamic time scales of minutes. Based on our tests and comparisons to alternative approaches, we conclude that DoG-HiT in combination with RML and Bayesian approaches, may enable us to do so already with existing EHT data sets.

Broader potentials for establishing fully unsupervised VLBI imaging frameworks have been further explored in this dissertation through the development of a genetic evolution algorithm MOEA/D. In contrast to DoG-HiT and DoB-CLEAN, this genetic algorithm does not require reducing the number of free parameters by data-driven choices, and instead samples the complete posterior with regard to the input parameters. Imaging with MOEA/D results in a hypersurface of non-dominated solutions that can be related to RML hyperparameter combinations. The algorithm is significantly faster than Bayesian sampling schemes, but still produces an image accompanied with a robustness estimate (although less simple to interpret). We demonstrate that the hypersurface of MOEA/D solutions represents effectively a multidimensional Pareto front, thus presenting a faster and better motivated alternative to parameter surveys with the potential to replace them in due time.

DoG-HiT, DoB-CLEAN, and MOEA/D are presently being actively used in VLBI frontline research, including imaging of the data from VLBI observations with the EHT and the GMVA. Their impact is fully demonstrated by the application examples presented in this dissertation which highlight in particular the following specific capabilities of these algorithms:

- DoG-HiT and MOEA/D recover robustly (polarimetric) images in an unsupervised way with small computational cost, even for extremely challenging data sets. The reduction in time necessary for the analysis is significant. At the same time, the human bias during imaging is reduced to a minimum.
- DoG-HiT is effectively the first VLBI imaging algorithm that can robustly recover rapid (polarimetric) movies at the event horizon scales.
- MOEA/D is the first global exploration technique that is fast, unsupervised, and simple enough to be applied to highly data-intensive extensions of the standard imaging problem, e.g. the reconstruction of dynamical movies.
- MOEA/D provides a unique approach to determining and quantifying the robustness of an image reconstruction.
- DoG-HiT and in particular DoB-CLEAN are capable of robustly recovering emission on a range of scales. This particularly provides the much needed capability of simultaneously imaging the extended (jet) emission together with an ultra-compact core, a feature that is currently missing from the VLBI data analysis pipelines.
- DoB-CLEAN effectively casts several novel capabilities of modern imaging algorithms to a CLEAN framework as well. In particular, it is the first

CLEAN algorithm that allows for super-resolution, adds reasonable regularization and solves the disparity between the CLEAN model and the CLEAN image.

- These three algorithms can provide (unsupervised) guidance to alternative imaging algorithms.
- Additionally, we have developed and demonstrated great potential for surveys, e.g. for MOJAVE. DoG-HiT has an unmatched combination of resolution, automatization, and speed, that makes it (when fully parallelized on a cluster) best suited for these kind of survey observations.

These examples highlight that DoG-HiT, DoB-CLEAN, and MOEA/D do not only improve the quality of the recovered images, but add unique, new capabilities in a variety of settings. These algorithms are now firmly finding their place at the present frontline of analysis and imaging of state-of-the-art VLBI observations carried out with the EHT, the GMVA, and space VLBI.

Finally, the versatile tools developed for these algorithms implemented in the software packages *MrBeam* and *regpy* are of interest for wider range of inverse problems, thus further highlighting the multidisciplinary horizon of this work. The modular implementation, as well as the general optimization formulation, allow an easy knowledge transfer to closely related inverse problems, which has been demonstrated in this dissertation with the exemplary applications to Ly $\alpha$  forest tomography, the search for dark matter in cosmographic surveys, medical imaging and solar spectroscopy. In these examples, we have found more accurate estimates for the thermal state of the intergalactic medium in the quasi-linear regime of structure formation and improved forecasted bounds on the existence of ultra-light dilatons as a fraction of dark matter. Furthermore, we have provided software infrastructure to unify and compare algorithmic developments in VLBI, medical imaging and in solar spectroscopy that share great similarity in their problem formulation.

## 7 Outlook

CLEAN has been the standard in VLBI imaging for over four decades. However, the continued development of interferometric instruments and increasing demands on robustness and structural range of image reconstruction from VLBI data have been gradually highlighting important limitations of CLEAN. Based on the work presented in this dissertation, one can identify two major fields in which CLEAN needs to be replaced by more advanced imaging routines: for extremely sparse VLBI arrays with almost lost phase information (such as the EHT/ngEHT, GMVA) and for dense, highly data intensive arrays (such as the ngEHT, LOFAR, SKA, MeerKAT). In the former case, modern unsupervised algorithms that provide super-resolution, that are less user- and calibration-biased, and that can avoid the disparity between the model and the image are needed. The latter data regime requires faster, unsupervised imaging algorithms that scale better to the high amount of data and allow for robust reconstructions of images at ultra high dynamic ranges.

In this dissertation, we mainly focused on the first data regime and proposed novel algorithms (DoG-HiT, DoB-CLEAN, MOEA/D). These algorithms are superior to CLEAN in terms of accuracy, resolution, and supervision. We started to apply them in a broad range of VLBI experiments (EHT, RadioAstron, GMVA, EVN+eMerlin). However, a systematic application to denser, high dynamic range, and lower frequency arrays such as the SKA or MeerKAT has not been done by now. The issues related to these arrays differ from the ones that we discussed in this dissertation. For instance, rather than a weak phase stability and extreme sparsity, these arrays deal primarily with wide-field issues (direction-dependent calibration) and the high amounts of visibility data that needs to be processed. This requires a substantial change the in the philosophy of image reconstruction, although the imaging problem remains principally the same (sparsely sampled, noise-corrupted Fourier transform). In global VLBI, and in particular for the EHT, the dominant source of uncertainty is the sparsity of the uv-coverage, i.e. the problem of missing data. We directly refer to this problem in DoG-HiT and DoB-CLEAN particularly by fitting the wavelets to the uv-coverage and in MOEA/D by investigating the multimodality of the problem. For the SKA or LOFAR the situation is different: regularization primarily plays the role of stabilizing the reconstruction against noise and calibration corruptions and becomes the most important factor for achieving dynamic ranges that are not reachable with the coverage of the EHT. It is therefore questionable, whether MOEA/D, DoG-HiT and DoB-CLEAN will bring the same amount of improvements for these arrays. However, we would like to mention in this con-

text the large amount of recent publications on sparsity promoting, multiscalar imaging algorithms (Abdulaziz et al. 2019; Carrillo et al. 2012, 2014; Dabbech et al. 2018; Garsden et al. 2015; Girard et al. 2015; Pratley et al. 2018; Thouvenin et al. 2023a,b; Wiaux et al. 2009) all of which are similar in philosophy to DoG-HiT. These works highlight the huge potential and interest in multiscalar imaging. Especially, the transfer of developements and ideas that recently arose in the mm-VLBI community (see e.g. Akiyama et al. 2017a,b; Arras et al. 2022; Bouman et al. 2018; Broderick et al. 2020b, 2022b; Chael et al. 2016, 2018, 2023; Müller & Lobanov 2022, 2023a,b; Müller et al. 2023d; Roelofs et al. 2023; Tiede 2022) to SKA science may be of great interest.

Vice versa, recent developements in radio imaging indicate a roadmap for further developements for VLBI. In particular, we propose and currently develop the parts of the following imaging algorithm:

$$\hat{\mathcal{I}} \in \operatorname{argmin}_{\mathcal{I}} \left[ \sum_i S_{cltrace}^{mf}(\Gamma \mathcal{I}(t_i)), \sum_i R_{l^1}(\mathcal{I}(t_i)), R_{ngmem}(\mathcal{I}) \right], \quad (7.1)$$

in the sense of multiobjective optimization. Here  $S_{cltrace}^{mf}$  denotes the fit metric to the (probably time dynamic) closure traces in a multifrequency observation,  $\mathcal{I}(t_i)$  the time-variable and polarimetric wavelet coefficient array or neural network coefficients, and  $R_{ngmem}$  the ngMEM entropy functional (Mus & Marti-Vidal 2023). Such an algorithm would, once successfully implemented and developed, fit time-dynamic, polarimetric and multifrequency data (data term) at high numerical performance (fast forward fitting and evaluation of  $\Gamma$ ) with an almost unsupervised reconstruction (multiobjective cluster investigation with a small number of priors), in a completely self-calibration agnostic way (closure traces) with high image fidelity, specifically for time-variable sources (multiscalar penalization combined with novel ngMEM prior) at highest resolution (comparable to DoG-HiT). In conclusion, such an algorithm or close variants would solve most of the problems related to VLBI. While this dissertation explored the fundamental principles already and achieved several milestones on the way towards the next generation of imaging techniques, there is still substantial development work to be done to achieve such a high goal, in particular due to the degeneracies of the closure traces. In what follows we discuss several parts of the framework proposed above and the missing parts in more detail.

We demonstrated in Müller et al. (2023d) with MOEA/D already the usefulness of a multiobjective formulation for VLBI imaging, particularly when combined with natural selection criterions, and successfully developed an implementation for reconstructing the total intensity. Due to the flexible framework it is

rather easy to extend this technique. First of all, we work towards adding the capabilities to perform polarimetry and dynamical reconstructions to MOEA/D. This development is straightforward. We reuse the data terms and penalty terms developed for DoG-HiT (Müller & Lobanov 2023b) and do the minimization by the genetic algorithm instead (Müller et al. 2023d). Instead of the standard entropy functional, we propose to use the temporal and spatial ngMEM entropy proposed in Mus & Marti-Vidal (2023). A related publication is currently in preparation (Mus et al. 2023).

Broderick & Pesce (2020) proposed closure traces as a new closure quantity that is independent from any kind of corruptions (i.e. gains and d-terms). A first model-fitting application has been done recently in Albentosa-Ruiz & Marti-Vidal (2023). As a natural next step, we propose to do closure-only polarimetry, i.e. recover polarimetric structures independently from calibration effects. However, closure traces have some degeneracies, e.g. the total position, overall position angle and polarized intensity are lost. This results in a multimodal problem (Albentosa-Ruiz & Marti-Vidal 2023) that could only be tackled effectively by a global exploration technique. Albentosa-Ruiz & Marti-Vidal (2023) proposed a grid search. However, there is a great synergy to the evolutionary optimization developed for this dissertation. MOEA/D is specifically designed to deal with this kind of multimodal and multiobjective settings. The synergy between the multimodality in the fit to closure traces and MOEA/D is currently explored and left for a future work.

The algorithms described in this dissertation can also be applied for reconstructing images from multifrequency data. Multifrequency synthesis has been steadily gaining more interest from the community (Chael et al. 2023) due to its use in filling the uv-plane and the upcoming generation of multiband receivers planned for the ngEHT and the GMVA upgrade. Chael et al. (2023) implemented a multifrequency representation of the image at different frequencies in the forward model and demonstrated its performance on synthetic data, compare also the discussions in Roelofs et al. (2023). A similar representation may be also valid for multiscale imaging routines, in particular when the wavelets are fitted to the uv-coverage as proposed in Müller & Lobanov (2022, 2023a). The uv-coverage at every frequency band requires the use of a different subset of the wavelets that were fitted to band-combined multifrequency uv-coverage. Hence, DoB-wavelets may allow for an optimal separation and correlation analysis between adjunct frequency bands as well.

In this dissertation we highlighted the benefits of a multiscale approach to sparse VLBI data, particularly when the used wavelet functions are fitted to the uv-coverage and its defects. It is therefore natural to keep the ideas behind multi-

scalar imaging for the next generation of VLBI imaging algorithms. As a natural extension, we propose to study neural networks. A number of current studies explored the use of neural networks in radio interferometry (Aghabiglou et al. 2022; Dabbech et al. 2022; Sun et al. 2022; Terris et al. 2023), but applications to sparse VLBI arrays remain rare (Sun et al. 2022). Neural networks could be understood as an effective framework for hosting adaptive multiscalar dictionaries. Instead of defining a wavelet dictionary manually that is best suited to represent the image sparsely, we could identify the basis from the learning process. This analogy, however, should not be taken too far: a network is by construction non-linear, in stark contrast to a dictionary of wavelets. Our take on neural networks is in particular inspired by the Network Tikhonov (NETT) method proposed in Li et al. (2020). Li et al. (2020) proposed an autoencoder architecture as illustrated in Fig. 7.58. Such networks consist of an encoder, a sparse central layer, and a decoder. The network is trained on the image artifacts only, i.e. the training input are the corrupted data (e.g. the dirty image) and the output are the artifacts only. In this way, the autoencoder learns how to compress the spatial information of the image artifacts (i.e. sidelobe pattern of the beam) to the low-dimensional central layer. The architecture of the decoder is mirrored to the architecture of the encoder. The decoder translates the sparsified coefficients in the inner layer back in the image domain. The concept shares great synergies with DoG-HiT: we replace the wavelet coefficients with the coefficients in the central layer, replace the wavelet decomposition with the encoder part and the wavelet dictionary with the decoder part. NETT directly fits in the framework proposed for DoG-HiT, but instead of the dictionary  $\Gamma$  we apply the decoder network  $\Psi$ . After replacing the wavelet basis by networks, the minimization procedure stays the same. Hence, once the network is trained, we get the further benefits of DoG-HiT as well, i.e. NETT is automatically extended to dynamical reconstructions and polarimetry. Moreover, since the network is only trained on the artifacts (i.e. on the beams) it is agnostic to the image structure (and hence biases introduced during the training procedure). Network aided reconstruction methods are also expected to solve the scaling problem of CLEAN to large data sets (e.g. Terris et al. 2023), and this direction of research will certainly remain one of the prime focus of interest in the area of interferometric image reconstruction.

Finally, the ngMEM functional, effectively a time-variable variant of the entropy functional, is demonstrated to allow for superior performance compared to traditional MEM functionals (Mus & Marti-Vidal 2023) and is currently studied in combination with MOEA/D for the reconstruction of time-variable movies (Mus et al. 2023). We already noted in Müller & Lobanov (2023b) that while mr-support imaging offers encouraging, super-resolving movies even with sparse

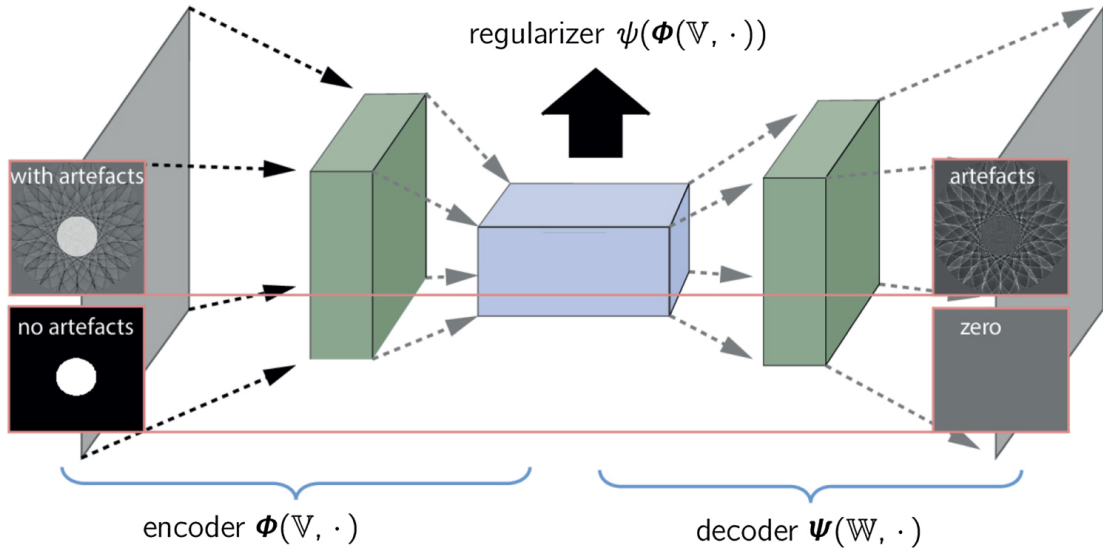


Figure 7.58: Schematic illustration of the Neural Network Tikhonov (NETT) method. The image structure with artifacts is projected to the artifacts only by an autoencoder. The autoencoder consists of an encoder network, a low-dimensional central layer, and a decoder network that is mirrored to the encoder. The regularizer is extracted from the central layer. Image adapted from Li et al. (2020) by CC.BY 3.0.

observationally coverage, the combination with a more powerful regularization term that takes the temporal correlation into account may improve the reconstruction quality significantly.

In conclusion, multiscale imaging algorithms and global exploration techniques continue to make impact in the field of VLBI, demonstrating their superior performance in comparison to the more conservative approach of CLEAN. These algorithms (among others DoG-HiT, DoB-CLEAN, MOEA/D) do not only improve the reconstruction quality, resolution or supervision, but provide fundamental new constraints and capabilities that would be impossible to attain with CLEAN. These developments will play a major role in the data analysis for the next generation of frontline VLBI experiments, e.g. the ngEHT or the ngVLA. They are pivotal to reach the scientific goals of these and other next generation radio interferometric instruments and facilities.

For this dissertation we explored some of the key concepts and fundamental developments for the next generation of VLBI imaging algorithms. Based on these key concepts, we presented a clear algorithmic roadmap forward that may allow for completely unsupervised, calibration-independent, near real time (time-dynamic and polarimetric) reconstructions at super-resolution with a substantially improved reconstruction accuracy.

## References

- Abdulaziz, A., Dabbech, A., & Wiaux, Y. 2019, *MNRAS*, 489, 1230
- Ables, J. G. 1974, *A&AS*, 15, 383
- Aghabiglou, A., Terris, M., Jackson, A., & Wiaux, Y. 2022, arXiv e-prints, arXiv:2210.16060
- Akiyama, K., Ikeda, S., Pleau, M., et al. 2017a, *AJ*, 153, 159
- Akiyama, K., Kuramochi, K., Ikeda, S., et al. 2017b, *ApJ*, 838, 1
- Albentosa-Ruiz, E. & Marti-Vidal, I. 2023, arXiv e-prints, arXiv:2303.04052
- ALMA Partnership, Brogan, C. L., Pérez, L. M., et al. 2015, *ApJ*, 808, L3
- Arras, P., Frank, P., Leike, R., Westermann, R., & Enßlin, T. A. 2019, *A&A*, 627, A134
- Arras, P., Bester, H. L., Perley, R. A., et al. 2021, *A&A*, 646, A84
- Arras, P., Frank, P., Haim, P., et al. 2022, *Nature Astronomy*, 6, 259
- Arvanitaki, A., Huang, J., & Van Tilburg, K. 2015, *Phys. Rev. D*, 91, 015015
- Assirati, L., Silva, N. R., Berton, L., Lopes, A. A., & Bruno, O. M. 2014, *Journal of Physics: Conference Series*, 490, 012020
- Bahcall, J. N. & Salpeter, E. E. 1965, *ApJ*, 142, 1677
- Bauer, J. B., Marsh, D. J. E., Hložek, R., Padmanabhan, H., & Laguë, A. 2020, *MNRAS*, 500, 3162
- Beck, A. & Teboulle, M. 2009, *SIAM J. Imaging Sciences*, 2, 183
- Becker, K., Backer, M., & Schwarz, J. 2006, *String Theory and M-Theory - A Modern Introduction* (Cambridge University Press)
- Becker, G. D., Bolton, J. S., Haehnelt, M. G., & Sargent, W. L. W. 2011, *MNRAS*, 410, 1096
- Becker, G. D., Hewett, P. C., Worseck, G., & Prochaska, J. X. 2013, *MNRAS*, 430, 2067

- Benvenuto, F., Schwartz, R., Piana, M., & Massone, A. M. 2013, *A&A*, 555, A61
- Bergé, J., Brax, P., Métris, G., et al. 2018, *Phys. Rev. Lett.*, 120, 141101
- Bhatnagar, S. & Cornwell, T. J. 2004, *A&A*, 426, 747
- Bi, H. G. & Davidsen, A. F. 1997, *ApJ*, 479, 523
- Biscani, F. & Izzo, D. 2020, *Journal of Open Source Software*, 5, 2338
- Blackburn, L., Pesce, D. W., Johnson, M. D., et al. 2020, *ApJ*, 894, 31
- Blandford, R. D. & Znajek, R. L. 1977, *MNRAS*, 179, 433
- Blandford, R. D. & Payne, D. G. 1982, *MNRAS*, 199, 883
- Blandford, R., Meier, D., & Readhead, A. 2019, *ARA&A*, 57, 467
- Boccardi, B., Perucho, M., Casadio, C., et al. 2021, *A&A*, 647, A67
- Boera, E., Murphy, M. T., Becker, G. D., & Bolton, J. S. 2014, *MNRAS*, 441, 1916
- Bolton, J. S., Becker, G. D., Haehnelt, M. G., & Viel, M. 2014, *MNRAS*, 438, 2499
- Bong, S.-C., Lee, J., Gary, D. E., & Yun, H. S. 2006, *ApJ*, 636, 1159
- Bontekoe, T. R., Koper, E., & Kester, D. J. M. 1994, *A&A*, 284, 1037
- Bouman, K. L., Johnson, M. D., Dalca, A. V., et al. 2018, *IEEE Transactions on Computational Imaging*, 4, 512
- Boyd, S. & Vandenberghe, L. 2004, *Convex Optimization* (Cambridge University Press)
- Briggs, D. S. 1995, PhD thesis, New Mexico Institute of Mining and Technology
- Broderick, A. E., Gold, R., Karami, M., et al. 2020a, *ApJ*, 897, 139
- Broderick, A. E., Pesce, D. W., Tiede, P., Pu, H.-Y., & Gold, R. 2020b, *ApJ*, 898, 9
- Broderick, A. E. & Pesce, D. W. 2020, *ApJ*, 904, 126
- Broderick, A. E., Gold, R., Georgiev, B., et al. 2022a, *ApJ*, 930, 1
- Broderick, A. E., Pesce, D. W., Gold, R., et al. 2022b, *ApJ*, 935, 61

- Broyden, C. G. 1970, *IMA Journal of Applied Mathematics*, 6, 76
- Burke, B. F., Graham-Smith, F., & Wilkinson, P. N. 2019, *An introduction to radio astronomy* (Cambridge university press)
- Byrd, R. H., Lu, P., & Nocedal, J. 1995, *SIAM Journal on Scientific and Statistical Computing*, 16, 1190
- Cai, X., Pereyra, M., & McEwen, J. D. 2018a, *MNRAS*, 480, 4154
- Cai, X., Pereyra, M., & McEwen, J. D. 2018b, *MNRAS*, 480, 4170
- Candès, E., Romberg, J., & Tao, T. 2006, *IEEE Trans. Information Theory*, 52, 489
- Candès, E., Wakin, M., & Boyd, S. 2007, *Journal of Fourier Analysis and Applications*, 14, 877
- Carilli, C. L. & Barthel, P. D. 1996, *A&A Rev.*, 7, 1
- Carilli, C. L. & Thyagarajan, N. 2022, *ApJ*, 924, 125
- Carrillo, R. E., McEwen, J. D., & Wiaux, Y. 2012, *MNRAS*, 426, 1223
- Carrillo, R. E., McEwen, J. D., Van De Ville, D., Thiran, J.-P., & Wiaux, Y. 2013, *IEEE Signal Processing Letters*, 20, 591
- Carrillo, R. E., McEwen, J. D., & Wiaux, Y. 2014, *MNRAS*, 439, 3591
- Casadio, C. 2016, PhD thesis, Institute of Astrophysics of Andalusia
- Caucci, S., Colombi, S., Pichon, C., et al. 2008, *MNRAS*, 386, 211
- Centers, G., Blanchard, J., Conrad, J., et al. 2021, *Nature Communications*, 12
- Chael, A. A., Johnson, M. D., Narayan, R., et al. 2016, *ApJ*, 829, 11
- Chael, A. A., Johnson, M. D., Bouman, K. L., et al. 2018, *ApJ*, 857, 23
- Chael, A. A., Issaoun, S., Pesce, D. W., et al. 2023, *ApJ*, 945, 40
- Chambolle, A. & Pock, T. 2011, *Journal of Mathematical Imaging and Vision*, 40, 120
- Chatterjee, K., Chael, A., Tiede, P., et al. 2023, *Galaxies*, 11
- Cheung, C. C., Harris, D. E., & Stawarz, L. 2007, *ApJ*, 663, L65
- Chirenti, C. & Rezzolla, L. 2016, *Phys. Rev. D*, 94, 084016

- Choudhury, T., Srianand, R., & Padmanabhan, T. 2001, *ApJ*, 559, 29
- Clark, B. G. 1980, *A&A*, 89, 377
- Cohen, M. H. 2009, *Journal of Astronomical History and Heritage*, 12, 141
- Combettes, P. L. & Pesquet, J.-C. 2011, *Proximal Splitting Methods in Signal Processing*, ed. H. H. Bauschke, R. S. Burachik, P. L. Combettes, V. Elser, D. R. Luke, & H. Wolkowicz (New York, NY: Springer New York), 185–212
- Cornwell, T. J. & Evans, K. F. 1985, *A&A*, 143, 77
- Cornwell, T. J., Braun, R., & Briggs, D. S. 1999, in *Astronomical Society of the Pacific Conference Series*, Vol. 180, *Synthesis Imaging in Radio Astronomy II*, ed. G. B. Taylor, C. L. Carilli, & R. A. Perley, 151
- Cornwell, T. J. 2008, *IEEE Journal of Selected Topics in Signal Processing*, 2, 793
- Coupinot, G., Hecquet, J., Auriere, M., & Futaully, R. 1992, *A&A*, 259, 701
- Dabbech, A., Onose, A., Abdulaziz, A., et al. 2018, *MNRAS*, 476, 2853
- Dabbech, A., Terris, M., Jackson, A., et al. 2022, *ApJ*, 939, L4
- Debye, P. J. W. 1909, *Mathematische Annalen*, 67, 535
- Doeleman, S., Blackburn, L., Dexter, J., et al. 2019, in *Bulletin of the American Astronomical Society*, Vol. 51, 256
- Donoho, D. 2006, *IEEE Trans. Information Theory*, 52, 128
- Duval-Poo, M. A., Piana, M., & Massone, A. M. 2018, *A&A*, 615, A59
- Event Horizon Telescope Collaboration, Akiyama, K., Alberdi, A., et al. 2019a, *ApJ*, 875, L1
- Event Horizon Telescope Collaboration, Akiyama, K., Alberdi, A., et al. 2019b, *ApJ*, 875, L4
- Event Horizon Telescope Collaboration, Akiyama, K., Alberdi, A., et al. 2021a, *ApJL*, 910, 48
- Event Horizon Telescope Collaboration, Akiyama, K., Alberdi, A., et al. 2021b, *ApJL*, 910, 43
- Event Horizon Telescope Collaboration, Akiyama, K., Alberdi, A., et al. 2022a, *ApJ*, 930, L12

- Event Horizon Telescope Collaboration, Akiyama, K., Alberdi, A., et al. 2022b, *ApJ*, 930, L14
- Ewen, H. I. & Purcell, E. M. 1951, *Nature*, 168, 356
- Fabian, A. C., Rees, M. J., Stella, L., & White, N. E. 1989, *MNRAS*, 238, 729
- Fabian, A. C., Sanders, J. S., Ettori, S., et al. 2000, *MNRAS*, 318, L65
- Fanaroff, B. L. & Riley, J. M. 1974, *MNRAS*, 167, 31P
- Faucher-Giguère, C.-A., Lidz, A., Hernquist, L., & Zaldarriaga, M. 2008, *ApJ*, 688, 85
- Felix, S., Bolzern, R., & Battaglia, M. 2017, *ApJ*, 849, 10
- Fletcher, R. & Reeves, C. M. 1964, *The Computer Journal*, 7, 149
- Fletcher, R. 1970, *The Computer Journal*, 13, 317
- Foster, J. W., Rodd, N. L., & Safdi, B. R. 2018, *Phys. Rev. D*, 97, 123006
- Frieden, B. R. 1972, *Journal of the Optical Society of America (1917-1983)*, 62, 511
- Fromm, C. M., Cruz-Osorio, A., Mizuno, Y., et al. 2022, *A&A*, 660, A107
- Gabuzda, D. C., Nagle, M., & Roche, N. 2018, *A&A*, 612, A67
- Gabuzda, D. C. 2021, *Galaxies*, 9, 58
- Gaikwad, P., Rauch, M., Haehnelt, M. G., et al. 2020, *MNRAS*, 494, 5091
- Gallerani, S., Choudhury, T. R., & Ferrara, A. 2006, *MNRAS*, 370, 1401
- Gallerani, S., Kitaura, F. S., & Ferrara, A. 2011, *MNRAS*, 413, L6
- Garsden, H., Girard, J. N., Starck, J. L., et al. 2015, *A&A*, 575, A90
- Garzilli, A., Bolton, J. S., Kim, T.-S., Leach, S., & Viel, M. 2012, *MNRAS*, 424, 1723
- Garzilli, A., Theuns, T., & Schaye, J. 2020, *MNRAS*, 492, 2193
- Gheller, C. & Vazza, F. 2022, *MNRAS*, 509, 990
- Giovannini, G., Savolainen, T., Orienti, M., et al. 2018, *Nature Astronomy*, 2, 472

- Girard, J. N., Garsden, H., Starck, J. L., et al. 2015, *Journal of Instrumentation*, 10, C08013
- Globus, N. & Levinson, A. 2016, *MNRAS*, 461, 2605
- Goan, E. & Fookes, C. 2020, in *Case Studies in Applied Bayesian Data Science : CIRM Jean-Morlet Chair, Fall 2018*, ed. K. Mengersen, P. Pudlo, & C. Robert, *Lecture Notes in Mathematics* (Cham, Switzerland: Springer), 45–87
- Goldfarb, D. 1970, *Mathematics of Computation*, 24, 23
- Gómez, J. L., Lobanov, A. P., Bruni, G., et al. 2016, *ApJ*, 817, 96
- Gonzalez, R. & Woods, R. 2006, *Digital Image Processing* (3rd Edition)
- Goupillaud, P., Grossmann, A., & Morlet, J. 1984, *Geoexploration*, 23, 85, seismic Signal Analysis and Discrimination III
- GRAVITY Collaboration, Abuter, R., Amorim, A., et al. 2019, *A&A*, 625, L10
- GRAVITY Collaboration, Abuter, R., Aymar, N., et al. 2022, *A&A*, 657, A82
- Greiner, M., Vacca, V., Junklewitz, H., & Enßlin, T. A. 2016, arXiv e-prints, arXiv:1605.04317
- Griswold, M. A., Jakob, P. M., Heidemann, R. M., et al. 2002, *Magnetic Resonance in Medicine: An Official Journal of the International Society for Magnetic Resonance in Medicine*, 47, 1202
- Gull, S. F. & Daniell, G. J. 1979, in *Astrophysics and Space Science Library*, Vol. 76, IAU Colloq. 49: Image Formation from Coherence Functions in Astronomy, ed. C. van Schooneveld, 219
- Gunn, J. E. & Peterson, B. A. 1965, *ApJ*, 142, 1633
- Hadamard, J. & Morse, P. M. 1953, *Physics Today*, 6, 18
- Hamaide, L., Müller, H., & Marsh, D. J. E. 2022, *Phys. Rev. D*, 106, 123509
- Hand, N., Feng, Y., Beutler, F., et al. 2018, *AJ*, 156, 160
- Hees, A., Guéna, J., Abgrall, M., Bize, S., & Wolf, P. 2016, *Phys. Rev. Lett.*, 117, 061301
- Hestenes, M. R. & Stiefel, E. 1952, *Journal of research of the National Bureau of Standards*, 49, 409

- Hewish, A., Bell, S. J., Pilkington, J. D. H., Scott, P. F., & Collins, R. A. 1968, *Nature*, 217, 709
- Hey, J. S. 1946, *Nature*, 157, 47
- Hiss, H., Walther, M., Hennawi, J. F., et al. 2018, *ApJ*, 865, 42
- Högbom, J. A. 1974, *A&AS*, 15, 417
- Högbom, J. A. 1979, in *Astrophysics and Space Science Library*, Vol. 76, IAU Colloq. 49: Image Formation from Coherence Functions in Astronomy, ed. C. van Schooneveld, 237
- Horowitz, B., Lee, K.-G., White, M., Krolewski, A., & Ata, M. 2019, *ApJ*, 887, 61
- Huang, F., Akao, J., Vijayakumar, S., Duensing, G. R., & Limkeman, M. 2005, *Magnetic Resonance in Medicine: An Official Journal of the International Society for Magnetic Resonance in Medicine*, 54, 1172
- Hui, L. & Gnedin, N. Y. 1997, *MNRAS*, 292, 27
- Hurford, G. J., Schmahl, E. J., Schwartz, R. A., et al. 2002, *Sol. Phys.*, 210, 61
- Ikeda, S., Tazaki, F., Akiyama, K., Hada, K., & Honma, M. 2016, *PASJ*, 68, 45
- Jansky, K. G. 1933, *Nature*, 132, 66
- Janssen, M., Falcke, H., Kadler, M., et al. 2021, *Nature Astronomy*, 5, 1017
- Janssen, M., Radcliffe, J. F., & Wagner, J. 2022, *Universe*, 8, 527
- Junklewitz, H., Bell, M. R., Selig, M., & Enßlin, T. A. 2016, *A&A*, 586, A76
- Kim, J. Y., Krichbaum, T. P., Lu, R. S., et al. 2018, *A&A*, 616, A188
- Kim, J. Y., Krichbaum, T. P., Broderick, A. E., et al. 2020, *A&A*, 640, A69
- Kim, J.-Y., Savolainen, T., Voitsik, P., et al. 2023, accepted for publication in *ApJ*, arXiv e-prints, arXiv:2304.09816
- Kirsch, A. 2011, *An Introduction to the Mathematical Theory of Inverse Problems*, 2nd edn., Vol. 120 (Springer)
- Kitaura, F. S., Gallerani, S., & Ferrara, A. 2012, *MNRAS*, 420, 61
- Knollmüller, J. & Enßlin, T. A. 2019, arXiv e-prints, arXiv:1901.11033

- Kramer, J. A. & MacDonald, N. R. 2021, *A&A*, 656, A143
- Krolewski, A., Lee, K.-G., White, M., et al. 2018, *ApJ*, 861, 60
- Krucker, S., Hurford, G. J., Grimm, O., et al. 2020, *A&A*, 642, A15
- Lalee, M., Nocedal, J., & Plantenga, T. 1998, *SIAM Journal on Optimization*, 8, 682
- Landweber, L. 1951, *American Journal of Mathematics*, 73, 615
- Lannes, A., Anterrieu, E., & Marechal, P. 1997, *A&AS*, 123, 183
- Lauterbur, P. C. 1973, *Nature*, 242, 190
- Lee, K.-G., Hennawi, J. F., White, M., Croft, R. A. C., & Ozbek, M. 2014a, *ApJ*, 788, 49
- Lee, K.-G., Hennawi, J. F., Stark, C., et al. 2014b, *ApJL*, 795, L12
- Lee, S.-S., Petrov, L., Byun, D.-Y., et al. 2014c, *AJ*, 147, 77
- Lee, K.-G., Hennawi, J. F., White, M., et al. 2016, *ApJ*, 817, 160
- Lee, K.-G. & White, M. 2016, *ApJ*, 831, 181
- Levenberg, K. 1944, *Quarterly of Applied Mathematics*, 2, 164
- Li, F., Cornwell, T. J., & de Hoog, F. 2011, *A&A*, 528, A31
- Li, D. & Pan, Z. 2016, *Radio Science*, 51, 1060
- Li, H., Schwab, J., Antholzer, S., & Haltmeier, M. 2020, *Inverse Problems*, 36, 065005
- Liang, Z.-P., Boada, F., Constable, R., et al. 1992, *Rev Magn Reson Med*, 4, 67
- Lidz, A., Faucher-Giguère, C.-A., Dall’Aglia, A., et al. 2010, *ApJ*, 718, 199
- Line, J. L. B., Mitchell, D. A., Pindor, B., et al. 2020, *PASA*, 37, e027
- Lister, M. L., Aller, M. F., Aller, H. D., et al. 2018, *ApJS*, 234, 12
- Lobanov, A. 2005, arXiv e-prints, astro-ph/0503225
- Lobanov, A. 2017, *Nature Astronomy*, 1, 0069
- Lockhart, W. & Gralla, S. E. 2022a, *MNRAS*, 509, 3643
- Lockhart, W. & Gralla, S. E. 2022b, *MNRAS*, 517, 2462

- Lustig, M., Donoho, D. L., Santos, J. M., & Pauly, J. M. 2008, IEEE signal processing magazine, 25, 72
- Maisinger, K., Hobson, M. P., & Lasenby, A. N. 2004, MNRAS, 347, 339
- Mallat, S. G. 1989, IEEE Transactions on Pattern Analysis and Machine Intelligence, 11, 674
- Marquardt, D. W. 1963, Journal of the Society for Industrial and Applied Mathematics, 11, 431
- Marsh, D. J. E. 2011, Phys. Rev. D, 83, 123526
- Massa, P., Schwartz, R., Tolbert, A. K., et al. 2020, ApJ, 894, 46
- Massa, P., Perracchione, E., Garbarino, S., et al. 2021, A&A, 656, A25
- Mazur, P. O. & Mottola, E. 2004, Proceedings of the National Academy of Science, 101, 9545
- McQuinn, M. & Upton Sanderbeck, P. R. 2016, MNRAS, 456, 47
- Mertens, F. & Lobanov, A. P. 2015, A&A, 574, A67
- Mertens, F., Lobanov, A. P., Walker, R. C., & Hardee, P. E. 2016, A&A, 595, A54
- Miyoshi, M., Kato, Y., & Makino, J. 2022, ApJ, 933, 36
- Mizuno, Y., Fromm, C. M., Younsi, Z., et al. 2021, MNRAS, 506, 741
- Mo, H., van den Bosch, F. C., & White, S. 2010, Galaxy Formation and Evolution
- Mohan, N. & Rafferty, D. 2015, PyBDSF: Python Blob Detection and Source Finder, Astrophysics Source Code Library, record ascl:1502.007
- Moreau, J. 1962, Comptes Rendus Hebdomadaires des Séances de l'Académie des Sciences, Paris, 255
- Morozov, V. 1967, Dokl. Akad. Nauk SSSR, 175, 1225
- Mouri Sardarabadi, A., Leshem, A., & van der Veen, A.-J. 2016, A&A, 588, A95
- Muckley, M., Riemenschneider, B., Radmanesh, A., et al. 2021, IEEE transactions on medical imaging, PP
- Müller, H., Behrens, C., & Marsh, D. J. E. 2020, MNRAS, 497, 4937

- Müller, H., Behrens, C., & Marsh, D. J. E. 2021, *MNRAS*, 503, 6202
- Müller, H. & Lobanov, A. P. 2022, *A&A*, 666, A137
- Müller, H. & Lobanov, A. P. 2023a, *A&A*, 672, A26
- Müller, H. & Lobanov, A. P. 2023b, accepted for publication by *A&A*, arXiv:2303.11877
- Müller, H. & Lobanov, A. P. 2023c, in Proceedings of 15th European VLBI Network Mini-Symposium and Users' Meeting — PoS(EVN2022), Vol. 428, 056, doi: <https://doi.org/10.22323/1.428.0056>
- Müller, H., Mus, A., & Lobanov, A. P. 2023d, accepted for publication in *A&A*, EHT review, arXiv:2304.12107
- Murenzi, R. 1989, in *Wavelets. Time-Frequency Methods and Phase Space*, ed. J.-M. Combes, A. Grossmann, & P. Tchamitchian, 239
- Murphy, M. T., Kacprzak, G. G., Savorgnan, G. A. D., & Carswell, R. F. 2019, *MNRAS*, 482, 3458
- Murtagh, F., Starck, J. L., & Bijaoui, A. 1995, *A&AS*, 112, 179
- Mus, A. & Marti-Vidal, I. 2023, in preparation
- Mus, A., Müller, H., Lobanov, A. P., & Marti-Vidal, I. 2023, in preparation
- Narayan, R. & Nityananda, R. 1984, in *Indirect Imaging. Measurement and Processing for Indirect Imaging*, ed. J. A. Roberts, 281
- Narayan, R. & Nityananda, R. 1986, *ARA&A*, 24, 127
- Nayak, K., Lim, Y., Campbell-Washburn, A., & Steeden, J. 2020, *Journal of Magnetic Resonance Imaging*, 55
- Nesterov, Y. E. 1983, *Doklady Akademii Nauk*, 269, 543
- Nusser, A. & Haehnelt, M. 1999, *MNRAS*, 303, 179
- Offringa, A. R. & Smirnov, O. 2017, *MNRAS*, 471, 301
- Onose, A., Carrillo, R. E., Repetti, A., et al. 2016, *MNRAS*, 462, 4314
- Onose, A., Dabbech, A., & Wiaux, Y. 2017, *MNRAS*, 469, 938
- Ozbek, M., Croft, R. A. C., & Khandai, N. 2016, *MNRAS*, 456, 3610

- Palanque-Delabrouille, N., Yèche, C., Borde, A., et al. 2013, *A&A*, 559, A85
- Palanque-Delabrouille, N., Yèche, C., Baur, J., et al. 2015, *J. Cosmology Astropart. Phys.*, 2015, 011
- Pantin, E. & Starck, J. L. 1996, *A&AS*, 118, 575
- Park, J. & Algaba, J. C. 2022, *Galaxies*, 10, 102
- Penzias, A. A. & Wilson, R. W. 1965, *ApJ*, 142, 419
- Pichon, C., Vergely, J. L., Rollinde, E., Colombi, S., & Petitjean, P. 2001, *MNRAS*, 326, 597
- Planck Collaboration, Aghanim, N., Akrami, Y., et al. 2020, *A&A*, 641, A1
- Ponsonby, J. E. B. 1973, *MNRAS*, 163, 369
- Porqueres, N., Jasche, J., Lavaux, G., & Enßlin, T. 2019, *A&A*, 630, A151
- Porqueres, N., Hahn, O., Jasche, J., & Lavaux, G. 2020, *A&A*, 642, A139
- Pötzl, F. M., Lobanov, A. P., Ros, E., et al. 2021, *A&A*, 648, A82
- Pratley, L., McEwen, J. D., d’Avezac, M., et al. 2018, *MNRAS*, 473, 1038
- Pritchard, J. R. & Loeb, A. 2012, *Reports on Progress in Physics*, 75, 086901
- Pruessmann, K. P., Weiger, M., Scheidegger, M. B., & Boesiger, P. 1999, *Magnetic Resonance in Medicine: An Official Journal of the International Society for Magnetic Resonance in Medicine*, 42, 952
- Pruessmann, K. P., Weiger, M., Börnert, P., & Boesiger, P. 2001, *Magnetic Resonance in Medicine: An Official Journal of the International Society for Magnetic Resonance in Medicine*, 46, 638
- Pushkarev, A. B., Kovalev, Y. Y., Lister, M. L., & Savolainen, T. 2017, *MNRAS*, 468, 4992
- Rau, U. & Cornwell, T. J. 2011, *A&A*, 532, A71
- Ravishankar, S. 2021, *Machine Learning for Medical Image Reconstruction, From Cells to galaxies talk* at URL: <https://vimeo.com/656714350/5b64a49cc2>
- Reber, G. 1944, *ApJ*, 100, 279
- Regpy. 2019, "regpy: Python tools for regularization methods", <https://github.com/regpy/regpy>

- Ricarte, A., Johnson, M. D., Kovalev, Y. Y., Palumbo, D. C. M., & Emami, R. 2023, *Galaxies*, 11, 5
- Ricci, L., Boccardi, B., Nokhrina, E., et al. 2022, *A&A*, 664, A166
- Riederer, S. J., Tasciyan, T., Farzaneh, F., et al. 1988, *Magnetic resonance in medicine*, 8, 1
- Robinson, A. & Terlevich, R. J. 1994, *The Nature of Compact Objects in Active Galactic Nuclei* (Cambridge University Press)
- Robson, I. 1996, *Active galactic nuclei* (Wiley-Praxis Series in Astronomy and Astrophysics)
- Roelofs, F., Janssen, M., Natarajan, I., et al. 2020, *A&A*, 636, A5
- Roelofs, F., Blackburn, L., Lindahl, G., et al. 2023, *Galaxies*, 11, 12
- Rollinde, E., Theuns, T., Schaye, J., Pâris, I., & Petitjean, P. 2013, *MNRAS*, 428, 540
- Rorai, A., Carswell, R. F., Haehnelt, M. G., et al. 2018, *MNRAS*, 474, 2871
- Sakai, N., Saida, H., & Tamaki, T. 2014, *Phys. Rev. D*, 90, 104013
- Santos, M., Bull, P., Alonso, D., et al. 2015, in *Advancing Astrophysics with the Square Kilometre Array (AASKA14)*, 19
- Sault, R. J. & Wieringa, M. H. 1994, *A&AS*, 108, 585
- Schaye, J., Theuns, T., Rauch, M., Efstathiou, G., & Sargent, W. L. W. 2000, *MNRAS*, 318, 817
- Schmahl, E. J., Pernak, R. L., Hurford, G. J., Lee, J., & Bong, S. 2007, *Sol. Phys.*, 240, 241
- Schwab, F. R. & Cotton, W. D. 1983, *AJ*, 88, 688
- Schwab, F. R. 1984, *AJ*, 89, 1076
- Schwarz, U. J. 1978, *A&A*, 65, 345
- Seiberlich, N., Breuer, F. A., Blaimer, M., et al. 2007, *Magnetic Resonance in Medicine: An Official Journal of the International Society for Magnetic Resonance in Medicine*, 58, 1257
- Shanno, D. F. 1970, *Mathematics of Computation*, 24, 647

- Snell, R., Kurtz, S., & Marr, J. 2019, *Fundamentals of Radio Astronomy: Astrophysics, Astronomy and Astrophysics* (CRC Press, Taylor & Francis Group)
- Sodickson, D. K. & Manning, W. J. 1997, *Magnetic Resonance in Medicine*, 38, 591
- Sodickson, D. 2021, *Introduction to Medical Imaging for Radio Astronomers, From Cells to galaxies talk* at URL: <https://vimeo.com/639618113/ca92064bc1>
- Starck, J.-L., Bijaoui, A., Lopez, B., & Perrier, C. 1994, *A&A*, 283, 349
- Starck, J.-L. & Murtagh, F. 1994, *A&A*, 288, 342
- Starck, J.-L., Murtagh, F., Querre, P., & Bonnarel, F. 2001, *A&A*, 368, 730
- Starck, J.-L., Donoho, D.-L., & Candès, E.-J. 2003, *A&A*, 398, 785
- Starck, J.-L. & Murtagh, F. 2006, *Astronomical image and data analysis*, 2nd edn. (Springer)
- Starck, J.-L., Murtagh, F., & Fadili, J. 2015, *Sparse image and signal processing: Wavelets and related geometric multiscale analysis*, second edition, 1st edn. (Cambridge University Press), 1–423
- Stark, C. W., White, M., Lee, K.-G., & Hennawi, J. F. 2015, *MNRAS*, 453, 311
- Stewart, I. M., Fenech, D. M., & Muxlow, T. W. B. 2011, *A&A*, 535, A81
- Stollnitz, E., Derosé, T., & Salesin, D. 1994, *IEEE Computer Graphics and Applications*, 15
- Sun, H., Bouman, K. L., Tiede, P., et al. 2022, *ApJ*, 932, 99
- Taylor, G., Carilli, C., & Perley, R. 1999, *Synthesis Imaging in Radio Astronomy II*
- Telikova, K. N., Shternin, P. S., & Balashev, S. A. 2019, *ApJ*, 887, 205
- Terris, M., Dabbech, A., Tang, C., & Wiaux, Y. 2023, *MNRAS*, 518, 604
- Thiébaud, É. & Young, J. 2017, *Journal of the Optical Society of America A*, 34, 904
- Thompson, A. R., Moran, J. M., & Swenson, George W., J. 2017, *Interferometry and Synthesis in Radio Astronomy*, 3rd Edition (Springer)

- Thouvenin, P.-A., Abdulaziz, A., Dabbech, A., Repetti, A., & Wiaux, Y. 2023a, MNRAS, 521, 1
- Thouvenin, P.-A., Dabbech, A., Jiang, M., et al. 2023b, MNRAS, 521, 20
- Tiede, P., Pu, H.-Y., Broderick, A. E., et al. 2020, ApJ, 892, 132
- Tiede, P. 2022, The Journal of Open Source Software, 7, 4457
- Tikhonov, A. 1963a, Soviet Mathematics Doklady, 4, 1035
- Tikhonov, A. 1963b, Soviet Mathematics Doklady, 4, 1624
- Turner, M. S. 1983, Phys. Rev. D, 28, 1243
- Tytler, D., Kirkman, D., O’Meara, J. M., et al. 2004, ApJ, 617, 1
- Uecker, M., Zhang, S., Voit, D., et al. 2010, NMR in Biomedicine, 23, 986
- Urry, C. M. & Padovani, P. 1995, PASP, 107, 803
- van Cittert, P. H. 1934, Physica, 1, 201
- Varah, J. M. 1983, SIAM Journal on Scientific and Statistical Computing, 4, 164
- Wakker, B. P. & Schwarz, U. J. 1988, A&A, 200, 312
- Walker, R. C., Hardee, P. E., Davies, F. B., Ly, C., & Junor, W. 2018, ApJ, 855, 128
- Walsh, D., Carswell, R. F., & Weymann, R. J. 1979, Nature, 279, 381
- Walther, M., Oñorbe, J., Hennawi, J. F., & Lukić, Z. 2019, ApJ, 872, 13
- Weaver, H., Williams, D. R. W., Dieter, N. H., & Lum, W. T. 1965, Nature, 208, 29
- Weir, N. 1992, in Astronomical Society of the Pacific Conference Series, Vol. 25, Astronomical Data Analysis Software and Systems I, ed. D. M. Worrall, C. Biemesderfer, & J. Barnes, 186
- Wernecke, S. J. & D’Addario, L. R. 1977, IEEE Transactions on Communications, 26, 351
- Wiaux, Y., Jacques, L., Puy, G., Scaife, A. M. M., & Vanderghenst, P. 2009, MNRAS, 395, 1733
- Wilkinson, P. N., Readhead, A. C. S., Purcell, G. H., & Anderson, B. 1977, Nature, 269, 764

- Yao-Yu Lin, J., Pesce, D. W., Wong, G. N., et al. 2021, arXiv e-prints, arXiv:2110.07185
- Zabora, D., Ryabov, M., Sukharev, A., & Petrenko, M. 2022, *Astronomical and Astrophysical Transactions*, 33, 89
- Zaroubi, S., Viel, M., Nusser, A., Haehnelt, M., & Kim, T. S. 2006, *MNRAS*, 369, 734
- Zernike, F. 1938, *Physica*, 5, 785
- Zhang, Q. & Li, H. 2007, *IEEE Transactions on Evolutionary Computation*, 11, 712
- Zobnina, D. I., Aller, H. D., Aller, M. F., et al. 2022, arXiv e-prints, arXiv:2211.15624
- Zu, Y., Narayanan, S. S., Kim, Y.-C., et al. 2013, *JAMA Otolaryngology–Head & Neck Surgery*, 139, 1312

## Acknowledgements

HM received financial support for this research from the International Max Planck Research School (IMPRS) for Astronomy and Astrophysics at the Universities of Bonn and Cologne. This work was partially supported by the M2FINDERS project funded by the European Research Council (ERC) under the European Union's Horizon 2020 Research and Innovation Programme (Grant Agreement No. 101018682).

## Data Availability

We will make our algorithms and our software available soon in the second release of MrBeam <sup>6</sup> and/or on reasonable request. The already published first version already contains proprietary versions of the algorithms DoG-HiT and DoB-CLEAN. Our software makes use of the publicly available ehtim (Chael et al. 2016, 2018), regpy (Regpy 2019), WISE (Mertens et al. 2016), and pygmo (Biscani & Izzo 2020) packages. Observational data and concrete imaging pipelines will be made publicly available upon acceptance by the journals with respect to the respective data policies.

---

<sup>6</sup><https://github.com/hmuellergoe/mrbeam>

## Personal acknowledgement

Finally, I would like to take the time to say thank you to whoever helped me to finish this project. First of all my thanks goes to Andrei. This dissertation would have never come to life without your scientific guidance. I truly did not only appreciate your scientific advice, but also your career and life advice and our non-scientific discussions that made working in Bonn a pleasure. Thank you!

I thank Prof. Anton Zensus for welcoming me in his group and giving me the opportunity to conduct my thesis in his group. My gratitude goes also to the further member of my thesis advisory committee (Prof. Andreas Eckart, Eduardo, Olaf) and of my examination committee (Prof. Yaping Shao, Prof. Jean-Luc Starck, Dr. Matthias Subroweit).

I would like to thank my friends and colleagues from the VLBI group Aleksei, Alejandro, George, Hui-Hsuan, Luca, Jong, Maria, Vieri, Sebastiano, Jack, Dae-won and especially my office mates Jan, Joana and Petra for sharing their time and office with me (even when I was in a grumpy mood) and all the beautiful memories. I will never forget our soccer games, pub evenings, and all our bullshit discussions.

From suffering from homesickness in the first months until completely identifying with the 'Rheinland' (and especially Beuel), I would like to thank all my friends who helped to make Bonn my second home. In particular I would like mention Timo and Karl.

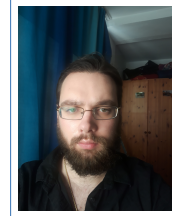
In closing, I would like to thank my supportive family and closest friends: my sister Katharina, my brother Björn and 'bro' Moritz, and specifically my parents Jörg and Birgit. You stood by me unconditionally! Specifically I thank my mother for the support over all the years. I would have loved to celebrate the finish of this dissertation together with you!

# Hendrik Müller

## Curriculum Vitae

Kölnstr. 190  
53111 Bonn

✉ [hmueller@mpifr-bonn.mpg.de](mailto:hmueller@mpifr-bonn.mpg.de)



---

### Personal Data

Name Hendrik Müller  
Birth 17.12.1996  
Nationality German

---

### Current Position

since Sept. 2020 **Doctoral Researcher**, *International Max Planck Research School at Max Planck Institute for Radioastronomy, Bonn, Germany*  
Thesis title: "*Advanced VLBI Imaging*",  
Scientific Advisor: Andrei Lobanov (Max Planck Institute for Radioastronomy)  
Academic Advisor: Anton Zensus (Max Planck Institute for Radioastronomy)  
Examiners: Anton Zensus (Max Planck Institute for Radioastronomy), Andreas Eckhart (Institute for Astrophysics, Cologne), Jean-Luc Starck (Service d'Astrophysique, CEA Saclay)

---

### Education

Apr. 2019–May 2020 **M.Sc. Physics**, *Georg-August-University Göttingen*  
Overall grade of Master's examination: very good (1.0). The Master's degree is awarded "with distinction". The Master's degree has been achieved with the research focus in "Astrophysics and Geophysics".  
Master's Thesis: "*Cosmography with the Lyman- $\alpha$  forest*",  
Supervisors: Christoph Behrens (Institute for Astrophysics Göttingen), David Marsh (Institute for Astrophysics Göttingen)  
Grade of thesis: very good, 1.0

Apr. 2019–Aug. 2020 **M.Sc. Mathematics**, *Georg-August-University Göttingen*  
Not completed yet. Current average grade: very good (1.3). The Master's degree is studied with research focus "Numerical and Applied Mathematics".

- Okt. 2015 – Nov. 2018 **B.Sc. Physics, Georg-August-University Göttingen**  
Overall grade of Bachelor's examination: very good (1.1). The Bachelor's degree is awarded "with distinction". The Bachelor's degree has been achieved without special research focus.
- Bachelor's Thesis: *"Reconstruction of Real Part of Scattering Greens Function from the Imaginary Part and Application to Iterative Regularization"*,  
Supervisors: Thorsten Hohage (Institute for numerical and applied mathematics Göttingen), Laurent Gizon (Max Planck Institute for Solar System Research Göttingen)  
Grade of thesis: very good, 1.0
- Okt. 2015 – Mar. 2019 **B.Sc. Mathematics, Georg-August-University Göttingen**  
Overall grade of Bachelor's examination: very good (1.2). The Bachelor's degree is awarded "with distinction". The Bachelor's degree has been achieved with research focus in "Numerical and Applied Mathematics".
- Bachelor's Thesis: *"Reconstruction of Real Part of Scattering Greens Function from the Imaginary Part and Application to Iterative Regularization"*,  
Supervisors: Thorsten Hohage (Institute for numerical and applied mathematics Göttingen), Laurent Gizon (Max-Planck-Institute for Solar System Research Göttingen)  
Grade of thesis: very good, 1.0
- July 2015 **Abitur, Max Planck Gymnasium Göttingen**  
Overall grade of examination: very good (1.0)

---

## Outreach

30. May 2023 **Outreach Talk, Schlecht gestellte inverse Probleme: Was schwarze Löcher, Beatboxing und Pyramiden gemeinsam haben, Bonn**
- 26.-29. May 2023 **Supervisor and Lecturer at Orpheus-seminar for talented scholar students, Training for international Physics Olympiad, Munich**
- 14.-18. Oct. 2021 **Supervisor and Lecturer at Orpheus-seminar for talented scholar students, Training for international Physics Olympiad, Virtual**
- Oct. 2015-Feb. 2020 **Organization of the mathematics Olympiad in Lower Saxony, Göttingen**
- 8.-11. Oct. 2015 **Supervisor and Lecturer at Orpheus-seminar for talented scholar students, Training for international Physics Olympiad, Leipzig**

---

## Publications

(\* first-author contribution to major publication)

### Accepted Publications

- Jul. 2023 **\*Peer-reviewed journal paper, Using multiobjective optimization to reconstruct interferometric data. Part I, Müller, H., Mus, A. and Lobanov, A., 2023**  
A&A, 675, A60 **shared first-authorship**
- Jul. 2023 **Peer-reviewed journal paper, RadioAstron Space-VLBI Imaging of Jets in nearby Radio Galaxies V: The jet of M87 at 22GHz, Kim, J.Y, Savolainen, T., Voitsik, P. et.al., 2022**  
ApJ, 952, 1

- May. 2023 \* **Peer-reviewed journal paper**, *Dynamic and polarimetric VLBI imaging with a multiscalar approach*, **Müller, H.**, and Lobanov, A., 2023  
A&A, 673, A151
- Feb. 2023 \* **Peer-reviewed journal paper**, *Multi-scale and multi-directional VLBI imaging with CLEAN*, **Müller, H.**, and Lobanov, A., 2023  
A&A, 672, A26
- Feb. 2023 **Peer-reviewed journal paper**, *Accretion Flow Morphology in Numerical Simulations of Black Holes from the ngEHT Model Library: The Impact of Radiation Physics*, Chatterjee, K., Chael, A., Tiede, P. et.al., 2023  
Galaxies, 11, 2, 38
- Feb. 2023 **Conference Paper**, *Multiscale VLBI Imaging*, **Müller, H.**, and Lobanov, A., 2023  
Proceedings of the 15th European VLBI Network Mini-Symposium and Users' Meeting
- Jan. 2023 **Peer-reviewed journal paper**, *The ngEHT Analysis challenges*, Roelofs, F., Blackburn, L., Lindahl, G. et.al., 2023  
Galaxies, 11, 1
- Dec. 2022 \* **Peer-reviewed journal paper**, *Searching for dilaton fields in the Ly-alpha forest*, Hamaide, L., **Müller, H.**, and Marsh, D.J.E., 2022  
Ph. Rev. D, 106, 12, **shared first-authorship**
- Oct. 2022 \* **Peer-reviewed journal paper**, *DoG-HiT: A novel VLBI Multiscale Imaging Approach*, **Müller, H.** and Lobanov, A., 2022  
A&A, 666, A137
- Aug. 2022 **Software Release**, *MrBeam*, **Müller, H.**, 2022  
<https://github.com/hmuellergoe/mrbeam>
- Jun. 2021 \* **Peer-reviewed journal paper**, *A novel estimator for the equation of state of the IGM by Ly  $\alpha$  forest tomography*, **Müller, H.**, Behrens, C. and Marsh, D.J.E., 2021  
MNRAS, 503, 6202-6222
- Mar. 2021 **Software Release**, *Reglyman*, **Müller, H.**, 2021  
<https://github.com/hmuellergoe/reglyman>
- Oct. 2020 \* **Peer-reviewed journal paper**, *An Optimized Ly $\alpha$  Forest Inversion Tool Based on a Quantitative Comparison of Existing Reconstruction Methods*, **Müller, H.**, Behrens, C. and Marsh, D.J.E., 2020  
MNRAS, 497, 4937-4955
- Publications in Preparation**
- 2023 \* **Peer-reviewed journal paper**, *Using multiobjective optimization to reconstruct interferometric data (II): polarimetry and dynamics*, Mus, A., **Müller, H.**, Lobanov, A., 2023  
to be submitted to A&A, **shared first-authorship**

- 2023 **\*Peer-reviewed journal paper**, *Polarimetric imaging from the closure traces*, **Müller, H.**, Albetosa-Ruiz, E., Mus, A., Kim, J. and Lobanov, A. (order to be declared), 2023  
to be submitted to A&A
- 2023 **\*Peer-reviewed journal paper**, *VLBI meets STIX: synergies in imaging*, **Müller, H.**, Massa, P., Mus, A. and Kim, J. (order to be declared), 2023  
to be submitted to A&A
- 2023 **\*Peer-reviewed journal paper**, *Multiresolution Imaging of the innermost wispl region of the Crab Nebula*, **Müller, H.**, Lobanov, A. and Muxlow, T. (order to be declared), 2023  
to be submitted to A&A

### Professional Experience

#### Professional Memberships

- since Oct. 2021 **M2FINDERS project**, *grant agreement No 101018682*
- since Oct. 2020 **Event-Horizon-Telescope Collaboration**
- since Sept. 2020 **Bonn-Cologne Graduate School of Physics and Astronomy**
- since Sept. 2020 **International Max Planck Research School for Astronomy and Astrophysics**
- Mar. 2023 **Scientific Integrity workshop of the Bonn-Cologne Graduate School**, *Virtual*
- Nov. 2022 **Gravity: Common Lecture Week by the MPIs for Gravitational Physics and Radio Astronomy**, *Remagen*
- Oct. 2022 **Resolve Workshop**, *Bonn*
- May. 2022 **NRAO Synthesis Imaging Workshop**, *Virtual*
- May. 2022 **Polarization in VLBI: tools for advanced calibration and analysis**, *Bonn*
- Nov. 2021 **From Vision to Instrument: Designing the Next-Generation EHT to Transform Black Hole Science**, *Virtual*

#### Teaching Experience

- Oct. 2015-today **Training of talented scholar students for international scientific contests**  
Organization Orpheus-seminars, organization mathematics olympiad of lower saxony

- Oct. 2018 **Undergraduate Teaching Assistant**, *Georg-August-University Göttingen*  
Tutoring exercise to lecture "Grundlagen des Experimentierens"

#### Organizational Skills

- Mar. 2023 **Organization of International Max Planck Research School (IMPRS) Conference**
- Dec. 2022 **Chair of LOC: EHT wintermeeting 2022**

- Sep. 2022 **Leading splinter discussions at 'From cells to Galaxies' conference, St. Paul**
- Jun. 2022-today **Organization of monthly VLBI-imaging talk series**
- Jul. 2022 **Organization of International Max Planck Research School (IMPRS) Conference**  
[Communicative Skills](#)
- Jul. 2023 **Contributed Talk**, *European Astronomical Society Annual Meeting*, Krakow, Using multiobjective optimization to reconstruct interferometric data
- Mar. 2023 **Seminar Talk**, *Thursday Seminar (VLBI)*, Bonn, Everything you need to know about Multiscale-CLEAN
- Mar. 2023 **Seminar Talk**, *CosmoStat Seminar*, Paris, Towards unsupervised VLBI imaging
- Feb. 2023 **Poster**, *BASP Frontiers*, Villars Sur Ollon, Towards unsupervised VLBI imaging
- Jan. 2023 **Contributed Talk**, *International Max Planck Research School (IMPRS) Conference*, Bonn, Advanced VLBI Imaging
- Dec. 2022 **Contributed Talk**, *EHT wintermeeting 2022*, Virtual, Towards unsupervised VLBI imaging
- Nov. 2022 **Seminar Talk**, *BASP Heriot-Watt group seminar*, Virtual, Towards unsupervised VLBI imaging
- Oct. 2022 **Contributed Talk**, *Resolve Workshop*, Bonn, Synergies between MRI and VLBI: Real Time Dynamic Imaging
- Oct. 2022 **Invited Talk**, *Workshop: Science enabled with Multi-Band Receivers and Frequency Phase Transfer*, Bonn, Imaging with wavelets and neural networks
- Oct. 2022 **Seminar Talk**, *Institute for experimental physics Hamburg: Journal Club*, Hamburg, Searching for Dilaton Fields in the Ly-alpha Forest
- Sep. 2022 **Contributed Talk**, *From cells to galaxies*, St. Paul, Real Time Dynamic Imaging in Radio Interferometry and MRI
- Sep. 2022 **Seminar Talk**, *Lebedev Astrospace center: group seminar*, Virtual, Multiscale VLBI imaging
- Aug. 2022 **Seminar Talk**, *ngEHT: Algorithms and Inference working group*, Virtual, Multi-scale VLBI imaging
- Aug. 2022 **Poster**, *17th Patras Workshop on Axions, WIMPs and WISPs*, Mainz, Towards optimal extraction of dark matter signal from the Ly-alpha forest
- Jul. 2022 **Contributed Talk**, *15th EVN Symposium & Users Meeting: Providing the Sharpest View of the Universe*, Cork, Multiscale VLBI imaging

- Jun. 2022 **Contributed Talk**, *Assembling the ngEHT: Community-Driven Science to a Global Instrument*, Granada, Blind Multiscale Imaging
- Apr. 2022 **Contributed Talk**, *International Max Planck Research School (IMPRS) Conference*, Bonn, Advanced Image Analysis for radio interferometry
- Apr. 2022 **Seminar Talk**, *M2FINDERS Seminar*, Bonn, Qualitative Comparison of VLBI imaging softwares
- since Feb. 2022 **Several Talks**, *EHT working groups: Imaging (C1), Polarimetry (C4) and MCFE (D3)*, Virtual, Presenting current working group results
- [Observations](#)
- May 2023 **Observing Support for GMVA observations in Effelsberg**
- 2022 **Observing Grant**, *EVN+eMerlin*, Multiresolution Imaging of the innermost wispy region of the Crab Nebula, 24h  
PI: Hendrik Müller
- Mar. 2022 **AOC monitoring for EHT observations**
- Oct. 2021 **Observing Support for GMVA observations in Effelsberg**
- Jan. 2020 **Astronomical Observing Course**, Observation of the extended narrow line region in Mrk 6 with the Galilei telescope at Asiago Astrophysically Observatory

---

### Internships and Side-Activities

- Apr. 2020-Jun.2020 **Undergraduate Research Assistant**, *Georg-August-University Göttingen*, Supervised by Thorsten Hohage (Institute for numerical and applied mathematics)  
Developing an interface for proximal regularization methods in *regpy*.
- Feb. 2019-July 2019 **Undergraduate Research Assistant**, *Georg-August-University Göttingen*, Supervised by Thorsten Hohage (Institute for numerical and applied mathematics)  
Developing the python toolbox *regpy* for inverse problems, special focus on an interface for coefficient estimation problems in partial differential equations with *ngsolve*.
- Apr. 2017-July 2017 **Project Lab Course**, *Georg-August-University Göttingen*, Supervised by Ingo Gregor (Institute for Biophysics Göttingen) and Jörg Enderlein (Institute for Biophysics Göttingen)  
Construction of a hybrid rocket engine, grade: 1.0

---

### Voluntary work

- May 2022 **Supervisor and organizer at 'Football is more' soccer camp for disabled children**, *Bonn*
- Jan. 2022-today **Voluntary security steward at home games of Bonner SC (Regionalliga and Mittelrheinliga)**
- Sept. 2021-today **Fan support of Bonner SC (professional soccer club)**

Sept. 2021-Mar. 2022 **'Research and Data Analysis' group for Volt Bonn (political party)**, *Analyzing and monitoring of elections*

## Awards

Okt. 2017-Sept. 2018 **Deutschlandstipendium**

Okt. 2016-Sept. 2017 **Niedersachsenstipendium**

2015 **Awards for Abitur examination**, *Awarded with the "Abiturpreis" by "Deutsche Physikalische Gesellschaft", Awarded with the "Abiturpreis" by "Deutsche Mathematiker Gesellschaft", Awarded by the old-philological association in lower saxony, E-fellows scholarship*

2015 **1.prize and participation in the final of "Bundeswettbewerb für Mathematik"**

2015 **German final for the international physics olympiad**

2013 **Exhibitor at "Ideenexpo 2013"**

2006-2015 **Several successful participations at mathematics Olympiad, Bundeswettbewerb Mathematik, physics Olympiad and chemistry Olympiad and more scientific competitions.**

## Language Skills

German **Native language**

English **Fluent**

## Computing Skills

Programming **Python**, *excellent, in daily use*  
**C/C++**, **Matlab**, **Mathematica**, *good*

Markuplanguages **LaTeX**, *excellent*

Software **ehetim**, **MrBeam**, **regpy**, **reglyman**, *developer*

**Difmap**, **pygmo**, **Tensorflow**, *good*

**AIPS**, **CASA**, **Themis**, **SMILI**, *basic*

**Sched**, **Topcat**, **Aladin**, **IRAF**, *basic*

**Comsol**, **Gnuplot**, *basic*

**Office**, *good*

Bonn, July 26, 2023



Hendrik Müller